16th International Workshop on Computational Electronics

Book of Abstracts

June 4-7, 2013
Nara, Japan

Nobuya Mori
Siegfried Selberherr (eds.)

Co-sponsored by
Inoue Foundation for Science
Nara Visitors Bureau
Support Center for Advanced Telecommunications Technology Research

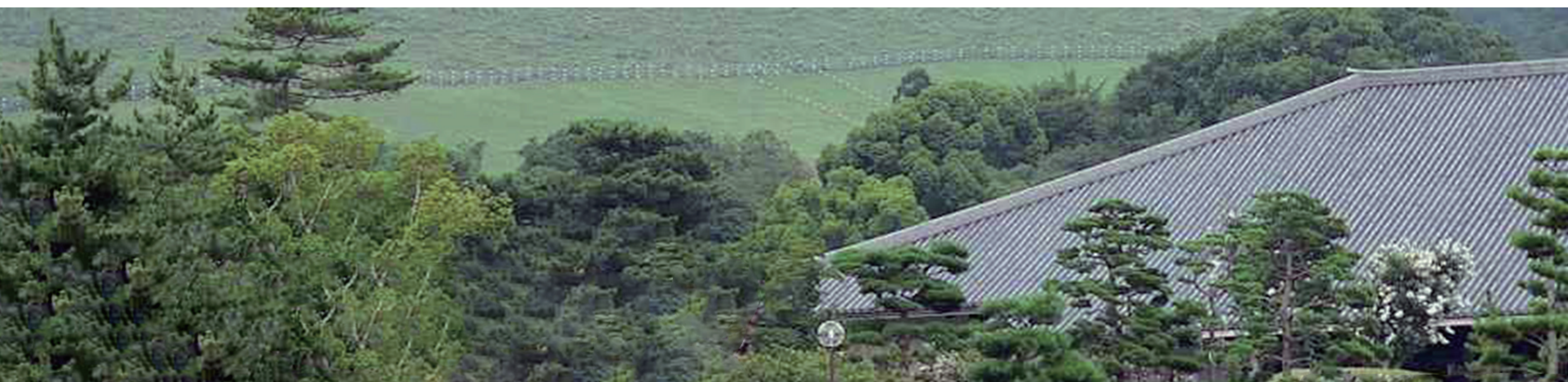

16th International Workshop on Computational Electronics

Book of Abstracts

Nobuya Mori
Siegfried Selberherr (eds.)

ISBN 978-3-901578-26-7

© 2013 Society for Micro- and Nanoelectronics
c/o Technische Universität Wien
Gußhausstraße 27-29, A-1040 Wien, Austria

Editorial

This volume contains the abstracts of the 16th International Workshop on Computational Electronics (IWCE 2013), held at Nara Prefectural New Public Hall, Nara, Japan on June 4–7, 2013. Over the years the workshop has become the main international forum for discussing on the current trends and future directions for computational electronics. The workshop continues a series of events initiated in 1992, when the first IWCE was organized by the Beckmann Institute of the University of Illinois Urbana-Champaign, Illinois, USA. The following events were held at University of Leeds, Leeds, UK (1993), Portland, Oregon, USA (1994), Arizona State University, Arizona, USA (1995), Notre Dame University, Indiana, USA (1997), Osaka University, Osaka, Japan (1998), University of Glasgow, Glasgow, UK (2000), University of Illinois Urbana-Champaign, Illinois, USA (2001), Villa Mondragone, Monte Porzio Catone (Rome), Italy (2003), Purdue University, West Lafayette, Indiana, USA (2004), TU Wien, Vienna, Austria (2006), University of Massachusetts, Amherst, Massachusetts, USA (2007), Tsinghua University, Beijing, China (2009), University of Pisa, Italy (2010), and University of Wisconsin, Madison, Wisconsin, USA (2012). Additional information can be found at the IWCE web page `http://www.iwce.org`.

The main themes of interest for IWCE 2013 are: 1) Ab-initio and atomistic simulations, 2) Quantum transport theory and techniques, 3) Quantum transport simulation, 4) Semiclassical transport theory and simulation, 5) Device physics and technology CAD, 6) Optical processes and optoelectronic devices, 7) Thermal/phonon transport and electron-phonon interaction, 8) Graphene and 2D semiconductors, 9) Spin and memory devices, and 10) Wide band-gap materials and energy applications.

The scientific program of IWCE 2013 is organized in a single-session format and comprises 4 invited lectures, 10 invited talks, 51 contributed talks, and 60 poster presentations. The distribution of the abstracts reflects the international nature of the workshop: 44 from Japan, 24 from USA, 10 from Austria and UK, 7 from France, 6 from Korea, 4 from China, Italy, and Taiwan, 3 from Switzerland, 2 from Finland and Germany, and 1 form Belgium, Iran, Spain, Sweden, and Vietnam.

The book of abstracts is printed from camera-ready manuscripts provided by the authors. The editors are not responsible for any inaccuracies, comments, or opinions given in the abstracts.

We would like to express our sincere appreciation to the authors for their effort to provide high-quality contributions. We thank the International Advisory Committee for the nomination of the invited speakers and the Program Committee for careful evaluation of the submitted abstracts.

Nobuya Mori
Siegfried Selberherr
Editors, IWCE 2013 Book of Abstracts

Committee Members

Conference Organizers

Nobuya Mori (Chair, Osaka University, Japan)
Yoshinari Kamakura (Local, Osaka University, Japan)
Siegfried Selberherr (Publication, TU Wien, Austria)

Program Committee

(Anant) M. P. Anantram (University of Washington, USA)
Andrea Bertoni (Institute of Nanoscience - CNR, Modena, Italy)
Philippe Dollfus (Universite Paris-Sud, France)
Massimo V. Fischetti (University of Texas at Dallas, USA)
Koichi Fukuda (AIST, Japan)
Robert W. Kelsall (University of Leeds, UK)
Hans Kosina (TU Wien, Austria)
Masaaki Kuzuhara (University of Fukui, Japan)
Yiming Li (National Chiao Tung University, Taiwan)
Mathieu Luisier (ETH Zurich, Switzerland)
Massimo Macucci (University of Pisa, Italy)
Umberto Ravaioli (University of Illinois at Urbana-Champaign, USA)
Ganesh Shankar Samudra (National University of Singapore, Singapore)
Satofumi Souma (Kobe University, Japan)
Michael A. Stroscio (University of Illinois-Chicago, USA)
Shinichi Takagi (University of Tokyo, Japan)
Andreas Wacker (Lund University, Sweden)
Takanobu Watanabe (Waseda University, Japan)
Zhiping Yu (Tsinghua University, China)

Advisory Committee

Shela Aboud (Stanford University, USA)
Aldo Di Carlo (University of “Rome Tor Vergata”, Italy)
Philippe Dollfus (Universite Paris-Sud, France)
Massimo V. Fischetti (University of Texas at Dallas, USA)
Stephen M. Goodnick (Arizona State University, USA)
Joseph Jerome (Northwestern University, USA)
Robert W. Kelsall (University of Leeds, UK)
Gerhard Klimeck (Purdue University, USA)
Irena Knezevic (University of Wisconsin, Madison, USA)
Paolo Lugli (Technical University Munich, Germany)
Massimo Macucci (University of Pisa, Italy)
Nobuya Mori (Osaka University, Japan)
Wolfgang Porod (University of Notre Dame, USA)
Nobuyuki Sano (Tsukuba University, Japan)
Siegfried Selberherr (TU Wien, Austria)
Mincheol Shin (Korea Advanced Institute of Science and Technology, Korea)
Michael A. Stroscio (University of Illinois-Chicago, USA)
Dragica Vasileska (Arizona State University, USA)

Time Table and Session Chairpersons

Time	June 4	June 5	June 6	June 7
8:30–9:00			Registration	
9:00–9:05		Opening	Session D R. W. Kelsall	Session H I. Knezevic
9:05–10:45		Session A C. Hamaguchi		
10:45–11:15			Break	
11:15–13:00		Session B M. Macucci	Session E Y. Li	Session I M. V. Fischetti
12:30–13:30	Registration			
13:00–14:30			Lunch	
13:30–18:00	Short Course N. Mori (Break 15:30–16:00)			
14:30–16:30		Session C P. Dollfus	Session F M. A. Stroscio	Session J S. M. Goodnick
16:15–16:45			Break	
16:30–18:30		Poster Session		
16:45–18:30			Session G H. Kosina	
18:00–20:00	Registration & Welcome Reception			
19:30–21:30			Banquet	

Lecture 50+10 min

Invited 25+5 min

Contributed 12+3 min

IWCE 2013 Program

June 4

Short Course: Quantum Theory of Electron Transport

S1 13:30–14:30

T. Ando (*Tokyo Institute of Technology*)
"Electronic and Transport Properties of Graphene" 14

S2 14:30–15:30

J.R. Barker (*University of Glasgow*)
"The Non-Equilibrium Green Function Approach to Quantum Transport in Nano-Structures" 16

15:30–16:00 *Coffee Break*

S3 16:00–17:00

M.V. Fischetti (*University of Texas at Dallas*)
"Pseudopotential-based Calculation of Electronic Structure and Transport in Nanostructures" 18

S4 17:00–18:00

C. Hamaguchi (*Osaka University, Sharp*)
"$\boldsymbol{k} \cdot \boldsymbol{p}$ Perturbation and Energy Bands of Semiconductors" 20

18:00–20:00 *Registration and Welcome Reception*

June 5

9:05–9:15 Opening and Welcome Remarks
N. Mori (*Osaka University*)

Session A: Quantum Transport Theory and Techniques

A1 9:15–9:45 **[invited talk]**

I. Knezevic (*University of Wisconsin-Madison*)
"Master Equations in Quantum Transport" 22

A2 9:45–10:15 **[invited talk]**

M. Trovato and L. Reggiani (*Universitá di Catania, Universitá del Salento*)
"A Nonlocal Formulation of Quantum Maximum Entropy Principle Including Fractional Exclusion Statistics" 24

A3 10:15–10:30

P. Marconcini, D. Logoteta, and M. Macucci (*Università di Pisa*)
"A Sinc-Based Approach for the Solution of Differential Transport Problems with Periodic Boundary Conditions" 26

A4 10:30–10:45

B. Fu and M.V. Fischetti (*University of Texas at Dallas*)
"Open-Boundary-Condition Ballistic Quantum Transport using Empirical Pseudopotentials" 28

10:45–11:15 *Coffee Break*

Session B: 2D Semiconductor and Graphene

B1 11:15–11:45 **[invited talk]**

S. Salahuddin (*University of California, Berkeley*)
"Electronics with 2D Semiconductors and their Heterostructures" 30

B2 11:45–12:00

F. Zahid, L. Liu, Y. Zhu, J. Wang, and H. Guo
(*University of Hong Kong, Nanoacademic Technologies, McGill University*)
"Tight-Binding Modeling of the Band Structures of Monolayer, Bilayer, and Bulk MoS_2" 32

B3 12:00–12:15

S. Berrada, V. Hung Nguyen, A. Alarcón, D. Querlioz, J. Saint-Martin, A. Bournel, C. Chassat, and P. Dollfus (*University of Paris-Sud, L_Sim*)
"Graphene Nanomesh Transistors with High On/Off Ratio and Good Current Saturation" 34

B4 12:15–12:30

N. Sule, K.J. Willis, S.C. Hagness, and I. Knezevic (*University of Wisconsin-Madison*)
"Effects of Charged Impurity Clusters on the Conductivity of Supported Graphene" 36

B5 12:30–12:45

M. Manoharan, S. Inoue, and H. Mizuta (*JAIST, University of Southampton*)
"First-Principles Study of CO_2 and NH_3 Adsorption on Armchair Graphene Nanoribbon" 38

B6 12:45–13:00

A. Afzalian, A. Lherbier, J.-C. Charlier, and D. Flandre (*Université catholique de Louvain*)
"Multiscale Simulation of Epoxide Adsorbate Functionalization on Graphene Nanoribbons" 40

13:00–14:30 *Lunch*

Session C: Quantum Transport and Fluctuation

C1 14:30–14:45

Y. Wang, Y. He, G. Klimeck, and T. Kubis (*Purdue University*)
"Nonequilibrium Green's Function Method: Algorithm for Regular and Irregular Leads" 42

C2 14:45–15:00

W.G. Vandenberghe and M.V. Fischetti (*University of Texas at Dallas*)
"Determination of Bound States in a Device with Transmitting Boundary Conditions" 44

C3 15:00–15:15

W. Goes, M. Toledano-Luque, O. Baumgartner, F. Schanovsky, B. Kaczer, and T. Grasser
(*TU Wien, imec*)
"A Comprehensive Model for Correlated Drain and Gate Current Fluctuations" 46

C4 15:15–15:30

S. Ravandi, B. Fu, W.G. Vandenberghe, S. Aboud, and M.V. Fischetti
(*University of Texas at Dallas, Stanford University*)
"Pseudopotential-Based Study of Gate Leakage and Contact Resistance beyond the 10 nm Node" . . 48

C5 15:30–15:45

A. Martinez, J.R. Barker, and M. Aldegunde (*Swansea University, University of Glasgow*)
"Impact of Dielectric Induced Dynamical Many-Body Correlation Effects on the Transfer Characteristic of Si Nanowire Transistor" 50

C6 15:45–16:00

L. Gerrer, S. Ling, S.M. Amoroso, A.M. El-Sayed, M.B. Watkins, A.L. Shluge, and A. Asenov (*University of Glasgow, University College London, Gold Standard Simulations*)
"Negative Bias Temperature Instabilities: A Multiscale Approach from First Principles to TCAD Time-Dependent Variability Simulations" 52

C7 16:00–16:15

M. Uematsu, K.M. Itoh, G. Mil'nikov, H. Minari, and N. Mori
(*Keio University, Osaka University, JST CREST*)
"Width Dependence of RDD-Induced Current Fluctuation in Silicon Nanowire Transistors" 54

C8 16:15–16:30

C.-Y. Chen, Y.-Y. Chen, and Y. Li (*National Chiao Tung University*)
"Multi-Fin Bulk FinFET Characteristic Fluctuation Induced by Process Variation and Random Dopant" 56

16:30–18:30 **Poster Session**

June 6

Session D: Semiclassical Transport

D1 9:00–9:30 **[invited talk]**

T. Sadi (*Aalto University*)
"The Monte Carlo Approach for Investigating Electrothermal Effects in Nanostructures" 58

D2 9:30–9:45

D. Rideau, Y.M. Niquet, O. Nier, P. Palestri, D. Esseni, V.H. Nguyen, F. Triozon, I. Duchemin, D. Garetto, L. Smith, L. Silvestri, F. Nallet, C. Tavernier, and H. Jaouen
(*STMicroelectronics, IMEP-LAHC, SP2M, CEA-LETI, University of Udine, Synopsys*)
"Mobility in FDSOI Devices: Monte Carlo and Kubo Greenwood Approaches Compared to NEGF Simulations" 60

D3 9:45–10:00

S. Oki, T. Misawa, and Y. Awano (*Keio University*)
"Quasi Self-consistent Monte Carlo Particle Simulations of Local Heating Properties in Single Layer Graphene Nano-channel FETs" 62

D4 10:00–10:15

E.A. Towie, C. Riddet, and A. Asenov (*University of Glasgow*)
"3D Monte Carlo Simulation of III-V Implant-Free Quantum-Well and FinFET MOSFETs" 64

D5 10:15–10:30

R. Hathwar, M. Saraniti, and S.M. Goodnick (*Arizona State University*)
"Full Band Monte Carlo Simulation of Silicon Nanowires and Junctionless Nanowire MOSFETs" .. 66

D6 10:30–10:45

K. Kukita, I.N. Adisusilo, and Y. Kamakura (*Osaka University, JST CREST*)
"Influence of Phonon Dispersion Relation on Thermal Resistance in Silicon Nanostructures" 68

10:45–11:15 *Coffee Break*

Session E: Spin and Memory Deives

E1 11:15–11:45 **[invited talk]**

V. Sverdlov, H. Mahmoudi, A. Makarov, D. Osintsev, J. Weinbub, T. Windbacher, and S. Selberherr (*TU Wien*)
"Modeling Spin-Based Devices in Silicon" 70

E2 11:45–12:15 **[invited talk]**

B. Magyari-Kop̈e and Y. Nishi (*Stanford University*)
"Modeling the Resistive Switching Process in Transition Metal Oxide Based Non-Volatile Memory Devices" 72

E3 12:15–12:30

A. Makarov, V. Sverdlov, and S. Selberherr (*TU Wien*)
"Structural Optimization of MTJs with a Composite Free Layer" 74

E4 12:30–12:45

D. Osintsev, V. Sverdlov, and S. Selberherr (*TU Wien*)
"Influence of Surface Roughness Scattering on Spin Lifetime in Silicon" 76

E5 12:45–13:00

A. Papp, G. Csaba, and W. Porod (*University of Notre Dame*)
"Non-Boolean Computing Using Spin Waves" 78

13:00–14:30 *Lunch*

Session F: Quantum Transport and Optics

F1 14:30–15:00 **[invited talk]**

U. Hetmaniuk, Y. Zhao, and M. Anantram (*University of Washington*)
"A Nested Dissection Approach to Modeling Transport in Nanodevices" 80

F2 15:00–15:15

M. Lindskog, D.O. Winge, and A. Wacker (*Lund University*)
"Nonequilibrium Green's Function Simulations of THz Quantum Cascade Lasers" 82

F3 15:15–15:30

A. Grier, Z. Ikonić, A. Valavanis, J.D. Cooper, D. Indjin, and P. Harrison (*University of Leeds*)
"Density Matrix Model Applied to GaAs and GaN-Based Terahertz Quantum Cascade Lasers" 84

F4 15:30–15:45

O. Baumgartner, Z. Stanojević, and H. Kosina (*TU Wien*)
"Modeling of the Effects of Band Structure and Transport in Quantum Cascade Detectors" 86

F5 15:45–16:00

N. Cavassilas, F. Michelini, and M. Bescond (*IM2NP*)
"Quantum Calculation of Solar Cell Efficiency" 88

F6 16:00–16:15

W. Hu, M.M. Rahman, T. Okada, A. Higo, Y. Li, and S. Samukawa
(*Tohoku University, JST CREST, National Chiao Tung University*)
"Simulation of Type-II Ge/Si Quantum Dot Solar Cells" 90

16:15–16:45 *Coffee Break*

Session G: Inelastic Scattering and Thermal Transport

G1 16:45–17:15 **[invited talk]**

M. Bescond, H. Mera, N. Cavassilas, C. Li, and M. Lannoo (*IM2NP*)
"Inelastic Scattering in Nano-devices: One-Shot Current Conserving Approach" 92

G2 17:15–17:30

H. Mera, M. Lannoo, N. Cavassilas, and M. Bescond (*IM2NP*)
"SCBA Made Simple" 94

G3 17:30–17:45

R. Rhyner and M. Luisier (*ETH Zürich*)
"Phonon-Limited Low-Field Mobility in Silicon Nanowires: NEGF Quantum Transport vs. Linearized Boltzmann" 96

G4 17:45–18:00

H. Karamitaheri, N. Neophytou, and H. Kosina (*TU Wien*)
"Thermal Conductivity of Si Nanowires Using Atomistic Phonon Dispersions" 98

G5 18:00–18:15

J. Hattori and S. Uno (*Ritsumeikan University, JST CREST*)
"Impact of Impurity Mass on Ballistic Phonon Thermal Transport in Silicon Nanowires" 100

G6 18:15–18:30

T. Imamoto and T. Endoh (*Tohoku University, JST CREST*)
"Improvement of Self-Heating Effect Employing Vertical-Channel Field-Effect-Diode 1T-DRAM" 102

19:30–21:30 *Banquet*

June 7

Session H: Graphene and Novel Materials

H1 9:00–9:30 **[invited talk]**

S. Islam, V.E. Dorgan, A.Y. Serov, A. Behnam, K.L. Grosse, M.-H. Bae, and E. Pop (*University of Illinois at Urbana-Champaign, Korea Research Institute of Standards and Science, Stanford University*)
"Electro-Thermal Transport in Graphene Devices" 104

H2 9:30–9:45

S. Aboud, J. Kim, and M.V. Fischetti (*Stanford University, University of Texas at Dallas*)
"DFT Study of Electronic Transport Properties in Supported Armchair Graphene Nanoribbons" . . . 106

H3 9:45–10:00

S.B. Touski, M. Pourfath, and H. Kosina (*University of Tehran, TU Wien*)
"Electronic Transport in Graphene Nanoribbons in the Presence of Substrate Surface Corrugation" 108

H4 10:00–10:15

M. Manoharan and H. Mizuta (*JAIST, University of Southampton*)
"Ab-initio Study of Edge Defects in Graphene Nanoribbon" 110

H5 10:15–10:30

V. Nam Do, H. Anh Le, and P. Dollfus
(*Hanoi University of Science and Technology, University of Paris-Sud*)
"Electron Transport Characteristics of Graphene-Metal Interfaces" 112

H6 10:30–10:45

Z. Jiang, M.A. Kuroda, Y. Tan, D.M. Newns, G.J. Martyna, M. Povolotskyi, T.B. Boykin, T. Kubis, and G. Klimeck (*Purdue University, IBM TJ Watson Research Center, University of Alabama in Huntsville*)
"Tight-Binding Modeling of Intermediate Valence Compound SmSe for Piezoelectronic Devices" . 114

10:45–11:15 *Coffee Break*

Session I: Dissipation and Transport in Nanostructures

I1 11:15–11:45 **[invited talk]**

Y. Asai (*AIST*)
"Non-equilibrium Low-Energy Transport Physics of Electron and Phonon at Nanoscale" 116

I2 11:45–12:00

H. Ryu, S. Lee, Y.-H. Matthias Tan, M. Füshsle, J.A. Miwa, S. Mahapatra, M.Y. Simmons, L.C.L. Hollenberg, and G. Klimeck (*KISTI, Samsung Advanced Institute of Technology, Purdue University, University of New South Wales, University of Melbourne*)
"Tight-Binding Simulations of Channel Modulation in a Single Atom Transistor" 118

I3 12:00–12:15

Y. Tanimura and A. Sakurai (*Kyoto University*)
"An Approach to Quantum Transport Based on Reduced Hierarchy Equations of Motion" 120

I4 12:15–12:30

T. Ono (*Osaka University*)
"Ab-initio Study on Scattering Potentials of Defects on Ge(001) Surfaces" 122

I5 12:30–12:45

X. Gao, D. Mamaluy, E. Nielsen, R. Muller, R. Young, N. Bishop, M. Lilly, and M. Carroll
(*Sandia National Laboratories*)
"Efficient Self-Consistent Quantum Transport Simulator for Quantum Well Devices" 124

I6 12:45–13:00

M. Macucci and P. Marconcini (*Università di Pisa*)
"Is There a Mesoscopic Braess Paradox?" 126

13:00–14:30 *Lunch*

Session J: Engineering Applications

J1 14:30–14:45

V.P. Georgiev, S. Markov, L. Vilà-Nadal, A. Asenov, and L. Cronin (*University of Glasgow*)
"Molecular-Metal-Oxide-nanoelectronicS (M-MOS): Achieving the Molecular Limit" 128

J2 14:45–15:00

A. Scheinemann and A. Schenk (*Integrated Systems Laboratory*)
"Defect Analysis with TCAD-Based DLTS Simulation" 130

J3 15:00–15:15

Z. Stanojević, O. Baumgartner, K. Schnass, M. Karner, and H. Kosina (*TU Wien, Global TCAD Solutions*)
"VSP – a Quantum Simulator for Engineering Applications" 132

J4 15:15–15:30

S.-H. Park, N. Kharche, D. Basu, Z. Jiang, S.K. Nayak, C.E. Weber, and G. Klimeck
(*Purdue University, Intel, Brookhaven National Laboratory, Rensselaer Polytechnic Institute*)
"Scaling Effect on Specific Contact Resistivity in Nano-scale Metal-Semiconductor Contacts" 134

J5 15:30–15:45

K. Alam, S. Takagi, and M. Takenaka (*University of Tokyo*)
"Thickness Dependent Performance of (111) GaAs UTB nMOSFETs" 136

J6 15:45–16:00

J. Lee, Y. Lee, H. Choi, and M. Shin (*KAIST*)
"Quantum Simulation of III-V Double Gate Schottky Barrier MOSFETs" 138

J7 16:00–16:15

A. Wang and T. Endoh (*Tohoku University, JST CREST*)
"Reduction of Self-Heating Effect in CMOS Inverter of Vertical MOSFET by Common-Gate Layout" 140

J8 16:15–16:30

K. Fukuda, T. Mori, W. Mizubayashi, Y. Morita, A. Tanabe, M. Masahara, T. Yasuda, S. Migita, and H. Ota (*AIST*)
"A Compact Model for Wire-Type Tunnel FETs Considering Tunneling Path Lengths" 142

Posters

P1 Y. Wang, F. Zahid, Y. Zhu, L. Liu, J. Wang, and H. Guo (*University of Hong Kong, Nanoacademic Technologies, McGill University*) "Band Offsets of $Al_xGa_{1-x}As$/GaAs Heterojunction from Atomistic First Principles" 144

P2 S.M. Aspera, H. Kasai, H. Kishi, N. Awaya, S. Ohnishi, and Y. Tamai (*Osaka University, Sharp*) "Resistive Switching in RRAM Devices through First Principles Calculation: Oxygen Vacancy Induced Electron Conduction Path in HfO_2" 146

P3 H.M. Rafferty, A.D. Burnett, Z. Ikonić, and R.W. Kelsall (*University of Leeds*) "Electronic Structure of Interface Defects in Epitaxially Grown Germanium on Silicon" 148

P4 B. Liu, R. Akis, and D.K. Ferry (*Arizona State University*) "Some Considerations on Conductance Fluctuations in Mesoscopic Structures" 150

P5 P. Schwaha, J.M. Sellier, M. Nedjalkov, I. Dimov, and S. Selberherr (*TU Wien, AVL List, Bulgarian Academy of Sciences*) "The Ultimate Equivalence Between Coherent Quantum and Classical Regimes" 152

P6 Y. Hanashiro and M. Morifuji (*Osaka University*) "Effect of Defective Connection to Electrodes in Atomic Scale Conductors" 154

P7 H.-H. Park, C. Jeong, S. Jin, W. Choi, Y.-T. Kim, U.-H. Kwon, K.-H. Lee, and Y. Park (*Samsung Electronics*) "Calculation of Alloy Scattering Mobility in SiGe FETs Based on Atomistic Tight-Binding Approach" 156

P8 K. Gärtner and T. Koprucki (*Weierstrass Institute*) "Generalization of the Scharfetter-Gummel Scheme to Strictly Monotonous Carrier Density State-Equations" 158

P9 S. Sho, S. Odanaka, and A. Hiroki (*Osaka University, Kyoto Institute of Technology*) "Analysis of Carrier Transport in Si and Ge MOSFETs Including Quantum Confinement and Hot Carrier Effects" 160

P10 Z. Yin, L. Meng, Q. Chen, and G. Chen (*University of Hong Kong*) "A Frequency-Dependent QM/EM Method: Multi-Scale Simulation of Electronics" 162

P11 M. Luisier (*ETH Zürich*) "How Far Can We Accelerate Full-Band Atomistic Device Simulations through Graphics Processing Units (GPUs)?" 164

P12 A. Suzuki, T. Kamioka, H. Imai, Y. Kamakura, and T. Watanabe (*Waseda University, Osaka University, JST CREST*) "Accelerated Parallel Computing of Carrier Transport Simulation Utilizing Graphic Processing Units" 166

P13 H. Imai, T. Kamioka, Y. Kamakura, K. Ohmori, K. Shiraishi, M. Niwa, K. Yamada, and T. Watanabe (*Waseda University, Osaka University, University of Tsukuba, JST CREST*) "Effect of Interface Roughness on Carrier Transport in Asymmetric Channel: An EMC/MD Simulation Study" 168

P14 J.A. Morales Escalante, I.M. Gamba, A. Majorana, Y. Cheng, C.-W. Shu, and J.R. Chelikowsky (*University of Texas at Austin, Universitá degli Studi di Catania, Michigan State University, Brown University*) "Deterministic DG Solvers for EPM-Boltzmann-Poisson Transport" 170

P15 T.T. Trang Nghiêm, J. Saint-Martin, and P. Dollfus (*University of Paris-Sud*) "New Self-Consistent Phonon-Electron BTE Solver for the Simulation of Ultra-Small DG-MOSFET" 172

P16 M. Kimura, M. Hirako, T. Yamaoka, and S. Tani (*Ryukoku University*) "Device Simulation of Hall Effect around Grain Boundaries in Poly-Si Films" 174

P17 M. Kimura and A. Nakashima (*Ryukoku University*) "Comparison of Off-Leakage Current between LTPS and HTPS TFTs" 176

P18 J. Wang, G. Du, K. Wei, L. Zeng, and X. Liu (*Peking University*) "Mixed-Mode Simulation of Reconfigurable Si Nanowire Schottky Barrier Transistors Based Circuits" 178

P19 M. Ono and T. Tezuka (*AIST*) "SNM Improvement for SRAMs Composed of High Mobility Channel MOSFETs" 180

P20 S.R. Mehrotra, A. Paul, J. Cho, M. Povolotskyi, and G. Klimeck (*Purdue University, GLOBALFOUNDRIES*) "Effect of Fin Tapering in Nanoscale Si FinFETs" 182

P21 C.-H. Chen, Y. Li, and S.-Y. Chu (*National Cheng-Kung University, National Chiao Tung University*) "On Rounding and Taper Fins of FinFET Varactors" 184

P22 K. Matsuda (*Tokushia Bunri University at Kagawa*) "Modeling of Stress-Induced Effects on Depletion Layer Capacitance in MOS Capacitor" 186

P23 T. Sasaki and T. Endoh (*Tohoku University, JST CREST*) "Gate Leakage Reduction of Vertical MOSFET with High-k Dielectric Film Employing Gate Dielectric Capacitance Oriented Design" 188

P24 A. Itagaki, M. Muraguchi, and T. Endoh (*Tohoku University, JST CREST*) "Intrinsic Region Length Dependence of Vertical Double Gate IMOS" 190

P25 H. Takeda, K. Uejima, K. Takeuchi, and M. Hane (*Renesas Electronics*) "Junction Leakage Variability Simulation Considering Random Discrete Dopants" 192

P26 M. Aldegunde, A. Martinez, and J.R. Barker (*Swansea University, University of Glasgow*) "Impact of Scaling on the Variability in Multigate Transistors" 194

P27 G. Mil'nikov, T. Zushi, M. Tomita, T. Watanabe, Y. Kamakura, and N. Mori (*Osaka University, Waseda University, JST CREST*) "Surface Roughness and Electron Transport Statistics in Si Nanowires" . . 196

P28 M.S. Choi, M.A. Stroscio, and M. Dutta (*University of Illinois at Chicago*) "Effect of the Size and the Separation of Metal Nanodots on the Electromagnetic Enhancement to Surface-Enhanced Raman Spectroscopy" 198

P29 H. Yasuda (*NICT*) "Terahertz Quantum Cascade Laser Using AlGaAs Wells for Higher-Temperature Operation" 200

P30 T. Kotani, H. Yoshikawa, T. Miyake, P. Lugli, and C. Hamaguchi (*TU München, Sharp*) "Polarization Dependent Optical Absorption Properties of Quantum Dot Superlattices" 202

P31 H. Yoshikawa, T. Kotani, Y. Kuzumoto, M. Izumi, Y. Tomomura, and C. Hamaguchi (*Sharp*) "Optical Absorption in InAs/$In_{0.48}Ga_{0.52}P$ Quantum Dot Superlattices" 204

P32 A. Tanaka, M. Morifuji, and M. Kondow (*Osaka University*) "Optical Coupling between Whispering-Gallery Mode and Waveguide Mode in Photonic Crystal" 206

P33 P. Kivisaari, T. Sadi, J. Oksanen, and J. Tulkki (*Aalto University*) "Coupled Monte Carlo-Drift-Diffusion Simulation of Transport in III-N LEDs" 208

P34 Y.W. Hwang, H.G. Lee, and T.Y. Won (*Inha University*) "Numerical Analysis on the Electrical and Optical Properties in Multilayer OLED Device" 210

P35 H.G. Lee, Y.W. Hwang, and T.Y. Won (*Inha University*) "Computational Analysis on Recombination Rate for Organic Light Emitting Diodes" 212

P36 M.-Y. Lee and Y. Li (*National Chiao Tung University*) "Comprehensive Study on Reflectance of Si_3N_4 Subwavelength Structures for Silicon Solar Cell Applications Using 3D Finite Element Analysis" . 214

P37 N. Zhang, M. Dutta, and M.A. Stroscio (*University of Illinois at Chicago*) "Interface Phonon Modes of Dual-Gate MOSFET System" 216

P38 F.G. Ruiz, I.M. Tienda-Luna, A. Godoy, L. Donetti, and F. Gámiz (*University of Granada*) "Impact of the Phonon Confinement and Geometry on the Mobility of Si-Nanowires" 218

P39 M. Aldegunde, R. Valin, A. Martinez, and J.R. Barker (*Swansea University, University of Glasgow*) "Dependence of Matthiessen's Rule on Complex Phonon Self-Energies: A NEGF Study" 220

P40 J.H. Oh, M.-G. Jang, and M. Shin (*KAIST, Electronics and Telecommunication Research Institute*) "Phonon Scattering at the Interface between Elastically Dissimilar Materials" 222

P41 T. Tanaka and K.M. Itoh (*Keio University*) "Effective Deformation Potential in Ultrathin SOI" 224

P42 V. Talbo, J. Saint-Martin, D. Querlioz, S. Retailleau, and P. Dollfus (*University of Paris-Sud*) "Thermoelectric Properties of Si-Based Single-Electron Transistors" 226

P43 P. Marconcini, D. Logoteta, and M. Macucci (*Università di Pisa*) "Symmetry-Dependent Conductance Behavior in Graphene-Based Double-Dot Structures" 228

P44 M. Ohnishi, K. Suzuki, and H. Miura (*Tohoku University*) "Change of the Electronic Properties of Carbon Nanotubes Cause by Three-Dimensional Strain Field" 230

P45 S. Honda, K. Inuduka, and N. Sano (*University of Tsukuba*) "Effect of σ-Band for Conduction of Metal/Graphene/Metal Junctions" 232

P46 S. Souma, T. Nakano, H. Nagai, and M. Ogawa (*Kobe University*) "Effect of Axial Strain on Switching Behavior of Carbon Nanotube Tunneling Field Effect Transistors" 234

P47 T. Akiyama, M. Ueyama, E. Nishimura, M. Ogawa, and S. Souma (*Kobe University*) "Quantum Dynamical Simulation of Photo-Induced Graphene Switch" 236

P48 T. Windbacher, O. Triebl, D. Osintsev, A. Makarov, V. Sverdlov, and S. Selberherr (*TU Wien*) "Switching Optimization of an Electrically Read- and Writable Magnetic Logic Gate" 238

P49 M. Purahmad, M.A. Stroscio, and M. Dutta (*University of Illinois at Chicago*) "Modeling the Effect of Nanowire Size on the Piezoelectric Nanogenerators Output" 240

P50 Y. Hiramatsu, N. Mori, and Y. Kamakura (*Osaka University, JST CREST*) "Modeling of Current Distribution through Metal-Insulator-Metal Diodes with Tunnel Barrier Roughness" 242

P51 H. Mahmoudi, T. Windbacher, V. Sverdlov, and S. Selberherr (*TU Wien*) "Optimization of Spin-Transfer Torque Magnetic Tunnel Junction-Based Logic Gates" 244

P52 H. Koike, T. Ohsawa, and T. Endoh (*Tohoku University*) "Verification of Simulation Time Improvement for SPICE Simulator Using Built-in MTJ Model" 246

P53 Y. Yoshida, H. Koike, M. Muraguchi, S. Ikeda, T. Hanyu, H. Ohno, and T. Endoh (*Tohoku University*) "A Model Reflecting Preheat Effect by Two-step Writing Technique for High Speed and Stable STT-MRAM" 248

P54 M. Matsubara, J. Godet, L. Pizzagalli, and E. Bellotti (*Boston University, Institut P'*) "Structural and Electronic Properties of Threading Screw Dislocations in GaN" 250

P55 K. Kodama, H. Tokuda, and M. Kuzuhara (*University of Fukui*) "Dependence of Gate-to-Drain Distance on Electron Velocity in AlN/GaN HEMTs" 252

P56 E. Bellotti, S. Shishehchi, and F. Bertazzi (*Boston University, DELEN and IEIIT-CNR*) "A Full-Band Monte-Carlo Study of Carriers Transport in III-Nitrides Alloys" 254

P57 N.M. Shrestha, Y.Y. Wang, Y. Li, and E.Y. Chang (*National Chiao Tung University*) "Effect of AlN Spacer Layer on AlGaN/GaN HEMTs" 256

P58 K. Nomura, T. Ishikawa, T. Kondoh, A. Kawamoto, T. Matsumori, T. Sugiyama, and Y. Nishibe (*Toyota Central R&D Laboratories*) "A Fast Doping Profile Optimization Method for Power Devices" 258

P59 E. Momox, N. Zakhleniuk, and N. Balkan (*University of Essex*) "Hydrodynamic and Drift-Diffusion Modelling of GaN-based Gunn Diodes" 260

P60 K. Matsuura, M. Miyake, A. Ueno, and H.J. Mattausch (*Hiroshima University*) "Investigation of SiC p-i-n Diode Reverse-Recovery Effect for Compact Modeling" 262

Electronic and transport properties of graphene

Tsuneya Ando
Department of Physics, Tokyo Institute of Technology
2-12-1 Ookayama, Meguro-ku, Tokyo 152-8551, Japan
e-mail: ando@phys.titech.ac.jp

Graphene was fabricated first by mechanical exfoliation in 2004 and the conductivity modulation by the gate was demonstrated and the quantum Hall effect was observed in 2005. Since then, various experimental and theoretical investigations have been performed to reveal its exotic properties. Actually, graphene has been a subject of theoretical study prior to the experimental realization because of the peculiar electronic structure also responsible for intriguing properties of carbon nanotubes [1]. Several reviews have already been published [2]–[4]. The purpose of this paper is to give a brief review on characteristic features of electronic states and transport properties in graphene mainly from a theoretical point of view.

The graphene has a honeycomb lattice with two carbon atoms in a unit cell. The Fermi level lies in the so-called π bands consisting of the p_z orbital perpendicular to the plane. The π bands have a linear dispersion and cross at the K and K' points at the corner of the first Brillouin zone. Because the Fermi level lies at the crossing points, electronic properties are dominated by those states. Within the effective-mass approximation or the $\mathbf{k}\cdot\mathbf{p}$ scheme, the electron motion is governed by Weyl's equation for neutrino or the Dirac equation with vanishing mass.

An important feature is the presence of a topological singularity at $\mathbf{k} = 0$. A neutrino has a helicity and its spin is quantized into the direction of the wave vector. The spin eigenfunction changes its sign under a 2π rotation. Correspondingly, the pseudo-spin wave function acquires phase $-\pi$ due to Berry's phase when the wave vector $\mathbf{k}$ is rotated around the origin along a closed contour. For the present pseudo spin, this sign change can be understood in terms of Berry's phase when the wave vector moves along a closed contour around $\mathbf{k} = 0$. The sign change occurs only when the contour encircles $\mathbf{k}=0$ but not when the contour does not contain $\mathbf{k}=0$. This topological singularity at $\mathbf{k}=0$ is the origin of the absence of backscattering in metallic carbon nanotubes [5], [6].

The singularity also leads to the presence of a Landau level at $\varepsilon=0$ independent of the magnetic-field strength [7]. It is responsible for the singular diamagnetic susceptibility $\chi \propto -\delta(\varepsilon)$ [2], [7], [8]. Further, the nanotube has a strong magnetic anisotropy and tends to align in the field direction [9], which has been extensively used in the observation of the Aharonov-Bohm effect in optical absorption [10]. This singularity is considered as the origin of the peculiar behavior in the transport properties of graphene, such as the minimum conductivity in the absence of a magnetic field, the quantum Hall effect, and the dynamical conductivity [2].

The neutrino equation for $\mathbf{F}$ is invariant under the special time-reversal operation S, $\mathbf{F}^S = K\mathbf{F}^*$, where $\mathbf{F}^*$ stands for the complex conjugate of $\mathbf{F}$ and $K = -i\sigma_y$ satisfying $K^2 = -1$ [1]. When S is operated twice, the wave function changes its sign, i.e., $\mathbf{F}^{S^2} = (\mathbf{F}^S)^S = -\mathbf{F}$. This S symmetry, characteristic to the symplectic universality class, is not destroyed by scatterers unless their potential range is not smaller than the lattice constant. In this case the quantum correction to the conductivity becomes positive and the conductivity exhibits a weak anti-localization behavior [11].

The special time reversal S is different from the real time reversal T in which the K and K' points are exchanged corresponding to the complex conjugate wave functions. When being repeated, the wave function returns to the original with the same sign. A system with this T symmetry belongs to the orthogonal universality class. In the presence of usual scatterers with their potential range larger than the lattice constant, the K and K' points can be regarded as independent because their coupling can safely be neglected. In this case this T symmetry

978-3-901578-26-7 © 2013 Society for Micro- and Nanoelectronics

is irrelevant and only the S symmetry prevails. In the presence of short-range scatterers causing inter-valley scattering between the K and K' points, the S symmetry is destroyed and the T symmetry becomes relevant [11], [12]. Therefore, the symmetry crossover between the symplectic and orthogonal classes occurs due to short-range scatterers. The change from the anti-localization behavior in the symplectic case to the weak-localization behavior in the orthogonal case for the quantum correction to the conductivity has been demonstrated [11], [13].

The equi-energy line of graphene in the vicinity of the K or K' points has a small trigonal warping. Effects of the warping can be included as a higher-order $\mathbf{k}\cdot\mathbf{p}$ term [2]. This term destroys the S symmetry and the symmetry of the system changes into unitary when the trigonal warping is appreciable. Further, the lattice strain and the nonzero curvature of the nanotube gives rise to an effective vector potential or Aharonov-Bohm flux, and therefore destroys the S symmetry [2].

Inter-layer interaction in bilayer graphene destroys the linear dispersion into an approximate parabolic dispersion with a trigonal warping [14], [15]. Electronic states of multi-layer graphene depend critically on the number of layers. This becomes clear if we consider only the major coupling terms and neglect other small parameters considered in bulk graphite. In fact, for odd-layer graphene, the Hamiltonian can be decomposed into those of bilayers with different interlayer coupling and that of a monolayer graphene, while for even-layer graphene, the Hamiltonian can be decomposed into those of bilayers only [16]. A perpendiculor electric field or asymmetry between two layers opens up an energy gap in bilayer graphene.

There have been various theoretical and experimental investigations on dominant scattering mechanisms, including effects of charged impurities [17], [18] and environmental dielectric screening effect [19], resonance scattering effects due to strong and short-range scatterers [20], etc. A recent theoretical study showed that the minimum conductivity is sensitive to effective potential range of dominant scatterers [21] in agreement with experiments [22]. The bilayer graphene exhibits the similar behavior [23]. The appearance of effective vector potential due lattice distortion [24] was used for the prediction of magneto-phonon resonances [25]. Interfaces between monolayer and bilayer graphenes were shown to exhibit peculiar dependence on incident angle because of the chiral electron motion, giving rise to valley polarization of transmitted electron [26], and characteristic Landau-level structure [27].

REFERENCES

[1] T. Ando, J. Phys. Soc. Jpn. **74**, 777 (2005).
[2] T. Ando, Physica E **40**, 213 (2007).
[3] A. H. Castro Neto, F. Guinea, N. M. Peres, K. S. Novoselov, and A. K. Geim, Rev. Mod. Phys. **81**, 109 (2009).
[4] D. S. L. Abergel, V. Apalkov, J. Berashevich, K. Ziegler, and T. Chakraborty, Adv. Phys. **59**, 261 (2010).
[5] T. Ando and T. Nakanishi, J. Phys. Soc. Jpn. **67**, 1704 (1998).
[6] T. Ando, T. Nakanishi, and R. Saito, J. Phys. Soc. Jpn. **67**, 2857 (1998).
[7] J. W. McClure, Phys. Rev. **104**, 666 (1956).
[8] M. Koshino and T. Ando, Phys. Rev. B **75**, 235333 (2007).
[9] H. Ajiki and T. Ando, J. Phys. Soc. Jpn. **62**, 2470 (1993); J. Phys. Soc. Jpn. **63**, 4267 (1994) (Erratum).
[10] S. Zaric, G. N. Ostojic, J. Kono, J. Shaver, V. C. Moore, M. S. Strano, R. H. Hauge, R. E. Smalley, and X. Wei, Science **304**, 1129 (2004).
[11] H. Suzuura and T. Ando, Phys. Rev. Lett. **89**, 266603 (2002).
[12] T. Ando and K. Akimoto, J. Phys. Soc. Jpn. **73**, 1895 (2004).
[13] E. McCann, K. Kechedzhi, V. I. Falko, H. Suzuura, T. Ando, and B. L. Altshuler, Phys. Rev. Lett. **97**, 146805 (2006).
[14] E. McCann and V. I. Falko, Phys. Rev. Lett. **96**, 086805 (2006).
[15] M. Koshino and T. Ando, Phys. Rev. B **73**, 245403 (2006).
[16] M. Koshino and T. Ando, Phys. Rev. B **76**, 085425 (2007).
[17] T. Ando, J. Phys. Soc. Jpn. **75**, 074716 (2006).
[18] K. Nomura and A. H. MacDonald, Phys. Rev. Lett. **96**, 256602 (2006).
[19] L. A. Ponomarenko, R. Yang, T. M. Mohiuddin, M. I. Katsnelson, K. S. Novoselov, S. V. Morozov, A. A. Zhukov, F. Schedin, E. W. Hill, and A. K. Geim, Phys. Rev. Lett. **102**, 206603 (2009).
[20] A. Toyoda and T. Ando, J. Phys. Soc. Jpn. **79**, 094708 (2010).
[21] M. Noro, M. Koshino, and T. Ando, J. Phys. Soc. Jpn. **79**, 094713 (2010).
[22] A. K. Geim and K. S. Novoselov, Nat. Mater. **6**, 183 (2007).
[23] T. Ando, J. Phys. Soc. Jpn. **80**, 014707 (2011).
[24] H. Suzuura and T. Ando, Phys. Rev. B **65**, 235412 (2002).
[25] N. Mori and T. Ando, J. Phys. Soc. Jpn. **80**, 044706 (2011).
[26] T. Nakanishi, M. Koshino, and T. Ando, Phys. Rev. B **82**, 125428 (2010).
[27] M. Koshino, T. Nakanishi, and T. Ando, Phys. Rev. B **82**, 205436 (2010).

The Non-Equilibrium Green Function Approach to Quantum Transport in Nano-Structures

J.R. Barker
College of Science and Engineering, University of Glasgow, Glasgow G12 8LT, Scotland, UK
e-mail: john.barker@glasgow.ac.uk

MANUSCRIPT

The Non-Equilibrium Green Function (NEGF) formalism was established 50 years ago [1-3] to describe non-equilibrium quantum statistical mechanics in *open systems* [4-6]. Clever algorithm development [7-10] and the wide availability of powerful computer technology has made the technically complex NEGF formalism a practical simulation tool for studying transport in nanostructured devices. The central concept is the 8-dimensional Green Function $G[\mathbf{r},t;\mathbf{r}',t']$ that describes the quantum mechanical probability amplitude for a carrier to propagate from a position $\mathbf{r}$ at time t to another position $\mathbf{r}'$ at time t' within a many-body interacting system that is driven out of thermal equilibrium by applied fields. G is rarely calculated directly, instead we may compute physically interesting properties such as the charge density, current density and local density of states in computationally efficient schemes. NEGF theory is a highly technical formalism [1-6] because the need to establish a *non-equilibrium* many-body perturbation theory leads to consideration of four different types of coupled Green functions. The general case is reviewed and we show the connection with semi-classical Boltzmann transport theory. Our main focus is on *stationary systems* where the Green functions depend on two position coordinates and energy. Four different Green functions are required: we consider the *retarded* and *advanced* Green functions $G^R(\mathbf{r},\mathbf{r}';E)$, $G^A(\mathbf{r},\mathbf{r}';E)$, (describing the dynamical states and quantum dynamics) and the so-called *lesser* and *greater* Green Functions $G^<(\mathbf{r},\mathbf{r}';E)$,$G^>(\mathbf{r},\mathbf{r}';E)$ (correlation functions that pick up the mainly statistical or thermodynamic properties). A simple picture is developed of the basic NEGF *simulation methodology*. Useful *visualisation techniques* are described based on the quantum hydrodynamic velocity field. We start with the *projection algorithms* [7-10] that reduce the computational domain to a finite device region at the expense of introducing a self-energy correction that takes account of coupling to the leads/contacts/environment. Criteria are then developed for choosing between full complexity *3D spatial modelling* versus the lower dimensional *modal decomposition* method in confined nanostructures [11-12]. NEGF methods are particularly useful in *quasi-ballistic* systems where the complexity of the self-consistent electrostatic architecture of the device (including atomistic treatment of the scattering on individual impurities and surface/interface roughness) may be incorporated *non-perturbatively* [13-15]. *Non-ballistic* nanostructures [16] are now becoming of interest for which *many-body self-energy* models are required to describe both elastic and inelastic scattering. Examples include *gate-all-around* (GAA) silicon nanowire (SNW) devices (Fig.1) that are *non-ballistic* because: (i) the electron-phonon interactions [18, 19] are enhanced by confinement effects and (ii) long-range remote phonon scattering from interfacial regions. Self-energies are generally *non-diagonal* [17] and this renders the standard Green function algorithms intractable. To reduce the numerical complexity many adopt approximations to the electron-phonon self-energies. We review important self-energy models including: electrostatic [20], Hartree, exchange and correlation, carrier-phonon/plasmon. We examine the errors created by common approximations to self-energies that arise from the diagonality approximation or violation of the requirements for physical causality [21] and we

978-3-901578-26-7 © 2013 Society for Micro- and Nanoelectronics

discuss a strategy for efficient accurate numerical calculation.

REFERENCES

[1] J. Schwinger, J. Math. Phys. **2**, 407 (1961).
[2] L.V. Keldysh, *Diagram Techniques for non-equilibrium processes*, Soviet Physics, JETP **20**, 1018 (1965) [Zh. Eksp. Teor. Fiz. 47, 1515 (1964)].
[3] L.P. Kadanoff and G. Baym, *Quantum Statistical Mechanics* (W.A. Benjamin,inc New York, 1962).
[4] J. Rammer and H. Smith, *Quantum field-theoretical methods in the transport theory of metals*, Reviews of Modern Physics, **58,** 323 (1986).
[5] H. Haug and A. P. Jauho, *Quantum kinetics in transport and optics of semiconductors* (Springer, Heidelberg, 1996).
[6] K. Balzer and M. Bonitz, *Nonequilibrium Green's Functions Approach to Inhomogeneous Systems,* Lecture Notes in Physics **867** (Springer, 2013).
[7] C. Caroli, R. Combescot, D. Lederer, P. Nozieres and D. Saint-James, *Direct Calculation of the Tunnelling Current*, Journal of Physics C: Solid State Physics, **4**, 916 (1971).
[8] R. Lake, G. Klimeck, R.C. Bowen, and D. Jovanovic, *Single and multiband modeling of quantum electron transport through layered semiconductor devices*, Journal of Applied Physics, **81**, 7845 (1997).
[9] S. Datta, *Electronic transport in mesoscopic systems* (Cambridge University Press, Cambridge, 1997).
[10] A. Svizhenko, M. P. Anantram, T. R. Govindan, B. Biegel, and R. Venugopal*, Two-dimensional quantum mechanical modelling of nanotransistors*, Journal of Applied Physics, **91**, 2343 (2002).
[11] J. R. Barker, M. Finch, J. Pepin and M. Laughton, *Theory of non-linear transport in quantum waveguides*, Solid State Electronics **32**, 1155 (1989).
[12] R. Venugopal1, Z. Ren, S. Datta, M. S. Lundstrom, and D. Jovanovic, *Simulating quantum transport in nanoscale transistors: Real versus mode-space approaches*, Journal of Applied Physics, **92**, 3730 (2002).
[13] A. Martinez, M. Bescond, J.R. Barker, A. Svizhenko, M. P. Anatram,C. Millar and A. Asenov, *A self-consistent full 3-D real space NEGF simulator for studying nonperturbative effects in nano-Mosfets,* IEEE Transactions on Electron Devices, **54**, 2213 (2007).
[14] J.R. Barker, A. Martinez, A. Svizhenko, M.P. Anatram, and A. Asenov, *Green Function study of quantum transport In ultrasmall devices with embedded atomistic clusters*, J. Phys.: Conf. Ser. 35, 233-246 (2006).
[15] A. Martinez, J.R. Barker, A. Svizhenko, M.P. Anantram, M. Bescond, A. Asenov, *Ballistic Quantum Simulators for Studying Variability in Nanotransistors,* Journal of Computational and Theoretical Nanoscience, **5**, 2289 (2008)
[16]A. Martinez, N. Seone, A. R. Brown, J. R. Barker and A. Asenov, *Variability in Si Nanowire MOSFETs Due to the Combined Effect of Interface Roughness and Random Dopants: A Fully 3D NEGF Simulation Study*,
[17] M. Aldegunde, A. Martinez and J. R. Barker, *Study of Discrete Doping Induced Variability in Junctionless Nanowire MOSFETs using Dissipative Quantum Transport Simulations,* IEEE Electron Device Letters, Vol. 33, 194 (2012)
[18] J R Barker, A Martinez and M Aldegunde, *Compliant energy and momentum conservation in NEGF simulation of electron-phonon scattering in semiconductor nano-wire transistors,*Journal of Physics: Conference Series, **367**, 012012 (2012)
[19] M. Aldegunde, A. Martinez and J. R. Barker, *Study of individual phonon scattering mechanisms and the validity of Matthiessen's rule in a gate-all-around silicon nanowire transistor,* Journal of Applied Physics, **113**, 014501 (2013)
[20] C. Li, M. Bescond and M. Lannoo, *GW investigation of interface-induced correlation effects on transport properties in realistic nanoscale devices*, Physical Review B **80**, 195318 (2009).
[21] J.R Barker, and A. Martinez*, Self-energy Models for Scattering in Semiconductor Nanoscale Devices: Causality Considerations and the Spectral Sum Rule,* submitted for publication.

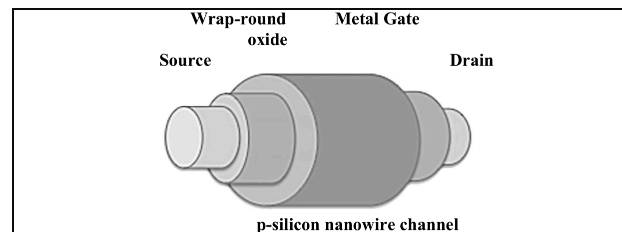

Fig. 1. Schematics of a nano-scale transistor. Channel dimensions: 2.2nm X 6 nm [21]

Pseudopotential-based calculation of electronic structure and transport in nanostructures

M. V. Fischetti
Department of Materials Science and Engineering, University of Texas at Dallas, 800 W. Campbell Road, Richardson, Texas 75080, USA
e-mail: max.fischetti@utdallas.edu

ABSTRACT/SYNOPSIS

This short course describes the use of empirical pseudopotentials (EPs) to study the electronic properties and transport in nanometer-scale structures, discussing the calculation of the band structure and wavefunctions, of the matrix elements determining scattering rates, and on open-boundary-condition quantum transport. The EP approach is compared to other approaches presented in these short courses (Density Functional Theory, DFT, tight-binding, and $\boldsymbol{k}\cdot\boldsymbol{p}$ perturbation theory).

CRYSTAL HAMILTONIAN AND PSEUDOPOTENTIALS

The course begins with a brief overview of the main physical approximations required to simplify the 'exact' crystal Hamiltonian with emphasis on plane-wave methods: The adiabatic (Born-Oppenheimer) approximation to separate the ionic and electronic degrees of freedom; The single-electron and mean-field approximations (Hartree and Hartree-Fock); The concept of 'density functional' to handle exchange and correlation [1]; And, finally, 'model potentials' and 'pseudopotentials' [2,3], both self-consistent (DFT) and empirical. EPs, when suitably calibrated and using 'relaxed' atomic coordinates, are then argued to represent a satisfactory compromise between physical accuracy and computational efficiency.

EMPIRICAL PSEUDOPOTENTIALS AND NANOSTRUCTURES

As an illustration of the practical use of EPs, the case of bulk Si is discussed also in its numerical details [4]. The idea of 'supercell' is then introduced with examples relative to transport in two dimensions (thin Si bodies, III-V hetero-layers, graphene) and in one dimension (Si nanowires, carbon nanotubes, graphene nanoribbons) [5,6].

SCATTERING PROCESSES

Next, the discussion moves to the use of EPs to calculate matrix elements (and so, scattering or transition rates, or self-energies) for some important collision processes. In particular, the rigid-(pseudo)ion approximation [7] is used to compute the electron-phonon matrix elements in Si inversion layers and in graphene. Results from semiclassical full-band transport studies (mobility and Monte Carlo) are then presented. Next, we describe the use of EPs to model atomic roughness (and its effect on electronic transport) at surfaces/interfaces/line-edges in thin bodies, nanowires (NWs) and armchair-edge graphene nanoribbons (AGNRs).

BALLISTIC QUANTUM TRANSPORT WITH OPEN BOUNDARY CONDITIONS

The last section of this short course deals with the study of ballistic quantum transport in nanostructures. The treatment of open boundary conditions at the 'contacts' is discussed presenting a full-band extension of the 'Quantum Transmitting Boundary Method' [8] using EPs and the example of ballistic transport in a small Si NW.

REFERENCES

[1] W. Kohn and L. J. Sham, *Self-Consistent Equations Including Exchange and Correlation Effects*, Phys. Rev. **140,** A1133 (1965).
[2] W. A. Harrison, *Pseudopotentials in the theory of metals*, Frontiers in Physics, (University of Virginia, 1966).
[3] V. Heine, *The Pseudopotential Concept*, Solid State Phys. **24,** 1 (1970).
[4] M. L. Cohen and T. K. Bergstresser, *Band Structures and Pseudopotential Form Factors for Fourteen Semiconductors of the Diamond and Zinc-blende Structures*, Phys. Rev. **141**, 789 (1966).
[5] The EPs used here are from Y. Kurokawa, S. Nomura, T. Takemori, and Y. Aoyagi, Phys. Rev. B **61**, 12616 (2000) for C; from W. Wang and A. Zunger, J. Phys. Chem. **98**, 2158 (1994) for Si; from L. Bellaiche, S.-H. Wei, and A. Zunger, Phys. Rev. B **54**, 17568 (1996) and K. A. Mäder and A. Zunger, Phys. Rev. B **51**, 10462 (1995) for III-Vs.
[6] M. V. Fischetti, Bo Fu, S. Narayanan, and J. Kim, *Semiclassical and Quantum Electronic Transport in Nanometer-Scale Structures: Empirical Pseudopotential Band Structure, Monte Carlo Simulations and Pauli Master Equation*, in "Nano-Electronic Devices: Semiclassical and Quantum Transport Modeling", D. Vasileska and S.M. Goodnick Eds. (Springer, New York, 2011), pp. 183-247.

[7] J. M. Ziman, *Electrons and Phonons*, Oxford University Press (Oxford, UK, 1960).
[8] C. S. Lent and D. J. Kirkner, *The Quantum Transmitting Boundary Method*, J. Appl. Phys. **67**, 6353 (1990).

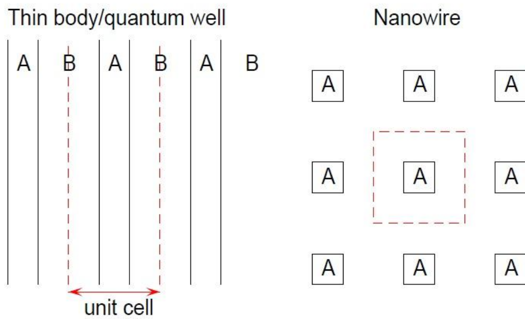

Fig. 1. Schematic diagram illustrating the concept of 'supercell': The nanostructure is replicated along one direction (*left*, thin body, 2DEG) or on the plane (*right*, nanowire/nanotube, 1DEG) to recover periodicity and make a plane-wave analysis possible.

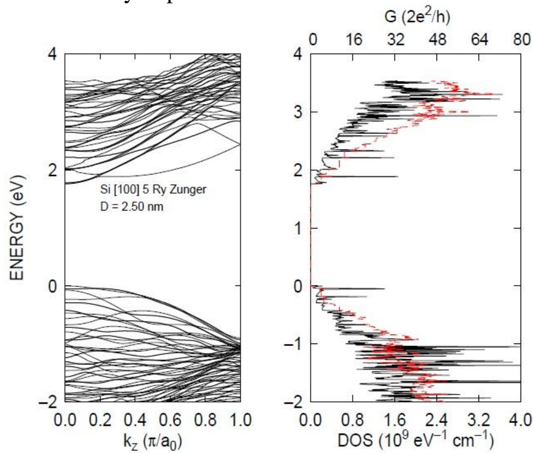

Fig. 2. Band structure (*left*) and density-of-states (*right*, solid black line, bottom scale) and ballistic conductance (*right*, dashed red line, top scale) for a 2.5 nm-diameter cylindrical [100] Si nanowire obtained using empirical pseudopotentials (M. V. Fischetti, unpublished).

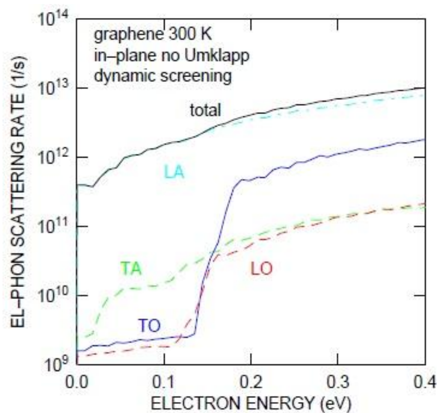

Fig. 3. Dynamically screened electron phonon scattering rate in graphene at zero density calculated using EPs and the rigid-ion approximation (M. V. Fischetti and S. Aboud, unpublished).

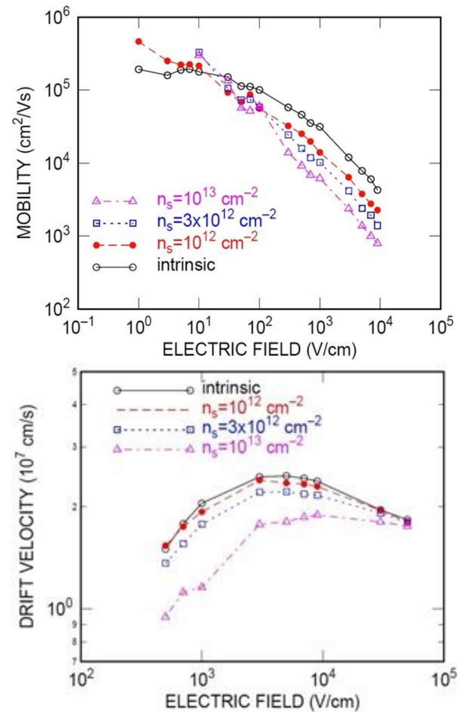

Fig. 4. Field-dependent mobility (*top*, calculated from the longitudinal diffusion coefficient) and drift-velocity (*bottom*) in graphene obtained using the rigid-ion scattering rates (courtesy S. Narayanan, UT-Dallas PhD Thesis).

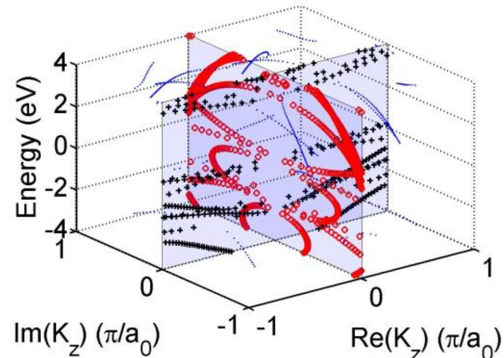

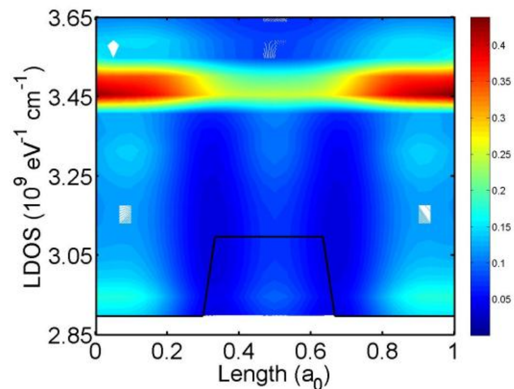

Fig. 4. *Top*: Complex band structure for a Si NW with 1 cell x1 cell square cross-section. This information is needed by the full-band QTBM. *Bottom*: Local density-of-states for the same Si NW in the presence of a rectangular potential barrier simulating the effect of a gate potential (courtesy Bo Fu, UT-Dallas Ph.D. Thesis).

$\boldsymbol{k} \cdot \boldsymbol{p}$ Perturbation and Energy Bands of Semiconductors

C. Hamaguchi
Professor Emeritus of Osaka University
Advanced Technology Research Laboratories, Sharp Corporation,
2613-1 Ichinomoto-cho, Tenri, Nara 632-8567, Japan
e-mail: hamaguchi-c@r6.dion.ne.jp

INTRODUCTION TO $\boldsymbol{k} \cdot \boldsymbol{p}$ PERTURBATION THEORY

Dresselhaus *et al.* [1] and Luttinger and Kohn [2], [3] introduced $\boldsymbol{k} \cdot \boldsymbol{p}$ perturbation theory to analyze the valence band structure of Ge and Si and later Kane [4], [5] extended $\boldsymbol{k} \cdot \boldsymbol{p}$ theory to include conduction bands. Cardona and Pollak [6] proposed $\boldsymbol{k} \cdot \boldsymbol{p}$ perturbation method to calculate energy bands in Ge and Si. In this lecture, the $\boldsymbol{k} \cdot \boldsymbol{p}$ perturbation theory is discussed in detail. First we show the energy band calculations of Ge and Si in the Brillouin zone and then we will show how to implement the spin–orbit interaction. In the second part we will discuss the analysis of the valence bands based on the second order perturbation of $\boldsymbol{k} \cdot \boldsymbol{p}$ Hamiltonian and the valence band parameters are determined. In the last part we discuss Luttinger Hamiltonian so called 4×4 (heavy and light hole bands), 6×6 (heavy, light and spin–orbit split off valence bands), and 8×8 (including the lowest conduction band) Luttinger Hamiltonian [7].

ENERGY BAND CALCULATIONS BY $\boldsymbol{k} \cdot \boldsymbol{p}$ THEORY

Schrödinger equation for an electron in a crystal is written as

$$\left[-\frac{\hbar^2}{2m}\nabla^2 + V(\boldsymbol{r})\right]\Psi(\boldsymbol{r}) = \mathcal{E}\Psi(\boldsymbol{r}). \tag{1}$$

The eigen function Ψ is given by Bloch function

$$\Psi(\boldsymbol{r}) = u_{\boldsymbol{k}}(\boldsymbol{r})\exp(\mathrm{i}\boldsymbol{k}\cdot\boldsymbol{r}) \tag{2}$$

where $u_{\boldsymbol{k}}(\boldsymbol{r})$ is a periodic function and $\boldsymbol{k}$ is the wave vector. Putting Eq. (2) into Eq. (1), we obtain

$$\left[-\frac{\hbar^2}{2m}\nabla^2 + V(\boldsymbol{r}) + \frac{\hbar}{m}(\boldsymbol{k}\cdot\boldsymbol{p})\right]u_{n,\boldsymbol{k}}(\boldsymbol{r}) = \left(\mathcal{E}_n(\boldsymbol{k}) - \frac{\hbar^2k^2}{2m}\right)u_{n,\boldsymbol{k}}(\boldsymbol{r}) \tag{3}$$

Above equation reduces to $[H_0 + V(\boldsymbol{r})]u_{\boldsymbol{k}}(\boldsymbol{r}) = \mathcal{E}_n(0)u_{\boldsymbol{k}}(\boldsymbol{r})$ for $\boldsymbol{k} = 0$ which gives the eigen states at the Γ point. When we know the eigen states at $\boldsymbol{k} = 0$ we may obtain the eigen states $\boldsymbol{k} \neq 0$ by treating $H_1 = (\hbar/m)\boldsymbol{k}\cdot\boldsymbol{p}$ as a perturbing term.

The first part of this lecture deals with the following items.

1.1 Derivation of $\boldsymbol{k} \cdot \boldsymbol{p}$ Hamiltonian.
1.2 Determination of 15×15 matrix of $\boldsymbol{k} \cdot \boldsymbol{p}$ Hamiltonian and of the parameters.
1.3 Eigen states obtained by 15×15 pseudopotential Hamiltonian matrix.
1.4 Energy band calculations.

The second part will deal the analysis of the valence bands and derivation of Luttinger Hamiltonian.

2.1 Second order $\boldsymbol{k} \cdot \boldsymbol{p}$ perturbation.
2.2 Spin–orbit interaction.
2.3 6×6 $\boldsymbol{k} \cdot \boldsymbol{p}$ matrix of Dresselhaus *et al.*
2.4 6×6 $\boldsymbol{k} \cdot \boldsymbol{p}$ Luttinger Hamiltonian.
2.5 8×8 $\boldsymbol{k} \cdot \boldsymbol{p}$ Luttinger Hamiltonian.

CONCLUSION

This lecture gives an introduction to $\boldsymbol{k} \times \boldsymbol{p}$ perturbation theory to understand the energy band structures of semiconductors. The theory is used to analyze quantum structures such quantum well, quantum dot and quantum dot superlattices.

REFERENCES

[1] G. Dresselhaus: A.F. Kip, and C. Kittel: Phys. Rev. **98** (1955) 368
[2] J.M. Luttinger and W. Kohn: Phys. Rev. **97** (1955) 869
[3] J.M. Luttinger: Phys. Rev. **102** (1956) 1030
[4] E.O. Kane: J. Phys. Chem. Solids, **1** (1956) 82
[5] E.O. Kane: J. Phys. Chem. Solids **1** (1957) 249
[6] M. Cardona and F.H. Pollak: Phys. Rev. **142** (1966) 530
[7] C. Hamaguchi: "*Basic Semiconductor Physics*", (Springer 2010), Chapter 1 and Chapter 2.

978-3-901578-26-7 © 2013 Society for Micro- and Nanoelectronics

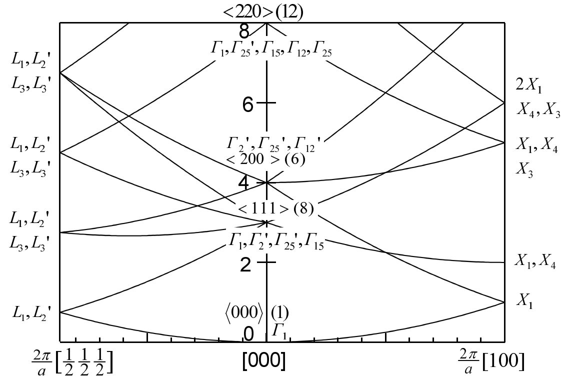

Fig. 1. Empty lattice bands of fcc crystals, where the degeneracy in the parentheses and the representations are shown.

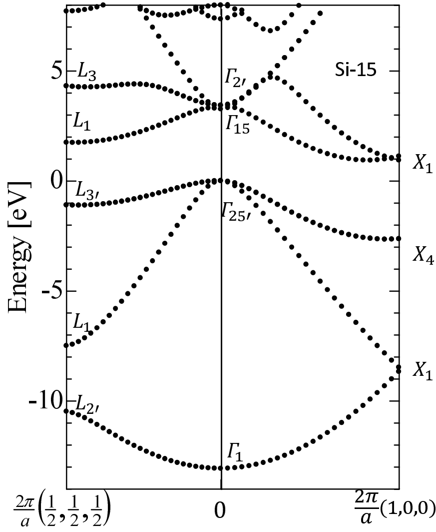

Fig. 2. Energy band structure of Si calculated by empirical pseudopotential method with 15 plane waves.

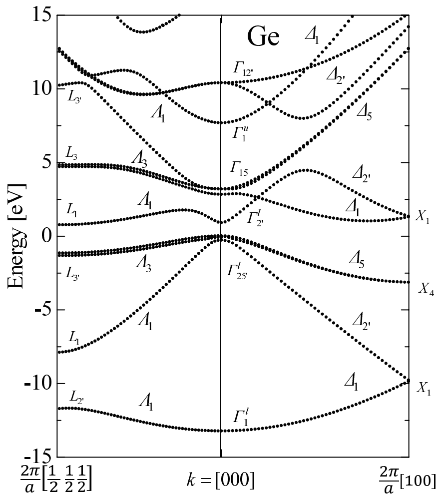

Fig. 3. Energy band structure of Ge calculated by 15×15 $\boldsymbol{k} \cdot \boldsymbol{p}$ method with spin–orbit interaction.

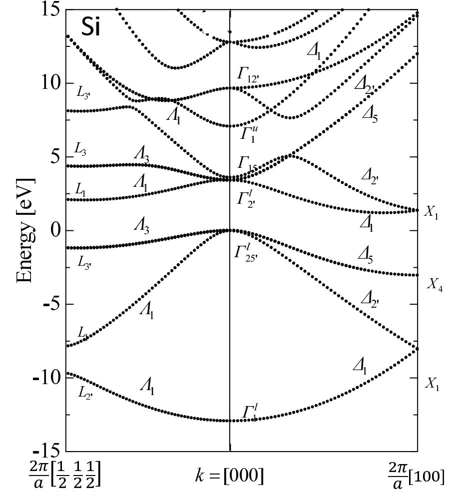

Fig. 4. Energy band structure of Si calculated by 15×15 $\boldsymbol{k} \cdot \boldsymbol{p}$ method.

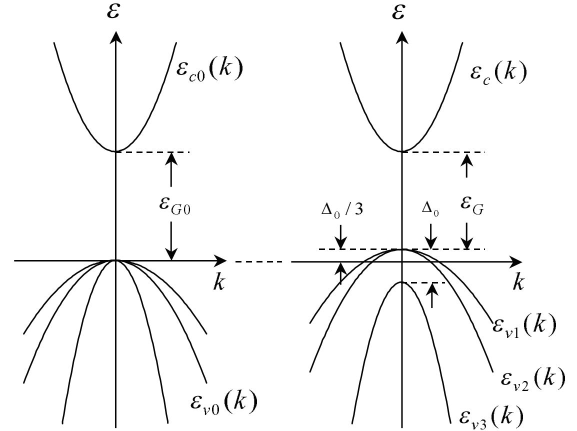

Fig. 5. Valence band structure. The left figure is without spin–orbit interaction and the right figure shows the bands with spin–orbit interaction.

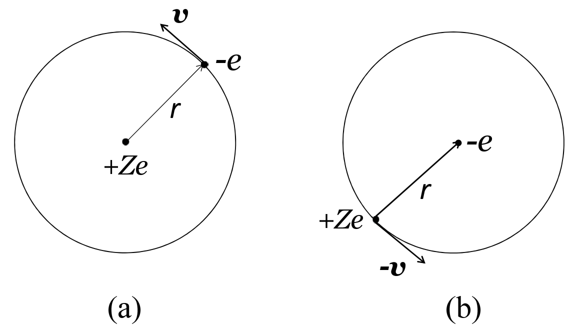

Fig. 6. (a) Bohr orbital motion of an electron $-e$ with the velocity $\boldsymbol{v}$ as seen by the nucleus Ze is interpreted from the point of view of the electron as (b) the nucleus Ze is moving with velocity $-\boldsymbol{v}$ around the electron.

Master Equations in Quantum Transport

Irena Knezevic
Electrical and Computer Engineering, University of Wisconsin-Madison, USA
e-mail: knezevic@engr.wisc.edu

In the theory of small, few-level open systems, the term "master equation" refers to equations that describe the evolution of the open system's full statistical operator (usually called the reduced statistical operator or the reduced density matrix) in the presence of coupling with reservoirs, which have an infinite number of degrees of freedom and are responsible for the irreversibility in the open system's evolution [1,2]. Traditionally, the reservoirs are considered bosonic and can have various spectral function [1], although the question of small open systems coupled with fermionic reservoirs has been receiving a lot of attention in recent years [3].

Electronic systems in semiconductor nanostructures are open quantum systems, exchanging particles and information with the contacts, rapidly dephasing reservoirs of charge. The term master equation is somewhat more broad when referring to electronic transport calculations. On the one hand, we have few-level models (e.g. the resonant-level models used for quantum dots) for which master equations continue to refer to the dynamics of the full reduced statistical operator [4,5]. On the other hand, if we strive to account for the generally continuous single-particle spectrum of an electron in a nanostructure (e.g. when capturing current in structures without resonances) and the fact that many electrons are available to populate them, then calculating the full many-body reduced statistical operator becomes both intractable and unnecessary, as much information can be obtained from the single-particle quantities. In this case, master equations can refer to the equations for the time evolution of the single-particle density matrix (e.g. Redfield-type equations [6] or generalized semiconductor Bloch equations [7]), its Wigner transform (i.e. the Wigner equation [8]), or just its diagonal terms (e.g. the Pauli master equation [9]).

Master equations as used in quantum transport in nanostructures can be divided in two groups based on the treatment of the interaction with the contacts: Markovian equations, in which just the current state of the contacts plays a role (obtained in the weak-coupling limit, large-bias limit, or singular coupling limit) and non-Markovian equations, in which details of the contact evolution over a finite time in the past affects the state of the open electronic system. Non-Markovian (also known as memory) effects are critical in resolving the short-time dynamics of electronic systems, such as in the interaction of electrons with ultrafast electromagnetic fields or when looking at the fluctuations of charge and current.

In this talk, I will review recent progress on the use of various Markovian and non-Markovian master equations in quantum transport. I will discuss issues such as complete positivity of the map when deriving approximations for master equations, the relationship between master equations and diagrammatic techniques, and address some of the problems that stem from the separation of contacts from the active region and tracing out of the contact degrees of freedom.

I will also present work [10] on completely positive non-Markovian dynamics in two terminal structures that can be obtained based on the approximation of rapid relaxation in the contacts due to electron-electron scattering. Self-consistent coupling of the Schrödinger equation, Poisson equation, continuity equation, and a master equation obtained by coarse-graining over the contact relaxation time results in non-Markovian transient response of nanostuctures, such as a silicon *nin* diode (Fig. 1) or a GaAs/AlGaAs tunneling diode (Fig. 2).

This work has been supported by NSF (award 0547415) and DOE (award DE-SC0008712).

References

[1] H.-P. Breuer and F. Petruccione, *The Theory of Open Quantum Systems* (Oxford University Press, Oxford, 2002).
[2] R. Alicki and K. Lendi, *Quantum Dynamical Semigroups and Applications* (Springer, 1987).
[3] X. Zheng *et al.*, J. Chem. Phys. 129, 184112 (2008)
[4] P. Zedler *et al.*, Phys. Rev. B 80, 045309 (2009); G. Schaller *et al.*, Phys. Rev. B 80, 245107 (2009)
[5] J. N. Pedersen and A. Wacker, Physica E 42, 595 (2010).
[6] I. V. Ovchinnikov and D. Neuhauser, J. Chem. Phys. 122, 024707 (2005)
[7] F Rossi, A Di Carlo, and P Lugli, Phys. Rev. Lett. 80, 3348 (1998).
[8] D. Querlioz and P. Dollfus, *The Wigner Monte-Carlo Method for Nanoelectronic Devices* (Wiley 2010); M. Nedjalkov *et al.* , Annals of Physics 328, 200 (2013).
[9] M.V. Fischetti, J. Appl. Phys. 83, 270 (1998); *ibid*, Phys. Rev. B 59, 4901 (1999)
[10] I. Knezevic, Phys. Rev. B 77, 125301 (2008); B. Novakovic and I. Knezevic, Fortschritte der Physik 61, 323-331 (2013).

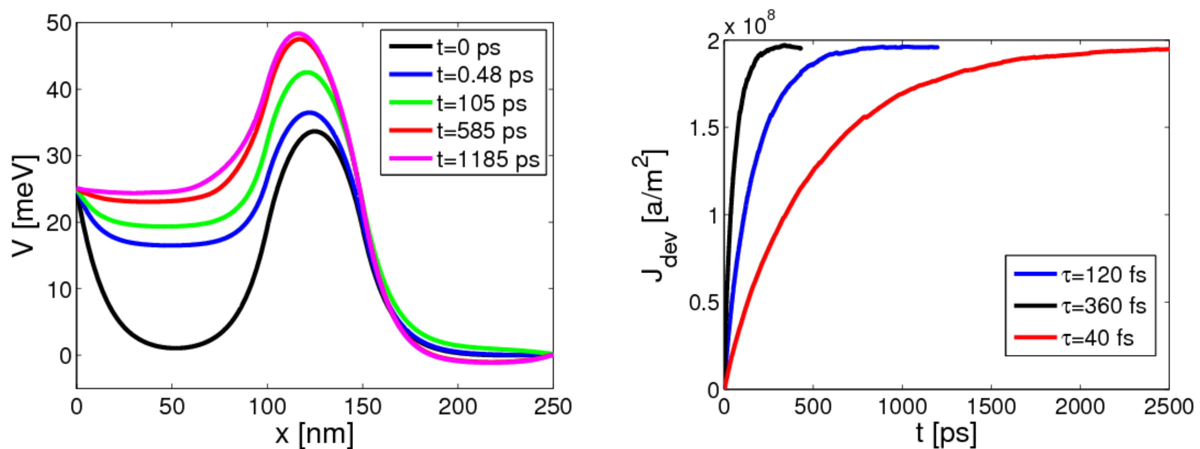

Fig. 1: (Left) Time evolution of the potential profile in a silicon *nin* diode. (Right) Transient current in the active region of the *nin* diode for different values of the momentum relaxation time in the contacts [10].

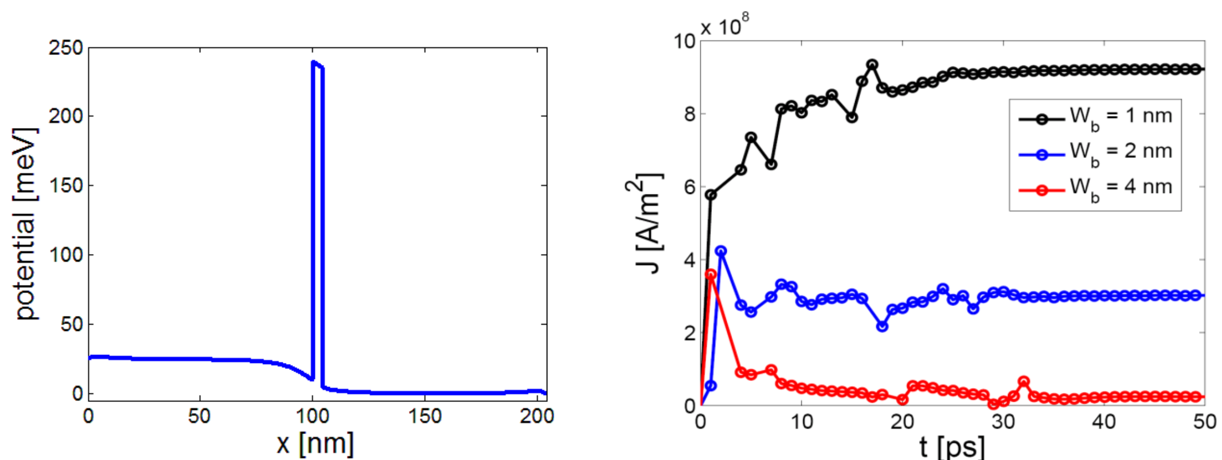

Fig. 2: In a GaAs/AlGaAs tunnel barrier (potential profile in left panel), the finite time needed to empty the well to the left of the barrier, connected to the relaxation time in the contacts, affects the shape of the transient (right).

A Nonlocal Formulation of Quantum Maximum Entropy Principle Including Fractional Exclusion Statistics

M. Trovato and L. Reggiani*
Dipartimento di Matematica, Universitá di Catania, Viale A. Doria, 95125 Catania, Italy
*Dipartimento di Matematica e Fisica ”Ennio De Giorgi” and CNISM, Universitá del Salento,
Via Arnesano s/n 73100 Lecce, Italy
e-mail: trovato@dmi.unict.it

INTRODUCTION

In thermodynamics and statistical mechanics entropy is the fundamental physical quantity to describe the evolution of a statistical ensemble. Its microscopic definition was provided by Boltzmann through the celebrated expression $S = k_B \ln \Gamma$, where k_B is the Boltzmann constant and Γ is the number of microstates exploiting the given macroscopic properties. In this context, it is well known that in classical mechanics the entropy: i) allows the violation of the uncertainty principle [1], [2]; ii) can be considered as a special case of the so-called *Boltzmann-Gibbs-Shannon* entropy that enables one to apply results of information theory to physics [1], [3]. In particular, by introducing the principle of maximum entropy (MEP) it was found possible to derive rigorous hydrodynamic (HD) models based on the *moments* of the distribution function to all orders of a power expansion and including appropriate closure conditions [4], [5]. Accordingly, making use of the Lagrange multipliers technique, it was found possible to construct the set of evolution equations for the macro-variables of interest.

Apart from some partial attempts [3], [6], this is no longer the case in quantum mechanics. Here, the main difficulties concern with: i) the definition of a proper quantum entropy that includes particle indistinguishability; ii) the formulation of a global quantum MEP (QMEP) that allows one to obtain a quantum distribution function both for thermodynamic equilibrium and nonequilibrium configurations. From one hand, in the framework of a nonlocal quantum theory, the generalization of the corresponding Lagrange multipliers is also an open problem. Fron another hand, a rigorous formulation of quantum HD (QHD) closed models is a demanding issue for many kinds of problems in quantum systems like, interacting fermionic and bosonic gases, quantum turbulence, quantum fluids, quantized vortices, nuclear physics, confined carrier transport in semiconductor heterostrucures, phonon and electron transport in nanostructures, nanowires and thin layers.

The aim of this talk is to address the above drawbacks by defining a quantum entropy in terms of the *reduced density matrix*, thus explicitly incorporating quantum statistics into problems involving a system of identical particles. As a further step, with respect to the uncertainty principle, starting from the Wigner representation we formulate a quantum maximum entropy principle which, in the framework of information theory, allows us to obtain a non-local theory for the system under study. As a final step, we determine a closed quantum hydrodynamic model for the macroscopic variables used as constraints in the QMEP approach.

THE NONLOCAL QMEP

By considering the Wigner formalism [7], the QMEP was asserted as the fundamental principle of quantum statistical mechanics when it becomes necessary to treat systems in partially specified quantum mechanical states [8]. Recently, in a series of papers [5], [8], [9] we have presented a set of results addressing this problem by emphasizing the role played by a proper formulation of a QMEP to close quantum hydrodynamic models

978-3-901578-26-7 © 2013 Society for Micro- and Nanoelectronics

in the framework of Extended Thermodynamics. Here, we present a rigorous nonlocal formulation of QMEP by including explicitly Fermi statistics, Bose statistics and, more generally, fractional exclusion statistics (FES).

Relevant results of the present investigation are:
(i) The development of a generalized quantum kinetic equation, in the mean field approximation, for the reduced Wigner function.
(ii) The construction of Extended Quantum Hydrodynamic models evaluated exactly to all orders of $\hbar$.
(iii) The definition of a generalized quantum entropy as global functional of the reduced density matrix.
(iv) The formulation of a quantum version of the maximum entropy principle obtained by determining an explicit functional form of the reduced density operator, which requires the consistent introduction of nonlocal quantum Lagrange multipliers within a Moyal expansion.
(v) The development of a quantum-closure procedure that, for a set of relevant quantum regimes, includes nonlocal statistical effects in the corresponding quantum hydrodynamic systems, both in thermodynamic equilibrium and nonequilibrium conditions.
(vi) The extension of QMEP in the framework of FES.
In particular, within point (vi) the anionic systems satisfying FES [9] are proven to generalize all the results available in the literature in terms of both the kind of statistics and the nonlocal description for excluson gases. Finally gradient quantum corrections are explicitly given at different levels of degeneracy, and classical results are recovered when $\hbar \to 0$.

We remark, that for many years the nonlocal gradient corrections have been extensively tested in real applications such as atomic, surface, nuclear physics, and electronic properties of clusters [10]. Analogously, density gradient expansions have been used to describe capture confinement and tunnelling processes for devices in the deca-nanometer regime by showing a very good agreement both with available experiments and other microscopic methods [11]. We conclude, that the novelty of the present approach allows one to describe the Wigner gradient expansions in the framework of quantum statistics by including also gradient thermal corrections and vorticity terms. As a consequence, the major results outlined above can have relevant applications in quantum turbulence, quantum fluids and quantized vortices. Accordingly, the QMEP including FES is here asserted as the most advanced formulation of the fundamental principle of quantum statistical mechanics.

References

[1] A. Wehrl, *General properties of entropy*, Review of Modern Physics **50**, 221 (1978).

[2] G. Manfredi, M. R. Feix, *Entropy and Wigner functions*, Physical Review E **62**, 4665, (2000);

[3] E.T. Jaynes, *Information Theory and Statistical Mechanics*, Physical Review **106**, 620 (1957); E.T. Jaynes, *Information Theory and Statistical Mechanics. II*, **108**, 171 (1957).

[4] M. Trovato, P. Falsaperla, *Full nonlinear closure for a hydrodynamic model of transport in silicon*, Physical Review B, **57**, 4456-4471 (1998); M. Trovato, L. Reggiani, *Maximum entropy principle within a total energy scheme: Application to hot-carrier transport in semiconductors*, Physical Review B, **61**, 16667-16681 (2000); M. Trovato, L. Reggiani, *Maximum-entropy principle for static and dynamic high-field transport in semiconductors*, Physical Review B, **73**, 245209-1-17 (2006).

[5] M. Trovato, L. Reggiani, *Maximum entropy principle and hydrodynamic models in statistical mechanics*, Rivista del Nuovo Cimento, **35**, 99-266 (2012) and references therein.

[6] Y. Alhassid, R. D. Levine, *Connection between the maximal entropy and the scattering theoretic analyses of collision processes*, Physical Review A **18**, 89 (1978); P. Degond, C. Ringhofer, *Quantum Moment Hydrodynamics and the Entropy Principle*, Journal of Statistical Physics **112**, 587 (2003).

[7] M. Hillery, R. O'Conell, M. Scully, E. P. Wigner, *Distribution Functions in Physics: Fundamentals*, Physics Reports **106**, 121 (1984).

[8] M. Trovato, L. Reggiani, *Quantum maximum entropy principle for a system of identical particles*, Physical Review E **81** 021119-1-11 (2010); M. Trovato, L. Reggiani, *Quantum maximum-entropy principle for closed quantum hydrodynamic transport within aWigner function formalism*, Physical Review. E **84**, 061147-1-29 (2011);

[9] M. Trovato, L. Reggiani, *Quantum Maximum Entropy Principle for Fractional Exclusion Statistics*, Physical Review letters **110**, 020404-1-5 (2013),

[10] W. Yang, *Gradient correction in Thomas-Fermi theory*, Physical Review A **34**, 4575 (1986); P. Tarazona and E. Chacon, *Exact solution of approximate density functionals for the kinetic energy of the electron gas*, Physical Review B **39**, 10366 (1989); E. Engel, P. LaRocca, and R. M. Dreizler, *Gradient expansion for $Ts[n]$: Convergence study for jellium spheres*, Physical Review B **49**, 16728 (1994).

[11] M. G. Ancona and A. Svizhenko, *Density-gradient theory of tunneling: Physics and verification in one dimension*, Journal of Applied Physics, **104**, 073726 (2008); M.G. Ancona, *Density-gradient theory: a macroscopic approach to quantum confinement and tunneling in semiconductor devices*, Journal of Computational Electronics **10**, 65 (2011);

A sinc-based approach for the solution of differential transport problems with periodic boundary conditions

P. Marconcini, D. Logoteta, and M. Macucci
Dipartimento di Ingegneria dell'Informazione, Università di Pisa, Via G. Caruso 16, I-56122 Pisa, Italy
e-mail: p.marconcini@iet.unipi.it

INTRODUCTION

A well-known method to solve a differential problem, and in particular a Schrödinger or Dirac transport equation, with periodic boundary conditions, is based on substituting each of the functions appearing in the differential system with its Fourier transform and solving the problem in terms of the Fourier coefficients of the unknown functions. A proper frequency cut-off has to be chosen to limit the size of the problem.

This approach is generally preferable to a direct real-space solution based on a finite-difference discretization scheme, since it avoids the errors related to the discretization of the derivatives. It can thus be shown that the precision of a solution found with the Fourier-space approach considering only N frequencies is generally better than that of a solution obtained with the direct-space finite-difference approach considering a grid of N points.

Here we discuss the possibility to obtain, working in the direct space, a method equivalent to that used in the reciprocal-space domain, and thus the same accuracy, using a particular set of basis functions in the solution of the problem.

METHOD AND RESULTS

The method is based on the use in the direct space of the following sampling functions for the quantities periodic with period $L = N\Delta$ (where Δ is the size of the considered direct-space mesh and N is the number of samples in the period):

$$g_\ell(x) = \sum_{\alpha=-\infty}^{\infty} \operatorname{sinc}\left(\frac{x - (\ell + \alpha N)\Delta}{\Delta}\right) \quad (1)$$

(where $\operatorname{sinc}(x) = \sin(\pi x)/(\pi x)$). In Fig. 1 we show an example of these basis functions for $N = 20$ and $\ell = 10$: it is clearly periodic with the same period L as the functions we are expanding.

In detail, assuming band-limited wave functions and potentials, we express them in terms of sinc functions using the sampling theorem and then, after some analytical elaborations, we find the correct expressions for all of the terms appearing in the transport equations, in the form of $g_\ell(x)$ function expansions. This allows us to obtain a direct space approach equivalent to that in the Fourier space and thus with the same accuracy properties.

As an example, we apply this method to solve the Dirac transport equation in an armchair graphene nanoribbon with the potential varying only in the transverse direction, which (as we have shown in [1], [2]) can be recast into a form with periodic boundary conditions. In particular, for the two transversal potentials represented in Fig. 2, we obtain the longitudinal wave vectors represented on the Gauss plane in Figs. 3 and 5, and, for the longitudinal wave vector with largest real part, the transverse envelope functions shown in Figs. 4 and 6. These results coincide with those obtained with the Fourier-space approach [1], [2] using a number of frequencies identical to the number of samples considered within the period in the direct-space domain.

REFERENCES

[1] P. Marconcini, D. Logoteta, M. Fagotti, M. Macucci, *Numerical solution of the Dirac equation for an armchair graphene nanoribbon in the presence of a transversally variable potential*, Proceedings of the 14th International Workshop on Computational Electronics, p. 53 (2010).
[2] M. Fagotti, C. Bonati, D. Logoteta, P. Marconcini, M. Macucci, *Armchair graphene nanoribbons: $\mathcal{PT}$-symmetry breaking and exceptional points without dissipation*, Phys. Rev. B **83**, 241406(R) (2011).

978-3-901578-26-7 © 2013 Society for Micro- and Nanoelectronics

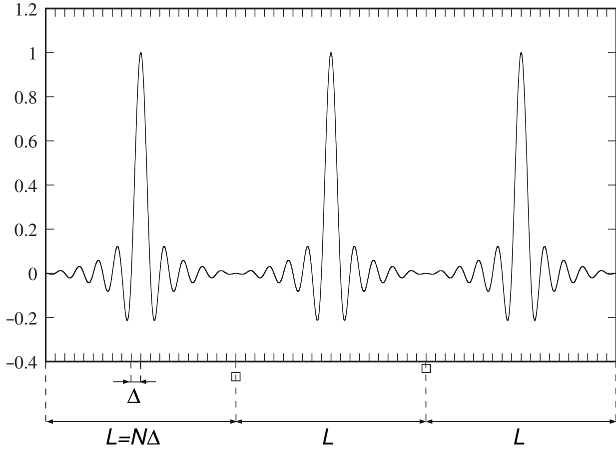

Fig. 1. Sinc basis function for $N = 20$ and $\ell = 10$ (three periods have been represented).

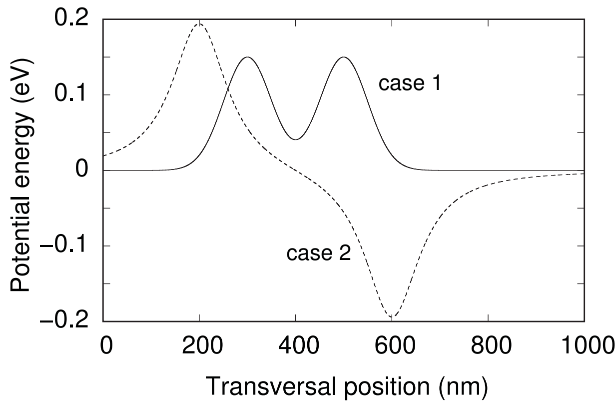

Fig. 2. The two transverse potentials for which the longitudinal wave vectors and transverse envelope functions of a 1 μm wide armchair nanoribbon have been computed using the sinc-based approach.

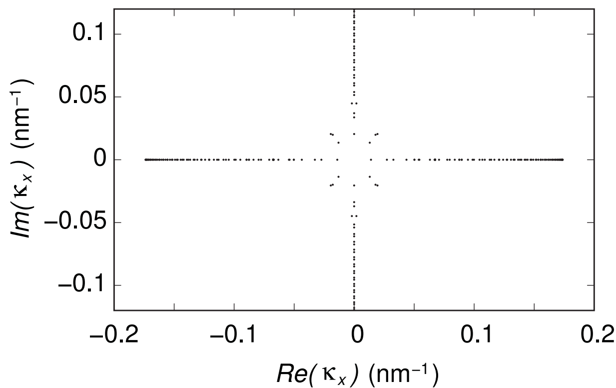

Fig. 3. Longitudinal wave vectors, represented on the Gauss plane, for the armchair nanoribbon in the presence of the potential of case 1 of Fig. 2.

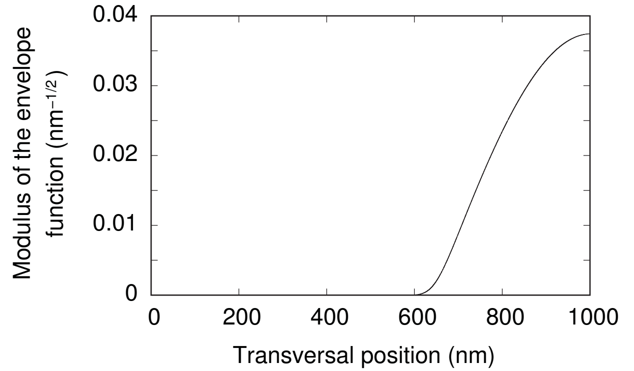

Fig. 4. Modulus of a transverse envelope function (corresponding to the longitudinal wave vector with largest real part) for the armchair nanoribbon in the presence of the potential of case 1 of Fig. 2.

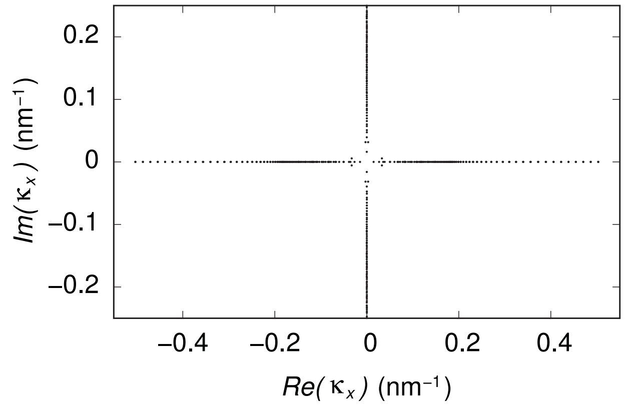

Fig. 5. Longitudinal wave vectors, represented on the Gauss plane, for the armchair nanoribbon in the presence of the potential of case 2 of Fig. 2.

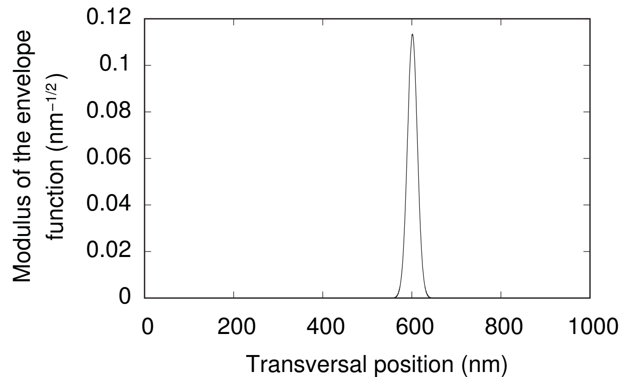

Fig. 6. Modulus of a transverse envelope function (corresponding to the longitudinal wave vector with largest real part) for the armchair nanoribbon in the presence of the potential of case 2 of Fig. 2.

Open-Boundary-Condition Ballistic Quantum Transport using Empirical Pseudopotentials

B. Fu and M. V. Fischetti
Dept. of Materials Science and Engineering, UT Dallas, Richardson, Texas 75080, USA
e-mail: bo.fu@utdallas.edu

Introduction

Moore's law aggressively pushes CMOS technology into the nanometer scale. Finite size and quantum confinement change the band structure, which deviates significantly from the bulk. Meanwhile, the study of electronic transport requires a quantum mechanical approach. Based our previous work on quantum transport using the Pauli Master Equation with effective mass [1], we developed an atomistic full band quantum transport model using empirical pseudopotentials to provide improved physical insight into novel nanodevices.

Method

The Schrödinger equation with lattice potential $V^{lat}(r)$ and external potential $V^{ext}(r)$ can be written as

$$\left[-\frac{\hbar^2\nabla^2}{2m}+V^{lat}(r)+V^{ext}(r)\right]\psi(r)=E\psi(r), \quad (1)$$

where the wave function $\psi(r)$, in order to account for the effect of the spatially varying external potential, can be approximated by the envelop function $\phi_G^k(r)$,

$$\psi_k(r)=\sum_G \phi_G^k(r)e^{iGr}. \quad (2)$$

Substituting Eq. (2) into Eq. (1), we have

$$\sum_{G'}\Big\{\Big[-\frac{\hbar^2\nabla^2}{2m}-\frac{i\hbar^2G'\nabla}{m}+\frac{\hbar^2{G'}^2}{2m}+V^{ext}(r)\Big]\delta_{GG'} +V_{GG'}\Big\}\phi_{G'}^k(r)=E(k)\phi_{G'}^k(r). \quad (3)$$

Equation (3) can be solved accounting for the open boundary conditions with a nontrivial extension of the Quantum Transmitting Boundary Method (QTBM) [2].

Simulation Results

We simulate Si nanowires using local empirical pseudopotential parameters from Zunger [3]. These devices have a cross section of 1x1 cells (0.384 nm x 0.384 nm). Each unit cell, containing 9 Si atoms and 12 H atoms terminating the surface, is isolated by one cell of vacuum in the x-y plane. Figure 1 shows the band structure and the density of states. Injected and reflected states are chosen according to the complex band structure shown in Fig. 2. In order to reduce computational cost, in Fig. 3 we compare results obtained using different restricted subsets of reflected states, considering that states with a large imaginary component of their wavevector result in a small contribution to the charge. Keeping the cross section fixed, we have considered nanowires with length of 1, 3, 6, and 9 cells. As an illustration, we show in Fig. 4 a particular wavefunction in nanowire 3-cell long. For these devices, source, channel and drain each shares 1/3 of the total length. The charge density is set to 10^6cm^{-1} in the S/D region and 10^0cm^{-1} in the channel. In Fig. 5 we show the self-consistent potential for a 9-cell long device and in Fig. 6 we compare the characteristics for devices of different length.

Conclusion

We have presented a nontrivial extension of QTBM to account for the full band structure and improved the computational efficiency by ignoring a subset of evanescent waves. For the application, we have shown simulation results of Si nanowires.

References

[1] B. Fu, and M.V. Fischetti, IWCE13 (2009)
[2] C.S. Lent and D.J. Kirkner, Journal of Applied Physics **67**, 6353 (1990).
[3] S.B. Zhang, C. Yeh, and A. Zunger, Phys. Rev. B **48**, 11204 (1993).

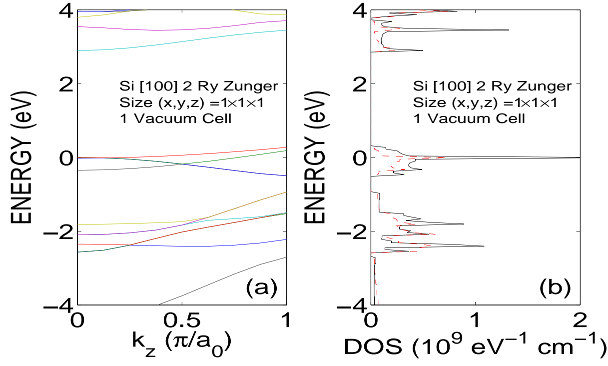

Fig. 1. Empirical pseudopotential band-structure (a) and density of states (b) for a [100] Si nanowire.

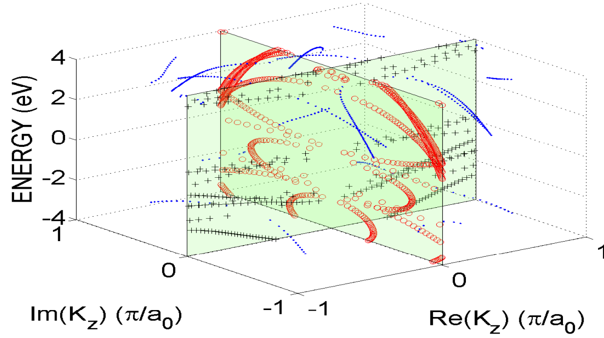

Fig. 2. Complex band structure of a Si [100] nanowire. Black crosses and red circles denote real and imaginary wavevectors, respectively, while the blue symbols denote fully complex wavevctors. The green planes show the projections of the dispersion onto the real and imaginare kz-planes.

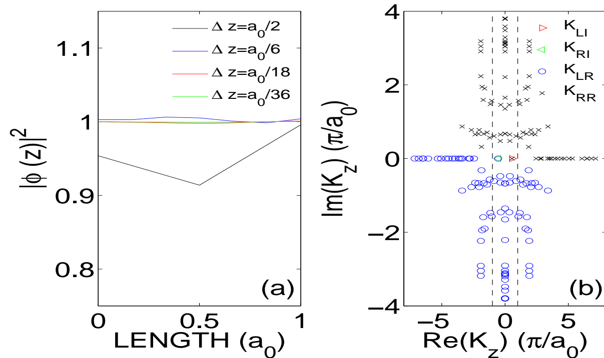

Fig. 3. Evolvement of propagating waves (a) under different choices of real space discretization Δz and reflected states k_z (b) at an incoming energy E=-1.5V.

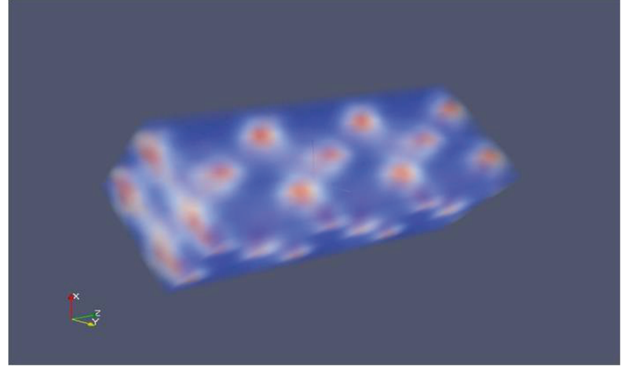

Fig. 4. Squared amplitude of a propagating wavefunction in a 3-cell long Si nanowire calculated using empirical pseudopotentials.

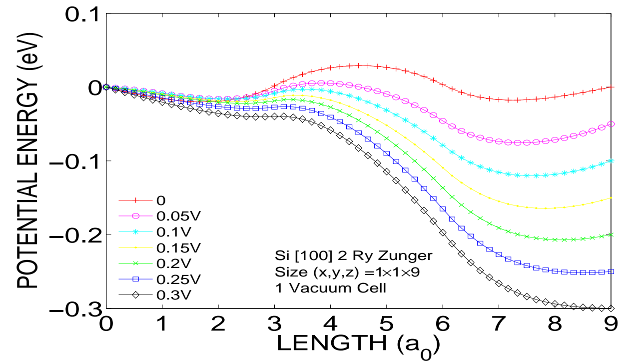

Fig. 5. Self-consistent potential energy for a 9-cell Si nanowire as a function of the applied bias.

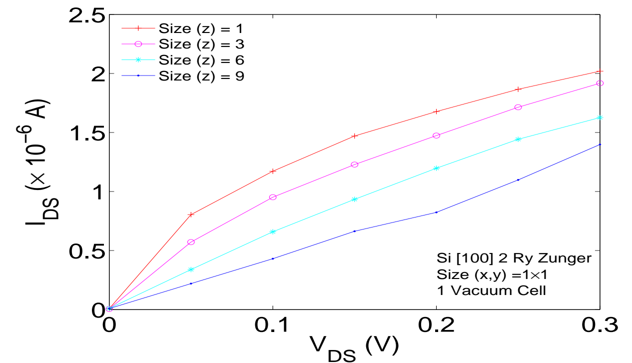

Fig. 6. I-V characteristics of 1, 3, 6 and 9-cell Si nanowires.

Electronics with 2D Semiconductors and their Heterostructures

Sayeef Salahuddin
Department of Electrical Engineering and Computer Sciences,
University of California Berkeley, CA

Two dimensional layered materials such as metal dichalcogenides are currently being investigated extensively due to their potential application in next generation electronics. One of the main reasons for 2D materials to be of interest is their inherent advantage in terms of electrostatics. As the channel length of the transistor is downscaled, there is a need to reduce the 'effective' body thickness as well to make sure that 2-D electrostatic effects are reduced [2].To understand why this is the case, one may define an *effective screening length* λ, which is the characteristic length within which potential variations along the length of the channel are screened out [3]. This means that, beyond a length of λ, the channel can effectively screen out the electric field coming from the drain, thereby maintaining a 1-D electrostatic profile. For ultra-scaled MOSFETs it is then desirable to have λ as small as possible. While the exact form of λ depends on the details of the device structure, for single and double gate geometries it can be approximated by [3] –

$$\lambda = \sqrt{\frac{\varepsilon_s d_s d_{ox}}{\varepsilon_{ox}}} \quad \text{(single-gate)} \qquad (1)$$

$$\lambda = \sqrt{\frac{\varepsilon_s d_s d_{ox}}{2\varepsilon_{ox}}} \quad \text{(double-gate)} \qquad (2)$$

Here, ε_s and d_s denote the dielectric constant and thickness of the semiconductor respectively and ε_{ox} and d_{ox} are the respective quantities for the oxide. From (1) and (2), it is clear that to have λ as small as possible, d_s needs to be small (thin films). Surely, in this context the 2D materials represent the best possible scenario that nature has to offer. We have recently shown using atomistic simulations [4] that it transistors that use these 2D materials as channel could potentially be highly attractive for low power applications (see Fig. 1.).

Nonetheless, 2D semiconductor di chalcogenides could be particularly interesting for developing new heterostructures. The 2D nature and compensated surface indicate that such heterostructures could be made to be abrupt and defect free. Additionally the possible configurations in which such heterojunctions could be extremely large. For example, one could make these vertically or horizontally. Going beyond just 2D-2D heterostructures it is possible to make them from 3D-2D, 1D-2D interfaces as well. Here, we shall discuss some of our recent work on heterostructures comprised of MoS_2 and amorphous Si. When 3D amorphous Si is combined with 2D MoS_2, a van der Waals diode can be formed that then leads to significantly higher performance for photo detection in terms of sensitivity and speed compared to state of the art. Experimentally such junctions can be formed by simply depositing amorphous Silicon layers on top of mechanically exfoliated MoS_2 layers. If large scale growth for 2D di-chalcogenides could be perfected, such heterotstructures could have a significant impact on future large area electronics applications.

ACKNOWLEDGEMENT

SS would like to thank National Science Foundation CAREER award for supporting this work. SS also thanks Mohammad Esmaeilii for collaborating on this worl.

REFERENCES

[1] B. Radisavljevic et al. Nature Nanotech. 6, 147–150 (2011).
[2J. Knoch, et al (IEDM) Tech. Dig., 173, 2008.
[3] J. Knoch, et al, IEEE Elect. Dev. Lett. 29, 372 (2008).
[4] Yoon et al, Nanoletters, vol. 11, no. 9, pp. 3768-3773, 2011.

 © 2013 Society for Micro- and Nanoelectronics

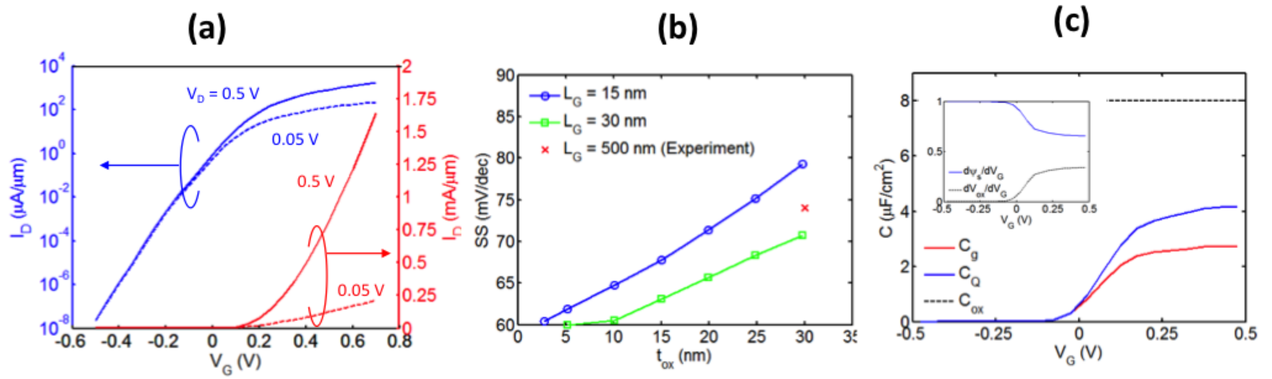

Fig. 1. (a) Transfer characteristic of a monolayer MoS_2 transistor in both log and linear scales. (b) The subthreshold swing as a function of gate oxide thickness for two different gate lengths. (c) Capacitance vs Voltage characteristics. Inset shows the change in surface potential ψ_s with gate voltage V_g . Results adopted from[4]).

Tight-binding modeling of the band structures of monolayer, bilayer, and bulk MoS_2

F. Zahid[1], L. Liu[2], Y. Zhu[2], J. Wang[1], and H. Guo[3,1]

[1]Department of Physics, The University of Hong Kong, Hong Kong SAR, China
[2]Nanoacademic Technologies Inc., Brossard, Quebec, J4Z 1A7, Canada
[3]Department of Physics, McGill University, Montreal, PQ, Canada, H3A 2T8
E-mail: fzahid@hku.hk

ABSTRACT

Molybdenum disulfide (MoS_2) belongs to a family of layered transition metal dichalcogenides (TMDC) in which the layers are held together by weak van der Waals forces, and it can be exfoliated mechanically to a single layer thickness. In its bulk form MoS_2 is an indirect band gap semiconductor which turns into a direct band gap semiconductor for monolayer structure [1]. This intrinsic semiconducting nature of MoS_2 is a major advantage over graphene as a channel material in field-effect transistors (FET). Recently, FET devices based on MoS_2 monolayer and bilayer have been fabricated in the experimental labs and demonstrated to have useful device performances [2]. Several theoretical studies of MoS_2 FET devices have also been reported [3,4], most of which are based on simplified description of the electronic structures within an effective mass approximation. However, we believe that due to the complex nature of the layered TMDC materials it may require more reliable, accurate, and atomistic treatment of the electronic structures.

Here, we report a parameterized non-orthogonal tight-binding (TB) model with sp^3d^5 orbitals, nearest-neighbor interactions, and spin-orbit coupling for bulk, monolayer and bilayer MoS_2. For the TB parameterization of the band structures we employed a recently developed software package named Nanoskif. Our TB scheme is based on the Slater-Koster model [5]. For the calculations of the target band structures we employ density functional theory (DFT) with the screened hybrid functional of Heyd, Scuseria, and Ernzerhof (HSE) [6] within a projector augmented-wave (PAW) pseudopotential plane-wave method as implemented in the VASP software package. It has been shown in previous studies that accurate band structures for a wide range of semiconductors can be obtained with the screened hybrid functional. Spin-orbit coupling is included self-consistently in all the calculations. For the structure relaxation we have taken into account of the van der Waals interactions between the layers of MoS_2. Excellent agreement with the experimental data for the band gaps is achieved by adjusting the screening parameter of the hybrid functional. In our tight-binding model with a same set of parameters (in total 96) we are able to reproduce accurately the band structures for three different forms of MoS_2: bulk, monolayer and bilayer. Another important feature of our tight-binding scheme is that it can be easily extended to other layered TMDC materials showing electronic characteristics similar to MoS_2 such as WS_2, WSe_2, and $MoSe_2$. The accuracy of our tight-binding fitting is validated by comparing the band structures (Fig.1), band gap values (Table 1) and the shape of the bands at the band edges (Fig.2) with our calculated *ab initio* results. The root-mean-square deviation of the fitting is within about 25 meV.

REFERENCES

[1] K. F. Mak, C. Lee, J. Hone, J. Shan, and T. F. Heinz, Phys. Rev. Lett. **105**, 136805 (2010).
[2] B. Radisavljevic, A. Radenovic, J. Brivio, V. Giacometti, and A. Kis, Nat. Nanotechnol. **6**, 147 (2011).
[3] Y. Yoon, K. Ganapathi, and S. Salahuddin, Nano Lett. **11**, 3768 (2011).
[4] L. Liu, S. B. Kumar, Y. Ouyang, and J. Guo, IEEE Trans. Electron Dev. **58**, 3042 (2011).
[5] J. C. Slater and G. F. Koster, Phys. Rev. **94**, 1498 (1954).
[6] J. Heyd, G. E. Scuseria, and M. Ernzerhof, J. Chem. Phys. **118**, 8207 (2003); **124**, 219906 (2006).
[7] A. R. Beal and H. P. Hughes, J. Phys. C **12**, 881 (1979).

978-3-901578-26-7 © 2013 Society for Micro- and Nanoelectronics

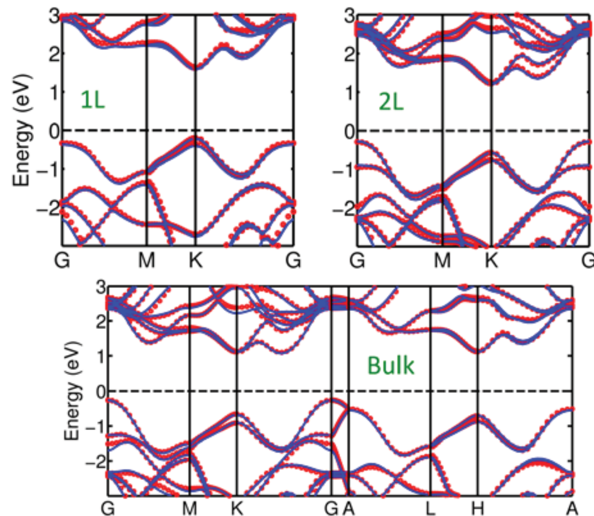

FIG. 1: Band structures for monolayer (1L), bilayer (2L), and bulk MoS_2 using screened hybrid density functional theory (blue lines) and our empirical tight-binding fitting (red dots). The zero in the energy axis is set at the Fermi level as shown by the dashed line. Spin-orbit coupling is included in the calculations.

Structures	Transitions	HSE (target)	TB (fitted)	Deviation (%)	Experiment
Monolayer	K_{v1} to K_c	1.786	1.805	1.06	1.90
	K_{v2} to K_c	1.974	1.969	0.24	2.05
Bilayer	Γ_v to K_c	1.480	1.516	2.41	1.60
	K_{v1} to K_c	1.779	1.792	0.76	1.88
	K_{v2} to K_c	1.980	1.987	0.35	2.05
Bulk	Γ_v to Σ_c	1.328	1.331	0.22	1.29
	K_{v1} to K_c	1.776	1.749	1.46	1.88
	K_{v2} to K_c	1.960	2.009	2.46	2.06

TABLE 1: Values of the band gap energies obtained from HSE calculations (target) and the tight-binding (TB) parameterization (fitted). Experimental data are obtained from Ref. 7 (for bulk) and Ref. 1 (for monolayer and bilayer). All the energies are in the unit of eV. The subscripts 'v' and 'c' stand for valence band and conduction band, respectively. The splitting of the valence band maximum at K point is given by K_{v1} (top) and K_{v2} (bottom), whereas Σ is the midpoint of the line joining the Γ and the K points.

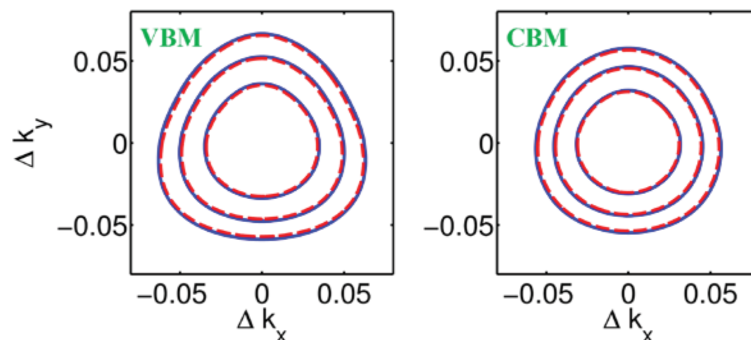

FIG. 2: Contour plots of the energies around the valence band maximum (VBM) and the conduction band minimum (CBM) for monolayer MoS_2 from screened hybrid density functional theory (blue solid lines) and empirical tight-binding fitting (red dashed lines). The contour lines are associated with $\Delta E = \pm(1/30)$, $\pm(1/15)$, and $\pm(1/10)$ eV, respectively, and the Δk_x and the Δk_y are in the unit of $2\pi/a$, where 'a' is the cell length.

Graphene Nanomesh Transistors with high on/off ratio and good current saturation

S. Berrada, V. Hung Nguyen*, A. Alarcón, D. Querlioz, J. Saint-Martin,
A. Bournel, C. Chassat and P. Dollfus
Institute of Fundametal Electronics, CNRS, Univ. of Paris-Sud, Orsay, France
*L_Sim, SP2M, UMR-E CEA/UJF Grenoble 1, INAC, Grenoble, France
e-mail: salim.berrada@u-psud.fr

INTRODUCTION

Pristine graphene is a semimetal with excellent transport properties [1]. However, its gapless character limits the possible range of applications of graphene transistors (GFET), as it yields small on/off current ratio and poor saturation behaviour [2]. Bilayer graphene and graphene nanorribons are graphene based materials that exhibit bandgap, but their use in GFETs remains a difficult task. In fact, bilayer graphene offers quite low bandgaps – around 130 meV [3] – and the fabrication of narrow-enough (sub-3 nm) ribbons with good edge roughness control remains challenging. Recently, the fabrication of graphene nanomesh (GNM) – a regular array of antidots separated by a sub-10 nm distance (see Fig. 1a) – has been reported [4]. Depending on the periodicity and the neck width of GNM lattice, bandgaps up to several hundreds of meV have been predicted to appear in large sheets of graphene [5,6]. Similar result can be obtained in superlattices of graphane-like islands formed by patterned adsorption of hydrogen atoms [7]. This kind of bandgap nanoengineering offers new possibilities to design improved devices delivering large currents [8].

MODEL, SIMULATED DEVICE AND RESULTS

In the present work, we investigate a GNM-based field-effect transistor (GNM-FET) by means of 3D numerical simulation. The model is based on the Green's function approach to solving a tight-binding Hamiltonian, self-consistently coupled to 3D Poisson's equation [9]. A 3D view of the simulated GNM-FETs is shown in Fig. 1b, with a gate length $L_G = 30$ nm and infinite width thanks to appropriate periodic boundary conditions along y direction. Comparison to a similar pristine graphene FET (GFET) is then provided.

The considered GNM has a bandgap of 508 meV, leading to an On/Off ratio as high as 1460 at $V_{DS} = 0.2$ V at room temperature. (Fig.2). We also note that increasing V_{DS} shifts the Dirac point (DP) toward higher V_{GS} for GNM-FETs while it is shifted toward lower V_{GS} for pristine GFETs, as shown in Fig. 3. This is due to the different conduction regimes that take place at DP for each device. The DP current (DPC) in pristine GFET results from the balance between the thermionic current and the chiral tunneling current through the gate-induced barrier [9]. In GNM-FET, the chiral tunneling is suppressed by the bandgap at DP. It can take place only at negative V_{GS}. The DP current is now resulting from the equilibrium between the thermionic current and the band-to-band tunneling current (BTBT). It is illustrated by the LDOS (for $k_y = 0$) and transmission at DP for $V_{DS} = 0.2$ V in Fig. 4. While at DP the chiral tunneling reduces when increasing V_{DS} in pristine GFET [9], the BTBT increases in GNM-FET. This explains why the DP moves differently as a function of V_{DS}. It is also remarkable that the GNM-FET provides a good saturation of current as a function of V_{DS} in the n-branch when the current is governed by the thermionic contribution. Indeed, thanks to the bandgap in the channel, the onset of BTBT is delayed to V_{DS} values higher than 0.5 V, which preserves a significant V_{DS} range of saturation.

We found the same behaviors for GNM-FETs with other neck widths and higher and lower energy gaps.

CONCLUSION

This work shows that well-designed GNM-FETs might offer both a high On/Off ratio and good saturation, making it a promising way to improve the operation of graphene based transistors.

978-3-901578-26-7 © 2013 Society for Micro- and Nanoelectronics

REFERENCES

[1] K.I. Bolotin et al., Solid-State Com 146 (2008) 351-355.
[2] Ph. Avouris, Nano Lett.10 (2010) 4285–4294.
[3] J.B. Oostinga et al., Nat. Mater. 7 (2008) 151-157.
[4] J. Bai, et al., Nat. Nanotechnol. 5 (2010) 190-194.
[5] T.G. Pedersen et al., Phys. Rev. Lett. 100 (2008) 136804.
[6] V. Hung Nguyen et al., J. Appl. Phys. 113 (2013) 013702.
[7] R. Balog et al., Nature Mater. 9 (2010) 315-319.
[8] V. Hung Nguyen, et al Nanotechnology 23 (2012) 065201.
[9] A. Alarcon et al., IEEE Trans. Electron Devices, 60 (2013) 985-991.

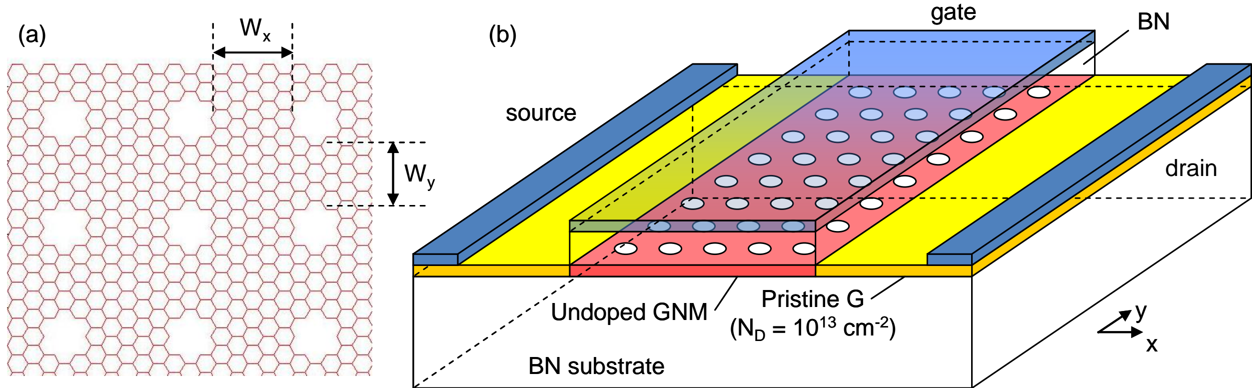

Fig. 1. (a) Typical view of a GNM lattice characterized by the neck widths W_x and W_y. (b) Schematic 3D view of the GNM-FET. The gate length is $L_G = 30$ nm, the BN gate insulator thickness is 2 nm. The GNM neck widths are $Wx \approx 1.1$ nm, $Wy \approx 0.9$ nm.

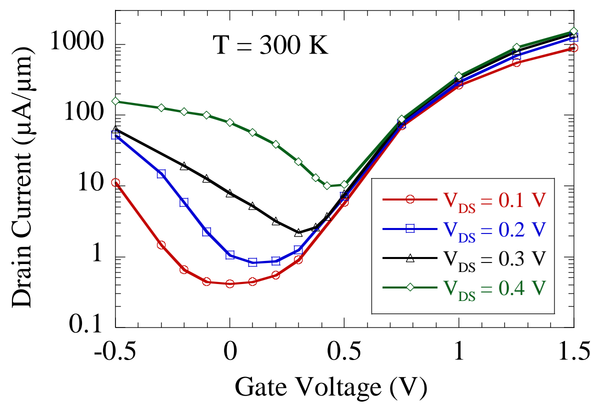

Fig. 2. Transfer characteristics of the GNM-FET.

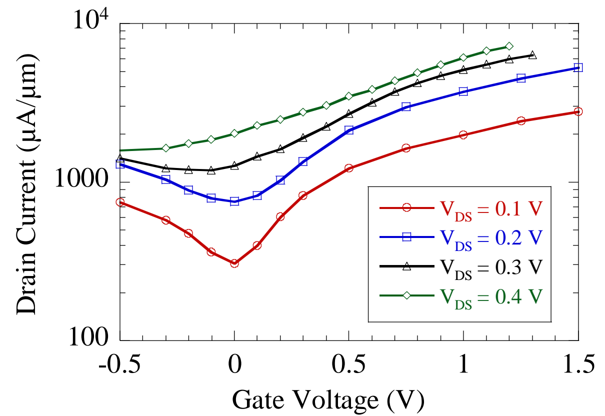

Fig. 3. Transfer characteristics of the Pristine GFET.

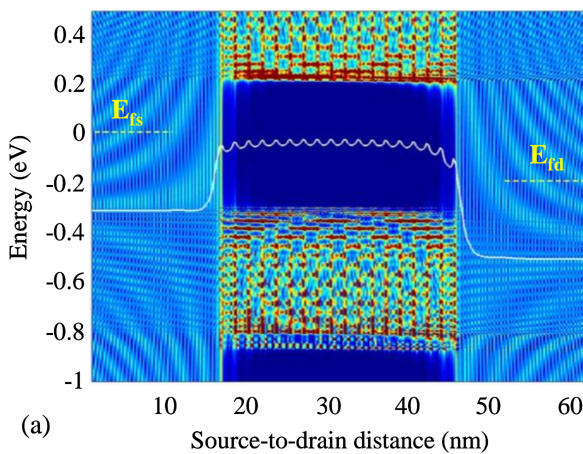

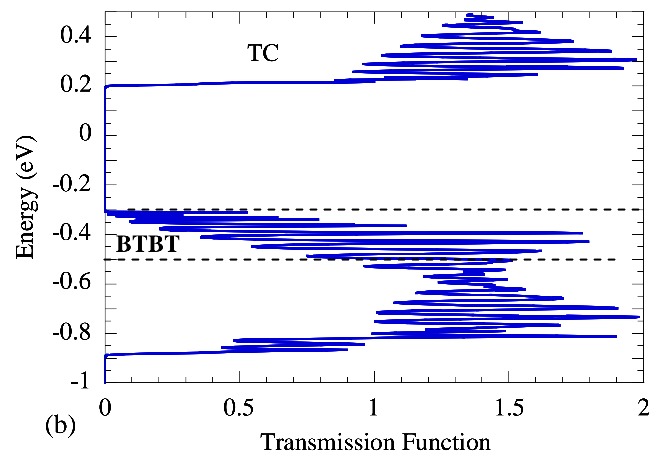

Fig. 4. (a) Local density of states for $k_y = 0$ in the GNM-FET for $V_{DS} = 0.2$ V, $V_{GS} = 0.1$ V (Dirac point). The potential profile at the center of the device is superimposed (line). (b) Corresponding transmission function, with contributions of thermionic current (TC) and band-to-band tunneling (BTBT).

Effects of charged impurity clusters on the conductivity of supported graphene

N. Sule,* K. J. Willis,† S. C. Hagness,* and I. Knezevic*
*University of Wisconsin Madison, Madison, WI 53706 USA
†AWR Corporation, 11520 North Port Washington Road, Mequon, WI 53092, USA
e-mail: sule@wisc.edu

Charged impurities can be introduced into graphene samples by typical fabrication and processing techniques, and can persist even after annealing [1]. Recent imaging experiments using scanning tunneling microscopy show electron-hole puddles in graphene with an average size of 20 nm [2], and point towards a clustered impurity distribution in graphene samples. It is evident that clustered or spatially correlated impurities play an important role in determining the conductivity of graphene [3], [4]. A reliable and quantitative determination of the effects of such impurities on carrier transport in graphene supported on $\mathrm{SiO_2}$ is important for the design of graphene-based applications. We have combined particle-based transport simulations using the ensemble Monte Carlo (EMC) method, with numerical long-range and short-range field solvers using the finite-difference time-domain (FDTD) technique and molecular dynamics (MD), respectively, to simulate the formation of electron-hole puddles, and study the effect of charged impurity distributions on the conductivity of graphene supported on $\mathrm{SiO_2}$. The coupled EMC-FDTD-MD algorithm has been used to calculate the high-frequency conductivity of bulk silicon [5], [6] with very good agreement to experimental data.

The simulated structure, shown in Figure 1, consists of a monolayer of graphene on top of an $\mathrm{SiO_2}$ substrate. Clusters of impurity ions are present at and near the interface between graphene and the substrate. We simulate an infinite graphene monolayer by using periodic boundary conditions on the fields and the carrier momentum. Doing so eliminates any edge-effects, thus focusing on the effects of impurities on carrier transport. The charged impurity clusters are stochastically initialized using a correlation length parameter to define the average size and distribution of the clusters.

By simulating carrier dynamics without any external fields, we calculate the steady-state electron and hole density distributions for a uniform random, as well as a clustered impurity distribution (Figs. 2a and b, respectively). The average size of the electron-hole puddles, calculated using the full width at half maximum (FWHM) of the normalized spatial auto-correlation functions of the density distributions, shown in Figs. 2c and d, are about 4 nm and 20 nm for the uniform random and clustered impurity distributions, respectively. Figure 2e shows a plot of the average electron-hole puddle size as a function of the average impurity cluster size. Thus, we show that impurity clusters between the sizes of 30 and 40 nm are responsible for producing electron-hole puddles quantitatively similar to those seen in experiments [2].

We calculate the conductivity in graphene as a function of the carrier density, under *dc* excitation for impurity-free, as well as for uniform random and clustered impurity distributions, with an impurity density of 10^{11}–10^{12} cm^{-2}, and average cluster size of 36 nm (Figs. 3a–d). It is seen that, for impurity densities greater than 10^{11} cm^{-2}, the distribution of impurities (random or clustered) significantly affects both the sublinearity and the slope of the linear region in the carrier-density dependence of conductivity. By turning off/on specific terms in the MD to elucidate the effect of short-range carrier-carrier and carrier-ion interactions, we find that the sublinearity in conductivity as a function of carrier density is due to direct and exchange carrier-carrier interactions limiting transport. Moreover, the slope of the linear region is strongly dependent on the short-range carrier-ion Coulomb interaction, and therefore on the density and distribution of the impurities.

In conclusion, we show that clustered impurities, as well as the resulting short-range carrier-ion, and carrier-carrier interactions play an important role in determining the room-temperature conductivity of supported graphene.

References

[1] Lin Yung-Chang, Lu Chun-Chieh, Yeh Chao-Huei, Jin Chuanhong, Suenaga Kazu, and Chiu Po-Wen, *Graphene Annealing: How Clean Can It Be?*, Nano Lett. **12**, 414–419 (2012).

[2] A. Deshpande, W. Bao, Z. Zhao, C. N. Lau, and B. J. LeRoy, *Imaging charge density fluctuations in graphene using Coulomb blockade spectroscopy*, Phys. Rev. B **83**, 155409 (2011).

[3] Yan Jun, and Fuhrer Michael, *Correlated Charged Impurity Scattering in Graphene*, Phys. Rev. Lett. **107**, 206601 (2011).

[4] Li Qiuzi, E. H. Hwang, E. Rossi, and S. Das Sarma, *Theory of 2D Transport in Graphene for Correlated Disorder*, Phys. Rev. Lett. **107**, 156601 (2011).

[5] K. J. Willis, S. C. Hagness, and I. Knezevic, *Terahertz conductivity of doped silicon calculated using the ensemble Monte Carlo/finite-difference time-domain (EMC/FDTD) simulation technique*, Appl. Phys. Lett. **96**, 6 (2010).

978-3-901578-26-7 © 2013 Society for Micro- and Nanoelectronics

[6] K. J. Willis, S. C. Hagness, and I. Knezevic, *Multiphysics simulation of high-frequency carrier dynamics in conductive materials*, J. Appl. Phys. **110** 063714 (2011).

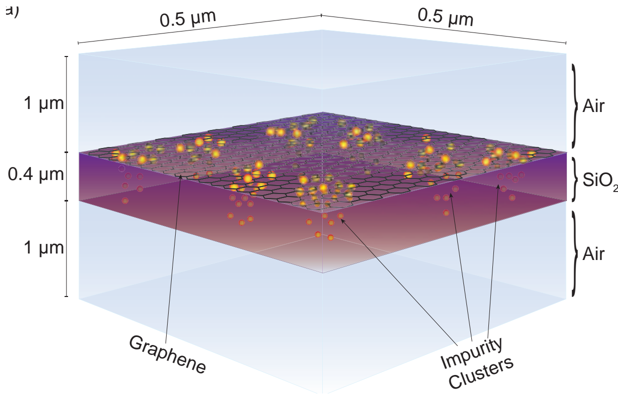

Fig. 1. A schematic of the simulated structure showing the graphene, SiO_2 substrate, and air layers, as well as impurity clusters between, and below the interface of graphene and the substrate.

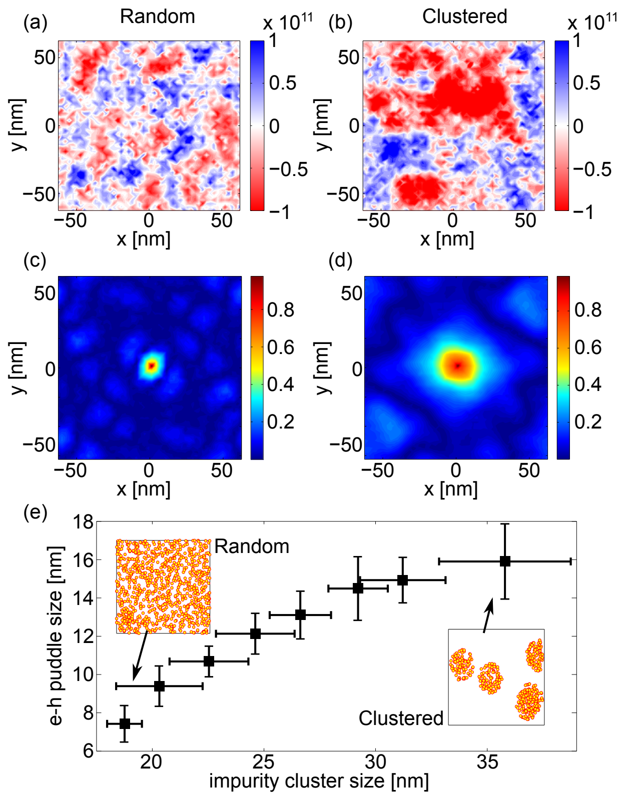

Fig. 2. Carrier-density distribution depicting the electron-holes puddles formed in graphene for (a) uniform random and (b) clustered impurity distributions with impurity density equal to 8×10^{11} cm^{-2}. The average size of the electron-hole puddles is estimated from the FWHM (yellow ring) of the normalized spatial auto-correlation function (SACF), is shown in (c) and (d), corresponding to the (a) random and (b) clustered impurity distributions, respectively. The estimated puddle size from (c) is 4 nm and that from (d) is 20 nm. (e) Plot of the mean electron-hole puddle size as a function of the mean impurity cluster size. Each data point in this plot is an average of 14 simulation runs and the error bars on data points denote the standard deviations.

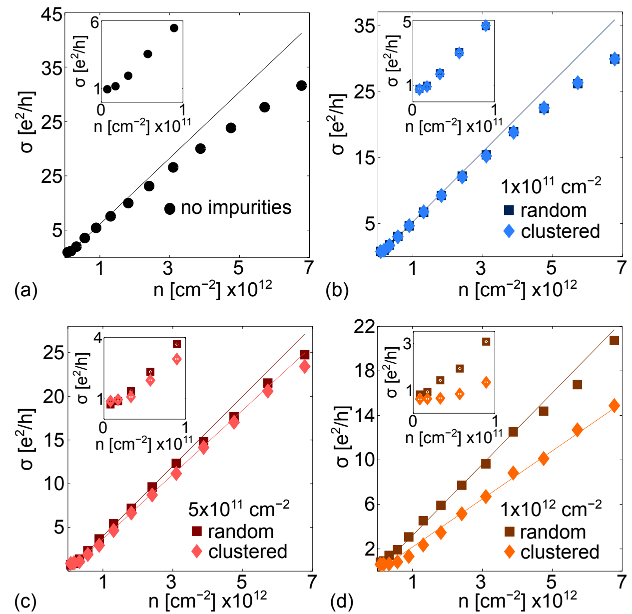

Fig. 3. Conductivity of graphene supported on an SiO_2 substrate as a function of the carrier-density for (a) impurity-free graphene, and for an impurity density of (b) 10^{11} cm^{-2}, (c) 5×10^{11} cm^{-2}, and (d) 10^{12} cm^{-2}. The square and diamond markers denote results for a uniform random and a clustered distribution of impurities, respectively. The insets in all of the above panels show a deviation from the linear decrease in conductivity at very low carrier densities ($< 10^{11}$ cm^{-2}), with the conductivity saturating near the value of e^2/h.

First-principles study of CO_2 and NH_3 adsorption on armchair graphene nanoribbon

M. Manoharan[1], Shinri Inoue[1], and Hiroshi Mizuta[1, 2]
[1]School of Materials Science, Japan Advanced Institute of Science and Technology, 1-1 Asahidai, Nomi, Ishikawa, 923-1292, Japan
[2]School of Electronic and Computer Science, University of Southampton, Southampton SO17 1BJ, U.K
e-mail: mano@jaist.ac.jp

Graphene is a most attractive candidate for high sensitivity gas sensor because graphene has highest surface-to-volume ratio. In this research, First-principle calculations are performed to study the adsorption of CO_2 and NH_3 gas molecules on armchair graphene nanoribbons (AGNR). The electronic and transmission properties are calculated based on Density functional Theory (DFT) and Non equilibrium green function formalization based on DFT implemented in the OpenMX package [1]. A system consisting of a central region connected to the left and right leads of infinite size, as shown in Fig. 1, is considered in this work. The structure given in Fig. 2 was used for initial configuration of the CO_2 adsorbed on AGNR.

To find the optimum distance between the molecule and the AGNR channel, adsorption energy calculations were performed. The adsorption energy is defined as $E_{Ads}=E_{AGNR-Gas}-(E_{AGNR} + E_{Gas})$, where $E_{AGNR-Gas}$ is the total energy of the AGNR with the gas molecule adsorption. E_{AGNR}, E_{Gas} are the energies of the isolated AGNR and the isolated corresponding gas molecule, respectively. The calculated adsorption energies of the CO_2 and NH_3 molecules are -0.1861 eV and -0.1528 eV, respectively. These results indicate that both CO_2 and NH_3 gas molecules are physisorptions nature on AGNR with the low adsorption energies.

In order to understand the charge transfer mechanism between the molecules and AGNR, the Mulliken population analyses were performed. The Table given in Fig. 3 shows the Mulliken population of each atom of the CO_2 and NH_3 molecules. It gives the values of the atomic charge transfer of each atom and the net charge transfer between the molecule and AGNR. For the CO_2 adsorption, we can see that there is small amount of 0.008679 e charge transfer from the AGNRs to the CO_2 molecule. This indicates that CO_2 adsorption acts as acceptor. In contrast, there is 0.088381e charge transfer from the NH_3 molecule to the AGNR, which indicates that NH_3 act as donor.

Fig. 4 and Fig 5 show the density of states (DOS) and the transmission spectra of the pristine AGNR, AGNR with CO_2 adsorption and AGNR with NH_3 adsorption. In the case of the CO_2 adsorbed on AGNR, the DOS is modified weakly because the interaction between CO_2 molecule and ANGR is weak as indicated by the mulliken population analysis. The corresponding transmission spectrum shows the reduction of the transmission. However, the DOS and the transport spectrum are changed considerable in the case of NH_3 adsorption. The emergence of the mid-gap state and the reduction in the transmission can be noticed for the NH_3 adsorption, which is consistent with the strong interaction between the NH_3 molecule and the AGNR indicated by the mulliken population analysis. Fig. 6 shows the IV characteristics of the AGNR device with a CO_2 and NH_3 molecules. Even though a small charge transfer occurs in the CO_2 adsorption the reduction in the current is remarkable, which is attributed to the remote Coulomb scattering [2].

The analysis of the charge transfers demonstrate that NH_3 and CO_2 absorbed on AGNR exhibit n-type and p-type doping, respectively. The remarkable reduction of the current with the CO_2 adsorption indicates the dominant nature of the remote Coulomb scattering.

REFERENCES

[1] http://www.openmx-square.org/
[2] Y Sato, K Takai, T Enoki Nano letters, 11, 3468–3475, 2011

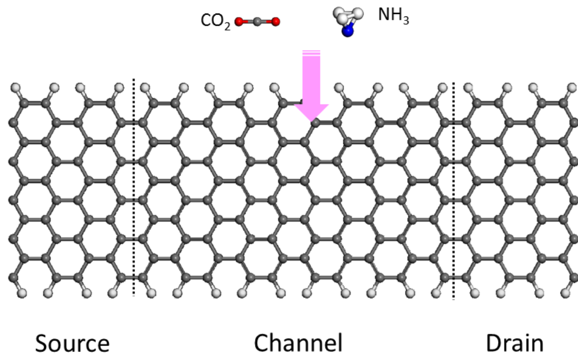

Fig. 1. The Configuration of the AGNR device treated by the transport calculation.

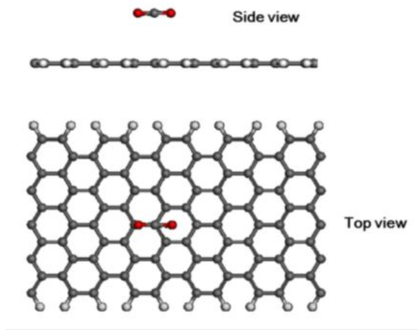

Fig. 2. Side view, and top view of the initial configuration of CO_2 molecule on the AGNR channel.

	CO_2			NH_3			
	C	O(1)	O(2)	N	H(1)	H(2)	H(3)
Mulliken population (*e*)	3.999	6.004	6.003	5.879	0.676	0.676	0.6766
Total charge transfer (*e*)	-0.008848 -> Acceptor-like			0.1346 -> Donor-like			

Fig. 3. Mulliken population analysis result of the CO_2 and NH_3 molecules on the AGNR channel.

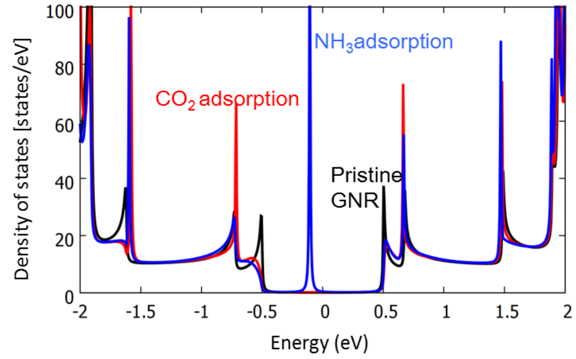

Fig. 4. Density of states of the Pristine AGNR, the AGNR with a single CO_2 molecule adsorption, and the AGNR with a single NH_3 molecule adsorption.

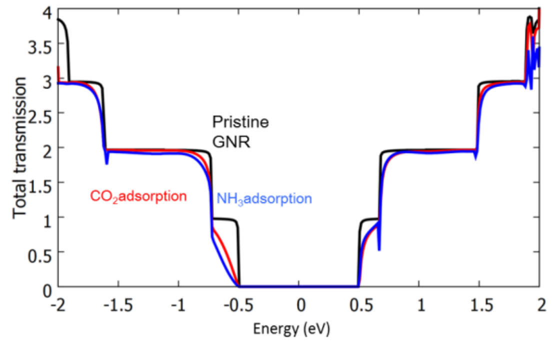

Fig. 5 The transmission spectrum of the Pristine AGNR, the AGNR with a single CO_2 molecule adsorption, and the AGNR with a single NH_3 molecule adsorption**.**

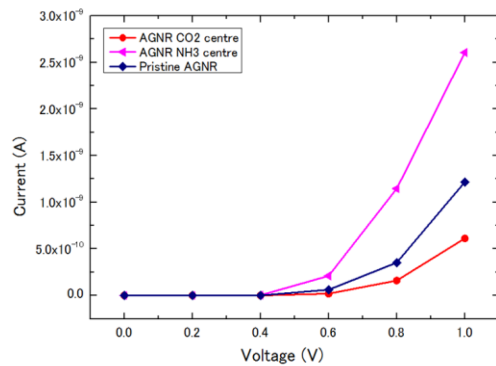

Fig. 6 I-V characteristics of a single molecule of CO_2, NH_3 adsorbed on AGNR and the pristine GNR.

Multiscale Simulation of Epoxide Adsorbate Functionalization on Graphene Nanoribbons:

A. Afzalian, A. Lherbier*, J.-C. Charlier*, and D. Flandre
ICTEAM Institute, Université catholique de Louvain (UCL), Louvain-la Neuve, Belgium,
*IMCN Institute, Université catholique de Louvain (UCL), Louvain-la Neuve, Belgium,
e-mail: Aryan.afzalian@uclouvain.be

Chemical functionalization of graphene has retained much attention of late, because of its promise to open a gap as needed for transistor operation [1,2]. Determining the impact of specific surface adsorbed molecules is also very relevant for bio or chemical sensing applications for which graphene excellent properties have been demonstrated [3]. Among the studied groups, epoxide adsorbates, easily produced by ozone decomposition on graphene surface, have shown interesting properties [1,2] and will be considered here as a case of study. At the device level, simulating the possibilities offered by functionalization require to innovatively combine traditional ab initio material property methods with tools used for charge transport such as NEGF (Non Equilibrium Green's Functions). Here, we investigate the possibility to use such a multi-scale approach by simulating a full graphene nanoribbon (GNR)-FET using a Self-Consistent NEGF code and a Tight-Binding (TB) Hamiltonian model with local perturbation parameters related to the local epoxide surface functionalization fitted to match DFT ab initio results.

N=12 armchair (12-a)-GNRs with $2x10^{13}cm^{-2}$ N-doped source and drain contacts with and without chemical functionalization were simulated using our 3D self-consistent NEGF solver. A real space (RS) TB Hamiltonian based on a set of orthogonal p_z orbitals, one for each atom, a first nearest neighbor (1N) interactions and including edge perturbation was used [4]. Locally, the ozone decomposition resulting in epoxide surface functionalization consists in an oxygen atom covalently bound to two carbons atoms. Here we have used a renormalized version of the accurate TB Hamiltonian model fitted to DFT results presented in [2] that yields band structure in good agreement with DFT results obtained using the SIESTA package [5] in the energy range relevant for transport (Fig. 1).

Fig. 2 shows the resulting $I_D(V_G)$ characteristics with 0 and 1 functionalized oxygen atom at various positions in the central slab of the channel. The device properties are changed and depend on bound position. To explain this behavior, the conduction (E_C) and valence (E_V) energy subbands profile versus channel direction x were extracted by solving a transversal Schrödinger equation for each slab Hamiltonian [6]. 1st E_C and E_V are shown together with a plot of the current spectrum in Fig. 3. As can be seen, a local barrier in the central slab, stronger for E_V than for E_C, is created when the functionalization happens at the upper edge of the slab ($y=y_6$). In this case the highest barrier, hence the lowest current, is observed for the oxygen atom bound to the x=2 and x=3 atoms of the slab (x- position), while the barrier is lower when bounded to the x=3 and x=4 atoms (x\) (see Fig. 1 for slab positioning notations). When functionalization happens closer to the center ($y=y_4$), the barrier height decreases, hence an increasing current. In the case of the x- position a localized potential well is observed instead of a barrier. This moves the transition from p-type to n-type conduction to lower V_G and increases the minimum off-current.

As a conclusion, the multi-scale approach on surface functionalization we propose here seems promising for simulating the impact of innovative nanoscale material layers or defects on device performances. The simple device analysis obtained here on band edges and current performances corroborates and translates to the device level material results such as n and p-type conductance asymmetry and position related variability observed by DFT simulation at low epoxide defect concentration [1,2].

978-3-901578-26-7 © 2013 Society for Micro- and Nanoelectronics

ACKNOWLEDGEMENT

This work was supported by F.R.S.–F.N.R.S, Belgium.

REFERENCES

[1] N. Leconte et al., *Damaging Graphene with Ozone Treatment: A Chemically Tunable Metal–Insulator Transition, ACS Nano*, **4** (7), 4033 (2010).
[2] A. Cresti, et al., *Oxygen Surface Functionalization of Graphene Nanoribbons for Transport Gap Engineering*, ACS Nano, **5** (11), 9271 (2011).
[3] F. Schedin et al., *Detection of Individual Gas Molecules Adsorbed on Graphene,* Nat. Mater., **6**, 652 (2007).
[4] Y.-W. Son, et al., *Energy gaps in graphene nanoribbons*, Phys. Rev. Lett., **97**, 216803 (2006).
[5] J.M. Soler et. al., *The SIESTA method for ab initio order-N materials simulation*, J. Phys. Cond. Mater., **14**, 2745 (2002).
[6] R. Grassi, et al., *Mode space approach for tight-binding transport simulation in graphene nanoribbon FETs*, IEEE Trans. on Nanotechnology, vol. 10, pp. 371-378, 2011.

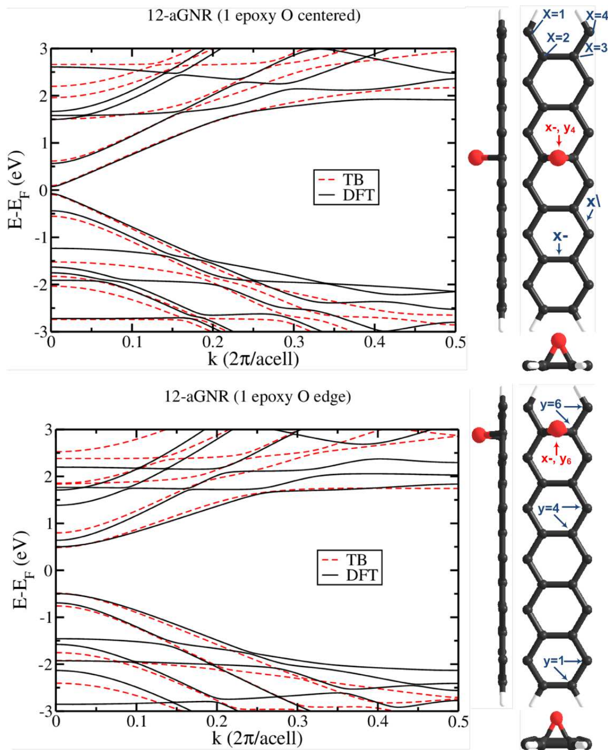

Fig. 1. 12-a-GNRs band structure extracted from DFT and a renormalized simpler version of the accurately fitted TB Hamiltonian model proposed in [2] for an epoxy oxygen atom in 2D graphene. This simpler version consists in renormalizing the on-site energy terms of both covalently bound carbon atoms by a shift of +15.597eV. The unit cell used for the band structure calculation (see atomic structure of the slab in the right panel, with C-atoms in black and O-atom in red) is repeated periodically along the transport (x) direction. Two different positions for the O-atom (top: x-, y_4, bottom: x-, y_6) are shown. Band structures obtained by the simplified TB model show a reasonably good agreement with DFT results in the energy range relevant for transport.

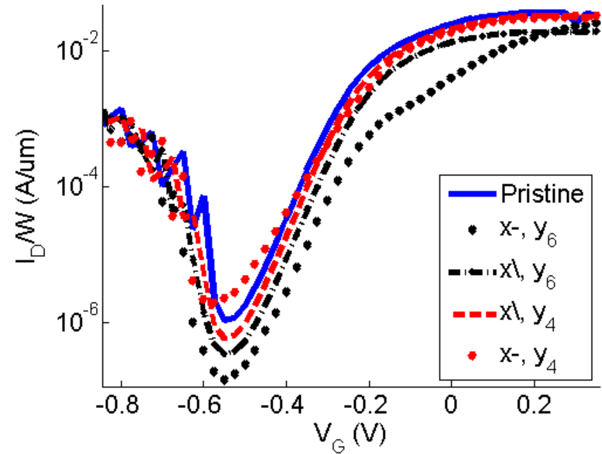

Fig. 2. Simulated $I_D(V_G)$ curves of a 12-a-GNRs with and without chemical functionalization. Source (S) and drain (D): $2x10^{13}cm^{-2}$ N-doped, 60 C-atoms long each. Channel: intrinsic doping, 120 C-atoms long. A bottom gate with an equivalent oxide thickness of 0.5nm was assumed. On top and side of the GNR a 25nm air layer is simulated. D voltage V_D=0.3V.

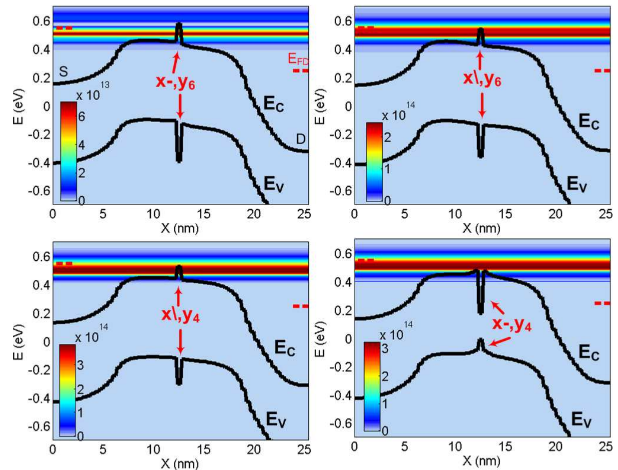

Fig. 3. First conduction and valence subband minimums $E_C(x)$ and $E_V(x)$ respectively (black line) and current spectrum J(x,E) in A/J (surface plot) along the channel for the 4 different epoxide functionalization cases of Fig. 2 . V_G=-0.125V. The positions of S and D Fermi levels are also indicated by a red dashed line at S and D side.

Nonequilibrium Green's function method: Algorithm for regular and irregular leads

Yu Wang, Yu He, Gerhard Klimeck and Tillmann Kubis
Network for Computational Nanotechnology,
Purdue University, West Lafayette, Indiana, USA, 47906
e-mail: wang1613@purdue.edu

INTRODUCTION

State of the art semiconductor devices face coherent quantum effects such as confinement and tunneling, as well as incoherent scattering with device imperfections and phonons. Over the last decade, the non-equilibrium Green's function method (NEGF) became the standard approach to model open nanoscale devices [1]. In this method, leads are either considered to be homogeneous or periodic [2,3]. In reality, however, leads have irregularities in their geometry, doping and alloy structure. Therefore, a method for solving regular as well as irregular leads is introduced in this work.

METHOD

The electronic transport has been solved with the atomistic tight binding NEGF implementation of the multipurpose nanodevice simulation tool NEMO5 [4]. All devices in this abstract are nanowires represented in the atomistic tight binding basis. Nevertheless, this method is applicable on any band structure model, geometry and periodicity (verified within NEMO5). Random alloys results have been averaged over 50 samples of discrete random distributions of the alloy atoms. The surface Green's functions of the leads are solved in a recursive Green's function (RGF) method [5,6]. Hereby, the lead portion that is considered explicitly in the RGF routine is determined by convergence of the lead surface Green's functions. This standard iterative approach is combined with an imaginary damping potential in leads that grows exponentially with increasing distance from the lead/device interface [6]. This damping potential allows limiting the numerical lead size to a few nanometers and is therefore essential for an efficient lead method.

All devices in this abstract are nanowires given in tight binding representation. Observables in the device such as the transmission and the density are obtained with the standard NEGF formula.

RESULTS AND DISCUSSION

To first verify the new lead algorithm, NEGF calculations with the iterative lead method are compared with NEGF calculations with leads solved in the well established transfer matrix method. Atomistic tight-binding NEGF simulations of a homogeneous Si 0.6nm $\times$ 0.6nm nanowire of 4.3 nm length with homogeneous Si leads have been performed using NEMO5. Figure 1 shows that the transmission coefficients resulting in both lead methods agree to a very high precision. Small deviations of the new iterative method are due to imperfect converged lead results typically close to band edges.

The new method can handle leads with arbitrary geometries. Figure 2 illustrates a benchmark device of a 12 nm long, 2 by 0.5 nm wide nanowire. The leads become wider with increasing distance to the device. The transmission of this device is calculated twice: first, only the homogeneous wire section is explicitly considered, while the rest is treated as leads (Fig.2 a). Second, a portion of the leads are explicitly included in the device. Since no bias is applied to the structure, the transmission coefficients of both situations have to agree – as confirmed by the results in Fig.3.

The new lead method can handle leads with random distribution of alloy atoms. Figure 4 shows the transmission in a GaAs nanowire with a 1.1 nm $\times$ 1.1 nm cross section and a length of 5 nm for 3 material configurations: pure GaAs in leads and wire, $In_{0.1}Ga_{0.9}As$ random alloy only in the wire, and $In_{0.1}Ga_{0.9}As$ alloy in the wire and the leads. NEGF results with randomness are averaged over 50 samples. The reduction of the transmission shows the large impact of alloy scattering in device and leads.

978-3-901578-26-7 © 2013 Society for Micro- and Nanoelectronics

Conclusion

A new algorithm is introduced for contact self-energies of general leads in the NEGF formalism. In contrast to existing methods, this method allows to model leads that include randomness fluctuations, such as random alloys and (not shown) random impurities.

ACKNOWLEDGEMENT

This work is support by nanoHUB.org computational resources and by the SRC task 2141.

References

[1] S. Datta, *Quantum Transport: Atom to Transistor*, Cambridge University Press, Cambridge (2005).

[2] M. Luisier, A. Schenk, W. Fichtner, G. Klimeck, *Atomistic simulation of nanowires in the sp3d5s* tight-binding formalism: from boundary conditions to strain calculations*, Phys. Rev. B 74, 205323 (2006).

[3] M. P. L. Sancho and J. M. L. Sancho, *Quick iterative scheme for the calculation of transfer matrices: Application to Mo (100)*, J. Phys. F, Met. Phys. 14, 5 (2000).

[4] S. Steiger, M. Povolotskyi, H.-H. Park, T. Kubis, and G. Klimeck, *NEMO5: A Parallel Multiscale Nanoelectronics Modeling Tool*, IEEE Trans. on Nano. 10, 1464 (2011).

[5] R. Lake, G. Klimeck, R. C. Bowen, D. Jovanovic, *Single and multiband modeling of quantum electron transport through layered semiconductors devices*, J. Appl. Phys. 81, 7845 (1997).

[6] T. Kubis, *Quantum transport in semiconductor nanostructures*, Verein zur Förderung des Walter Schottky Instituts der Technischen Universität München e.V., Garching (2009).

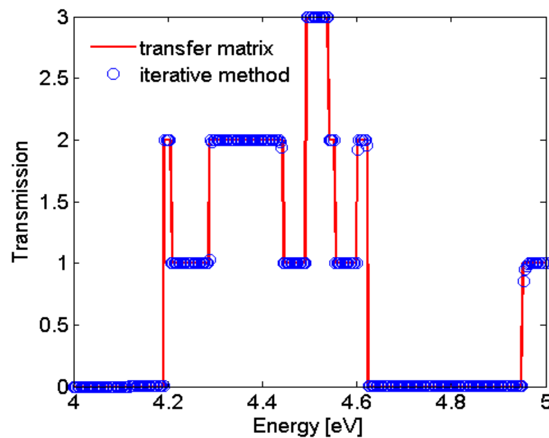

Fig. 1. Transmission coefficient of a homogeneous Si nanowire calculated in the transfer matrix (line) and the new iterative method (symbols).

Fig. 2. 12nm Si nanowire with a 2nm × 0.5nm cross section and conical leads when (a) only the wire is the active device (dark region) and (b) 2.7 nm of the leads are explicitly included.

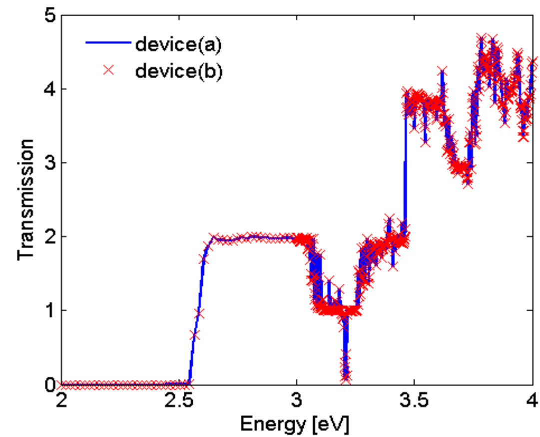

Fig. 3. Comparison of the transmission coefficient of the devices in Fig. 2 (a) (line) and Fig. 2(b) (symbols)..

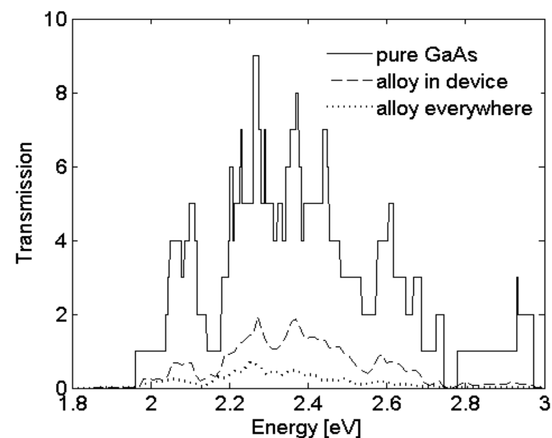

Fig. 4. Comparison of transmission in the pure and alloyed nanowire described in the main text.

Determination of bound states in a device with transmitting boundary conditions

W.G. Vandenberghe and M.V. Fischetti
Department of Materials Science and Engineering, University of Texas at Dallas, Richardson, TX-75080, USA

INTRODUCTION

Quantum transmitting boundary conditions are often imposed to determine the states in an electronic device with contacts. Transmitting boundary conditions also form the basis for most non-equilibrium Green's function (NEGF) simulations of semiconductor devices. The states in the device are calculated by considering a wavefunction with an incoming component from one mode and one contact with outgoing/decaying components in other contacts. In the wavefunction formalism the charge density is calculated by

$$n(\mathbf{r}) = \int \mathrm{d}E f_{\mathrm{L}}(E) \sum_i |\psi_{i,\mathrm{L}}(\mathbf{r};E)|^2 + f_{\mathrm{R}}(E) \sum_i |\psi_{i,\mathrm{R}}(\mathbf{r};E)|^2 \quad (1)$$

or in the non-equilibrium Green's function formalism

$$n = \int \mathrm{d}E f_{\mathrm{L}}(E) \mathrm{diag}\left(G^{\mathrm{R}}(E)\Gamma_{\mathrm{L}}(E)G^{\mathrm{A}}(E)\right) + f_{\mathrm{R}}(E)\mathrm{diag}\left(G^{\mathrm{R}}(E)\Gamma_{\mathrm{R}}(E)G^{\mathrm{A}}(E)\right). \quad (2)$$

BOUND STATES

Despite their widespread use, Eqns. (1) and (2) do not correctly describe the charge in a device if bound states are present. Moreover, even when bound states are not expected to occur in the final solutions, bound states may emerge during an iterative self-consistent process and must be properly identified and accounted for[1].

In the case of a one-dimensional potential profile, at least one bound state will be present if the potential in the device region is lower than the potential in either contact. In a two- or three-dimensional potential profile, there is no straightforward criterion for determining whether or not bound states are present.

METHOD TO DETERMINE BOUND STATES

In general the solution of the states associated with either contact are the solution of a linear system of the form

$$(E\mathbb{1} - H - \Sigma(E))\,\Psi_{\mathrm{L,R}} = I_{\mathrm{L,R}} \quad (3)$$

where $\Sigma(E)$ incorporates the outgoing waves in all contacts and the right hand side $I_{\mathrm{L,R}}$ accounts for the incoming waves from left or right.

If there are bound states in the system, they will be a solution of the homogeneous system

$$(E\mathbb{1} - H - \Sigma(E))\,\Psi_{\mathrm{D}} = 0. \quad (4)$$

which presents a non-linear eigenvalue problem. To solve this problem, we propose a Newton's method.

DISCUSSION

Fig. 1 shows the one-dimensional Pöschl-Teller potential which presents a textbook example of a bound state in a system with a continuous spectrum. We determine the bound states using our method. Fig. 2 and Fig. 3 show a two-dimensional canyon potential and the wavefunction of the first bound state respectively. We use an 8-band $k \cdot p$ Hamiltonian determining the CdTe/HgTe bandstructure [2] (Fig. 5) to calculate the bound states in a CdTe/HgTe/CdTe sandwich (Fig. 4). The first conduction and valence band wavefunctions are shown in Fig. 6 for two different HgTe layer thicknesses. The bound state energies are plotted as a function of HgTe layer thickness in Fig. 7 which reveals the topological insulator transition at $w \approx 6.7\,\mathrm{nm}$[3].

CONCLUSION

We have discussed the presence of bound states in a system with contacts. We have given a method to calculate the bound states and illustrated our method for the case of a one-dimensional potential, a two-dimensional potential and a one-dimensional heterostructure using the $k \cdot p$ method.

REFERENCES

[1] W. R. Frensley. *Rev. Mod. Phys.*, 62:745–791, Jul 1990.
[2] E. G. Novik, A. Pfeuffer-Jeschke, T. Jungwirth, V. Latussek, C. R. Becker, G. Landwehr, H. Buhmann, and L. W. Molenkamp *Phys. Rev. B*, 72:035321, Jul 2005.
[3] B. A. Bernevig, T. L. Hughes, and S.-C. Zhang. *Science*, 314(5806):1757–1761, 2006.

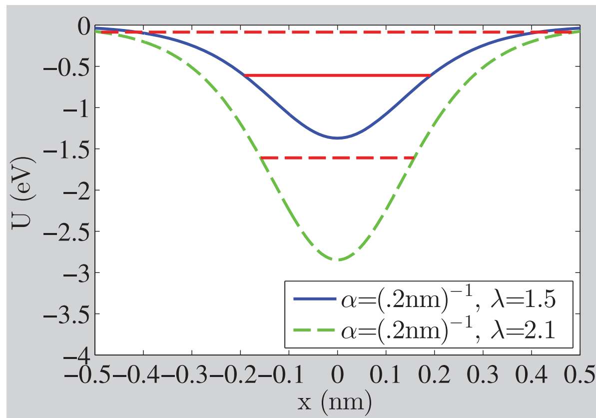

Fig. 1. Illustration of the Pöschl-Teller potential and its bound states.

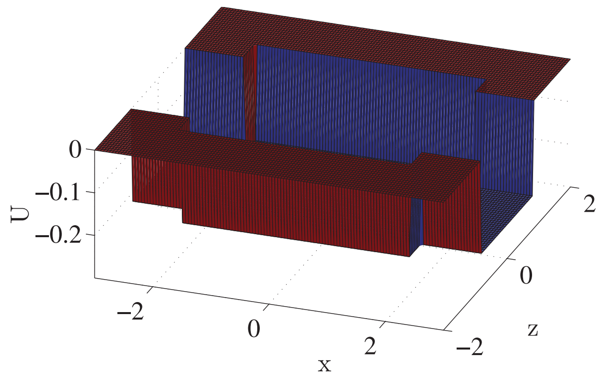

Fig. 2. Illustration of two-dimensional canyon potential harboring a bound state.

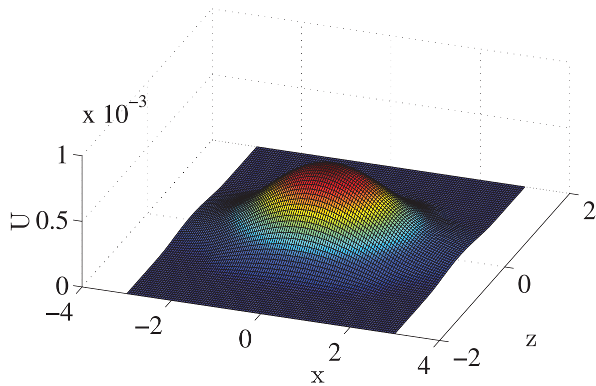

Fig. 3. Square amplitude of the first bound state in the canyon potential illustrated in Fig. 2.

Fig. 4. Illustration of a CdTe/HgTe/CdTe sandwich.

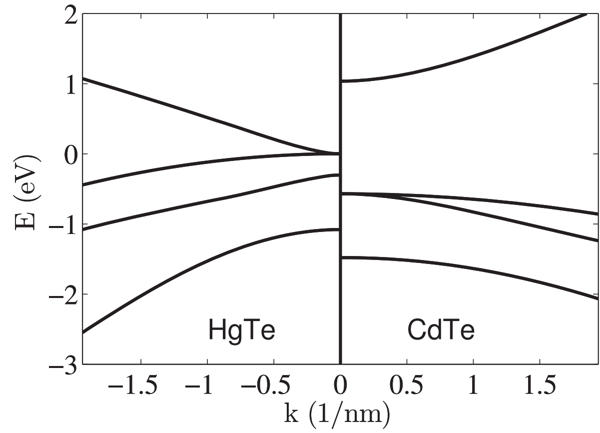

Fig. 5. Illustration of the bulk HgTe (left) and CdTe (right) bandstructure.

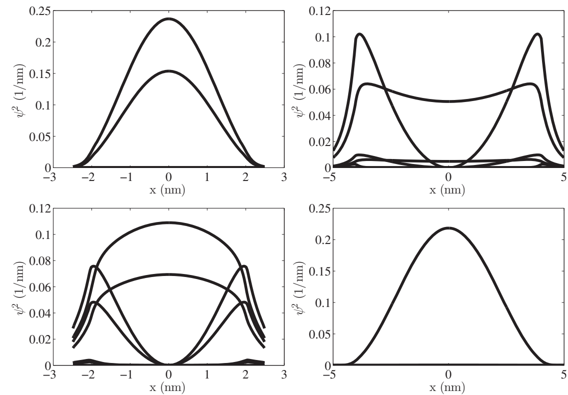

Fig. 6. $k \cdot p$ envelope functions of first conduction (top) and valence (bottom) bands for a 4 nm (left) and a 8 nm (right) sandwich.

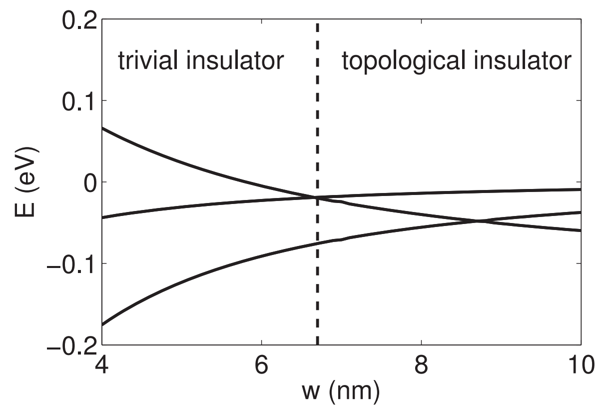

Fig. 7. Evolution of the bound state energies as a function of HgTe thickness. The transition from trivial to topological insulator can be observed at the critical thickness $w \approx 6.7\,\text{nm}$.

A Comprehensive Model for Correlated Drain and Gate Current Fluctuations

W. Goes*, M. Toledano-Luque†, O. Baumgartner*, F. Schanovsky*, B. Kaczer†, and T. Grasser*
*Institute for Microelectronics, TU Wien, Vienna, Austria †imec, Leuven, Belgium

Introduction

Decades ago Andersson *et al.* [1] studied in detail the occurrence of gate current fluctuations in MOS tunnel diodes. As random telegraph noise (RTN) in the drain current has emerged as a serious reliability issue for MOS devices, recent investigations [2, 3] revealed that the fluctuations in the drain and the gate current can be correlated (see Fig. 1). The drain noise has also been investigated in the context of the bias temperature instability (BTI) and is traced back to the capture and emission of substrate charge carriers in the gate oxide. It may be argued that the captured charge locally repels the inversion layer thereby decreasing the direct tunneling current. However, the gate current fluctuations due to this effect can be ruled out due to their small magnitude [4].

Andersson et al. suggested a microscopic picture, in which the capture and emission processes are simply described by a SRH theory. As shown in [5], such a model cannot account for the features usually observed in BTI and noise measurements [5]. However, a multistate model based on nonradiative multiphonon (NMP) processes [6, 7] was proposed that is consistent with all these observations: (*i*) It yields uncorrelated capture (τ_{cap}) and emission (τ_{em}) times. (*ii*) It predicts a strong field dependence of τ_{cap}, ascribed to different curvatures in adiabatic potentials. (*iii*) It can explain the frequency dependence of τ_{cap} by the introduction of an additional metastable state [8]. As an additional benchmark of this model we apply the multistate model to explain correlated drain and gate current fluctuations.

Modeling

The trapping dynamics in the multistate model [5] are illustrated by the state diagram in Fig. 2. In this model the defect features two charge states (positive and neutral) with each having a secondary metastable state besides its equilibrium configuration. The actual hole capture or emission proceed via an NMP transition, whose corresponding rate k can be formulated as an energy integral of the form

$$k = k_0 \int D_{\mathrm{p}}(E) f_{\mathrm{p/n}}(E) \lambda_{\mathrm{p}}(E) f(c_i, c_f, \Delta q_{\mathrm{s}}, \Delta E)\,\mathrm{d}E. \quad (1)$$

$D_{\mathrm{p}}(E)$ and $\lambda_{\mathrm{p}}(E)$ denote the valence band density of states in the inversion layer and the hole WKB factor, respectively. $f_{\mathrm{p/n}}(E)$ is the occupancy with the corresponding charge carrier type and $f(c_i, c_f, \Delta q_{\mathrm{s}}, \Delta E)$ the semiclassical lineshape function (see Fig. 3). The latter gives the probability for an NMP transition and is associated with the intersection of two adiabatic potential energy surfaces along a reaction path. These potentials are usually described by harmonic oscillators, whose parabolic potentials are defined by their curvatures c_i and c_f, their spatial distance Δq_{s}, and their energy separation ΔE in a configuration coordinate diagram ($\Delta E = E - E_{\mathrm{t}}$ for hole capture and $\Delta E = E_{\mathrm{t}} - E$ for hole emission with E_{t} being the trap level). In this study we employ an analytical form [9] for the high-temperature limit of the lineshape function. It accounts for the quadratic electron-phonon coupling using different curvatures of the two parabolic potentials ($c_i \neq c_j$) and is proven to give an excellent approximation at usual device operation temperatures. Also, all combinations of NMP transition rates for electrons and holes from the substrate and the poly gate have been incorporated into our simulations. Besides those NMP transitions, the state diagram in Fig. 2 also involves pure thermal transitions, which are associated with a structural rearrangement and modeled using Arrhenius-type expressions [5].

The full hole capture process encompasses the transition pathway from the neutral state 1 to the positive state 2 over the metastable state 2′ while the respective emission process simply proceeds in the reverse direction. Their respective rates are calculated using first passage times. The trap-assisted tunneling (TAT) current responsible for the gate leakage fluctuations is assumed to be caused by the transitions $1'_{\mathrm{s}} \leftrightarrow 1'_{\mathrm{p}}$ over the state 2 as outlined in Fig. 2.

Results

The multistate model was tested for its ability to also correctly predict the gate leakage fluctuations. For this purpose, we evaluated the model against the experimental data for the nanoscaled pFET device investigated in [2]. Fig. 4 demonstrates that the field and temperature dependence observed for the magnitude of the gate fluctuations is well reproduced by the multistate model. Interestingly, the data exhibit no temperature activation, usually reminiscent of some kind of elastic tunneling. The defect in our fits is located close to the substrate interface ($x_{\mathrm{t}} = 4$ Å) so that the hole capture and emission with the substrate occurs on much shorter timescales than the hole emission into the poly gate. As a consequence, the gate leakage is controlled by the NMP transitions rate $2 \rightarrow 1'_{\mathrm{p}}$, whose configuration coordinate diagram is depicted in Fig. 5. Considering all bandstates, the integral (1) has its dominant contributions from the bandstates that intersect the parabola U_2 around its minimum. These transitions feature negligible NMP barriers so that the overall transition k yield no temperature activation. The multistate model also yields a good agreement for the capture and emission times extracted from the noise measurement (see Fig. 6). Both simulations were carried out for the same set of parameters in order to ensure that the model captures both the gate leakage and the trapping phenomenon at the same time.

Conclusion

This study successfully demonstrates that the multistate model not only describes the charge capture and emission as in BTI and RTN but also gives an explanation for the gate fluctuations caused by TAT. As such, the multistate model provides a comprehensive description of oxide defects causing BTI and gate leakage, thereby further corroborating the validity of this model.

Acknowledgements

This work has received funding from the Austrian Science Fund (FWF) project n° 23390-N24 and the European Communitys FP7 n° 261868 (MORDRED).

References

[1] M. Andersson et al., Phys.Rev.B **41**, 9836 (1990).
[2] M. Toledano-Luque et al., Proc.IRPS (2012).
[3] C.-Y. Chen et al., Proc.IRPS (2011).
[4] O. Baumgartner et al., Proc.SISPAD (2008).
[5] T. Grasser et al., Proc.IRPS (2010), pp. 16 –25.
[6] K. Huang et al., Proc.RoyalSoc. of London. Ser. A **204**, 406 (1950).
[7] A. Palma et al., Phys.Rev.B **56**, 9565 (1997).
[8] T. Grasser et al., Proc.IEDM (2012), pp. 19.6.1–19.6.4.
[9] F. Schanovsky et al., Journ. Comp. Electronics **11**, 218 (2012).

 © 2013 Society for Micro- and Nanoelectronics

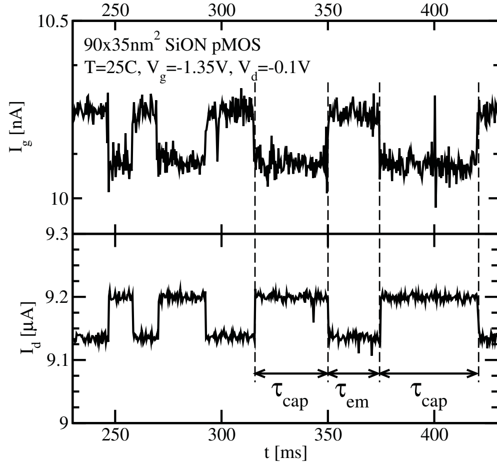

Fig. 1. Simultaneously recorded I_g (upper panel) and I_d traces (lower panel) [2]. Upon the hole capture (after a time period of τ_cap), the charged defect reduces I_d to a lower level for electrostatic reasons. At the same time a significant increase in I_g is observed, meaning that an additional conductive path over the defect has been opened. When the hole is emitted after a time period of τ_em, I_d returns to its previous level and the conductive path is closed again.

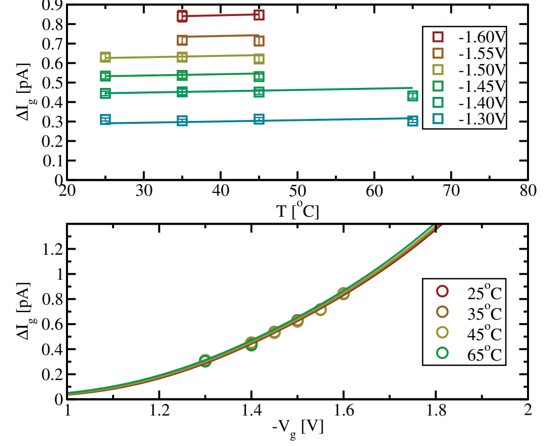

Fig. 4. The step heights of the I_g fluctuations vs. temperature for different gate biases (upper panel). The experimental data (syms) show virtually no temperature dependence — a fact that is usually not associated with a transition over an NMP barrier. Nevertheless, the fit to the experimental data demonstrates that the multistate model is capable of explaining this surprising behavior for reasons given in Fig. 5. The same data are plotted as a function of the gate bias (lower panel).

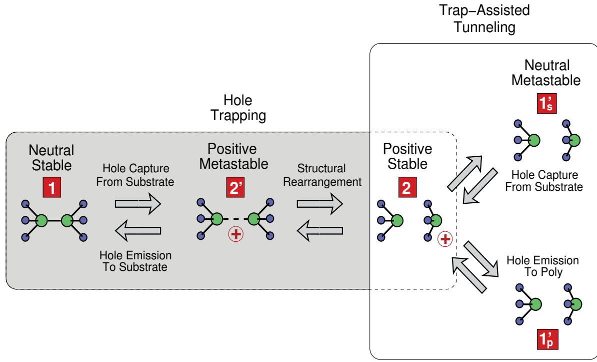

Fig. 2. State diagram of the multistate model. The defect is present in a neutral (1, 1′) and a positive (2, 2′) charge state, where each of them has a second metastable state marked by the prime (1′, 2′). The NMP transitions 1 ↔ 2′ and 2 ↔ 1′ occur between different charge states while the thermal transitions 2 ↔ 2′ connect the positive states 2 and 2′. The subscripts s and p refer to the case where the hole is in the substrate or the poly gate.

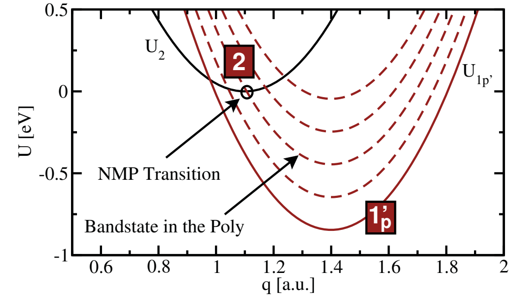

Fig. 5. Schematic configuration coordinate diagram for the transition $2 \rightarrow 1'_\mathrm{p}$. The red and the black parabola correspond to the case where the hole is located at the poly or the defect, respectively. When the full width of valence band states (red dashed parabolas) is taken into account, there always exists one red parabola that intersects the black one in its minimum. Then the NMP transition proceeds without a barrier and therefore shows no temperature dependence. Note, however, that for different gate biases different band states become dominant, which affects the WKB factor and gives rise to the observed field dependence in Fig. 4.

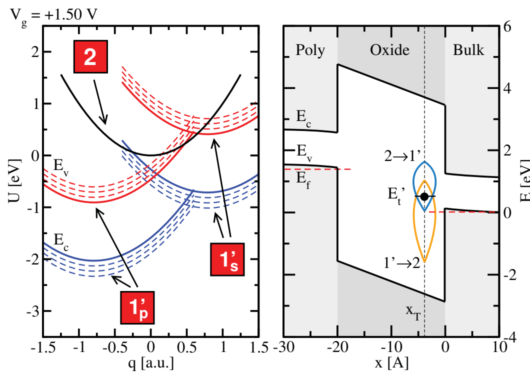

Fig. 3. Left: Adiabatic potential energy surfaces extracted from the fits to the pMOS in [2]. Our simulations consider NMP transitions from all conduction (blue) and valence (red) band states involving charge carriers from the poly gate (left) and the bulk (right). Right: Lineshape functions for the transition 1′ ↔ 2 plotted into the bandenergy diagram. The width of the lineshape functions corresponds to the probability for the respective NMP transition and can be envisioned as a density of trap levels. There are two different lineshape functions, one for hole capture (orange) and one for hole (turquoise) emission. The thermodynamic trap levels E'_t is located at the point where their respective lineshape functions intersect.

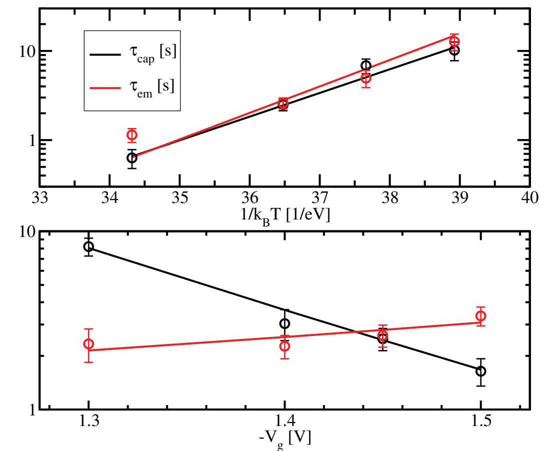

Fig. 6. Comparison of measured (syms) and simulated (lines) for τ_cap and τ_em. A good agreement with the experimental data is obtained for the temperature (upper panel) and the gate bias (lower panel) dependence.

Pseudopotential-based study of gate leakage and contact resistance beyond the 10 nm node

S. Ravandi[1], Bo Fu[1], W. G. Vandenberghe[1], S. J. Aboud[2], and M. V. Fischetti[1*]
[1]Department of Materials Science and Engineering, University of Texas at Dallas, Richardson, TX 75080
[2]Energy Resources Engineering, Stanford University, Stanford CA 94305, USA
*e-mail: max.fischetti@utdallas.edu

ABSTRACT

Scaling FETs according to the 2011 ITRS-Roadmap and employing the empirical-pseudopotential band structure of Si and InAs thin-bodies, we show that quantum confinement causes an unacceptably large on-state gate-current leakage at gate lengths of ~5 nm. This suggests that intrinsically 2D (*e.g.*, of the graphene/graphane structure or dichalcogenides) or 1D (*e.g.*, CNTs) channels are required at 5 nm. We also report a DFT study of the metal/III-V contact resistance and present results for InAs/Mo showing that the target of 10^{-9} Ω cm^2 may be hard to achieve.

GATE LEAKAGE

The use of thinner bodies in FD-SOIs, multi-gate (MG) and nanowire (NW) FETs dictated by scaling causes an upward energy shift of the bottom of the conduction band and so an increase of the gate current (Fig. 1). Using ITRS scaling rules [1], scaling the body and insulator thickness, t_{body} and t_{ins}, linearly with gate length, L_G, adopting the EOT (0.8nm) and t_{body} (11.3nm) of the 2011 ITRS Roadmap[1] for MG-FETs at the 21 nm node, we show in Fig. 2 how the gate current, I_G, increases with decreasing gate-length. For MG-FETs I_G has been estimated in the on-state as:

$$I_G = e\int_0^{L_G} dx \quad n_s(x)\frac{\pi\hbar}{m_e t_{body}^2} T_{WKB}[\Phi_B - E_0, F_{ins}(x)]$$

where $T_{\mathrm{WKB}}[\Phi_B\text{-}E_0,F_{ins}(x)]$ is the WKB tunneling probability across the gate insulator for a barrier Φ_B reduced by the energy E_0 of the ground-state subband determined by quantum confinement (Fig. 3), $F_{ins}(x)$ is the electric field across the insulator at the position x along the channel assuming a linear source-to-drain voltage drop, and $n_s(x) = \varepsilon_{ins}F_{ins}(x)/e$ is the electron sheet density at x. The term $\pi\hbar/(m_e t_{body}^2)$ is the `attempt to escape' frequency of an electron of effective mass m_e in the ground-state subband. As seen in Fig. 2, I_G can become comparable to the on-current at short L_G. An ideal Si/HfO_2 combination appears satisfactory at ~5 nm, but the lower ε_{ins} of Al_2O_3 (resulting in physically thinner insulating layers) results in an excessively high I_G. Similarly, despite a larger semiconductor/insulator barrier, the lower InAs mass results in large quantum-confinement effects. The advantage of `intrinsically' low-dimensionality channels (of the 2D graphene /graphane structure or chalcogenides, or of the 1D CNT structure) is evident in Fig. 2 (bottom). In this case electrons are confined by the ionic potentials and the damaging effect of scaling the body thickness is avoided, in addition to allowing for thicker insulating layers. We conclude that this confinement-induced gate leakage constitutes a serious scaling limit at the 5 nm gate-length.

CONTACT RESISTIVITY

Using the DFT band-structure of Mo and InAs shown in Fig. 4, we have evaluated the InAs/Mo contact resistance [2], assuming the interface located at z=0 and conservation of parallel momentum, from:

$$\frac{1}{\rho_c} = \int_{-\infty}^{\infty} dE \frac{\partial f_S(E)}{\partial E}$$
$$\left\{ 2e^2 \sum_{n,m} \int_{\Omega_C} \frac{d\mathbf{k}}{(2\pi)^3} \upsilon_{M,n,z}(\mathbf{K},k_z) T(\mathbf{k},n,m) \delta[E - E_{M,n}(\mathbf{k})] f_M[E_{M,n}(\mathbf{k})] \right\}$$

where n and m denote the Mo and InAs bands, the integration domain Ω_c extends over 'energy-conserving' wave vectors $\boldsymbol{k}$=$(\boldsymbol{K},k_z)$ (*i.e.*, $E_M(\boldsymbol{K},k_z) = E_s(\boldsymbol{K},k_z')+\Phi$, where Φ is the band-discontinuity and k_z' is the normal component of the InAs wave-vector), and E_M, E_S , f_M and f_S are the dispersion and Fermi functions of Mo and InAs. Ignoring here the (all important!) overlap factor between Mo *d*-waves and InAs *sp*-waves, the 'transmitted flux' $T(\mathbf{k},n,m)$ $\upsilon_{M,n,z}(\boldsymbol{k})$ is taken as min[$\upsilon_{M,n,z}(\boldsymbol{K},k_z)$, $\upsilon_{S,m,z}(\boldsymbol{K},k_z')$], the smallest of the Mo and InAs 'normal' velocity. The InAs resistance and the InAs/Mo contact resistance are shown in Fig. 4: The ITRS required 10^{-9} Ω cm^2 is at the limit of what can be practically achieved.

REFERENCES

[1] 2011 ITRS Roadmap, www.ITRS.org.. These scaling rules are very 'relaxed'. Thus, the gate current estimated here is a 'best case' scenario, but the devices do not exhibit the desired electrostatic integrity. The ITRS workgroup is at work to fix this problem (Kwok Ng, private communication).

[2] See a similar study – ignoring the effect of the metal -- by A. Baraskar *et al.*, "*High doping effects on in-situ ohmic contacts to n-InAs*", 22nd IEEE International Conference on Indium Phosphide and Related Materials, Kagawa, Japan (May 2010).

978-3-901578-26-7 © 2013 Society for Micro- and Nanoelectronics

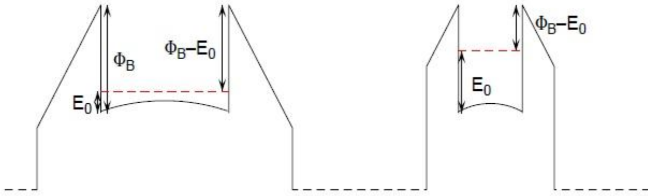

Fig. 1. Schematic diagram illustrating the reduction of the channel/insulator barrier caused by quantum confinement.

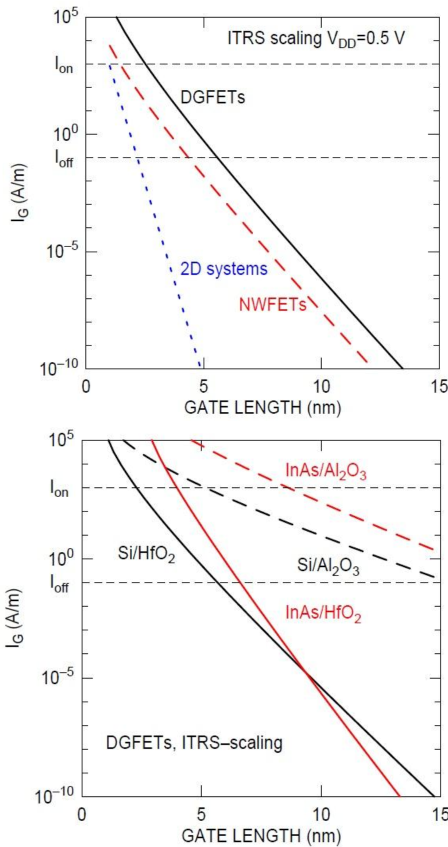

Fig. 2. *Top:* Gate current in scaled MGFETs employing a 'toy' semiconductor (m^*= 0.25 m_0 , nonparabolicity parameter -2.0/eV Φ_B=2.75 eV) and different device designs. '2D systems' refers to graphene (t_{body}≈0.3nm). Note their excellent behavior. *Bottom*: The same but for DG/MG-FETs only and for 'realistic' Si or InAs bodies and HfO_2 or Al_2O_3 insulators. The 2011 ITRS Roadmap scaling rules have been used in both plots.

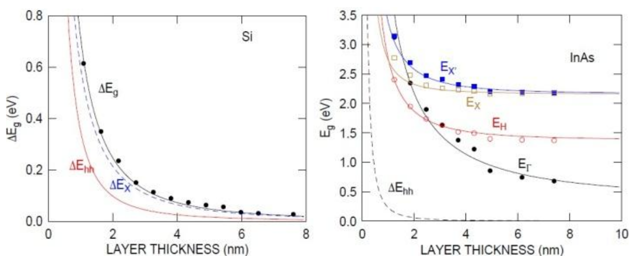

Fig. 3. Change of the gap at various 2D symmetry points for Si (H-terminated, left) and InAs (terminated by an *ad-hoc* insulator, right) thin layers *vs*. layer-thickness calculated using empirical pseudopotentials. Empirical fits to these results (lines) are employed in Fig. 2 (bottom).

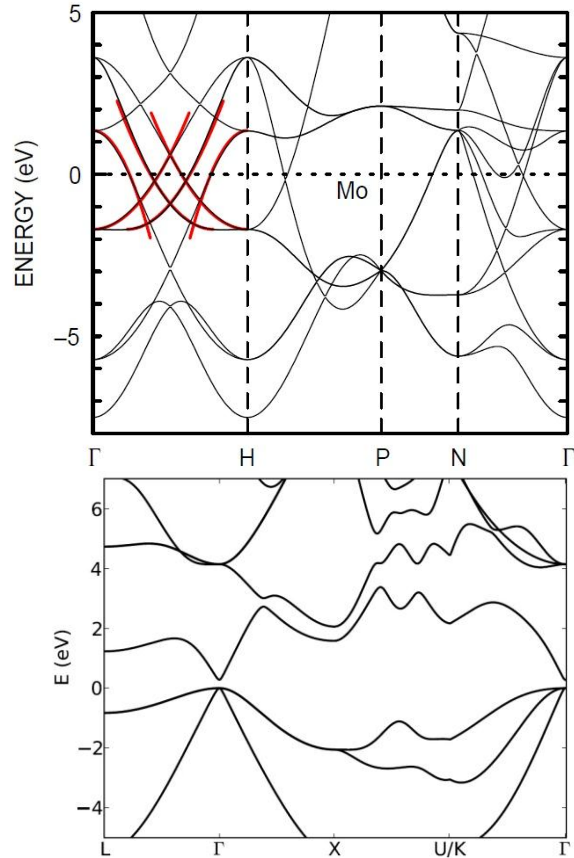

Fig. 4. DFT (Quantum Espresso) calculation of the band structure of Mo (left) and InAs (right). The thick (red) lines in the top frame show effective-mass fits to the Mo bands used to obtain the results of Fig. 5 for the (100) interface.

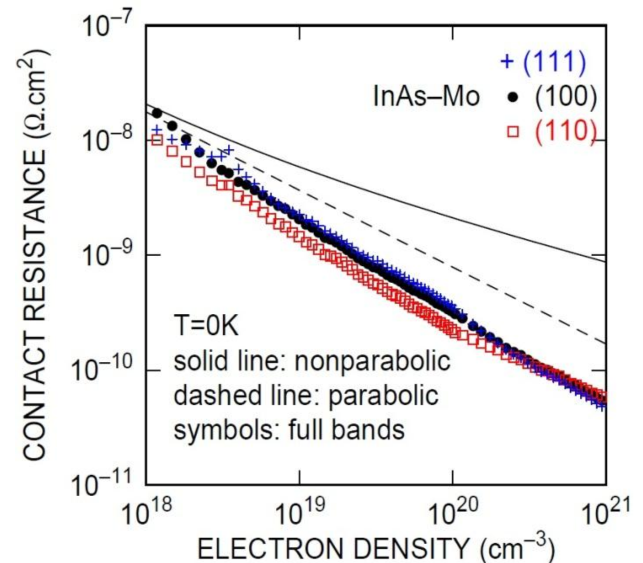

Fig. 5. Contact resistivity at the InAs/Mo interface as a function of InAs carrier density (doping). The lines show the results obtained using effective-mass models for Mo and InAs (parabolic and non-parabolic), while the symbols show results obtained using the full band structure of InAs. Since perfect wavefunction matching between the *d*-like Mo wavefunctions and the *sp*-like InAs wavefunctions has been assumed, these results should be taken as lower bounds for the contact resistivity.

Impact of dielectric induced dynamical many-body correlation effects on the transfer characteristic of Si Nanowire transistor

A. Martinez, J. R. Barker*, and M. Aldegunde
College of Engineering, Swansea University, Singleton Park SA2 8PP
Swansea, UK
*School of Engineering, University of Glasgow, Glasgow G12 8LT, UK
e-mail: a.e.martinez@swansea.ac.uk

Quantum transport has become an essential tool for the TCAD community, as electron confinement and tunneling are important for designing and predicting nanometre devices. The inclusion of phonon scattering for relative large nanotransistor structures is still very time consuming. Futhermore, the efficient incorporation of many body effects such as exchange and correlation into the TCAD simulation remains in progress [1,2]. One of the effects, which becomes important in small structures, is the so-called dielectric confinement [3]. In the case of open systems this effect is not included in the self-consistent Hartree-Fock potential and needs to be added to the self-energy of the electron in the one particle Schrödinger equation. Ref. 1 calculated the effect of this self-energy for different nanowire transistor cross sections. However, the numerical calculation of the self-energy is very time consuming, as it is required for every point in the nanowire.

In this work, we have derived analytical formulae for the calculation of the space-dependent electrostatic self-energy for cylindrical nanowire transistors using an exact Fourier-Bessel analysis that is adapted to square nanowires. The effect of the self-energy in the I_D-V_G characteristic of Si gate-all-around nanowire transistors is studied for different oxide thickness. Two cross-sections (2.2x2.2 nm^2, 3.6x3.6 nm^2) have been considered and two different oxide thickness (0.8, 1.2 nm). Ballistic and dissipative (including phonon scatterings) [4] Non-Equilibrium Green Function simulations for a nanowire transistor with 14/10/14 nm for source/gate/drain are carried out. Fig. 1 shows the self-energy for the 2.2x2.2 nm^2 cross-section and 1.2 nm oxide thickness calculated in one of the planes at the middle of the cross section and perpendicular to one of the confinement direction. There is a substantial downshift (~ 0.1 eV) of the self-energy in the gate relative to the source self energy. This downshift is exhibited in Fig. 2, where the conduction band profile is consequently shifted up to 0.1 eV downwards by the correction. Similarly, in Fig. 2, there is an energy shift downward in source and drain relative to the case without self-energy. This is due to the dielectric confinement and the Neumann boundary condition in source and drain. The corresponding ballistic and dissipative I_D-V_G characteristics are plotted in fig 3. Fig. 4 shows the I_D-V_G characteristics for the 2.2x2.2 nm^2 cross-section and 0.8 nm oxide thickness. Fig. 5 shows the $(I_{DS}-I_D)/I_{DS}$ ratio for ballistic and dissipative simulations. I_{DS} (I_D) denotes the drain current with (without) self-energy included. Fig. 6 shows the corresponding ballistic I_D-V_G for the 3.6x3.6 nm^2 nanowire transistors. In general, the inclusion of the self-energy increases the off current several orders of magnitude for both cross sections and the on current eight times for the small cross section and two times for the large cross section. The effect diminishes rapidly with thicker oxides and wider cross sections. The increase of current due to the electrostatic self-energy correction is smaller when phonon scattering is considered.

References

[1] C. Li et al, Phys. Rev. B **80**, 195318 (2009).
[2] A. Martinez et al proceedings of IWCE conference (2013), 10.1109/IWCE.2012.6242845.
[4] M. Aldegunde, J. Appl. Phys. **110**, 094518 (2011);
[3] C. Delerue, M. Lannoo, *Nanostructures*, Springer (2004).

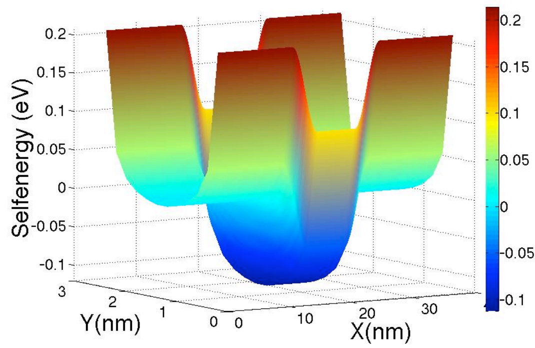

Fig. 1. Self-energy for the 2.2x2.2 nm^2 with 0.8 oxide thickness

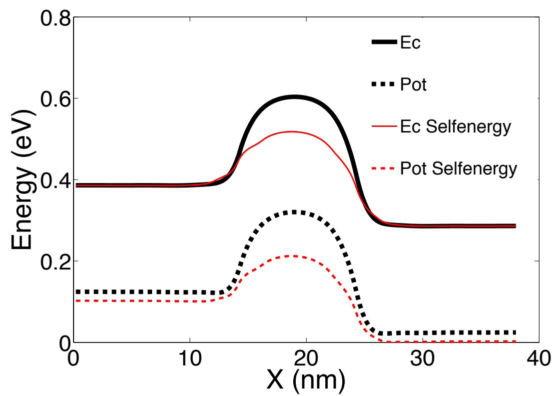

Fig. 2. Conduction band and electrostatic potential energy at Vg=0.6 V for the case of Fig. 1 showing self-energy effects.

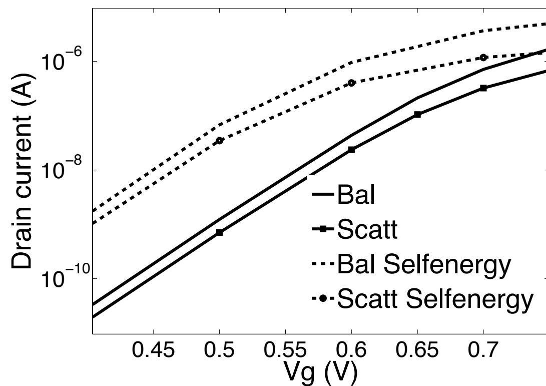

Fig. 3. I_D-V_G for the 2.2x2.2 nm^2 cross section and 1.2 nm oxide thickness device. Dissipative simulations are shown with symbols.

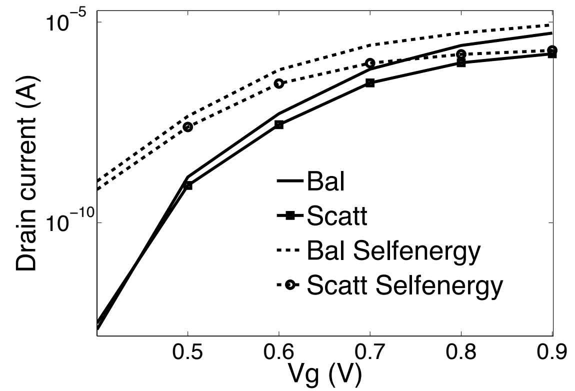

Fig. 4. I_D-V_G for the 2.2x2.2 nm^2 cross-section and 1.2 nm oxide thickness device. Dissipative simulations are shown with symbols.

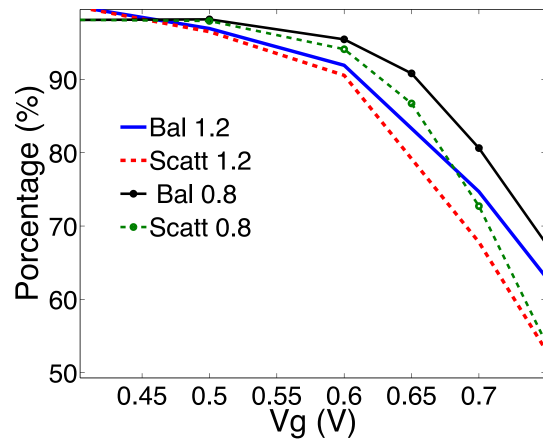

Fig. 5. Drain current increase due to the renormalization of the electron energy. The ballistic and dissipative simulations are shown for the 1.2 and 0.8 oxide thickness cases

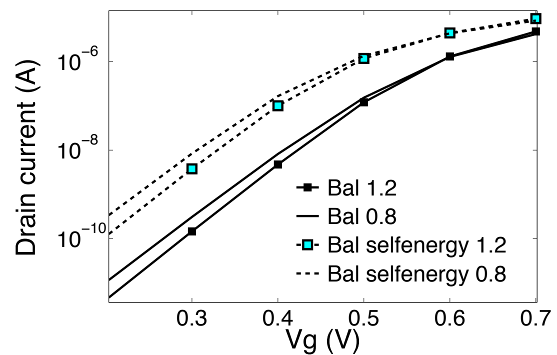

Fig. 6. I_D-V_G for the 3.6x3.6 nm^2 cross-section device.

Negative Bias Temperature Instabilities: A Multiscale Approach from First Principles to TCAD Time-Dependent Variability Simulations

L. Gerrer*, S. Ling**, S. M. Amoroso*, A. M. El-Sayed**, M. B. Watkins**, A. L. Shluger** and A. Asenov*,+
* Device Modelling Group, University of Glasgow, e-mail: louis.gerrer@glasgow.ac.uk
** Department of Physics and Astronomy, University College London
+ Gold Standard Simulations Ltd, Glasgow G12 8QQ, Scotland, UK

Introduction: Oxide aging and in particular Negative Bias Temperature Instabilities (NBTI) is one of the major threats for device reliability [1]. All traps related effects are now considered as a time-dependent variability, drastically impacting design margins [2, 3]. A robust design aiming oxide reliability impacts reduction relies on a better understanding of the traps properties and, in turn, of their dynamics and their impact on devices, including their interaction with the statistical variability (SV) induced by the atomistic nature of dopants [4]. In this work we present for the first time a unified simulation framework from first principles simulation to TCAD statistical simulations of the time-dependent impact of NBTI on device performances. Defect properties obtained by full oxide processing first principles simulations are used as an input in a drift diffusion simulator, including a physics-based trapping/detrapping model in presence of SV. Existing compact model extraction tools [5] can easily extend these results to the ultimate multiscale simulation tool, from first principles to circuit simulations.

Simulation methodology: Realistic Si/SiO_2 interface models, each of which containing 408 atoms, with 3 nm thick SiO_2 and 3 nm thick Si substrate, were generated by performing molecular dynamics simulations with a proper annealing procedure [6] using the ReaxFF force field [7]. Atomic positions were further refined at density functional theory level using the HSE functional [8]. A prototype defect, i.e. three-coordinated silicon atom in the oxide region dubbed as neutral E' centre, as shown in Figure 1, was identified in the resulting structures as a possible candidate for being responsible of interface traps related effects such as BTI degradation. A uniform distribution, given in Figure 2, of the trap levels associated with this defect in its 0/+ states were determined by shifting its positions, thus demonstrating the impact of the chemical environment on the defect properties. The 0 to + state transition occurs by capturing a hole and switches back when capturing an electron, the latter event being modelled by a simpler model of hole emission, as illustrated in Figure 2. Note that the ++ state features an important reaction energy barrier, leading to much longer term oxide degradation and is not considered in this work.

The defects are implemented in an oxide reliability module on top of GSS quantum corrected, drift diffusion simulator GARAND [9], designed for statistical simulations of SV impact on devices performances. A random position (x_T,y_T) is assigned to each trap, the trap depth into the oxide being fixed at 0.3nm to emulate interface defects. A random energy E_T, uniformly distributed in the obtained trap level range is assigned to each trap. The traps are initially in neutral state 0, after solving the device electrostatic and the current continuity equation, the average hole capture times $<\tau_c>$ are computed for each traps, considering the tunnelling current reaching the trap over the trap cross-section area $\sigma_T=10^{-14}$ cm^2 [10]. Averages hole emission times $<\tau_e>$ are evaluated to respect the SRH balance [11]. Those average values feed a Kinetic Monte-Carlo engine, which randomly chooses the next trap to be charged/discharged and randomly extracts the simulation time step, following an exponential distribution of average value $<\tau_c>$ and $<\tau_e>$ and then reproducing the stochastic character of trapping phenomena. The corresponding charge is assigned in the oxide area using a cloud-in-cell technic and the loop is repeated until the stopping condition has been reached, as shown in the flowchart in Figure 3.

NBTI analysis: 3D simulations of a well-scaled 25nm PMOS device were performed at operating voltages; Figure 4 already shows that these realistic traps will charge at high gate bias and discharge at low gate bias. Figures 5 and 6 give time constants distributions of simulated traps; without/with SV induced by Random Dopants Fluctuations (RDF) and Metal Gate Granularity (MGG); an additional source of variability is induced by trap levels distributions. Figure 7 presents BTI charge traces with/without variability and Figure 8 gives threshold voltage shifts ΔV_T for a single occupied trap and after 0.1 s. of simulated stress for devices with an average trap density of 10^{12} cm^{-2}. The average dynamic impact on V_T is higher for devices with SV but traps are slower on average; dispersions are much higher when variability is considered.

Conclusions: We have presented a multiscale oxide reliability simulation methodology, starting from molecular simulation up to device level large ensemble simulations, demonstrating the SV/trap variability to be determinant both in defects dynamics and impacts.

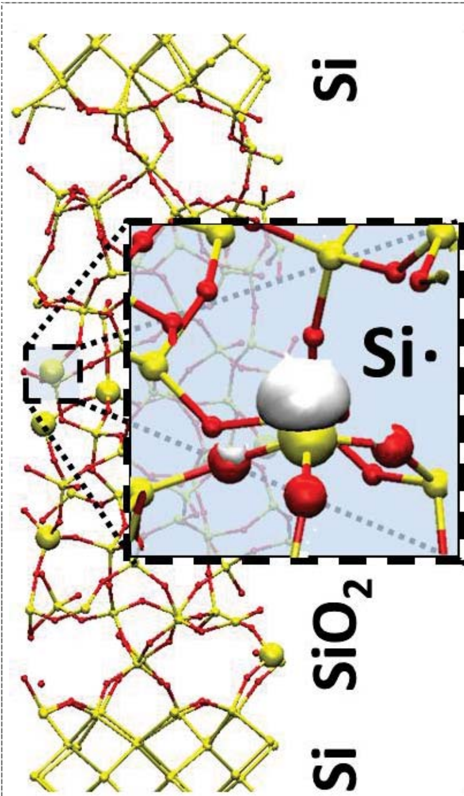

Fig.1 E' centre at the Si/SiO$_2$ interface, obtained by first principle simulations of oxide melting and annealing. The '+' state presents one hole and one electron localized on the Si$_{3C}$, one electron delocalizes in the Si conduction band (CB). The chemical environment of the defect impacts the defect energy level.

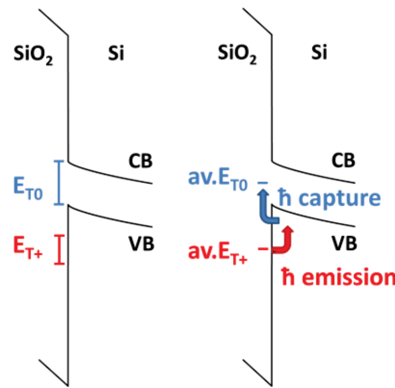

Fig.2 Traps level ranges from first principle simulations in both states E_{T0} ε [3.27, 4.39], E_{T+} ε [5.19, 5.91], (eV, from SiO$_2$ Cond. band).

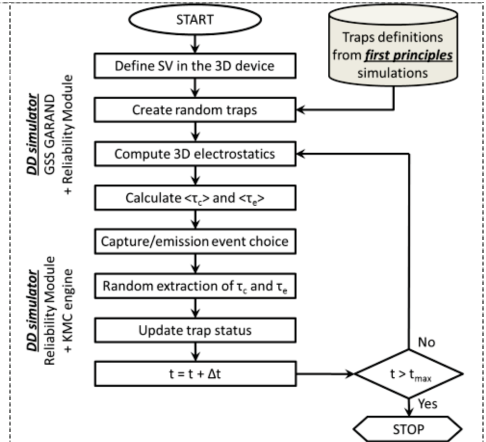

Fig.3 Flowchart of dynamic simulation of time-dependent variability, including first principles inputs.

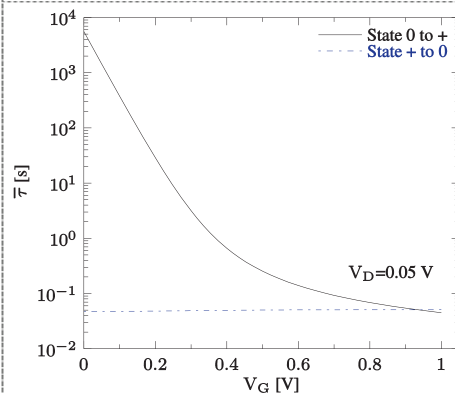

Fig.4 Transition time from a state to another as a function of the gate voltage; in this model holes emission are considered instead of electron capture.

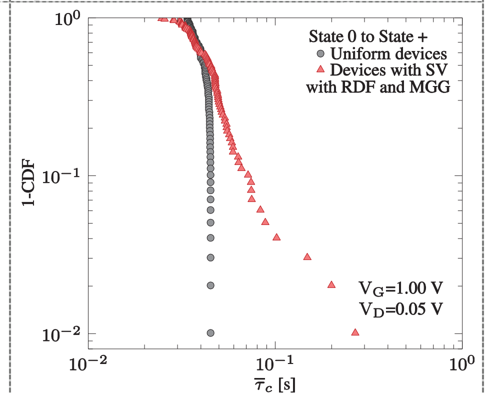

Fig.5 Hole capture time distribution, switching the state from 0 to +. Devices with SV feature RDF and MGG whereas only the trap position is random in uniform devices.

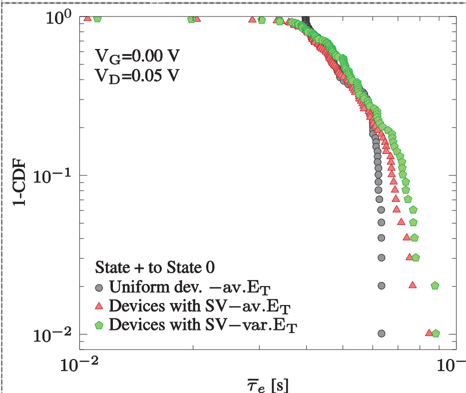

Fig.6 Hole emission time distribution, switching the state from + to 0; in uniform and SV devices with average trap levels; in SV devices with distributed trap levels to account for chemical environment impact.

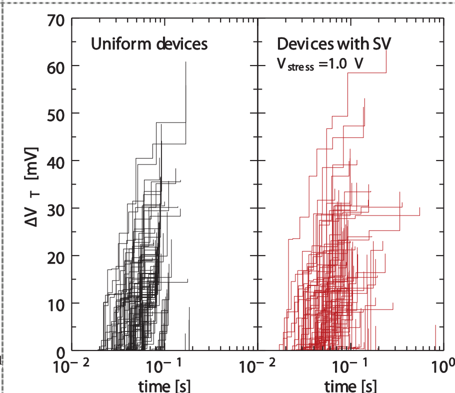

Fig.7 BTI charge traces for uniform devices and devices with SV including a poissonian distributed number of traps with an average of 4; only trapping is considered in this figure, to avoid heavy traces from RTN behaviour.

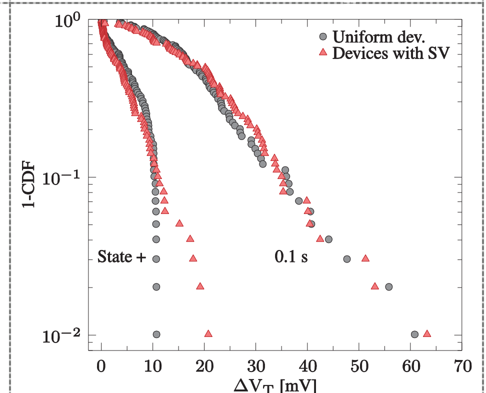

Fig.8 ΔV_T distributions induced by one single charged defect in its + state and extracted distributions after 10^2 s. of stress for uniform and devices with SV.

References

[1] K. V. Aadithya, Design, Automation & Test in Europe Conference & Exhibition (DATE), 2011. **[2]** S. V. Kumar et al., Proc. of 7th International Symposium on Quality Electronic Design (ISQED'06), pp. 27-29, 2006. **[3]** N. Tega et al., Symp. on VLSI Tech. and Circ., pp.50-51, 2009. **[4]** A. Asenov et al., Trans. Elec. Dev., vol. 50, no. 9, pp. 1837-1852, 2003. **[5]** L. Gerrer et al., Proc. of Int. Rel. Phys. Symp (IRPS), 2013. **[6]** N. L. Anderson et al., Phys. Rev. Letts. 106, 206402, 2011. **[7]** A. C. T. van Duin et al., J. Phys. Chem. A 107, 3803, 2003. **[8]** J. Heyd et al., J. Chem. Phys. 118, 8207, 2003. **[9]** http://www.goldstandardsimulations.com. **[10]** S.M. Amoroso et al., "3D MC simulation of the programming dynamics and their statistical variability in nanoscale charge-trap memories", Proc. IEDM, 2010, pp. 540-543.

Acknowledgment

Work supported by European 7th framework collaborative project entitled "Modeling of the reliability and degradation of next generation nanoelectronic devices".

Width Dependence of RDD-Induced Current Fluctuation in Silicon Nanowire Transistors

Masashi Uematsu[†], Kohei M. Itoh[†], Gennady Mil'nikov[*†], Hideki Minari[*†], and Nobuya Mori[*†]

School of Fundamental Science and Technology, Keio University, Yokohama 223-8522, Japan

[*]Graduate School of Engineering, Osaka University, Osaka 565-0871, Japan

[†]Japan Science and Technology Agency (JST), CREST, Tokyo 102-0076, Japan

e-mail: uematsu@a3.keio.jp

Fluctuation of device characteristics due to random discrete dopant (RDD) distribution is becoming a major concern for nanoscale transistors [1]. Effects of the RDD distribution are usually analyzed with a randomly generated dopant distribution. The actual RDD distribution, however, should be correlated with the process condition, and can be different from a mathematically generated one. We have studied the effects of RDD in silicon nanowire (Si NW) transistors with a square cross-section of 3 nm × 3 nm by using realistic implanted and annealed arsenic (As) distributions [2]–[4]. In this study, we investigate the effects of the NW size on the current fluctuation of NW transistors.

Discrete random As distributions in Si NWs are obtained using Sentaurus kinetic Monte Carlo (KMC) simulator [5]. Si NWs (w nm wide, w nm high, and 30 nm long) covered with 1 nm-thick SiO_2 and with a thick mask are implanted with As (0.5 keV, 2×10^{14} cm^{-2}) and annealed at 1000 °C with a hold time of 0 s [Fig. 1(a)]. For studying the effects of the NW size, we simulate two types of NWs of w = 3 nm and 5 nm. Statistical variations are investigated by using different discrete As distributions [Fig. 1(b)], which are generated by preforming the KMC simulation with different random seeds. The active As distributions obtained through the KMC simulation are introduced into n-type gate-all-around Si NW MOSFETs [Fig. 1(c)]. The drain-current–gate-voltage (I_d–V_g) characteristics are calculated by non-equilibrium Green's function method with an effective mass approximation [6]. The discrete impurities are treated with a cloud-in-cell charge assignment scheme.

Figure 2 shows histograms of a number of active As atoms in the Si NWs. We simulate 100 different discrete As distributions for each device structure. We find that about 30% of As atoms implanted into the Si region are active in the Si NWs. The average active As density in the source and drain (S/D) extensions is $N_{S/D} \approx 1.8\times10^{20}$ cm^{-3}. The standard deviation of $N_{S/D}$ is smaller for w = 5 nm, in accordance with the law of large numbers. Active As density profiles are plotted in Fig. 3. Dopant atoms diffuse into the channel region with the lateral abruptness of ~2.5 nm/dec, which causes large variability of the device characteristics [3].

Figure 4 shows calculated I_d–V_g characteristics at V_d = 0.05 V. We find that the I_d–V_g curves of the 5 nm NWs show larger fluctuation compared with those of the 3 nm NWs, especially in the lower V_g region. We also find that in the lower V_g region the log I_d-distribution for w = 3 nm is significantly asymmetric while that for w = 5 nm is fairly symmetric (see Figs. 5 and 6). The smaller I_d fluctuation for w = 3 nm is partially due to the short tail (virtually no tail) in the log I_d-distribution for the lower I_d side. This short tail may be attributed to the fact that the 3 nm NW transistor has better gate control compared to the 5 nm NW device.

We acknowledge Dr. Ignacio Martin Bragado for fruitful discussions on KMC modeling.

REFERENCES

[1] S. Roy and A. Asenov, Science **309**, 388 (2005).
[2] N. Mori *et al.*, Int'l Workshop on Comput. Electron. (Madison, USA, 2012).
[3] M. Uematsu *et al.*, IEDM Tech. Digest, p. 709 (2012).
[4] M. Uematsu *et al.*, Nanoscale Research Lett., **7**, 685 (2012).
[5] Sentaurus Process User Guide, Version F-2011.09, Synopsys, Inc. (2011).
[6] H. Takeda and N. Mori, J. Comput. Electron. **4**, 31 (2005).

978-3-901578-26-7 © 2013 Society for Micro- and Nanoelectronics

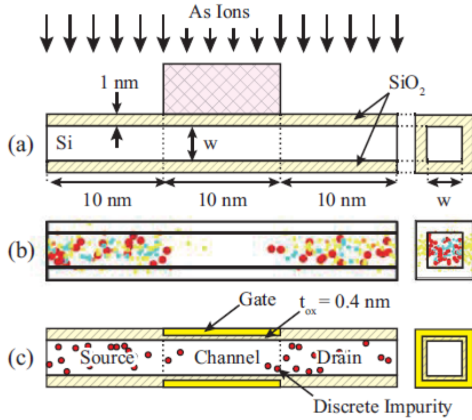

Fig. 1. (a) KMC simulation. (b) Discrete As distribution in the Si NW. Red dots show active As atoms in Si, light blue As clusters, orange As at the oxide/Si interface, and yellow As in the oxide. (c) Device structure for NEGF calculation.

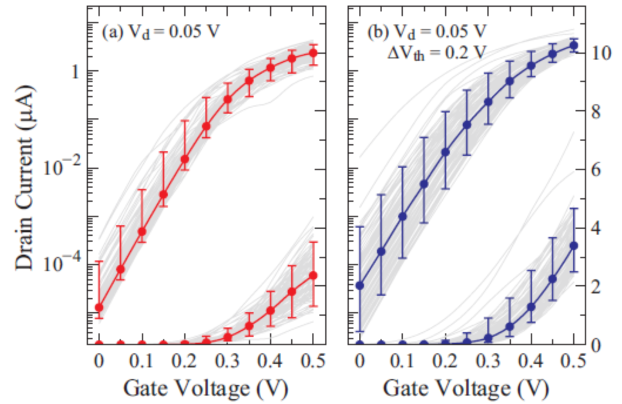

Fig. 4. I_d–V_g characteristics for w = 3 nm (a) and 5 nm (b). Close circles show the median ($I_{50\%}$). The upper error bars represent 95 percentile while the lower error bars represent 5 percentile values ($I_{95\%}$ and $I_{5\%}$).

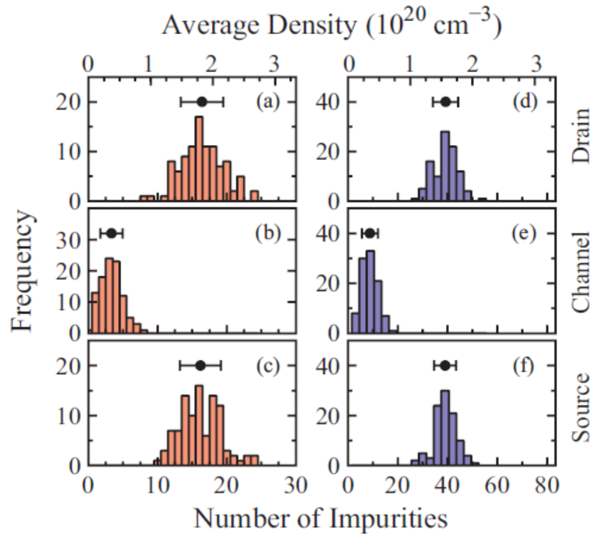

Fig. 2. Histogram of a number of active As atoms in the Si NWs of w = 3 nm (a, b, c) and 5 nm (d, e, f).

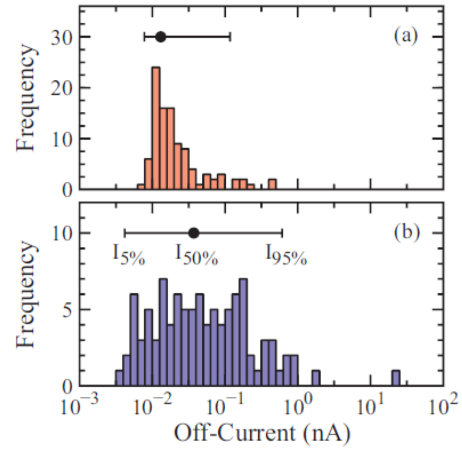

Fig. 5. Histogram of the off-current for w = 3 nm (a) and 5 nm (b) at V_d = 0.05V and V_g = 0.0 V.

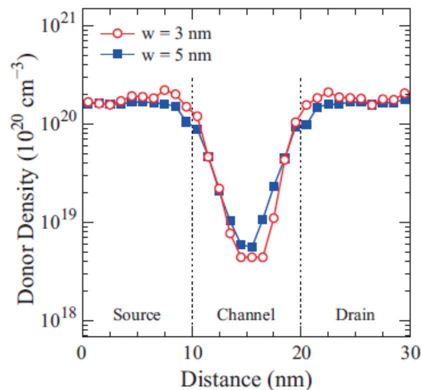

Fig. 3. Active As density profile along the source-to-drain direction for w = 3 nm (circles) and 5 nm (squares).

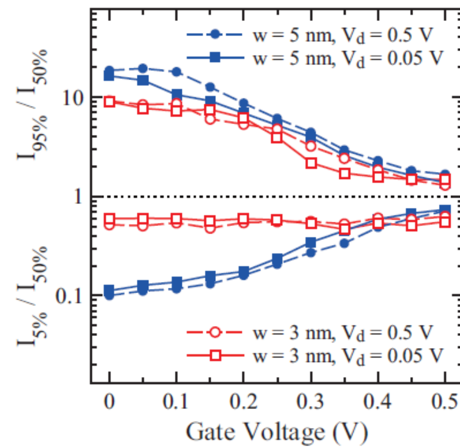

Fig. 6. $I_{95\%}/I_{50\%}$ and $I_{5\%}/I_{50\%}$ as a function of V_g. Open (closed) marks correspond to w = 3 nm (5 nm), and squares (circles) represent V_d = 0.05V (0.5 V).

Multi-Fin Bulk FinFET Characteristic Fluctuation Induced by Process Variation and Random Dopant

Chieh-Yang Chen, Yu-Yu Chen, and Yiming Li*
Parallel and Scientific Computing Laboratory, Department of Electrical and Computer Engineering, National Chiao Tung University, 1001 Ta-Hsueh Road, Hsinchu 300, Taiwan
e-mail: ymli@faculty.nctu.edu.tw

I. INTRODUCTION

Device scaling has suffered sizeable statistical variation in device parameter and has increased the short-channel effect (SCE) [1-2]. To overcome the variation and SCE, 3D transistor, such as bulk FinFET in sub-22-nm has been one of competitive solutions [3-4]. Impurity dopants are continuously adopted for tuning device characteristics. Recent simulations have been reported for single SOI and bulk FinFET device's characteristic fluctuation [5-7]. However, the multi-fin bulk FinFET's random dopants fluctuation (RDF) and the process variation effect (PVE) including the variations of silicon fin's fin height (Hf), fin width (Wf), and gate length (Lg) have not been clearly explored yet.

In this work, 16-nm-gate HKMG multi-fin bulk FinFET devices are simulated for both the RDF and PVE. Experimentally validated 3D quantum-mechanically corrected device simulation is intensively performed to statistically analyze the impact of RDF and PVE on the device characteristic fluctuation.

II. SIMULATION AND RESULTS DISCUSSION

As shown in Fig. 1(a), we study the single-fin and multi-fin (four fins) bulk FinFET in which both the channel length and device width are 16 nm and silicon fin height is 32 nm. We randomly generate 1,327 dopants in a large cube of $(96\ \text{nm})^3$, in which the equivalent doping concentration is $1.5\times10^{18}\text{cm}^{-3}$. The large cube is partitioned into sub-cubes. The number of dopants in the sub-cubes may vary from 0 to 14, and the average dopant number is 6. (Similarly, for the FinFET's Hf of 32 nm; devices are with 2,654 dopants in $96 \times 192 \times 96\ \text{nm}^3$ cube and average dopant number is 12) These sub-cubes are then mapped into the device channel region for 3D device simulation, as shown in plot Fig. 1(a). Fig. 1(c) shows the diagram of the fin's process variation. And, the fin's variation includes the Hf, Wf, and Lg which varies follow the table in Fig. 1(c).

As shown in Figs. 2(a) and 2(b), the single-fin's I_D-V_G characteristics are fluctuated by the RDF and PVE, respectively. The PVE varying with respect to each factor the Hf, the Lg, and the Wf, is further shown in Figs. 2(c)-(e). The solid line shows the nominal case with a channel doing of $1.5\times10^{18}\ \text{cm}^{-3}$ and V_{th} is experimentally calibrated to 140 mV. Similarly, as shown in Fig. 3, we simulate the four-fin's I_D-V_G characteristic for the devices suffering the RDF and PVE. We stimulate the σV_{th} resulting from the RDF and PVE, as shown in Fig. 4. Compared with the single fin device, the multi-fin device can suppress the V_{th} fluctuation of RDF about 48% owing to the increase of fin numbers and the enhanced screening effect. The more we increase the fin number, the more we suppress the fluctuation; nevertheless, the improvement will be limited by the geometry aspect of fin which should be subject to further investigation. For the suppression of PVE, it is merely 10% due to different fin shape. As shown in Fig. 5, we list the normalized σV_{th}, σI_{on}, and σI_{off} for both the cases of single- and multi-fin resulting from the PVE and RDF. The multi-fin structure can effectively suppress the fluctuation from RDF and PVE on V_{th} and I_{on}, but the variation of I_{off} is increased for the case of multi-fin devices.

III. CONCLUSIONS

In this work, we have statistically performed the 3D device stimulation to estimate the multi-fin device's fluctuation. The results indicate that the multi-fin device can successfully suppress RDF by 48% and PVE by 10% on σV_{th}, compared with the single-fin device.

ACKNOWLEDGEMENT

This work was supported in part by the Taiwan National Science Council (NSC) under Contract No. NSC-101-2221-E-009-092 and a 2012-2013 tsmc grant.

REFERENCES

[1] Y. Li et al., in: *IEDM Tech. Digest* 171(2012).
[2] Y. Li et al., *IEEE T ED* 57 (2010) 437.
[3] K. J. Kuhn et al. in: *IEDM Tech. Digest* 171(2012).
[4] C.-H. Lin et al., in: *Proc. Symp. VLSI Tech*., 2.3 (2012).
[5] H.-W. Su et al., in: *Proc. IEEE DRC* 109 (2012).
[6] X. Wang et al., in: *IEDM Tech. Digest* 103 (2011).
[7] H.-W. Cheng et al., in: Proc. *IEEE SISPAD* 287 (2011).

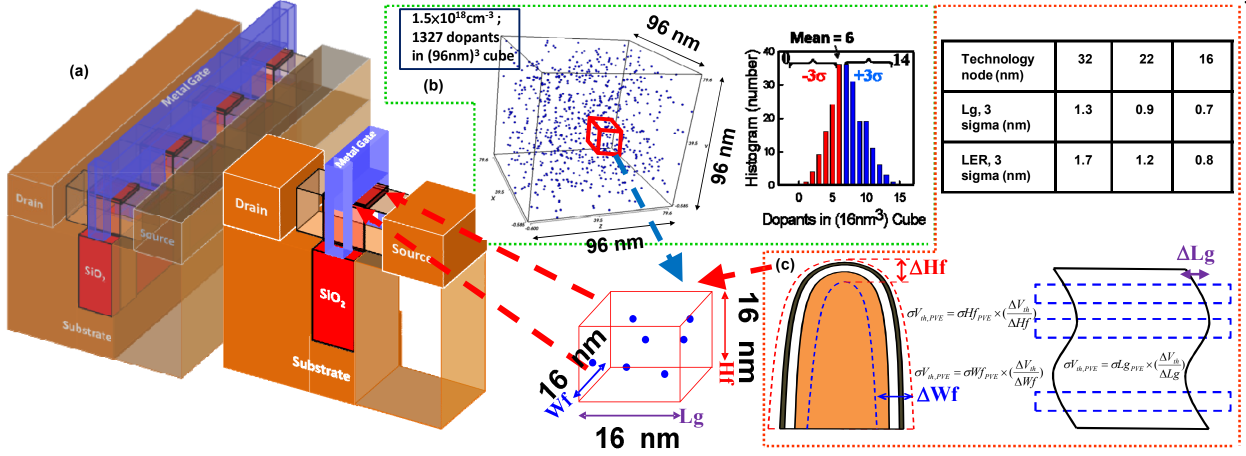

Fig. 1. (a) An illustrate of the device structure for both the single- and Multi-fin. (b) We randomly generate 1,327 dopants in a large cube of (96 nm)^3, in which the equivalent doping concentration is 1.5 x 10^{18} cm^{-3}. The large cube is partitioned into sub-cubes. The number of dopants in the sub-cubes may vary from 0 to 14, and the average dopant number is 6. (Similarly, for FinFET AR2 devices: 2,654 dopants in 96 x 192 x 96 nm^3 cube and average dopant number is 12). The AR2 is defined as Fin height / Fin width = 2. These sub-cubes are then mapped into the device channel region for 3D device simulation, as shown in plot (a). (b) The diagram of fin's process variation. Fin's variation includes the Hf, Wf, and Lg which varies follow the inset table.

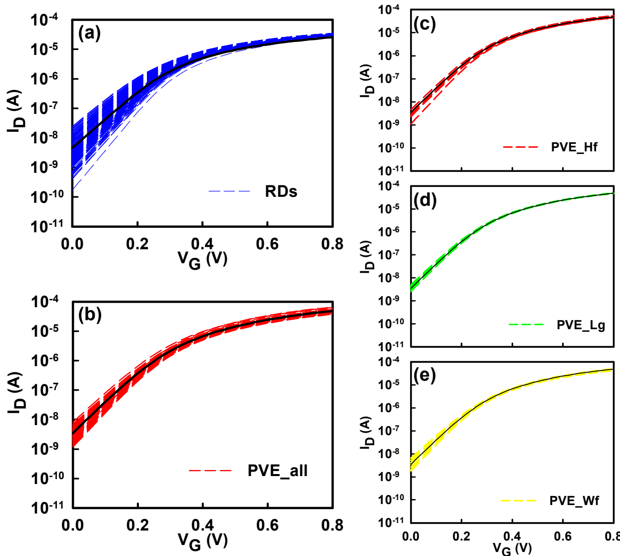

Fig. 2. The single-fin's I_D-V_G characteristics for (a) RDF, (b) PVE. (c) Hf, (d) Lg, and (e) Wf are each factor's impact. The solid line in each plot shows the nominal case with a channel doing 1.5x10^{18} cm^{-3} and the V_{th} is equal to 140 mV.

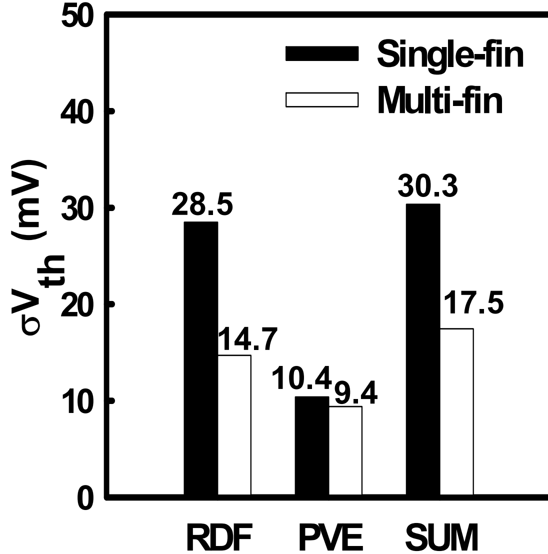

Fig. 4. Plot of the σV_{th} calculated from the devices with the RDF, PVE, and their statistical sum: $(\sigma^2 V_{th,RDF} + \sigma^2 V_{th,PVE})^{0.5}$.

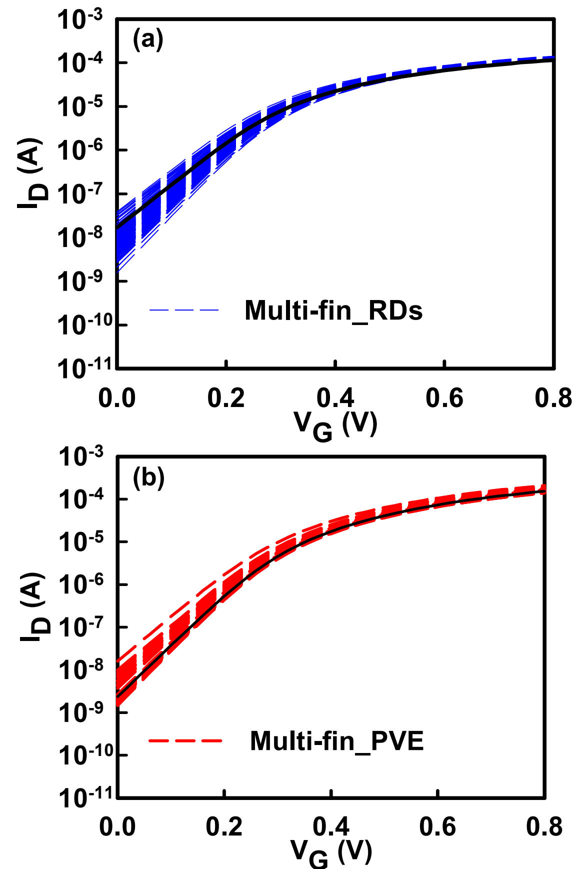

Fig. 3. The multi-fin's I_D-V_G characteristics for both the (a) RDF and (b) PVE, where the fin number is 4.

	Normalized σV_{th} (%)	Normalized σI_{on} (%)	Normalized σI_{off} (%)
PVE_Hf	5.3	5.5	20.7
PVE_Lg	2.5	0.5	12.0
PVE_Wf	4.3	4.3	23.1
PVE_all	7.4	12.0	37.7
RDF	20.4	4.2	99.3
Multi-fin RDF	9.7	3.2	64.8
Multi-fin PVE	6.8	6.2	65.3

Fig. 5. The first 4 rows are the normalized σV_{th}, σI_{on}, and σI_{off} of the single-fin and the last two rows are the multi-fin's PVE and RDF. The multi-fin structure effectively suppresses the fluctuation from both the RDF and PVE on V_{th} and I_{on}.

The Monte Carlo approach for investigating electrothermal effects in nanostructures

T. Sadi
Department of Biomedical Engineering and Computational Sciences,
Aalto University, P.O.Box 12200, FI-00076 Aalto, Finland.
e-mail: toufik.sadi@aalto.fi

INTRODUCTION

Device miniaturization has continued to revolutionize the semiconductor industry for decades. Shrinking device dimensions allowed cramming more components onto integrated circuits (ICs), giving rise to an increased functionality of electronic products. Considering the reported miniaturization trends, as described e.g. by Moore's law [1], the continuous increase in the packing density of ICs have also been followed by an exponential increase in on-chip heat generation. In fact, and for many years, it has been suggested that such trends may not be sustained without significant improvements in cooling technology or fundamental changes in device designs, as unrealistic power density levels and temperatures were predicted. Hot-spots, the low thermal conductivity in thin films and nanowires, and the thermal resistance at interfaces, are but few examples of the difficult challenges faced in guaranteeing the operation of next-generation nanodevices with minimized self-heating. Therefore, for future technology developments, a fundamental understanding of thermal transport at the nanoscale is a necessity. In this context, the development of reliable simulation methods for coupled electron and phonon transport is essential to address all these issues.

SIMULATION METHOD

The simulation work presented here relies on a very well-established Monte Carlo (MC) simulator accounting for self-heating using phonon statistics [2]. The electrothermal simulator self-consistently couples a three-dimensional (3D) electronic trajectory (MC) simulation with the solution of the heat diffusion equation. The Monte Carlo method is very suitable for the simulation of electron transport in semiconductor nanodevices, as it is free from low-field near-equilibrium approximations. More importantly, the method is well-suited for electrothermal modeling, since it allows a detailed microscopic description of electron-phonon scattering. This feature provides an inherent and direct prediction of the spatial distribution of heat generation.

SIMULATION WORK, RESULTS AND DISCUSSIONS

The simulator is employed to study the electrothermal phenomenon in a variety of nanodevices, ranging from conventional Si- and III-V-based field-effect transistors (FETs) to nanowire FET devices. The advantages of using the simulation method are demonstrated. These include: (i) the accurate determination of the spatial heat generation distribution, (ii) the possibility of studying the contribution of the individual phonon populations to heat generation, and (iii) the possibility of accurately studying the effect of self-heating on the microscopic properties of electron transport [3]. The microscopic analysis of self-heating provides a direct means of understanding device electronic and thermal properties, e.g. thermal management and charge confinement in low-dimensional structures. As an example, Figs. 1 and 2 demonstrate a comparison of the electrothermal performance of three mainstream heterostructure devices, including submicron Si, III-As and III-N HEMTs [3]. Fig. 1 shows the variation of the local peak temperature with the input power. From Fig. 1, it can be concluded that GaN HEMTs give the best thermal performance because of the high thermal conductivity of the SiC substrate used in this case. SiGe HEMTs provide the poorest thermal performance mainly due to the very low thermal conductivity of SiGe alloys. Fig. 2 shows the variation of the current reduction due to self-heating with

978-3-901578-26-7 © 2013 Society for Micro- and Nanoelectronics

the maximum reduction in the electron velocity in the channel. Since the slope of each curve is directly proportional to the 2DEG concentration, this parameter reflects the extent of charge confinement in each device. Fig. 2 indicates how GaN HEMTs provide the best confinement, mainly due to the presence of polarization effects near the channel. Further results will be reported from the simulation of the electrothermal behavior of advanced structures, such as metal-insulator-semiconductor FETs (MISFETs) with a single InAs nanowire channel. In spite of a low average heat dissipation (few orders of magnitude lower than in conventional HEMTs), simulations predict significant local temperatures due to the high current density levels and the poor thermal management in these nanowire structures.

Acknowledgment

I would like to thank Robert W. Kelsall and Neil. J. Pilgrim from Leeds University, and Jean-Luc Thobel and François Dessenne from the Université Lille 1, for their significant contribution to the simulation work. I would also like to thank Prof. Frank Schwierz from the Technical University of Ilmenau for advice.

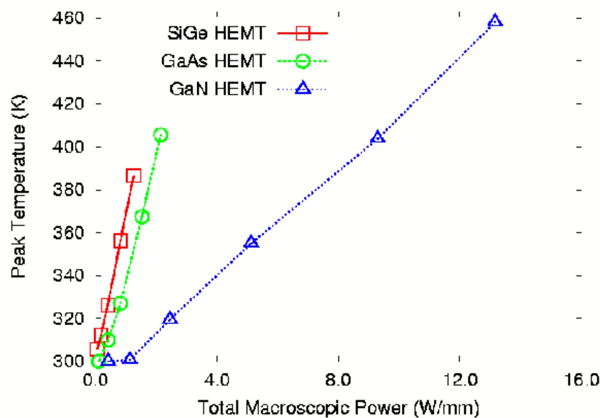

Fig. 1. Variation of the peak temperature with the macroscopic power dissipation for submicron SiGe, GaAs and GaN HEMTs, with a gate length of 200 nm [3].

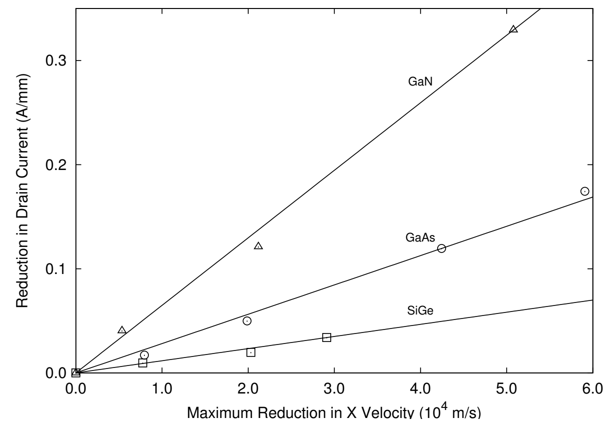

Fig. 2. Variation of the electrothermal reduction in the drain current with the electrothermal reduction in the peak x velocity in the channel for submicron SiGe, GaAs and GaN HEMTs, with a gate length of 200 nm [3].

References

[1] G.E. Moore, *Cramming More Components onto Integrated Circuits*, Electronics Magazine **38**, (1965)

[2] T. Sadi, R.W. Kelsall, N.J. Pilgrim, *Investigation of Self-Heating Effects in Submicrometer GaN/AlGaN HEMTs Using an Electrothermal Monte Carlo Method*, IEEE Trans. Electron Devices **53**, 2892 (2006)

[3] T. Sadi, R.W. Kelsall, N.J. Pilgrim, J.-L. Thobel and F. Dessenne, *Monte Carlo Study of Self-Heating in Nanoscale Devices*, J. Comp. Elec. **11**, 118 (2012)

Mobility in FDSOI Devices: Monte Carlo and Kubo Greenwood Approaches Compared to NEGF Simulations

D. Rideau[1], Y. M. Niquet[3], O. Nier[1,2,4,5] , P. Palestri[5], D. Esseni[5], V. H. Nguyen[3], F. Triozon[4], I. Duchemin[3], D. Garetto[6], L. Smith[8] , L. Silvestri[7], F. Nallet[7], C. Tavernier[1], H. Jaouen[1]

[1)] STMicroelectronics, 850, rue J. Monnet, BP. 16, 38921 Crolles, France ;
[2)]IMEP-LAHC, MINATEC 3 Parvis Louis Néel, 38016 Grenoble,
[3)] SP2M, UMR-E CEA/UJF-Grenoble 1, INAC, Grenoble, France; [4)] CEA-LETI, Campus MINATEC, 17 rue des Martyrs, 38054 Grenoble, France ;
[5)] DIEGM, University of Udine, Via delle Scienze 208, 33100 Udine, Italy;
[6)] Synopsys, 12 Rue Lavoisier, FR-38330 Montbonnot St Martin, France ; [7)] Synopsys, Thurgauerstrasse 40, CH-8050 Zürich, Switzerland ; [8)] Synopsys, Inc., 700 E. Middlefield Rd., Mountain View, CA.

1. Introduction

This paper presents a thorough comparison of mobility calculations in Fully-Depleted Silicon on Insulator (FDSOI) devices. Semi-classical approaches, such as the Kubo-Greenwood (KG) and the multi-subband Monte Carlo (MSMC) methods, are compared to quantum Non-Equilibrium Green's Functions (NEGF) results. All solvers use purely parabolic band structures for electrons with a Si/SiO_2 barrier of 3.15 eV and an oxide effective mass of 0.5 m_0. The considered scattering mechanisms include phonon and surface roughness (SR). The phonon scattering parameters of Ref [1] and SiO_2/Si roughness parameters of Ref. [2] are used in all simulations to guarantee consistent comparisons. The front gate stack of the devices is made of 2 nm of SiO_2 and of 2 nm of HfO_2. The undoped silicon active layer thickness varies from T_{Si}=2 nm up to T_{Si}=10 nm and the BOX thickness is 25 nm.

2. Scattering time based approaches

Semi-classical approaches such as the Kubo Greenwood and the MSMC have often been used to calculate the mobility in FDSOI devices [1-5]. However a direct comparison between published results is difficult, because either model parameters or SR profiles are different. In this abstract, we provide a comparison between two KG solvers, namely the STM in-House UTOX solver [6] and the commercial SBAND solver [7]. We extended the comparison to the Udine University MSMC solver [1,5].

All solvers treat the interaction with acoustic phonons as an isotropic, elastic mechanism while inter-valley phonon scattering is treated as isotropic with fixed phonon energies. SR scattering is treated as an elastic, anisotropic mechanism within either the Prange-Nee approximation [1,5,7], the generalized Prange-Nee model [2,6], or the Gamiz numerical approach [3,6]. The matrix elements are screened with a scalar Lindhard approach.

3. NEGF

NEGF mobility calculations have been performed with the TB_SIM solver from CEA [8]. We generated periodic random SR samples [4] with width W=20 nm and length L=30 nm (see Figure 1). We then built devices made of these units repeated once, twice (L= 60 nm), and up to three times (L= 90 nm). One nanometer of SiO_2 is included in the effective mass Hamiltonians on both sides of the film. The resistance of the devices was next computed in a mode space approach, including electron-phonon scattering. As expected, it is proportional to the length (that is, to the number of units, see Figure 2), allowing for an accurate extraction of the resistance of the SR sample. We finally computed the phonon-limited mobility μ_{PH} in smooth films and extracted an "effective" surface roughness-limited mobility μ_{SR} from Matthiesen's rule. The obtained μ_{SR} is, therefore, the SR mobility to be combined with the phonon mobility to recover the total mobility given by the NEGF calculation. We stress that a direct "surface roughness only" NEGF calculation (no phonons) would bring even lower SR mobilities, as the absence of inelastic pathways for electron scattering strengthens localization. We have verified that the width and length of the SR sample are large enough to limit statistical bias ($\Delta\mu_{SR}/\mu_{PH}$ = 2.5%).

5. Results and Discussion

Figure 3 shows the phonon-limited mobility as a function of the active layer thickness. All solvers are in excellent agreement. We therefore now focus on the SR mobility.

There are two closely related approaches to compute the impact of a local fluctuation of the electrostatic potential due to SR. The former one, derived from the well-known Prange-Nee approximation, regroups SR models described in [1,2,4,5]. The latter approach, originally proposed by F. Gamiz [1,3], consists in a numerical evaluation of the scattering potential. As shown in Figure 4, two independent Poisson-Schrodinger calculations of the electrostatic potential are performed: the first one in the considered device, and a second one on the same device with the front or the back SiO_2/Si interface shifted by Δ. Figure 5 shows that the mobility obtained with this numerical approach agrees well with the usual Prange-Nee-based approaches.

Figure 6 compares the SR-limited mobility obtained with the semiclassical methods to the NEGF results. The former solvers, in close agreement one with each other, clearly overestimate the SR-limited mobility with respect to NEGF. This is further emphasized in Figure 7, which shows the SR-limited mobility as a function of T_{SI}. The results of S. Jin [2] have also been reported on this figure. They account for carrier density fluctuations and image charge effects, but are still above NEGF data. In figure 8, the total mobility is compared to measurements [9]. It appears that the widely used set of parameters for phonon [1] and SR [2] leads to mobilities larger than experimental data. Figure 9 shows the mobility obtained with optimized parameters. All phonon deformation potentials have been increased by 20%. Additionally the SR parameter Δ has been increased to 0.67 nm in KG calculations (but not in NEGF).

To conclude, we have shown that semi-classical approaches are in excellent agreement with quantum NEGF simulations for electron-phonon scattering, yet not for SR scattering. This sheds new light on the explanation of mobility degradation in thin films.

References

[1] D. Esseni *et al*., Elec. Devices, IEEE Transactions on, **12**, 2445 (2003).
[2] S. Jin *et al*., Elec. Devices, IEEE Transactions on, **54**, 2191 (2007).
[3] F. Gamiz *et al*., J. Appl. Phys., **89**, 1764 (2001) ; *ibid*. **94**, 392 (2003).
[4] S.M. Goodnick *et al*., Phys. Rev. B **32**, 8171 (1985).
[5] D. Esseni *et al*., « Nanoscale MOS Transistors: Semi-Classical Transport and Applications », Cambridge Univ. Press (2011).
[6] UTOX regroups a series of k.p-Schrodinger-based tools including a KG solver. D. Garetto *et al*., Proc. Nanotech Conference (2010)
[7] http://www.synopsys.com/Tools/TCAD/
[8] http://inac.cea.fr/L_Sim/TB_Sim/
[9] K. Uchida *et al*., proc. IEDM 47 (2002).

978-3-901578-26-7 © 2013 Society for Micro- and Nanoelectronics

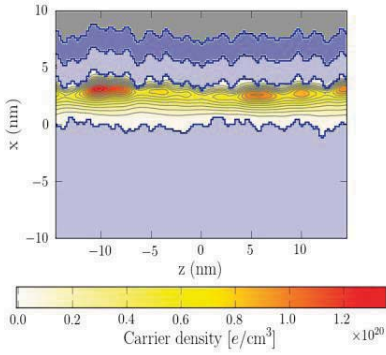

Figure 1 : Carrier density with NEGF in a 4 nm thick FDSOI film. Interface roughness generated with an exponential autocorrelation function (Δ=0.47 nm and Λ=1.3 nm).

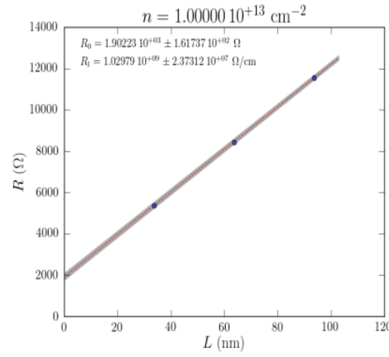

Figure 2 : NEGF resistance of the FDSOI film as a function of length. The slope gives the mobility, while the intercept at L=0 is the quantum "ballistic" resistance.

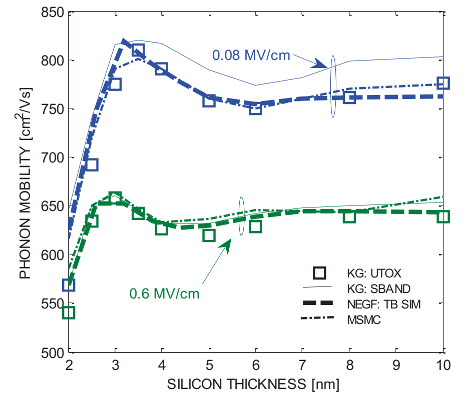

Figure 3 : Comparison of phonon-limited electron mobility in FDSOI devices as a function of active layer thickness. Phonon parameters from [1].

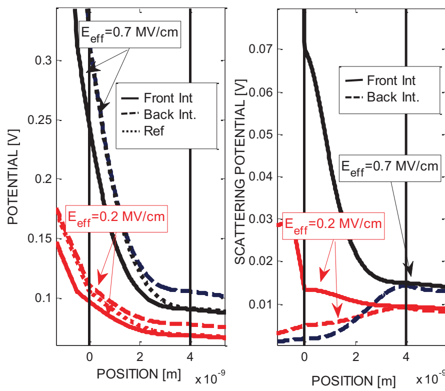

Figure 4 : Electrical potential changes (left) in a 4 nm thick FDSOI device (Ref.) for front and back interface fluctuations (Δ=0.47 nm) and associated scattering potentials (right) defined as the difference between the potential in the reference device and the one in the device with a shifted front or back interface.

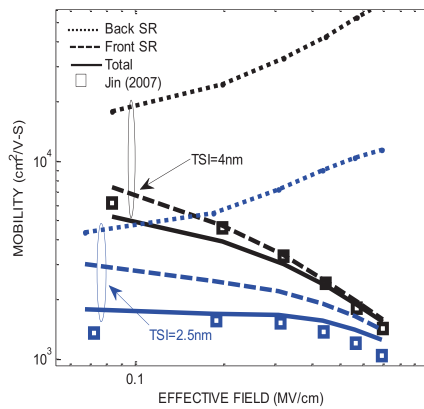

Figure 5 : SR-limited electron mobility calculated with Gamiz [3] approach in FDSOI: Influence of the Back interface roughness and comparison with Jin [2] model (density fluctuation and polarization terms neglected).

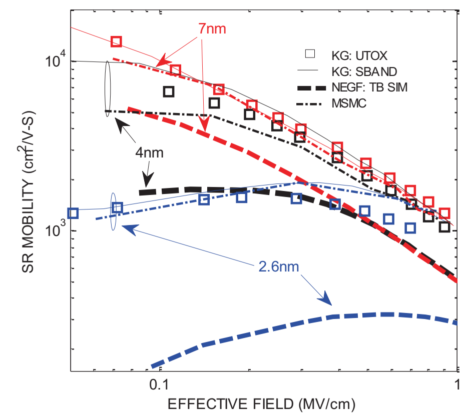

Figure 6 : SR-limited electron mobility for T_{SI}=2.6 nm, 4 nm and 7 nm: scattering time-based methods and NEGF predictions (exponential SR autocorrelation with Δ=0.47 nm; Λ=1.3 nm).

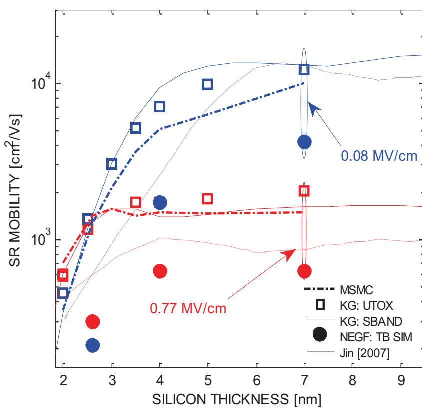

Figure 7 : SR-limited electron mobility vs T_{SI}. Summary of simulation results with present solvers and comparison with S. Jin results [2]. (effective field E_{eff}=0.08 and 0.77 MV/cm; exponential SR autocorrelation with Δ=0.47 nm; Λ=1.3 nm).

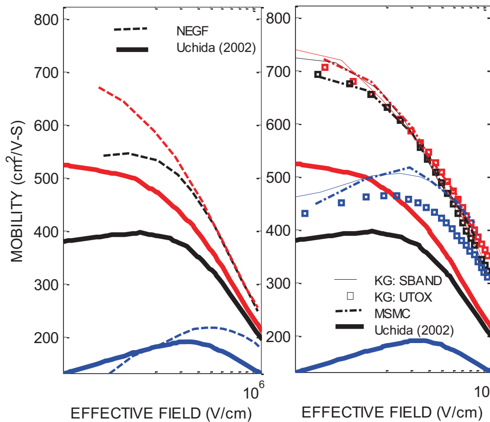

Figure 8 : Total electron mobility in a 2.5 nm, 4 nm and 7 nm FDSOI film calculated with NEGF (left) and scattering time-based methods (right). Comparison with experimental data from K. Uchida [9] (From top-to-bottom: T_{Si}=2.48, 4.3, 7.4 nm).

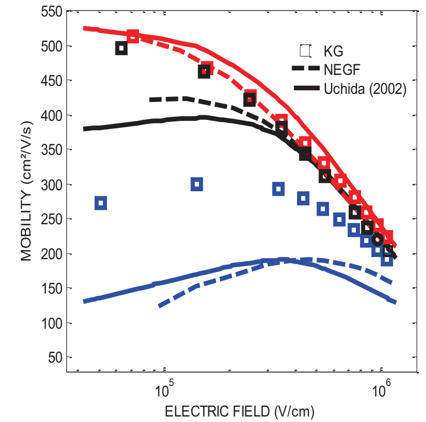

Figure 9 : NEGF with enhanced phonon deformation potentials (+20%) compared to KG results with enhanced phonon (+20%) and SR parameters (Δ=0.67 nm; Λ=1.3 nm).

Quasi Self-consistent Monte Carlo Particle Simulations of Local Heating Properties in Single Layer Graphene Nano-channel FETs

S. Oki, T. Misawa, and Y. Awano
Keio University, Yokohama 223-8522, Japan
E-mail: awano@elec.keio.ac.jp

Abstract

In this paper, we report a new algorithm for Monte Carlo quasi self-consistent particle simulations of both electron and phonon transport in nanometer-channel FETs, based on computer time saving considerations. We simulate a local heating properties of a Single layer graphene (SLG) FETs for the first time, comparing with that of a conventional GaAs devices.

Introduction

Due to high density integration of LSIs and high power applications, thermal management becomes more and more important. Besides, Graphene has received much attention as an emerging research material for future nanoelectronics, because of its excellent electrical, thermal and mechanical properties.

In an advanced electron device scaled below or comparable to the size of electron mean-free-path, Monte Carlo particle simulation method has been used as the most reliable and accurate method to calculate non-stationary electron transport [1]. Similarly, when the mean-free-path of the phonon becomes comparable to the size of device, thermal properties should be analysed for non-stationary state phonon transport. Monte Carlo particle method for both electron and phonon transport [2] must be the most accurate theoretical approach. However, because of a large difference in time-scale between electron and phonon transport phenomena, such a self-consistent simulation with realistic computer time must be very difficult and important for future phonon engineering. In this paper, we propose a new quasi self-consistent algorithm for Monte Carlo method with a reasonable computing time and report electrical and thermal properties of Single layer Graphene (SLG) nano-FETs for the first time.

Simulation Method

Figure 1 shows the algorithm of our simulation. It consists of two parts; an electron transport part to obtain spatial distributions of phonon emission and absorption and a phonon transport part to estimate local heating in the device. In this process, we developed two simulation procedures. First, we made a program to estimate a local temperature from phonon spatial distribution, where we used a Bose-Einstein distribution function, phonon density of states and phonon generation rate, which were obtained by Monte Carlo simulations (Fig. 2). Secondly, we developed a new algorithm, which made it possible to calculate long time phonon transport by introducing different time steps for electron and phonon transport simulations (Fig. 3). In the new algorithm, first, we only calculate electron transport for a short period of time ΔT and obtain phonon spatial distribution. Then, only phonon transport is calculated for long period of time, where phonon particles are generated at each time step of ΔT based on the simulated spatial distribution of phonons. After that, we calculate a local temperature in the channel and electron-phonon scattering rates. By repeating this process, we can analyse phonon transport for a long period of time in extremely short computation time. By these methods, we succeeded in calculating both electron and phonon transports self-consistently for a reasonable computation time. The phonon velocity is derived from the phonon dispersion curve of SLG [4]. The phonon-phonon scattering rate is assumed to be a constant value for each material.

Results and Discussion

Using the new method, we succeeded in analyzing local heating phenomena in nano-scale Single layer graphene (SLG) FETs, quantitatively. Figures 4 show the simulated results of SLG and GaAs channel temperature at 500 ns after applying voltage to the device. The gate length Lg is 100 nm. Figure 5 shows the peak channel temperature

978-3-901578-26-7 © 2013 Society for Micro- and Nanoelectronics

between both devices. The local heating in the SLG channel is much smaller than that of GaAs channel. It is probably due to high speed optical and acoustic phonon transport in SLG, even though the heat generation rate in SLG is much higher than that of GaAs.

CONCLUSION

Thermal property of SLG-channel nano-FETs is simulated. We developed two kinds of simulation procedures for Monte Carlo method, which lead to quasi self-consistent simulations of electron and phonon transport in nano-sale devices for a reasonable computing time. Our method can be applied other materials for power device applications, in which a local heating is more crucial in determining device performance.

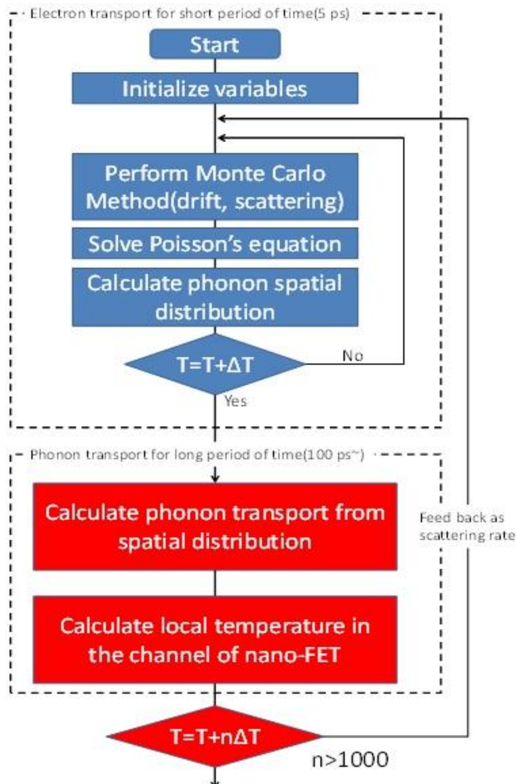

Fig. 1 Algorithm of Quasi Self-consistent Monte Carlo method for electron and phonon transport

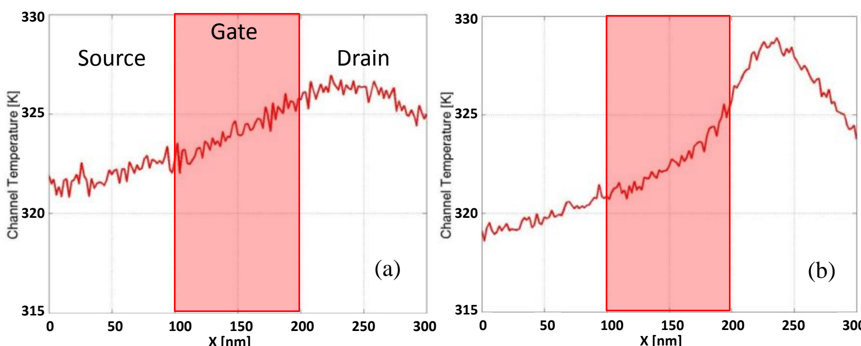

Figs. 4 Local temperature 500 ns after applying voltage to (a) Graphene channel and (b) GaAs channel FETs (Lg=0.1 μm)

ACKNOWLEDGEMENT

The authors would like to thank Professor K. Tomizawa of Meiji University and Professor S. Murakami of Tokyo Institute of Technology for their helpful suggestions and discussions. This research is supported by JSPS through its FIRST Program.

REFERENCES

[1] N. Harada et al., APEX, 1, (2008) 024002
[2] Y. Kamakura, et al., SISPAD 2010, (2010) pp. 89 - 92
[3] D. L. Mafra, et al., Phys. Rev. B 76 (2007) 23340

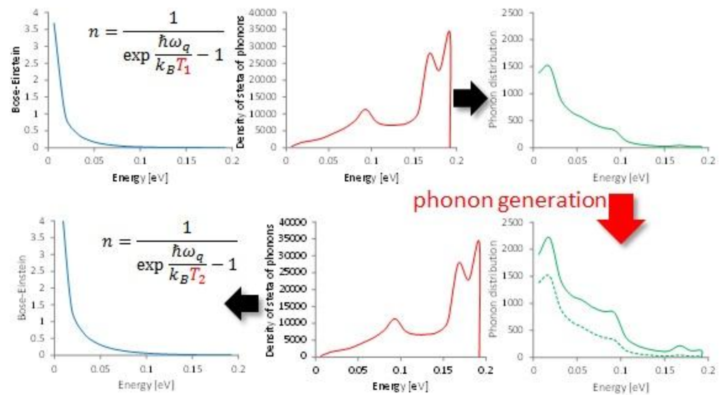

Fig. 2 Schematic of estimation method of a local temperature from phonon population

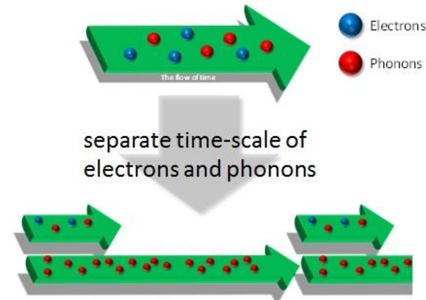

Fig. 3 Schematic of quasi self-consistent simulation procedure for both electron and phonon transport

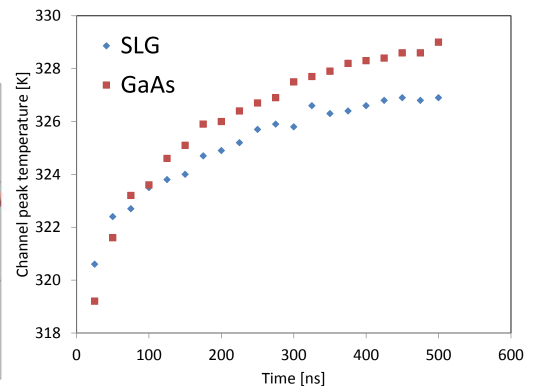

Fig. 5 Local heating in SLG and GaAs channel FETs (Lg=0.1 μm)

3D Monte Carlo Simulation of III-V Implant-Free Quantum-Well and FinFET MOSFETs

E. A. Towie[1], C. Riddet[1] and A. Asenov[1,2]
[1] Device Modelling Group, University of Glasgow, G12 8LT Glasgow, Scotland U.K
[2] Gold Standard Simulations Ltd., G12 8LT Glasgow, U.K.
e-mail: ewan.towie@glasgow.ac.uk

Introduction

Following the 2011 edition of the International Roadmap for Semiconductors (ITRS), the III-V/Ge CMOS technology has moved from the "Emerging Materials Devices" areas to the "Process, Integration and Devices" and "Front End Process" areas of the ITRS, which strongly implies that this technology could be utilized at and beyond the 10nm technology node [1]. To extract the greatest benefit from III-V materials, various new transistor architectures have been considered including the Implant-Free Quantum-Well (IFQW) structure and the multi-gate FinFET structure [2]-[4]. In this work we compare the performance of these two III-V nMOSFET architectures designed for the 10nm CMOS technology generation employing $In_{0.53}Ga_{0.47}As$ as the channel material with a high-κ Al_2O_3 gate oxide and a metal gate.

Devices and Methodology

For the purpose of this work the transistors have been designed to have similar structural details. The structure of the n-type IFQW MOSFET is illustrated in Fig. 1 and the n-type FinFET in Fig. 2. The MOSFET dimensions and doping for the transistors are given in Tables 1-2. Both have an Al_2O_3 gate oxide with a Si_3N_4 lateral spacer. The source and drain regions are epitaxial, in-situ doped raised $In_{0.53}Ga_{0.47}As$, the channel is $In_{0.53}Ga_{0.47}As$ and the substrate is lattice matched $In_{0.52}Al_{0.48}As$. The IFQW transistor has a channel of thickness t_{chn}= 3.75nm and the FinFET has a fin width of W_{fin}= 10nm, and height H_{fin}= 25nm. The channel width of the IFQW is 15nm, and for the FinFET it is $W_{fin}+2\times H_{fin}$= 60nm. Both transistors also include the diffusion of dopants from the source/drain regions into the channel layer [5], which is referred to as sub-diffusion.

The 3D MC module of GARAND [6] is used in this study and provides accurate physical treatment of the non-equilibrium transport in short channel transistors. The MC simulator uses an analytical ellipsoidal, non-parabolic description of the band structure for the III-V materials. Carrier statistics are evaluated using a fully degenerate Fermi-Dirac model that includes the Pauli-Exclusion Principle. Quantum corrections are implemented using a density-gradient approach, which has been calibrated for these devices against a 1D Poisson-Schrodinger solver. The MC module employs the typical scattering mechanisms in III-V materials and the scattering parameters have been calibrated to match the experimentally measured velocity-field and bulk mobility characteristics (Figs. 3-4).

Results

The I_D-V_G characteristics for the two devices are given in Fig. 5 and shows the relationship of drive current per unit width between device architectures. We can report the SS is vastly improved from 88mV/decade in the IFQW to 68mV/dec in the FinFET, and DIBL improves from 85mV/V to 29mV/V. Fig. 6 presents the electron sheet density (per unit width) and velocity of the device with the FinFET having increased electron density in the channel but lower electron velocity. Due to the low DOS of InGaAs, the larger electron density in the FinFET channel increases the impact of degeneracy and forces the electrons into the heavier effective mass L-valleys (see Fig. 7). To conclude, the FinFET structure offers a large improvement in electrostatic control but at higher gate bias doesn't offer improved drive current.

 © 2013 Society for Micro- and Nanoelectronics

REFERENCES

[1] ITRS, International Technology Roadmap for Semiconductors. [Online]. Available: http://www.itrs.net/Links/2011ITRS/

[2] B. Benbakhti et al., Microelectronic Eng., v. 88, p. 358, 2011.

[3] E. A. Towie, S. Liao, C. Riddet, A. Asenov, "Performance Investigation of Implant-Free Quantum-Well InGaAs MOSFET Using Comprehensive Monte Carlo Simulation", unpublished.

[4] M. Radosavljevic et al., IEDM 2011, pp. 33.1.1–33.1.4.

[5] J. Mitard et al., VLSI-T 2011, p. 134.

[6] A. Asenov et al., J Comput Electron, v. 8, p. 349, 2009.

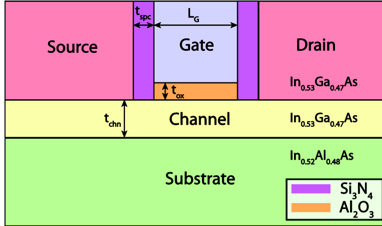

Fig. 1. Device structure of the III-V n-type Implant-Free Quantum-Well MOSFET.

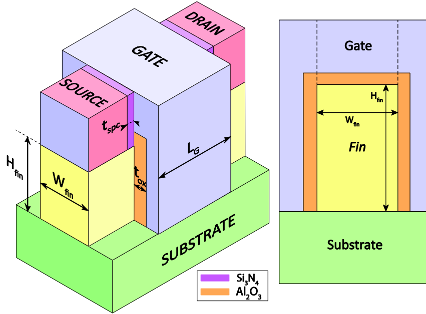

Fig. 2. Device structure of the III-V n-type FinFET MOSFET.

Table 1: IFQW and FinFET structure dimensions.

L_G [nm]	EOT [nm]	T_{ox} [nm]	t_{spc} [nm]
15	0.51	1.125	2

Table 2: IFQW and FinFET doping concentrations.

Src/Drn [cm^{-3}]	Chn. [cm^{-3}]	Subs. [cm^{-3}]
9.1×10^{19}	1.82×10^{17}	3.65×10^{18}

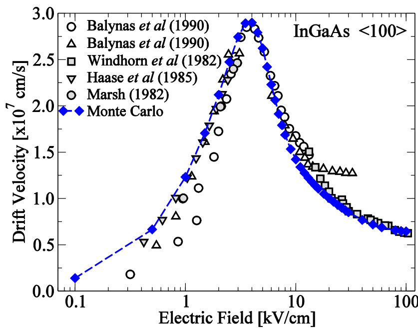

Fig. 3. Calibrated velocity-field characteristic from Monte Carlo simulation for $In_{0.53}Ga_{0.47}As$.

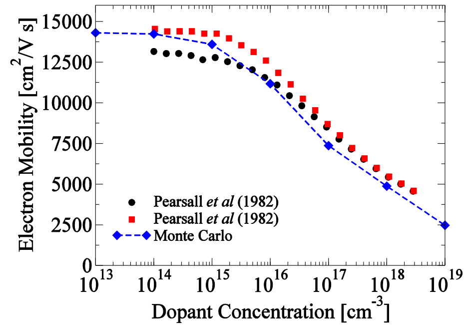

Fig. 4. Calibrated bulk mobility from Monte Carlo simulation for $In_{0.53}Ga_{0.47}As$.

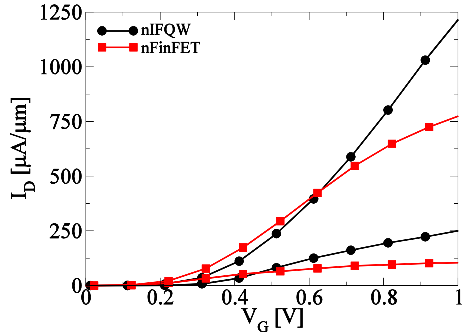

Fig. 5. I_D-V_G characteristics of the III-V nMOSFETs for I_{OFF}= 0.1μA/μm.

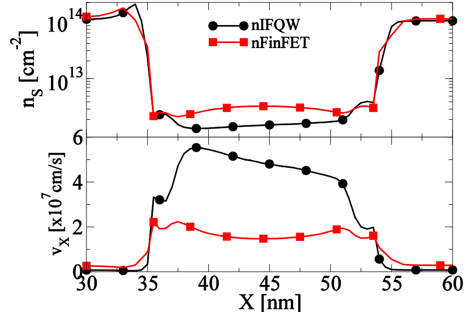

Fig. 6. Sheet density and carrier velocity at V_G=V_D=1V.

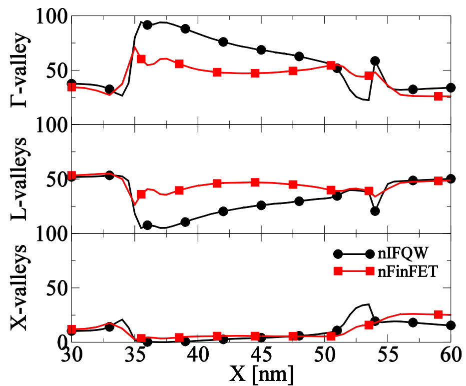

Fig. 7. Conduction band valley occupation [%] at V_G=V_D=1V.

Full Band Monte Carlo Simulation of Silicon Nanowires and Junctionless Nanowire MOSFETs

R. Hathwar, M. Saraniti and S. M. Goodnick
Center for Computational Nanoscience, Arizona State University
e-mail: rhathwar@asu.edu

INTRODUCTION

Junctionless nanowire MOSFETs have recently gained popularity since its debut fabrication at the Tyndall National Institute [1]. The device is simple to fabricate setting it as a strong future contender for the semiconductor industry. Simulations of such nanowire transistors have either involved the assumption of ballistic transport [2] or an effective mass approximation to the nanowire band structure in order to calculate the mobility [5]. In this work we implement a full band Monte Carlo simulation of such devices. The band structure is obtained from a semi-empirical $sp^3d^5s^*$ tight binding (TB) model including spin [3] and deformation potential scattering is included. Results are presented on the mobility of nanowires using k-space simulation, as well as I-V characteristics for device structures such as junctionless nanowire MOSFETs.

NUMERICAL PROCEDURE

The device structure considered is a gate all around junctionless transistor. The oxide thickness is 2nm. The source and drain are doped to 10^{20}cm^{-3} while the channel is doped to 10^{19}cm^{-3}. The device is divided into slabs along the transport direction (axis of the nanowire). Each slab is considered as an individual material with its own band structure and scattering rates. The deformation potential scattering is calculated using the method outlined in [4] modified slightly to include full band optical phonon dispersion. In treating the acoustic modes we still assume a linear dispersion relation as well as the equipartition approximation. The 1D scattering rates are calculated from every k_x to k'_x (assuming the transport direction is the x-axis) and stored in lookup tables [6]. The Poisson equation is solved self-consistently with the Schrödinger equation (through the band structure and scattering rates). To couple 1D transport to a 3D Poisson's solver, we assume that the carrier has a smeared-like charge along the confined directions. The charge distribution at atom m along the confined direction of the wire (for each slab) is assumed to be the carrier charge weighted by $\Sigma|C^2_{lm}|$ over the l orbitals of the atom. This is shown in Fig. 1. The potential obtained from the Poisson solver is then entered back into the TB calculation and new band structures and scattering rates are recalculated for every slab. To make this computationally practical, the band structures and scattering rates are recalculated only every 0.5ps till convergence is reached.

RESULTS

The k-space simulations are run once the band structure and scattering rates for a slab is calculated and stored. The simulations are run till steady state is reached. Interesting physical insights such as particle position and/or valley occupancy in the band structure can be obtained from such a simulation as is shown in Fig. 3. Fig 4. shows the variation of mobility versus nanowire width considering just deformation potential scattering. A plot of the scattering rate versus energy for a 5nmx5nm silicon nanowire is shown in Fig. 2. The rates are lower than that of the bulk material due to the lower density of states of the 1D system. A plot of I_D versus V_G for a 3nmx3nm silicon nanowire junctionless MOSFET is shown in Fig. 5.

REFERENCES

[1] J-P Colinge, C-W Lee, A. Afzalian, N. D. Akhavan *Nature Nanotechnology* **5**, 225-229 (2010).
[2] M. Aldegunde and A. Martinez, *IWCE*, 2012, 1-4.

[3] M.Luisier, A. Schenk, W. Fichtner, *Phys Rev* ***B*** 74, 205323 (2006).
[4] R.Kotlyar, *JAP* **111**, Issue 12, 123718-123718-11.
[5] A.K.Buin, A.Verma, and M.P. Anantram, *J. Appl. Phys.* **104**, 053716 (2008).
[6] M.Saraniti, S.M.Goodnick, *IEEE Transactions on Electronic Devices*, Vol **47**, No. 10, 2000.

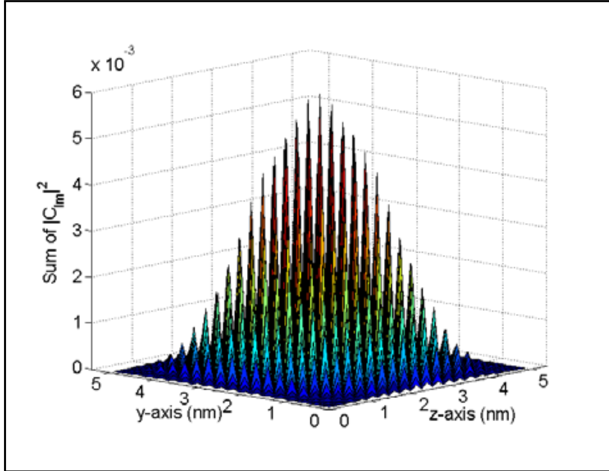

Fig. 1. The distribution of the carrier charge at the 1st CB at the gamma valley in a 5nmx5nm Si nanowire.

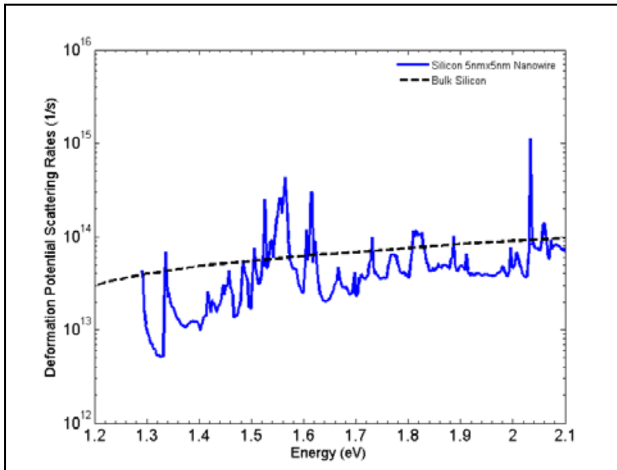

Fig. 2. Deformation potential scattering rates of a Si 5nmx5nm nanowire as compared to the bulk rates calculated by the EPM method.

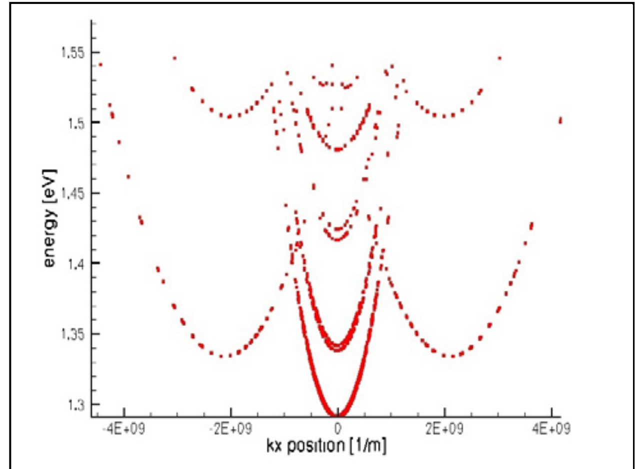

Fig. 3. Position, in k-space, of 20000 carriers taken at steady state in a 5nmx5nm Si nanowire under an applied electric field of 1kV/cm along the axis of the wire.

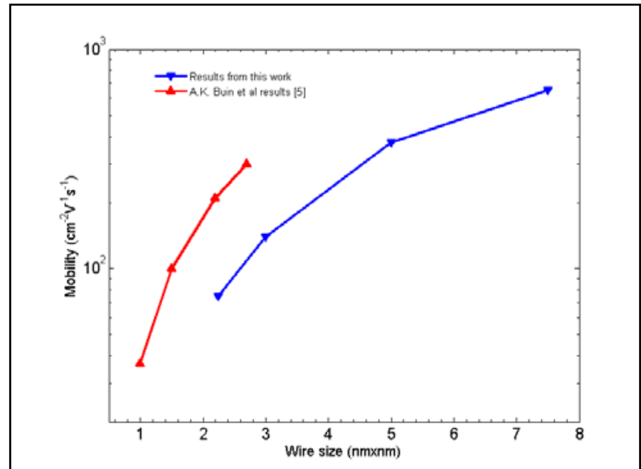

Fig. 4. Phonon limited mobility at steady state for different wire widths (inverted triangles) against the values calculated by [5] (triangle).

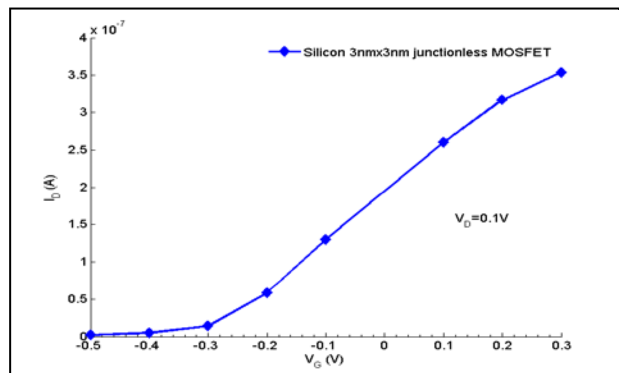

Fig. 5. I_D-V_G curve for 3nmx3nm Si nanowire junctionless MOSFET at V_D=0.1V.

Influence of Phonon Dispersion Relation on Thermal Resistance in Silicon Nanostructures

Kentaro Kukita*, Indra Nur Adisusilo* and Yoshinari Kamakura*†
*Graduate School of Engineering, Osaka Univ., 2-1 Yamada-oka, Suita, Osaka 565-0871, Japan
†Japan Science and Technology Agency (JST), CREST, Kawaguchi, Saitama 332-0012, Japan
e-mail: kukita@si.eei.eng.osaka-u.ac.jp

INTRODUCTION

The accurate understanding of the thermal conduction properties in nanoscale regime becomes important because of the scaling of the electronic devices. In this study, we analyze the thermal resistance in Si nanostructures using a Monte Carlo (MC) method for solving the phonon Boltzmann transport equation, and discuss the quasi-ballistic transport properties depending on the phonon dispersion relation model.

SIMULATION METHOD AND RESULTS

Figure 1 shows a dispersion relation of phonons in bulk Si calculated with adiabatic bond charge model [1]. In many of the previous works, approximated dispersion curves were employed; e.g., as shown in Fig. 1, the dispersion relation were expressed by the analytical curve fitted only to [100] (Γ–X) direction [2]. In this study, we compare the [100] model to the more accurate approach, in which the phonon density of states and the group velocity averaged over constant-energy surfaces were calculated from the realistic dispersion relation and implemented as look-up tables (full-band model) in the phonon MC simulator [3,4].

Figure 2 shows the phonon average group velocity v as a function of temperature T. Note that the [100] model exhibits higher velocities, which is mainly due to the lack of TA2 branch having low group velocities. We have confirmed, however, that both two models can yield the correct thermal conductivity $\kappa(T)$ of bulk Si by adjusting the phonon scattering rates. Considering that κ is expressed as $\sim Cv\lambda/3$ (where C and λ are the heat capacity and phonon mean free path, respectively), lower λ value is needed for [100] model as shown in Fig. 3.

To investigate the difference between the two models, we have simulated the steady state temperature distribution in the simple one-dimensional structure of Si as shown in Fig. 4. Figure 5 shows the calculated thermal resistances R_{th} as a function of the device length L. In the large L limit, the two models exhibit the same R_{th}, while the discrepancy was found in the small L region. As illustrated in Fig. 6, when $L \gg \lambda$, the phonon transport property is considered to be diffusive, and R_{th} is a function of κ. Since the scattering rate parameters for the both models were adjusted to yield the experimental κ, the both same R_{th} were obtained. On the other hand, when $L \ll \lambda$, the ballistic transport nature, which depends on v but not λ, becomes dominant, and thus [100] model shows lower R_{th}.

SUMMARY

We have analyzed the thermal resistance in Si nanostructures using the MC method. It has been demonstrated that the correct implementation of the phonon dispersion relation is essential to accurately simulate the thermal conduction properties in the quasi-ballistic transport regime.

REFERENCES

[1] W. Weber, *Adiabatic bond charge model for the phonons in diamond, Si, Ge, and α-Sn*, Phys. Rev. B **15**, 4789 (1977).
[2] P. Chantrenne, J. L. Barrat, X. Blase, and J. D. Gale, *An analytical model for the thermal conductivity of sil- icon nanostructures*, J. Appl. Phys. **97**, 104318 (2005).
[3] K. Kukita and Y. Kamakura, *Monte Carlo Simulation of Phonon Transport in Silicon Thin films Including Realistic Dispersion Relation*, Proc. Int. Workshop on Comp. Elec., pp. 63-64, 2012.
[4] K. Kukita, I. N. Adisusilo and Y. Kamakura, "Impact of Quasi-Ballistic Phonon Transport on Thermal Properties in Nanoscale Devices;: A Monte Carlo Approach," Tech. Dig. IEDM, pp. 411-414, 2012.

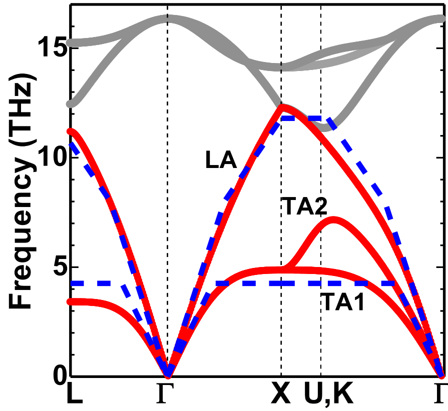

Fig. 1. Phonon dispersion curves for bulk Si obtained from adiabatic bond charge model [1]. Only acoustic phonons (TA1, TA2, and LA) were considered in this work. Lines are the approximated curves used in the previous work [2].

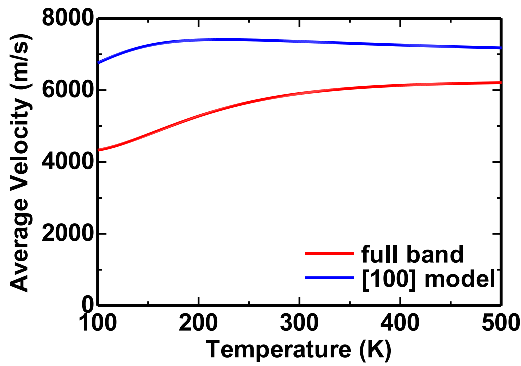

Fig. 2. Average group velocity of acoustic phonons as a function of temperature. The results calculated from a realistic dispersion relation (red line) and approximated model (blue line) are compared.

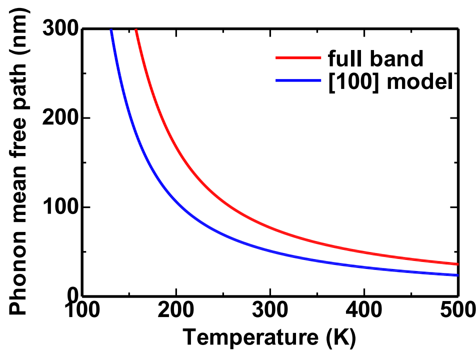

Fig. 3. Phonon mean free path as a function of temperature. Realistic dispersion relation (red line) and approximated model [2] (blue line) are compared.

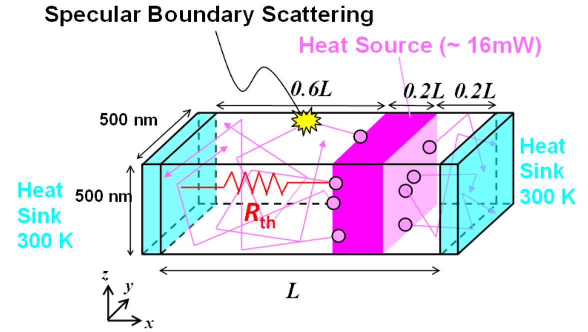

Fig. 4. Schematic view of the 1D structure to investigate the thermal resistance R_{th} in Si device with various L.

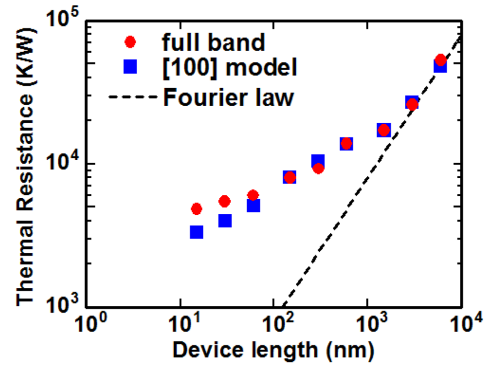

Fig. 5. Simulated $R_{\rm th}$ as a function of L. MC simulation results with the full band model and [100] phonon dispersion model are compared. The dashed line represent the theoretical dependence based on the Fourier law.

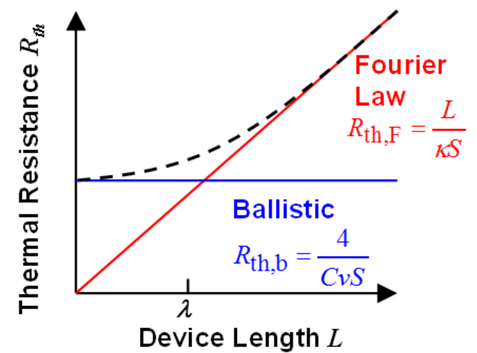

Fig. 6. Schematic view showing L-dependence of R_{th} described with the Fourier law and the ballistic transport model.

Modeling Spin-Based Devices in Silicon

V. Sverdlov, H. Mahmoudi, A. Makarov, D. Osintsev, J. Weinbub, T. Windbacher, and S. Selberherr
Institute for Microelectronics, TU Wien, Gußhausstraße 27–29/E360, 1040 Wien, Austria
e-mail: sverdlov@iue.tuwien.ac.at

Continuous miniaturization of CMOS devices made the breath taking increase in performance of integrated circuits become a magnificent reality. Numerous tough problems were solved on this exciting journey; however, growing technological challenges and soaring costs will gradually bring CMOS scaling to an end. This puts foreseeable limitations to the future performance increase, and research on alternative technologies and computational principles becomes paramount.

The spin of an electron possesses several exciting properties suitable for future devices. It is characterized by two projections on a chosen axis – up or down, and it can change its orientation rapidly by utilizing an amazingly small amount of energy. Employing spin, as a compliment to electron charge, opens new exciting opportunity for developing conceptually new non-volatile nanoelectronic devices for future low power applications [1].

Silicon, the main material of microelectronics, is characterized by weak spin-orbit interaction and zero-spin nuclei, which gives rise to a long spin lifetime. This makes silicon perfectly suited for spin-driven applications. Spin propagation through an undoped 350μm thick silicon wafer [2] gives hope for fabrication of silicon spin-based devices in the near future increasingly likely.

The success of microelectronics has been assisted by smart Technology Computer-Aided Design tools. Because a commercial support for spin applications is entirely absent it is mandatory to develop a simulation environment for spin-based devices in silicon [3]. Understanding spin-polarized transport in silicon and in compatible hysteretic materials facilitates inventing, modeling, and optimizing prototypes of spin-based switches and memory devices for the 21st century.

The canonical spin field-effect transistor (SpinFET) proposed by Datta and Das [4] is a switch which employs the electron spin to modulate the current through the device. The SpinFET is composed of a semiconductor channel region sandwiched between two ferromagnetic contacts. The source contact injects spin-polarized electrons in the semiconductor. The gate-voltage-dependent spin-orbit interaction in the channel is used to modulate the current through the SpinFET. It causes the electron spin to precess during the electron propagation through the channel. Only the electrons with their spins aligned to the drain contact's magnetization can leave the channel through the drain contact, thus contributing to the current. For practical realization of a SpinFET it is mandatory to solve the problem of spin injection and detection as well as spin propagation, control, and manipulation [5]. Successful spin injection from different ferromagnets into a number of semiconductors through several oxides has been demonstrated [5-7]. Regardless the undoubted progress, the level of spin accumulation which displays several orders of magnitude discrepancy [5] with the standard theory is not yet understood.

Close to interfaces the spin diffusion length and relaxation time at room temperature appear to be shorter with much weaker temperature dependence than in the bulk [7]. Thus, external spin relaxation mechanisms due to the presence of a Si/SiO_2 interface become central, and methods to boost the spin lifetime in MOSFETs are needed. We utilize a spin-dependent **k·p** Hamiltonian [8], where only the [001] valleys are included. Without strain the unprimed subbands are degenerate. This degeneracy produces a large mixing between the spin-up and spin-down states from the opposite valleys, resulting in hot spots characterized by strong spin relaxation. The hot spots are defined by the condition $D\varepsilon_{xy} - \hbar^2 k_x k_y \left(\frac{1}{m_t} - \frac{1}{m_0}\right) = 0$, where D = 14eV is the shear strain deformation potential, m_t is the transverse mass, and ε_{xy} is shear strain. In strained samples the hot spots are moved away from the center of the two-dimensional Brillouin zone (Fig.1), which reduces

their contribution to spin relaxation. Thus, strain used to enhance on-current in nano-CMOS can significantly boost spin lifetime [9] (Fig.2).

The spin-orbit interaction in silicon films is due to the interface-induced inversion symmetry breaking [10]. Silicon nanowires with [100] orientation display a stronger modulation of the conductance as function of spin-orbit interaction and are preferred for practical realizations of SpinFETs [11]. However, the channel length required to manipulate spin is about a micron. The spin degree can be introduced into nano-CMOS by using ferromagnetic source and drain contacts [1], however, due to the low spin injection efficiency at room temperature [12], it has not yet been realized. Many new ideas to build spin-based devices have been recently introduced [5], [13]. To be successful, these devices must operate at room temperature and be compatible with CMOS. Albeit many exciting inventions are lying ahead, the practical option for the near future is to benefit from combining CMOS with magnetic tunnel junctions (MTJs). MTJ-based spin transfer torque MRAM is CMOS compatible, non-volatile, and close to production. A combination of a MTJ with a MOSFET to a pseudo-spin-MOSFET appears to be very beneficial [14]. Arrays made of MTJs offer new opportunities to build non-conventional non-volatile logic-in-memory systems [15].

This work is supported by the European Research Council through the grant #247056 MOSILSPIN.

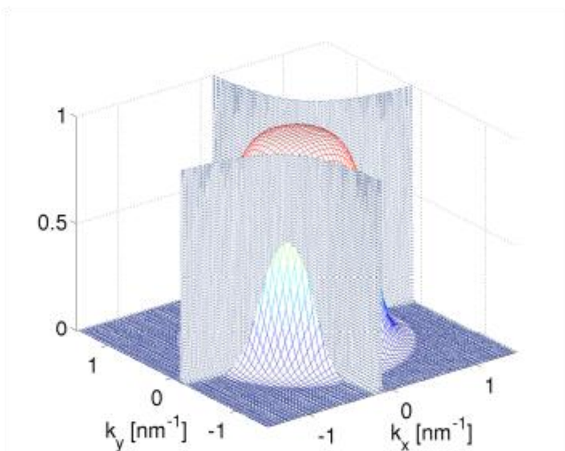

Fig. 1. Spin relaxation hot spots in strained samples.

References

[1] S. Sugahara and J. Nita, *Spin-transistor electronics: an overview and outlook*, Proc. IEEE **98**, 2124 (2010).

[2] B. Huang, D. J. Monsma, and I. Appelbaum, *Coherent spin transport through a 350 micron thick silicon wafer*, Phys.Rev.Lett. **99**, 177209 (2007).

[3] http://www.iue.tuwien.ac.at/index.php?id=software.

[4] S. Datta and B. Das, *Electronic analogue of the electro-optical modulator*, Appl.Phys.Lett. **56**, 665 (1990).

[5] R. Jansen, *Silicon spintronics*, Nature Materials **11**, 400 (2012).

[6] C.H. Li, O.M.J. van t'Erve, and B.T. Jonker, *Electrical injection and detection of spin accumulation in silicon with magnetic metal/silicon dioxide contacts*, Nature Commun. **2**, 245 (2011).

[7] T. Suzuki et al., *Room-temperature electron transport in highly doped Si channel*, Appl.Phys.Express **4**, 023003 (2011).

[8] P. Li and, H. Dery, *Spin-orbit symmetries of conduction electrons in silicon*, Phys.Rev.Lett. **107**, 107203 (2011).

[9] D. Osintsev, V. Sverdlov, and S. Selberherr, *Spin lifetime enhancement by shear strain in thin silicon-on-insulator films*, Proc. 223rd ECS Meeting, accepted (2013).

[10] M. Prada, G. Klimeck, and R. Joynt, *Spin–orbit splittings in Si/SiGe quantum wells: from ideal Si membranes to realistic heterostructures*, New J.Phys. **13**, 013009 (2011).

[11] D. Osintsev et al., *Temperature dependence of the transport properties of spin field-effect transistors built with InAs and Si channels*, Solid-State Electron. **71**, 25 (2012).

[12] S. Zhang et al., *Electrical spin injection and detection in silicon nanowires trough oxide tunnel barrier*, Nano Lett., online version **DOI:** 10.1021/nl303667v (2013).

[13] J. Fabian et al., *Semiconductor spintronics*, Acta Physica Slovaca **57**, 565 (2007).

[14] Y. Shuto et al., *Design and performance of pseudo-spin-MOSFET using nano-CMOS devices*, Proc. IEDM, 685 (2012).

[15] H. Mahmoudi, V. Sverdlov, and S. Selberherr, *MTJ-based implication logic gates and circuit architecture for large-scale spintronic stateful logic systems*, Proc. ESSDERC, 254 (2012).

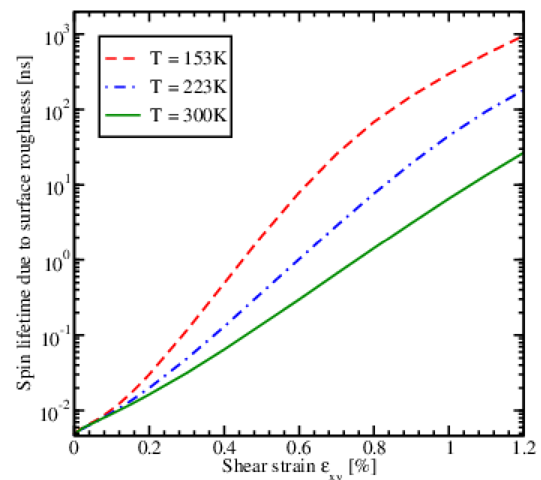

Fig. 2. Spin lifetime enhancement by shear strain.

Modeling the Resistive Switching Process in Transition Metal Oxide Based Non-Volatile Memory Devices

B. Magyari-Köpe and Y. Nishi
Department of Electrical Engineering, Stanford University
e-mail: blankamk@stanford.edu

INTRODUCTION

Binary transition metal oxides TiO_x, NiO_x, HfO_x, AlO_x, TaO_x have been recently proposed as possible materials for embedded non-volatile memory modules. Currently, a major bottleneck in determining the scalability, retention and endurance of these devices, is the lack of detailed understanding of resistive switching mechanism. Generally, the process of forming in transition metal oxides systems includes either the diffusion of oxygen vacancies to cluster into filaments [1-5] or the diffusion of oxygen atoms away from the oxide region to form a thin interfacial reduced oxide. During electroforming, oxygen vacancies or ions are believed to drift due to the applied bias (Fig. 1), trap electrons or holes and facilitate the formation of vacancy ordered domains [4]. Then, during the reset process, the ordered vacancy domains are disconnected and a high resistance state is achieved. Another, slightly different mechanism is based on the potential barrier change between the electrode and the oxide by modulating the Schottky barrier height.

DISCUSSION

Filamentary models for transition metal oxides had been proposed theoretically [4] and the formation energy implications of a conductive filament channel formation corresponding to the "ON" state or LRS [6-8] was investigated (Fig. 2). The rupturing/dissolution process of the so formed filament, i.e. switching to the "OFF" state of the memory operation with HRS characteristics, is illustrated in Fig, 3. Preferential impurity doping [9] in these types of systems can favorably affect the transition process between the "ON" and "OFF" states (Fig. 4). In addition, the effect of electron and hole trapping during the switching process under applied electrical field were recently explained [10]. Hole injection into an oxygen reduced transition metal oxide that contain a formed filament were found to favor the dissolution, while electron injection induces filament formation, respectively. A schematic illustration of this process is shown in Fig. 5.

CONCLUSION

Atomistic modeling approaches based on quantum mechanical principles were used to elucidate the formation of filaments in ReRAM devices and a switching mechanism is proposed.

ACKNOWLEDGEMENT

The calculations were partially done using the NSF supported National Nanotechnology Infrastructure Network's computation cluster at Stanford University. In addition, the use of the Center for Nanoscale Materials was supported by the U. S. Department of Energy, Office of Science, Office of Basic Energy Sciences, under Contract No. DE-AC02-06CH11357.

REFERENCES

[1] B. Magyari-Köpe et al., J. Mater. Sci., 47, 7498, 2012.
[2] L. Zhao et al., *MRS Proc.,* 1430, 1103, 2012
[3] D. Duncan et al., *MRS Proc.,* 1430, 980, 2012.
[4] S.G. Park et al., *Phys. Rev. B*, 82, 115109, 2010.
[5] H.-D. Lee et al., *Phys. Rev. B,* 81, 193202, 2010.
[6] S.G. Park et al., *Tech. Digest VLSI Tech. Symp.,* 2011.
[7] B. Magyari-Köpe et al., *Nanotechn.* 22, 254029*,* 2011.
[8] S.G. Park et al., *EDL*, 32, 197, 2011.
[10] L. Zhao et al., *APL*, 102, 083506, 2013.
[9] K. Kamiya et al., *APL*, 100, 073502, 2012; *Tech. Digest IEDM,* 2012.

 © 2013 Society for Micro- and Nanoelectronics

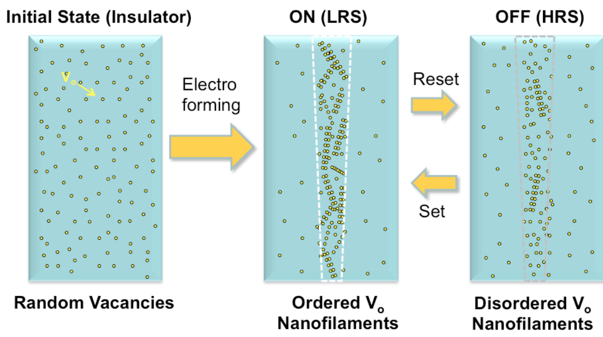

Fig. 3. Schematic switching model incorporating nano-filaments formation and disruption.

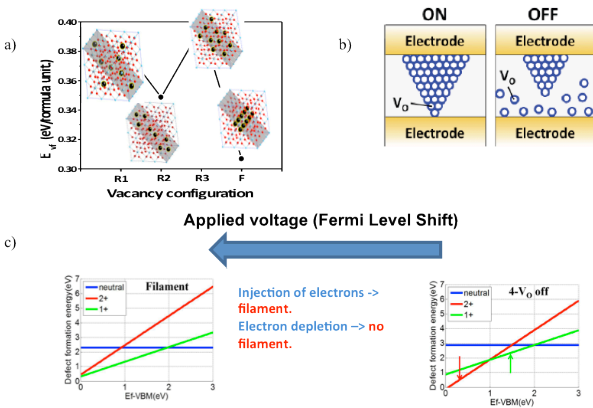

Fig. 2 a) Oxygen vacancy ordering is shown to be energetically favored over random configurations b) Schematic view of cohesion ("ON" state) to isolation ("OFF" state) transition of the filament formed by oxygen vacancies. c) The "ON"-"OFF" transition driven by the applied electric field induces filament stabilization/destabilization depending on electron or hole injection.

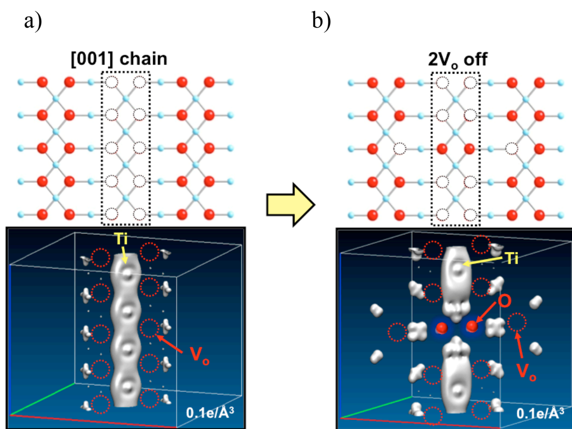

Fig. 3. Oxygen vacancy configurations and the corresponding partial defect charge densities. a) Ordered vacancy chain b) Disrupted oxygen vacancy chain.

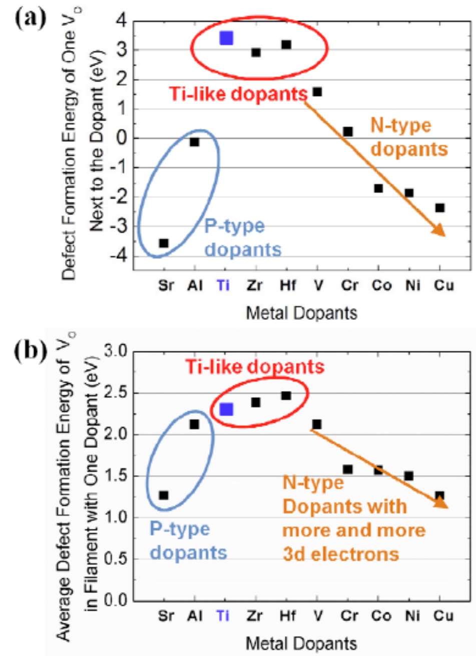

Fig. 4 a) Calculated formation energies of single oxygen vacancy next to different types of dopants. (b) Calculated average formation energies of oxygen vacancies in the filament doped with the metal dopants.

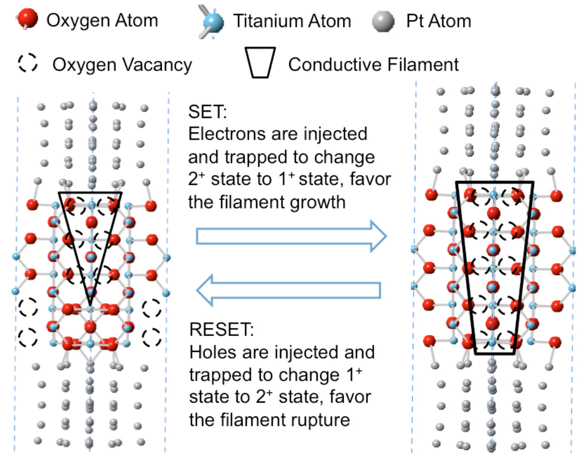

Fig. 5. Schematic view of electron and hole trapping process and their effect on the switching mechanism.

Structural Optimization of MTJs with a Composite Free Layer

A. Makarov, V. Sverdlov, and S. Selberherr
Institute for Microelectronics, TU Wien, Gußhausstraße 27-29, 1040 Wien, Austria
e-mail: {makarov | sverdlov | selberherr}@iue.tuwien.ac.at

INTRODUCTION

New types of spintronics devices utilizing magnetization switching by current, such as spin-torque transfer RAM and spin-torque oscillators, have been intensely developed based on MgO magnetic tunnel junctions (MTJs) with a large magneto-resistance ratio [1], [2] (Fig.1a). At the same time the research on new materials and architectures for MTJ structures has recently gained momentum. A MTJ with a composite free layer (C-MTJ) was proposed [3-5]. The free magnetic layer of such a structure consists of two equivalent parts of half-elliptic form separated by a narrow non-magnetic spacer (Fig.1b). The C-MTJs demonstrate a substantial decrease of the switching time and switching current as compared to the standard MTJ with the monolithic free layer.

In this work we present a structural optimization of C-MTJs (Fig.1b) by means of extensive micromagnetic simulations and propose a new structure of the composite free layer, C2-MTJ (Fig.1c).

SIMULATIONS AND RESULTS

In C2-MTJs the free layer consists of two ellipses with the major axes *a/2* and *b* (*a>2b*) inscribed into a rectangle $a\times b$. This structure is easier to fabricate as compared to the previous generation of C-MTJs (Fig.1b). The simulations are based on the magnetization dynamics described by the LLG equation with the additional spin torque terms [3-5].

We found that both C-MTJ and C2-MTJ composite structures have the same switching time (Fig.2), i.e. the fast switching in C2-MTJ is preserved (Fig.3b) as compared to the monolithic M1-MTJ. Despite the modification in shape, the C2-MTJ is characterized by the same thermal stability as C-MTJ (Fig.4). Note, that the C2-MTJ exhibits the same switching time as the monolithic structure (M2-MTJ) with one small ellipse (Fig.3a), while possessing nearly a two times larger thermal stability factor (Fig.5). The dependence of the width of the standard deviation on the composite layer thickness is shown in Fig.6 for several values of the short axis. A C2-MTJ with $52.5\times25\text{nm}^2$ cross section, as well as C-MTJs [4], has the width of the standard deviation of switching times $\sim10^{-3}$ns, while for a MTJ with $52.5\times10\text{nm}^2$ cross section the value is considerably larger (0.3-1ns).

Next, we look at the magnetization dynamics of the left and right part of the C2-MTJ free layer separately (Fig.7). We found that the peculiarity of the switching behavior of C-MTJs [4], where the switching occurs mostly in the *x-y* plane, is preserved in C2-MTJs (Fig.7). Thus, the switching barrier in a C2-MTJ is practically equal to the thermal stability barrier defined by the shape anisotropy, as confirmed in Fig.8.

CONCLUSION

We proposed the new C2-MTJ structure with a composite free layer. Our simulations show that, while preserving all the advantages of the C-MTJs, the newly proposed structure can be easier fabricated, offering great potential for STT-MRAM performance optimization.

ACKNOWLEDGEMENT

The work is supported by the European Research Council through the grant #247056 MOSILSPIN.

REFERENCES

[1] A. Fukushima et al., *Trans. on Magn.* **48**, 4344 (2012).
[2] R. Sbiaa et al., *Phys. Stat. Solidi RRL* **12**, 413 (2011).
[3] A. Makarov et al., *IWCE*, 225 (2012).
[4] A. Makarov et al., *SISPAD*, 229 (2012).
[5] A. Makarov et al., *SSDM*, 402 (2012).

978-3-901578-26-7 © 2013 Society for Micro- and Nanoelectronics

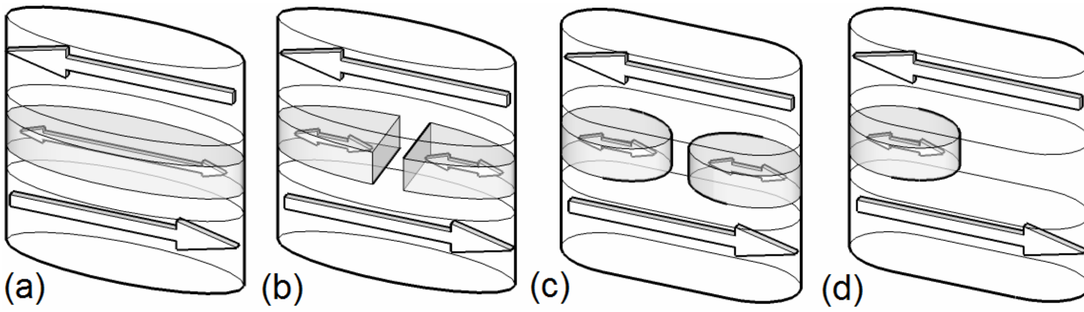

Fig. 1. Schematic illustration of penta-layer MTJs with monolithic free layer M1-MTJ (a) and M2-MTJ (d), and composite free layer C-MTJ (b) and C2-MTJ (c).

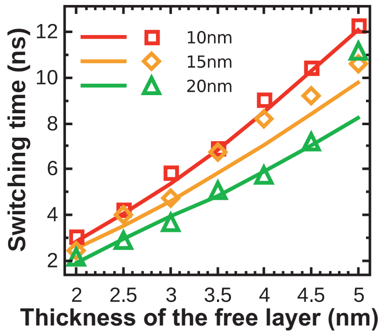

Fig. 2. Switching time of the C-MTJ (symbols) and C2-MTJ (lines) as function of the thickness of the free layer. The long axis is fixed at 52.5nm and the thickness of the fixed layers are 5nm. Dependences are shown for short axes of 10nm, 15nm, and 20nm length.

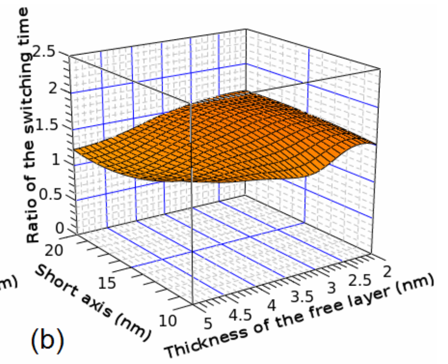

Fig. 3. Ratio of the switching times in the monolithic structure and composite structure as function of thickness of the free layer and short axis length. The long axis is fixed at 52.5nm. Dependences are shown for ratio: M2-MTJ vs. C2-MTJ (a), M1-MTJ vs. C2-MTJ (b).

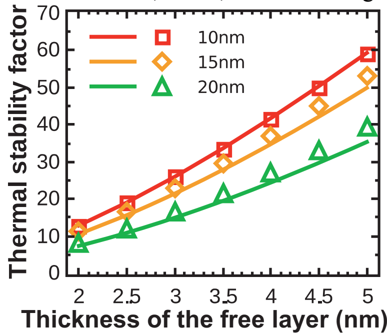

Fig. 4. Thermal stability factor for C-MTJ (symbols) and C2-MTJ (lines) as function of the thickness of the free layer. The long axis is fixed at 52.5nm and the thickness of the fixed layers are 5nm. Dependences are shown for short axes of 10nm, 15nm, and 20nm length.

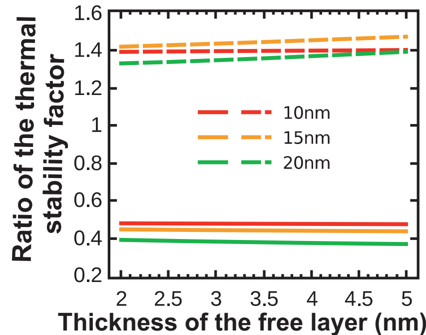

Fig. 5. Ratio of the thermal stability factor for monolithic structure and composite structure as function of thickness of the free layer and short axis length. The long axis is fixed at 52.5nm. Dependences are shown for ratio: M2-MTJ vs. C2-MTJ (solid lines), M1-MTJ vs. C2-MTJ (dotted lines).

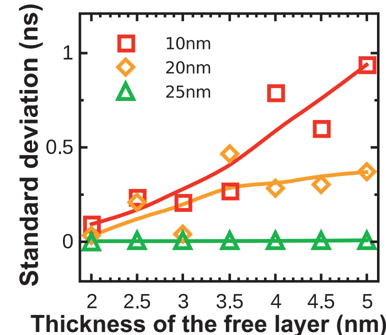

Fig. 6. The standard deviation of the switching time distribution in the composite structure as a function of thickness of the free layer. The long axis is fixed at 52.5nm and the thickness of the fixed layers are 15nm. Dependences are shown for short axes of 10nm, 20nm, and 25nm length.

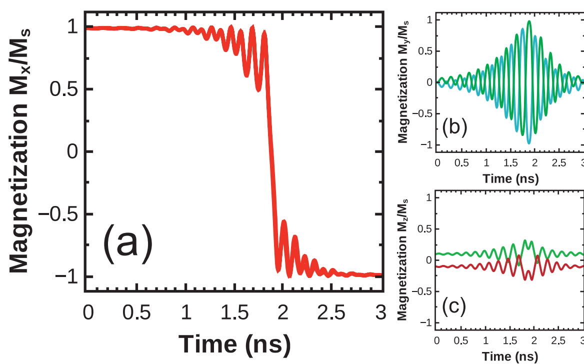

Fig. 7. Magnetization components as a function of time for a MTJ element of 52.5×20nm^2 with a composite free layer (C2-MTJ). The magnetization of the left and right half is shown separately.

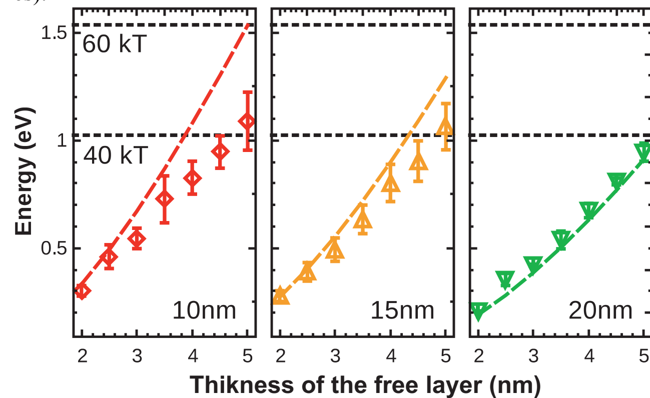

Fig. 8. Thermal energy (lines) vs. switching energy (symbols) barriers for C2-MTJ. The long axis is fixed at 52.5nm and the thickness of the fixed layers are 5nm. Dependences are shown for short axes of 10nm, 15nm, and 20nm length.

Influence of Surface Roughness Scattering on Spin Lifetime in Silicon

D. Osintsev, V. Sverdlov, and S. Selberherr
Institute for Microelectronics, TU Wien, Gußhausstraße 27–29/E360, 1040 Wien, Austria
E-mail: {Osintsev|Sverdlov|Selberherr}@iue.tuwien.ac.at

Silicon is an ideal material for spintronic applications [1] due to long spin lifetime, however, considerable spin relaxation in gated silicon structures was experimentally observed [2]. Surface roughness scattering determines the transport in the channel at high carrier concentration N_s in thin silicon films [3].

Here we investigate the spin relaxation due to surface roughness. The surface roughness scattering matrix elements are proportional to the square of the product of the subband wave function derivatives at the interface [4, 5]. To find the corresponding matrix elements for spin relaxation we use the effective **k·p** Hamiltonian for the two relevant valleys along the *OZ*-axis [6, 7] with the spin degree of freedom properly included [8-10].

The relaxation time τ is calculated as a thermal average with the Fermi function $f(\varepsilon)$

$$\frac{1}{\tau} = \frac{\int \frac{1}{\tau(\mathbf{K_1})} f(\varepsilon)\big(1-f(\varepsilon)\big)\, d\mathbf{K_1}}{\int f(\varepsilon)\, d\mathbf{K_1}} \qquad (1)$$

of the rate [4,8,9]

$$\frac{1}{\tau(\mathbf{K_1})} = \frac{4\pi}{\hbar} \sum_{i,j=1,2} \int_0^{2\pi} \pi\Delta^2 L^2 \frac{1}{\epsilon_{ij}^2(\mathbf{K_2}-\mathbf{K_1})} \frac{\hbar^4}{4m_l^2} \left[\frac{d\Psi^*_{i\sigma\mathbf{K_1}}}{dz}\frac{d\Psi_{j\sigma'\mathbf{K_2}}}{dz}\right]^2_{z=\pm\frac{t}{2}}$$
$$\times \exp\left(\frac{-(\mathbf{K_2}-\mathbf{K_1})^2 L^2}{4}\right) \frac{|\mathbf{K_2}|}{\left|\frac{\partial\varepsilon(\mathbf{K_2})}{\partial\mathbf{K_2}}\right|} \frac{1}{(2\pi)^2}\, d\varphi, \qquad (2)$$

where ε is the electron energy, $\mathbf{K_{1,2}}$ are the in-plane wave vectors, σ, σ' are the spin projections on a chosen axis, ϵ_{ij} is the dielectric permittivity, L is the autocorrelation length, Δ is the mean square value of the surface roughness fluctuations. In case the wave vector dependence of the derivatives of the wave functions $\Psi_{i\sigma\mathbf{K}}$ on $\mathbf{K}$ can be ignored [4, 5], the rate (2) is approximated as

$$\frac{1}{\tau(\mathbf{K_1})} = \frac{2\pi\Delta^2 L^2}{\hbar} \sum_{i,j=1,2} \frac{\hbar^4}{4m_l^2} \left[\frac{d\Psi^*_{i\sigma\mathbf{K}\to\mathbf{0}}}{dz}\frac{d\Psi_{j\sigma'\mathbf{K}\to\mathbf{0}}}{dz}\right]^2_{z=\pm\frac{t}{2}}$$
$$\times \exp\left(\frac{-(\mathbf{K_2^2}+\mathbf{K_1^2})L^2}{4}\right) \frac{m_t}{2\pi\hbar^2} 2\pi I_0\left(-\frac{L^2 K_1 K_2}{2}\right), \qquad (3)$$

where I_0 is the modified Bessel function of the first kind.

Through all simulations we use a film thickness of 2.48nm. Fig. 1 shows the dependence of the surface roughness limited mobility on shear strain. A good agreement between the results calculated with (2) and (3) is observed confirming the standard approximation of neglecting the wave vector dependence in the matrix elements [4]. In the absence of strain the mobility is higher for higher electron concentrations N_s, in agreement with [3]. For $N_s = 10^{12}\text{cm}^{-2}$ the mobility increases with tensile shear strain because of the reduction of the transport effective mass [6]. For $N_s = 5 \cdot 10^{12}\text{cm}^{-2}$ an opposite trend is observed, because of the increase of intrasubband scattering with strain within the second subband (Fig. 2), which gets split from the first one due to strain-induced valley splitting (inset in Fig. 2). The occupation of the second subband remains substantial even at high strain as confirmed by the Fermi level dependence (inset in Fig. 2). This increase of the intrasubband scattering overcompensates the mobility enhancement due to the reduced transport mass, resulting in an overall decrease of the surface roughness limited mobility at high N_s (Fig. 1).

To evaluate the electron spin relaxation we take the matrix elements on the wave functions with the opposite spin projections $\sigma' = -\sigma$ corresponding to the spin flip events. Normalized spin relaxation matrix elements display sharp peaks at the same values of strain, where the intersubband splitting is reduced. These minima determine the positions of the narrow hot spots.

Fig. 4 shows the dependence of the spin lifetime on temperature for an unstrained film. While the temperature increases, the number of the hot spot points which lie in the energy range determined by the term $f(\varepsilon)\big(1-f(\varepsilon)\big)$ increases. In combination with the Fermi level lowering this results in the reduction of the spin lifetime with temperature due to increased surface roughness scattering, in complete analogy with the momentum relaxation time behavior [3].

For higher shear strain values the hot spots are pushed to higher energies (Fig. 5) away from the subband minima (inset in Fig. 5). This leads to a strong increase of the spin lifetime shown in Fig. 6. This also demonstrates that the approximation of the independence of the matrix elements on the wave vectors used to obtain (3) is inappropriate for evaluation of the spin lifetime. Indeed, while the momentum relaxation time changes insignificantly with strain, the spin relaxation time increases by orders of magnitude. Thus, shear strain used to enhance mobility can also be used to increase spin lifetime.

References

[1] R. Jansen, Nat.Mater. **11**, 400–408 (2012).
[2] T. Suzuki *et al.*, *Appl.Phys.Express* **4**,023003(1-3) (2011).
[3] K. Uchida, J. Koga, and S. Takagi, J.App.Phys. **102**, 074510 (2007).
[4] M. V. Fischetti *et al.*, J.App.Phys. **94**, 1079 (2003).
[5] S. Jin, M.V. Fischetti, T.-W. Tang, IEEE Trans. Electron Devices **54**(9), 2191–2202 (2007).
[6] G.L. Bir, G.E. Pikus, "*Symmetry and strain-induced effects in semiconductors*", New York/Toronto: J. Wiley & Sons, 1974.
[7] V. Sverdlov, "*Strain-induced effects in advanced MOSFETs*", Springer, 2011.
[8] P. Li, H. Dery, Phys.Rev.Lett. **107**, 107203 (2011).
[9] Y. Song, H. Dery, Phys.Rev.B **86**, 085201 (2012).
[10] V. Sverdlov *et al.*, Proc. IWCE (2013).

This work is supported by the European Research Council through the grant #247056 MOSILSPIN. The computational results have been achieved in part using the Vienna Scientific Cluster (VSC).

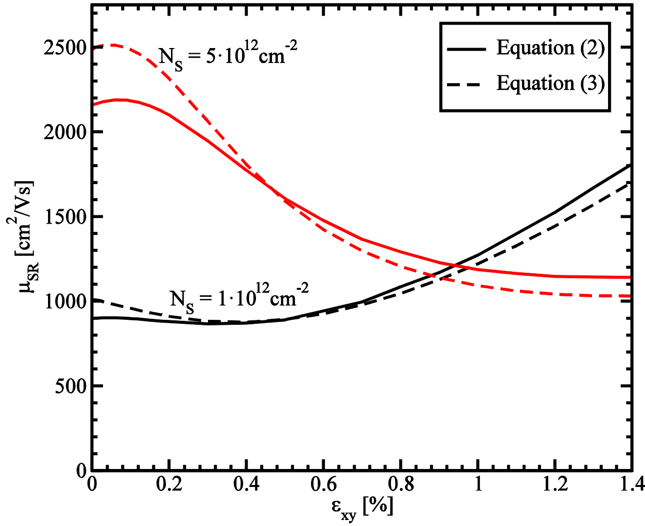

Fig. 1. Dependence of the surface roughness limited electron mobility calculated with (2) and (3) on shear strain for different values of the electron concentration.

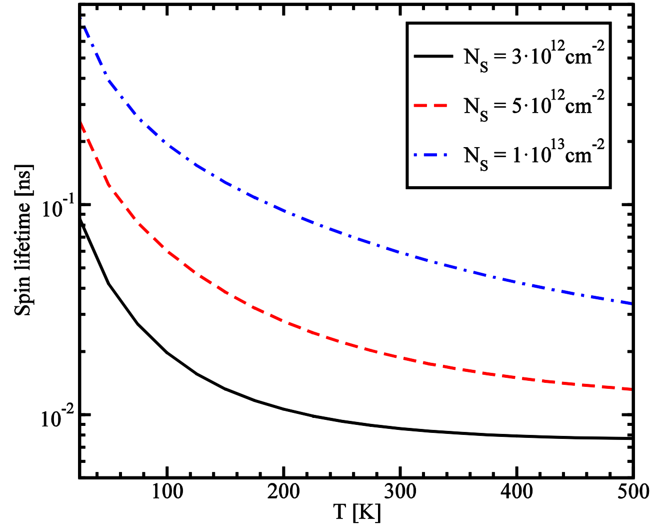

Fig. 4. Dependence of the spin lifetime on temperature for different values of the electron concentration in unstrained film.

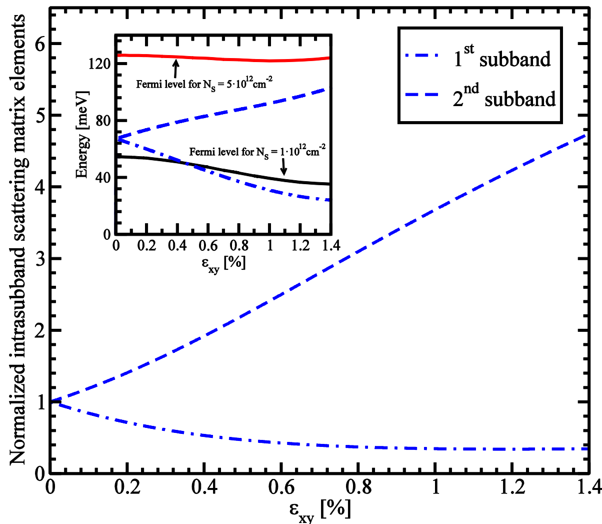

Fig. 2. Normalized intrasubband scattering matrix elements as a function of shear strain. The inset shows the dependence of subband energies and Fermi levels on shear strain.

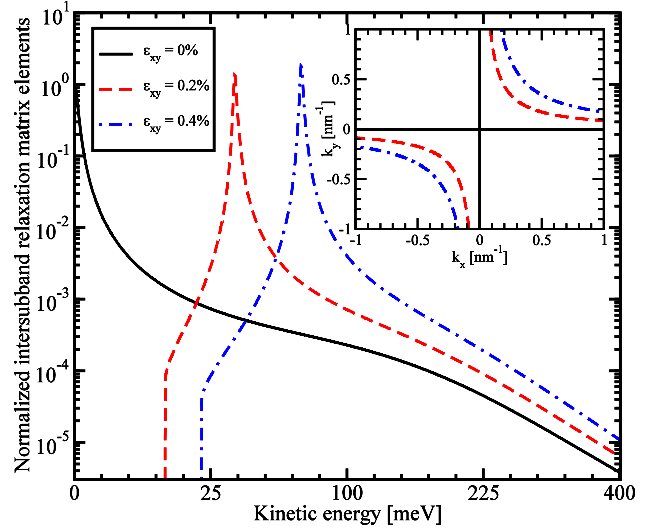

Fig. 5. Normalized intersubband relaxation matrix elements as a function of the conduction electrons kinetic energy in [110] direction. The inset shows the positions of the hot spots for different values of shear strain.

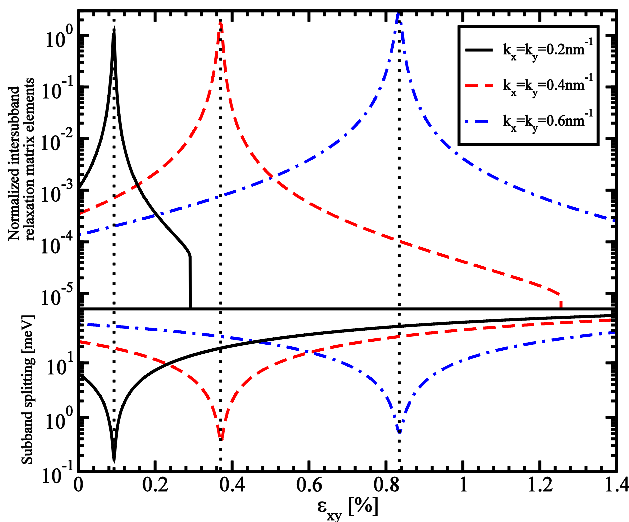

Fig. 3. Normalized intersubband relaxation matrix elements and subband splitting as a function of shear strain for different values of the wave vectors.

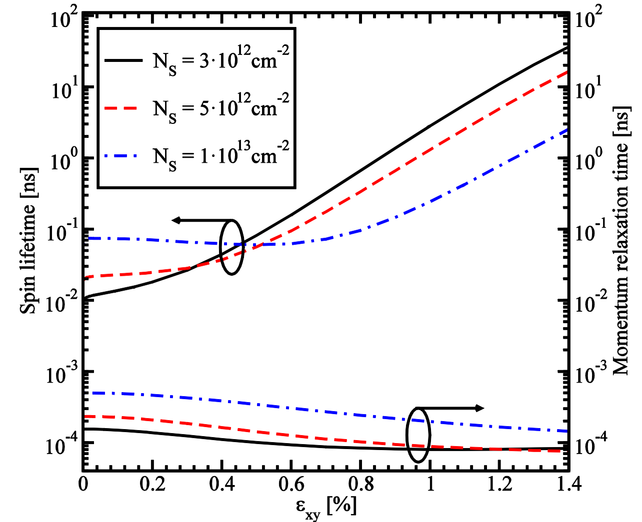

Fig. 6. Spin lifetime and momentum relaxation time as a function of shear strain for different values of electron concentration at room temperature.

Non-Boolean Computing Using Spin Waves

A. Papp*+, G. Csaba*, W. Porod*
*Center for Nano Science and Technology, University of Notre Dame, Notre Dame, USA
+Pazmany Peter Catholic University, Budapest, Hungary
e-mail: {appap,gcsaba,porod}@nd.edu

INTRODUCTION

Spin waves display similar interference behavior as optical waves, but at much shorter wavelengths (<100 nm), and they are also more straightforwardly generated on-chip. This gave rise to a number of proposals for 'spin wave computing' devices [1][2], aimed at mimicking on the nanoscale the behavior of optical logic gates, switches, and interconnections.

Moreover, spin waves could be well-suited for non-Boolean algorithms as well, such as pattern recognition using interference [3][4]. By means of micromagnetic simulations, we show that spin-waves can perform computational primitives that are well established in optics. Spin-wave based computing media can be straightforwardly integrated with CMOS units to form a general-purpose signal processing system.

SPIN-WAVE OPTICAL ELEMENTS

The system that motivates this work is sketched in Fig. 1. The spin-wave sources and the phase shifters can create an arbitrary wavefront (just as in the in-line holography scheme of Gabor [3]), and the interference pattern is read out at the opposite boundary of the device.

For spin-wave sources we use AC driven spin-torque sources, where a locally-oscillating magnetic moment injects spin waves into a thin Permalloy film (Fig 2). The physical structure of the spin-torque sources is identical to that of a spin-torque oscillator, but they are not used in the self-oscillating regime. For self-oscillating sources the phase is difficult to control, while for the driven oscillators it is straightforwardly linked to the driving source.

Multiple, coherently-driven spin-torque sources can realize line sources (Fig 3.), akin to a laser source in a real optical system. Placing slits (Fig 4.) or a lens (Fig 5.) in the path of the wave, one can imitate interference and focusing phenomena known from optics. Most importantly, a phase shifter (Fig. 6) can be realized by applying a local magnetic field, which changes the phase velocity of the wave.

NON-BOOLEAN COMPUTING USING SPIN WAVES

Placing the above-simulated optical components in the system of Fig. 1, one arrives at a device that can execute a sequence of optical processing steps, such as holographic pattern recognition or Fourier transformation. CMOS circuitry can control the flow of the optical primitives and perform additional (Boolean-based) pre- and post-processing steps.

ACKNOWLEDGEMENT

We thank G. Bourianoff, D. Nikonov (Intel Corp.), and A. Csurgay (Pazmany University, Budapest) for stimulating discussions, and the NSF-SRC 'Nanoelectronics Beyond 2020' grant for financial support.

REFERENCES

[1] T. Schneider, A. A. Serga, B. Leven, B. Hillebrands, R. L. Stamps, and M. P. Kostylev. *Realization of spin-wave logic gates.* Applied Physics Letters 92, no. 2 (2008): 022505-022505.
[2] A. Khitun, M. Bao, and K. L. Wang. *Magnonic logic circuits.* Journal of Physics D: Applied Physics 43, no. 26 (2010): 264005.
[3] D. Gabor: *Nobel Lecture: Holography, 1948-1971.* Nobelprize.org. 24 Feb 2013 http://www.nobelprize.org/nobel_prizes/physics/laureates/1971/gabor-lecture.html
[4] D. Feitelson: *Optical Computing: A Survey for Computer Scientists* The MIT Press 1992

978-3-901578-26-7 © 2013 Society for Micro- and Nanoelectronics

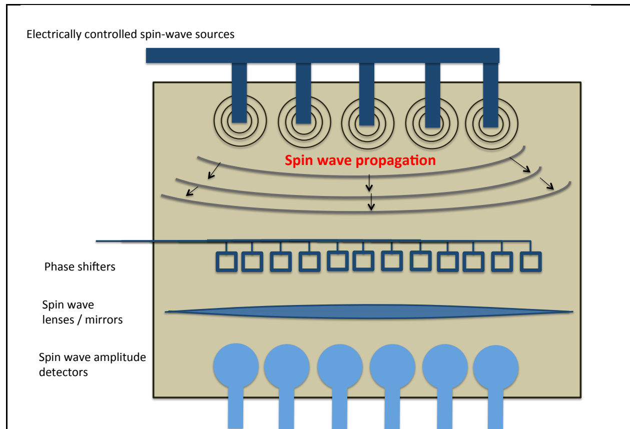

Fig. 1. Sketch of a spin-wave based computing system, with sources, phase shifters and detectors. A standard CMOS circuitry is used to configure the input oscillators and read-out the resulting spin-wave amplitudes.

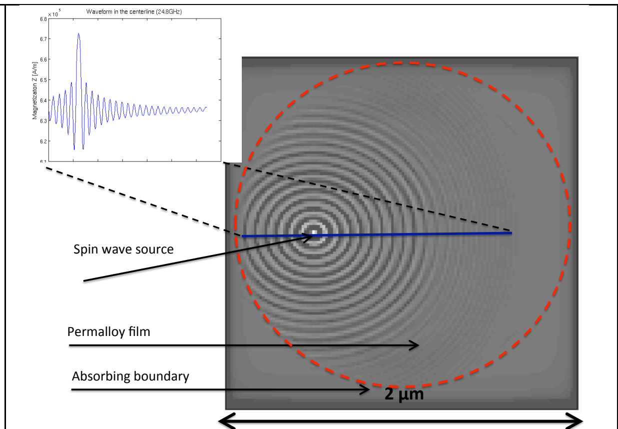

Fig. 2. Spin-wave distribution generated by a singe 30 nm diameter spin-torque source. The source is placed on a 5 nm thick Permalloy film. There is a constant 1.0 T magnetic film pointing 80° to the film plane. The decay of spin wave intensity is close to a *1/r* law, as expected from a point source.

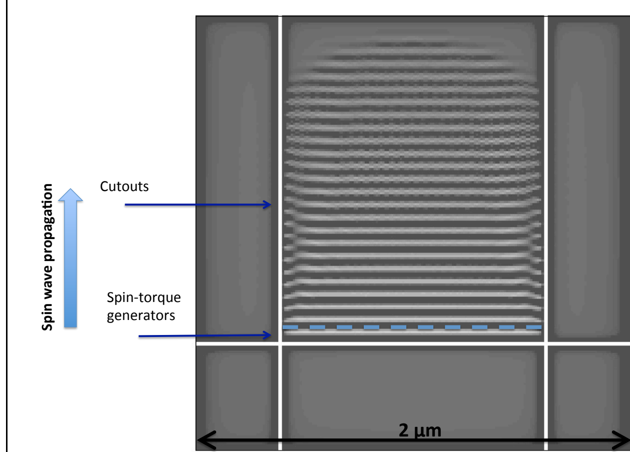

Fig. 3. A series of spin-torque sources are acting as a line source. The contour plot shows the out-of-plane component of the magnetization distribution.

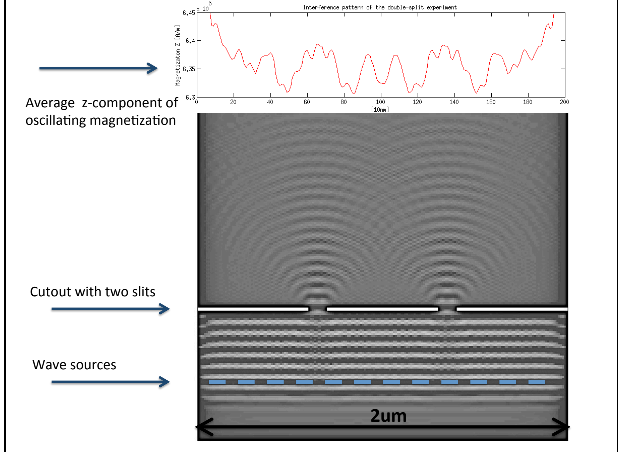

Fig. 4. A double-slit interference pattern from spin waves

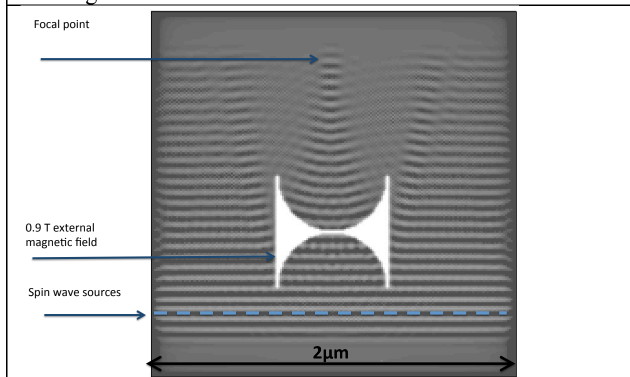

Fig 5. A focusing lens can be made by applying a local magnetic field, which changes the phase velocity of the spin waves. In this calculation the external field is altered in a 'negative lens' shape, focusing the waves.

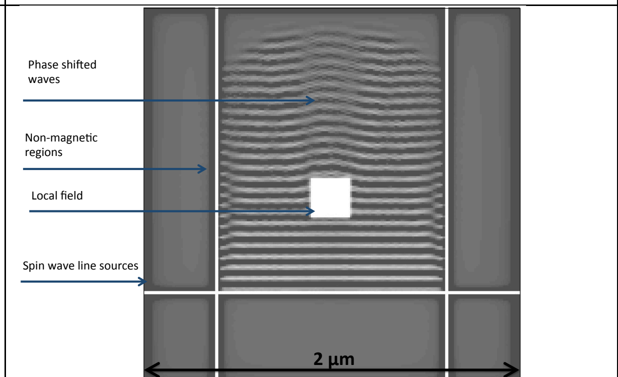

Fig. 6. An area with a variable magnetic field can act as a tunable phase shifter. A B_z = 0.7 T magnetic field applied in the white area in the center.

A Nested Dissection Approach to Modeling Transport in Nanodevices

U. Hetmaniuk, Y. Zhao*, and M. Anantram*
Department of Applied Mathematics, University of Washington,
Box 353925, Seattle, WA 98195-353925, U.S.A.
e-mail: hetmaniu@uw.edu
*Department of Electrical Engineering, University of Washington,
Box 352500, Seattle, WA 98195-2500, U.S.A.
e-mail: zhaoyq@uw.edu, anant@uw.edu

With the advent of smaller nanoelectronic devices, where quantum mechanics is central to the device operation, quantum mechanical simulations have become a necessity. The non-equilibrium Green's function (NEGF) method [1] has emerged as a powerful modeling approach for these nanodevices and nanomaterials.

A typical NEGF-based simulation solves the Green's function equations,

$$\begin{cases} \mathbf{A}(E)\,\mathbf{G}^r(E) = \mathbf{I} \\ \mathbf{A}(E)\,\mathbf{G}^<(E) = \mathbf{\Sigma}^<\left(\mathbf{G}^r(E)\right)^\dagger \end{cases} \quad (1)$$

where the sparse matrix $\mathbf{A}$ is defined by

$$\mathbf{A} = E\mathbf{I} - \mathbf{H} - \mathbf{\Sigma}_{Lead} - \mathbf{\Sigma}_{Phonon}. \quad (2)$$

$\mathbf{G}^r(E)$ is the retarded Green's function, describing local density of states, and $(\mathbf{G}^r(E))^\dagger$ its Hermitian conjugate. $\mathbf{G}^<(E)$, the lesser Green's function, represents the electron correlation function for energy level E; the diagonal elements of $\mathbf{G}^<(E)$ represent the electron density per unit energy. $\mathbf{I}$ is the identity matrix and $\mathbf{H}$ the system Hamiltonian. $\mathbf{\Sigma}_{Lead}$ represents the self-energy matrix due to the leads and $\mathbf{\Sigma}_{Phonon}$ corresponds to the self-energy governing electron-phonon scattering. The matrix $\mathbf{\Sigma}^<$ corresponds to the lesser self-energy. Solving (1) for the diagonal of $\mathbf{G}^<$ at many energies E is a computationally intensive part of NEGF-based simulations.

The most common approach to compute blocks of $\mathbf{G}^r$ and $\mathbf{G}^<$ is the recursive Green's function method [4]. Recent advances utilize the nested dissection method [2] to exhibit a significant speedup. These new algorithms exploit a sparse block $\mathbf{LDL}^T$-factorization of $\mathbf{A}$ and re-use this factorization to fill in all diagonal blocks of the Green's functions in a specific order. The main difference between RGF and these methods is the replacement of *layers* of grid points organized along a specific direction with *arbitrarily-shaped clusters* of grid points organized in a binary tree. Such choice allows to *fold* and to *extract* in any physical direction when following the binary tree, generated by the nested dissection.

The present contribution introduces an algorithm for calculating diagonal blocks of $\mathbf{G}^<$ with partitions from METIS [3]. The developed method has a reduced complexity compared to the established recursive Green's function approach. For a device with N_y layers and N_x grid points per layer, as shown in Figure 1, the complexity for RGF is $\mathcal{O}(N_x^3 N_y)$ while the proposed algorithm exhibits a complexity $\mathcal{O}(N_x^2 N_y)$. Numerical experiments on a quantum well superlattice and a carbon nanotube demonstrate significant speedups over the recursive method.

References

[1] S. Datta, *The non-equilibrium Green's function (NEGF) formalism: An elementary introduction*, International Electron. Devices Meeting, pp. 703-706 (2002).
[2] A. George, *Nested dissection of a regular finite element mesh*, SIAM J. Numer. Anal, vol. 10, pp. 345-363 (1973).
[3] G. Karypis and V. Kumar, *A fast and high quality multilevel scheme for partitioning irregular graphs*, SIAM J. Sci. Comput., vol. 20, pp. 359-392 (1998).
[4] A. Svizhenko, M. Anantram, T. Govindam, B. Biegel, R. Venugopal, *Two-dimensional quantum mechanical modeling of nanotransistors*, J. Appl. Physics, vol. 91, pp. 2343 (2002).

978-3-901578-26-7 © 2013 Society for Micro- and Nanoelectronics

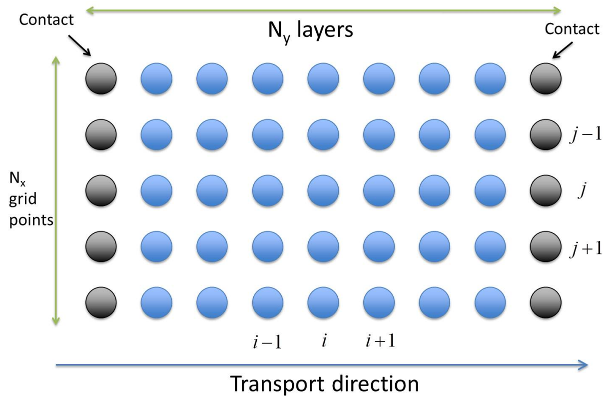

Fig. 1. Nano-device partitioned into N_y layers. Each layer contains N_x grid points.

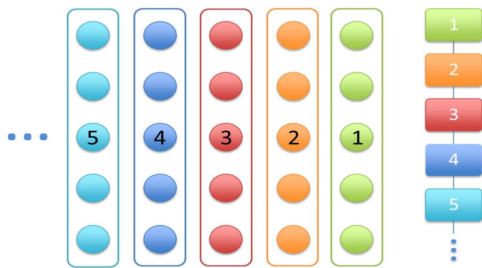

Fig. 2. Partition generating the RGF algorithm.. The first pass advances one layer at a time from left to right along the y-direction and, recursively, folds the effect of left layers into the current layer. The second pass marches one layer at a time from right to left along the y-direction and, recursively, extracts the diagonal blocks and the nearest neighbor off-diagonal blocks for the final result.

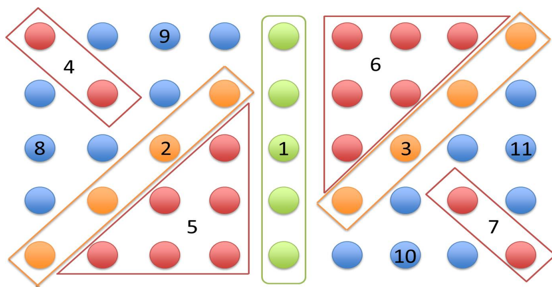

Fig. 3. Partition generated by METIS for system including dense layers at two ends.

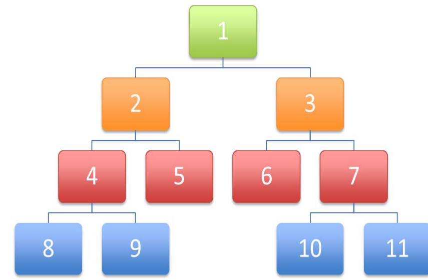

Fig. 4. Binary tree relating the different clusters of grid points. The first pass folds all *clusters* of grid points on the same level, while climbing up. The second pass extracts the diagonal blocks one level at a time, while marching down.

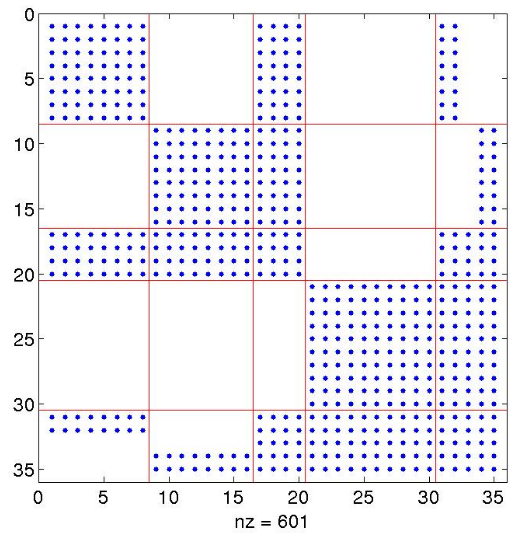

Fig. 5. Typical distribution of computed elements for $\mathbf{G}^r$ and $\mathbf{G}^<$.

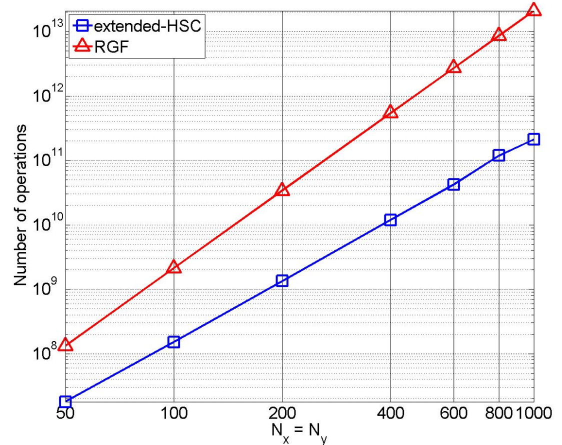

Fig. 6. Comparison of number of operations between our algorithm (blue) and RGF (red).

Nonequilibrium Green's function simulations of THz quantum cascade lasers

M. Lindskog*, D. O. Winge, and A. Wacker
Division of Mathematical physics, Lund University, Box 118 Lund, Sweden
* e-mail: martin.lindskog@teorfys.lu.se

We simulate THz quantum cascade lasers (QCLs) [1] with the nonequilibrium Green's function (NEGF) method [2][3], in which relevant observables, such as the energy resolved carrier density

$$\rho(z,E)=\sum_{\mathbf{k}}\sum_{\alpha,\beta}\Im\{G^{<}_{\alpha,\beta}(\mathbf{k},E)\phi^{*}_{\beta}(z)\phi_{\alpha}(z)\}$$

are expressed in terms of the Green's functions of the system, in this case the lesser Green's function $G^{<}$, and the basis wavefunctions with z-component $\phi_\alpha(z)$. The NEGF method allows for a detailed analysis of the transport, since the spatially and energy resolved carrier and current densities, as well as the density of states, can be obtained from the Green's functions.

Fig. 1 shows the conduction band edge, the Wannier-Stark states, and the carrier densities of the THz QCL from Ref. [4]. The simulated and measured current densities are shown in Fig. 2.

This phonon-photon-phonon (PPP) design [5] relies on two phonon resonances (with energy $E_{\rm LO}$) occuring between the lower laser state (LLS) and the extraction state e (with splitting $\Delta E_{\rm LLS,e}$), as well as between the injection state i and the upper laser state (ULS) (with splitting $\Delta E_{\rm i,ULS}$) at a bias where i and e also align. These phonon and tunneling resonances create population inversion between the ULS and LLS, which allows for a lasing transition between those states.

The carrier densities in Fig. 1 show that carriers accumulate in the LLS due to the mis-match between $\Delta E_{\rm LLS,e}$ and $E_{\rm LO}$, as well as in e, which is due to the thick injection barrier. Had this barrier been more narrow, the tunneling coupling at higher biases would be larger, meaning that biases where $\Delta E_{\rm LLS,e}$ and $\Delta E_{\rm i,ULS}$ are better aligned to $E_{\rm LO}$ could be reached.

The design in Fig. 3, described in Ref. [6], is an improvement of the one previously discussed, albeit $\Delta E_{\rm LLS,e}$ does not match $E_{\rm LO}$ either. The current density is peaked at a bias greater than the bias of the tunneling resonance i/e, since both $\Delta E_{\rm LLS,e}$ and $\Delta E_{\rm i,ULS}$ are better matched to $E_{\rm LO}$. We identify the lack of mean field potential in the rate equation (RE) model used for design optimization as one of the causes for the mis-match of the resonances. In contrast, the NEGF model takes mean field and the real part of the self energies into account, which alters the energy levels and thus the bias at which different phonon and tunneling resonances occur.

As temperature increases, inversion decreases due to thermal backfilling from e to LLS as well as from ULS to i. A better matching of the biases giving tunneling and phonon resonances respectively, would reduce the backfilling and increase the population inversion.

The simulated gain profile and experimental laser spectra are shown in Fig. 4.

Conclusion

The experimental current densities as well as gain profiles of two THz QCLs have been reproduced with the NEGF model. The results for the gain spectra are significantly better than with a simple RE model. The energetically and spatially resolved transport dynamics suggest improvements of the design.

References

[1] R. Koehler *et. al*, Nature **417**, 156 (2002)
[2] A. Wacker and S. C. Lee, Phys. Rev. B **66**, 245314 (2002).
[3] A. Wacker, M. Lindskog, and D. O. Winge, IEEE J. Sel. Top. Quant. Electron. (2013), in press.
[4] E. Dupont *et. al*, J. Appl. Phys. **111**, 073111 (2012)
[5] M. Yamanishi *et. al* , Opt. Express **16**, 20748 (2008)
[6] S. G. Razavipour *et. al* (2013), unpublished

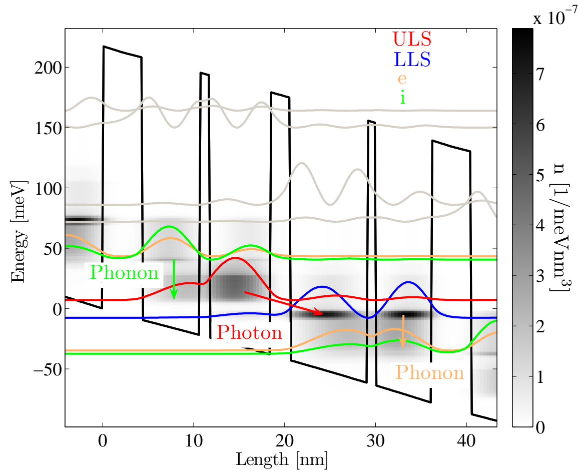

Fig. 1. Carrier densities and electronic states for the structure presented in Ref. [4], at operation bias. $T = 50$ K. The carriers accumulate in the LLS since the extraction energy does not match E_{LO}.

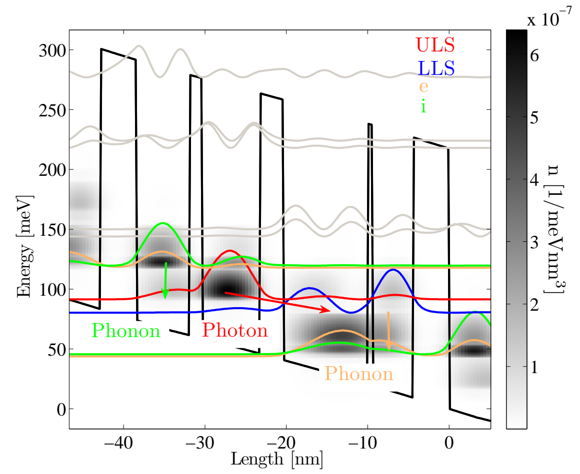

Fig. 3. Carrier densities and electronic states for the structure presented in Ref. [6] at operation bias. $T = 50$ K. Carriers accumulate in the injection and extraction states since the injection energy is not matched to E_{LO}, and the e/i states are not aligned to a high degree at this bias.

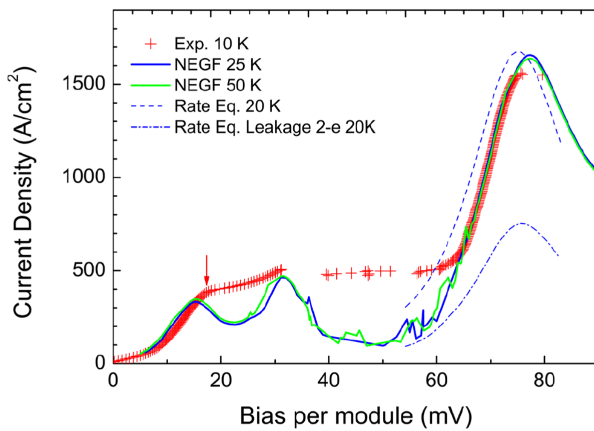

Fig. 2. Current density of the structure in Ref. [4] as a function of applied bias. Even though the rate equation model predicts the behaviour well, the NEGF is better in predicting the correct lasing frequency at different biases and identifying effects such as leakage currents and dispersive gain. Figure from Ref. [4].

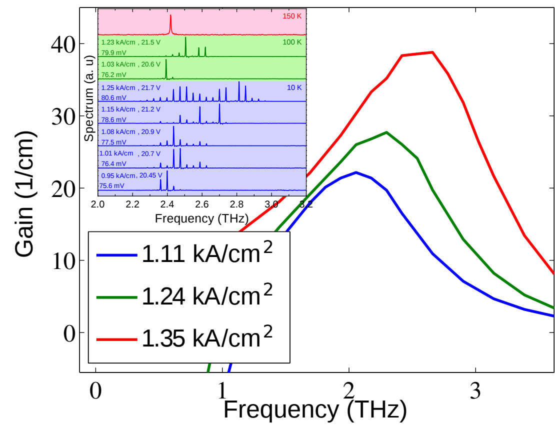

Fig. 4. NEGF simulated gain profile at T = 50 K of the structure presented in Ref. [6]. The inset shows experimental results. The qualitative agreement is good, showing a similar reduction of the laser frequency as bias is decreased from the bias of the maximum of the current density. The NEGF model also gives very similar lasing frequencies as seen experimentally.

Density Matrix Model Applied to GaAs and GaN-based Terahertz Quantum Cascade Lasers

A. Grier, Z. Ikonić, A. Valavanis, J. D. Cooper, D. Indjin, and P. Harrison
Institute of Microwaves and Photonics, School of Electronic and Electrical Engineering,
University of Leeds, Leeds LS2 9JT, United Kingdom
e-mail: el09a2g@leeds.ac.uk

INTRODUCTION

Quantum cascade lasers (QCLs) are compact sources of coherent radiation that can emit in the terahertz (THz) region of the electromagnetic spectrum. However, room temperature operation has not yet been achieved in THz QCLs; the current highest temperature operation is 199.5 K at 3.22 THz using an AlGaAs/GaAs stucture [1]. Advances in theoretical modelling have contributed to the development of such optimized and novel devices and both Monte Carlo and rate-equation models of QCLs can give good agreement with experimental results [2]. However, these semi-classical models do not account for coherent transport which is thought to be important in THz QCLs due to the typically thick injection barriers and can predict unrealistic results. Like non-equilibrium Green's functions (NEGF), density matrix (DM) modelling accounts for tunnelling but is less computationally intensive which allows for its use as a simulation tool. To reach higher temperatures, it is necessary to suppress the performance degradation mechanisms which occur. These include thermal backfilling and thermally activated LO phonon scattering which occurs as electrons gain enough in-plane kinetic energy to emit an LO phonon and relax to the lower laser level non-radiatively. Therefore, we aim to investigate and then apply the DM approach to the AlGaN/GaN system which has been considered promising due to its higher LO phonon energy (92 meV) compared to that of GaAs (36 meV) [3].

METHOD

The density matrix method outlined in Ref. 4 allows for coherent modelling of a QCL structure with any number of states. Additionally, the Hamiltonian in the Liouville equation can be be altered to include further submodules in each period so that intra-period transport is modelled coherently. We first model a GaAs structure measured experimentally in Ref. 5 to compare gain/current vs applied field using the rate equation approach, the DM approach, and the DM approach with two submodules per period [6]. The Armadillo C++ linear algebra library [7] is used to solve the Liouville equation in the DM calculations. In the first implementation of the DM approach (Figs. 1 and 4) tunnelling transport only through the injection barrier is considered. Fig. 2 illustrates the unrealistic spikes in current density and gain when electrons scatter between spatially extended subbands (as in Fig. 3) using the rate equation approach.

The formalism is then applied to InAlGaN/GaN (Fig. 5) and AlGaN/GaN THz QCLs with polarization fields included. To calculate tight-binding energies, wavefunctions and coupling strengths it is necessary to remove pyro- and piezo-electric fields from the isolating barriers to maintain periodicity of the bandstructure. Optimizations are limited to diagonal transition designs to account for an enhanced Frölich interaction which is thought to suppress gain in nitride systems [8].

ACKNOWLEDGEMENT

This work was supported by the EPSRC.

REFERENCES

[1] S. Fathololoumi et al., *Terahertz quantum cascade lasers operating up to ∼ 200 K with optimized oscillator strength and improved injection tunneling*, Opt. Exp., **30**, 003866 (2012).
[2] V. D. Jovanović et al., *Influence of doping density on electron dynamics in GaAs/AlGaAs quantum cascade lasers*, J. Appl. Phys., **99**, 103106 (2006).
[3] V. D. Jovanović, D. Indjin, Z. Ikonić, and P. Harrison, *Simulation and design of GaN/AlGaN far-infrared ($\lambda \sim 34\,\mu m$) quantum-cascade laser*, Appl. Phys. Lett., **84**, 2995 (2004).
[4] T. V. Dinh, A. Valavanis, L. J. M. Lever, Z. Ikonić, and R. W. Kelsall, *An extended density matrix model applied to silicon-based terahertz quantum cascade lasers*, Phys. Rev. B., **85**, 235427 (2012).
[5] L. Lever et al., *Terahertz ambipolar dual-wavelength quantum cascade laser*, Opt. Exp., **17**, 22 (2009).
[6] G. Beji, Z. Ikonić, C. A. Evans, D. Indjin, and P. Harrison *Coherent transport description of the dual-wavelength ambipolar terahertz quantum cascade laser*, J. Appl. Phys., **109**, 013111 (2011).
[7] C. Sanderson, *Armadillo: An Open Source C++ Linear Algebra Library for Fast Prototyping and Computationally Intensive Experiments*, Technical Report, NICTA (2010).
[8] H. Yasuda, T. Kubis, I. Hosako, and K. Hirakawa, *Non-equilibrium Green's Function calculation for GaN-based terahertz quantum cascade laser structures*, J. Appl. Phys., **111**, 083105 (2012).

978-3-901578-26-7 © 2013 Society for Micro- and Nanoelectronics

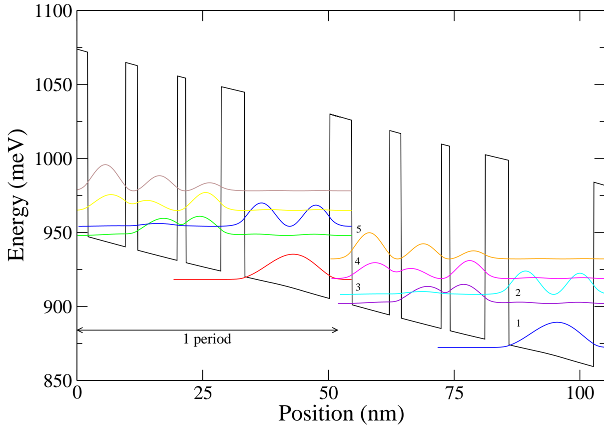

Fig. 1. Energy-band diagram of the ambipolar THz QCL in Ref. 5 at 9 kV/cm. The lasing transition is from state 4 to 3.

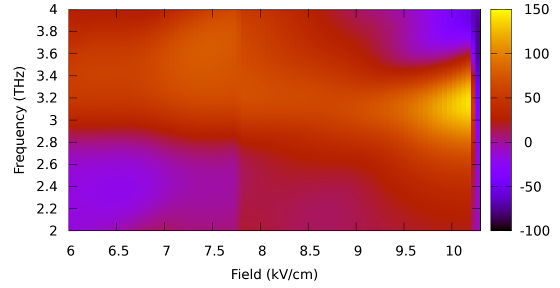

Fig. 4. Simulated gain (or negative absorption) per cm for the ambipolar THz QCL in Ref. 5 at 80 K with an excess electron temperature of 10 K using the density matrix approach.

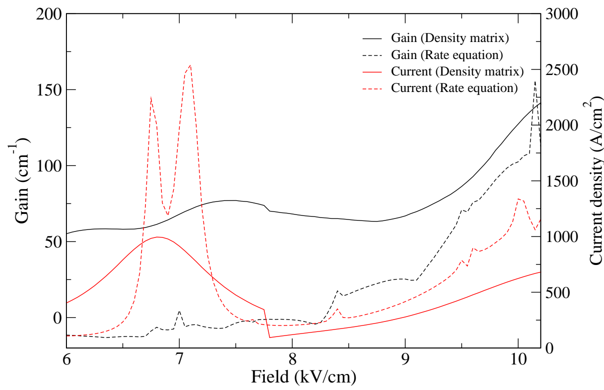

Fig. 2. Current density and gain as a function of forward bias for the ambipolar THz QCL in Ref. 5 at 80 K with an excess electron temperature of 10 K.

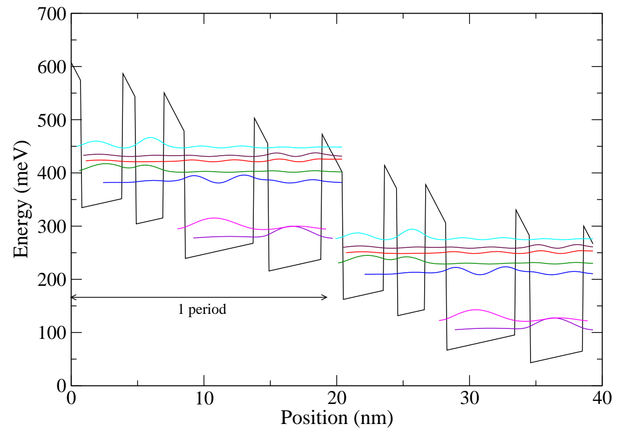

Fig. 5. Energy-band diagram of the GaN THz QCL in Ref. 8 at a forward bias of 80 kV/cm with the tight-binding scheme to obtain the localized wavefunctions shown.

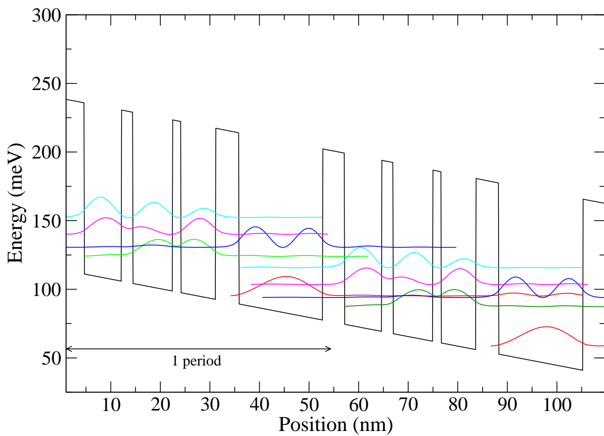

Fig. 3. Energy-band diagram of the ambipolar THz QCL in Ref. 5 at 7 kV/cm without the tight-binding approach. This leads to an extended state 1 wavefunction providing an unrealistic resonant LO phonon current path.

Modeling of the Effects of Band Structure and Transport in Quantum Cascade Detectors

Oskar Baumgartner, Zlatan Stanojević, and Hans Kosina
Institute for Microelectronics, TU Wien, Gußhausstraße 27–29, A–1040 Wien, Austria
Email: {baumgartner|stanojevic|kosina}@iue.tuwien.ac.at

One of the essential technologies in modern photonic systems are semiconductor heterostructures. The first use of a QCL as a photo-detector has been reported by [1] and was since then refined for infrared and terahertz wavelengths [2] leading to the current quantum cascade detectors (QCD).

The operating principle of a QCD is outlined in Fig. 1. A ground level electron is excited to a higher state by absorbing a photon. Due to the asymmetric design, the electron relaxes in a preferred direction into the quantum well of the next cascade. This concept reduces dark current and dark current noise.

We use the semi-classical Pauli master equation (PME) [3], [4] to model current transport through the multi-layer semiconductor heterostructure. We developed an efficient Monte Carlo (MC) simulator in C++ as part of the Vienna-Schrödinger-Poisson (VSP) simulation framework [5]. The versatility of the simulator was successfully demonstrated by the design and automatized optimization of a bi-functional QCL and QCD device [6]. The Hamiltonian includes the band edge formed by the heterostructure, and thus, coherent tunneling is accounted for through the delocalized eigenstates. Transport occurs via scattering between the subbands. Due to the periodicity of the device, periodic boundaries are imposed on the PME. As scattering sources, we currently consider non-polar acoustic and optical phonons, and polar optical phonons as well as alloy disorder, intervalley processes and interface roughness. The incorporated model for stimulated emission and absorption of photons is essential for the description of a QCD. For the calculation of the rates the effect of in-plane nonparabolicity can be included.

Band nonparabolicity in cross-plane direction is essential to determine the subbands in QCDs. We employed a two-band $\mathbf{k}\cdot\mathbf{p}$ [7] and a four-band $\mathbf{k}\cdot\mathbf{p}$ Hamiltonian. The periodic wavefunctions (Fig. 1) are picked automatically by a reliable algorithm. For the in-plane transport treatment we investigated three approaches: (I) parabolic effective (density of states) mass as input parameter; (II) parabolic effective mass measured by $\langle\psi_i|m(z)|\psi_i\rangle$ for each subband, (III) non-parabolic dispersion $\mathcal{E}(1+\alpha\mathcal{E}) = \frac{\hbar^2 k^2}{2m}$ fitting the mass m and nonparabolicity coefficient α to the numerical subband structure determined by the Schrödinger equation.

As a test device we use a mid-infrared QCD operating at a wavelength of $4.7\,\mu\text{m}$. The design of the InGaAs/InAlAs QCD is taken from [2] (device N1022) and all simulation results are compared to the measurements therein. We calculate the responsivity, which relates the incoming photon flux to the detected current, for each combination of band structure model (2-band/4-band $\mathbf{k}\cdot\mathbf{p}$) and in-plane dispersion of the transport model (parabolic, non-parabolic, parameters obtained using methods (I)-(III) as outlined above). Each simulation takes about ten minutes. Fig. 2 and Fig. 3 depict the responsivity for parabolic transport with the well mass as input parameter. The 4-band $\mathbf{k}\cdot\mathbf{p}$ model shows a considerably better agreement with measurement. Using method (II) instead of (I) to determine the subband mass does not influence the result (Fig. 4). Finally, Fig. 5 shows the results for method (III), which show the best agreement with measurements.

In conclusion, we presented a versatile simulator, that allows quick simulation studies of QCLs and QCDs, while still accurately capturing the relevant physics. The importance of nonparabolicity to correctly describe the behavior of QCDs is shown.

Acknowledgment: This work was supported by the Austrian Science Fund program IR-ON (F2509).

References

[1] D. Hofstetter *et al.*, Appl. Phys. Lett. **81**, 2683 (2002).
[2] F. Giorgetta *et al.*, IEEE Journal of Quantum Electronics **45**, 1039 (2009).
[3] R. C. Iotti *et al.*, Phys. Rev. B **72**, 125347 (2005).
[4] C. Jirauschek *et al.*, J. Appl. Phys. **101**, 086109 (2007).
[5] O. Baumgartner *et al.*, *SISPAD* (2011), pp. 91–94.
[6] B. Schwarz *et al.*, Appl. Phys. Lett. **101**, 191109 (2012).
[7] C. Sirtori *et al.*, Phys. Rev. B **50**, 8663 (1994).

978-3-901578-26-7 © 2013 Society for Micro- and Nanoelectronics

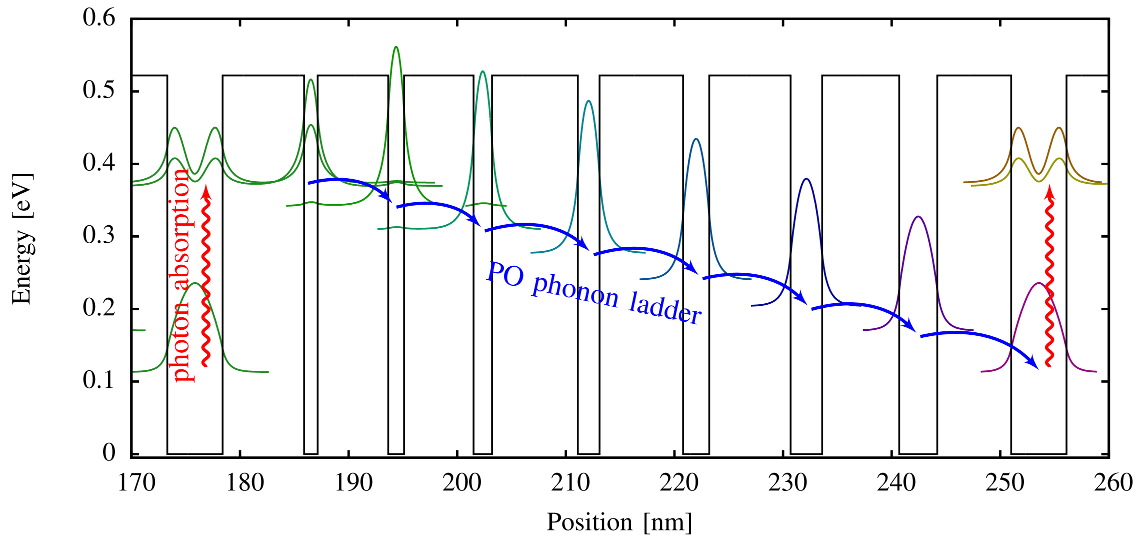

Fig. 1. Calculated wave functions of the QCD from [2] using a four-band $\mathbf{k}\cdot\mathbf{p}$ model; electrons are excited to higher states by absorbing photons. The polar optical phonon ladder causes the electron to preferably relax towards the next cascade.

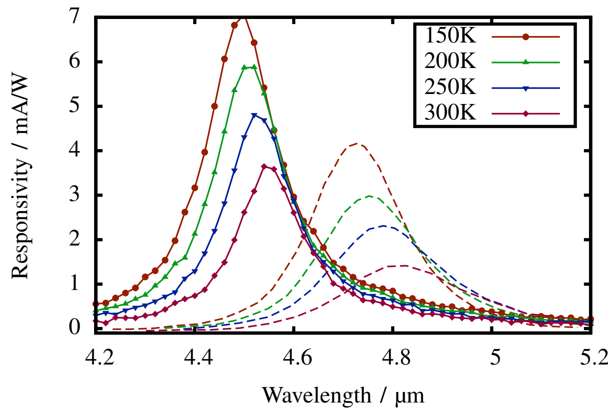

Fig. 2. Calculated responsivity (solid) of the QCD compared to measurements of [2] (dashed); cross-plane band structure modeled with a two-band $\mathbf{k}\cdot\mathbf{p}$ Hamiltonian. In-plane dispersion in the transport model is assumed parabolic with the effective mass set to the well material effective mass.

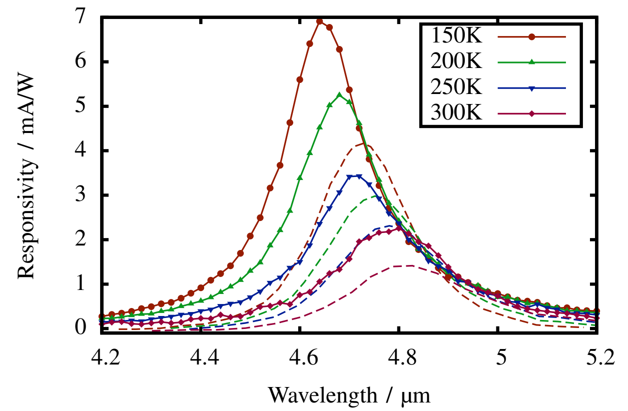

Fig. 3. Same as Fig. 2, but with a four-band $\mathbf{k}\cdot\mathbf{p}$ Hamiltonian; the wavelengths of the peak responsivity agree closer with measurements than for the two-band $\mathbf{k}\cdot\mathbf{p}$ Hamiltonian.

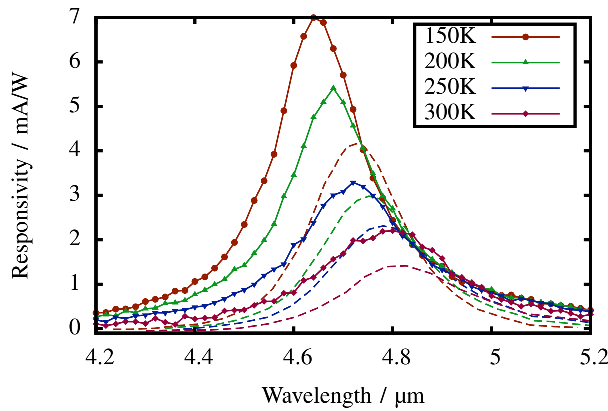

Fig. 4. Same as Fig. 3 but the mass for the parabolic in-plane dispersion in the transport model has been averaged for each subband; no visible improvement is observerd using this model.

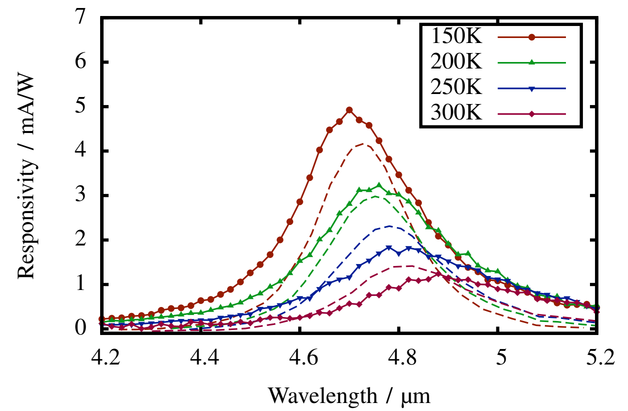

Fig. 5. Same as Fig. 3 but the in-plane dispersion in the transport model is assumed non-parabolic with the effective mass and non-parabolicity coefficient fitted to the subband structure; inclusion of nonparabolicity has substantial effects on the responsivity.

Quantum calculation of solar cell efficiency

Nicolas Cavassilas, Fabienne Michelini, Marc Bescond
IM2NP, UMR CNRS 7334, Bât. IRPHE, 13384 Marseille, France
e-mail: nicolas.cavassilas@im2np.fr

INTRODUCTION

Third-generation solar cells [1] based on quantum effects represent promising candidates to overcome the Schockley-Queisser limit [2]. Most of the solar cell simulations consider carrier transport from a semi-classical approach [3]. However, these models are no longer suitable to describe electronic transport in nano-structured devices. So far, few quantum simulations have been reported [4]. These models, computationally challenging, have been applied to specific studies with generally a monochromatic incident light. However, assuming the entire sun spectrum is essential to model solar cells and calculate the power conversion efficiency (PCE). We present a quantum transport model considering the black-body spectra for the incident light. Inspired by the excellent results achieved by *Alta Device* [5], we focus on thin GaAs *p-i-n* junctions. We analyze the different negative contributions to photovoltaic (PV) current *versus* the applied voltage.

DEVICE and MODEL

The considered GaAs *p-i-n* junction is detailed Fig. 1. The invariance of the potential in the transverse plan permits to separate the 2D dispersion from the 1D transport. The 1D transport modelling is based on the non-equilibrium Green's function formalism with two one-band effective mass Hamiltonians (conduction and valence) coupled by the electron-photon interaction. The 1D electric potential is self-consistently calculated using Poisson's equation. Electron-phonon scattering is included through polar optical phonon interactions. Photon incident flux is assumed to propagate along the electron transport direction with a power P_{sun}=1000Wm^{-2} (AM1.5 Global standard) and the spectra profile of the black-body at 6000K. In electron-photon interaction we assume a decrease of the light intensity according to an absorption coefficient of 2.7 10^{4}cm^{-1}.

RESULTS and DISCUSSION

Figure 2 shows the current characteristics *J-V* and the corresponding power ($P=J.V$) obtained without phonon scattering. These results agree rather well with experimental results [6]. The PV current is maximum for V=0. The corresponding spectra is shown Fig. 3 *versus* position along the transport direction. In addition to the expected positive current we show a negative contribution at the device edges (labeled as LEC for Large Energy Contribution). Carriers generated at energy larger than the junction barrier are less sensitive to electric field and may reach the wrong contact. The power is maximum for V=0.75V with a PCE (P/P_{sun}) of 20.9%. For that bias, the LEC increases with respect to V=0 due to the reductions of both the electric field and the junction barrier (Fig. 4). In spirit of the *Alta Device* cell [5], $Al_{0.38}Ga_{0.62}As$ is used in the *p*-type extremity. This allows to reduce the LEC for electrons and PCE reaches 22.3% (Fig. 5). For larger bias (*e.g.* V=0.85 V) the power is strongly reduced. As shown in Fig. 6, the current spectrum depicts the emergence of a new negative contribution (labeled as MRC for Majority Recombination Contribution) which vanishes when switching-off the photon emission. Due to the low electric field, majority carriers reach the central region and recombine radiatively. It follows a negative current of majority carriers. Finally, phonon scattering incorporation reduces PCE maximum down to 16.5% (against 20.9%).

In conclusion, this study highlights two behaviors limiting the efficiency of thin solar cells. While the MRC is expected to be reduced in a thicker junction, we clearly show that the LEC can be reduced by the use of an heterojunction.

[1] M.A. Green, Physica E 14 (2002).
[2] W. Schockley, H. Queisser, J. Appl. Phys. 32 (1961).
[3] K. Yoshida *et al.*, Appl. Phys. Lett. 97, 133503 (2010).
[4] U. Aeberhard, J Comput, Electron 10, 394 (2011).
[5] I.C. Kizilyalli *et al.*, US Patent 2010/0126570 A1.
[6] M.A. Green *et. al.*, Prog. Photovolt: Res. Appl. 20 (2012).

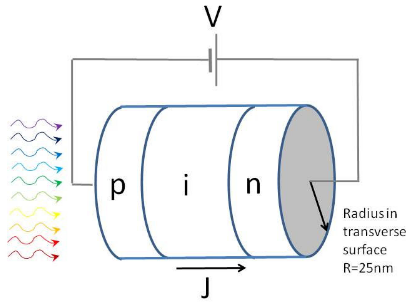

Fig. 1. Schematic representation of the considered *p-i-n* junction (N_D=N_A=10^{25}m^{-3}, L_n=L_p=10nm, L_i=160nm). The transport axis is discretized (Δx=0.2nm), as well as the transverse wave vector **k** (Δk=π/R). For GaAs we assume an energy band-gap Eg=1.43eV, and effective masses of the valence and conduction bands equal to m_v=0.51m_0 and m_c=0.07m_0 respectively (m_0 being the free electron mass).

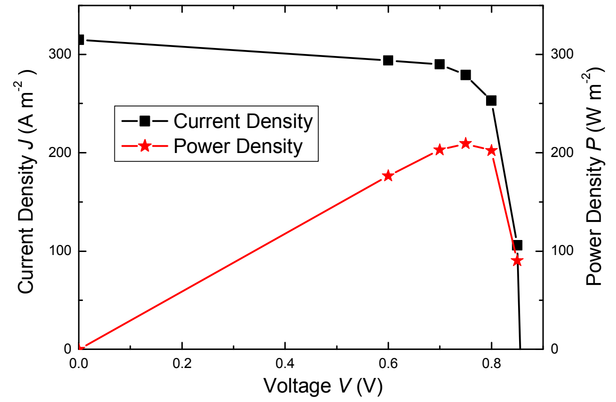

Fig. 2. Current-density J *versus* applied voltage V obtained without phonon scattering and the corresponding generated power density P.

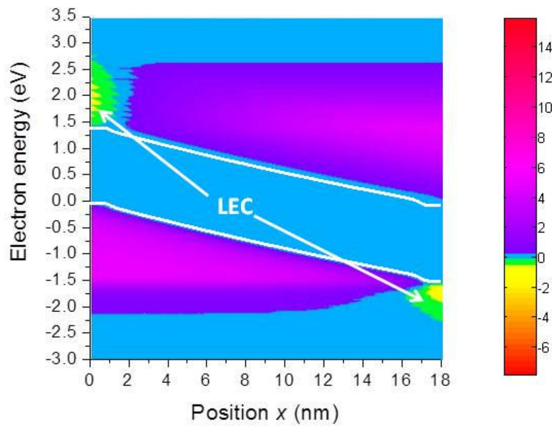

Fig. 3. Current spectra (in arbitrary units) *versus* position along transport axis x for V=0V. Valence and conduction band-edges are also shown (white lines).

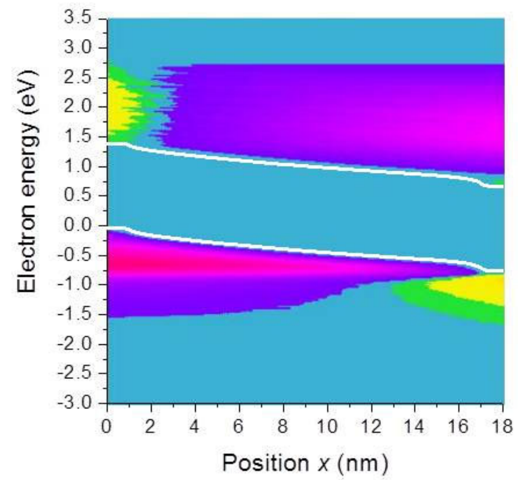

Fig. 4. Like Fig. 3 with V=0.75V.

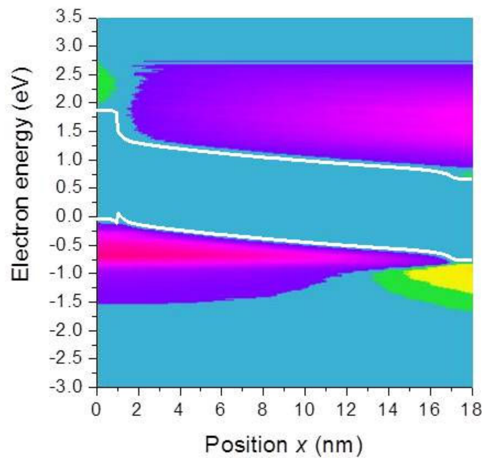

Fig. 5. Like Fig. 3 with V=0.75 V and $Al_{0.38}Ga_{0.62}As$ added at the p-type material extremity. For the AlGaAs/GaAs heterojunction we took bands offset given by ΔE_c=0.3eV and ΔE_v=0.19eV.

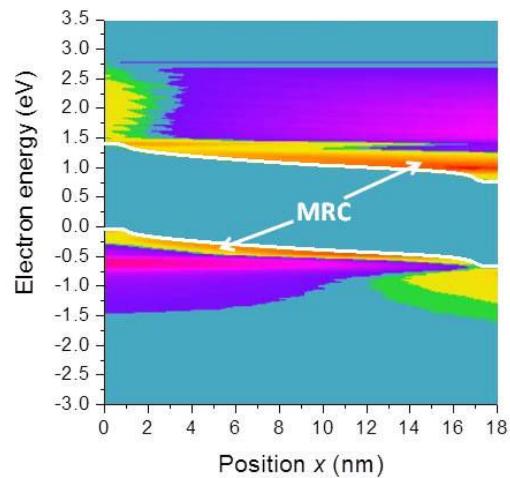

Fig. 6. Like Fig. 3 with V=0.85V.

Simulation of Type-II Ge/Si Quantum Dot Solar Cells

Weiguo Hu[1,2], Mohammad Maksudur Rahman[1,2], Takeru Okada[1], Akio Higo[4], Yiming Li[3,4,*], and Seiji Samukawa[1,2,4,*]
[1]Institute of Fluid Science, Tohoku University, Sendai 980-8577, Japan
[2]Japan Science and Technology Agency, CREST, Tokyo 102-0075, Japan
[3]Department of Electrical and Computer Engineering, National Chiao Tung Universit, Hsinchu 300, Taiwan
[4]WPI Advanced Institute for Materials Research, Tohoku University, Sendai 980-8577, Japan
*e-mail: ymli@faculty.nctu.edu.tw (Y. Li); samukawa@ifs.tohoku.ac.jp (S. Samukawa)

INTRODUCTION

Silicon solar cells have faced their limitation of conversion efficiency for many years. Quantum dot solar cell brings us a great interest to break this frustrating limitation. Combining neutral beam etching with bio-template, advanced nano-process technique was utilized to fabricate superlattices; in particular, for Si nanodisk array [1]. In this study, a 3D finite element method (FEM) is advanced for type-II Ge/Si quantum dot solar cells, which is integrated into the detailed balance transport equation to calculate the conservation efficiency of intermediate band solar cell (IBSC) [2-4].

THE COMPUTATIONAL MODEL

The electronic structure is solved on the basis of envelope-function approximation [3-4]:

$$\left(-\frac{\hbar^2}{2m^*}\nabla^2 + V\right)\psi = E\psi. \quad (1)$$

In the IBSC, the electron conduction current is described as the continuty functions:

$$\frac{dn}{dt} = (G_{VC} - R_{VC}) + (G_{IC} - R_{IC}) + \frac{1}{q}\frac{dJ_n}{dx}. \quad (2)$$

Photovoltage V equals to quasi fermi level splitting between the conduction and valence bands.

$$V = \mu_{VC} = Ef_C - Ef_V. \quad (3)$$

The detailed balance process determines the carrier's chemical potential:

$$G_{VI}(x) - R_{VI}(x) = G_{IC}(x) - R_{IC}(x). \quad (4)$$

RESULTS AND DISCUSSION

As shown in Fig. 1(a), Ge/Si is a typical type-II quantum structure under stress-free conditions. The hole was strongly localized in the Ge QD with a 0.095-eV ground-confined level; however, electrons freely moved in the Si matrix. In a realistic structure, the large lattice mismatch generally induces compressive stress, as shown in Fig. 1(b), which slightly confines the electrons. This additional confinement enhances the optical transition matrix significantly. The 3D FEM simulation enables us to calculate stress distribution. Figure 2 shows the miniband formation in a Ge/Si QD superlattice. Several clear minibands are evident. The miniband induced by the heavy holes ground state are substantially separated from the continuous valence band and other minibands, which have sub-bandgaps several tens of times larger than the thermal energy. With the suggested device structure in Fig. 3, we calculated the I-V curves, as shown in Fig. 4. Under one-sun, the Si QD only improved the efficiency very little, as shown in Fig. 5; however, under the concentration application, the most attractive commercial applications, its conversion efficiency drastically increase to more than 42% under 200X concentration. As shown in Fig. 6, for one-sun applications, H-passivation Si or regrowthing amorphous Si has a great potential to achieve 45%.

CONCLUSION

Ge/Si QD superlattice is especially for concentration application; and with H-passivation Si or regrowth to fabricate amorphous Si matrix, it has a potential to achieve 45% under 1-sun.

ACKNOWLEDGEMENT

Y. Li in this work was supported in part by the Taiwan National Science Council (NSC) under Contract No. NSC-101-2221-E-009-092.

REFERENCES

[1] W. Hu, M. Igarashi, M.-Y. Lee, Y. Li, and S. Samukawa, in: *IEDM Tech. Digest*, 2012, p. 6-1.
[2] A. Martí, E. Antolín, C. R. Stanley, C. D. Farmer, N. López, P. Díaz, E.Cánovas, P. G. Linares, and A. Luque, *Phys. Rev. Lett.* **97**, 247701 (2006).
[3] W. Hu, Y. Harada, A. Hasegawa, T. Inoue, O. Kojima, and T. Kita, *Prog. Photovolt: Res. Appl.*, in press (2013).
[4] W. Hu, M. F. Budiman, M. Igarashi, M.-Y. Lee, Y. Li, S. Samukawa, *Mathematical and Computer Modelling*, in press (2013).

978-3-901578-26-7 © 2013 Society for Micro- and Nanoelectronics

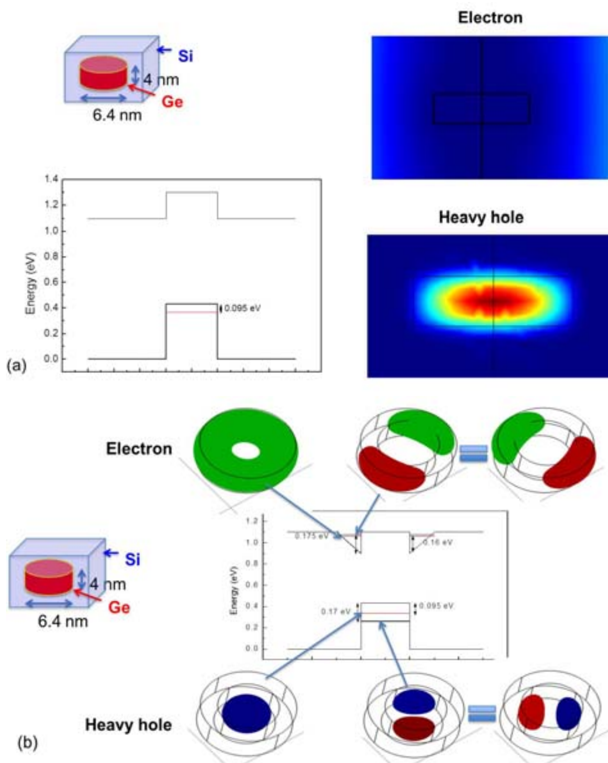

Fig. 1. The quantum level and wavefunction in single Ge/Si QD (a) without stress and (b) with stress.

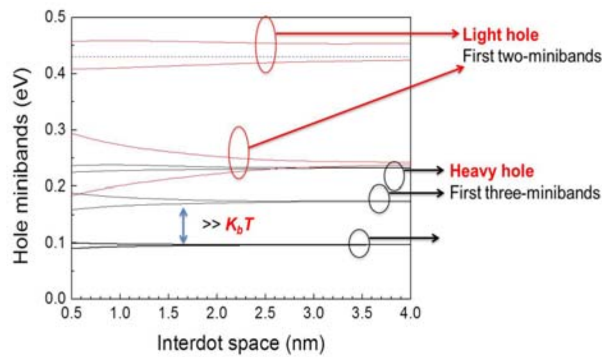

Fig. 2. The miniband formations in the Ge/Si QD superlattice.

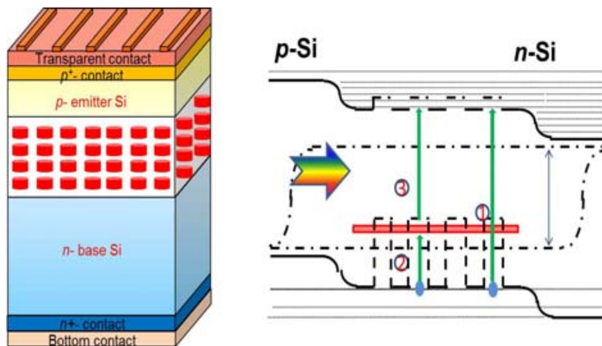

Fig. 3. The explored Ge/Si IBSC's device structure for solar cell applications and the corresponding band profile.

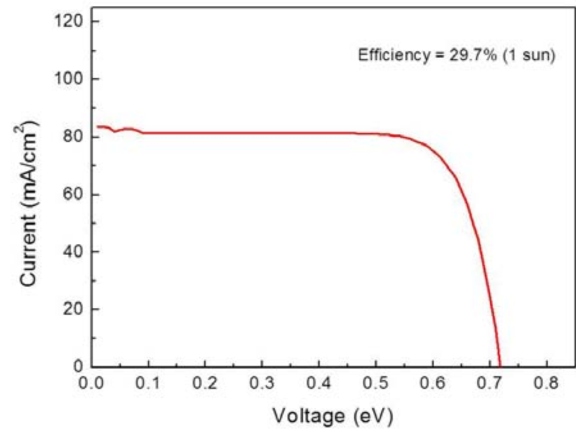

Fig. 4. The simulated I-V profile of the Ge/Si IBSC (one-sun, 5800 K blackbody).

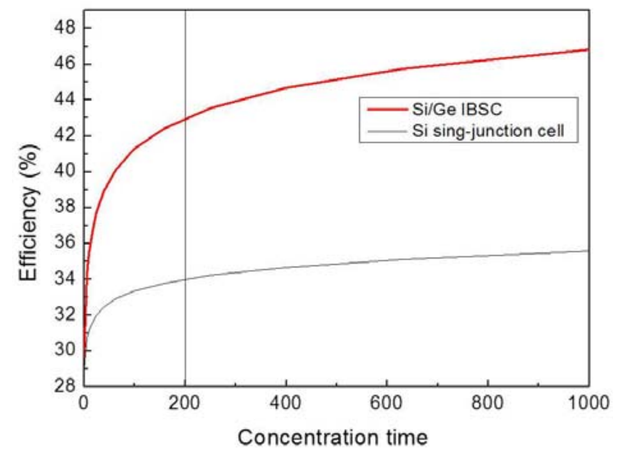

Fig. 5. The plot of conversion efficiency as a function of concentration time. The proposed structure possesses the improved conversion efficiency compared with the conventional one.

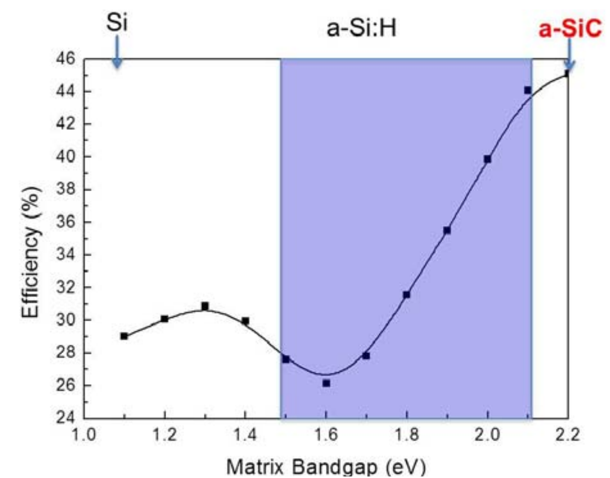

Fig. 6. The conversion efficiency under one-sun as a function of matrix bandgap. With H-passivation treatment, amorphous Si bandgap would gradually increase to 2.1 eV, and thus, the conversion efficiency has a potential to approach 45%.

Inelastic scattering in nano-devices: One-shot current conserving approach

M. Bescond, H. Mera, N. Cavassilas, C. Li, and M. Lannoo
IM2NP, UMR CNRS 7334, Bat. IRPHE, 13384 Marseille, France
e-mail: marc.bescond@im2np.fr

In the last twenty years the non-equilibrium Green's functions (NEGF) formalism has demonstrated its efficiency to model quantum transport in nanoscale devices [1]. In particular, NEGF formalism has been extensively developed to treat inelastic scattering. The description of inelastic scattering by phonons and/or photons is based on the so-called selfconsistent Born approximation (SCBA), which is computationally very challenging when applied to realistic devices. In this work we present a one-shot current conserving approach to treat electron-phonon scattering and apply it to the modeling of n-type nano-transistors while avoiding the self-consistent SCBA procedure.

Let us start with the lowest order approximation (LOA), which within the SCBA is nothing but a perturbative expansion to first order in the interaction. We consider an ideal linear chain where electrons interact with one optical phonon mode [2]. Figure 1 shows the left (I_L) and right (I_R) currents calculated with the LOA for various arbitrary electron-phonon coupling M and applied voltages V. We note that LOA perfectly satisfies the current conservation law. Figure 2 compares the right spectral currents obtained with the ballistic regime, the SCBA and LOA. While SCBA spectrum depicts several well-resolved phonon emission peaks, the LOA only accounts for the emission of one phonon. For larger electron-phonon coupling M the LOA spectral current takes negative values signaling the failure of the LOA. Fortunately, given the ballistic current I_0 and a first-order correction ΔI, one can build the first Padé approximant, $I_0/(1 - \Delta I/I_0)$, to analytically-continue the perturbative Born series [3]. This is the simplest current-conserving one-shot approximation. We illustrate the application of the LOA and LOA analytically continued (LOA-AC), by considering electron-phonon scattering in Silicon double-gate and nanowire transistors (Fig. 3(a-b)).

For DG-transistor, current degradations as a function of the gate voltage obtained with the three approaches (SCBA, LOA, and LOA-AC) are shown in Fig. 4. We note that LOA overestimates the current degradation while its analytic continuation faithfully reproduces the SCBA results [4].

Nanowire transistor constitutes a relevant case since its transport properties are found to be strongly impacted by electron-phonon interactions. Indeed, $I_D - V_G$ current characteristics of Fig. 5 show that LOA fails in describing the phonon scattering influence. The breakdown of the LOA is mainly due to interactions with acoustic phonons which induce negative values of current spectrum (Fig. 6). Interestingly even in this case, the LOA-AC still provides current characteristics close to those of SCBA [5].

Therefore, we present a one-shot current conserving approach well suited to model inelastic transport in n-type nano-transistors with highly doped leads. This challenges the currently adopted view that heavy self-consistent calculations are required to preserve conservation laws.

This work is supported by the QUASANOVA and SIMPSSON contracts funded by the ANR.

REFERENCES

[1] H. Haug and A.-P. Jauho, *Quantum Kinetics in Transport and Optics of Semiconductors* (Springer, New York, 1996).
[2] H. Mera, M. Lannoo, N. Cavassilas and M. Bescond, Phys. Rev. B (R) **86**, 161404 (2012).
[3] H. Mera, M. Lannoo, N. Cavassilas and M. Bescond, *Nanoscale device modelling using a conserving analytic continuation technique*, submitted (2013).
[4] N. Cavassilas, M. Bescond, H. Mera, and M. Lannoo, Appl. Phys. Lett. **102**, 013508 (2013).
[5] M. Bescond, C. Li, H. Mera, N. Cavassilas, and M. Lannoo, *Inelastic scattering in n-type nanowire field-effect-transistors: One-shot current conserving approach*, to be submitted (2013).

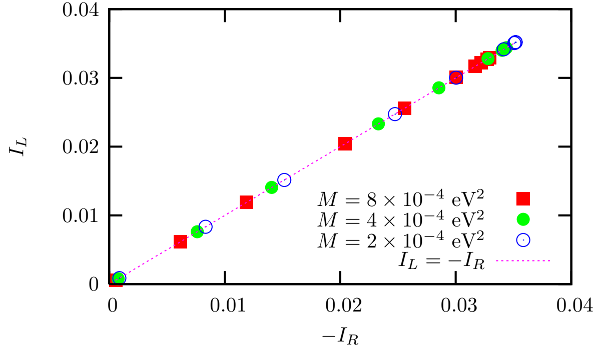

Fig. 1. Current conservation in the LOA calculated for an ideal linear chain. The model is numerically shown to exactly satisfy current conservation $I_L = -I_R$. The graph has been obtained for different electron-phonon couplings (M) and applied bias voltages (0< V <0.4 V). M represents the square of the matrix elements of the electron-phonon interaction.

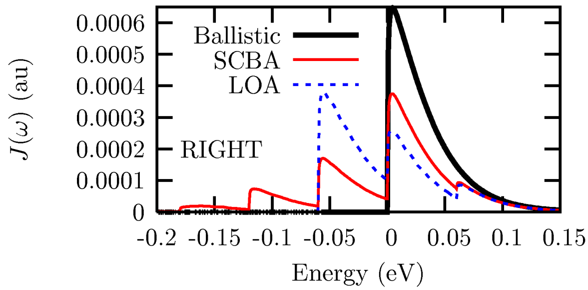

Fig. 2. Current spectrum of the linear chain at the right interface calculated in the ballistic regime (bold solid line), the SCBA (solid line) and the LOA (dashed line). $V = 0.2$ V and $M = 4.10^{-4}$ eV^2.

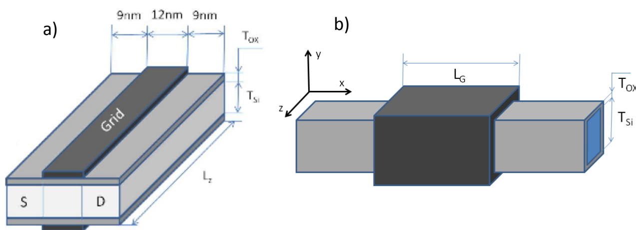

Fig. 3. Schematic representation of the devices considered in this work: a) the double-gate (DG) MOSFET and b) the nanowire (NW) MOSFET for which T_{OX}=1 nm, T_{Si}=2 nm and L_G=15 nm. Source/drain doping is N_D=10^{20}cm^{-3}.

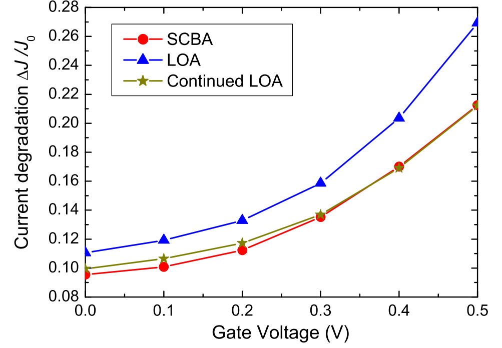

Fig. 4. Current degradation with respect to the ballistic result (J_0) when considering the SCBA (circles), the LOA (triangles) and the LOA-AC (stars) for the DG-MOSFET shown in Fig. 3a).

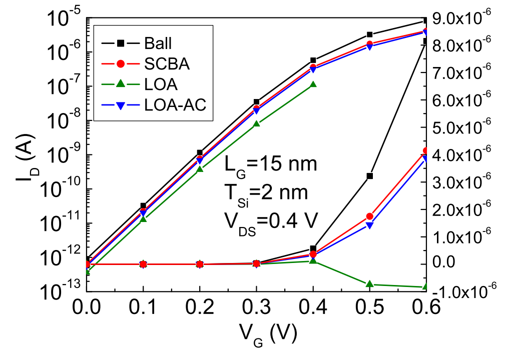

Fig. 5. $I_D - V_G$ current characteristics for Si NW transistor shown Fig. 3b), in the ballistic limit (squares), the SCBA (circles), the LOA (triangles), and the LOA-AC (reversed triangles).

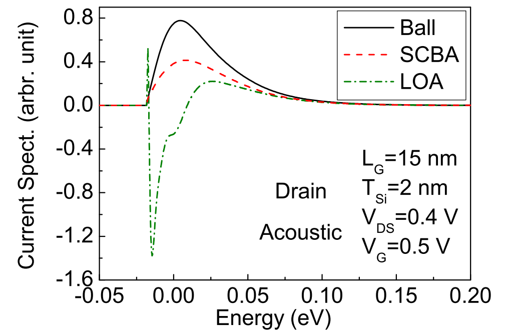

Fig. 6. Influence of acoustic phonon scattering on drain-edge current spectra in the NW transistor. Three models are shown: the ballistic regime (solid line), SCBA (dashed line) and LOA (dash-dot line).

SCBA Made Simple

H. Mera, M. Lannoo, N. Cavassilas and M. Bescond
IM2NP–UMR CNRS 7334, Aix-Marseille Université, 49 Rue Juliot Curie, Boîte Postale 146, and
Technopole Chateau–Gombert, 13384 Cedex 13, Marseille.
e-mail: hexmera@hotmail.com

Non-equilibrium Green's function (NEGF) techniques are commonly applied to the understanding and design of novel nanoelectronic devices. In many situations one needs to take into account interactions such as the electron-phonon/photon or electron-electron. Accounting for these within NEGF is theoretically and computationally challenging. Inexpensive approximations to treat interactions are thus very much in need. Selfconsistency is considered to be essential for conservation laws to be obeyed. According to this view it is necessary to iterate NEGF equations to selfconsistency, thus further complicating matters.

The purpose of this study is to provide a generalization and a full theoretical justification of our previous work at the lowest order [1-3]. We provide an infinite family of conserving but not fully selfconsistent approximations. We illustrate the performance of the newly developed approximations by considering the calculation of the photocurrent in a bias molecular-junction model.

In the NEGF method one accounts for interactions by means of a Dyson equation of the form

$$G=g+g\Sigma[G]G, \quad (1)$$

where $\Sigma[G]$ is a Φ-derivable selfenergy that accounts for interactions and g is the noninteracting NEGF. Because the selfenergy is itself a functional of G, Eq. (1) needs to be solved selfconsistently. The standard way of iterating Eq. (1) is based on writing it as $G=[g^{-1}-\Sigma[G]]^{-1}$ leading to

$$G_n=[g^{-1}-\Sigma[G_{n-1}]]^{-1}. \quad (2)$$

Unfortunately iterating Eq. (2) leads to a sequence of G_n's which are not conserving. Eq. (2) leads only to one conserving approximation, the fully self-consistent one. In strongly interacting systems many iterations might be needed for Eq. (2) to converge.

In this work we show how one can generate conserving approximations from the Born series for the NEGF. In the Born series the fully selfconsistent G is expanded as a partial power series in the interaction strength parameter, M^2, up to the desired order:

$$g_N = g + \sum_{n=1}^{N} \delta g_n M^{2n} , \quad (3)$$

where the δg_n are M-independent coefficients. We will show that g_N is conserving. To estimate the SCBA current, $I[G]$, we evaluate instead $I[g_N]=I_{N/0}$, which is a Born series for the current. With $I_{N/0}$ we can calculate a Padé table of approximations, $I_{P/Q}$. Because g_N is conserving, observables calculated from it satisfy whatever conservation laws they ought to satisfy.

In Fig. 1 we show the photocurrent as a function of source-drain bias, calculated for a molecular junction model for various values of M. We compare the SCBA currents with those obtained from $I_{N/0}$ (top panel) and the diagonal Padé sequence $I_{P/P}$ (bottom panel). For small values of M, Fig. 1(a), the Born series works well, reproducing the full SCBA result. As M increases the Born series breaks down (see Fig 1(b) and (c)). In contrast the Padé approximations $I_{P/P}$, Fig. 1(d-f), work well or any value of M. The 1/1 Padé approximate is a two-shot conserving approximation.

We believe these techniques will lead to improved recipes for the nanodevice simulation accounting for inelastic scattering.

References

[1] M. Bescond, invited talk at IWCE2013.
[2] H. Mera *et al*. Phys. Rev. B (R) **86**, 161404 (2012)
[3] N. Cavassilas *et al*. App. Phys. Lett. **102**, 013508 (2013)

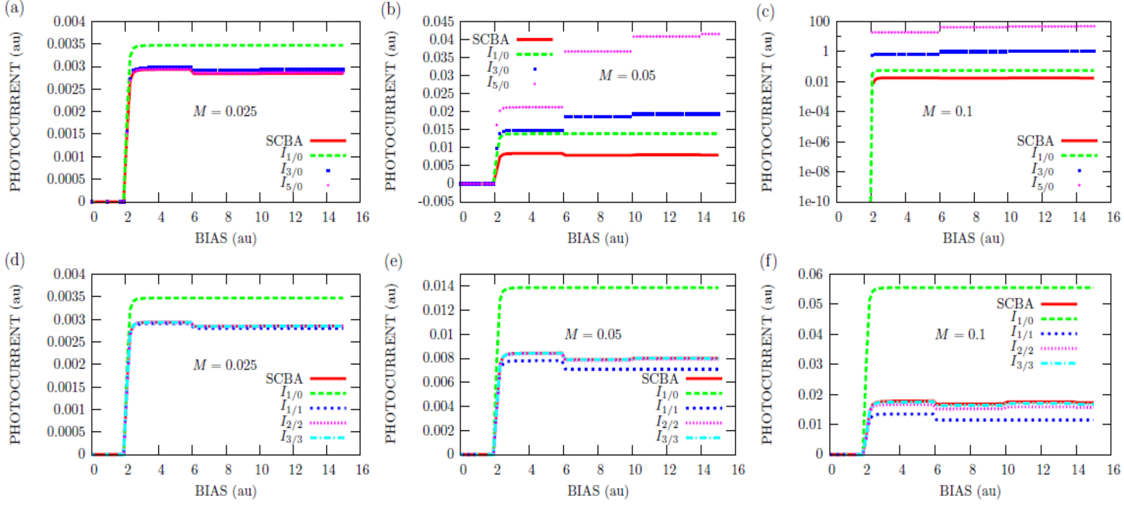

FIG. 2: Photocurrent as a function of source-drain bias. In (a)-(c) we show a comparison between currents calculated from the SCBA and the Born series, $I_{N/0}$ for n = 1, 3 and 5, for the values of M shown. (a) When interactions are weak the SCBA current is well approximated by currents calculated from the Born series for the NEGF. (b-c) The Born series is divergent. Outside its radius of convergence the estimates become worse and worse as M is increased. In (d)-(f) we compare SCBA currents with those obtained from the first three diagonal elements of the Padé table, $I_{P/P}$, P=1,2,3. For M small or large the Padé approximants give fairly good approximations for the SCBA current. In particular the two-shot approximate $I_{1/1}$ is both accurate and computationally inexpensive.

Phonon-Limited Low-Field Mobility in Silicon Nanowires: NEGF Quantum Transport vs. Linearized Boltzmann

R. Rhyner and M. Luisier
Integrated Systems Laboratory, ETH Zürich, 8092 Zürich, Switzerland, e-mail: rhyner@iis.ee.ethz.ch

Introduction Quantum transport simulations of nanoscale devices in a full-band and atomistic basis are computationally very intensive, especially those including electron/hole-phonon scattering in the Non-equilibrium Green's Function (NEGF) formalism [1]. To investigate realistic structures with such an approach, it is necessary to introduce physical and numerical approximations. However, even in these cases, the computational burden remains very high as compared to semi-classical simulations with the drift-diffusion model.

Here, we propose to check and validate the approximations made in dissipative quantum transport (QT) simulations through comparisons with the exact solution of the linearized Boltzmann Transport Equation (LB). Although it does not allow for the simulation of current characteristics as QT, the LB method is particularly well-suited to compute low-field mobilities in bulk and nanostructures. Using the same electron/hole tight-binding parametrization and phonon bandstructure model in the QT and LB approaches, we calculate the electron and hole mobility in bulk Si and ultrascaled Si nanowires as shown in Fig. 1. A careful analysis of the results shows that the QT simplifications work well for electrons, but are less accurate for holes.

Method In the quantum transport case, low-field mobilities are calculated within the NEGF formalism [2] using the dR/dL method [3]. The linearized Boltzmann Transport Equation is solved exactly in the stationary regime [4] to obtain reference mobility values. All the simulations use the same nearest-neighbor $sp^3d^5s^*$ tight-binding model to describe the electron and hole properties in Si [5] and the same valence-force-field (VFF) method for phonons [6]. The electron/hole-phonon interactions are derived from the first order Taylor-expansion of the tight-binding Hamiltonian ($\nabla\mathbf{H}_{ln}$) around the equilibrium lattice positions R_l and R_n. The strain parametrization has therefore a strong influence on the electron-phonon coupling strength.

As depicted in Fig. 2, the NEGF formalism accounts for electron-phonon interactions through scattering self-energies $\mathbf{\Sigma}_{nn}^{<>}(E)$ while the LB approach relies on transition matrix elements $S(b,k_x;b',k_x')$ based on Fermi's Golden Rule . For computational reasons, the scattering self energies are assumed diagonal and use a simplified form factor $\widetilde{\mathbf{V}}$. With LB, all the scattering elements can be taken into account (LB FULL) or only the diagonal ones (LB APPROX), as in the NEGF calculations.

Results As a first step, we compare the bulk mobility of Si computed with NEGF and LB to experimental data. The goal is not only to determine whether the two approaches agree, but also how close they are to reality. Once that confidence in the models is obtained, nanowires can be considered. Note that the calculation of bulk mobilities requires the coupling of transverse momentum, which is not shown in Fig. 2, but performed anyway. Two different strain models are investigated, labeled *old* [7] and *new* [8]. Mobility results are reported in Fig. 3. For electrons, a good agreement between the NEGF and LB approach (both FULL and APPROX) can be observed, especially with the *new* strain model where the values are close to the experimental data. For holes, LB reproduces the experimental values reasonably well, but NEGF greatly overestimates them. This discrepancy needs further investigations.

We now consider free-standing silicon nanowires with different diameters and crystal orientations as schematized in Fig. 1. The QT mobilities are obtained by simulating three different nanowire lengths (20, 30, and 40 nm) at a low applied voltage ΔV=10^{-4} V and low doping concentrations N_A, N_D=10^{16} cm^{-3}. Based on the resulting channel resistance, the dR/dL method is applied. In the LB calculations, the Fermi level matches the QT one. In Fig. 4 and 5 the electron mobilities for two crystal orientations and different diameters are plotted. A good agreement between QT, LB FULL, and LB APPROX is achieved. Figure 6 shows the hole mobility in $\langle 110\rangle$-oriented Si nanowires with different diameters. The QT mobilities still agree well with LB APPROX, where only the diagonal elements of the scattering matrix are taken into account, but they are too large as compared to LB FULL. This indicates an underestimation of the hole-phonon coupling strength with diagonal self-energies only.

Conclusion A NEGF quantum transport simulator and the linearized Boltzmann Transport Equation have been compared by means of the calculation of low-field mobilities in Si bulk and nanowires. A good agreement between the NEGF and LB results is demonstrated where we apply the same diagonal approximation, validating the simplification made to the electron/hole-phonon form factor. There are still discrepancies to address between NEGF and LB FULL. Once they are solved, the LB approach could be used to efficiently parametrize the electron/hole-phonon coupling strength of the NEGF formalism so that experimental mobility values can be reproduced for materials other than Si.

References [1] M. Luisier, *Proc. ACM/IEEE Conf. Supercomput.* 2010, pp. 1-11. [2] M. Luisier, G. Klimeck, *Phys. Rev. B*, 80, 155430, 2009. [3] K. Rim et al., *Tech. Dig. Int. Electron Devices Meet.* 4346, 2002. [4] W. Zhang et al., *Phys. Rev. B*, 82, 115319, 2010. [5] T. B. Boykin et al., *Phys. Rev. B*, 69, 115201, 2004. [6] Z. Sui, I. P. Herman, *Phys. Rev. B*, 48, 17938, 1993. [7] T. B. Boykin et al., *Phys. Rev. B*, 76, 035310, 2007. [8] T. B. Boykin et al., *Phys. Rev. B*, 81, 125202, 2010.

978-3-901578-26-7 © 2013 Society for Micro- and Nanoelectronics

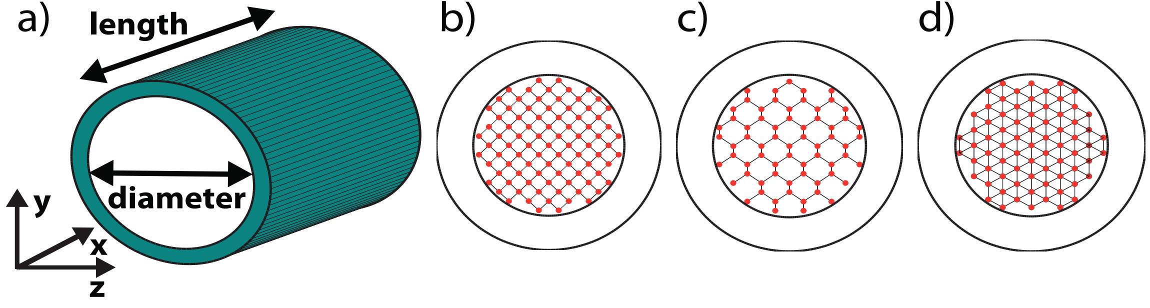

Fig. 1. (a) Schematic view of the nanowire structures simulated in this work. The diameter and length vary between 2.0 and 3.5 nm and 20 and 40 nm, respectively. Three different cross sections are considered (b) $\langle 100\rangle$, (c) $\langle 110\rangle$ and (d) $\langle 111\rangle$.

$$\textbf{NEGF:}\quad \widetilde{\mathbf{V}}^{ij}_{nlln}(\omega_{ph}) = \sum_{\lambda}\int_{-\pi}^{\pi}\frac{dq_x}{2\pi}\cdot\mathbf{V}^{i}_{nl}(\lambda,q_x)\cdot\left(\mathbf{V}^{j}_{ln}(\lambda,q_x)\right)^{*}\quad \text{with}\quad \omega_{ph}-\Delta_E/\hbar\leq\omega_\lambda(q_x)\leq\omega_{ph}+\Delta_E/\hbar$$

$$\mathbf{\Sigma}^{\lessgtr}_{nn}(E)\approx\sum_{l,i,j}\sum_{\omega_{ph}}\widetilde{\mathbf{V}}^{ij}_{nlln}(\omega_{ph})\cdot\nabla_i\mathbf{H}_{nl}\cdot\left(n_{ph}(\omega_{ph})\cdot\mathbf{G}^{\lessgtr}_{ll}(E\mp\hbar\omega_{ph})+(n_{ph}(\omega_{ph})+1)\cdot\mathbf{G}^{\lessgtr}_{ll}(E\pm\hbar\omega_{ph})\right)\cdot\nabla_j\mathbf{H}_{ln}$$

$$\textbf{LB:}\quad S(b,k_x;b^{'},k_x^{'})\approx\frac{1}{\hbar}\sum_{\lambda}\int_{-\pi}^{\pi}dq_x\left|\sum_{n,l,i}\left(\mathbf{c}_n(b^{'},k_x{'})\right)^{*}\cdot\mathbf{c}_l(b,k_x)\cdot\nabla_i\mathbf{H}_{nl}\cdot\mathbf{V}^{i}_{nl}(\lambda,q_x)\right|^2\cdot\delta_{k_x^{'},k_x+q_x+Q_x}$$

$$\cdot\left[\left(n_{ph}(\omega_\lambda(q_x))+\frac{1}{2}\mp\frac{1}{2}\right)\cdot\delta(E^{b^{'}}_{k_x^{'}}-E^{b}_{k}\mp\hbar\omega_\lambda(q_x))\right]$$

Fig. 2. Comparison of the electron/hole-phonon equations in the NEGF and Linear Boltzmann approaches for nanowires. The indices i,j refer to spatial coordinates $\{x,y,z\}$, n, l to the atomic positions while b/λ indicates the electron/phonon mode. The variables k_x/q_x represent the electron/phonon wavevector, Q_x a primitive phonon wavevector, $E/\hbar\omega$ the electron/phonon energy, n_{ph} the equilibrium phonon distribution (Bose-Einstein), $\mathbf{G}$ is the electron Green's Function and $\mathbf{c}$ the electron eigenvectors resulting from the tight-binding Hamilton matrix $\mathbf{H}$. The term $\nabla\mathbf{H}$ describes the derivative of the tight-binding Hamilton matrix, $\mathbf{V}$ is the electron/hole-phonon scattering form factor, and $\widetilde{\mathbf{V}}$ its approximated value in the NEGF calculations [2]. In LB, the squared absolute value allows for either taking all the scattering elements ($n_1n_2\rightarrow n_1l_1l_2n_2$, LB FULL) into account or applying the same diagonal approximation ($nn\rightarrow nlln$, LB APPROX) as in the NEGF formalism.

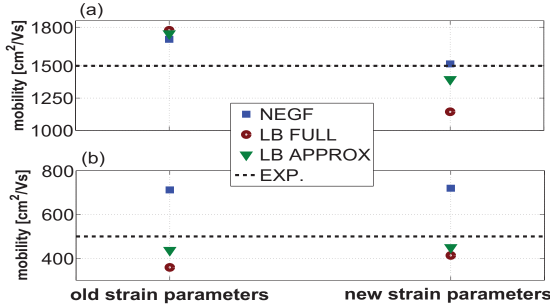

Fig. 3. (a) Electron mobility in bulk silicon. Comparison between the *old* [7] and *new* [8] strain model and the experimental value of pure silicon (dashed line). The blue squares refer to the NEGF simulations, red circles to LB FULL, and green triangles to LB APPROX. (b) Same as (a), but for holes.

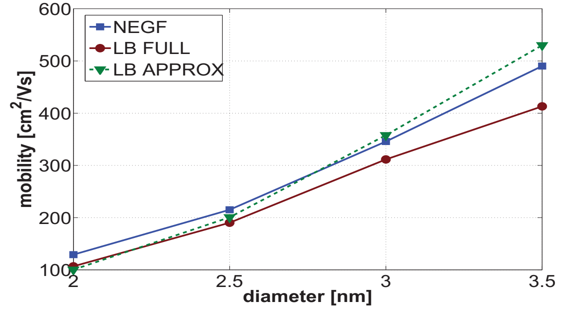

Fig. 4. Electron mobility in a $\langle 100\rangle$-oriented silicon nanowire for diameters comprised between 2 and 3.5 nm. The blue line with square refers to NEGF, the red line with circles to LB FULL, and the green line with triangles to LB APPROX. In all these simulations, the *old* strain model is used.

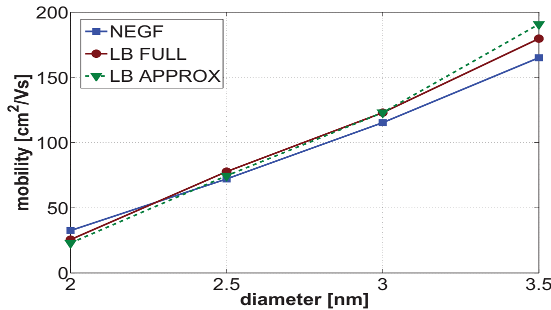

Fig. 5. Same as in Fig. 4, but for electrons along the $\langle 111\rangle$ crystal orientation.

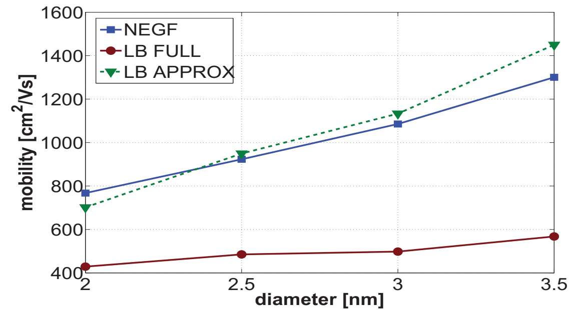

Fig. 6. Same as in Fig. 4 and 5, but for holes along the $\langle 110\rangle$ crystal orientation.

Thermal Conductivity of Si Nanowires Using Atomistic Phonon Dispersions

H. Karamitaheri, N. Neophytou, and H. Kosina
Institute for Microelectronics, TU Wien, Gußhausstraße 27–29/E360, 1040 Wien, Austria
e-mail: {karami | neophytou | kosina}@iue.tuwien.ac.at

INTRODUCTION

The thermal properties of Si nanowires (NWs) are of high interest for a variety of applications such as thermal management and thermoelectricity. Most simulation studies to date use the Si bulk dispersion within a confined geometry. The phonon dispersion in ultra-narrow 1D NWs, however, is different from the bulk dispersion, and can lead to different thermal properties. In this work, we study the thermal conductivity (κ_l) of ultra-narrow silicon NWs using the full-band confined phonon dispersion and Boltzmann transport theory.

COMPUTATIONAL METHOD

We calculate the phonon dispersion using the modified valence force field method which captures the phonon details in the entire Si Brillouin Zone [1]. The lattice thermal conductivity is calculated using the BTE for phonons as [2]:

$$\kappa_l = \sum_{\alpha,q} \frac{\hbar^2 \omega_\alpha(q)^2}{k_\mathrm{B}^2 T} \frac{e^{(\hbar\omega_\alpha(q)/k_\mathrm{B}T)}}{\left[e^{(\hbar\omega_\alpha(q)/k_\mathrm{B}T)} - 1\right]^2} \tau_\alpha(q) v_\alpha(q)^2$$

where $v_\alpha(q)$ is the group velocity of a phonon with wavevector q in subband α. For the calculation of the relaxation times, we follow the bulk formalism for Umklapp scattering, $\tau_\mathrm{U}^{-1} = \mathrm{B}\omega_\alpha(q)^2 T \exp(-\mathrm{C}/T)$ [3]. For boundary scattering we use $\tau_\mathrm{B}^{-1} = (1-p)/(1+p) v_\alpha(q)/D$, where D is NW diameter and p is specularity parameter given by $p(q) = \exp(-4q^2\Delta_\mathrm{rms}^2)$ [3] where $\Delta_\mathrm{rms} = 0.3$ nm. NWs have a finite phonon density of states (*DOS*) at low frequencies, in contrast to bulk. Therefore, the bulk scattering model for Umklapp scattering causes divergence in κ_l. To remove the singularity, as proposed by Mingo [4], an additional second order 3-phonon scattering rate can be introduced as $\tau_\mathrm{U2}^{-1} = \mathrm{A}T^2$. Finally, the overall relaxation rate is computed using Mathiensens rule.

RESULTS AND DISCUSSION

Figure 1 shows the Umklapp scattering-limited κ_l for NWs in the <100>, <110>, and <111> orientations, vs. D. To obtain this, we use $\mathrm{A} = 15000\ 1/\mathrm{sK}^2$, which provides good agreement with molecular dynamics (MD) results [5]. Our results also show good agreement with results from MD [5] and NEGF simulations [6] in a large temperature range (especially above 200 K), as shown in Fig. 2 and 3. In ultra-narrow NWs, however, the most important scattering mechanism is boundary scattering [5]. Its effect as a function of p at $T = 200$ and 300 K is shown in Fig. 4. Here, we use a constant p for all q-points. The conductivity increases as p increases (specular boundaries) as expected. The solid symbols show κ_l when we consider a q-dependent p. The empty symbols with errorbars are MD results from [5]. Interestingly, the effective p is ~ 0.8, indicating that the overall scattering is almost specular, even for such narrow NWs ($D = 2$ nm), in contrast to what normally assumed for nanostructures. The low-q phonons have high p and undergo mostly specular scattering on the surfaces. This low scattering rate at low frequencies, the high group velocity of acoustic branches, as well as the non-zero *DOS* at low frequency, result in a major κ_l contribution of the low frequency phonons (inset of Fig. 5). The cumulative κ_l vs. mean-free-path (MFP) is shown in Fig. 5. For Umklapp-limited scattering (blue), the heat is carried by phonons with MFPs from a few nanometers to a few microns. In the presence of boundary scattering, however, almost 50% of the heat is carried by phonons with MFPs of a few nanometers. The contribution of phonons with $\lambda > 3\ \mu$m is not affected by boundary scattering because these are low frequency phonons, that undergo mostly specular boundary scattering.

978-3-901578-26-7 © 2013 Society for Micro- and Nanoelectronics

Acknowledgment

This work was supported by the European Commission, grant 263306 (NanoHiTEC).

References

[1] A. Paul, M. Luisier, and G. Klimeck, J. Comput. Electron **9**, 160 (2010).

[2] Z. Aksamija and I. Knezevic, Phys. Rev. B **82**, 045319 (2010).

[3] C. Jeong, S. Datta, and M. Lundstrom, J. Appl. Phys. **111**, 093708 (2012).

[4] N. Mingo and D. A. Broido, Nano Lett. **5**, 1221 (2005).

[5] D. Donadio and G. Galli, Nano Lett. **10**, 847 (2010).

[6] M. Luisier, Phys. Rev. B **86**, 245407 (2012).

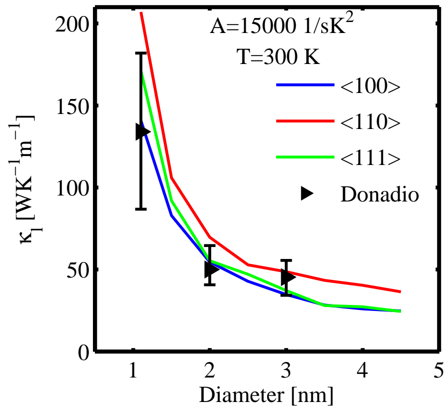

Fig. 1. Thermal conductivity of NWs vs. diameter at $T = 300$ K. The parameter for second order 3-phonon scattering processes is A $= 15000$ $1/\mathrm{sK}^2$. Symbols are MD results from [5].

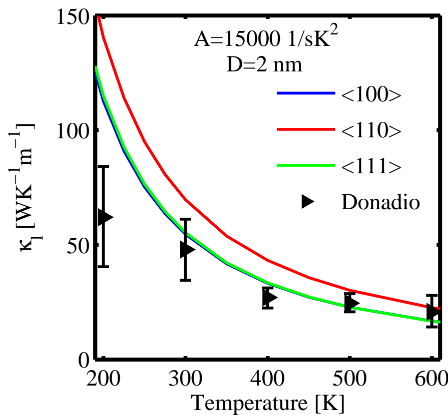

Fig. 2. Thermal conductivity of the $D = 2$ nm NWs vs. temperature. The parameter for second order 3-phonon scattering processes is A $= 15000$ $1/\mathrm{sK}^2$. Symbols are MD results from [5].

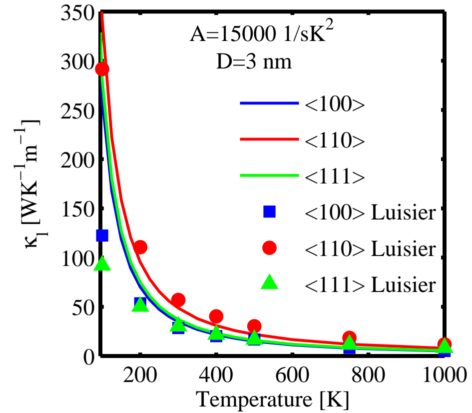

Fig. 3. Thermal conductivity of the $D = 3$ nm NWs vs. temperature. Symbols are NEGF results from [6].

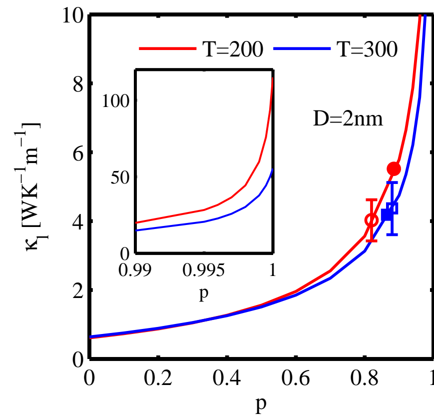

Fig. 4. The thermal conductivity of the $D = 2$ nm <111> NW vs. the boundary scattering specularity parameters p. Solid symbols show the results using a q-dependent p. Empty symbols with errorbars show MD results from [5]. Inset: zoom-in around $p \sim 1$.

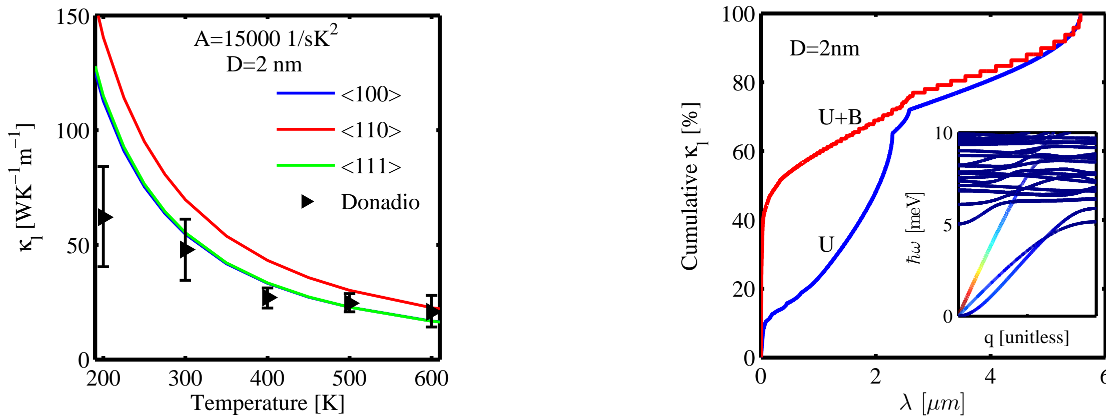

Fig. 5. The cumulative thermal conductivity of the $D = 2$ nm <111> NW vs. the phonon mean-free-path. Results for Umklapp-limited κ_l (U), and Umklapp plus boundary scattering-limited κ_l (U+B) are shown. Inset: The contribution of each mode in κ_l in the Umklapp scattering-limited case.

Impact of Impurity Mass on Ballistic Phonon Thermal Transport in Silicon Nanowires

Junichi Hattori[1,3] and Shigeyasu Uno[2,3]

[1]The Research Organization of Science and Technology, Ritsumeikan University, Kusatsu, Shiga, 525-8577, Japan
[2]Department of Electrical and Electronic Engineering, Ritsumeikan University, Kusatsu, Shiga, 525-8577, Japan
[3]JST, CREST, Chiyoda-ku, Tokyo 102-0075, Japan
E-mail: jhattori@fc.ritsumei.ac.jp

1. Introduction

Silicon nanowires (Si NWs) have been attracting a lot of interests as thermoelectric (TE) materials, which directly convert temperature gradients to electric fields and vice versa. The conversion efficiency is measured by the figure of merit, ZT. Si NWs have shown a relatively high ZT of about 0.5 at room temperature [1, 2]. Practical TE applications, however, require a higher ZT of at least unity. One way to improve ZT is impurity doping. Impurities behave as scattering sources for phonons and reduce the phonon thermal conductivity κ_p [3]. This reduction leads to an improvement in ZT, because $ZT \propto (\kappa_\text{p} + \kappa_\text{e})^{-1}$, where κ_e is the electron thermal conductivity. Recently, Lee and Hwang have closely examined κ_p in doped bulk Si using molecular dynamics simulations and confirmed its reduction due to doping [4]. They have also revealed that, in bulk Si doped with B or As, the doping-induced disorder of spatial distribution of atomic mass has a much larger contribution to the reduction in κ_p than the change of interatomic potential shape and the lattice strain. However, the mechanism through which the three phenomena directly caused by doping decrease κ_p has not yet been made clear. In this work, we study the doping impact on phonon thermal transport in Si NWs, especially the impact of impurity mass.

2. Dispersion Relations

We considered [001]-oriented ^{28}Si NWs with the unit cell shown in Fig. 1(a), and calculated the phonon dispersion relations in the NWs using the lattice dynamics method [5]. Figure 2 shows the results obtained for a pure and an ^{75}As-doped ^{28}Si NW. In our study, doped NWs differ from undoped ones only in the mass of the atoms substituted by impurity atoms. We assumed impurities not to change the interatomic potential shape and not to cause the lattice strain.

3. Ballistic Thermal Conductance

Phonon thermal conductance is given by

$$K = \sum_n \int_{-a_z/\pi}^{a_z/\pi} \hbar\omega_n v_n(q_z) \frac{\partial f(\omega_n)}{\partial T} \mathcal{T}_n(q_z) H(v_n(q_z)) \frac{\mathrm{d}q_z}{2\pi}, \quad (1)$$

where q_z is the phonon wavevector along the z-axis, ω_n the frequency in the nth dispersion branch, v_n the group velocity, f the Bose–Einstein distribution, $\mathcal{T}_n$ the transmission, and H the Heaviside function [6]. Figure 3 shows K in the ballistic limit ($\mathcal{T}_n(q_z) \to 1$), K_bal, in ^{28}Si NWs randomly doped with ^{11}B, ^{27}Al, ^{31}P, or ^{75}As [see Fig. 1(c)]. Regardless of dopant type, doping decreases K_bal. As can be seen in Fig. 2, on the whole, phonons in the ^{75}As-doped NW have a smaller ω_n than those in the undoped NW. This is attributed to the tendency, $\omega_n \propto \langle m\rangle^{-1/2}$, where $\langle m\rangle$ is the average atomic mass. If a dispersion relation scales down (up) in terms of ω_n, its constituent branches become flat (steep). Note also that some degenerate modes are split in the doped NW. This is because impurities break the orderliness of atomic mass distribution. The mode splitting (MS) flattens dispersion branches more strongly than the change of $\langle m\rangle$, as shown in Fig. 4. The figure shows the change of v_n in ^{75}As-doped ^{28}Si NWs as a function of the doping concentration. The flattening of dispersion branches means a reduction in v_n, which decreases K_bal through (1).

The MS effect on K_bal in a ^{28}Si NW with a unit cell having one impurity atom at the center [see Fig. 1(d)] is shown in Fig. 5 as a function of the impurity mass. Regardless of whether the impurity atom is heavier or lighter than ^{28}Si, the MS effect increases with increasing mass difference between the two atoms. The MS effect is generally evaluated as the mass-difference scattering rate [3], which is proportional to $\Gamma = \sum_i n_i(1 - m_i/\langle m\rangle)^2$. Here, n_i and m_i are the relative concentration and the mass of ith nuclide, respectively. Figure 6 shows the MS effect as a function of Γ. In terms of the scattering rate, even though NWs are doped with various impurities at various concentrations, if they have the same Γ, they are expected to experience the same MS effect. However, the MS effect in NWs heavily doped with impurities having a small mass difference is larger than that in NWs lightly doped with impurities having a large mass difference.

4. Conclusions

The impact of impurity mass on phonon thermal transport in doped Si NWs was studied in detail with atomistically calculated dispersion relations. The mass disorder induced by impurities reduces the phonon group velocity and thereby thermal transport properties.

978-3-901578-26-7 © 2013 Society for Micro- and Nanoelectronics

[1] A. I. Boukai *et al.*, *Silicon nanowires as efficient thermoelectric materials*, Nature **451**, 168 (2008).
[2] A. I. Hochbaum *et al.*, *Enhanced thermoelectric performance of rough silicon nanowires*, Nature **451**, 163 (2008).
[3] M. Asheghi *et al.*, *Thermal conduction in doped single-crystal silicon films*, J. Appl. Phys. **91**, 5079 (2002).
[4] Y. Lee and G. S. Hwang, *Mechanism of thermal conductivity suppression in doped silicon studied with nonequilibrium molecular dynamics* Phys. Rev. B **86**, 075202 (2012).
[5] A. Paul *et al.*, *Modified valence force field approach for phonon dispersion: from zinc-blende bulk to nanowires*, J. Comput. Electron. **9**, 160 (2010).
[6] J. Hattori and S. Uno, *Impact of Isotope Doping on Phonon Thermal Transport in Silicon Nanowires*, Jpn. J. Appl. Phys. (to be published).

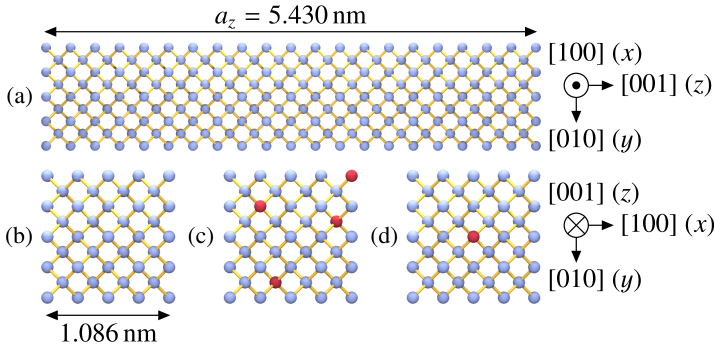

Fig. 1. (a) Side view of a unit cell of the Si NWs considered in this work. The unit cell is repeated periodically along the [001] direction in the NWs. Also, it contains 410 atoms. (b)–(d) Top views of cross sections of the NWs without and with impurities, which are shown by the dark red atoms.

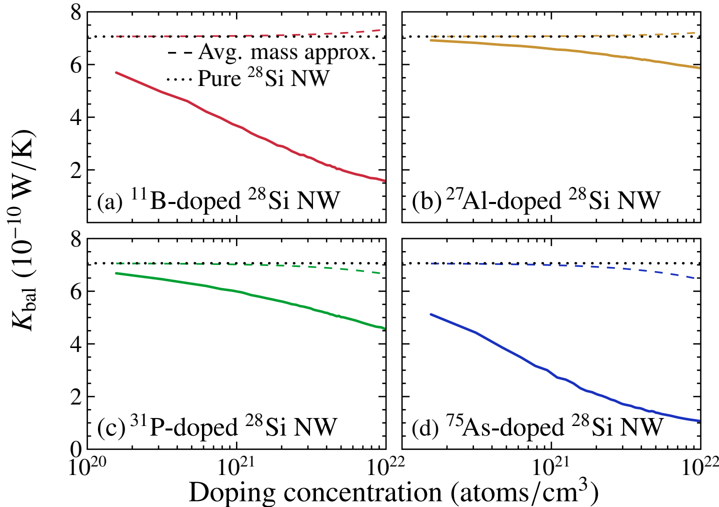

Fig. 3. Ballistic thermal conductance K_{bal} in ^{28}Si NWs randomly doped with (a) ^{11}B, (b) ^{27}Al, (c) ^{31}P, or (d) ^{75}As at 300 K, plotted as a function of the doping concentration N_{i}. The results for each N_{i} were averaged over 15 samples to reduce the fluctuation. The dotted lines represent K_{bal} in a pure ^{28}Si NW. Also, the dashed lines show K_{bal} obtained under the assumption that the masses of all the atoms in a NW are equal to their average.

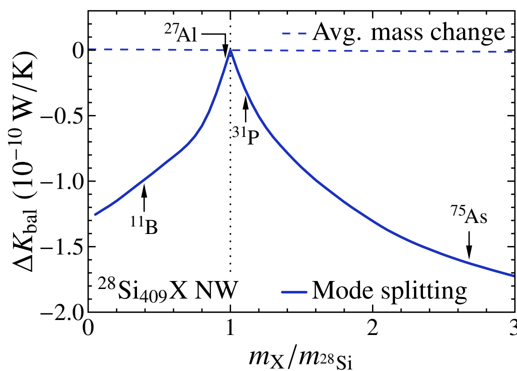

Fig. 5. Variations of K_{bal} due to the mode splitting (solid line) and the change of average atomic mass (dashed line). The calculation was done for ^{28}Si NWs having one impurity atom per unit cell. Each impurity atom was located at the center of each unit cell, as shown in Fig. 1(d). The horizontal axis represents the atomic mass of the impurity divided by that of ^{28}Si.

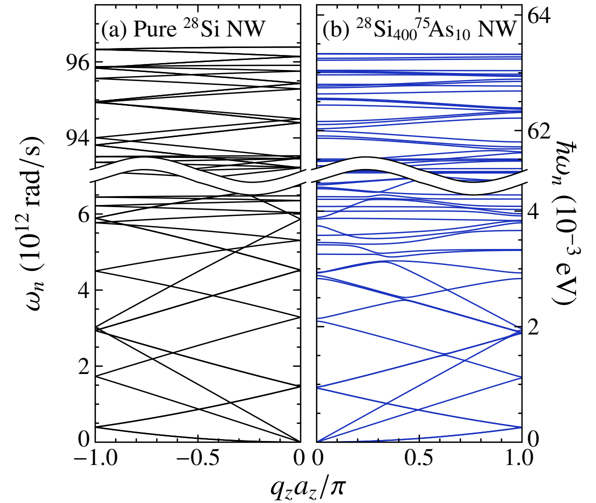

Fig. 2. Dispersion relations of phonons in (a) a pure ^{28}Si NW and (b) a $^{28}\mathrm{Si}_{400}{}^{75}\mathrm{As}_{10}$ NW. The horizontal axes represent the phonon wavevector along the z-axis, q_z, and the vertical axes the phonon frequency, ω_n.

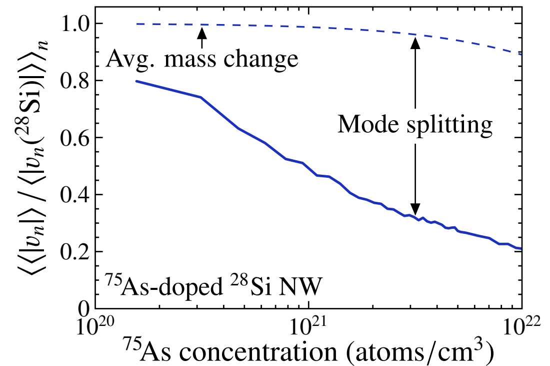

Fig. 4. Ratio of average phonon speed in a dispersion branch in an ^{75}As-doped ^{28}Si NW to that in the corresponding dispersion branch in a pure ^{28}Si NW, averaged over all the branches. The horizontal axis represents ^{75}As concentration.

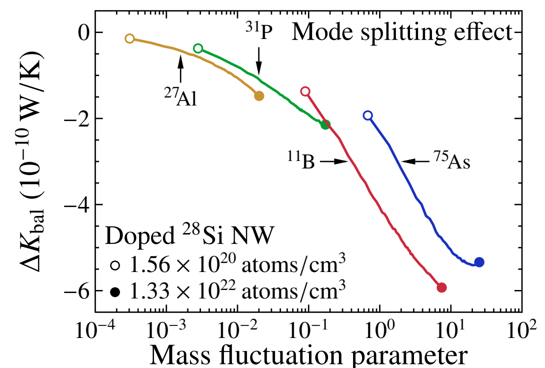

Fig. 6. Mode splitting effects on K_{bal} in ^{11}B-, ^{27}Al-, ^{31}P-, and ^{75}As-doped ^{28}Si NWs, plotted as a function of the mass fluctuation parameter Γ. In the calculation, the doping concentration was varied from 1.56×10^{20} (one) to 1.33×10^{22} atoms/cm^3 (85 atoms per unit cell).

Improvement of Self-Heating Effect Employing Vertical-Channel Field-Effect-Diode 1T-DRAM

T. Imamoto[1, 2], and T. Endoh[1, 2]
[1]Graduate School of Engineering, Tohoku University, [2]JST-CREST
Aramaki aza Aoba 6-6, Aoba-ku, Sendai, Japan, 980-8579, E-mail: endoh@riec.tohoku.ac.jp

INTRODUCTION

Capacitorless 1T-DRAM has been developed to overcome the scaling limitations of conventional 1 transistor 1 capacitor DRAM cells [1]. Previously, we proposed the Field Effect Diode (FED) type vertical 1T-DRAM with negative hold Bit Line (BL) voltage scheme for excellent hold characteristics and low voltage operation [2]. In this paper, the excellent thermal characteristics of our proposed 1T-DRAM compared to the conventional vertical channel 1T-DRAM using Single Transistor Latch (STL) [3] are analyzed in detailed through Sentaurus 3-D device simulator [4] including the Self-Heating Effect (SHE).

MEMORY CELL STRUCTURE AND OPERATION VOLTAGES

Figure 1 (a) and (b) show the schematics of the conventional STL type vertical 1T-DRAM and the FED type vertical 1T-DRAM. The STL type is based on the vertical double gate MOSFET. On the other hand, the FED type is based on the vertical cylindrically p-i-n diode with surrounding gate. Both the STL type and the FED type, an ideal cell size of $4F^2$ can be achieved due to vertical structure. Simulated memory cell design parameters and memory cell operation voltages are shown in Table I and II. Because the highest BL voltage (V_{BL}) is applied in the whole memory operation, the transient thermal characteristics of write “1” operation are focused in this study.

EVALUATION OF SELF-HEATING EFFECT IN THE STL TYPE AND THE FED TYPE 1T-DRAM

Write “1” operation of the STL type and the FED type 1T-DRAM are shown in Fig. 2 and Fig. 3. In the STL type, maximum lattice temperature in the memory cell increased 143K and reaches the value of 443K at 45nsec as BL current (I_{BL}) is increased. Moreover, as maximum lattice temperature is increased, I_{BL} is also increased. This feedback effect is due to the intrinsic bipolar effect. On the other hand, the FED type shows the excellent thermal characteristics. After V_{BL} is applied to -1.1V, $|I_{BL}|$ increases sharply while the STL type increases gradually. In the FED type, peak value of the maximum lattice temperature is only 301.2K at 46nsec with 1.2K rise of temperature. Figure 4 (a) and (b) show the hole distribution along the channel direction of the STL type and the FED type. Hole can be stored under the G_1 within 60nsec access time. Lattice temperature distributions in the memory cell after write “1” operation (time=60nsec) are shown in Fig. 5. In the STL type, maximum lattice temperature is reached 352K while the FED type is reached 300.3K. From all, it is shown that the FED type shows excellent thermal characteristics and can nearly avoid SHE.

CONCLUSION

Excellent thermal characteristics of the FED type 1T-DRAM are presented for the first time by comparing to the conventional STL type 1T-DRAM. Vertical channel type FED 1T-DRAM has the potential to extend scaling limitations.

ACKNOWLEDGEMENT

This work has been supported in part by a grant from “Research of Innovative Material and Process for Creation of Next-generation Electronics Devices” of CREST under the Japan Science and Technology Agency (JST).

REFERENCES

[1] T. Ohsawa, et al., *IEEE J. Solid-State Cir.*, pp. 1510-1522, 2002.
[2] T. Imamoto, et al., Ext. Abs. Int. Conf. SSDM, 2012, pp.588-589
[3] W. Kwon, et al., Jpn. J. Appl. Phys. 49 2010.
[4] http://www.synopsys.com/

978-3-901578-26-7 © 2013 Society for Micro- and Nanoelectronics

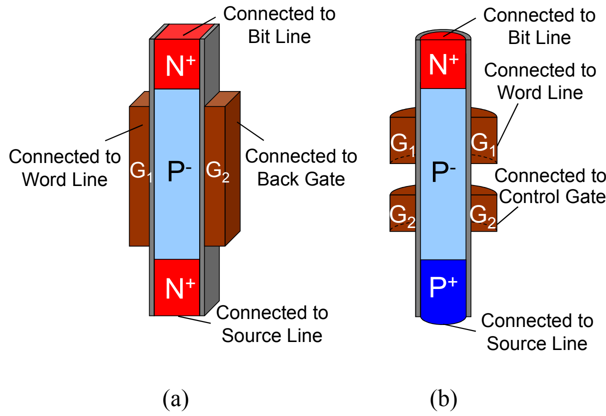

(a) (b)

Fig. 1. The schematics of the vertical channel capacitorless 1T-DRAM cell. (a) Single Transistor Latch (STL) type and (b) Field Effect Diode (FED) type.

Table I. Memory cell design parameters.

Parameter	STL type	FED type
Silicon thickness (T_{Si})	20nm	
Silicon pillar diameter (D)		20nm
Gate length (L_G)	50nm	60nm
Control Gate length (L_{CG})		50nm
Oxide thickness (T_{OX})	5nm	

Table II. Memory cell operation voltages.

	STL type		FED type	
	WRITE"1"	HOLD	WRITE"1"	HOLD
V_{BL}	2.0V	0.0V	-1.1V	-0.6V
V_{WL}	-1.0V	-2.0V	0.0V	-2.0V
V_{CG}			0.3V	
V_{BG}	1.0V			
V_{SL}	0.0V			
V_{Sub}	0.0V			

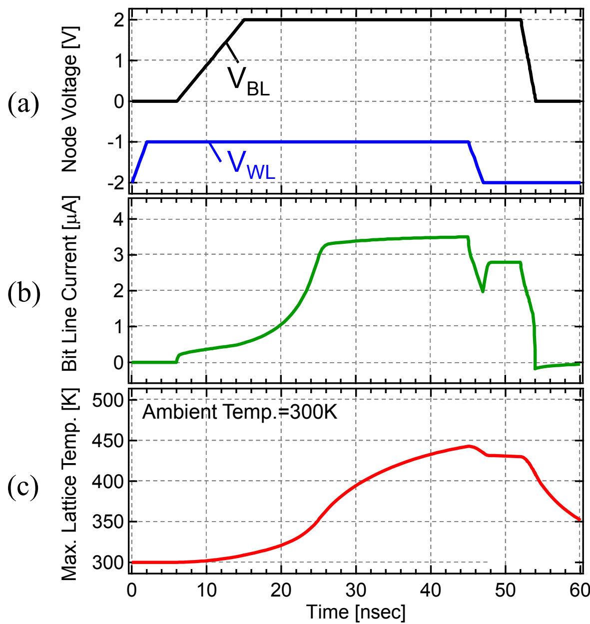

Fig. 2. Write "1" operation of the STL type 1T-DRAM cell. (a) Node voltage (b) Bit line current and (c) Maximum lattice temeprature.

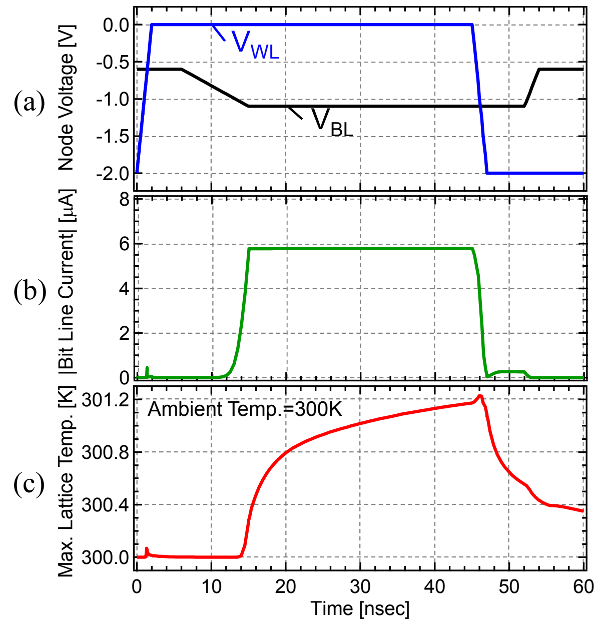

Fig. 3. Write "1" operation of the FED type 1T-DRAM cell. (a) Node voltage (b) Bit line current and (c) Maximum lattice temperature.

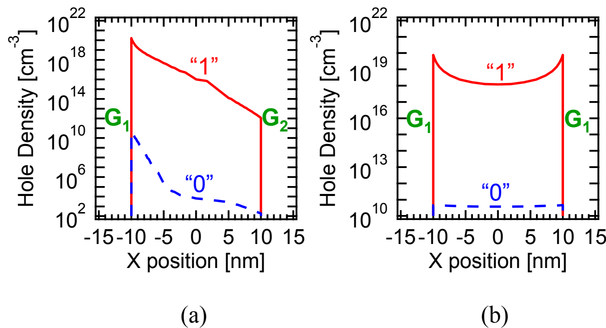

(a) (b)

Fig. 4. Distribution of hole density along the channel direction. (a) STL type and (b) FED type.

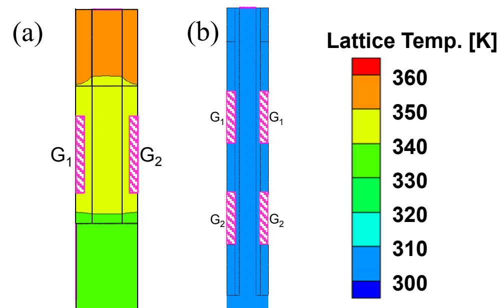

Fig. 5. Distribution of lattice temperature after write "1" operation (time=60nsec). (a) STL type and (b) FED type.

Electro-Thermal Transport in Graphene Devices

S. Islam[1], V.E. Dorgan[1], A.Y. Serov[1], A. Behnam[1], K.L. Grosse[1], M.-H. Bae[1,2], E. Pop[1,3*]

[1]Electrical & Computer Engineering, Univ. Illinois Urbana-Champaign, Urbana, IL 61801, U.S.A.
[2]Korea Research Institute of Standards and Science, Daejeon 305-340, Republic of Korea
[3]Electrical Engineering, Stanford University, Stanford, CA 94305, U.S.A. • E-mail: epop@illinois.edu

We have used simulations verified by extensive experimental data to understand the (coupled) electrical and thermal behavior of graphene transistors and interconnects. Using infrared thermal imaging [1] we uncovered that graphene transistors (GFETs) heat up non-uniformly during high-field operation, due to varying carrier density and E-field along the channel. A hot spot forms at the location of maximum field (minimum carrier density), and its position depends on the applied voltages (Fig. 1) [1].

In addition, using scanning Joule expansion microscopy (SJEM) [2] we have uncovered that thermoelectric effects become important at graphene-metal contacts. For instance, approximately one-third of the temperature rise at graphene contacts is controlled by Peltier effects and about two-thirds by Joule effects, but this proportion will shift in favor of the Peltier effect as graphene contact resistance is improved in future technologies [2].

Self-Consistent Device Modelling

We have developed self-consistent GFET simulations coupling the drift-diffusion equations, Poisson equation, heat diffusion equation, and thermoelectric contact effects [1-5]. These models can simultaneously fit (and extract) graphene mobility, contact resistance, Seebeck effect, thermal conductivity, and thermal conductance to the substrate. The models are best applied in devices larger than the electron and phonon mean free paths in graphene (20-100 nm), where most experimental data are available.

We have recently extended this work to understand current saturation in sub-micron GFETs on SiO_2/Si substrates (Figs. 2-3). We uncovered that strong self-heating limits the maximum current to ~1 mA/μm, but self-heating also "helps" achieve better current saturation and lower output conductance ($g_o = \partial I/\partial V_{ds}$) which is important for amplifier gain [3]. Interestingly, devices shorter than about 0.5 μm benefit from heat sinking at the contacts, which simultaneously reduces their current saturation [3].

Grain Boundaries & Suspended Graphene

We have also used non-equilibrium Green's functions (NEGF) to investigate heat flow at grain boundaries (GBs) in graphene grown by chemical vapour deposition (CVD). We found that "not all defects are created equal", in other words that line defects scatter phonons more strongly than GBs (Fig. 4) [4].

Most recently, we have succeeded in suspending graphene devices to examine the extreme case of coupled electro-thermal behaviour at high field [5] (Figs. 5-6). We uncovered the *intrinsic* drift velocity saturation in graphene, as well as the thermal conductivity k scaling up to ~2000 K (Fig. 6). Interestingly, graphene k decreases as $\sim T^{-1.7}$ while graphite k as $\sim T^{-1.1}$ at high temperature, likely due to a stronger second-order three-phonon scattering which must be further investigated.

Conclusion

Graphene devices present an interesting set of challenges, due to their high in-plane mobility and thermal conductivity, but poor thermal coupling to the environment [6]. Our simulations coupled with experiments have shed physical insight into such coupled behaviour, particularly at high-fields typical of modern devices. Challenges remain in understanding, e.g., the behaviour of GFETs on "well-matched" substrates such as BN, and on highly insulating substrates such as plastics.

Acknowledgement

This work was supported in part by the Office of Naval Research (ONR), by the Nanotechnology Research Initiative (NRI), and by a National Science Foundation (NSF) CAREER Award to E.P.

References

[1] M.-H. Bae, S. Islam, V.E. Dorgan, E. Pop, *Scaling of High-Field Transport and Localized Heating in Graphene Transistors*, ACS Nano **5**, 7936 (2011)
[2] K. Grosse, M.-H. Bae, F. Lian, E. Pop, W.P. King, *Nanoscale Joule heating, Peltier cooling and current crowding at graphene-metal contacts*, Nature Nano **6**, 287 (2011)
[3] S. Islam, Z. Li, V.E. Dorgan, M.-H. Bae, E. Pop, *Role of Joule Heating on Current Saturation and Transient Behavior of Graphene Transistors*, IEEE Electron Device Lett. **34**, 166 (2013)
[4] A.Y. Serov, Z.-Y. Ong, E. Pop, *Effect of Grain Boundaries on Thermal Transport in Graphene*, Appl. Phys. Lett., **102**, 033104 (2013)
[5] V.E. Dorgan, A. Behnam, H. Conley, K. Bolotin, E. Pop, *High-Field Electrical and Thermal Transport in Suspended Graphene*, Nano Lett, DOI:10.1021/nl400197w (2013)
[6] E. Pop, V. Varshney, A.K. Roy, *Thermal Properties of Graphene: Fundamentals and Applications*, MRS Bulletin 37, 1273 (2012)

978-3-901578-26-7 © 2013 Society for Micro- and Nanoelectronics

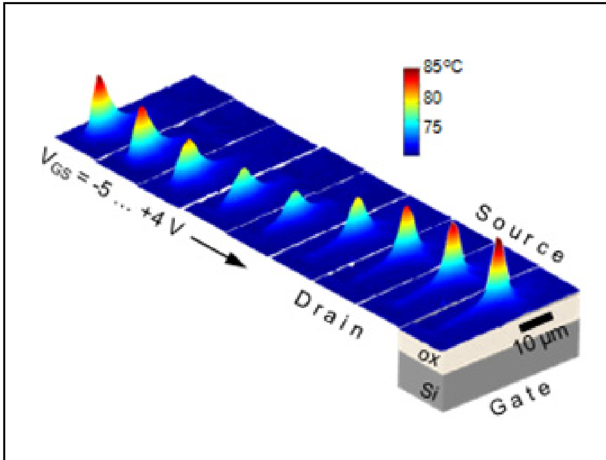

Fig. 1. Infrared (IR) thermal imaging of graphene field-effect transistor (GFET) during operation, from [1]. The figure is a sequence of IR images taken at varying V_{GS} as labeled, and V_{DS} = 12 V. A hot spot forms at the location of highest field, and "moves" along the channel as the voltages are varied [1].

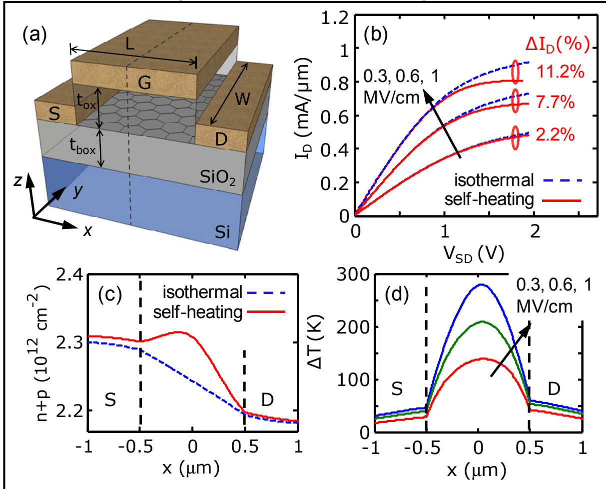

Fig. 2. (a) Simulated GFET (L=1 μm). (b) Effect of self-heating on current saturation, (c) on carrier densities, (d) on temperature rise along the channel [3].

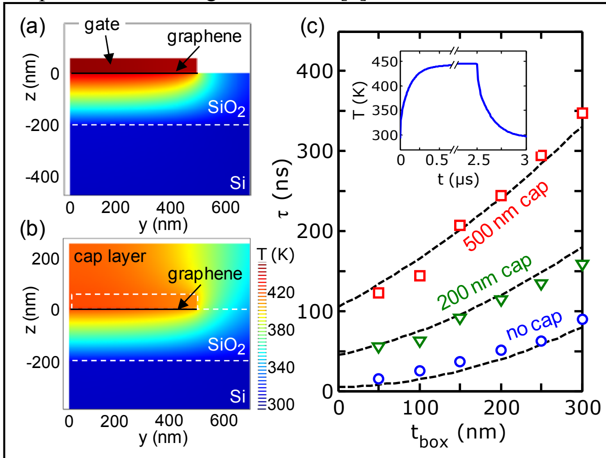

Fig. 3. Simulated thermal transient of a GFET (see Fig 2), (a) without and (b) with a capping layer. (c) Thermal time constants of a GFET are in the range 30-300 ns, much slower than electrical switching time constants [3].

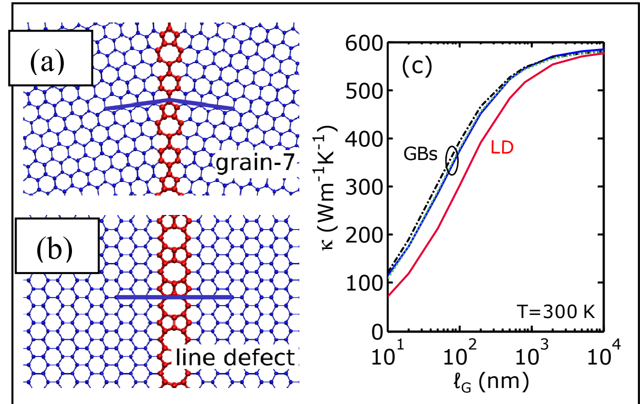

Fig. 4. (a) Schematic of grain boundary (GB) and (b) line defect (LD) in graphene. (c) Computed thermal conductivity of graphene with GBs and LDs, as a function of grain size (or average distance between defects) ℓ_G [4].

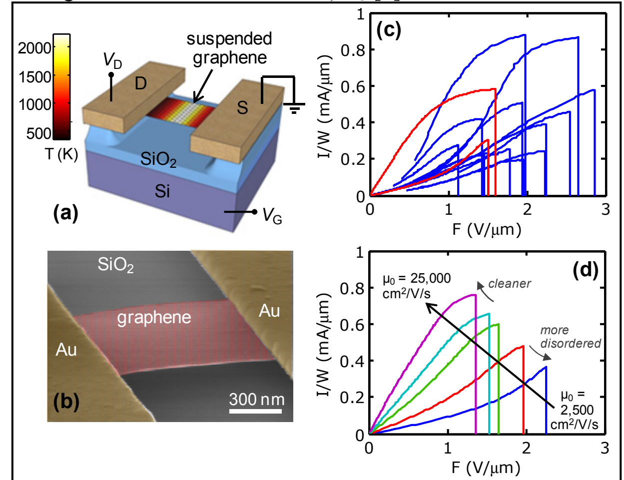

Fig. 5. (a-b) Schematic and experimental suspended graphene, the extreme case of electrical and thermal coupled transport at high field. (c) Experimental data across 15 suspended devices (red: exfoliated, blue: CVD-grown graphene). (d) Simulation of suspended devices explaining the different types of behavior seen at high-field [5].

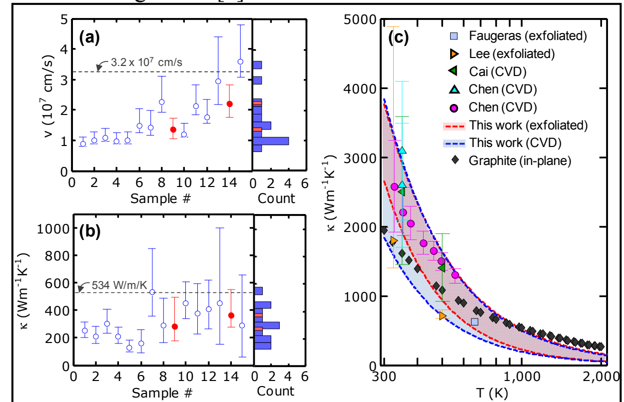

Fig. 6. Summary of *intrinsic* high-field properties of suspended graphene across 15 samples: (a) saturation velocity, (b) thermal conductivity at 1000 K, (c) thermal conductivity *k* scaling at high temperature, and comparison to previous data and to graphite [6]. Graphene *k* appears to drop more steeply at high *T* than graphite. See ref. [5] for in-depth discussion.

DFT Study of Electronic Transport Properties in Supported Armchair Graphene Nanoribbons

S. Aboud, J. Kim*, and M. V. Fischetti*
Energy Resources Engineering Department, Stanford University, Stanford, CA, USA
*Department of Materials Science, University of Texas Dallas, Richardson, TX, USA
e-mail: shela.aboud@stanford.edu

INTRODUCTION

Armchair graphene nanoribbons (AGNR) hold great promise in nano-electronics because of the capability of opening a semiconducting gap in narrow ribbons[1]. However the effective use of AGNR in devices may be limited by structural and chemical modifications from a variety of sources including the support material, edge effects, width variability, doping and defects which all change the trends in the bandgap scaling. In this work we use density functional theory (DFT)[2] simulations to investigate how structural and chemical variability in AGNRs influence electron transport through changes in the band-structure and phonon modes as a function of the type of edge functionalization (H-,H_2-,O-, and OH-) and support material (h-BN, SiO_2, and HfO_2).

EDGE FUNCTIONALIZATION AND SUPPORT MATERIALS

Theoretical calculations predict that the band gap of hydrogen-terminated ribbons of width less than ~15nm is sensitive to the number of atomic layers[3]. The oscillatory dependence of the gap on the number of atomic layers along the ribbon width is attributed to the aromaticity of the graphene: This can be understood through the spatial distribution of the Clar-resonance structures (Clar sextets[4]) that become more localized because of the formation of the edge states, as illustrated in Fig. 1. Chemical functionalization of the edges, defects at the edges and in the bulk of the ribbon modify the aromaticity of the ribbons, and therefore the bandstructure. For AGNRs terminated by single hydrogen atoms the band gap oscillates as a function of the number of carbon atoms along the ribbon width, N, as: Eg(3N+1) >Eg(3N) > Eg(3N+2), as shown in Fig. 2a. *Ab initio* thermodynamic calculation[5] can be used in conjunction with the DFT simulations to look at the stability of different functional groups on the edges as a function of temperature and partial pressure of surrounding gases. Figure 3 shows a plot the surface free energy as a function of hydrogen chemical potential. As can be seen, terminating the edge carbon atoms with two hydrogen atoms is more thermodynamically stable except at extremely low hydrogen partial pressures. The trend in the band gap scaling changes for ribbons terminated by double hydrogen atoms as: Eg(3N)>Eg(3N+2)>Eg(3N+1), as shown in Fig. 2b. Under actual environmental conditions a combination of single- and double-hydrogen terminations will exist making it difficult to see this scaling trend experimentally, consistent with what has been observed. An analysis of ribbons with various terminations, including oxygen atoms, hydroxyls, and various concentrations of single- and double-hydrogen atoms will be presented. In addition, the low field mobility and ballistic conductance in AGNRs with various surface terminations will be calculated using the Empirical Pseudopotential Method (EP)[6], benchmarked to the DFT results.

The substrate material used to support graphene-based devices can affect electronic transport significantly, often degrading the mobility[5]. In this work we consider three different substrates: h-BN, SiO_2 and HfO_2. Graphene supported by h-BN and SiO_2 (modeled as (001) α-quartz) is shown in Fig 4. Investigations of the coupling between the graphene or AGNR flexural modes and the polar modes of the substrates and its effect on the carrier mobility will be discussed.

REFERENCES

[1] See for example, A. K. Geim and K. S. Novoselov, Nature Materials, 6, 183-191 (2007)
[2] The DFT calculations are carried out with the projector augmented wave (PAW) method using VASP and QE. The exchange-correlation functions are represented with

978-3-901578-26-7 © 2013 Society for Micro- and Nanoelectronics

the PBE model of the generalized gradient approximation (GGA) and van der Waals interactions are accounted for with the DFT-D2 method of Grimme.
[3] V. Barone, O. Hod, G. E. Scuseria, Nano Lett. **6**, 2748 (2006)
[4] E. Clar, The Aromatic Sextet; Wiley: London 1972.
[5] K. Reuter and M. Scheffler, Phys. Rev. B 65, 035406 (2002); X.-G. Wang, A. Chaka, and M. Scheffler, Phys. Rev. Lett. 84 3650 (2000).
[6] M. V. Fischetti and S. Narayanan, J. Appl. Phys. **110**, 083713 (2011).

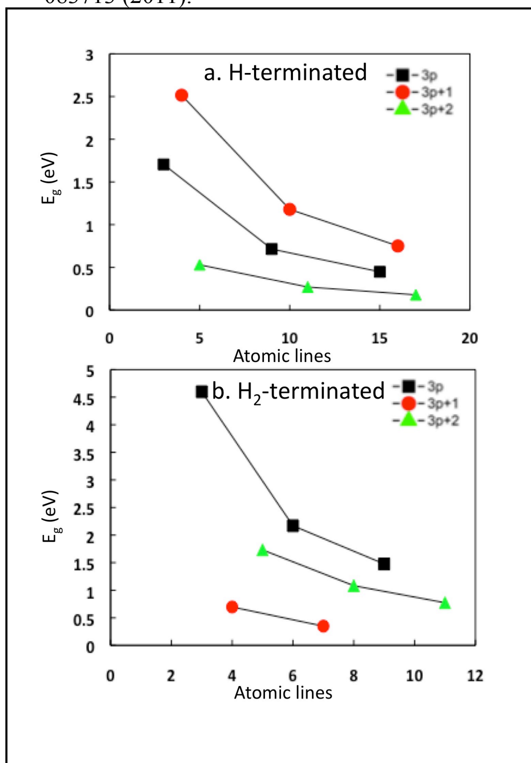

Fig. 1. Band gap of a) H-terminated and b) H2-terminated edges of AGNR as a function of the number of atoms along the ribbon width.

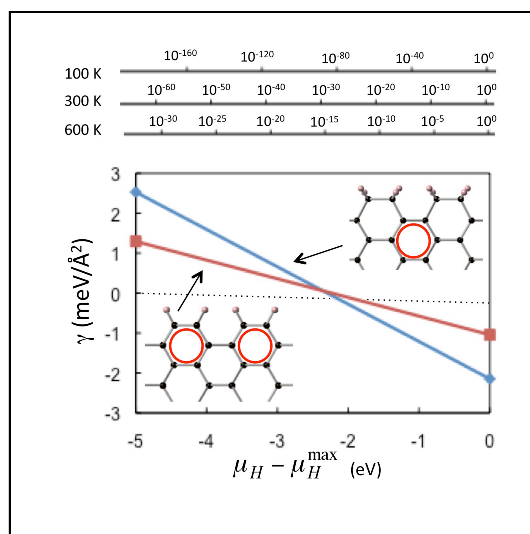

Fig. 2. Edge free energy of AGNR terminated with a single hydrogen atom (red line) and a double hydrogen atom (blue line) as a function of hydrogen chemical potential. The structure with the lower free energy is the most stable. The partial pressures of hydrogen for various temperatures are given on the top axis.

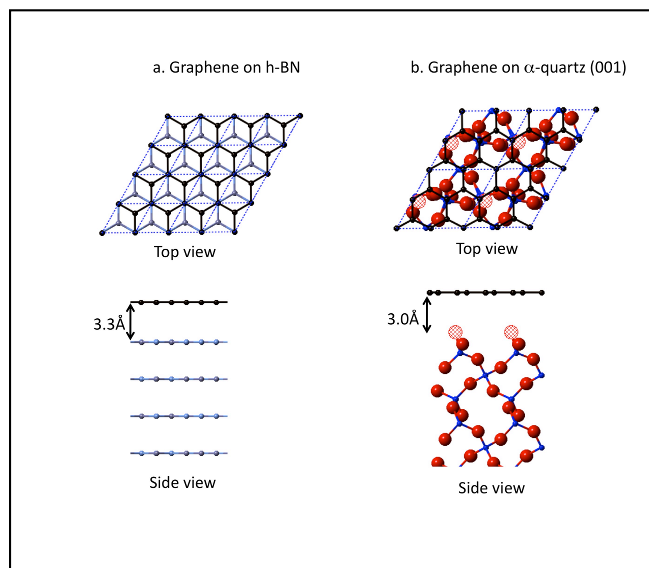

Fig. 3. Graphene supported by a) h-BN and b) α-quartz.

Electronic Transport in Graphene Nanoribbons in the Presence of Substrate Surface Corrugation

S. B. Touski*, M. Pourfath*† H. Kosina†
*School of Electrical and Computer Engineering, University of Tehran, P.O.BOX 14395-515, Tehran, Iran
†Institute for Microelectronics, Technische Universität Wien, Gußhausstraße 27–29/E360, A-1040 Wien, Austria
pourfath@iue.tuwien.ac.at

Graphene is a two-dimensional material which has attracted the attention of many scientists over the past few years. To use graphene for electronic applications it should be placed on a substrate. The surface of any substrate has always a degree of corrugation. Substrate surface corrugation affects the surface morphology which in turn modulates the electronic properties of devices placed on such substrates. In this work the role of surface corrugation parameters on the electronic properties of armchair graphene nanoribbons (AGNRs) is studied, employing the non-equilibrium green's function formalism along with a tight-binding description of the electronic bandstructure. The mean free path as functions of the geometrical and corrugation parameters is extracted and discussed.

Surface corrugation affects the bonding lengths between carbon atoms which in turn modulates the hopping parameters [1]. Pereira and co-workers used a rate of decay $dt_{ij}/dl = -6.4\text{eV}/\text{Å}$ and proposed an exponential dependence of the hopping parameter on the bonding length [2, 3]:

$$t_{ij}(l) = t_0 \exp\left[-3.37\,(l/a_{cc} - 1)\right] \qquad (1)$$

$a_{cc} = 0.142\text{nm}$ is the bonding length at equilibrium and l is the bonding length in the presence of strain or corrugation. The small bending of p_z-orbitals due to corrugation has only a weak effect. It has been shown that the effect of the hopping parameter modulation due to bonding length variation dominates that of orbital bending [4].

Surface corrugation of the substrate is a statistical phenomenon which can be modeled by a Gaussian auto-correlation function (ACF) [5, 6]:

$$R(x, y) = \delta h^2 \exp\left(-\frac{x^2}{{L_x}^2} - \frac{y^2}{{L_y}^2}\right) . \qquad (2)$$

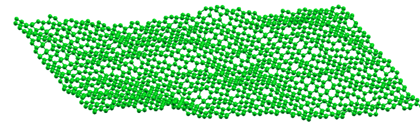

Fig. 1. 3D sketch of a corrugated AGNR.

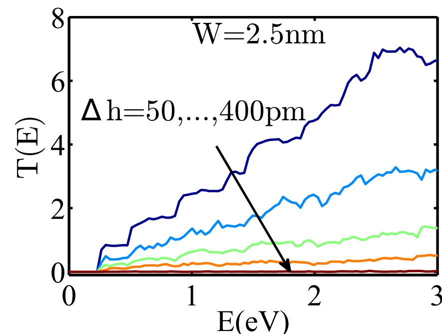

Fig. 2. The average transmission probability as a function of energy at various corrugation amplitudes. $W = 2.5\text{nm}$, $L = 100\text{nm}$, and $L_x, L_y = 25\text{nm}$.

L_x and L_y are the correlation lengths along the x and y-direction, respectively, and δh represents the root mean square of height fluctuations. To generate surface corrugation in the spatial domain (see Fig. 1) the ACF is Fourier transformed to obtain the spectral function. A random phase is applied and the achieved function is inverse Fourier transformed [7]. Using this method many devices are created for a given set of geometrical and corrugation parameters. Each sample is simulated separately followed by taking the ensemble average of the results.

The average transmission probability as a func-

978-3-901578-26-7 © 2013 Society for Micro- and Nanoelectronics

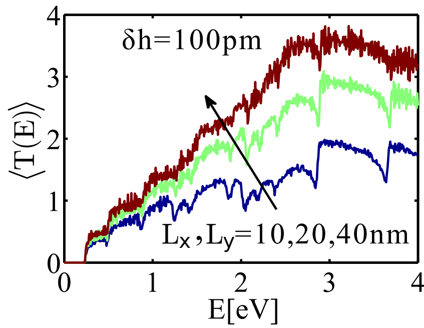

Fig. 3. The average transmission probability at various correlation lengths. $W = 2.5$nm, $L = 85$nm, and $\delta h = 50$pm.

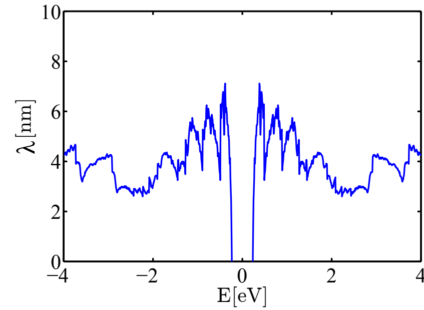

Fig. 5. The mean free path as a function of energy. $W = 2.5$nm, $L_x, L_y = 15$nm, $\delta h = 150$nm.

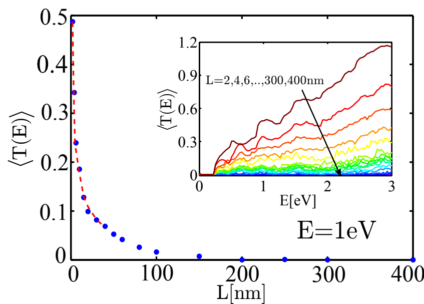

Fig. 4. The average transmission probability as function of length at $E = 1$eV. $W = 2.5$nm , $L_x, L_y = 15$nm, and $\delta h = 250$pm. The dashed-line is a fitted curve for extracting the MFP.

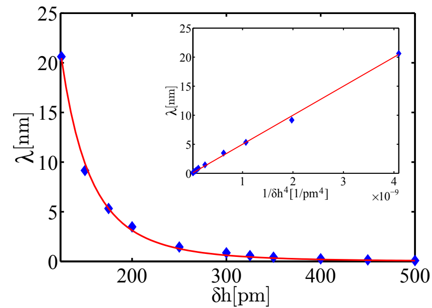

Fig. 6. The dependency of the MFP on the corrugation amplitude. The inset indicates that the MFP scales as $\lambda \propto \delta h^{-4}$. $L_x = L_y = 15$nm, $W = 5$nm.

tion of energy for different δh is shown in Fig. 2. As corrugation amplitude increases the transmission probability decreases due to an increased carrier scattering rate. On the other hand, the average transmission probability increases with the corrugation correlation length, see Fig. 3. A larger correlation length implies a smoother height variation which results in smaller bonding length modulation.

To quantify the role of surface corrugation on the electronic properties of AGNRs the mean free path (MFP) as function of the corrugation parameters can be investigated. In the diffusive transport regime the transmission is inversely proportional to the channel length:

$$T(E) = N_{\text{ch}}(E)/(1 + L/\lambda(E)) \ , \qquad (3)$$

where $\lambda(E)$ represents the MFP of carriers. To extract the MFPs at each energy a curve based on Eq. (3) is fitted to the average transmission probability as a function of the channel length (Fig. 4) and the respective MFP at that particular energy is numerically extracted (Fig. 5). The MFP as a function of energy for $\delta h = 150$pm is shown in Fig. 6. The results indicate that the MFP scales as $\lambda \propto \delta h^{-4}$ with the corrugation amplitude.

Depending on the material type and cleaning process, typical values the corrugation amplitude are $168 - 360$pm, 75pm, and 24pm for SiO_2, Boron-Nitride, and Mica, respectively [6, 8]. Although smooth surfaces of Boron-Nitride and Mica substrates are better suited for graphene based devices, SiO_2 is more widely used in microelectronics. Therefore, the analysis of graphene based devices on SiO_2 substrates requires a careful study of the role of substrate corrugation on the electronic transport.

REFERENCES

[1] S. Koenig *et al.*, Nature Nanotech. **6**, 543 (2011).
[2] V. M. Pereira *et al.*, Phys. Rev. B **80**, 045401 (2009).
[3] A. H. Castro Neto *et al.*, Phys. Rev. B **75**, 045404 (2007).
[4] J. W. Klos *et al.*, Phys. Rev. B **80**, 245432 (2009).
[5] M. Ishigami *et al.*, Nano Lett. **7**, 1643 (2007).
[6] C. H. Lui *et al.*, Nature **462**, 339 (2009).
[7] A. Yazdanpanah *et al.*, IEEE Trans. on Electron Devices **59**, 433 (2012).
[8] C. Dean *et al.*, Nature Nanotech. **5**, 722 (2010).

Ab-initio study of edge defects in Graphene Nanoribbon

M. Manoharan[1] and Hiroshi Mizuta[1, 2]
[1]School of Materials Science, Japan Advanced Institute of Science and Technology, Japan.
[2]School of Electronic and Computer Science, University of Southampton, U.K.
e-mail: mano@jaist.ac.jp

Introduction

Graphene is studied widely for its potential applications of nanoscale electronic/photonic/ spintronic devices [1]. All the superior properties of graphene encourage us to downscale graphene devices. Unnecessarily, edge irregularities/defects are created in the geometrically constricted regions during electron/ion beam exposure in the device fabrication process. These defects strongly affect the electronic properties of the device and consequently its transport characteristics are also affected.

Model and Calculation method

The GNR channel sandwiched between semi-infinite graphene electrodes (shown in Fig. 1) was used for the quantum transport calculations. The electronic states were calculated by using the density functional theory (DFT). The quantum transport was calculated by using the non-equilibrium Green's function (NEGF) method which is implemented in the OpenMX package [2]. The edges of the GNR and the horizontal edges of the electrodes are terminated by hydrogen atoms.

Results and Discussion

At first one single vacancy defect is created in the GNR channel as shown in Fig. 2. This structure was geometrically optimized to realize the stable structure. After the geometrical optimization, the defect region is rearranged to the structure shown in Fig. 3. Carbon atoms in the defected region self-organized to form dangling bond-less structure, which is inherent property of the graphene.

To study the electronics and transmission properties of the geometrically optimized single vacancy defect channel, Density of States (DOS) calculation and transmission analysis was done. Fig. 4 and Fig. 5 show the DOS and the transmission spectrum of the GNR device with geometrically optimized channel, respectively. From the DOS plot inception of mid-gap states near the fermi-energy level can be clearly noticed. By comparing the DOS and transmission spectrum plots, it can be clearly understood that mid-gap states are not contributing to transmission of electrons across the electrodes. Moreover, the values of transmission coefficients are lower compared to the pristine GNR channel at a given energy (Fig. 6). This is due to scattering introduced by edge irregularities. Even though there is no dangling bond present in the channel, the self-assembled defect region leads to scattering of the electrons. This indicates that edge irregularities play a very important role in the carrier transport.

To study the impact of increase in the number of defects at the edge, we have simulated one, two, and three defects channel. Its transmission spectra are given in Fig. 6. From this result, we can clearly see the increase in the scattering with the increase in the defects. On the positive side, the widening of the transport bandgap can be clearly notice from this result. This helps us to realize wider bandgap in the Graphene. In the conference, results of zigzag GNR will also be presented.

References

[1] Geim, A. K. & Novoselov, K. S. The rise of graphene. Nature Mater. 6, 183–191 (2007).
[2] http://www.openmx-square.org/

978-3-901578-26-7 © 2013 Society for Micro- and Nanoelectronics

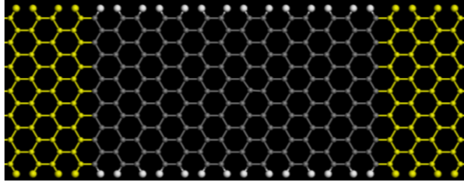

Fig. 1. Structure of the GNR channel sandwiched between semi-infinite graphene left and right electrodes (yellow coloured atoms).

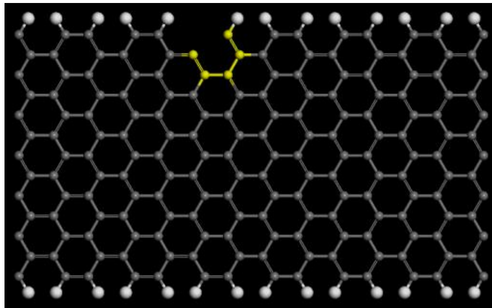

Fig. 2. GNR channel with single edge defect. The yellow bonds indicate the region of defect.

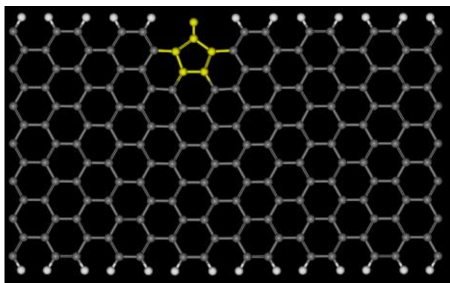

Fig. 3. Rearranged Single edge defect of the GNR channel after the geometrical optimization of the channel region.

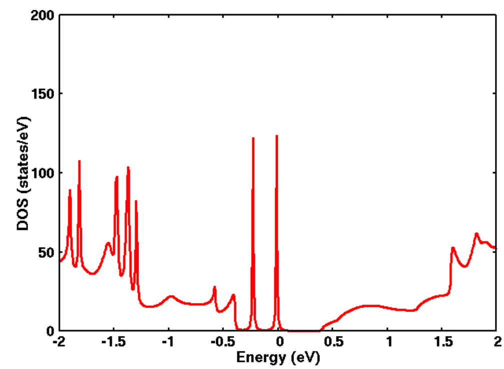

Fig. 4. Density of states of the geometrically optimized single edge defected GNR channel.

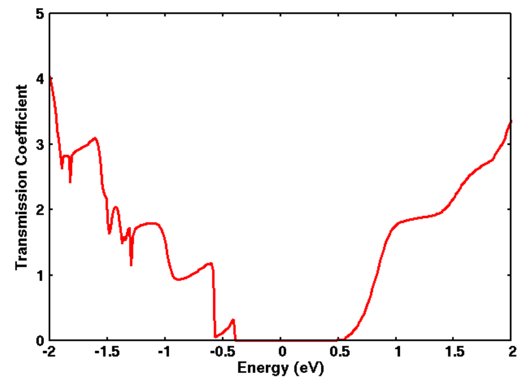

Fig. 5. Transmission spectrum of the geometrically optimized single edge defected GNR channel.

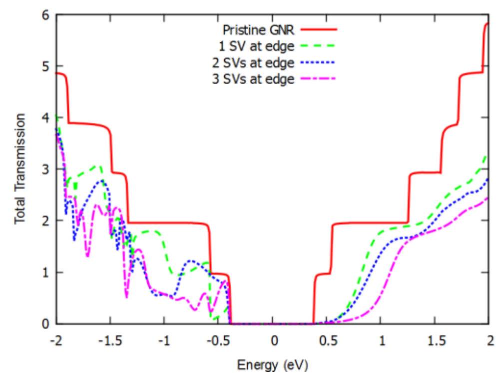

Fig. 6. Transmission spectra of the pristine GNR, and the GNR device with one, two, and three edge defects.

Electron transport characteristics of graphene-metal interfaces

V. Nam Do[1], H. Anh Le[1], and P. Dollfus[2]
[1] Advanced Institute for Science and Technology, Hanoi Univ. of Science and Technology, Vietnam
[2] Institute of Fundametal Electronics, CNRS, Univ. of Paris-Sud, Orsay, France
e-mail: vannam.do@gmail.com

Abstract

Due to extraordinary properties graphene is expected to become a material of choice for future applications in electronics. However, it has been shown that the interface with metal leads, the indispensable part of any graphene-based device, plays a crucial role in the transport of charges in the whole nanostructure [1-7]. Under-standing the phenomena induced by these interfaces may have therefore many technological implications. To tackle this problem from the theoretical point of view, it is mandatory to clarify two issues: (i) the electronic structure of graphene-metal (G-M) complexes at their interfaces, and (ii) the transfer of charges between metal leads and graphene.

To investigate the issue (i), we have used a first-principles approach for five typical G-M complexes, namely G-Cu, G-Au, G-Pt, G-Pd and G-Ti, i.e., for both noble and transition metals. We have used the VASP4.6 package which is based on the projector augmented-wave pseudo-potentials within the general gradient approximation. The resulting electronic structures are shown in Fig. 1. The results show the different effects of metals on the electronic structure of graphene. Metals as Cu and Au just cause slight changes in the electronic structure of graphene and preserve the Dirac cones at the K points. In contrast, in the case of d-bands metal as Pt, Pd and Ti, the graphene electronic structure shares many features with the metal and around the Fermi level we no longer see the typical form of the π-bands of graphene. These results are consistent with the available data obtained by different research groups [8-10].

Regarding the transport issue (ii), the ab initio approach may still be used to explore the transfer characteristics of the G-M interfaces by calculating physical quantities as the conductivity and/or the contact resistivity. However, we have considered a simplified description of sp-bands and d-bands fitted on first principles-ones, which allows us to study separately the contribution of these bands to the charge transfer through the G-M interface at low computational cost. Our approach, though simple, gives a clear picture of the charge transfer.

We have estimated the intrinsic values of the G-M contact resistivity by exploring the transport in M-G-M structures. Fig. 2 shows the three typical forms of the I-V curves for the five structures. We observe either a negative differential conductance (NDC) for Cu and Au, a positive differential conductance (PDC) for Pt and Pd, or a linear behavior for Ti. Combining these results with the analysis of the band structures leads us to conclude that in the former case (Cu, Au), the Fermi level is far from the d-band edge, the transport is governed by s electrons, which induces an NDC behavior. In contrast, for the G-Ti complex, the Fermi level stays in the middle of the dense d-band and the linear I-V form is understood as that of the regime of wideband limit. Finally, the PDC behavior of the Pt-G-Pt and Pd-G-Pd complexes is attributed to the fact that both the s- and d-electrons contribute to the current but not simultaneously.

References

[1] P. Blake, et al., Solid State Commun. **149**, 1068 (2009).
[2] K. Nagashio, T. Nishimura, K. Kita, and A. Toriumi, Appl. Phys. Lett. **97**, 143514 (2010).
[3] F. Xia, V. Perebeinos, Y.-M. Lin, Y. Wu, and P. Avouris, Nat. Nanotechnol. **6**, 179 (2011).
[4] R. Nouchi, T. Saito, and K. Tanigaki, J. Appl. Phys. **111**, 084314 (2012).
[5] J. A. Robinson, et al., Appl. Phys. Lett. **98**, 053103 (2011).
[6] J. Maassen, W. Ji, and H. Guo, Appl. Phys. Lett. **97**, 142105 (2010); Nano Lett. **11**, 151 (2011).
[7] S. Barraza-Lopez, M. Vanevic, M. Kindermann, and M. Y. Chou, Phys. Rev. Lett. **104**, 076807 (2010).
[8] G. Giovannetti, et al., Phys. Rev. Lett. **101**, 026803 (2008).
[9] Q. Ran, M. Gao, X. Guan, Y. Wang, and Z. Yu, Appl. Phys. Lett. **94**, 103511 (2009).
[10] C. Gong, G. Lee, B. Shan, E. M. Vogel, R. M. Wallace, and K. Cho, J. Appl. Phys. **108**, 123711 (2010).

978-3-901578-26-7 © 2013 Society for Micro- and Nanoelectronics

Fig.1. Electronic structure of graphene and of five G-M complexes, i.e. G-Cu, G-Au, G-Pt, G-Pd and G-Ti. The square black symbols guide the eyes to the typical π-bands of graphene formed by the hybridization of carbon pz-orbitals.

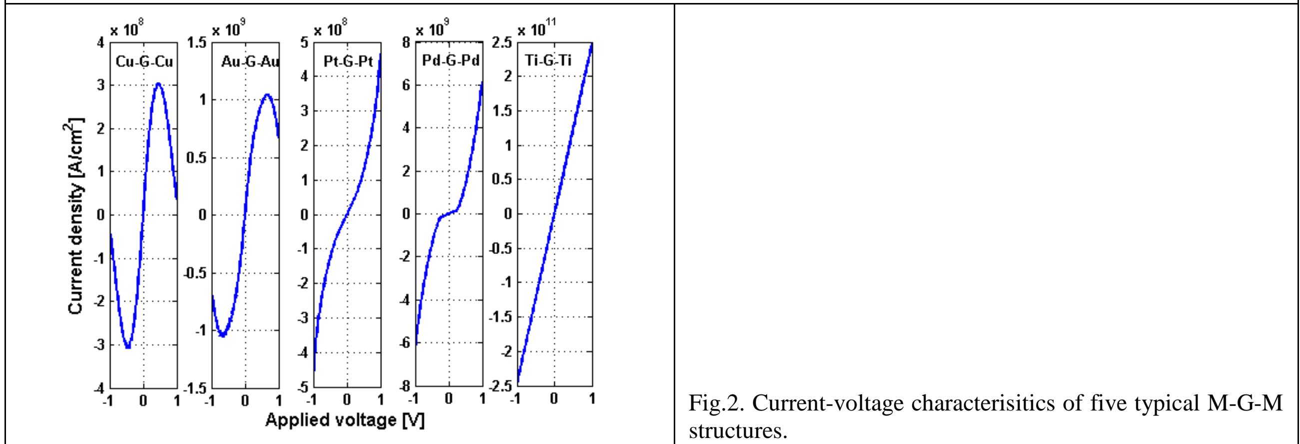

Fig.2. Current-voltage characterisitics of five typical M-G-M structures.

Tight-Binding Modeling of Intermediate Valence Compound SmSe for Piezoelectronic Devices

Zhengping Jiang, Marcelo A. Kuroda[*], Yaohua Tan, Dennis M. Newns[*], Glenn J. Martyna[*], Michael Povolotskyi, Timothy B. Boykin[†], Tillmann Kubis, Gerhard Klimeck
School of Electrical and Computer Engineering, Purdue University, West Lafayette, IN, 47906, USA
[*]Physical Sciences, IBM TJ Watson Research Center, Yorktown Heights, NY, 10520, USA
[†]Department of Electrical and Computer Engineering, The University of Alabama in Huntsville, Huntsville, Alabama 35899, USA
e-mail: jiang32@purdue.edu

Introduction

Scaling of MOSFET physical dimensions has enabled exponential growth of the total transistor number in a single chip. Today heat dissipation issues prevent any performance increases through clock frequency increases, since the supply voltage cannot be lowered. These fundamental power consumption issues have spurred the exploration of alternative switching mechanisms[1].

The Piezoelectronic Transistor (PET) has been proposed as a post-CMOS device for fast, low power switching[2, 3]. In this device the piezoresistive channel is filled with carriers through pressure induced via the expansion of a piezoelectric element. The mixed-valence compound SmSe is a good choice of PET channel material because of its pressure-induced Metal Insulator Transition (MIT). Performance prediction and optimization of a realistic, nano-scaled PET based on SmSe requires the understanding of quantum confinement, tunneling, and metal interface effects. To achieve this, a computationally efficient empirical tight binding (ETB) model is necessary. In this work, TB parameters are developed for SmSe and used in quantum transport simulations to explore the atomistic nature of material properties and the scaling limit of PET channel lengths.

Methods

Our parameterization of ETB features a basis transformation from DFT e.g. plane wave representation to an orthogonal TB basis i.e. Löwdin orbitals[4] and subsequent refinement by numerical optimization. First principle calculations within generalized gradient approximation with spin-orbit coupling and Hubbard-like, localized potential (GGA+SO+U) are performed with ELK [5]. Wavefunctions and bandstructure at the minimum-energy lattice constant are obtained. The DFT Hamiltonian is then constructed and transformed to the TB Hamiltonian[6]. Values of onsite energy and two center integrals for the TB basis are extracted following Slater and Koster notations[4]. Parameters are then refined with the simplex algorithm. Effects of strain are accounted for by additional parameters representing bond bending and stretching[7]. DFT bandstructures under hydrostatic strain are used as fitting targets. NEGF is employed to study the ballistic transport in SmSe with NEMO5 [8]. Currents are evaluated for different strains in a 6nm SmSe channel.

Discussion

The TB model is determined based on the analysis of a decomposition of DFT DOS into atom species and orbitals (Fig.1a-c). The TB model with second nearest neighbor coupling is implemented with *spdfs*[*] orbitals. Spin-orbit (SO) coupling for *p,d and f* orbitals are included for both atoms. The *4f* band splitting, which is included in DFT as Hubbard-type *U* has been considered in our model through *4f* SO coupling. In the energy range relevant to transport, the band dispersion is accurately reproduced as shown in Fig.1d. Detailed analysis shows that conduction band minimum energy and dispersion at the band minimum are mainly affected by second nearest neighbor Sm-Sm coupling of *d*-orbitals.

The MIT in SmSe is believed to originate from the bandgap reduction under pressure. Fig.2a shows the extracted indirect bandgap for SmSe under hydrostatic strain and uniaxial strain along

978-3-901578-26-7 © 2013 Society for Micro- and Nanoelectronics

the (100) direction. Although the TB parameters are fitted to bandstructure under hydrostatic strain, the good match obtained for uniaxial strain without modification of the parameters confirms good transferability of the TB parameters.

Figure 3a demonstrates the simulation domain in form of a thin film. The equilibrium Fermi level position is determined self-consistently (Fig.3a) and a 0.05V bias is applied in the drain contact. A ballistic current calculation shows that modulation of the resistance by 3 orders of magnitude is achieved by hydrostatic strain of 3% (Fig.3d). In the Hubbard model the *f*-electrons are supposed to be highly localized[9]. However, both DFT and TB bandstructure show a small effective mass at the top of valence band at Γ (Fig.1d) which gives rise to hole currents and increases the conductance (Fig.3d). The band width of *f*-band is found to be controlled by the nearest neighbor *p*-*f* coupling between Se and Sm atoms.

ACKNOWLEDGEMENT

nanoHUB.org computational resources operated by the Network for Computational Nanotechnology funded by NSF under EEC-0228390 are utilized in this work. The research was funded by IBM PhD fellowship.

REFERENCES

[1] T. N. Theis and P. M. Solomon, *Science*, vol. 327, pp. 1600-1601, 2010.
[2] D. M. Newns, *et al.*, *Advanced Materials,* 2012.
[3] D. M. Newns, *et al.*, *MRS Bulletin,* vol. 37, pp. 1071-1076, 2012.
[4] J. C. Slater and G. Koster, *Physical Review,* vol. 94, p. 1498, 1954.
[5] http://elk.sourceforge.net/.
[6] Y. Tan, *et al.*, *arXiv preprint arXiv:1210.8215,* 2012.
[7] T. B. Boykin, *et al.*, *Physical Review B,* vol. 66, 2002.
[8] S. Steiger, M. Povolotskyi, H-H. Park, T. Kubis, G. Klimeck, *IEEE Trans on nano,* vol. 10, 2011.
[9] G. Kotliar and D. Vollhardt, *Physics Today,* vol. 57, pp. 53-60, 2004.

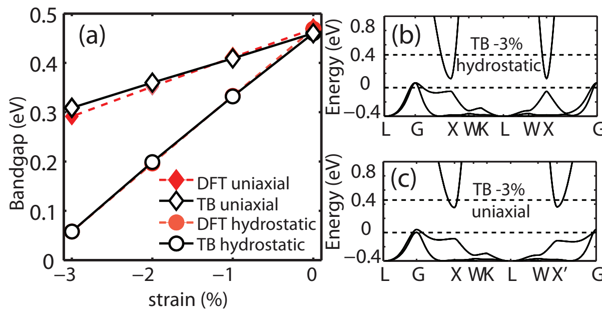

Fig. 2. Comparison of band gap modulations with strain calculated by DFT and TB. (a) Band gap extracted from DFT and TB band structure under hydrostatic and uniaxial strain. (b) TB band structure with 3% compressive hydrostatic strain in each direction. (c) TB band structure with 3% compressive uniaxial strain in growth direction. Dashed lines show bulk band edges in (b, c).

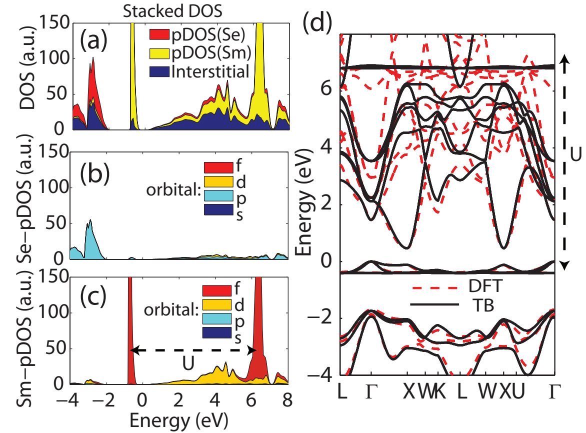

Fig. 1. Stacked DFT DOS and DFT/TB bandstructure comparison. (a) DOS within muffin-tin radius of Sm/Se and interstitial DOS. (b) DOS within Se atom decomposed by angular momentum. (c) DOS within Sm atom decomposed by angular momentum. (d) Band structure by *spdfs**+SO TB model without strain (black) and DFT band structure without strain (red). E=0 at top of valence

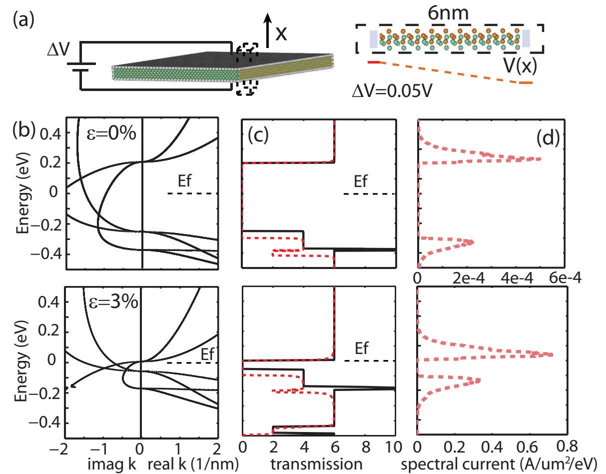

Fig. 3. Transport simulation for SmSe with hydrostatic strain. (a) Device configuration and supercell of simulation domain. (b) Real and imaginary band structure for 0% and 3% hydrostatic strain. (c) Transmission with 0V and 0.05V linear drop potential. (d) Vd=0.05V, spectral current with linear drop potential.

Non-equilibrium Low-Energy Transport Physics of Electron and Phonon at Nanoscale

Y. Asai
Nanosystem Research Institute (NRI) "RICS,"
National Institute of Advanced Industrial Science and Technology (AIST),
Umezono 1-1-1, Tsukuba Central 2, Tsukuba, Ibaraki 305-8568, Japan
e-mail: yo-asai@aist.go.jp

INTRODUCTION

Because electronic devices become smaller than before they were, first principle based non-equilibrium transport theory becomes applicable to some of the important devices in nanoelectronics nowadays. One of the examples is the resistive random access memories (ReRAMs) whose device length scale becomes smaller than 10 nano meter (nm) [1]. First principle transport theory, however, has some intrinsic limitations. Because it is based on a ballistic transport theory, it cannot take into account of scattering effects, heating effects, heat dissipation effects and the hopping conduction processes. All of these, however, have been a matter of intense investigations among condensed matter physics theorists. A theory describing all of these has been developed recently. In this talk of 16th IWCE, I will describe the present status of the theory in this respect.

THEORY

Because paramagnetic electronic correlation effect is mostly elastic, the largest contribution to the heating effects may come from electron-phonon interactions. [2] The interaction effects on electric current I are described by the following equation:

$$I = \frac{2e}{h}\int Tr[\Sigma_L^{>}(E)G_R^{<}(E) - \Sigma_L^{<}(E)G_R^{>}(E)]dE + \frac{2e}{h}\int Tr\left[\Sigma_L^{>}(E)G_{eph}^{<}(E) - \Sigma_L^{<}(E)G_{eph}^{>}(E)\right]dE$$

where $G_{eph}^{<(>)}(E) = G^R(E)\Sigma_{eph}^{<(>)}(E)G^A(E)$ and $G_R^{<(>)}(E) = G^R(E)\Sigma_R^{<(>)}(E)G^A(E)$. $\Sigma_{eph}^{<(>)}$ is the Keldysh component of the electron-phonon self-energy, which may be obtained by using the self-consistent Born approximation (SCBA) for example. $\Sigma_R^{<(>)}$ is the contact self-energy of the right terminal which is obtained by using surface electron Green's function of the right electrode terminal and the thermal equilibrium boundary condition. Electrode terminals are supposed to be thermalized and all the heat generetated by the electron-phonon interaction is supposed to be dissipated there. In order to take into account of the heat dissipation effect on the curret I, we take into account of phonon current as well as electron current whose schemes werer discussed in the reference [3].

APPLICATIONS

The theory [3] has been tested in some cases of single molecular junctions which are made of a single molecule and two bulk electrodes. Break junction techniques are applied to them and statistical analyses of the resulting data are made. Acurate experimental results comparable with the theory are thus obtained. The local heating effect [4,5], the cross over temperature dependence of the conductance describing both the tunneling and the hopping regions [6] and the zero bias anomaly (ZBA) of electric conductance [7] have been discussed. Good agreements between the theoretical and experimental results affirm the validity of the theory to describe low-energy

978-3-901578-26-7 © 2013 Society for Micro- and Nanoelectronics

transport physics and thermal physics of electron and phonon. [5-9]

RESULTS

The local heating effect result and the ZBA result are summarized in Figs. 1 and 2, respectively. As we apply the bias voltage V, the effective temperature T_{eff} defined in terms of the break junction life time [5,8,9] increases with small deviation from the estimate obtained by using bulk phonon theory, i.e., $T_{eff}^4 \propto V^2$. The deviation may come from the constriction effect on phonon current. In Fig.2, the ZBA behavior emerging in the inelastic tunneling spectrum (IETS: d^2I/dV^2 vs V spectrum) is shown. While the growth of peak and dip structures at positive and negative values on the voltage axis whose absolute value correspond to phonon energy is the well-known feature of the IETS, the growth of a structure close to $V=0$ is quite anomalous. This zero bias anomaly has been observed experimentally. Our theoretical results indicate that the ZBA comes from rattling motion of the molecule in the gap between the two electrodes. Our theory is capable to describe the low energy transport physics of our junction.

CONCLUSION

By including phonon transport as well as electron transport, our theory treating electron-phonon interaction within the SCBA can describe low energy transport physics and thermal physics problems including heat dissipation into the thermalized electrodes. Our theory should be very useful when it is applied to nanoelectronics problems.

REFERENCES

[1] T. Miyazaki, H. Nakamura, K. Nishio, H. Shima, H. Akinaga, and Y. Asai, unpublished results.

[2] Y. Asai, *Theory of inelastic electric current through single molecule*, **Phys. Rev. Lett**. 93, 246102-1-4 (2004).

[3] Y. Asai, *Nonequilibrium phonon effects on transport properties through atomic and molecular bridge junctions*, **Phys. Rev. B** 78, 045434-1-24 (2008).

[4] Y. Asai, H. Nakamura, J. Hihath, C. Bruot, and N.J. Tao, *Electron correlation enhancement of the diode property of asymmetric molecules*, **Phys. Rev. B** 84, 115436-1-5 (2011).

[5] Y. Asai, *Theory of local heating in single molecular bridge junctions*, **Phys. Rev. B**, 84, 085436-1-7 (2011).

[6] S. –K. Lee, R. Yamada, S. Tanaka, G. –S. Chang, Y. Asai, and H. Tada, *Universal Temperature Crossover Behavior of Electrical Conductance in a Single Oligothiophene Molecular Wire,* **ACS Nano**, 6, 5078-5082 (2012).

[7] Y. Asai, *Theory of zero-bias anomaly in low-temperature inelastic tunneling spectroscopy*, **Phys. Rev. B** 86, 201405(R)-1-4 (2012): Rapid Communications.

[8] Z. Huang, B. Xu, Y. Chen, M. Di Ventra, and N.J. Tao, *Measurement of Current-Induced Local Heating in a Single Molecule Junction*, **Nano Lett**. 6, 1240 (2006).

[9] Z. Huang, F. Chen, R. D'Agosta, P. A. Bennett, M. Di Ventra, and N.J. Tao, *Local ionic and electron heating in single-molecule junctions*, **Nature Nanotech**. 2, 698 (2007).

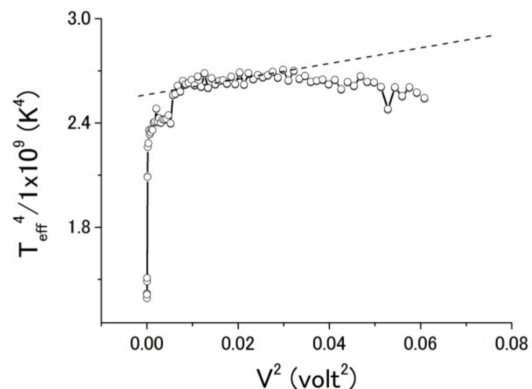

Fig. 1. The voltage dependence of the effective temperature T_{eff} estimated from the junction lifetime. The result agrees with experimental results qualitatively.

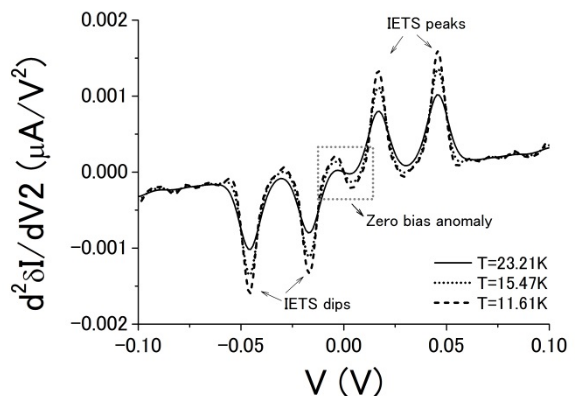

Fig. 2. The zero bias anomaly found in the IETS. The similar anomaly has been found experimentally.

Tight-binding Simulations of Channel Modulation in a Single Atom Transistor

Hoon Ryu*‡‖, Sunhee Lee†‡, Yui-Hong Matthias Tan‡, Martin Füchsle§, Jill A. Miwa§, Suddhasatta Mahapatra§, Michelle Y. Simmons§, Lloyd C. L. Hollenberg¶, and Gerhard Klimeck‡
*Korea Institute of Science and Technology Information, Daejeon 305-806, Republic of Korea
†Samsung Advanced Institute of Technology, Yongin, Gyeonggi-do 446-712, Republic of Korea
‡Network for Computational Nanotechnology, Purdue University, West Lafayette, IN 47907, USA
§Centre for Quantum Computer Technology, University of New South Wales, Sydney, NSW 2052, Australia
¶Centre for Quantum Computer Technology, University of Melbourne, Parkville, VIC 3010, Australia
‖e-mail: elec1020@gmail.com

Introduction

There has been remarkable progress in the use of a scanning tunneling microscope to pattern various highly phosphorus δ-doped Si (Si:P) devices [1], [2], [3]. The physical realization of a single atom transistor [3], is especially a quite remarkable achievement since it represents the ultimate limit of device downscaling. In this work, we not only perform the first tight-binding study of the gate-bias dependent shift of the electron ground state (1s(A)) in the single-atom channel, but also demonstrate strong connections between the modeling and the experiment confirming the demonstrated device is indeed a single atom transistor.

Modeling Approach

Based on the gate-bias dependent channel potential profiles that are obtained via the Thomas-Fermi approach [4], the energy-level quantizations formed by a single phosphorous atom in Si bulk are calculated with a 3-D Nanoelectronics MOdeling Tool for Petascale simulations (NEMO 3-D PETA), where the channel electronic structure is described with a $sp^3d^5s^*$ tight-binding model [5], [6]. Fig. 1(a) illustrates the simulation domain, where we only considered the gate modulation of the channel assuming the source and drain are grounded.

Result and Discussion

The equilibrium potential profile is shown in Fig. 1(b), where the 2-D surface plot on the doping plane as well as the 1-D plots along various line-cuts are presented. The phosphorous ions in highly δ-doped (1/4ML) nanowires that act as leads, pull down the conduction subbands into Si band gap creating a potential barrier over the low doped ($\sim 10^{15}/cm^3$) P-type Si channel. Strong electron confinement is created by a phosphorous atom in the channel.

Gate-bias dependent channel potential profiles are shown in Fig. 2 with energetic positions of 1s(A) state and Fermi-level. Higher gate bias reduces the channel barrier height and the energy level of 1s(A) state such that 1s(A) state meets the Fermi-level filling the first electron into the channel at the gate bias of 0.45V. Further increase of gate bias shifts up the channel potential and the 1s(A) state due to electron screening of the channel phosphorous ion. At the gate bias of 0.72V, the 1s(A) state again hits the Fermi-level filling the second electron. Fermi-level doesn't change since we assumed a zero source-drain bias for all the simulations.

The pattern of the channel modulation is summarized well in Fig. 3, which provides three strong connections to the experimental result reported in Ref. [3]. First, we obtain the energy needed to fill the first electron into the channel as 46.3 meV that is on top of the measured value. Second, the two gate-biasing points that fill a new electron into the channel, happen at Vg = 0.45 and 0.72V, where the experiment locates these *vertex points* at Vg = 0.45 (almost same) and 0.8V (10% inaccuracy). The third connection can be found from the slope of lines - the gate controllability over the 1s(A) state that is obtained as 0.15 where the experiment shows 0.12.

978-3-901578-26-7 © 2013 Society for Micro- and Nanoelectronics

Conclusion

Channel modulation in the physically realized single atom transistor (Ref. [3]) is simulated with a tight-binding approach. Results are discussed focusing on connections to the experiment that are strong enough to confirm that the device contains exactly a single phosphorous atom in the channel.

References

[1] A. Fuhrer *et al.*, Nano Lett. **9**, 707 (2009).
[2] B. Weber *et al.*, Science **335**, 64 (2012).
[3] M. Füchsle *et al.*, Nature Nanotech. **7**, 242 (2012).
[4] K. A. Chao, Phys. Rev. B **26**, 3463 (1982).
[5] G. Klimeck *et al.*, IEEE TED. **54**, 2079 (2007).
[6] S. Lee *et al.*, Phys. Rev. B **84**, 205309 (2011).

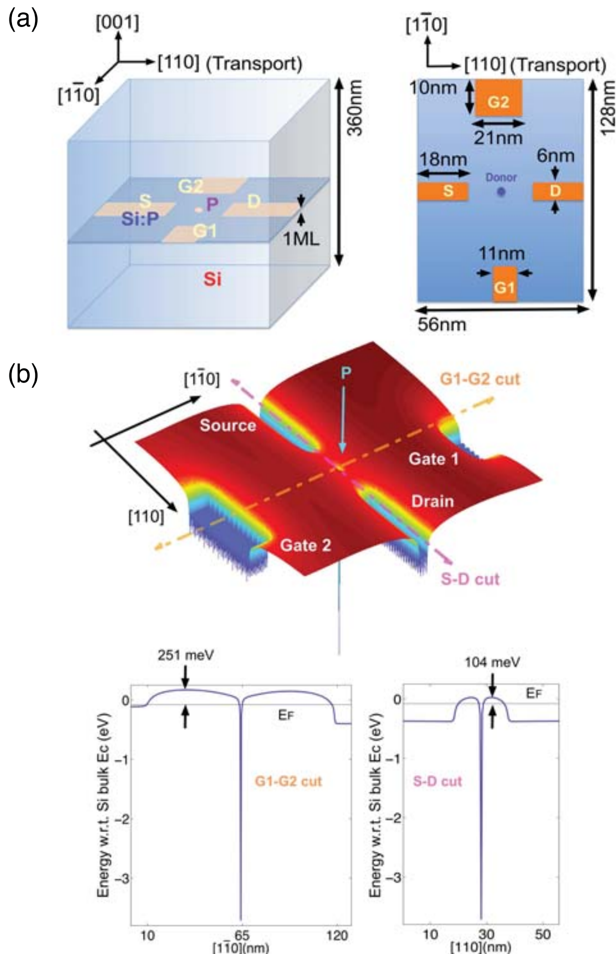

Fig. 1. (a) Simulation domain: (Left) a 3-D View (Right) a 2-D View onto the doping plane. (b) Potential profile at equilibrium on the doping plane. Densely δ-doped Si:P nanowires form leads and a single phosphorous atom creates a strong electron confinement in the channel. A zero energy references to the conduction band minimum of intrinsic Si bulk.

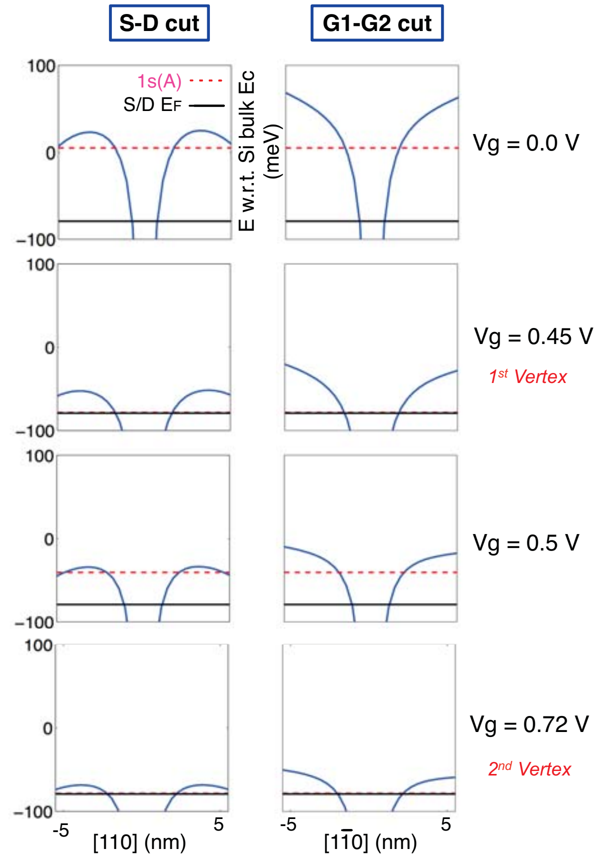

Fig. 2. Bias-dependent channel potential profile and 1s(A) state: The energetic level of electron ground state decreases with increasing gate bias such that source-drain Fermi-level meets the 1s(A) state at Vg=0.45V filling one electron in the channel. At larger gate bias, the 1s(A) state shifts up due to the electron screening over the channel phosphorous ion and decreases again filling the second electron at Vg=0.72V.

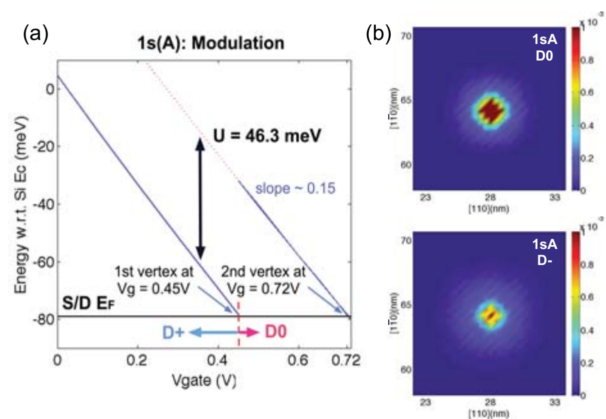

Fig. 3. (a) Gate modulation of 1s(A) state. Charging energy, lever-arm of gate bias, and the position of two vertex points (@Vg=0.45, 0.72V) demonstrate strong connections to experiment (Ref. [3]). (b) Electron wave functions at two vertex points showing a strong confinement even at the second vertex.

An Approach to Quantum Transport Based on Reduced Hierarchy Equations of Motion

Yoshitaka Tanimura and Atsunori Sakurai
Department of Chemistry, Graduate School of Science, Kyoto University, Kyoto 606-8502, Japan
e-mail: tanimura@kuchem.kyoto-u.ac.jp

The quantum dissipative dynamics of a tunneling process through double barrier structures is investigated on the basis of a rigorous treatment for the first time. We employ a Caldeira-Leggett Hamiltonian

$$\hat{H} = \frac{\hat{p}^2}{2m} + U(q;t) + \sum_j \left[\frac{\hat{p}_j^2}{2m_j} + \frac{1}{2} m_j \omega_j^2 \left(\hat{x}_j - \frac{c_j \hat{q}}{m_j \omega_j^2} \right)^2 \right]$$

with an effective potential calculated self-consistently, accounting for the electron distribution. The heat bath can be characterized by the spectral distribution function, defined by $J(\omega) = m\zeta\gamma^2\omega / \pi(\gamma^2 + \omega^2)$,where γ is the reciprocal of the correlation time of the noise induced by phonons and ζ is the electron-phonon coupling strengt. With this Hamiltonian, we employ reduced hierarchy equations of motion (HEOM) approach, which can deal with non-Markovian and non-perturbative system-bath interactions at finite temperature $\beta = 1/kT$ without approximation [1,2]. In the Wigner form the HEOM is expressed as [2-4]

$$\dot{W}^{(n)}_{j_1,\cdots,j_K}(t) = -\left[\hat{L} + \hat{\Xi}' + n\gamma + \sum_{k=1}^{K} j_k \nu_k \right] W^{(n)}_{j_1,\cdots,j_K}(t)$$
$$+ \frac{\partial}{\partial p} \left[W^{(n+1)}_{j_1,\cdots,j_K}(t) + \sum_{k=1}^{K} W^{(n)}_{j_1,\cdots,(j_k+1),\cdots j_K}(t) \right]$$
$$+ n\gamma \hat{\Theta}_0 W^{(n-1)}_{j_1,\cdots,j_K}(t) + \sum_{k=1}^{K} j_k \nu_k \hat{\Theta}_k W^{(n)}_{j_1,\cdots,(j_k-1),\cdots j_K}(t)$$

In the HEOM, the reduced density operator is expressed in the auxiliary hierarchy density matrix elements $W^{(n)}_{j_1,\cdots,j_K}$ with the cutoff $n + \sum_{k=1}^{K} j_k \gg \omega_c / \min(\gamma, 1/\beta\hbar)$, where the index n and j_k arises from the hierarchal expansion of noise correlation time and the kth Matsubara frequency $\nu_k \equiv 2\pi k / \beta\hbar$ and $-\hat{L}$ is quantum Liouvillian (time scale $\approx 1/\omega_c$). Other operatorswith ($c_k \equiv 2\gamma^2 / (\nu_k^2 - \gamma^2)$) are

$$\hat{\Xi}' = -\frac{m\zeta}{\beta} \left[1 - \frac{\beta\hbar\gamma}{2} \cot\left(\frac{\beta\hbar\gamma}{2} \right) - \sum_{k=1}^{K} c_k \right] \frac{\partial^2}{\partial p^2},$$
$$\hat{\Theta}_0 = \zeta \left[p + \frac{\beta\hbar\gamma}{2} \cot\left(\frac{\beta\hbar\gamma}{2} \right) \right], \quad \hat{\Theta}_k = \frac{mc_k\zeta}{\beta} \frac{\partial}{\partial p}.$$

Hysteresis and both single and double plateau-like behavior are observed in the negative differential resistance (NDR) region. We find two distinct types of current oscillations, with large and small oscillation amplitudes, respectively, in some parts of the plateau in the NDR region. The results of eigenstates analysis indicate that the first type is caused by a transition between ground tunneling states and adjacent excited states in the emitter basin, while the second type is caused by a transition between intermediate tunneling states and higher states. These two types of oscillation also appear differently in the Wigner space, with one exhibiting two piston engine-like motion and the other exhibiting tornado-like motion (Figs.4-5).

REFERENCES

[1] Y. Tanimura and R. Kubo, *Time Evolution of a Quantum System in Contact with a Nearly Gaussian-Markoffian Noise Bath*, J. Phys. Soc. Jpn. **58**, 101 (1989).
[2] Y. Tanimura, *Stochastic Liouville, Langevin, Fokker–Planck, and Master Equation Approaches to Quantum Dissipative Systems*, J. Phys. Soc. Jpn. **75**, 082001 (2006).
[3] A. Sakurai and Y. Tanimura, *An Approach to Quantum Transport Based on Reduced Hierarchy Equations of Motion: Application to a Resonant Tunneling Diode*, J. Phys. Soc. Jpn. **82**, 033707 (2013).
[4] A. Sakurai and Y. Tanimura, *Self-excited current oscillations in a resonant tunneling diode described by a model based on the Caldeira-Leggett Hamiltonian*, New J. of Phys. submitted.

978-3-901578-26-7 © 2013 Society for Micro- and Nanoelectronics

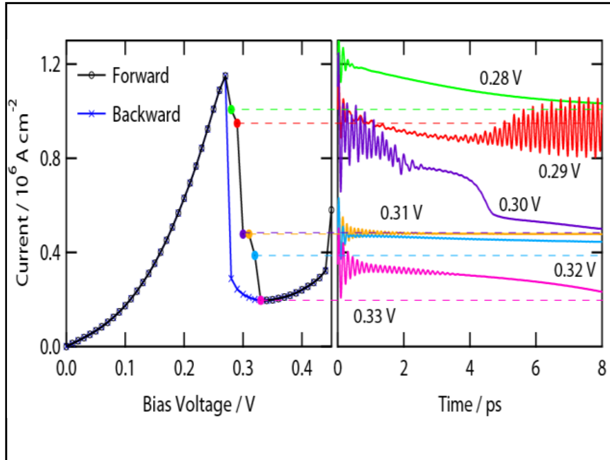

Fig. 1. The I-V characteristics and steady current.

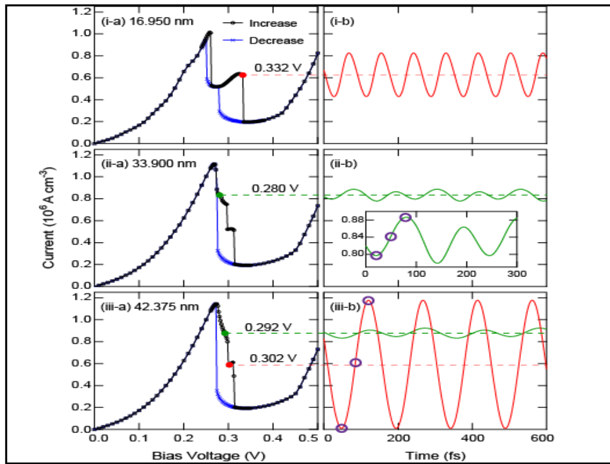

Fig. 2. The I-V characteristics for different contact region size.

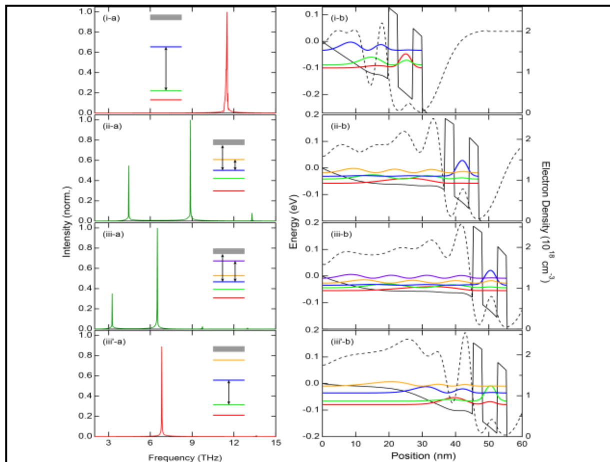

Fig. 3. The spectral distributions and the effective potential for the large (red) and small (green) oscillations in fig.2 (b).

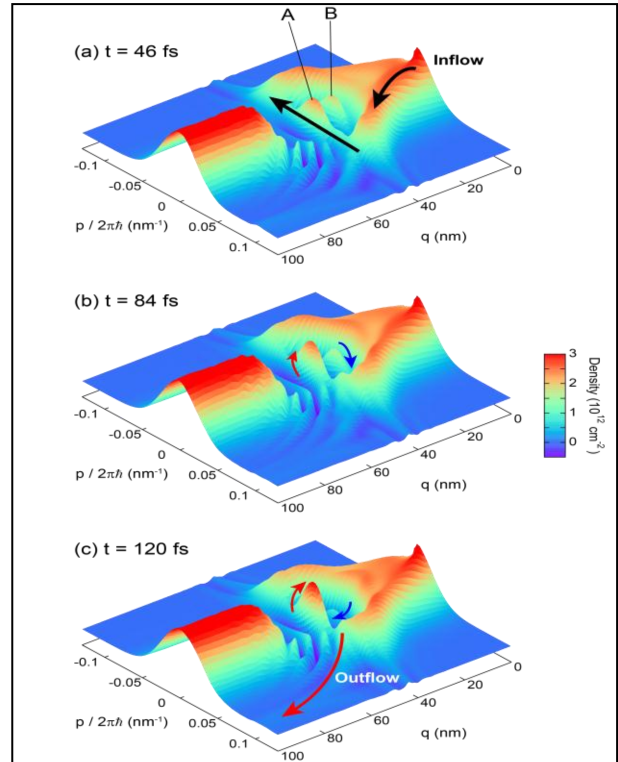

Fig.4. The snapshots of the Wigner distribution for small oscillation case(green curve) at the times marked in Fig.2(ii-b).

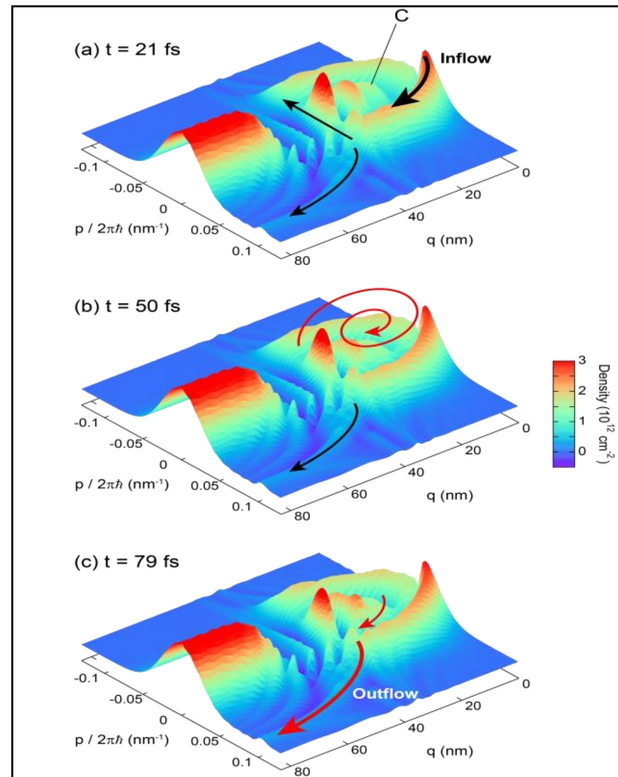

Fig.5. The snapshots of the Wigner distribution for large oscillation case (red curves) at the times marked in Fig.2(iii-b).

Ab-initio study on scattering potentials of defects on Ge(001) surfaces

T. Ono
Greduate School of Engineering, Osaka University, Suita, Osaka, 565-0871 Japan
e-mail: ono@prec.eng.osaka-u.ac.jp

INTRODUCTION

As new techniques for the nanoscale manipulation and modification of materials progress, the electron scattering properties of nanostructures are the focus of attention both experimentally and theoretically. Although scanning tunneling microscopy and mechanically controllable break junctions have been used to examine the scattering properties of nanoscale systems sandwiched between two electrodes, it is not easy to discuss the contribution of local chemical bonds to the electron scattering using these techniques. On the other hand, the spatial maps of the local density of states obtained by scanning tunneling spectroscopy can give us the images of standing waves, which provide important information about the dispersion relation of the electron scattering process at the potential barrier.

COMPUTATIONAL METHODS AND MODELS

I carried out first-principles calculation for obtaining the scattering potential of the defects on Ge(001) surfaces using a computational model shown in Fig. 1 [1]. The Ge-Ge dimer at the center of the scattering region is replaced by Ge-Si or Ge-Sn dimer as a defect. When the Si and Ge atoms are located at the lower and upper sides of the dimer, respectively, the dimer is referred as an SiL dimer. Other dimers are named in a similar manner. By calculating the scattering wave functions using the overbridging boundary-matching method [2], the standing waves in the spatial map of the local density of states are examined; the waves correspond to the image of the differential conductance obtained by scanning tunneling spectroscopy [3].

DISCUSSION

The charge density distribution of the scattering wave functions for the electrons propagating from both the left and right electrodes is investigated with an energy of E_F+0.55 eV, which corresponds to the spatial image of the differential conductance in the scanning tunneling spectroscopy spectrum [3]. The line profiles of the standing waves along the dimer row including the impurity atom are depicted in Fig. 2. It should be noted that the charge density of the π^* band above the lower atom of the dimer is larger than that above the upper atom. To demonstrate the period and phase shift of the standing waves clearly, the density of the standing waves is fitted by

$$\alpha(x) = A\cos(2k_x x + \varphi) \quad (1)$$

where A, φ, and k_x are the amplitude of the standing waves, phase shift of the standing waves, and Bloch vector in x direction, respectively. The fitting is carried out using the density of the standing waves above the lower atoms of the dimers, which are indicated by closed circles in Fig. 2.

The period of the standing wave and its phase shift are shown in Table I, in which they agree with those obtained by the experiment [3]. The scattering potential acts as a barrier when the electronegativity of the upper atom of the dimer is larger than that of the lower atom, while it becomes a well in the opposite case. The scattering potential is related to the stabilization of the π bands of the Ge(001) surface due to the difference in electronegativity between Ge and the impurity.

CONCLUSION

The scattering potential of the defects on Ge(001) surface is investigated by first-principles

calculation. The phase shifts of the standing waves due to the defects are in agreement with those obtained by experiments [3]. By calculating the reflection coefficients of the scattering wave functions, it was found that the scattering potentials of the SiL and SnU dimers act as a well, while those of the SiU and SnL dimers behave as a barrier. This characteristic is interpreted in terms of the electronegativity of the defects; when the electronegativity of the upper site of the dimer is large, the energy gap between the π and π^* bands increases, resulting in the generation of the potential barrier for the π^* electrons.

REFERENCES

[1] T. Ono, *Phys. Rev. B* **87**, 085311 (2013).

[2] K. Hirose, T. Ono, Y. Fujimoto, and S. Tsukamoto, *First Principles Calculations in Real-Space Formalism, Electronic Configurations and Transport Properties of Nanostructures* (Imperial College, London, 2005).

[3] K. Tomatsu, M. Yamada, K. Nakatsuji, F. Komori, B. Yan, C. Wang, G. Zhou, and W. Duan, *Phys. Rev. B* **78**, 081401 (2008).

Table I. Amplitude and phase shift of the standing waves around the Ge-Si and Ge-Sn dimers.

	Model			
	SiL	SiU	SnL	SnU
Amplitude (10^{-7}e/Å^3/eV/spin)	3.908	1.692	7.169	1.031
Phase shift (π rad)	0.221	-0.602	-0.650	0.142

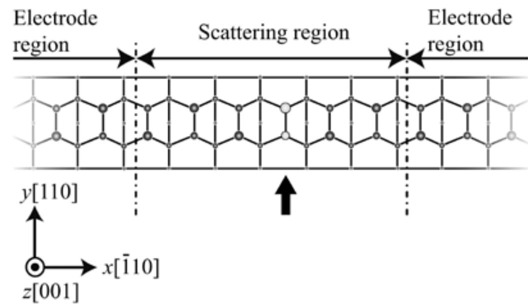

Fig. 1. Schematic image of computational model. Dark spheres are Ge atoms and light spheres represent the dimer replaced by a Ge-Si or Ge-Sn dimer, which is indicated by the arrow. Atoms are denoted by large and small spheres according to the distance from the surface. Reprinted from Ref. 1.

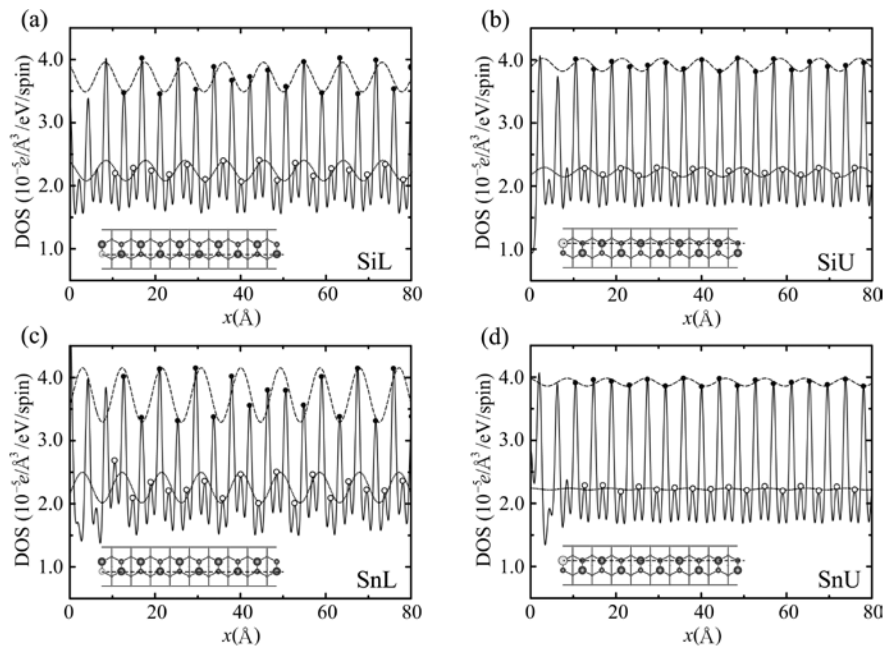

Fig. 2. Line profiles along dimer row including impurity atom indicated by dashed lines in insertions, where the meanings of symbols are the same as those in Fig. 1. Solid curve represents the standing wave. Dashed and dotted curves are fitted by Eq.~(1) using the densities above lower atoms of impurity side (closed circle) and upper atoms of impurity side (open circle), respectively. Reprinted from Ref. 1.

Efficient Self-Consistent Quantum Transport Simulator for Quantum Well Devices

X. Gao, D. Mamaluy, E. Nielsen, R. Muller, R. Young, N. Bishop, M. Lilly, M. Carroll
Sandia National Laboratories,
1515 Eubank SE, Albuquerque, NM 87123, USA
e-mail: xngao@sandia.gov

Silicon quantum dot systems have attracted enormous efforts [1-2] in the past decade to explore their potential as qubits for quantum computing due to the promise of long spin coherence times and the well-established Si manufacturing processes. We have developed a Quantum Computer Aided Design (QCAD) device simulator [3] that solves for electrostatic potential, single- and multi-electron wave functions and energies, and that has been extensively used to accelerate the development of Si double quantum dot (DQD) qubit work at Sandia National Laboratories. To model additional features of interest to experimentalists, such as current flow across tunnel barriers, we needed a carrier quantum transport capability. In principle, we have to solve a self-consistent 3D quantum transport problem for DQDs, which would require excessive development time and computing resources due to the inherent complexity of 3D transport and the relatively large size of DQDs (on the order of micrometers in each direction). Alternatively, we can first perform QCAD electrostatic simulations of DQDs, identify the tunnel barrier path of interest along which current flows, and then perform 1D self-consistent quantum transport simulations to obtain the current-voltage relation. This procedure allows for very fast simulation time and provides good general guidance on device designs.

To set the context, Figure 1(a) shows an experimental Si DQD with the gate insulators and top metal gate not shown. Under certain gate bias and interface charge conditions, the device is flooded with electrons in the left and right regions but a barrier is formed between the two dots as shown in Fig. 1(b). The potential energy profile across the barrier obtained from QCAD is given in Fig. 1(c). We want to know how the barrier will change and what is the tunnel current when applying a source-drain voltage to the barrier. The applied voltage in experiment can be relatively large with respect to k_BT, e.g., 50 mV at 4 K (about 143 k_BT), to overcome effects of any possible unknown defects around the barrier region. Because of the high voltage, we are required to have a self-consistent solution of quantum transport across arbitrary 1D barriers.

Our self-consistent transport is based on the Contact Block Reduction (CBR) method [4]. It turns out that when we apply the general 3D CBR approach to 1D applications, we obtain a set of very simple equations that allow for easy implementation and very fast simulation. In particular, within the CBR method, the transmission across arbitrary single or multiple barriers becomes trivial to compute and extremely fast compared to the standard techniques for a tri-diagonal Hamiltonian [5]. For example, when computing transmission as a function of energy across the barrier in Fig. 1(c) using Matlab, CBR takes only 1 s on one CPU of a 2.6 GHz laptop, whereas matrix inverse requires more than 1000 s.

The Poisson-CBR self-consistency is achieved by adapting the predictor-corrector scheme [6] to open systems [7]. The resulting nonlinear Poisson equation is solved by a straightforward Newton method as the Jacobian matrix is tri-diagonal in 1D. Electron density is computed using the LDOS obtained by CBR. The self-consistent loop often achieves convergence within just ten iterations. Figure 2 shows simulation results at T = 10 K of a test RTD device that contains several coupled resonant states. The current-voltage curve shows interesting characteristics: the increase in part (A) is mainly because source states (left side) are in

978-3-901578-26-7 © 2013 Society for Micro- and Nanoelectronics

resonance with the states in the well, as seen by the relatively sharp transmission and current spectrum at 45 and 50 mV, while the increase in part (B) is due to single-barrier tunneling and quantum interference from the right barrier which is below the source Fermi level at 0, with the interference effect seen by the broad peaks in transmission spectrum at 55 and 60 mV.

We will present the self-consistent Poisson-CBR simulation results of tunnel barriers in DQDs and compare with transport measurements at various gate conditions. We also intend to expand the code for ballistic transport through an arbitrary number of 1D barriers and release it under an Open Source license, which will allow people to quickly obtain *self-consistent* quantum transport solution in quantum-well types of devices for design guidance.

This work was supported by the Laboratory Directed Research and Development program at Sandia National Laboratories. Sandia is a multiprogram laboratory operated by Sandia Corporation, a Lockheed Martin Company, for the United States Department of Energy's National Nuclear Security Administration under Contract DE-AC04-94AL85000.

[1] B. E. Kane, Nature **393**, 133 (1998).
[2] T. M. Lu, et. al., Appl. Phys. Lett. **99**, 043101 (2011).
[3] X. Gao, et. al., Proceedings of 15th IWCE (2012).
[4] D. Mamaluy, et al., Phys. Rev. B **71**, 245321 (2005).
[5] S. Datta, *Quantum Transport Atom to Transistor* (2005).
[6] A. Trellakis, et. al., Appl. Phys. Lett. **81**, 7880 (1997).
[7] H. Khan, et. al., IEEE Trans. Elec. Dev. **54**, 784 (2007).

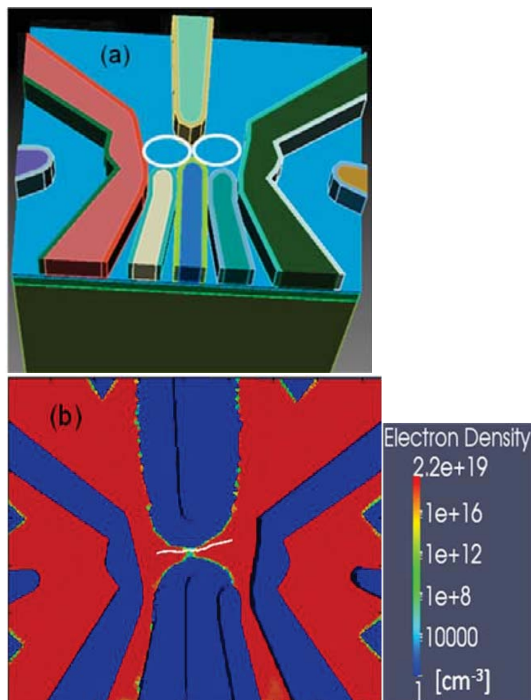

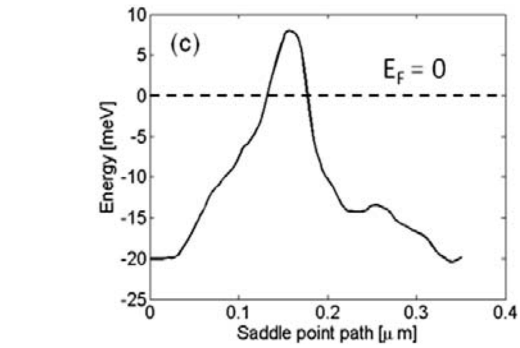

Fig.1. (a) Experimental Si DQD with depletion gates and Si substrate shown and the two white circles denote the dots. (b) Top view of electron density at the Si/SiO2 interface under certain conditions, with the left and right regions flooded with electrons but a barrier formed between the dots. Depletion gates are overlaid on the figure. The white curve across the barrier denotes the saddle-point path found by a searching algorithm in QCAD. (c) The potential energy barrier obtained in QCAD along the white curve with the left of the path as starting point.

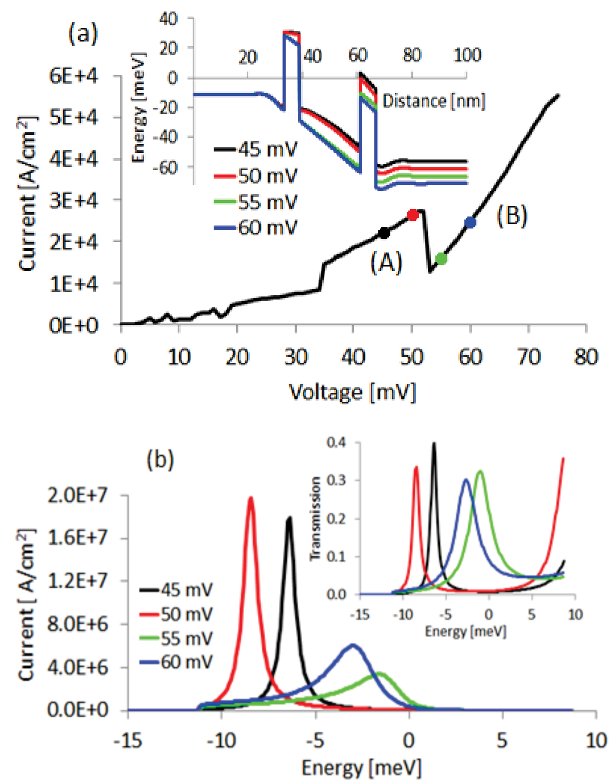

Fig.2. (a) Current-voltage relation of a test RTD at T = 10 K. The four circles denote the voltages at which the self-consistent band profiles are plotted in the inset. The small ripples in currents at low voltages are believed to be due to numerical noise. (b) Current spectrum at four voltage points, with the inset showing the corresponding transmission function.

Is there a mesoscopic Braess paradox?

M. Macucci, P. Marconcini
Dipartimento di Ingegneria dell'Informazione, Università di Pisa, via Caruso 16, 56122 Pisa, Italy
e-mail: macucci@mercurio.iet.unipi.it

INTRODUCTION

In a recent paper Pala *et al.* present an experiment and a numerical simulation of an interesting phenomenon that is interpreted as a mesoscopic analogous of the Braess paradox. They consider the structure reported in Fig. 1 and observe that, in "congestion" conditions (i.e., if the total number of modes propagating in the parallel channels is less than that in the leads), addition of the channel in the middle may, somewhat counterintuitively, lead to a decrease in conductance instead of an increase. This effect is interpreted with reference to the Braess paradox [2] in transportation theory, in which opening a new path in a particular road network used by noncooperative players may lengthen the average travel time between two locations.

Here we perform an analysis showing that this situation is actually a particular case of destructive quantum interference. In other words, addition of the third channel leads to suppression of transmission for some of the modes in the vertical channels, due to a "stub" effect (see, e.g. Ref. [3]), and this suppression prevails over the conductance increase due to the additional channel.

MODEL AND RESULTS

We consider the same material parameters (for InGaAs) and device geometry as in Ref. [1], and use a recursive Green's function approach [3] to compute the trasmission matrix, from which conductance is obtained via the Büttiker-Landauer formalism.

Let us first analyze the dependence of conductance through the structure as a function of the position of the exit lead: results are reported in Fig. 2 for the case of only two channels (solid line), adding a third channel in the middle (dashed line), and with a third channel shifted 500 nm away from the center (dotted line). We immediately notice that the paradoxical behavior is observed only when the entrance and exit lead are on opposite sides with respect to the third channel (otherwise the addition of the third channel leads to an increase of the conductance)

We observe that the third channel not only acts as an additional conducting path, but also as a "stub" for the vertical channels to which it is connected, thereby letting only part of the propagating modes pass without being attenuated. If the third channel is between the leads, such an attenuation will occur along both paths: the clockwise [Fig. 3(a)] and the counterclockwise one [Fig. 3(b)], otherwise the attenuation will affect only one [Fig. 3(d)] of the paths (although connected in two locations, the same modes will be affected). Thus, in the former case the attenuation prevails over the increase in conductance resulting from the new open path, while in the latter case the reverse happens.

To confirm this interpretation, we have performed a simulation adding a third channel with a barrier in the middle: in this way we still have a stub action leading to the conductance decrease, but there is no new path for conduction. In Fig. 4 we plot the overall conductance as a function of the position of the exit lead in the absence of the third channel (solid line), and in the presence of the third channel obstructed with a 20 nm thick and 0.1 eV high barrier (the Fermi energy is 60 meV) placed in the middle. It is apparent that conductance is suppressed more than when the third channel is unobstructed, although there is no new open path.

REFERENCES

[1] M. G. Pala, S. Baltazar, P. Liu, H. Sellier, B. Hackens, F. Martins, V. Bayot, X. Wallart, L. Desplanque, S. Huant, *Transport inefficiency in Branched-Out Mesoscopic Networks: an Analog of the Braess Paradox*, Phys. Rev. Lett. **108**, 076802 (2012).

[2] D. Braess, A. Nagurney, T. Wakolbinger, *On a Paradox of Traffic Planning*, Transportation Science **39**, 446 (2005).

[3] F. Sols, M. Macucci, U. Ravaioli, Karl Hess, *Theory for a quantum modulated transistor*, J. Appl. Phys. **66**, 3892 (1989).

978-3-901578-26-7 © 2013 Society for Micro- and Nanoelectronics

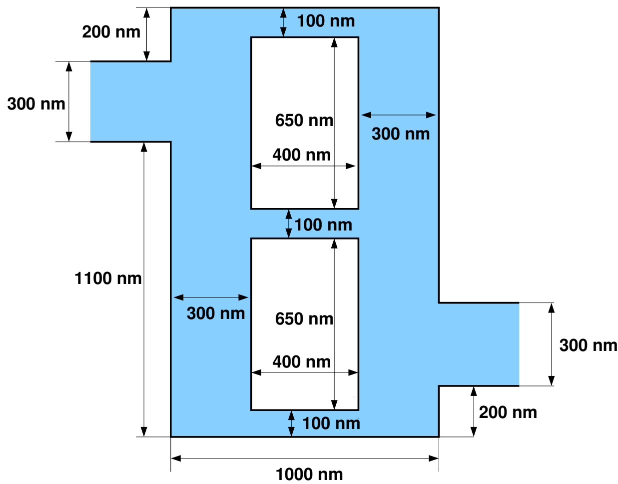

Fig. 1. Sketch of the considered structure

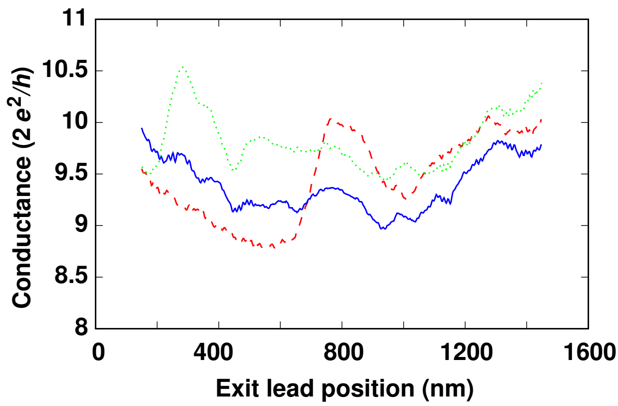

Fig. 2. Conductance as a function of the position of the center of the exit lead (measured from the bottom): for 2 channels (solid line), with the addition of the third channel in the middle (dashed line), and with the addition of the third channel shifted down by 500 nm (dotted line).

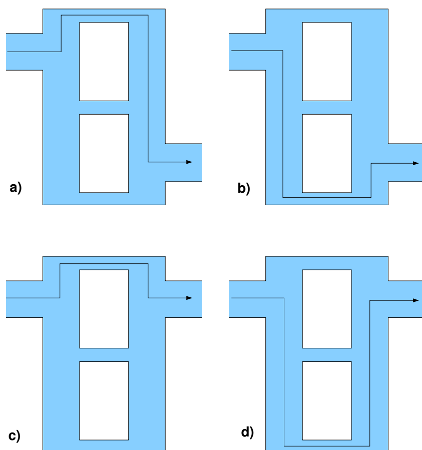

Fig. 3. Possible paths in the case of leads on opposite sides (a,b) and of leads on the same side (c,d) with respect to the third channel.

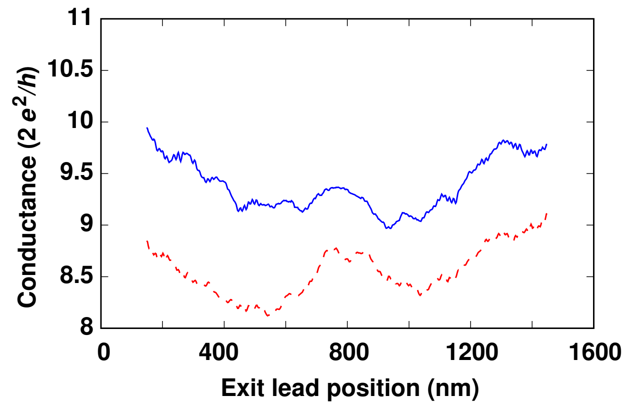

Fig. 4. Conductance as a function of the position of the exit lead for 2 channels (solid line) and for 3 channels (dashed line), but with an opaque barrier in the middle of the third channel.

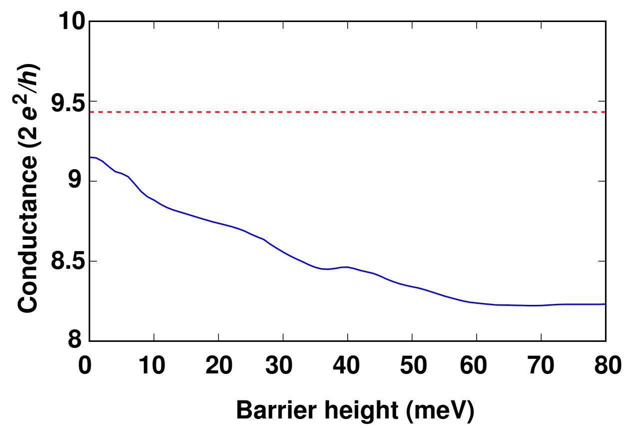

Fig. 5. Conductance as a function of the height of the barrier in the middle of the third channel, for the lead configuration of Fig. 1; the dashed line represents the conductance for the case of only 2 channels.

Molecular-Metal-Oxide-nanoelectronicS (M-MOS): Achieving the Molecular Limit

V. P. Georgiev[1], S. Markov[1], L. Vilà-Nadal[2], A. Asenov[1,§] and L. Cronin[2]
[1] Device Modelling Group, School of Engineering, University of Glasgow, G12 8LT Glasgow, UK
[§] Gold Standard Simulations Ltd., G12 8LT Glasgow, UK
[2]WestCHEM, School of Chemistry, University of Glasgow, G12 8QQ Glasgow, UK
e-mail: vihar.georgiev@glasgow.ac.uk

Introduction

In recent years interest in electronic, magnetic and optical structures and devices based on inorganic, organic, hybrid and nano-materials has increased significantly. An example of this is the EPSRC funded M-MOS Programme Grant, which provides an exciting opportunity for research in the field of molecular electronics based on hybrid nano-materials. Among the aims of this project is to study extensively, using 3D simulations, the interplay between variability, scalability and reliability of a non-volatile flash-memory cell, in which the charge-storing components constitute of a layer of polyoxometalates molecular clusters (POMs) – Fig.1. POMs are metal-oxide inorganic molecules formed by early transition metal ions and oxo ligands [1] – Fig.2. Importantly, they can undergo multiple times reversible reduction/oxidation, which makes them attractive candidates for multi-bit storage in flash memory cells. The use of redox-active molecules to form the floating gate (FG) could offer several very important advantages over the conventional polysilicon FG [2].

Discussion

In order to evaluate the idea of POMs, based non-volatile molecular memories, we developed a simulation flow that links the density functional theory (DFT) result to three-dimensional (3D) numerical flash cell simulations – Fig.3. The custom-built *Simulation Domain Bridge*, which establishes a connection between the two distinct modelling schemes (DFT for the molecular part and mesoscopic device modelling for the flash cell), was a vital step in this flow.

For the purpose of this paper we have designed an 18 nm x 18 nm square gate n-channel flash memory cell. The gate dielectric is assumed to be SiO_2 with thickness of 20 nm. The POMs layer is 4.5 nm above the Si substrate, where 3 nm are SiO_2 and 1.5 nm is balancing cation from the insulation barrier (see green chains in Fig.2). The molecular layer has a 4x4 rectangular planar arrangement of the POMs.

Using a floating gate built from 4x4 POMs with molecular formula $[W_{18}O_{54}(SO_3)_2]^{4-}$, arranged in a planar distribution, we calculated the drain current of the cell – Fig.4. The main assumption is that all of the POMs within the layer are simultaneously reduced by one (blue line) or two (red line) electrons. Adding (reducing) additional negative charges into the FG leads to lowering of the source-drain current and to a threshold voltage shift. Fig.5 reveals the increase of the threshold voltage, ΔV_{TH}, as a function of the sheet-charge density. ΔV_{TH} agrees well with the idealised analytical model. Moreover, reducing each POM by two electrons produces the same impact on V_{TH} as doubling the sheet density in the analytical dependence. A directly link can be established between the results presented in Fig.5 and the potential barrier profile along the channel shown in Fig.6. The height of the barrier in the channel determines the shift in $\Delta V_{TH.}$

References

[1] D.-L. Long, Y.-F. Song, E. F. Wilson, P. Kögerler, S.-X. Guo, A. M. Bond, J. S. J. Hargreaves, L. Cronin, *Angew. Chem. Int. Ed.* **47**, 4384-4387 (2008).
[2] J. Lee, S. H. Hur, J.-D. Choi, *IEEE Electron Device Letters* **23/5**, 264-266 (2002).

978-3-901578-26-7 © 2013 Society for Micro- and Nanoelectronics

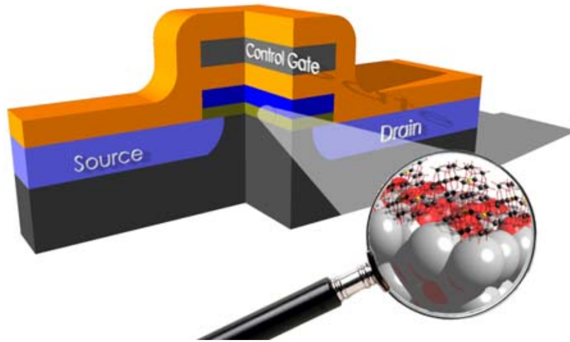

Fig. 1. Schematic representation of a single-transistor non-volatile memory cell, showing an array of polyoxometalate clusters (POMs) as part of the floating gate.

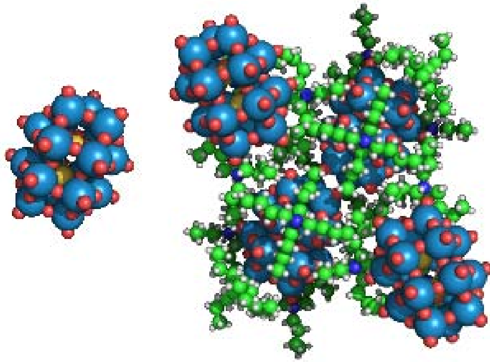

Fig. 2. Schematic representation of POMs cluster anions, $[W_{18}O_{54}(SO_3)_2]^{4-}$, with their cations (green chains). Colour scheme: O, red; W, blue; Se, yellow.

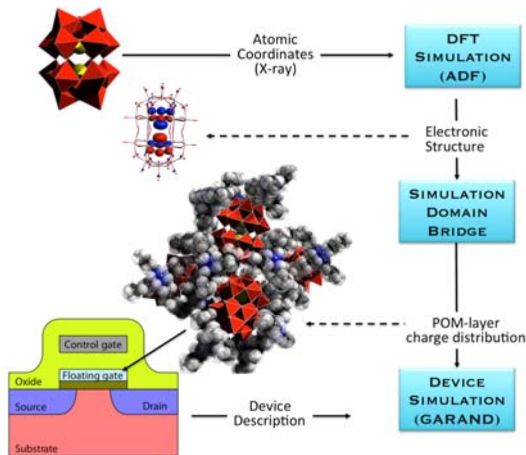

Fig. 3. Simplified block diagram of the simulation methodology, linking DFT and flash-cell modelling. The simulation domain bridge is developed in-house. The commercial simulators ADF and Garand are used for the DFT and three-dimensional device simulations respectively.

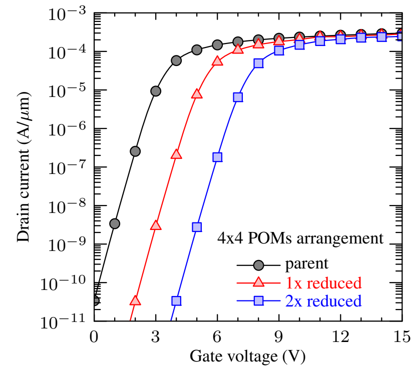

Fig. 4. Clear lowering of the source-drain current corresponding to the reduction of each POM simultaneously by 1(blue) and 2(red) electrons. The centres of all POMs are 4.5nm above the substrate.

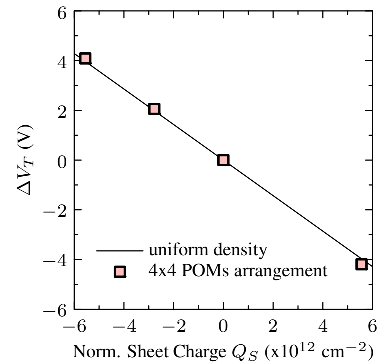

Fig. 5. Comparison of the threshold voltage shift ΔV_{TH} due to an idealised sheet charge in the oxide (line), and due to a POM-FG (symbols), versus sheet charge density (normalised by the electron charge).

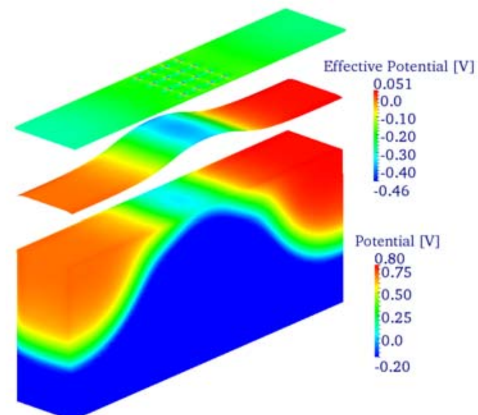

Fig. 6. Potential barrier profile along the channel of the flash-cell (2D elevated plot) and distribution of the effective potential of the simulated device (3D). Fingerprints of the twelve POMs placed in the floating gate are visible on the top (green) panel above the potential barrier profile along the channel.

Defect Analysis with TCAD-based DLTS Simulation

A. Scheinemann and A. Schenk
Integrated Systems Laboratory, ETH Zürich, Gloriastrasse 35, 8092 Zürich, Switzerland
e-mail: scheinemann@iis.ee.ethz.ch

Introduction

Although DLTS [1] is a wide-spread characterization technique and has been studied quite extensively, its key properties have to be reconsidered when facing the characterization of extended defects which are often observed in todays CMOS processes. In most cases the characterized samples contain more than one defect level. Hence, the measured capacitance transients are not single time constant exponential functions but superpositions of different decay processes in the form of $C(t) = \sum_{i=1}^{n} C_i(0)e^{-e_i t}$ where n is the number of different species and e_i is the emission rate containing the most important physical parameters of the defect. Furthermore, the spatial defect distributions in general cannot be assumed homogeneous, e.g. in the case of end-of-range (EOR) defects introduced during amorphising implants. This renders the use and fitting of analytical expressions to measured DLTS signals not applicable.

Methodology

Experiments on dedicated samples for the study of extended defects exhibit a multitude of different defect species some of which appear to be strongly broadened. In the majority of available literature DLTS peaks are compared to the analytical expression

$$S(T) = C_{\text{Trap}}(e^{-e_\nu(T,E_T,\sigma_\nu)t_1} - e^{-e_\nu(T,E_T,\sigma_\nu)t_2}) \ , \quad (1)$$

where C_{Trap} denotes the capacitance difference between filled and empty defects and e_ν with $\nu \in \{n,p\}$is the emission rate which couples the defect levels to the corresponding carrier band. This signal as it results from the original box car DLTS method introduced by Lang [1] as well as many other approaches using different correlation functions $\zeta(t)$ to obtain a temperature dependent signal

$$\hat{S} = \int_0^{t_S} \mathrm{d}t \, e^{-e_\nu(T,E_T,\sigma_\nu)t} \zeta(t) \quad (2)$$

are all based on simplifying assumptions which limit the usability of the analytical expression [2]–[5]. These limitations are easily overcome when the DLTS simulations are obtained with an advanced device simulation tool [6]. The transient relaxation of a device after an abrupt change in the applied bias is simulated which has the following advantages:

1) Instead of only thermal emission into one band e_ν all coupling processes (e_n, e_p, c_n, c_p) of the trap to all bands are evaluated.
2) Instead of homogeneous distributions an actual process-related and spatially resolved defect profile is used.
3) The occupation of defect levels is computed consistently with the position of the Fermi level.

In order to explain the broadening of DLTS spectra a coupling of different energy levels is implemented instead of just integrating over a distribution of independent energy levels,

$$\begin{aligned} \frac{\mathrm{d}n_i}{\mathrm{d}t} &= e_{p,i}(N_i - n_i) - e_{n,i}n_i \\ &+ c_{12,i}(N_i - n_i)n_{i+1} - e_{12,i}(N_{i+1} - n_{i+1})n_i \\ &- c_{12,i-1}(N_{i-1} - n_{i-1})n_i \\ &+ e_{12,i-1}(N_i - n_i)n_{i-1} \ . \end{aligned} \quad (3)$$

The set of coupled differential equations (3) resulting from the model in Fig. 1 is integrated numerically with a symplectic integrator to directly obtain a DLTS signal. This formalism is easily extended to N levels where only the neighboring levels are coupled to each other. Corresponding results of this numerical integration are compared in Figs. 4 and 5.

Results

The solution of the system (3) yields a substantial broadening of the DLTS signal as can be seen from Fig. 4 and, therefore, seems to represent a suitable model to explain very broad DLTS peaks. It differs from the S-Device simulation result where a uniform distribution of independent defect levels within an energy interval $E = E_C - 0.35e\text{V} \pm 0.15e\text{V}$ was assumed. The low-temperature tail of this peak was neither reproduced by the numerically integrated result nor by the S-Device simulation of the DLTS signal. This is probably because another level is present in the sample which cannot be resolved as a distinct peak in the DLTS measurement. Despite the use of simulated defect profiles, the amplitude of the DLTS peak, which is (beside other dependencies) directly proportional to the concentration of electrically active defects, is still a fitting parameter. It is not possible to predict the extent of decoration of the dislocation loops with other point-like impurities [8]. Hence, the concentration of peripheral interstitials in the dislocation loops can be deemed as an approximation to the maximum concentration of active defects. (see Fig. 3).

978-3-901578-26-7 © 2013 Society for Micro- and Nanoelectronics

Acknowledgement

The research leading to these results has received funding from the European Seventh Framework Program FP7/2007-2013) under the grant agreement No. 258547 (ATEMOX).

References

[1] D.V.. Lang , J. Appl. Phys., Vol. 45, No. 7, Jul. 7, 1974, pp. 3023 - 3032.
[2] C. Hardalov et al. and K Kirov et al., J. Appl. Phys., Vol. 71, No. 5, Mar. 1, 1992, pp. 2270 - 2273.
[3] A. Das and V.A. Singh and D.V. Lang, Semicond. Sci. Technol., Vol. 3, 1988, pp. 1177 - 1183.
[4] G.L. Miller and J.V. Ramirez and D.A.H. Robinson, J. Appl. Phys., Vol. 46, No. 6, Jun. 1975, pp. 2638 - 2644.
[5] A.A. Istrativ and O.F. Vyvenko and H. Hieslmair and E.R. Weber, Meas. Sci. Technol., Vol. 9, 1998, pp. 477 - 484.
[6] Synopsys Inc, Sentaurus Device User Guide, version F- 2011.09
[7] A. Schenk and U. Krumbein, J. Appl. Phys., Vol. 78, No. 5, Sep. 1, 1995, pp. 3185 - 3192.
[8] V. Moroz and M. Choi, ECS Trans. Vol. 33, No. 11m 2010, pp. 221-236.
[9] Private communications within the ATEMOX project. www.atemox.eu

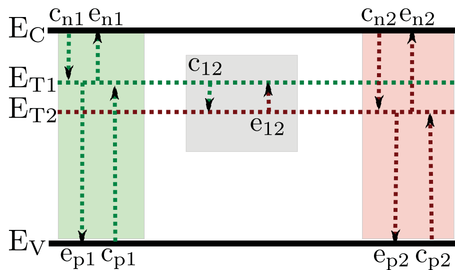

Fig. 1. Schematic representation of two defect levels (E_{t1} and E_{t2}) in the band gap. Each defect level couples to conduction and valence band. Furthermore, an inter-level coupling is represented by the coupling constants c_{12} and e_{12}. This model of the coupling of two defect levels from [7] is available in the commercial device simulator S-Device.

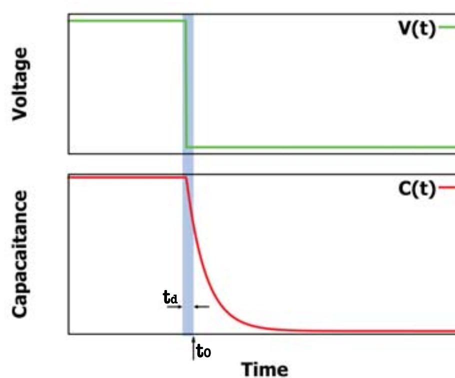

Fig. 2. Relation between voltage pulse configuration $V(t)$ and measured capacitance transient signal $C(t)$. A thorough description and analysis of the experimental setup can be found in [1]. Here t_d depicts the typical downtime of the instrumentation after the abrupt voltage change which leads to an overshoot in the detection hardware and hence a downtime which offsets the first measured point relative to the actual zero point of the switching process. For the device simulation C(t) curves are simulated for every temperature point. Script-based extraction of the necessary information from the simulation files is conducted to construct a DLTS signal.

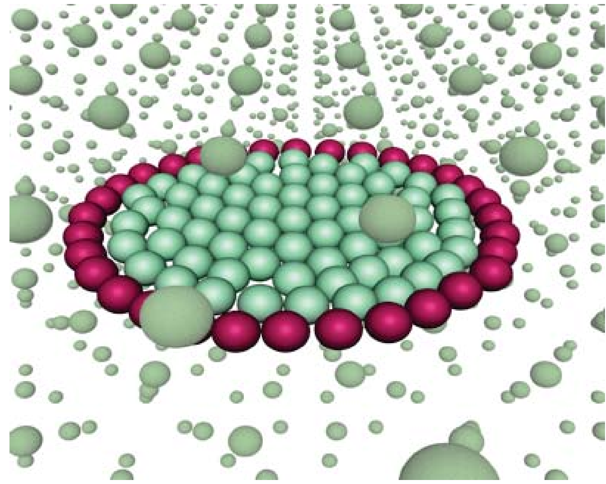

Fig. 3. Schematic visualization of the model for electrically active defects (red) in a dislocation loop.

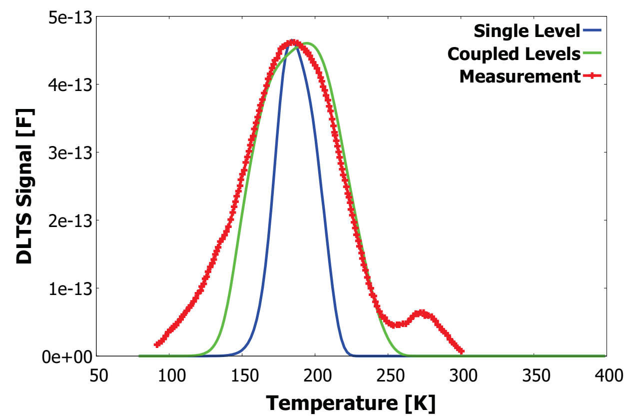

Fig. 4. Comparison of measured DLTS signal (red curve) [9] with numerically integrated signals for the single defect level (blue curve) and an ensemble of defect levels distributed over an interval of $\pm 0.15eV$ around the energy value $E_0 = E_C - 0.35eV$. (green curve) This energy interval is descretized into 15 smaller intervals and each of them is assigned to a normalized trap population. Energetic neighbouring populations are coupled to each other as demonstrated in Eq. (3).

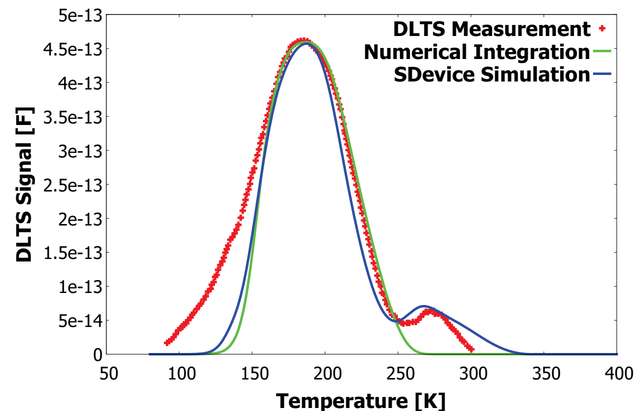

Fig. 5. Measured DLTS signal (red curve), numerically computed DLTS signal with parameters identical to those listed in the caption of Fig. 4. The blue line shows the S-Device simulation with the same energy distribution as used for the numerical solution. The defect levels in this device simulation are assumed to be independent.

VSP – a Quantum Simulator for Engineering Applications

Z. Stanojević, O. Baumgartner, K. Schnass*, M. Karner*, and H. Kosina
Institute for Microelectronics, TU Wien, Gußhausstraße 27–29/E360, 1040 Wien, Austria
*Global TCAD Solutions GmbH, Landhausgasse 4/1a, 1010 Wien, Austria
e-mail: (stanojevic,baumgartner,kosina)@iue.tuwien.ac.at, (k.schnass,m.karner)@globaltcad.com

State of the Art and Motivation

Several software packages exist that are concerned with some aspects of quantum-electronic computation. Codes began to appear in the late nineties as one-dimensional Schrödinger-Poisson solvers. Since then we have seen the development of academic codes such as nextnano^3 [1], NEMO 5 [2], tiberCAD [3], and tdkp/AQUA [4]. These feature accurate modeling of materials through advanced band structure models, and are able to include effects of strain or magnetic fields in the calculation.

Some of these tools are in fact a collection of specialized models tailored to specific tasks and offer little flexibility. Others demand considerable experience in semiconductor physics from the user to operate them properly.

In our work we are seeking to bridge this gap and provide a flexible, highly efficient simulation enviroment for quantum-electronic problems – the Vienna Schrödinger-Poisson framework (VSP) [5]. The framework is aimed at engineers, students with basic knowledge, and the experienced user.

Methods

A number of methods have been developed and adopted for the VSP. At the core of VSP lies a loop that solves the Poisson equation together with a carrier model self-consistently. Different carrier models can be picked: a classical equilibrium distribution, a system of quantized carriers using the parabolic band approximation, or a $\mathbf{k} \cdot \mathbf{p}$ band structure model with an arbitrary number of bands. A unified interface has been developed that allows the user to specifiy any kind of $\mathbf{k} \cdot \mathbf{p}$ Hamiltonian up to second order in $\mathbf{k}$. Arbitrary crystal orientations are possible. Strain and magnetic fields can be included.

Discretization of both real space and $\mathbf{k}$-space is based on a finite volume scheme described in [6], that accurately treats anisotropy, which is important when discretizing $\mathbf{k} \cdot \mathbf{p}$ Hamiltonians. The discretization is independent of the problem dimensionality and each model code works for one, two, and three dimensions. This ensures consistency when comparing problems of different dimensionality. As default, VSP automatically picks the most suitable numerical methods for the problem at hand.

On the numerical side, VSP employs established libraries for solving linear, nonlinear and eigenvalue problems. These are combined with methods that enhance the numerical preformance especially for eigenvalue problems, such as the shift-invert technique or subspace deflation. Scalable parallelization is provided, making the VSP a highly efficient tool.

Results

Figures 1 through 5 show three different devices analyzed using VSP: a p-type MOS capacitor, a p-type FinFET and a STM tip on an lightly p-doped Si substrate covered by a SiO_2 layer. The simulator was set up to obtain the carrier concentration self-consistently with the Poisson equation. The same simulation setup was used for all three devices – only the geometry changed. Three different carrier models were used: (I) classical unconfined carriers, (II) quantum-confined carriers in the parabolic band approximation, and (III) confined carriers with a $\mathbf{k} \cdot \mathbf{p}$ band structure for electrons modeled according to [7] and for holes according to [8] and [9].

Acknowledgment

This work has been supported by the Austrian Science fund through contracts F2509 and I841-N16.

978-3-901578-26-7 © 2013 Society for Micro- and Nanoelectronics

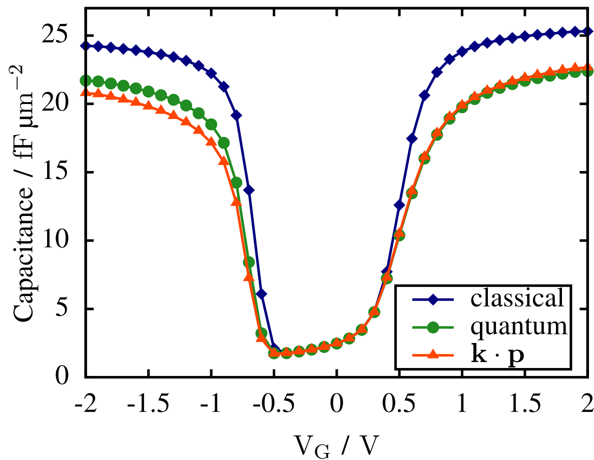

Fig. 1. CV-curve of a p-type MOS capacitor; classical, parabolic band quantum, and $\mathbf{k}\cdot\mathbf{p}$ quantum models are compared; a difference between the effective mass and $\mathbf{k}\cdot\mathbf{p}$ is visible in inversion due to the higher non-parabolicity of the valence band.

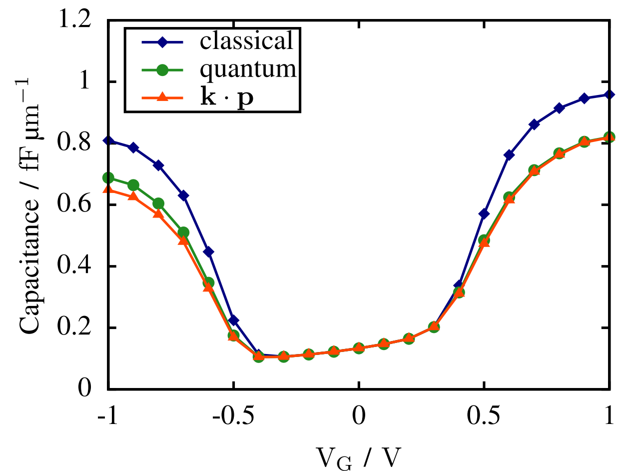

Fig. 3. CV-curve of a p-type FinFET; classical, effective mass quantum, and $\mathbf{k}\cdot\mathbf{p}$ quantum models are compared; here too, the quantum and $\mathbf{k}\cdot\mathbf{p}$ curves differ at inversion.

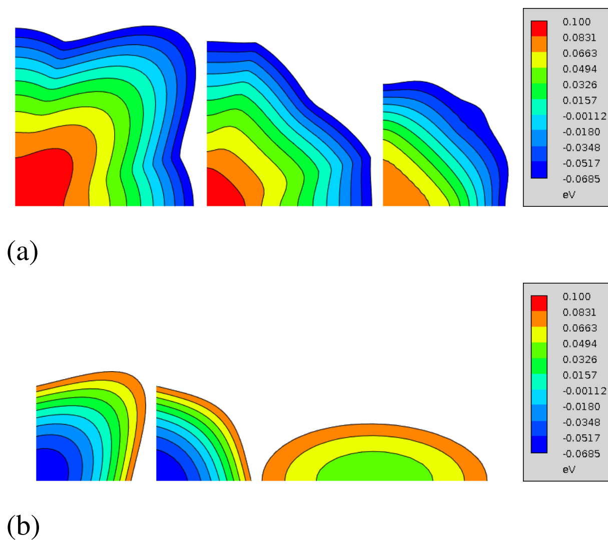

Fig. 2. Contour plots of the lowest three subbands in the p-type MOS capacitor calculated using a $\mathbf{k}\cdot\mathbf{p}$ band structure at inversion $V_G = -2\,\mathrm{V}$ (a) and accumulation $V_G = 2\,\mathrm{V}$ (b)

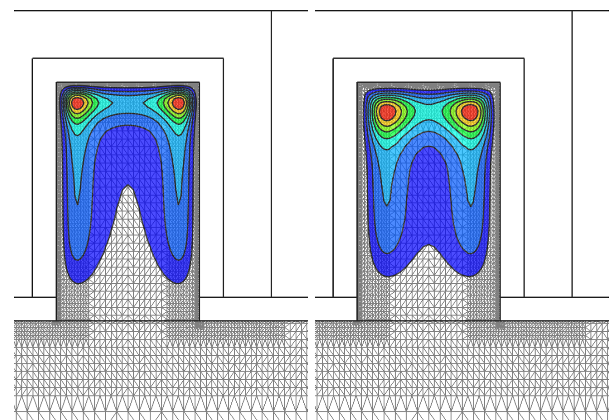

Fig. 4. Hole distribution in the FinFET at inversion $V_G = -1\,\mathrm{V}$; left: parabolic band approximation, right: $\mathbf{k}\cdot\mathbf{p}$ band structure

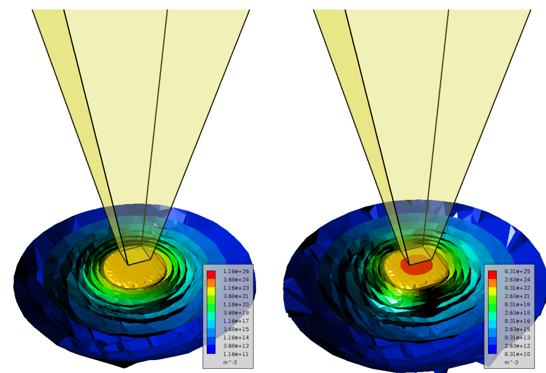

Fig. 5. Electron concentration under a STM tip biased at $4\,\mathrm{V}$; left: parabolic band approximation, right: $\mathbf{k}\cdot\mathbf{p}$ band structure

References

[1] S. Birner *et al.*, IEEE T. Electron. Dev. **54**, 2137 (2007).
[2] S. Steiger, *NEMO 5 User Manual*, NCN Purdue Univ.
[3] M. Auf der Maur *et al.*, IEEE T. Electron. Dev. **58**, 1425 (2011).
[4] R. G. Veprek, Ph.D. thesis, ETH Zürich, 2009.
[5] M. Karner *et al.*, J. Comput. Electron. **6**, 179 (2007).
[6] Z. Stanojevic *et al.*, *SISPAD* (2011), pp. 143 –146.
[7] J. C. Hensel *et al.*, Phys. Rev. **138**, A225 (1965).
[8] T. Manku *et al.*, J. Appl. Phys. **73**, 1205 (1993).
[9] Frank L. Madarasz *et al.*, J. Appl. Phys. **52**, 4646 (1981).

Scaling Effect on Specific Contact Resistivity in Nano-scale Metal-Semiconductor Contacts

S.-H. Park[*], N. Kharche[**], D. Basu[*], Z. Jiang, S. K. Nayak[***], C. E. Weber[*], and G. Klimeck
Purdue University, West Lafayette, IN 47907, USA
[*]Process Technology and Device Modeling Group, Intel Corporation, Hillsboro, OR 97124, USA
[**]Brookhaven National Laboratory, Upton, NY 11973, USA
[***]Rensselaer Polytechnic Institute, Troy, NY 12180, USA
e-mail: park43@purdue.edu

INTRODUCTION

Progressive downscaling has allowed semiconductor industries to continuing improve the performance of integrated circuits (ICs) [1]. The downscaling adversely affects the performance of interconnects. Specifically, the resistivity of metal interconnects and metal-semiconductor contacts increases due to downscaling. The metal-semiconductor contact resistance, which acts as a parasitic source and drain contact resistance of a device is becoming a performance limiting factor as it takes larger fraction of the total on-state resistance [2]. Hence, the contact resistance must be reduced to meet ITRS performance requirements of future technology nodes.

As metal-semiconductor interface shrinks simultaneously as device shrinks, it becomes questionable if the resistivity still can meet the ITRS requirements when it reaches to the certain scaling limit (sub-10nm). Specific contact resistivity (ρ_C) is one of important factors affecting total contact resistance, and it is determined by important factors such as metal-semiconductor Schottky barrier height and semiconductor doping. This paper investigates the effects of contact geometry, Schottky barrier height, and doping concentration on the specific contact resistivity.

DEVICE DESCIPTION AND SIMULATION APPROACH

To gain substantial insight we chose simple 2-D and 3-D metal-semiconductor junctions (Fig. 1 (a)). The source region is a metal contact, and channel and drain regions are heavily n-doped Si contact pads (Fig. 1 (b)). The theoretical modeling of nanoscale structure demands a proper treatment of quantum effects such as the energy-level quantization caused by quantum confinement. Hence, a 2-D / 3-D quantum transport solver based on a self-consistent solution of the non-equilibrium Green's function (NEGF) and Poisson equations using the real-space effective mass approximation is used to simulate the metal-semiconductor devices. To investigate the transport property of a pure metal wire. The sp3d5 empirical tight-binding method is adapted to account for the full-band structure of the model [3].

RESULTS AND DISCUSSION

The specific contact resistivity and the system conductance are calculated (Fig. 2). The higher doping concentrations in the Si contact pad and lower Schottky barrier indeed result in a lower specific contact resistivity (Fig. 3). The measured specific contact resistivity starts increasing when the dimensions of the metal-semiconductor interface are smaller than 5nm in 2-D and increasing over an order of magnitude in the 3D case. (Fig. 2). The observed scaling effect of the specific contact resistivity can be explained by invoking the concept of the total transmission [4]. As a measure of conductance, the net current flowing from source to drain is computed as following equations,

$$I = \frac{2q^2}{h}\int dE \sum_n T(E)M(E)f(E_{FS}-E_{FD})$$

,where $2q^2/h$ is the quantum conductance. T(E) is the transmission probability, and M(E) is the number of transverse modes. Since a small bias, 10 mV, is applied across the device, the conductance can be expressed to $\Sigma T(E)M(E)$. The conductance decreases as the size of the metal wire decreases (Fig. 4 and Fig. 5). However, as the ballistic conductance of metal wire decreases linearly, the ρ_C is independent of the size of metal interconnect (Fig. 5). However, the reduced number of discrete modes across the Schottky barrier shows quantum confinement like effect in the contact pad region. The conductance between two different materials can be simply expressed to,

$$G = \frac{2q^2}{h}\int dE \sum_n T(E)\left(\frac{1}{\frac{1}{M_2(E)}-\frac{1}{M_1(E)}}\right)$$

When $M_1(E) >> M_2(E)$, the total system conductance depends on M_2. Hence, the interface downsaling, which means narrower carrier injection points in the contact pad, works as a bottleneck in the system. In addition, the structural mismatch ($W_M < W_{Si}$) causing wave function mismatch, and the mismatch effect leads transmission resonances generating fluctuations in the transmission lines (Fig. 4).

Conclusion and Outlook

The key finding of this work is that the specific contact resistivity increases significantly when metal-Si contact dimensions drop below 5 nm due to the reduced number of discrete modes available for conduction across the Schottky barrier. The absolute magnitude of this scaling effect can be mitigated by reducing the Schottky barrier.

Acknowledgement

This work was supported by Intel Corporation and MSD/FCRP. The use of computational resources provided by nanoHUB.org operated by the Network for Computational Nanotechnology and funded by NSF is acknowledged.

References

[1] ITRS. "International Technology Roadmap for Semiconductors," http://www.itrs.net/Links/2010ITRS/. [2] S. H. Park et al., "Performance Comparisons of III-V and Strained-Si in Planar FETs and Nonplanar FinFETs at Ultrashort Gate Lengh (12nm)," *IEEE Trans. Electron Devices*, 2012. [3] N. Kharche et al., "Crystallographic Orientation Depedent Ballistic Transport in Nanoscale Copper and Aluminium Wires", unpublished. [4] S. Datta, "Electronic Transport in Mesoscopic Systems," Cambridge, 2009.

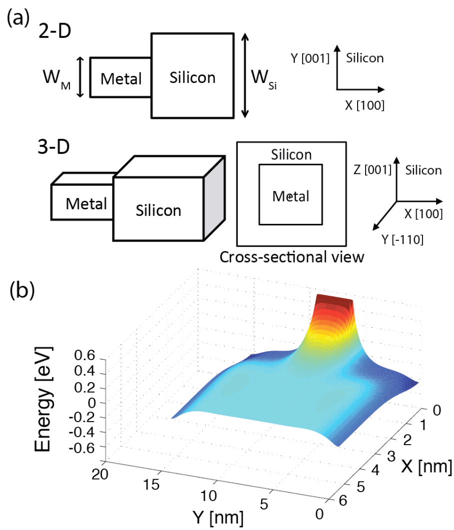

Fig. 1 (a) Schematics of the simulated contact structures (b) Potential profile of a contact model (W_M = metal-silicon interface width = 3 nm, W_{Si} = silicon width = 15 nm) and Schottky barrier height is set to 0.5 eV with $N_D = 2\times10^{20}$ cm^{-3}.

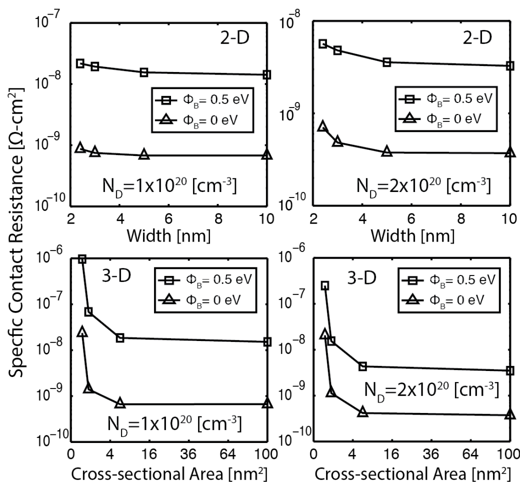

Fig. 2 Measured specific contact resistance for 2-D and 3-D structures for two given doping concentration N_D = 1×10^{20} cm^{-3} and 2×10^{20} cm^{-3} with Φ_B=0 eV sand 0.5 eV in semi-log scale. The dimension of metal wire is reduced from 10 nm to 2.4 nm while the dimension of contact pad is fixed at 15 nm in 2-D. The cross-section area of metal wire is varied from 10×10 nm^2 to 2.4×2.4 nm^2 in 3-D.

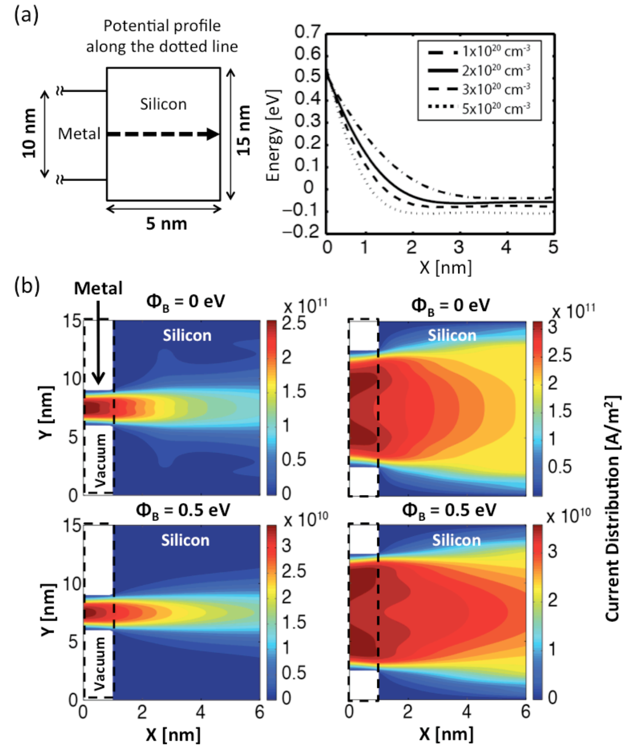

Fig. 3 (a) The potential profiles cut along the middle of structure in the transport direction in different doping concentrations (N_D = 1×10^{20} cm^{-3}, 2×10^{20} cm^{-3}, 3×10^{20} cm^{-3}, and 5×10^{20} cm^{-3}) with Φ_B = 0.5 eV (b) The current density spectrum from metal wire (W_M = 3 nm (left) and 10 nm (right) with fixed W_{Si} = 15 nm) to silicon pad with different Φ_B=0 eV and 0.5 eV and N_D = 2×10^{20} cm^{-3}.

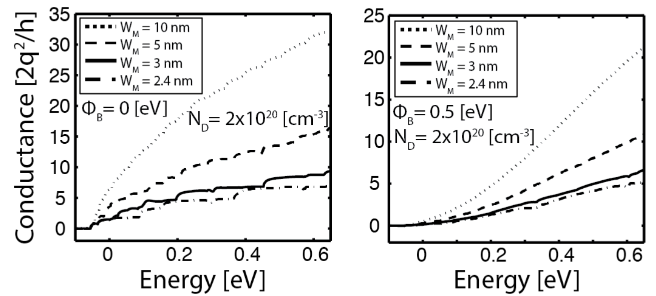

Fig. 4 Total transmission for 2-D structure (W_M = metal wire width, and W_{Si} = 15 nm) with Φ_B = 0 eV (left) and Φ_B = 0.5 eV (right) for N_D = 2×10^{20} cm^{-3}.

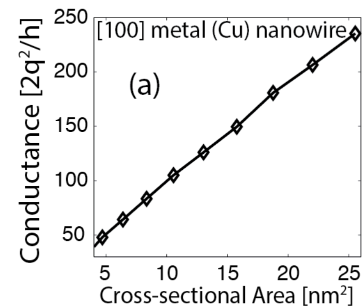

Fig. 5 The ballistic conductance of [100]-oriented Cu wires as a function of cross sectional area calculated using the sp^{3}d^5 tight-binding model.

Thickness dependent performance of (111) GaAs UTB nMOSFETs

K. Alam, S. Takagi, and M. Takenaka
Department of Electrical Engineering and Information Systems
The University of Tokyo, 7-3-1 Hongo, Bunkyo-ku, Tokyo 113-8656, Japan
e-mail: kalam@mosfet.t.u-tokyo.ac.jp, takagi@ee.t.u-tokyo.ac.jp

Electron transport in III-V semiconductors such as GaAs, InAs, GaSb, and InGaAs has drawn significant attentions due to high electron injection velocity (good side) and low density-of-states (DOS) (bad side) [1]–[3]. A solution to DOS bottleneck has been proposed by quantizing an ultra-thin-body (UTB) channel along the crystallographic <111> direction [3]–[6]. Using an atomistic tight binding (TB) top-of-the-barrier (ToB) model, Mehrotra *et al.* [4] have shown that a 2 nm thick (111) GaAs channel outperforms (100) Si and GaAs channels for an effective oxide thickness (EOT) larger than 0.3 nm. Studies on different orientations by Luisier [3] and Kim *et al.* [6] show that (111) GaAs and GaSb UTB channels outperform Si and Ge. In this work, the thickness dependent performance of a (111) GaAs UTB nMOSFET is studied using a ToB model that self-consistently solves $sp^3s^*d^5$ orbital basis Hamiltonian for electron density and two dimensional Poisson's equation for electrostatics. The Hamiltonian includes spin-orbit interaction and uses energy parameters of [7]. The device performance improves up to the UTB thickness of $\approx$ 3 nm and then it degrades.

A few conduction bands of (111) GaAs UTBs are shown in Fig. 1 for two different values of UTB thickness, T_{utb}. At thicker T_{utb}, the quantized L valley projects at a higher energy, Fig. 1(a), and the transport is primarily governed by the single Γ valley subband. With thinner T_{utb}, Fig. 1(b), the two valley subbands align in energy leading to many modes for transport.

The current-voltage characteristics for three T_{utb} are shown in Fig. 2. We use an EOT of 0.5 nm and a V_{DS} of 0.6 V. For performance comparison at the same gate bias, a potential barrier height of 0.5 eV is set at V_{GS} = 0 V for all the devices. At lower gate biases, the transport in 6.77 nm UTB is through the single mode from Γ valley (see Fig. 1 (a)). For 2.86 nm UTB, many modes from projected L valley get populated and the current is much higher. With increased bias, high energy modes of 6.77 nm UTB also get populated and the current is improved. For the 6.77 nm and 4.81 nm UTBs, the current at zero gate bias is almost same due to single mode transport. At intermediate biases, the current in 4.81 nm UTB is higher due to lower Γ-L energy separation. Finally, at very high gate biases, the current in both the UTBs is almost same due to significant population of the high energy modes.

In Figs. 3 and 4, we plot the current, electron sheet density, quantum capacitance, and the switching delay versus T_{utb} at a gate bias of 1.0 V. We choose this gate bias to make sure that all the devices operate in saturation. In the plots, the device performance improves with thinner channel until $T_{utb} \approx$ 3 nm. Beyond this thickness, the performance slightly degrades. This degradation is due to the double role of quantization. When $T_{utb} >$ 3 nm, the Γ-L energy separation is reduced with thinner UTB. This increases the number of available modes within the energy range of interest and the device performance is improved. When $T_{utb} <$ 3 nm, the lowest energy mode comes from L valley and the energy separation between the low energy modes is increased with thinner UTB. This reduces DOS, Fig. 5, and the device performance is degraded.

In summary, the double role of quantization is important in device design of (111) GaAs UTB nMOSFETs, especially for very thin channel.

Acknowledgment

This work was supported by Japan Society for Promotion of Sciences (JSPS) fellowship.

References

[1] M. Radosavljevic, B. Chu-Kung, S. Corcoran, G. Dewey, M. K. Hudait, J. M. Fastenau, J. Kavalieros, W. K. Liu, D. Lubyshev, M. Metz, K. Millard, N. Mukherjee, W. Rachmady, U. Shah, and R. Chau, "Advanced high-K gate dielectric for high-performance short-channel $In_{0.7}Ga_{0.3}As$ quantum well field effect transistors on silicon substrate for low power logic applications," in *Int. Electron Dev. Meet.* Baltimore, Maryland: IEEE, 2009, pp. 319–322.

978-3-901578-26-7 © 2013 Society for Micro- and Nanoelectronics

[2] M. Fischetti, L. Wangt, B. Yut, C. Sachs, P. M. Asbeck, Y. Taurt, and M. Rodwell, "Simulation of electron transport in high-mobility MOSFETs: Density of states bottleneck and source starvation," in *International Electron Devices Meeting*, 2007, pp. 109–112.

[3] M. Luisier, "Performance comparison of GaSb, strained-Si, and InGaAs double-gate ultrathin-body n-FETs," *Electron Dev. Lett.*, vol. 32, no. 12, pp. 1686–1688, 2011.

[4] S. Mehrotra, M. Povolotskyi, J. Lawy, T. Kubis, G. Klimeck, and M. Rodwell, "Design of high-current L-valley GaAs/$AlAs_{0.56}Sb_{0.44}$/InP(111) ultra-thin-body nMOSFETs," in *International Conference on Indium Phosphide and Related Materials*, University of California, Santa Barbara, 2012.

[5] M. Rodwell, W. Frensley, S. Steiger, E. Chagarov, S. Lee, H. Ryu, Y. Tan, G. Hegde, L. Wang, J. Law, T. Boykin, G. Klimek, P. Asbeck, A. Kummel, and J. Schulman, "III-V FET channel designs for high current densities and thin inversion layers," in *Device Research Conference (DRC)*, 2010, pp. 149–152.

[6] R. Kim, T. Rakshit, R. Kotlyar, S. Hasan, and C. E. Weber, "Effects of surface orientation on the performance of idealized III-V thin-body ballistic n-MOSFETs," *Electron Dev. Lett.*, vol. 32, no. 6, pp. 746–748, 2011.

[7] T. B. Boykin, G. Klimeck, R. C. Bowen, and F. Oyafuso, "Diagonal parameter shifts due to nearest-neighbor displacements in empirical tight-binding theory," *Phys. Rev. B*, vol. 66, no. 12, p. 125207, 2002.

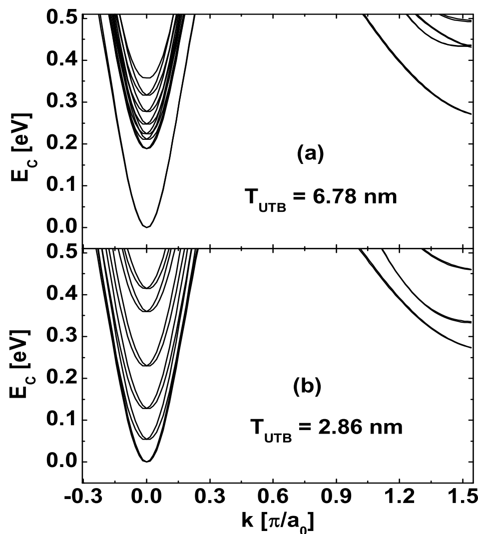

Fig. 1: A few conduction bands of the (111) GaAs UTB for two different values of UTB thickness. The conduction band bottom has been shifted to 0 for comparison. In the plots, positive k: $\Gamma - X$ and negative k: $\Gamma - L$.

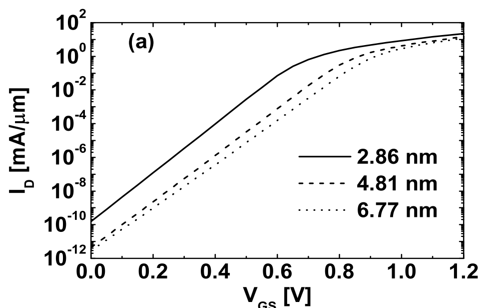

Fig. 2: Current-voltage characteristics for three different values of UTB thickness.

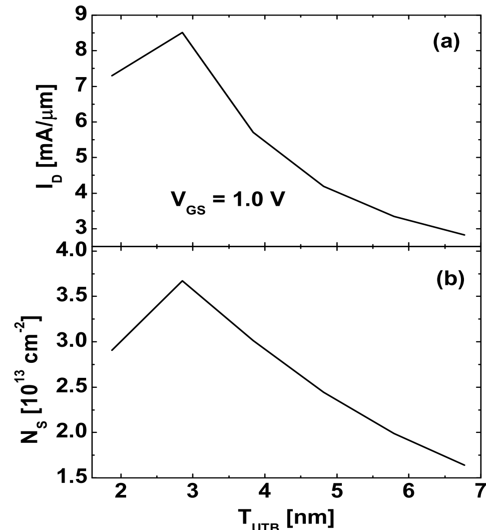

Fig. 3: Current and electron sheet density versus UTB thickness at a gate bias of 1.0 V.

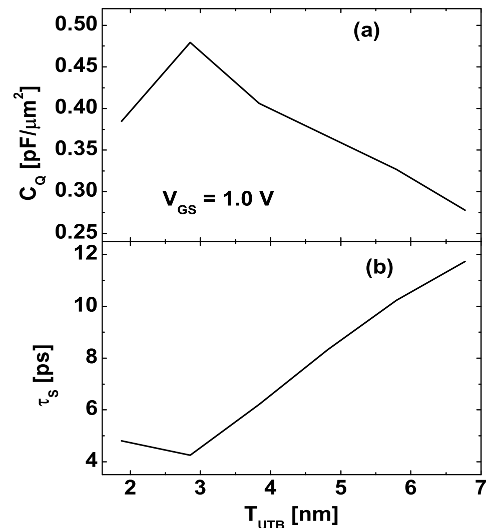

Fig. 4: Quantum capacitance and switching delay versus UTB thickness at a gate bias of 1.0 V.

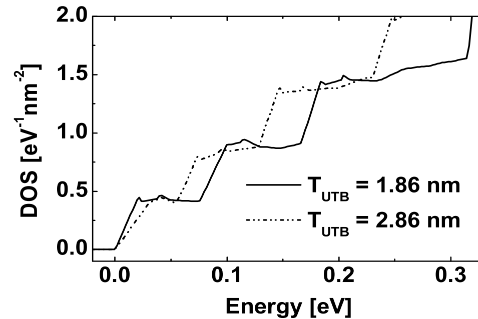

Fig. 5: Zero bias density of states at two different values of UTB thickness. Energy 0 is the conduction band bottom.

Quantum Simulation of III-V Double Gate Schottky Barrier MOSFETs

Jaehyun Lee, Yolum Lee, Howon Choi, and Mincheol Shin*
Dept. Electrical Engineering, Korea Advanced Institute of Science and Technology, Rep. of Korea
e-mail: mshin@kaist.ac.kr*

INTRODUCTION

Schottky barrier metal-oxide-semiconductor field-effect transistors (SB-MOSFETs) are one of the promising candidates for the future nano-scaled devices [1]. They have advantages of suppressing short channel effects due to low resistivity of ultra-shallow junction at source/drain. However, a major drawback of SB-MOSFETs is that on-state current (I_{on}) is considerably lower compared to conventional MOSFETs because SB-MOSFETs are operated by tunneling current (I_{tunn}) through SB [2]. In an attempt to enhance I_{on}, we proposed to adopt III-V materials as channel material such as InAs and GaAs which have small effective masses (m_{eff}), $0.023m_0$ and $0.063m_0$ in bulk, respectively. But the following issues are present with III-V SB-MOSFETs: III-V materials with narrow bandgap (E_g) such as InAs may suffer from high off-state current (I_{off}) [3], while those with wide E_g such as GaAs have a high SB height (SBH). In this work, we assess the performance limits of ultra-thin-body (UTB) III-V SB-MOSFETs compared with Si SB-MOSFETs.

SIMULATION APPROACH

The structure of double-gate UTB SB-MOSFETs is shown in Fig. 1. To describe the electron transport, the effective mass Hamiltonians were used with the effective masses adjusted by the $sp^3d^5s^*$ tight-binding method. The adjustment is crucial to properly take into account the quantization effect (QE) in UTB structure.

In this work, the electron transport was treated fully quantum mechanically because precise calculation of I_{tunn} is important in SB-MOSFETs. The electron density and potential were calculated by solving the non-equilibrium Green's function equation and Poisson's equation self-consistently [2]. Note that, although we focused on the electron transport in this work, we also calculated hole current to treat the ambipolar behavior of SB-MOSFETs and determine I_{off}. The six-band $k{\cdot}p$ Hamiltonian was used for hole transport calculation.

RESULTS AND DISCUSSION

The drain current (I_d) versus gate voltage (V_g) characteristics of InAs, GaAs, and Si SB-MOSFETs with T = 5nm are shown in Fig. 2. The gate length (L_g) is scaled as $L_g = 4T$, where T is a thickness of UTB, and equivalent oxide thickness (EOT) and SBH are 1nm and 0eV, respectively. The drain voltage (V_d) of 0.5V is applied.

Fig. 3 (a) shows I_d at the saturation region ($I_{d,sat}$) as W is decreased. $I_{d,sat}$ is defined as I_d when the minimum value of channel potential coincides with the value of potential at the top of drain-SB. Due to the low transconductance (See Fig. 2.), $I_{d,sat}$ of III-V SB-MOSFETs is less than that of Si SB-MOSFETs, which is contrary to expectation. Note that $I_{d,sat}$ of III-V SB-MOSFETs increases with W while that of Si SB-MOSFETs decreases. The latter is due to the usual behavior that the gate controllability becomes worse as W is increased. The reason for the former is the strong QE occurs due to small m_{eff}, which makes the effective SBH to increase and the number of subband to decrease. See Figs. 3 (c) and (d). The above QE can also explain that $I_{d,sat}$ of InAs SB-MOSFETs increases more steeply than that of GaAs SB-MOSFETs as shown in Fig. 3 (b).

The I_{on} and I_{off} versus W are shown in Fig. 4 (a) for the three channel materials. I_{on} was calculated with V_d after adjusting the gate work function such that I_{off} = 0.1μA/μm. If I_{off} does not satisfy with the criteria, it was measured by the lowest I_d in the ambipolar current graph. At T = 10nm, both InAs and GaAs SB-MOSFETs show higher I_{on} in comparison to Si SB-MOSFETs. However, InAs SB-MOSFETs show drastic decrease of I_{on} upon reduction of T. On the other hand, as shown in Fig.

978-3-901578-26-7 © 2013 Society for Micro- and Nanoelectronics

4 (b), I_{on}/I_{off} of InAs SB-MOSFETs becomes remarkably worse as T is increased, due to the fact that I_{off} increases sharply.

In InAs SB-MOSFETs, high I_{off} seriously limits the performance. We, therefore, propose to use gate underlap as a solution to improve the I_{off} behavior. Fig. 5 (a) shows the dependence of the I_{on}, I_{off}, and I_{on}/I_{off} on the gate position with the channel length (L_{ch}) of 25nm. Regardless of the gate position, SB-MOSFETs with gate underlap make both I_{on} and I_{off} to decrease. However, when the gate is placed near the source (underlap length: L_{u1} = 0nm and L_{u2} = 5nm, respectively; see Fig. 1 for the definition of L_{u1} and L_{u2}), I_{on} is comparable to the case with no underlap while I_{off} becomes lower. The dependence of I_{on}, I_{off}, and I_{on}/I_{off} of InAs SB-MOSFETs on L_{u2} is shown in Figs. 5 (b) and (c). We conclude that, as L_{ch} is increased (with L_{u1} and L_g fixed), I_{on}/I_{off} is improved exponentially.

Fig. 5 (d) shows the I_{on} versus SBH for GaAs and Si SB-MOSFETs with T = 5nm. Recall that SBH is set to 0V for all the materials considered in this work. Since the typical SBH for GaAs is 0.6eV, methods to lower SBH should be devised.

CONCLUSION

For the purpose of enhancing the performance of SB-MOSFETs, III-V materials having small m_{eff} such as InAs and GaAs are investigated. We have found that the enhancement in III-V SB-MOSFETs can be limited by I_{off} for narrow E_g materials. As a solution to overcome it, gate underlap has been suggested and its effect on the improvement on I_{off} has been investigated.

REFERENCES

[1] J. M. Larson and J. Snyder, *Overview and status of metal S/D Schottky barrier MOSFET technology*, IEEE Trans. Electron Devices **53**, 5, pp. 1048-1058 (2006).

[2] J. Guo and M. S. Lundstrom, *A computational study of thin-body, double-gate, Schottky barrier MOSFETs*, IEEE Trans. Electron Devices **49**, 11, pp. 1897-1902 (2002)

[3] Y. Zhao, D. Candebat, C. Delker, Y. Zi, D. Janes, J. Appenzeller, and C. Yang, *Understanding the Impact of Schottky Barriers on the Performance of Narrow Bandgap nanowire Field Effect Transistors*, Nano Lett. **12**, pp. 5331-5336 (2012)

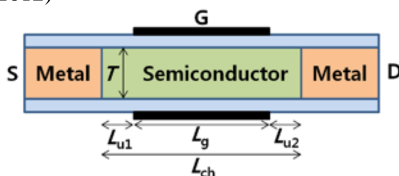

Fig. 1. The schematic diagram of UTB SB-MOSFETs.

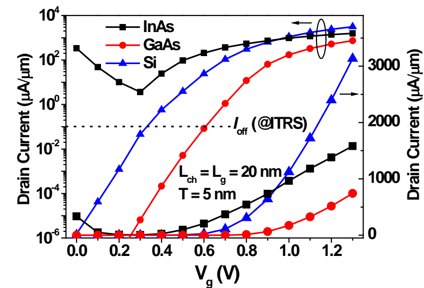

Fig. 2. I_d-V_g characteristics of InAs, GaAs, and Si SB-MOSFETs with T = 5 nm and L_g = 20 nm, displayed in the log scales (left axis) and linear scales (right axis).

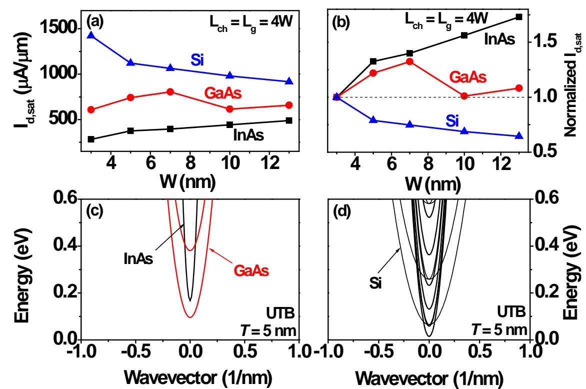

Fig. 3. (a) $I_{d,sat}$ and (b) normalized $I_{d,sat}$ of InAs, GaAs, and Si SB-MOSFETs are shown as W varies from 13nm down to 3nm. The figure shows the conduction subband structure of 5 nm thickness with (c) InAs, GaAs, and (d) Si channel. Energy is measured with reference to the bulk conduction band minima.

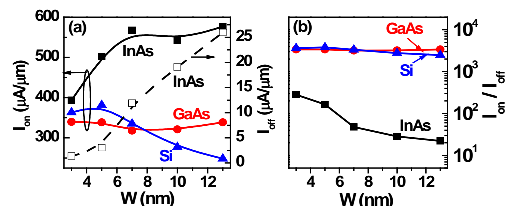

Fig. 4. The dependence of (a) I_{on}, I_{off} (InAs only), and (b) I_{on}/I_{off} on W is shown.

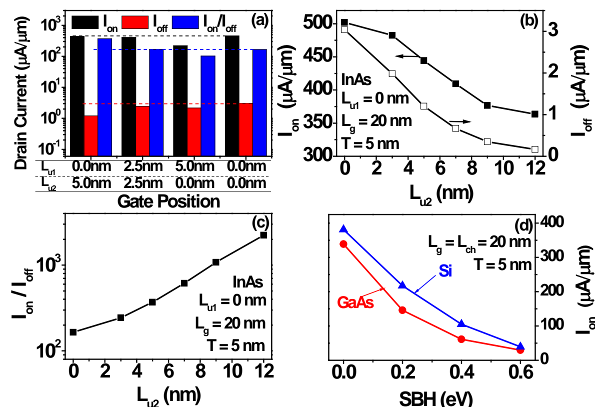

Fig. 5. (a) The graph shows the dependence of I_{on}, I_{off}, and I_{on}/I_{off} of InAs SB-MSFETs with gate underlap (L_{ch} = 25nm) and no underlap (L_{ch} = L_g = 20nm) on the gate position. (b) I_{on}, I_{off}, and (c) I_{on}/I_{off} versus L_{u2} of InAs SB-MOSFETs with asymmetric gate underlap are shown. (d) I_{on} of GaAs and Si SB-MOSFETs is shown as SBH varies from 0.0eV to 0.6eV.

Reduction of Self-Heating Effect in CMOS Inverter of Vertical MOSFET by Common-Gate Layout

A. Wang[1, 2], and T. Endoh[1, 2]
[1]Graduate School of Engineering, Tohoku University, [2]JST-CREST
Aramaki Aza-Aoba 6-6, Aoba-ku, Sendai, Japan, 980-8579, E-mail: endoh@riec.tohoku.ac.jp

INTRODUCTION

Very Large Scale Integration (VLSI) shows higher performance by improving the density year by year. However, higher density of VLSI induces a large current density, leading the increase of temperature in a circuit, which will degrade the performance of the circuit [1]. Therefore, it is important to restrain the self-heating effect in a circuit. One of efficient solvents to this problem is designing a high efficient heat dissipation layout of the circuit considering self-heating effect. In this paper, 22nm technology node CMOS Inverter composed of Vertical MOSFET [2,3] is investigated considering both electrical and thermal properties. It is clarified by 3D device simulation results that Vertical NMOS drain side is the hot spot and gate is one of the dominant heat radiation routes from the hot spot. It is also shown that common-gate layout have a thermal advantage than separate-gate layout by dissipating much heat from the hot spot.

SIMULATION METHOD

Figure 1 (a) and (b) show the layout of common-gate CMOS Inverter and separate-gate CMOS Inverter of Vertical MOSFET in the same footprint ($17F \times 7F$) . Table I shows the parameters used in the 3D device simulation. We assume the most severe thermal situation for the circuit, the case that all adjacent circuits are active. We attached thermal resistances equivalent to 12 layers of interconnect above the top of the simulation area (M1 metal) and 50μm Si substrate below the bottom of the simulation area.

RESULTS AND DISCUSSION

Figure 2 shows the power of two layout types are the same under dc operation when input voltage (*Vin*) from 0.4V to 0.55V, which shows the most high power due to the through current (I_T). When *Vin* is 0.46V, NMOS drain side shows the peak temperature (423K) as shown in Fig. 3. This is due to the difference of current density between NMOS and PMOS. It is important to release the heat from NMOS drain side, the hot spot in entire simulation area to maintain the performance of the circuit. Figure 4 shows the heat flux distribution when *Vin* is 0.46V. As from this figure, the heat of NMOS drain side dissipates via high thermal conductivity material tungsten (W) and silicon (Si) area. Particularly, in our simulation situation, dominant heat radiation routes are the paths toward drain contact, source contact and gate. Conducting much heat via gate, common-gate layout shows around 3% reduction of temperature raise than the separate-gate layout as shown in Fig. 5.

CONCLUSION

The self-heating effect in CMOS Inverter composed of Vertical MOSFET is analysed for the first time. It is shown that NMOS drain side is the hot spot in the circuit. Thus, it is important to dissipate heat from the NMOS drain side. One of the dominant heat radiation routes from NMOS drain side is gate. Thus, the common-gate layout for CMOS Inverter composed of Vertical MOSFET shows 3% reduction of temperature raise by conducting much heat from NMOS drain side to PMOS via gate, which is important to maintain high reliability of the circuit.

ACKNOWLEDGEMENT

This work has been supported in part by a grant from “Research of Innovative Material and Process for Creation of Next-generation Electronics Devices” of CREST under the Japan Science and Technology Agency (JST).

REFERENCES

[1] Semenov, O. et al., IEEE Transactions on , vol.6, no.1, pp. 17- 27, March 2006

[2] T. Endoh, T. Nakamura, and F. Masuoka, IEICE Trans. on Electronics, Vol.E80-C, No.7, pp.911-917, July 1997

[3] T. Endoh, K. Tanaka, Y. Norifusa, IEICE Trans. Electron, Special Issue on Fundamentals and Applications of Advanced Semiconductor Devices,2008

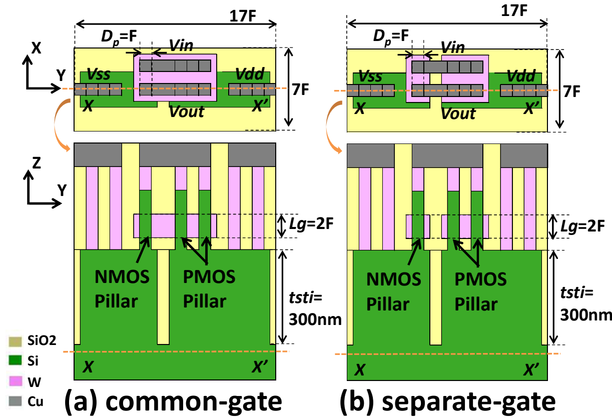

Fig. 1. (a) Layout of Common-Gate CMOS Inverter and (b) Separate-Gate CMOS Inverter of Vertical MOSFET.

Table I. Parameters for this simulation.

Parameters	
Feature Size (*F*)	22nm
Pillar Diameter (*Dp*)	*F* (=22nm)
Gate Length (*Lg*)	2*F* (=44nm)
Gate Oxide Thickness (*tox*)	1.2nm
STI thickness (*tsti*)	300nm
Ambient Temperature (*Tamb*)	400K
Power Supply (*Vdd*)	0.9V

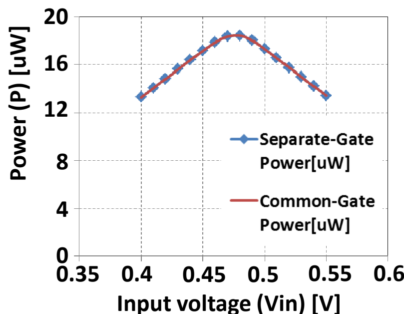

Fig. 2. Power for Vertical CMOS Inverter under dc operation due to the through current, where $P = Vdd \times I_T$. Here, Vdd is supply voltage and I_T is through current.

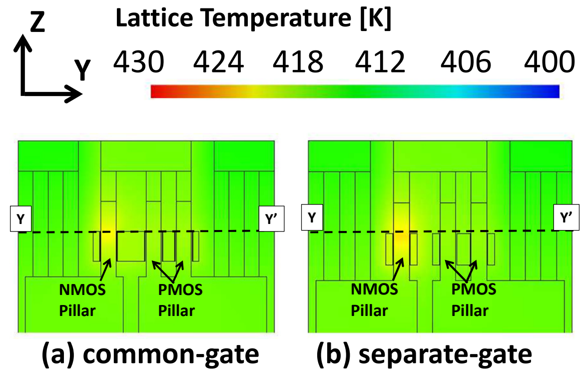

Fig. 3. Lattice temperature distribution under dc operation for (a) common-gate layout and (b) separate-gate layout when the bias recorded the highest peak temperature (Vin = 0.46V).

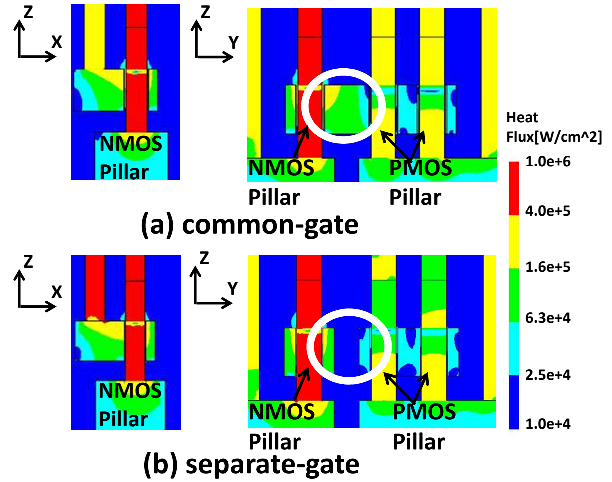

Fig. 4. Heat flux distribution for (a) common-gate layout and (b) separate-gate layout when the bias recorded the highest peak temperature (Vin = 0.46V).

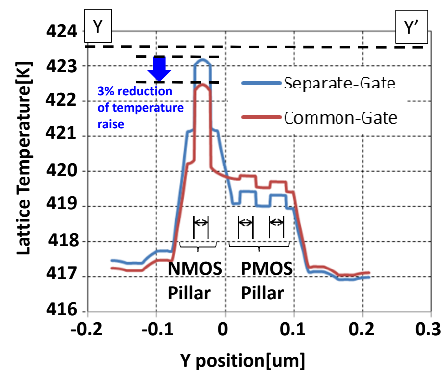

Fig. 5. Lattice temperature distribution for the cross-sectional view along the line Y-Y' in Fig. 3, under dc operation when the bias recorded the highest peak temperature (Vin = 0.46V), temperature raise: the rise of temperature from 400K.

A Compact Model for Wire-Type Tunnel FETs Considering Tunneling Path Lengths

Koichi Fukuda, Takahiro Mori, Wataru Mizubayashi, Yukinori Morita,
Akihito Tanabe, Meishoku Masahara, Tetsuji Yasuda, Shinji Migita, and Hiroyuki Ota
Collaborative Research Team Green Nanoelectronics Center (GNC),
National Institute of Advanced Industrial Science and Technology (AIST)
16-1 Onogawa, Tsukuba, Ibaraki 305-8569, JAPAN

Tunnel FET (TFET) is one of the key devices for low-power applications beyond CMOS [1]. However studies of TFET circuits are still in early stage because of the lack of a TFET compact model. Authors have reported a compact model of TFETs based on the nonlocal band to band tunneling (BTBT) model [2]. In this paper, the model is expanded to fin (double gate) and wire-type (cylinder) TFETs.

In the previous model in ref. [2], tunneling path is divided into two parts, vertical path at source gate overlap region, and horizontal path along gate insulator interface as shown in fig.1. The model agrees well with measured IV-curves (fig.2) of SOI-type planar TFETs developed by our group [3].

Since the key difference of the present model is the lateral potential profile along the gate insulator interface, the vertical profile considered in the previous work is not discussed in this paper. In our model, the potential profile is expressed by position dependent capacitances of each point along the gate insulator interface given by

$$\psi(x) = \frac{V_{source} \cdot C_{source}(x) + V_{gate} \cdot C_{gate}(x)}{C_{source}(x) + C_{gate}(x)} \quad (1)$$

where x denotes the distance from the source junction. The source and the gate capacitances of each point are obtained by numerical simulations and fitted to the following equations,

$$C_{gate}(x) \sim \frac{ax+b}{x+c} + F_{correction}(x) \quad (2)$$

$$C_{source}(x) \sim \frac{d}{x^e + f} \cdot G_{correction}(x) \quad (3)$$

Where *a~f...* are fitting parameters and *Fcorrection* and *Gcorrection* are correction functions to realize better accuracy. Simulated and fitted capacitances are compared in fig.3. Strong interaction is observed between the two capacitance components. This is the reason why eq. (2) and (3) require correction terms. Potential profiles obtained from the model are compared with simulations in fig.4. Wire-type TFET provides steeper potential profiles than fin-type does, and the steepness is increased by decreasing their feature sizes.

The tunnel distance $\lambda_{tunnel}(x)$ is obtained by

$$\psi(x + \lambda_{tunnel}(x)) = \psi(x) + E_g \quad (4)$$

where Eg is the bandgap. This $\lambda_{tunnel}(x)$ is used to calculate BTBT rates using Kane's formula.

$$G_{BTBT}(x) = A \cdot E^p \cdot exp\left(-\frac{\lambda_0}{\lambda_{tunnel}(x)}\right) \quad (5)$$

The drain current of TFET is obtained by,

$$I_d = \int G_{BTBT} dV \quad (6)$$

I-V curves of fin, wire and SOI-type silicon TFETs predicted by the present model are shown in fig.5. Steepness of the curves are better in an order of Wire > Fin > SOI. Drain saturation currents *Idsat* at the same gate bias is plotted as a function of fin-thicknesses or wire-diameters in fig.6. It should be mentioned that wire-type TFETs provide larger currents even in large wire diameters such as 50nm. This comes from the fact that wire-insulator interfaces are surrounded by the gate.

Eq. (1)~(6) are ready for implementations to our compact model of TFET described by Verilog-A languages. Thus we have built a basis for a set of TFET compact models consistent for bulk, SOI, Fin and Wire types.

ACKNOWLEDGEMENT

This research is granted by JSPS through FIRST Program initiated by CSTP.

REFERENCES

[1] Adrian M. Ionescu, Heike Riel, Nature 479, pp.329–337, 2011.
[2] K.Fukuda et al., Extended Abstract of SSDM, p.799 ,2012.
[3] T.Mori et al., Extended Abstract of SSDM, p.74, 2012.

978-3-901578-26-7 © 2013 Society for Micro- and Nanoelectronics

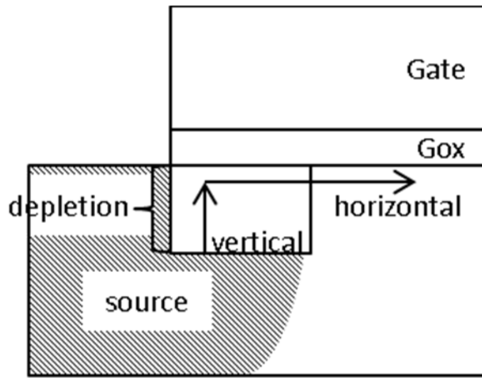

Fig. 1. Concept of the path length assumption in our model. The tunnel path is divided into two parts. This paper focuses on the horizontal tunnel path.

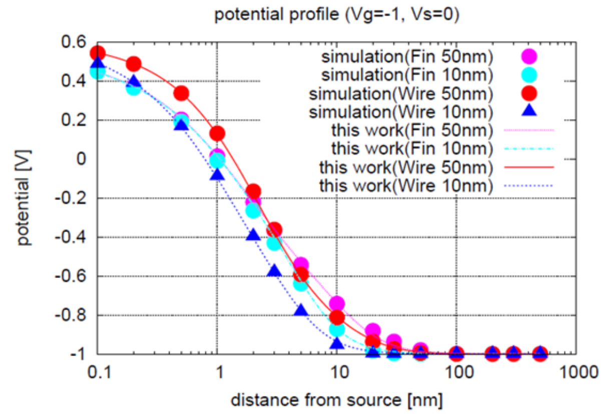

Fig. 4. Lateral potential profile compared with numerical simulation results. Potential profiles of wire-TFETs are steeper than those of fin-TFETs.

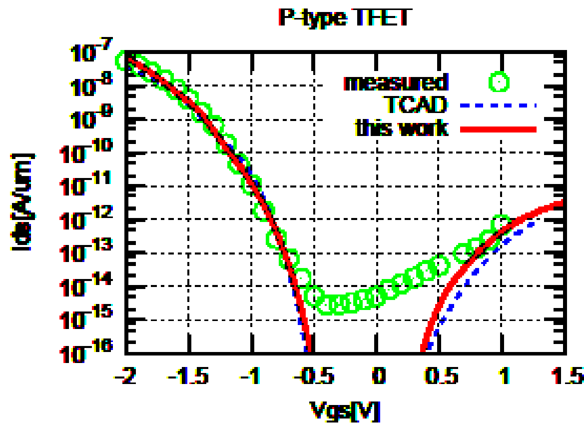

Fig. 2. Comparison of our model in ref. [3] with a measured IV curve of TFET fabricated by our group.

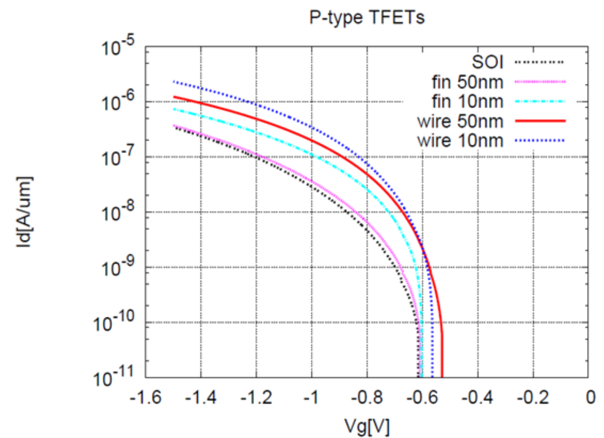

Fig. 5. Id-Vg characteristics predicted by the present model. Scaling merit is observed stronger in wire-TFETs.

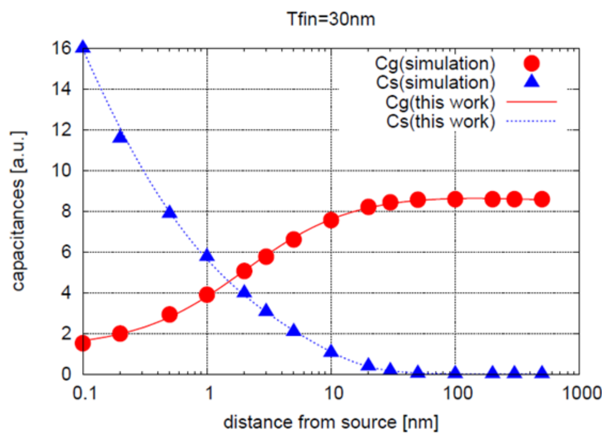

Fig. 3. Capacitances of the model and simulation results. Source and gate capacitances affect each other.

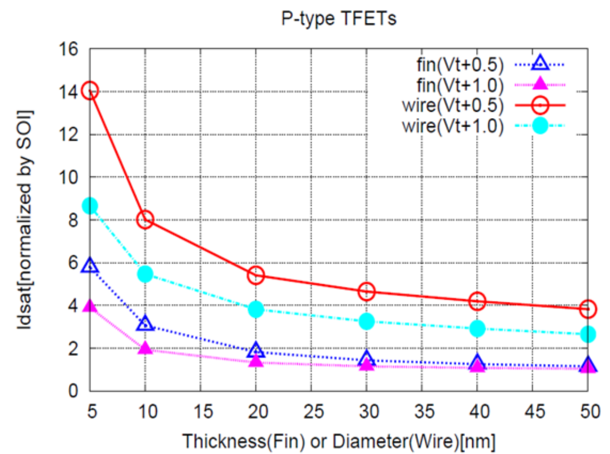

Fig. 6. Size scaling merits of saturation current at $Vg=Vt-0.5$, $Vt-1.0$ (Vt @ $Id=10^{-11}$[A/um]) of fin and wire-type TFETs. Currents are normalized by those of SOI-TFETs.

Band offsets of $Al_xGa_{1-x}As$/GaAs heterojunction from atomistic first principles

Yin Wang*§, Ferdows Zahid*, Yu Zhu†, Lei Liu†, Jian Wang*, and Hong Guo‡*
*Department of Physics and the center of theoretical and computational physics,
The University of Hong Kong, Pokfulam Road, Hong Kong SAR, China
†Nanoacademic Technologies, Montreal, PQ, Canada, H3A 2T8
‡Center for the Physics of Materials and Department of Physics,
McGill University, Montreal, PQ, Canada, H3A 2T8
§email:yinwang@hku.hk

The properties of III-V compound semiconductors and their heterojunctions have been relentlessly investigated due to their wide-ranging applications in electronic and optoelectronic technologies. One of most important electronic property of heterojunctions is the band offset which describes the relative alignment of the electronic bands across the junction interface. Accurate determination of band offsets is critical for understanding quantum transport properties of the heterojuncton. For many III-V materials systems, the band offset has been carefully measured experimentally.[1]

On the other hand, theoretical calculations of band offset have proven to be a serious challenge. This is because first principles method of density function theory (DFT) with local-density approximation (LDA) and generalized gradient approximation (GGA) underestimates the band gap (E_g) of semiconductors. Without a correct calculation of E_g for individual semiconductors, the calculated band offset between two semiconductors can be problematic. Another theoretical difficulty is when there are impurities: the predicted physical results must be averaged over multitudes of impurity configurations which is extremely costly in computation.

Considerable theoretical efforts have been devoted in the literature to correctly predict E_g. Apart from the GW and hybrid functional methods, for calculating E_g of pure semiconductors, the recently proposed modified Becke Johnson (MBJ) semilocal exchange was shown to give quite accurate values for many compounds with "cheap" computational cost.[2] To deal with the prohibitively large computation required for calculating configuration average for doped semiconductors, one wishes to compute the averaged physical quantity in one-shot without individually computing each impurity configuration as in the super-cell approach. In this regard, a widely used technique is the coherent potential approximation (CPA)[3] as implemented in Korringa-Kohn-Rostoker or linear muffin-tin orbital (LMTO)[4] DFT methods. Very recently, Ref.[5] has combined CPA with MBJ and reported the calculation of E_g for the semiconductor $In_xGa_{1-x}N$, the results are in excellent agreement with the measured data for the entire range of $x = 0$ to 1.

In this work, we employ the CPA-MBJ first principles approach as implemented in the Nanodsim[6] software package to quantitatively calculate the band offsets of two semiconductors with impurity doping. In particular, we consider the most important heterojucntion, between GaAs and $Al_xGa_{1-x}As$. Our calculated E_g of $Al_xGa_{1-x}As$ for the entire x range, and the calculated band offsets of the heterojunctions, are all quantitatively and excellently compare with the experimental data.

REFERENCES

[1] I. Vurgaftman, J.R.Meyer, and L.R. Ram-Mohan, J. Appl. Phys. **89**, 5815 (2001).
[2] F. Tran and P. Blaha, Phys. Rev. Lett. **102**, 226401 (2009).
[3] P. Soven, Phys. Rev. **156**, 809 (1967).
[4] I. Turek, V. Drchal, J. Kudrnovský, M. Šob, and P. Weinberger, *Electronic Structure of the Disordered Alloys, Surfaces and Interfaces* (Kluwer, Boston, 1977).
[5] M. César, Y. Ke, W. Ji, H. Guo, and Z. Mi, Appl. Phys. Lett. **98**, 202107 (2011).
[6] For details of the NEGF-DFT code with CPA-MBJ, see Nanoacademic Technologies, http://nanoacademic.ca/.

978-3-901578-26-7 © 2013 Society for Micro- and Nanoelectronics

TABLE I

ENERGIES OF THE CONDUCTION BAND MINIMA AT THE Γ, X, AND L POINTS WITH RESPECT TO THE VALENCE MAXIMUM AT THE Γ POINT IN UNITS OF ELECTRON VOLT. THE COLUMN OF LDA^v WERE OBTAINED BY THE VASP ELECTRONIC PACKAGE USING LDA, OTHER RESULTS WERE BY NANODSIM WHICH IMPLEMENTS THE DFT WITHIN TB-LMTO APPROACH. THE LAST COLUMN ARE THE EXPERIMENTAL VALUES FROM REF.[1].

material	Eg	LDA^v	LDA	MBJ	Expt.[1]
GaAs	E_g^Γ	0.493	0.761	1.518	1.519
	E_g^X	1.334	1.346	1.960	1.981
	E_g^L	0.948	1.100	1.691	1.815
AlAs	E_g^Γ	2.014	2.300	3.099	3.099
	E_g^X	1.312	1.307	2.258	2.24
	E_g^L	2.086	2.191	2.835	2.46

TABLE II

USING THE CPA-MBJ APPROACH IN THE NANODSIM ELECTRONIC PACKAGE, THE FOLLOWING TABLE LISTS THE CALCULATED VBO AND CBO OF GAAS/$AL_xGA_{1-x}AS$ HETEROJUNCTION.

x	0.1	0.2	0.3	0.4	0.5
VBO	0.070	0.114	0.167	0.222	0.280
CBO	0.050	0.145	0.238	0.276	0.230
x	0.6	0.7	0.8	0.9	1.0
VBO	0.337	0.397	0.459	0.532	0.593
CBO	0.210	0.190	0.167	0.161	0.148

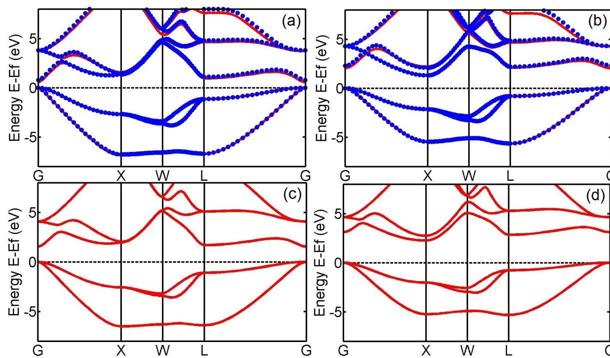

Fig. 1. (a,b) The band structures obtained with LDA: (a) for GaAs, (b) for AlAs. Red line is obtained by VASP, blue dots obtained by Nanodsim. A perfect agreement of the valence bands and a very good match of the conduction bands between these methods indicate that the TB-LMTO approach (Nanodsim) is quite accurate in calculating the physical properties of these materials. However, the band gaps were underestimated by LDA. (c,d) The band structures calculated with MBJ by Nanodsim: (c) for GaAs and (d) for AlAs. The MBJ band gaps are in good agreement with the experimental values at the Γ and X points, and within 7% for GaAs and 15% for AlAs to the experimental values at the L point, see Table I.

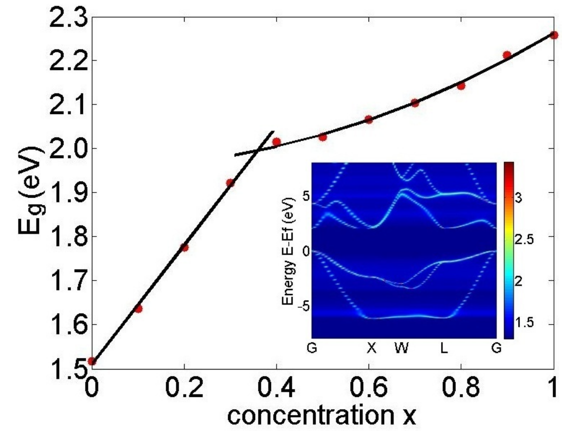

Fig. 2. The calculated band gaps of $Al_xGa_{1-x}As$ versus x by the CPA-MBJ approach. The two solid lines are fitting to the data in the two ranges of x. The alloy material changes from a direct-gap semiconductor to an indirect-gap one at a crossover point ($x \sim 0.36$) where the conduction band minima at Γ and X have the same energy value. Inset: the calculated DOS for the alloy $Al_{0.36}Ga_{0.64}As$ in logarithmic scale as a function of momentum k and energy E, revealing a broadened "band structure". The "conduction band" minima at Γ, X, and L points have essentially the same energy value for this alloy at $x \sim 0.36$.

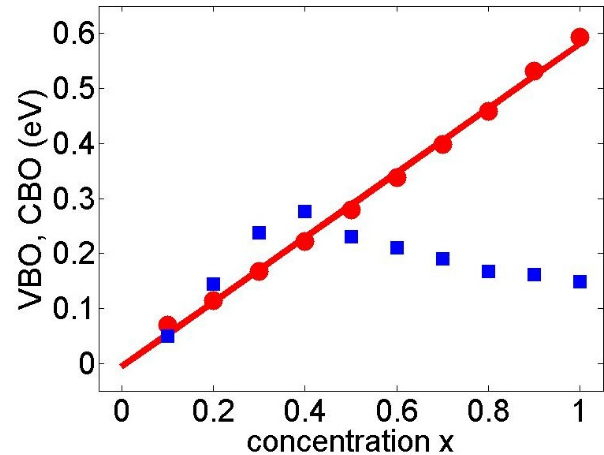

Fig. 3. Valence band offset (red dot) and conduction band offset (blue square) at different concentration x. The red line shows the linear fitting of the VBO, $VBO(x) \simeq 0.587x$ eV, which agrees reasonably with the experimental observation of $VBO(x) \simeq 0.55x$ eV. The GaAs/$Al_xGa_{1-x}As$ heterojunctions have the straddling type gap - the valence band maximum of GaAs is higher, while its conduction band minimum is lower.

Resistive Switching in RRAM Devices through First Principles Calculation: Oxygen Vacancy-Induced Electron Conduction Path in HfO_2

Susan Meñez Aspera, Hideaki Kasai, Hirofumi Kishi, Nobuyoshi Awaya*, Shigeo Ohnishi*, and Yukio Tamai*
Department of Applied Physics, Osaka University, Suita, Osaka 565-0871, Japan
*Corporate Research and Development Group, Sharp Corporation, 1 Asahi, Daimon-cho, Fukuyama 721-8522, Japan
e-mail: kasai@dyn.ap.eng.osaka-u.ac.jp

INTRODUCTION

The electrically induced nanoscale resistive switching in resistance random access memory (RRAM) devices gains considerable attention as a promising non-volatile memory device [1]. From among the different structures of RRAM devices, the metal-insulator-metal sandwiched type structure mostly incorporates with it a transition metal oxide (TMO) insulator material that alters its resistive property upon subject to moderate amount of set and reset pulse voltage. This "ON-OFF" resistive switching has been exemplified in various experimental studies [1,2] but the basic mechanism at the atomic level is still unclear. Here, we employed first principles calculation based on density functional theory (DFT) to analyze the mechanism of resistive switching through a known TMO used in RRAM devices, HfO_2.

RESISTIVE SWITCHING THROUGH OXYGEN VACANCIES

Experimental reports related to determining the switching mechanism in TMO-based RRAM [2] shows the existence of rowed (aligned) oxygen vacancies within the bulk TMO material upon subject to a relatively large amount of forming voltage. This causes change in the resistive property of the TMO from having insulator-like to having metallic-like properties. Thereafter, sufficiently small amount of set and reset pulse voltage is needed for the resistive switching. Therefore, the presence of rowed oxygen vacancies in HfO_2 was analyzed using DFT where results of the total density of states (TDOS) plots for bulk HfO_2 with rowed oxygen vacancies (Fig. 1) and plus charge carrier trapping (Fig.2) shows metallic properties [3]. This electron conduction path was also confirmed through the partial charge density distribution (Fig. 3) along the band crossing the Fermi level. Moreover, it was confirmed from the electrode(Ta)-TMO interaction that the layers of the TMO near the electrode interface have metallic properties with and without the presence of oxygen vacancies (Fig. 4). We thereby proposed a mechanism of resistive switching (Fig. 5) where oxygen vacancy migration from the interface layers to the bulk of the TMO HfO_2, and vice versa, determines the resistive property of the TMO.

CONCLUSION

We have used first principles calculation based on DFT to propose a mechanism of resistive switching in a TMO-based RRAM. The proposed mechanism is based on the presence of continuously aligned oxygen vacancies with charge carrier trapping and its migration between the electrode-TMO interface and its bulk.

REFERENCES

[1] R. Waser, and M. Aono, *Nanoionics-based resistive switching memories*, Nature Materials **6**, 833 (2007).
[2] P. Gonon, M. Mougenot, C. Vallée, C. Jorel, V. Jousseaume, H. Grampeix, and F. El Kamel. *Resistance switching in HfO_2 metal-insulator-metal devices.* Journal of Applied Physics **107**, 074507 (2010).
[3] S.M. Aspera, H. Kasai, H. Kishi, N. Awaya, S. Ohnishi, and Y. Tamai. *Realization of the Switching Mechanism in Resistance Random Access Memory™ Devices: Structural and Electronic Properties Affecting Electron Conductivity in a Hafnium Oxide-Electrode System Through First-Principles Calculations*. Journal of Electronic Materials **42**, 143 (2013).

978-3-901578-26-7 © 2013 Society for Micro- and Nanoelectronics

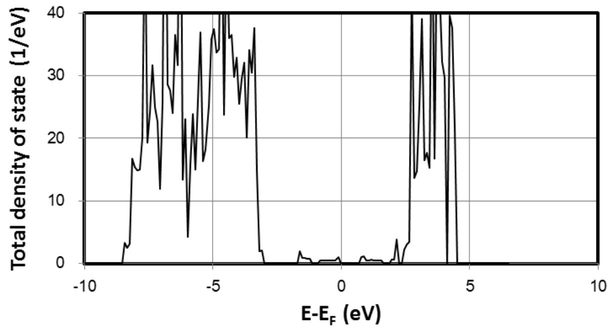

Fig. 1. Total density of states (TDOS) vs energy relative to the Fermi level (E-E_F) for bulk HfO_2 with rowed oxygen vacancies.

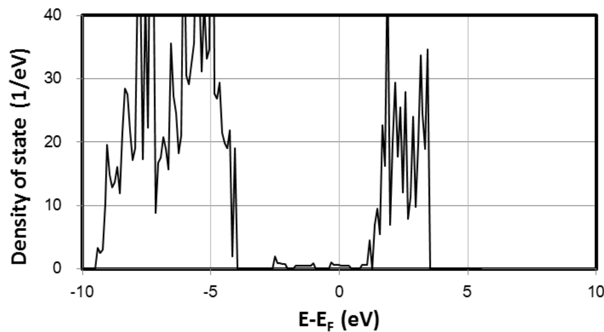

Fig. 2. Total density of states (TDOS) vs energy relative to the Fermi level (E-E_F) for bulk HfO_2 with rowed oxygen vacancies and charge carrier trapping.

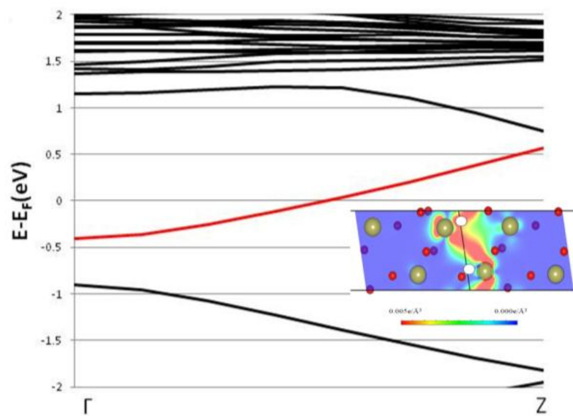

Fig. 3. Band structure plot near the Fermi level of bulk HfO_2 with rowed oxygen vacancies and charge carrier trapping. The highlighted red line shows the band passing through the Fermi level. *Inset*: partial charge density distribution plot for the band (shown in red) passing through the Fermi level. Green, red, and white spheres represents Hf atoms, O atoms and O vacancies, respectively. The colors indicate electron densities of until 0.005 e/Å^3.

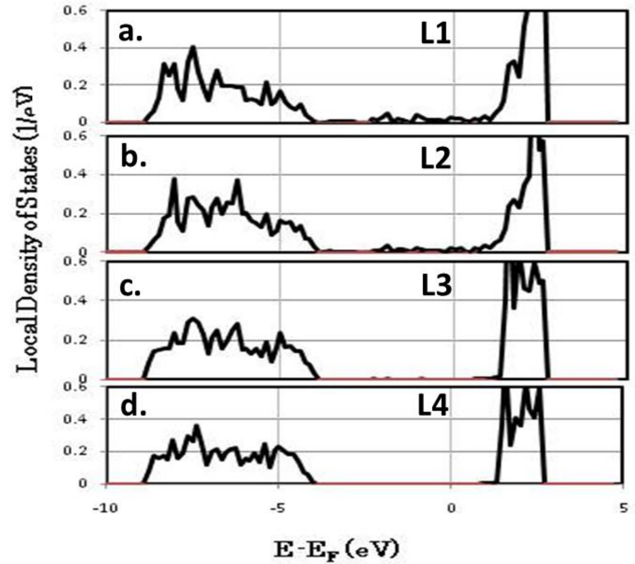

Fig. 4. Local density of states (LDOS) vs the energy relative to the Fermi level for HfO_2 layers (L1, L2, L3, and L4) near the electrode(Ta)-HfO_2 interface. L1 depicts the LDOS of the HfO_2 layer at the interface whereas L4 depicts the LDOS of the 4th layer of the HfO_2 bulk from the interface.

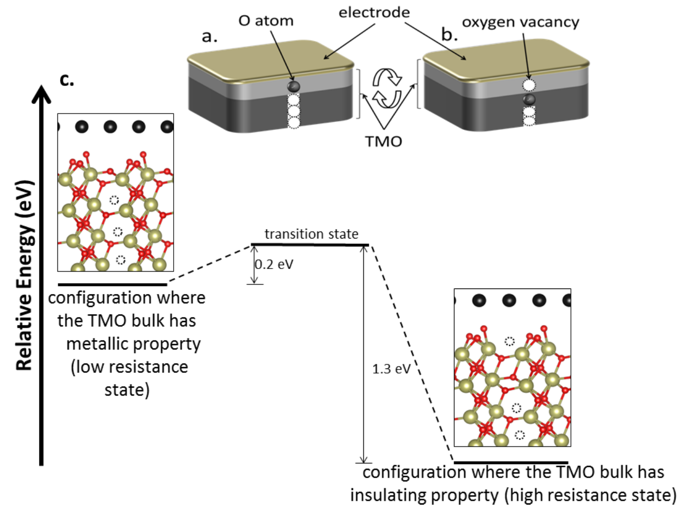

Fig. 5. Schematic illustration of the switching mechanism: a. high resistance state, b. low resistance state, and c. relative energies of the configuration with low and high resistance states, and the position of the transition state for oxygen vacancy migration. *Insets in Fig.5c*: configuration of the system. Green, red, white and black spheres represents Hf atoms, O atoms, O vacancies and Ta atoms, respectively.

Electronic Structure of Interface Defects in Epitaxially Grown Germanium on Silicon

H. M. Rafferty[1,*], A. D. Burnett[2], Z. Ikonic[1] and R. W. Kelsall[1]
[1] Institute of Microwaves and Photonics, School of Electronic and Electrical Engineering, University of Leeds, Leeds, LS2 9JT, UK.
[2] Astbury Centre for Structural Molecular Biology, University of Leeds, Leeds LS2 9JT, UK.
*e-mail: lechmr@leeds.ac.uk

Defects in the germanium/silicon epitaxial interface result in trap states which affect carrier recomination and transport, and thus device performance. Density functional theory (DFT) offers one method for characterising these states.

BACKGROUND

A number of devices rely on epitaxially grown germanium on silicon, including photodetectors, Stark modulators and lasers. There is a 4.2% lattice mismatch between these materials, hence germanium grown epitaxially on silicon will contain defects within some distance from the interface [1]. Line defects are either misfit dislocations—lines of dangling bonds where a mismatched plane terminates parallel to the heterointerface—or threading dislocations which occur where the side edges of the misfit dislocation terminate and usually glide along the (111) plane [2]. Defect structures create 'trap states'—allowed energy states within the forbidden band gap. Traps may act as recombination centres or inhibit transport over the interface, which can limit the repetition rate of devices such as photodetectors and may contribute to noise currents from detrapping of carriers outside the normal operating regime of a device. DFT offers one means of characterising the electronic structure of defects and hence the available states for carrier recombination and transport.

METHOD

The CASTEP simulation software [3] is used to calculate the electronic bandstructure for germanium and epitaxial interfaces of germanium grown on silicon, both for pure bulk and for cells containing extended misfit dislocations. CASTEP relies on periodic boundary conditions, and hence a misfit placed within a supercell will be replicated across the structure. However, first-principles calculations impose practical limits to the number of atoms which may be simulated, and one challenge is to ensure the calculated electronic states due to a dislocation are not unduly influenced by an adjacent periodic dislocation. A rhombohedral cell of germanium, in which the dislocation propagates along the [100] direction, was used to increase the spatial separation between dislocations while retaining practical numbers of atoms for simulation. In this orientation, a supercell one unit. cell deep in the plane of the dislocation may be created, allowing greater spatial separation in the remaining directions for the same volume of supercell. A repeated supercell constructed from 12×8×1 rhombohedral cells is shown in Fig. 1. The electronic bandstructure for bulk germanium without defects has been calculated using CASTEP, applying a norm-conserving pseudopotential and PW91 exchange-correlation functional. This has been repeated using 6×4×1 and 12×8×1 rhombohedral cells containing a single extended misfit dislocation. Comparison of these electronic structures allows identification of electronic states due to extended misfit dislocations in germanium.

DISCUSSION

For a supercell constructed of multiple primitive cells, the effective Brillouin zone represents only a portion of that of the primitive cell, and band folding takes place. A calculated bandstructure for bulk germanium using a 6×4×1 rhombohedral cell, demonstrating the reduced-scheme representation of a single band, is shown in Fig. 2. The electronic bandstructure for a 6×4×1 supercell containing a misfit dislocation is shown in Fig. 3. A number of additional energy states are observed in the bandgap for the material containing defects relative to the electronic structure for bulk material. This calculation may be repeated for various sizes of supercell and for the Ge/Si heterointeface.

ACKNOWLEDGEMENTS

This work is supported by the Engineering and Physical Sciences Research Council (EPSRC). Thanks also to Alex Valavanis, University of Leeds, for computational support.

REFERENCES

[1] V. A Shah, A. Dobbie, M. Myronov and D. R. Leadley. *Effect of layer thickness on structural quality of Ge epilayers grown directly on Si(001).*Thin Solid Films, **519**, 7911-7917 (2011).
[2] John E. Ayers. *Heteroepitaxy of Semiconductors: Theory, Growth and Characterisation.* CRC Press, (2007).
[3] S. J. Clark, M. D. Segall, C. J. Pickard, P. J. Hasnip, M. J. Probert, K. Refson and M. C. Payne. *First principles methods using CASTEP.* Z. Kristall, **220**, 567-570 (2005).

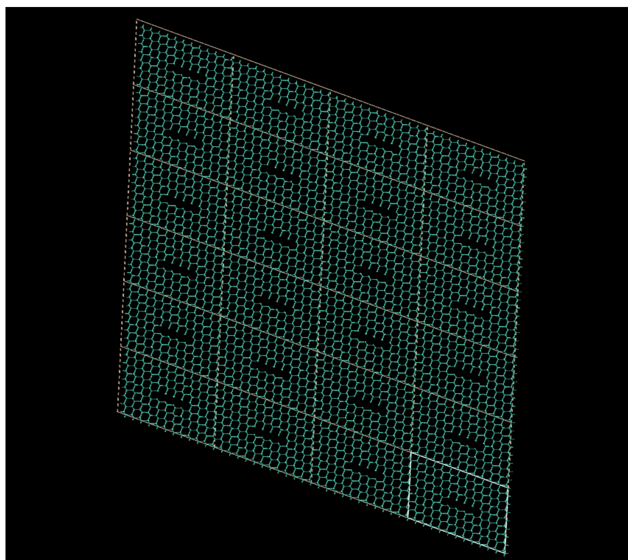

Fig. 1. Repetition of a 12 rhombohedral supercell of germanium containing a misfit dislocation.

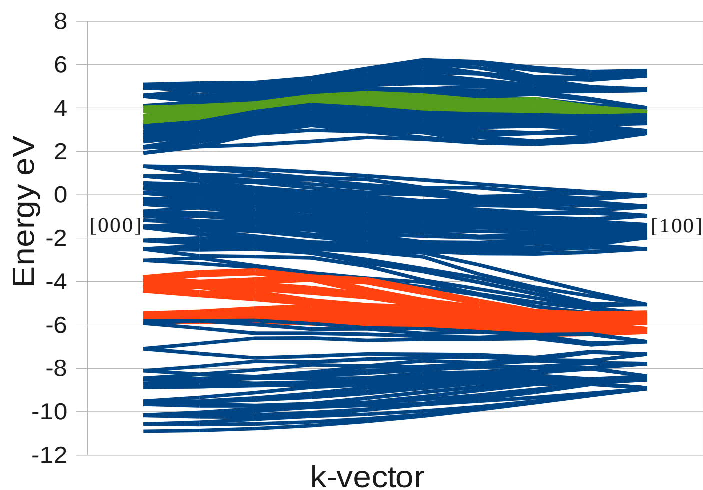

Fig. 2. Reduced-scheme bandstructure for a supercell of bulk germanium, with one folded valence band and one folded conduction band indicated.

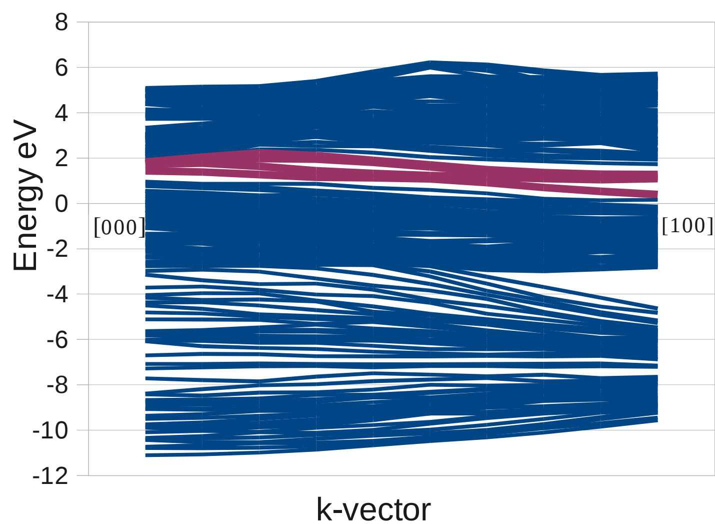

Fig. 3. Electronic bandstructure for a 6×4×1 supercell containing an extended misfit dislocation. The additional states due to the dislocation are highlighted.

Some Considerations on Conductance Fluctuations in Mesoscopic Structures

Bobo Liu, R. Akis, and D. K. Ferry
School of Electrical, Computer, and Energy Engineering, Arizona State University
Tempe, AZ 85287-5706 USA
e-mail: ferry@asu.edu

Universal conductance fluctuations have been observed in mesoscopic semiconductors for decades [1]. These fluctuations arise from the presence of a random potential in the semiconductor, which arises from e.g. impurities present in the material. The common theory suggests that the amplitude of these fluctuations will be a factor $\sqrt{2}$ smaller for magnetic field variation as compared to Fermi energy (or gate voltage) variation. This arises from breaking of time reversal symmetry in the magnetic field and a reduction in the diffuson channel in the quantum conductance. Within this small factor, it has been generally believed that a form of an "ergodic theorem" related the expected values for these two types of parameter sweep. Recently, experimental work on graphene has raised questions about such a theorem [2]. It was found that sweeps of gate voltage led to fluctuations that were more than a factor of 3 higher than sweeps of magnetic field.

Here, we explore Fermi sweep induced fluctuations versus magnetic field sweep induced fluctuations, to examine whether an ergodic theorem exists.

We use a recursive scattering matrix formulation to solve for the quantum transport through our active region, which is projected onto a discrete lattice in two dimensions. Here, the recursive approach follows that of Usuki [3] and our previous formulations. The use of a discrete lattice imposes a cosinusoidal band onto the eigenvalues of the slice Hamiltonian, and that allows us to study both the normal parabolic band behaviour and a quasi-linear energy behaviour near the center of the energy band. Thus, we can determine whether the observed effects in graphene [2] are unique to graphene or appear in any quasi-linear energy structure.

We find a range of results depending upon the precise structure and the level of the random potential. When a modest random potential is superimposed upon a weak quantum dot confinement, then we find for both parabolic and quasi-linear bands that the rms amplitude of the fluctuations is about 0.3 (in units of $2e^2/h$) for Fermi energy sweeps and about 0.28 for magnetic field sweeps. The former is close to the value of 0.36 expected from diagrammatic Green's function theory [1]. If the quantum dot is removed, the magnetic sweeps give smaller amplitude of order 0.1. If the amplitude of the random potential is increased to a large value, little change is seen in the Fermi energy sweeps (other than a reduction in overall conductance), but the fluctuations in the magnetic sweeps are reduced further to about 0.07.

These results suggest that there is no universal relationship between the two types of sweep, particularly no $\sqrt{2}$ connection, as the ratio of the amplitudes for the two sweeps can be found to vary from near 1 to more than 4. This further suggests that the observations in graphene [2] may be as much due to very strong disorder as to the uniqueness of the graphene energy structure.

[1] See, e.g., D. K. Ferry, S. M. Goodnick, and J. P. Bird, *Transport in Nanostructures*, 2nd Ed. (Cambridge Univ. Press, Cambridge, 2009) Ch. 7.

[2] G. Bohra, R. Somphonsane, N. Aoki, Y. Ochiai, R. Akis, D. K. Ferry, and J. P. Bird, "Nonergodicity and microscopic symmetry breaking of the conductance fluctuations in disordered mesoscopic graphene," Phys. Rev. B **86**, 405(R) (2012).

[3] T. Usuki, M. Saito, M. Takatsu, R. A. Kiehl, and N. Yokoyama, "Numerical analysis of ballistic-electron transport in magnetic fields by using a quantum point contact and a quantum wire," Phys. Rev. B **52**, 8244 (1995).

978-3-901578-26-7 © 2013 Society for Micro- and Nanoelectronics

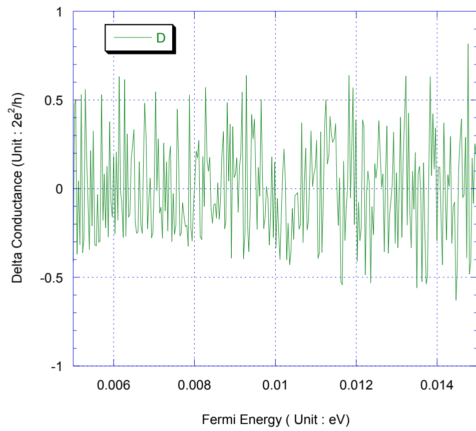

Fig. 1. Fluctuations for Fermi sweep in the parabolic regime. A small, soft walled quantum dot is also present.

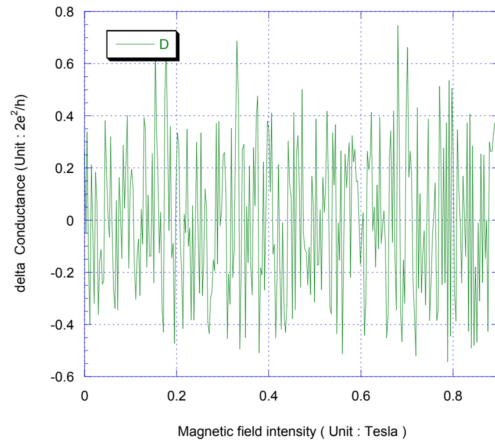

Fig. 2. Fluctuations for magnetic field sweep in the parabolic regime. A small, soft walled quantum dot is also present. The Fermi energy is 10 meV.

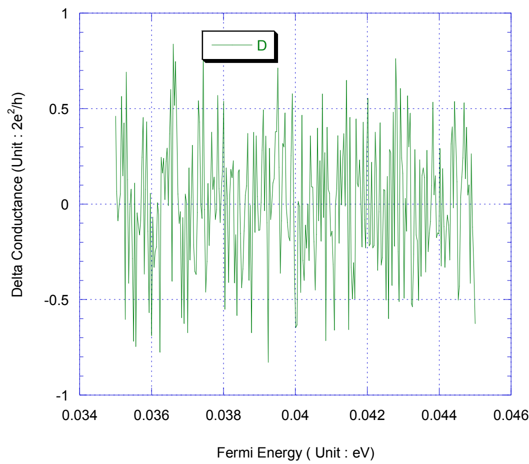

Fig. 3. Fluctuations for Fermi sweep in the quasi-linear regime. A small, soft walled quantum dot is also present.

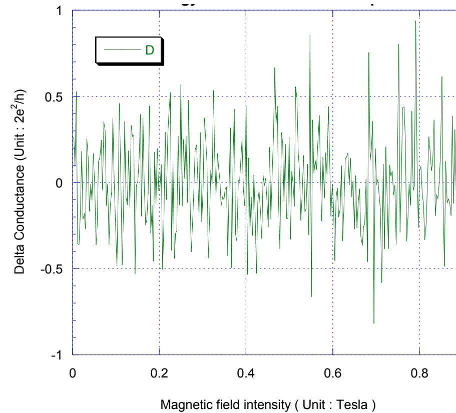

Fig. 5. Fluctuations for magnetic field sweep in the quasi-linear regime. A small, soft walled quantum dot is also present. The Fermi energy is 43 meV.

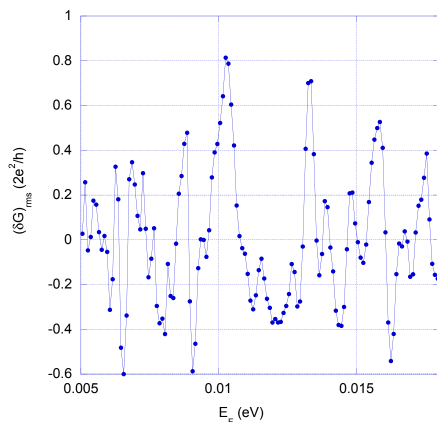

Fig. 2. Fluctuations for Fermi sweep in the parabolic regime, with no quantum dot potential, but with strong scattering.

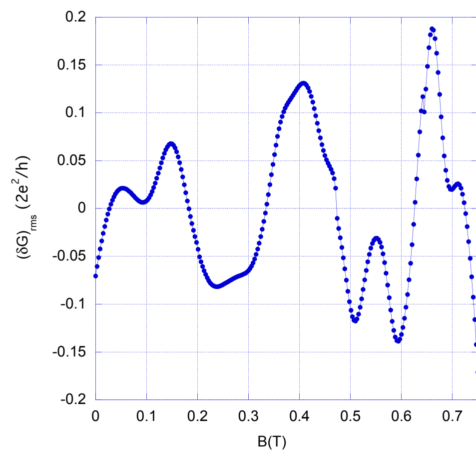

Fig. 5. Fluctuations for magnetic field sweep in quasi-linear regime for strong scattering. The Fermi energy is 58 meV

The Ultimate Equivalence Between Coherent Quantum and Classical Regimes

P. Schwaha[1,2], JM. Sellier[3], M. Nedjalkov[1], I. Dimov[3], S. Selberherr[1]

[1]Institute for Microelectronics, TU Wien, Gußhausstraße 27–29/E360, 1040 Wien, Austria
[2] AVL List GmbH, Hans-List-Platz 1, 8020 Graz, Austria
[3] IICT, Bulgarian Academy of Sciences, Acad.G.Bontchev str. Bl25A, 1113 Sofia, Bulgaria

The difference between the classical and the quantum mean values of a physical quantity associated with the evolution of an initial state may be evaluated by an estimate [1], which vanishes for up to quadratic potentials. In this case the commutator coincides with the Poisson bracket and the physical aspects are determined by the initial condition only. This ultimate parity may be used to setup benchmark experiments testing the properties of computational approaches. In particular, in the Wigner picture it holds:

$$\int dk' V_w(k-k')f(x,k',t) = -\frac{eE\partial f(x,k,t)}{\hbar\partial k} \quad (1)$$

showing the equivalence of the ballistic Boltzmann and coherent Wigner evolution for linear potentials $V(x) = Ex$. The choice of an initial condition $f(x,k,0) = N\delta(k)\delta(x)$ discards all quantum effects, so that the evolution is a simple acceleration of classical particles over a Newton trajectory. Why has this duality not yet been used as a reference for validation of Wigner transport simulation methods? The reason is that according to (1) V_w is a generalized function: $V_w(k) = \frac{eE}{\hbar}\delta'(k)$, which precludes any exact numerical treatment: even the standard, infinitely coherent in space, definition of the Wigner potential [2] diverges. This research aims at both, the development of an asymptotic approach as well as a validation of our Wigner particle model for this extreme case. The model accounts for mixed initial and boundary conditions and entangles particle attributes such as drift, generation and sign of the ergodic counterpart [3] with the concepts for momentum quantization, indistinguishable particles and annihilation at consecutive time steps. The key parameter in this approach is the finite coherence length L giving rise to the quantization $\Delta k = \pi/L$ of the momentum subspace, and a discrete Fourier expansion

$$V_w(n) = \int_{-L/2}^{L/2} \frac{e^{-in\Delta ks}}{i\hbar L}\Delta V(x\pm s)ds = -\frac{eEL}{\hbar\pi n}cos(\pi n)$$

The quantization imposes rules of cellular automata on the Boltzmann evolution [4]: The probability for a transition during a time dt to the next node n in field direction is proportional to the acceleration $dk = eEdt/\hbar$. This leads to a reference process, where the number of particles placed at the initial node gradually decreases in favour of the corresponding increase on the next node. Newton's law is recovered in the limit $L \to \infty$. The challenge now is to emulate the same process by generation of signed particles according to $V_w(n)$, which reside at a momentum grid during the evolution and may annihilate if having: opposite sign; identical phase space coordinates; identical evolution times. This illustrates their indistinguishability. Our simulations indeed demonstrate this behaviour: Figure 1 shows the initial peak which drops so that at $0.53ps$ the two adjacent nodes contain an equal number of particles, while after $1ps$ the transition is complete. However, an additional phenomenon is revealed by this evolution process: a pattern of oscillating values appears. We associate this with the fact that the equivalence between quantum and classical evolution is asymptotic only. The discrete quantum system is disturbed by the violation of the uncertainty principle in the initial condition. Indeed, with an increase of L the magnitude of the oscillations decreases, Figure 2. Another interesting phenomenon is the pulsing of the pattern in time: during a transition the oscillations are much higher than at its end, as if the solution tends to the classical shape at discrete points in time, Figure 1 and Figure 3. For $E = 10^4 V/m$ and $L = 200nm$ these instants are consistent with Newton's law: $\Delta k = eE\Delta t/\hbar$. It also validates the robust behaviour of our technique: the $5ps$ solution is obtained without any distortion due to annihilation. Figure 4 shows the dramatic increase of computational effort with increasing evolution time and the importance of annihilation to keep particle numbers under control. The fine structure and asymptotic behaviour of the analysed quantum process makes it an ideal candidate for benchmark simulations.

978-3-901578-26-7 © 2013 Society for Micro- and Nanoelectronics

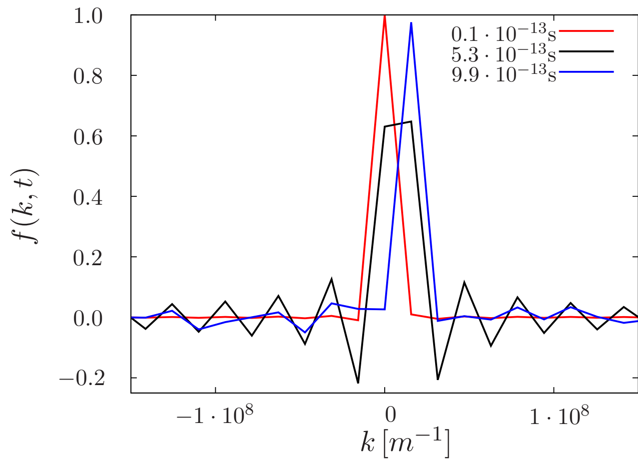

Fig. 1. The effect of the accelerating force is replaced by the Wigner potential with generation of positive and negative particles which reside on the grid in momentum space. The decrease of the initial peak is entirely due to the generation of negative particles at the zero node. These annihilate with the positive counterparts leading to a decrease of the initial condition. On the next node to the right positive particles are generated. The net effect is as in the cellular automata reference process. The transition of the peak between two neighbouring nodes is accompanied by increased oscillations, which are subside once the transition is complete.

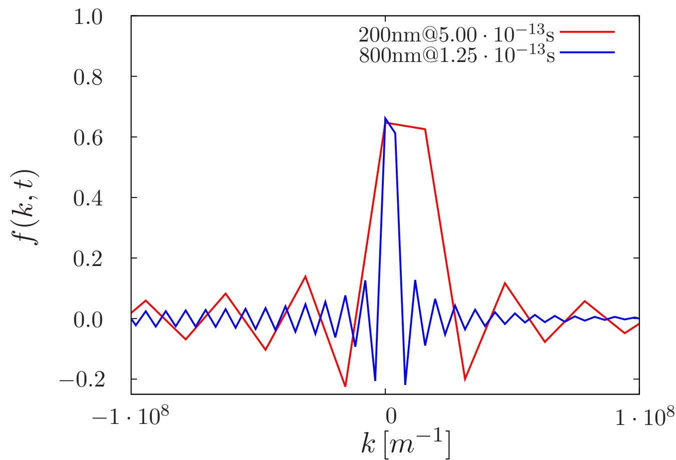

Fig. 2. An increase of the coherence length reduces the magnitude of the oscillations, demonstrating the expected asymptotic behaviour. The corresponding decrease of Δk reflects on the time required for half transfer, according to Newton's law, by reducing it 4 times.

ACKNOWLEDGEMENT

This work has been supported by the Austrian Science Fund Project FWF-P21685-N22, the project EC AComIn (FP7-REGPOT-2012-2013-1) and Bulgarian NSF Grants DMU 03/61 and DTK 02/44/2009.

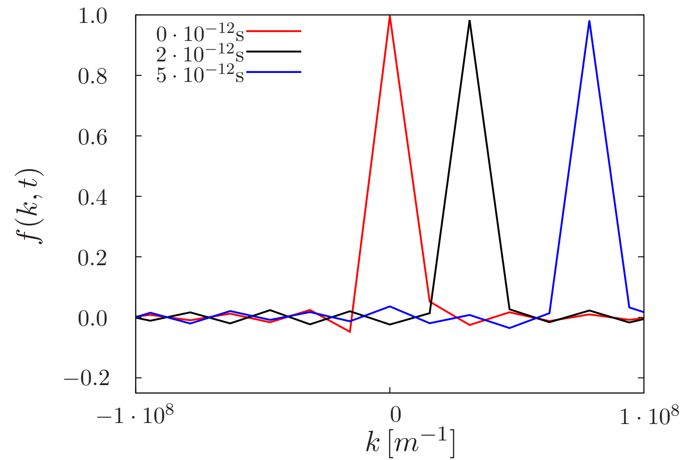

Fig. 3. The initial peak moves robustly for 5ps demonstrating the lack of any distortion due to the annihilation of particles. Points in time corresponding to Newton's law have much lower oscillations.

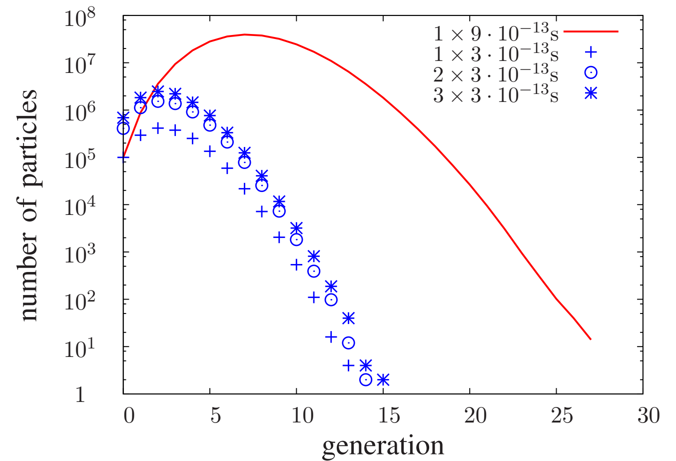

Fig. 4. An increase of the time step dramatically increases the number of generated particles as can be seen by comparing the number of generated particles for $9 \cdot 10^{-13}$s with $3 \times 3 \cdot 10^{-13}$s.

REFERENCES

[1] M. Nedjalkov, S. Selberherr, D.K. Ferry, D. Vasileska, P. Dollfus, D. Querlioz, I. Dimov, P. Schwaha: *Physical Scales in the Wigner-Boltzmann Equation*, Annals of Physics, **328**, 220, (2012).

[2] M. Nedjalkov, D. Querlioz, P. Dollfus, H. Kosina: *Wigner* Function Approach in: "Nano-Electronic Devices: Semiclassical and Quantum Transport Modeling", D. Vasileska, S.M. Goodnick (ed.); Springer, 289, (2011).

[3] M. Nedjalkov, H. Kosina, S. Selberherr, Ch. Ringhofer, D.K. Ferry: *Unified* Particle Approach to Wigner-Boltzmann Transport in Small Semiconductor Devices Physical Review B, **70**, 115319, (2004).

[4] G. Zandler, A. Di Carlo, K. Krometer, P. Lugli, P. Vogl, and E. Gornik: *A* Comparison of Monte Carlo and Cellular Automata Approaches for Semiconductor Device Simulation IEEE Electron Dev. Letters, **14**, 77, (1993).

Effect of defective connection to electrodes in atomic scale conductors

Y. Hanashiro, and M. Morifuji
Graduate School of Engineering, Osaka University, 2-1 Yamada-oka, Suita, Osaka 565-0871, Japan
Phone: +81-6-6879-7766 E-mail: yhanashiro@e3.eei.eng.osaka-u.ac.jp

INTRODUCTION

Owing to development of fabrication technologies, atomic scale conductors have been realized. Although electrodes are necessary in utilizing such conductors for electronic devices, it is difficult to create the electrodes with a conventional way such as metal heat bonding. If interface between the device and electrodes is defective, characteristics of the atomic scale device would be rectified or washed out due to large contact resistance.

In this study, we investigate how current-voltage characteristics of a small two-dimensional conductor change when connection between the device and the electrode is malfunction.

MODEL

Figure 1 shows the structure of the model we study. A two-dimensional conductor, which is depicted as the dark shaded region, is cladded by electrodes. By applying the effective mass approximation, the device is discretized by 10 mesh points in the longitudinal direction. We consider two structures with different width which are divided by 3 or 6 mesh points, respectively. We refer the 3×10 and 6×10 structures as (A) and (B), respectively. The mesh points, which have energy $\varepsilon + V_i$ (V_i: potential due to applied voltage), are connected by the nearest neighbor hopping integral t. To model the malfunction in connection to the electrodes, we set some of the hopping integrals between the device and electrodes to zero. We evaluated current through the device at 300 K by using the non-equilibrium Green's function method.

RESULTS

In Fig. 2, we show current-voltage characteristics of the structure (A). The solid curve shows the current for the case of perfect connection to the electrode. The dashed curve denotes the current with defect at the edge of the interface. The dot-dashed curve denotes the current with defect at the center of the interface. Position of the defect is schematically shown by the crosses in the insets. We observe that the defective connection reduces the current. Reduction of current due to defect located at the center of the interface is larger than that due to defect at the edge.

Fig. 3 shows current-voltage characteristics of the structure (B). The defective connection also reduces the current, however, in this case, effect of disconnection at the edge of the interface is larger than that at the center.

In Fig. 4, we show electron densities for the two structures. For both cases, the defect is located at the middle of the interface between the device and cathode. We observe that the electron distributions are quite different for the two samples.

DISCUSSION

Such difference in the effect of the position of the defect in the connection would be explained by difference in relevant lateral modes which are schematically shown in Fig. 5. In the structure (A), current flows mainly through the lowest mode. The current is largely affected by the defect at the center because it locates on the belly of the lowest mode. Whereas in the wider structure (B), the second mode is dominant for the current. In this case, the defect at the center of the interface, which locates at the node of the mode, has small effect on current.

REFERENCES

[1] H. Kawaura and T. Baba, Jpn. J. Appl. Phys., **42**, pp. 351-357, 2003.
[2] S. Datta, Quantum Transport: Atom to Transistor (Cambridge University Press, Cambridge, 2005)

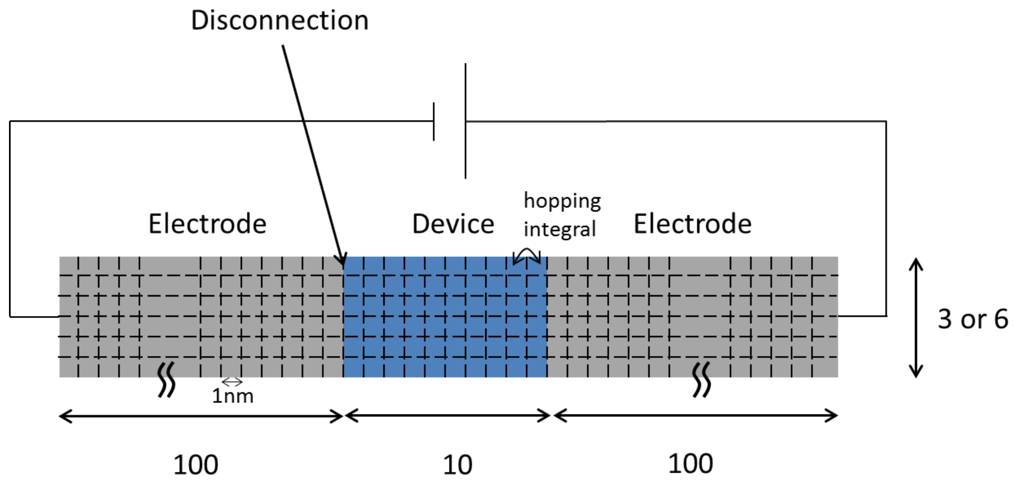

Fig. 1. Schematic structure of the device we studied. Discretized mesh points are connected by hopping integral, and there are disconnection between the electrode (cathode) and device.

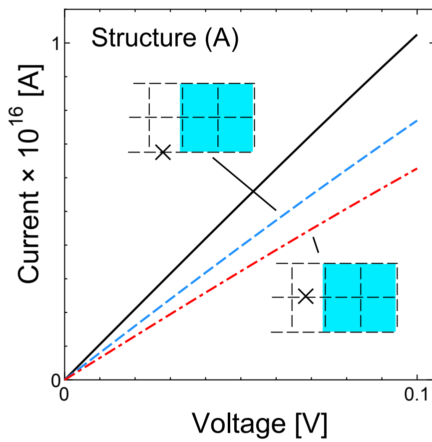

Fig. 2. Current-Voltage characteristics of the 3×10 device.

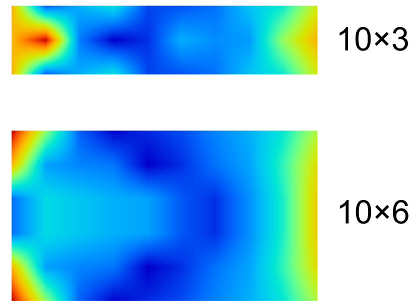

Fig. 4. Electron density when the connection was lost in the middle of the device

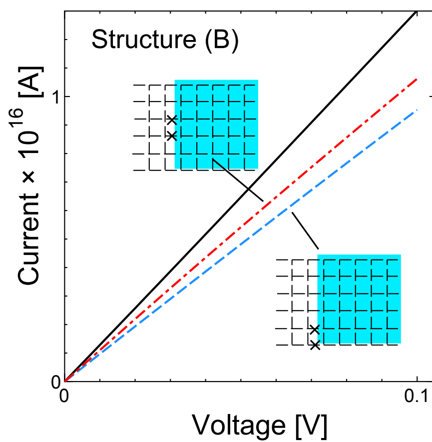

Fig. 3. Current-Voltage characteristics of the 6×10 device.

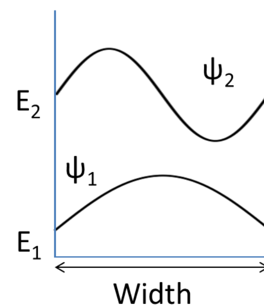

Fig. 5. Wave functions in the lateral direction are schematically shown.

Calculation of alloy scattering mobility in SiGe FETs based on atomistic tight-binding approach

Hong-Hyun Park, Changwook Jeong*, Seonghoon Jin, Woosung Choi,
Young-Tae Kim*, Ui-Hui Kwon*, Keun-Ho Lee*, and Youngkwan Park*
Samsung Semiconductor Inc., San Jose, California, USA
*Semiconductor R&D Center, Samsung Electronics, Hwasung-si, Gyeonggi-do, Korea
e-mail: honghyun.p@samsung.com

ABSTRACT

The use of SiGe alloy as a channel material is a promising way to overcome the low mobility problem of conventional Si-based field effect transistors. This paper presents an atomistic approach to alloy scattering mobility calculation and shows its application to SiGe channel field effect transistors.

INTRODUCTION

The calculation of alloy scattering mobility has become an important device modeling issue to determine the expected device performance of SiGe-based FETs. Usually, the calculation of alloy scattering mobility assumes an alloy scatterer in a simple analytical form with some fitting parameters [1], which is a good practical approach but has a limited predictability. Recently, Mehrotra et al. presented an atomistic approach to calculate the alloy scattering mobility in bulk SiGe materials, which describes an alloy system in atomistic level and requires no fitting parameters for the mobility calculation [2].

In this paper we extend the atomistic approach to be applicable to general devices as well as bulk materials. Also, we investigate the alloy scattering mobility in SiGe bulk, thin film, and thin film FETs.

CALCULATION METHOD

The following briefly shows a few steps to calculate the alloy scattering hole mobility in the channel region of a device.

Step 1: Perform a device simulation at a certain bias condition to obtain the solution and information needed for the following mobility calculation.

Step 2: Solve Schrodinger equations in a desired channel region of the device assuming no atomistic randomness due to alloy atoms. Alloy-averaged Hamiltonian matrices($H_{VCA}(\vec{k})$) are solved and corresponding eigenfunctions($|\vec{k}\rangle$) and velocities($v(\vec{k})$) are obtained.

Step 3: Calculate the ensemble average of the momentum relaxation time due to alloy scattering.

$$\frac{1}{\tau_x(\vec{k})} = \int d\vec{k}' \left\langle \frac{2\pi}{\hbar} \left| \langle \vec{k} | H_{alloy}(\vec{k}) - H_{VCA}(\vec{k}) | \vec{k}' \rangle \right|^2 \delta\left(E(\vec{k}) - E(\vec{k}')\right) \right\rangle \left(1 - \frac{v_x(\vec{k}')}{v_x(\vec{k})}\right)$$

, where $H_{alloy}(\vec{k})$ is a Hamiltonian matrix of a randomly generated SiGe alloy structure.

Step 4: Calculate the hole mobility according to Kubo-Greenwood formula.

$$\mu_x = \frac{\frac{q}{k_B T} \int d\vec{k}\, \tau_x(\vec{k}) \left| v_x(\vec{k}) \right|^2 f(E(\vec{k}))\left(1 - f(E(\vec{k}))\right)}{\int d\vec{k} \left(1 - f(E(\vec{k}))\right)}$$

RESULTS AND DISCUSSIONS

Hole alloy scattering mobility for SiGe bulk, thin film, and the channel of thin film transistors are calculated. $sp^3d^5s^*$ tight-binding basis with spin-orbit coupling and a valence band offset of 0.54eV between Si and Ge have been used throughout our calculations. Results and discussions are shown in the following page with figures and captions.

REFERENCES

[1] M. V. Fischetti and S. E. Laux, J. Appl. Phys. **80**, 2234 (1996)
[2] S. R. Mehrotra, A. Paul, and G. Klimeck, Appl. Phys. Lett. **98**, 173503 (2011).
[3] G. Busch and O. Vogt, Helv. Phys. Acta **33**, 437 (1960).

978-3-901578-26-7 © 2013 Society for Micro- and Nanoelectronics

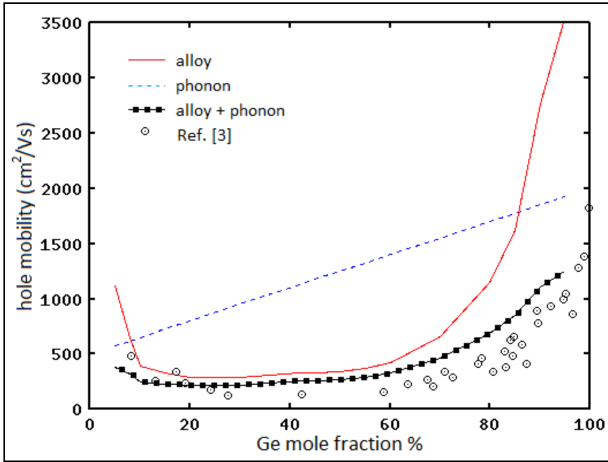

Fig. 1. Calculated hole mobility(red), estimated hole phonon mobility(dashed blue), and the total of the two(marked black) versus alloy mole fraction in bulk SiGe. Our calculation shows good agreement with Ref. [3].

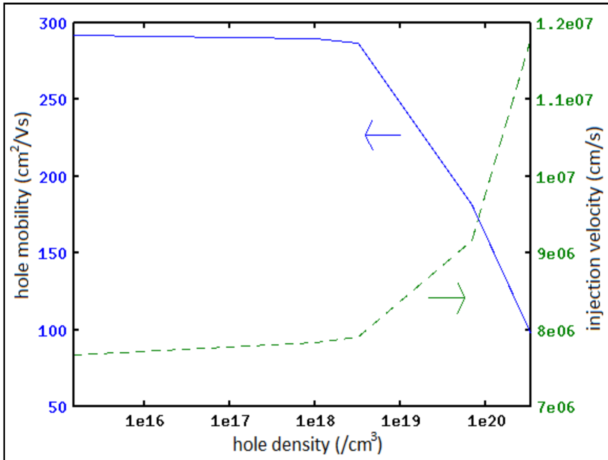

Fig. 2. Calculated hole alloy scattering mobility(blue) versus hole density in $Si_{0.7}Ge_{0.3}$ bulk. In degenerate semiconductors the alloy scattering mobility decreases due to rapid increase of alloy scattering rate even though the average carrier velocity increases as carrier density.

Figs. 4(a) and 4(b). Calculated hole alloy scattering mobility in the channel of thin film SiGe transistors with various alloy mole fraction and gate bias conditions. The thickness of the thin films is 11.7nm, and the transport and confinement directions are [110] and [1-10], respectively. (a) The numbers at markers are the surface hole densities(/cm^2) and a red line indicates a hole mobility with a fixed surface hole density of 1E13/cm^2. (b) There is a tendency for the alloy scattering mobility to decrease with increasing the carrier density.

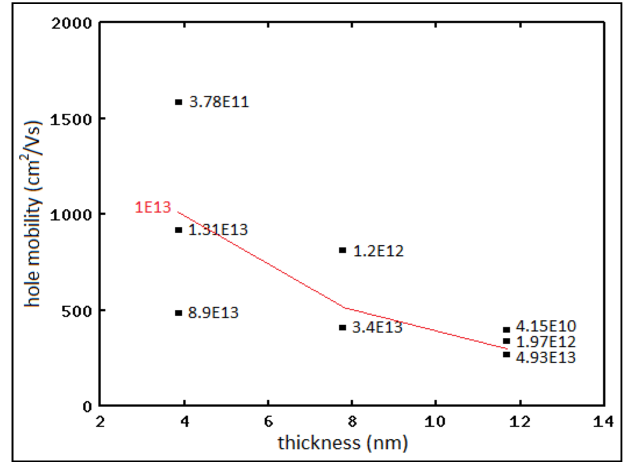

Fig. 3. Calculated hole alloy scattering mobility in thin film $Si_{0.7}Ge_{0.3}$ layers with different thicknesses and carrier densities. The transport and confinement directions are [110] and [1-10], respectively. The numbers at markers are the surface hole densities(/cm^2) and a red line indicates a hole alloy mobility with a fixed surface hole density of 1E13/cm^2.

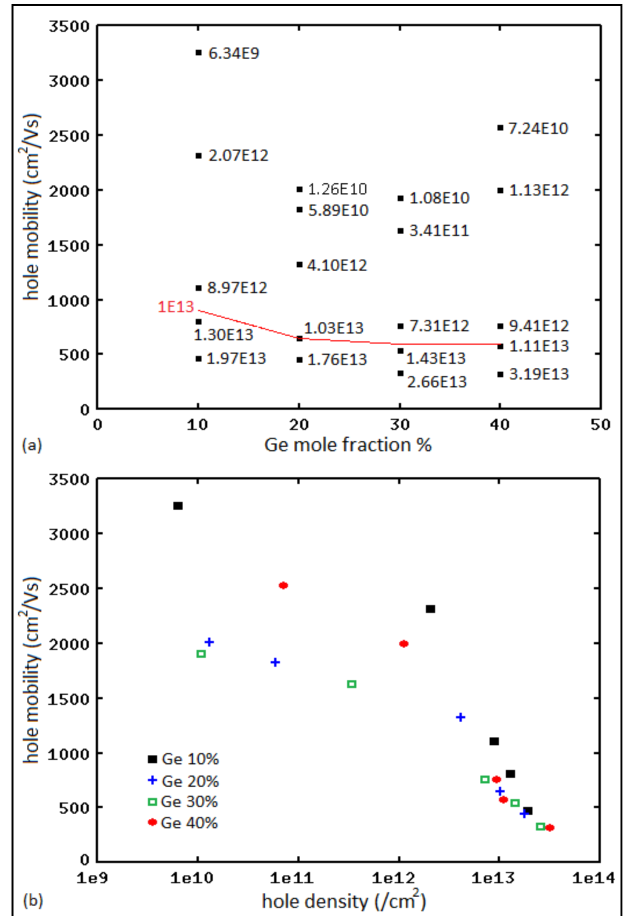

Generalization of the Scharfetter-Gummel scheme to strictly monotonous carrier density state-equations

K. Gärtner and T. Koprucki
Weierstrass Institute (WIAS), Mohrenstr. 39, 10117 Berlin, Germany
e-mail: gaertner@wias-berlin.de

ESSENTIAL GOALS OF THE DISCRETIZATION

Models for the carrier density n in semiconductors $n = N_c\mathcal{F}(\eta)$, η chemical potential, include all strictly monotonous distribution functions $\mathcal{F}(\eta)$ in the range defined by Boltzmann-statistics (strongest increase of density) and the Fermi-Dirac-integral of order -1 (weakest increase of density), compare Fig. 1. The latter one appears as vanishing disorder limit of the Gauss-Fermi-integral [1] for hopping transport in organic semiconductors and in phase-separation models [2], where a 'discrete chain rule' was used to get stability for the discrete problem.

Looking at analytic results for Fermi-Dirac-statistics (e.g. [3]) and comparing them to those for the Boltzmann case suggests, that it should be possible to get all nice properties also for the discrete problem in the $\mathcal{F}(\eta)$-case: uniqueness for small applied voltages; bounded, positive steady states; existence of a unique transient solution; dissipativity. Such results are expected to hold for restricted classes of material models for all boundary conforming Delaunay grids and all time steps.

The goal here is to generalize the Scharfetter-Gummel-scheme for the above described range. Up to now degenerate semiconductors may be most precisely handled by a local, non-symmetric Boltzmann approximation and an outer iteration [4]. This outer iteration multiplies the total computation time, while a much more complex current relation may triple the assembly effort only, a small fraction of the total time.

A FIRST APPROXIMATION

In [5] the approximation introduced by Blakemore [6] of the distribution function $\mathcal{F}_{1/2}(\eta)$ for small arguments

$$\mathcal{F}_B(\eta) = \frac{1}{e^{-\eta} + \gamma}, \quad 0 \le n \le \frac{N_c}{\gamma} \tag{1}$$

was investigated for the governing equation

$$\frac{d}{dx}\Big(q\mu N_c\mathcal{F}(\eta(\varphi,\psi))\frac{d}{dx}\varphi(x)\Big) = 0, \tag{2}$$

describing a constant current j along an edge $[x_a, x_b]$ and the boundary values of the quasi-Fermi potential $\varphi(x_a) = \varphi_a$ and $\varphi(x_b) = \varphi_b$. This case is sufficiently simple to obtain explicit expressions and to study the essentials of the non-Boltzmann case, namely the generalized Einstein relation, describing the nonlinear ratio between diffusion coefficient and mobility $D/\mu \sim g_3(n)$, see Fig. 2.

Using Eq. (2), changing variables from quasi-Fermi potential to chemical potential together with a linearity assumption of the electrostatic potential ψ results in the following integral equation for j along the edge

$$\int_{\eta_a}^{\eta_b} \frac{1}{\frac{j}{\mathcal{F}(\eta)} + \delta\psi} d\eta = 1. \tag{3}$$

Inserting the approximation $\mathcal{F}_B(\eta)$ results in a fixed point problem for the current [5]:

$$j = B(\delta\psi + \gamma j)e^{\eta_b} - B(-(\delta\psi + \gamma j))e^{\eta_a}, \tag{4}$$

where $B(x) = \frac{x}{e^x - 1}$ is the Bernoulli function. Due to the properties of the Bernoulli function this fixed point problem has a unique solution for the current and for all finite arguments. Solutions of Eq. (3) for given potentials are shown in Fig. 3 together with their Boltzmann counterparts.

 © 2013 Society for Micro- and Nanoelectronics

The general case

The approach is generalized to any strictly monotonous distribution function $\mathcal{F}(\eta)$, $-\infty < \eta < \infty$, by using a piecewise continuous approximation of the form

$$\mathcal{F}_i(\eta) = \frac{\sigma_i}{e^{-\eta} + \gamma_i}, \qquad \eta_i \le \eta \le \eta_{i+1},$$
$$\eta_a = \eta_0,\ \eta_b = \eta_{k+1}, \qquad \sigma_i > 0,\ \gamma_i > 0.$$

In this case the left hand side of equation (3) reads

$$\int_{\eta_a}^{\eta_b} \frac{d\eta}{\frac{j}{\mathcal{F}(\eta)} + \delta\psi} = \sum_{i=0}^{k} c_i,\ c_i = \int_{\eta_i}^{\eta_{i+1}} \frac{d\eta}{\frac{j}{\mathcal{F}_i(\eta)} + \delta\psi}.$$

Hence, a decomposition of unity $\sum_i c_i = 1$, $c_i > 0$, defines the current j. Simplifications for special choices of σ_i, γ_i and a detailed discussion of existence and uniqueness of a solution, which is supporting an implementation directly, will be in the focus of the talk.

Conclusion

The Scharfetter-Gummel scheme is extended to monotonous carrier density state equations in a unified way.

Acknowledgment

T. Koprucki thanks Deutsche Forschungsgemeinschaft, collaborative research center 787 "Semiconductor Nanophotonics", project B4 for support.

References

[1] G. Paasch and S. Scheinert. Charge carrier density of organics with Gaussian density of states: Analytical approximation for the Gauss-Fermi integral. *J. Appl. Phys.*, 107(10):104501, 2010.

[2] H. Gajewski and K. Gärtner. A dissipative discretization scheme for a nonlocal phase segregation model. *Z. Angew. Math. Mech.*, 85:815–822, 2005.

[3] H. Gajewski and K. Gröger. Semiconductor equations for variable mobilities based on Boltzmann statistics or Fermi–Dirac statistics. *Math. Nachr.*, 140:7–36, 1989.

[4] U. Bandelow, H. Gajewski, and R. Hünlich. Fabry–Perot Lasers: Thermodynamics-Based Modeling. In Joachim Piprek, editor, *Optoelectronic Devices*. Springer, 2005.

[5] T. Koprucki and K. Gärtner. Discretization scheme for drift-diffusion equations with a generalized Einstein relation. preprint 1738, WIAS.

[6] J.S. Blakemore. The Parameters of Partially Degenerate Semiconductors. *Proc. Phys. Soc. London A*, 65:460–461, 1952.

[7] V.L. Bonch-Bruevich and S.G. Kalaschnikov. *Halbleiterphysik*. VEB Deutscher Verlag Wissenschaften, 1982. Berlin.

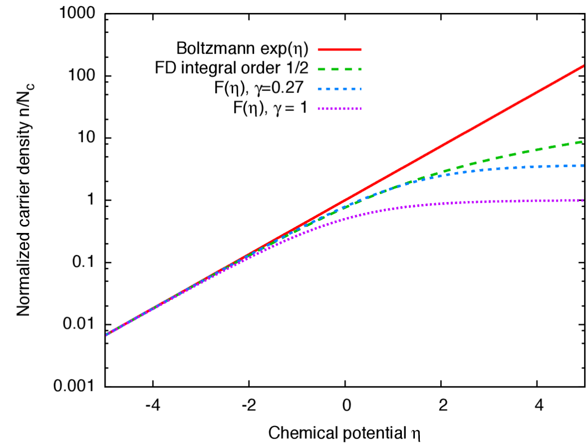

Fig. 1. Density in dependence of the chemical potential for different state equations.

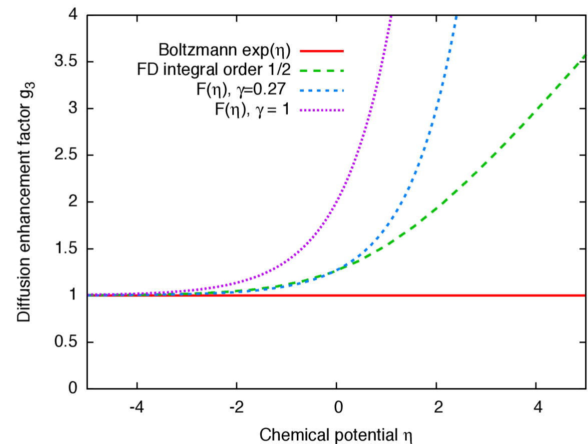

Fig. 2. Diffusion enhancement factor for different state equations, or: the generalized Einstein relation [7].

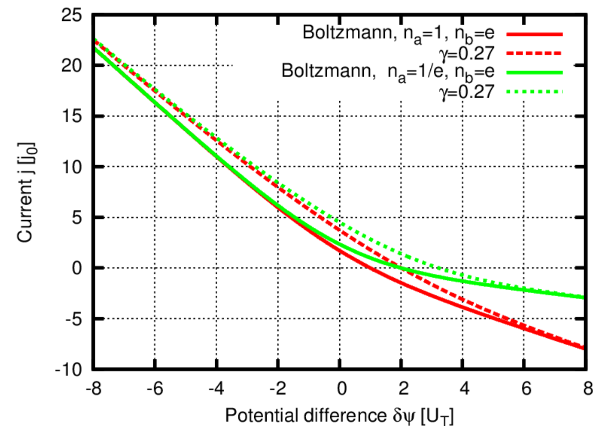

Fig. 3. Current comparison for different state equations.

Analysis of carrier transport in Si and Ge MOSFETs including quantum confinement and hot carrier effects

Shohiro Sho, Shinji Odanaka, and Akira Hiroki*
Graduate School of Information Science and Technology, Osaka University, Osaka, Japan
*Department of Electronics, Kyoto Institute of Technology, Kyoto, Japan
e-mail: *shohiro@cas.cmc.osaka-u.ac.jp

INTRODUCTION

New channel materials such as Ge and III-V semiconductors are needed to achieve high performance and low power in nanoscale CMOS devices[1]. A number of authors have presented numerical and theoretical studies of carrier transport in MOSFETs on high mobility substrates and Si [2], [3], [4].

In this paper, transport properties in Si and Ge n-MOSFETs are evaluated using a 4 moments quantum energy transport(QET) model[5]. The QET model allows analysis of carrier transport including quantum confinement and hot carrier effects.

4 MOMENTS QUANTUM ENERGY TRANSPORT MODEL

We develop a 4 moments QET model, assuming the classical form of the fourth moment tensor and neglecting quantum corrections in the diffusive contributions to the energy flux density[5]. For electrons, the carrier continuity and energy balance equations are derived as

$$\frac{1}{q} div J_n = 0, \tag{1}$$

$$\nabla \cdot S_n = -J_n \cdot \nabla\varphi - \frac{3}{2} kn \frac{T_n - T_L}{\tau_\epsilon}, \tag{2}$$

where φ, n and T_n are the electrostatic potential, electron density and electron temperature, respectively. q, k, τ_ϵ and T_L are the electronic charge, Boltzmann's constant, energy relaxation time, and lattice temperature. The quantum corrections of the current density J_n and energy flux density S_n are given by

$$J_n = q\mu_n(\nabla(n\frac{kT_n}{q}) - n\nabla(\varphi + \gamma_n)), \tag{3}$$

$$S_n = -\frac{\mu_s}{\mu_n}(\frac{5}{2}\frac{kT_n}{q} - \frac{\hbar^2}{24mq}\Delta \log n - \gamma_n)J_n - \frac{\mu_s}{\mu_n}\frac{5}{2}(\frac{k}{q})^2 q\mu_n n T_n \nabla T_n, \tag{4}$$

where μ_n and μ_s are the electron and energy flow mobilities, respectively. $\hbar$ and m are Plank's constant and effective mass. The quantum potential is written as

$$\gamma_n = \frac{\hbar^2}{6mq}\frac{\Delta\sqrt{n}}{\sqrt{n}}. \tag{5}$$

NUMERICAL RESULTS

Si and Ge n-MOSFETs with high-k/metal gate are examined. Selected material parameters are listed in Table I. Both devices have gate length L_g=35nm, EOT=0.7nm and the S/D dopings of $1.0 \times 10^{20} cm^{-3}$. The dielectric permittivity considered here is 22, and the value is known as "HfO_2". For metal gates, the work functions of 4.2 eV for Si devices, and 4.14 eV for Ge devices are adopted. Fig. 1 (a) and (b) shows comparisons of the classical and quantum mechanical average inversion layer depths versus effective normal field for Si and Ge n-MOSFETs. In both devices, the classical value is less than 1.0 nm, and the difference between two devices is small. The QM value of the Ge n-MOSFET is larger than that of the Si n-MOSFET by 0.8nm-1.2nm for a wide range of channel doping because of the low effective mass and high permittivity of Ge. This effectively reduces the charge control by the gate in Ge n-MOSFETs. The electron

density distributions perpendicular to the interface are shown in Fig. 2 (a) and (b). The results clearly indicate that the quantum confinement effect at the drain end of the channel is further reduced by the enhanced diffusion towards the bulk due to the high electron temperature. Fig. 3 shows electron density distributions of a double gate Si n-MOSFET with high-k/metal gate. The silicon layer thickness is 6nm. It is seen that the device exhibits two channels at the source end of the channel and a single channel at the drain end of the channel due to high electron temperature near the drain.

CONCLUSION

A 4-moments QET model allows simulations of quantum confinement transport with hot-carrier effects in Si and Ge n-MOSFETs. The charge control by the gate is effectively reduced in the Ge n-MOSFET due to low effective mass and high permittivity. The quantum confinement effect is further reduced by high electron temperature near the drain.

REFERENCES

[1] S. Takagi et al., Proceedings of IEDM 2012, pp.505-508.

[2] A. Rahman et al., Proceedings of IEDM 2003, pp.471-474.

[3] S. E. Laux, IEEE Trans. Elec. Devices, vol. 54(2007), pp.2304-2320.

[4] M. V. Fischetti et al., IEEE Trans. Elec. Devices, vol. 54(2007), pp.2116-2136.

[5] S. Sho and S. Odanaka, Journal of Comp. Phys., vol. 235(2013), pp.486-496.

TABLE I

SELECTED SEMICONDUCTOR MATERIAL PARAMETERS

semiconductor	Si	Ge
$\mu_{eff}(cm^2/Vs)$ [4]	400	1040
$E_G(eV)$	1.12	0.66
$\epsilon_R(\epsilon_0)$	11.7	16.0
$m_{eff}(m_0)$	0.26	0.10
$n_i(cm^{-3})$	1.105×10^{10}	2.0×10^{13}

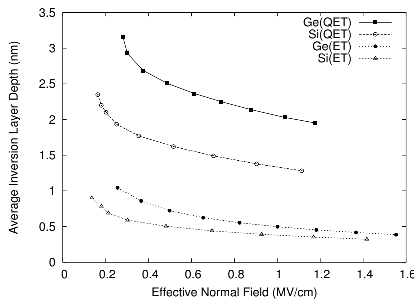

(a)

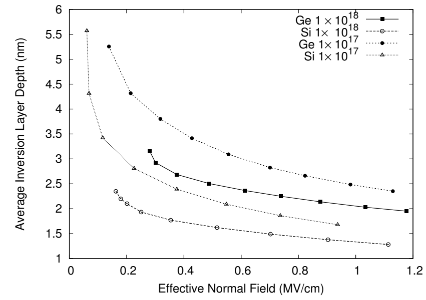

(b)

Fig. 1. Average inversion layer depth as a function of gate effective normal field for Si and Ge n-MOSFETs. (a) The results are calculated by the QET and ET models. The channel doping is $1.0 \times 10^{18} cm^{-3}$. (b) The uniform channel dopings are $1.0 \times 10^{18} cm^{-3}$ and $1.0 \times 10^{17} cm^{-3}$, respectively.

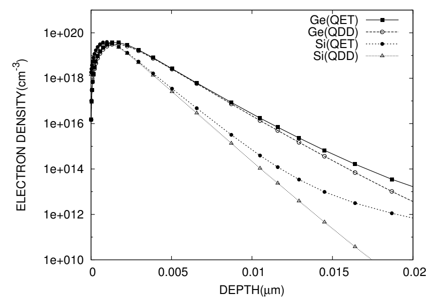

(a)

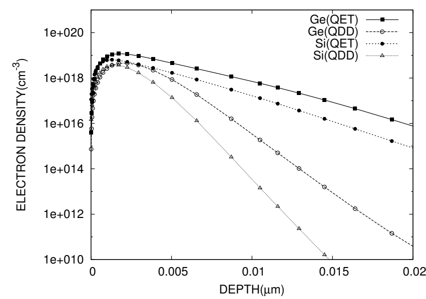

(b)

Fig. 2. Electron density distributions perpendicular to the interface for a 35nm MOSFET, (a) at the source end of the channel, (b) at the drain end of the channel. V_g=0.8V, V_d=0.8V.

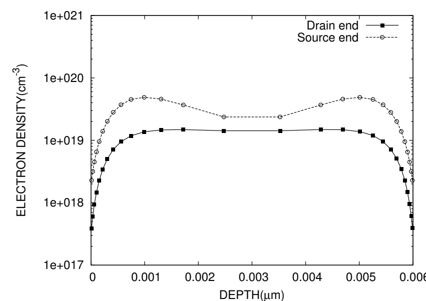

Fig. 3. Electron density distributions perpendicular to the interface at the source and drain end of the channel for a 35nm double gate Si n-MOSFET. V_g=0.8V, V_d=0.8V.

A Frequency-Dependent QM/EM Method: Multi-Scale Simulation of Electronics

Zhenyu Yin, Lingyi Meng, Quan Chen*, and Guanhua Chen
Department of Chemisty, The University of Hong Kong, Pokfulam, Hong Kong
*Department of Electrical and Electronic Engineering, The Univeristy of Hokng Kong, Pokfulam, Hong Kong
E-mail: zyyin@yangtze.hku.hk

Abstract

Because of fast development of fabricate technique, it is expected that the scale of transistor will go below 10nm in a few years. Under such scale, properties of electrons will be dominated by quantum mechanics effects. In order to handle such a situation, an amount of quantum mechanics methods have been developed. However, the most important defect of all these methods is extremely time-consuming during calculations, especially when more atoms contained. Therefore, when a system consists of a core device under atomic scale and a broader environment outside, a hybrid method which combines quantum mechanics (QM) and electromagnetic (EM) has been proposed, resulting in less accuracy but much faster speed comparing with purely QM solver if this system could still be dealt with by it. For the system mentioned above, its active core device which contributes most properties is simulated by QM solver, while the left environment part containing a large number of atoms which can hardly be solved by QM method, is calculated by EM solver. Moreover, effect on the interface and communications between two solvers should be considered. As a result, this QM/EM method balances the accuracy and efficiency.

The QM/EM method has been successfully developed in time-domain which can now solve steady-state [1] and time-dependent [2] problems. In this work, the application of this method is extended into frequency-domain. Within EM solver, system is treated classically by solving Maxwell's equations directly in frequency domain. Basing on time-dependent density functional method (TDDFT) and non-equilibrium green's function method (NEGF), electronic transport properties are investigated in QM solver. By defining a double-time Fourier transform, its energy spectrum can also be explored [3]. In order to realize an information exchange between QM and EM region, a coupled self-consistent scheme is adopted. Potential distribution V on the interface between two regions is solved by EM solver as the boundary conditions for QM solver. After accomplishment of QM simulation, current density J on the interface calculated by QM solver is fed back to EM solver as its boundary condition. This process is iterated until potential distribution and current density converge.

Basing on this QM/EM method, a carbon nanotube device depicted in Fig. 1 is studied in frequency domain. Result obtained directly from frequency region is compared with that from time-dependent calculation by a numerical Fourier transform $G(\omega) = I(\omega) / V(\omega)$. A very well agreement can be found in Fig. 2 upon frequency up to 0.6ev (~70THz) by this comparison, which validate this frequency-dependent QM/EM method.

References

[1] C. Y. Yam, L. Y. Meng, G. H. Chen*, Q. Chen, N. Wong*, *Multiscale quantum mechanics/electromagnetics simulation for electronic* device, Phys. Chem. Chem. Phys. **13**, 14365–14369 (2011).
[2] L.Y. Meng, C. Y. Yam, S. K. Koo, Q. Chen, N. Wong and G. H. Chen, *Dynamic Multiscale Quantum Mechanics/Electromagnetics Simulation Method*, J. Chem. Theory Comput., **8**, 1190 (2012).
[3] J. Q. Zhang, Z. Y. Yin, X. Zheng, C. Y. Yam and G. H. Chen, *Frequency-dependent response of emerging electronic devices*, arXiv:1301.0183.

978-3-901578-26-7 © 2013 Society for Micro- and Nanoelectronics

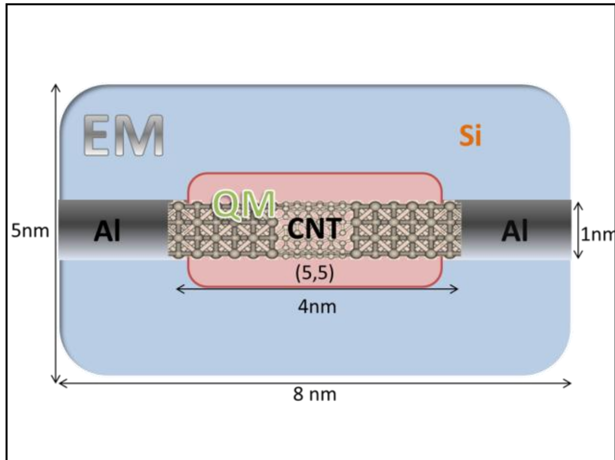

Fig. 1. A (5,5) CNT sandwiched by two aluminum leads in the center of a silicon environment

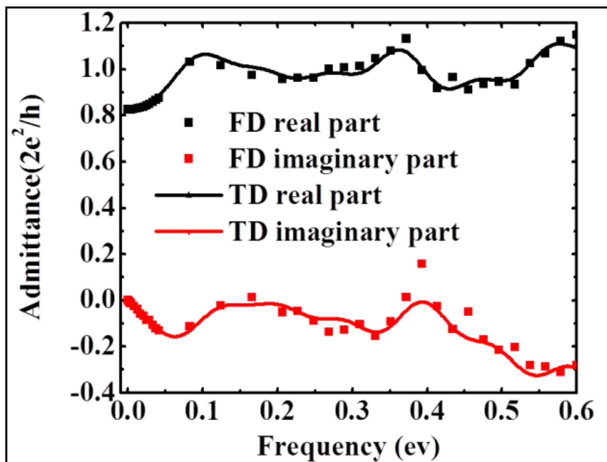

Fig. 2. Solid line: real (imaginary) part of dynamic admittance from time-dependent QM/EM calculation; dashed line: real (imaginary) part of dynamic admittance directly from frequency-dependent QM/EM method. A very well agreement can be found from this picture.

How far can we accelerate full-band atomistic device simulations through graphics processing units (GPUs)?

Mathieu Luisier
Integrated Systems Laboratory, ETH Zürich, 8092 Zürich, Switzerland, e-mail: mluisier@iis.ee.ethz.ch

Introduction As the size of transistors keeps shrinking, it becomes more and more important to include quantum mechanical, bandstructure, and atomistic effects to accurately simulate their properties. Hence, nano-TCAD tools that capture band non-parabolicity, atomic granularity, energy quantization, quantum confinement, and tunneling are required to design next-generation logic switches.

Advanced simulation models are computationally very intensive so they are either restricted to small devices or need some simplifications to be applied to realistic structures. For example, replacing the real-space by a mode space approach allows for the consideration of larger transistors [1]. At the algorithm level, a recursive Green's Function (RGF) solver [2-3] is faster than inverting an entire matrix. Finally, reducing the model complexity (tight-binding vs. DFT) decreases the computational burden.

Here, another approach based on novel hardware architectures is investigated to accelerate nanoelectronic device simulations: the usage of graphics processing units (GPUs). The transition from CPUs to GPUs demands for software modifications that can be significant. The purpose of this paper is to show what kind of speed-up can be obtained as function of the effort that is invested in code-rewriting.

Computational Strategy GPUs find their main application in 3D computer graphics and video cards, but can also be used as general-purpose computing units. Currently, they equip the largest supercomputer in the world called Titan and located at ORNL [4]. Usually, on each computational node, N_{GPU} GPUs are attached to N_{CPU} CPUs, as illustrated in Fig. 1(a). The total speed-up SU_{tot} that can be achieved when all the CPUs and GPUs work together, as compared to the case with CPUs only, is defined as

$$SU_{tot} = \frac{N_{GPU} \cdot SU_{GPU} + N_{CPU,working}}{N_{CPU}}, \quad (1)$$

where SU_{GPU} is the speed-up when comparing one single GPU with one single CPU and $N_{CPU,working}$ the number of CPUs that are actually working: due to the low memory of GPUs ($\leq$6 GB), $N_{CPU,working} < N_{CPU}$ so that the memory of the idle CPUs can be used to store GPU data.

To determine SU_{tot}, AMD Opteron 6272 CPUs with a frequency of 2.1 GHz and reaching a performance of P_{CPU}=16.8 GFlop/s [5] are selected. As GPUs, the Tesla K20 Kepler from NVIDIA with a peak performance of P_{GPU}=1170 GFlop/s are chosen [6]. Ideally, SU_{GPU}=P_{GPU}/P_{CPU}=70. However, even with an excellent programmer, SU_{GPU} will remain below 50 because it is difficult to fully exploit the GPU potential. Furthermore, a complete code rewrite in a GPU language is needed.

From Eq. (1) it appears that with multiple GPUs per node, the total speed-up SU_{tot} tends towards $N_{GPU} \cdot SU_{GPU}/N_{CPU}$: with 1 GPU for 4 CPUs, SU_{tot} $\approx$12.5 is possible. Many machines such as Titan at ORNL or Tödi at the Swiss National Supercomputing Centre (CSCS) [7] provide only one GPU for 16 CPUs. If two CPUs remain idle ($N_{CPU,working}$=N_{CPU}-2=14) for data storage, the maximum achievable speed-up SU_{tot}=4, obtained only after lots of code modifications. An attractive alternative when $N_{GPU} << N_{CPU}$ consists in off-loading only the code segments with heavy computations to the GPU. This hybrid approach requires less work and is tested here.

Results A full-band, atomistic quantum transport (QT) simulator based on the tight-binding model and the Non-equilibrium Green's Functions (NEGF) [8] is accelerated with GPUs. The algorithm that the QT solver uses to solve the NEGF equations [9] is slightly modified (200 lines of code) to off-load matrix operations to the GPUs.

Three applications are considered: a Si gate-all-around nanowire transistor, a non-flat graphene nanoribbon, and a Ge electron-hole bilayer tunneling transistor (EHBTFET) [10], as shown in Fig. 1(b-d). Some simulation results are depicted in Fig. 2 and 3. The time-to-solution with and without GPUs and the speed-up obtained with GPUs are reported in Fig. 4 as function of the number of CPUs (32 up to 4096) on Tödi at CSCS. An almost linear scaling of the time can be observed when the number of CPUs increases. More important, a speed up of 2 or more is obtained when GPUs are used, with a peak at 2.5 for the EHBTFET.

Conclusion In this paper, an acceleration of quantum transport simulations through GPUs has been presented. It is found that rewriting a TCAD simulator in a GPU language is only beneficial if a computer with several GPUs per node is available. Otherwise, off-loading code segments to the GPU brings useful speed-ups with much less efforts. Note that other accelerators such as the many integrated cores (MIC) from Intel are emerging with potential greater speed-up and less code modifications than GPUs.

References
[1] R. Venugopal et al., J. Appl. Phys. **92**, 3730 (2002). [2] R. Lake et al., J. Appl. Phys. **81**, 7845 (1997). [3] A. Svizhenko et al., J. Appl. Phys. **91**, 2343 (2002). [4] www.olcf.ornl.gov/titan/ [5] www.amd.com/la/Documents/Opteron_6000_QRG.pdf [6] www.nvidia.com/object/tesla-servers.html [7] www.cscs.ch/ [8] M. Luisier et al., Phys. Rev. B **74** 205323 (2006). [9] T. B. boykin et al., Phys. Rev. B **77** 165318 (2008). [10] L. Lattanzio et al., IEEE Elec. Dev. Lett. **33** 167 (2012).

978-3-901578-26-7 © 2013 Society for Micro- and Nanoelectronics

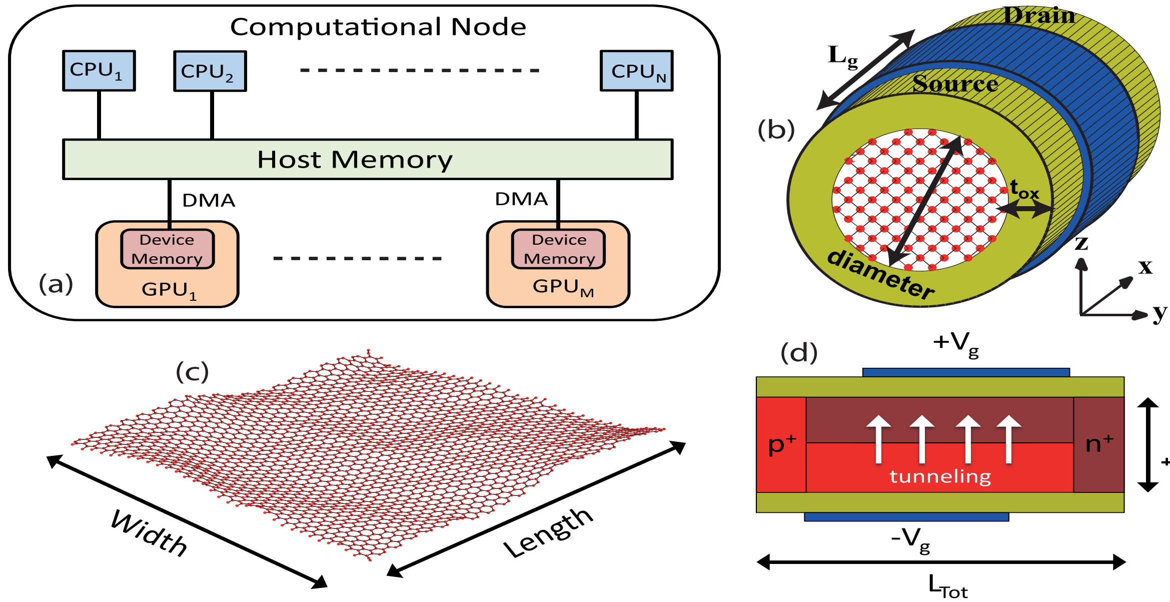

Fig. 1. (a) Schematic view of a typical computational node including N shared memory CPUs (hosts) and M GPUs (devices) connected through direct memory access (DMA). (b-d) Illustration of the nanoelectronic devices simulated in this work with either CPUs only or CPUs+GPUs. (b) Si gate-all-around nanowire field-effect transistor (GAA NW FET) with a diameter of d=4 nm, a gate length L_g=20 nm, and composed of N_A=31372 atoms. (c) Non-flat graphene nanoribbon (GNR) of width w=20 nm and length L=120 nm (N_A=97440). (d) Ge electron-hole bilayer tunneling field-effect transistor (EHBTFET) [10] made of N_A=42600 atoms with a body thickness t_{body}=10 nm and a total length L_{tot}=170 nm.

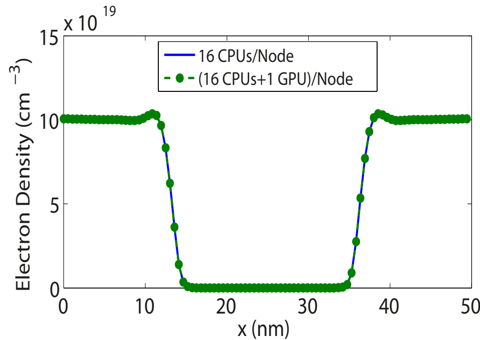

Fig. 2. Comparison of the electron density in the Si NW FET shown in Fig. 1(b) obtained with (dashed green line with circles) and without (solid blue line) the GPUs.

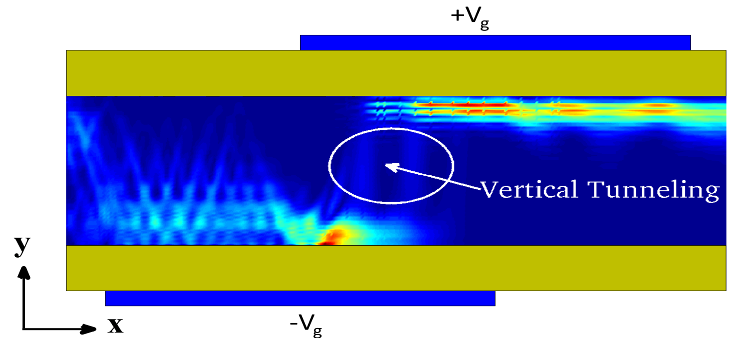

Fig. 3. Spatially-resolved ON-current flowing through the EHBTFET shown in Fig. 1(d). With GPUs, the simulation time could be reduced by a factor close to 2.5 as compared to CPUs only. Vertical tunneling paths appear clearly in the plot.

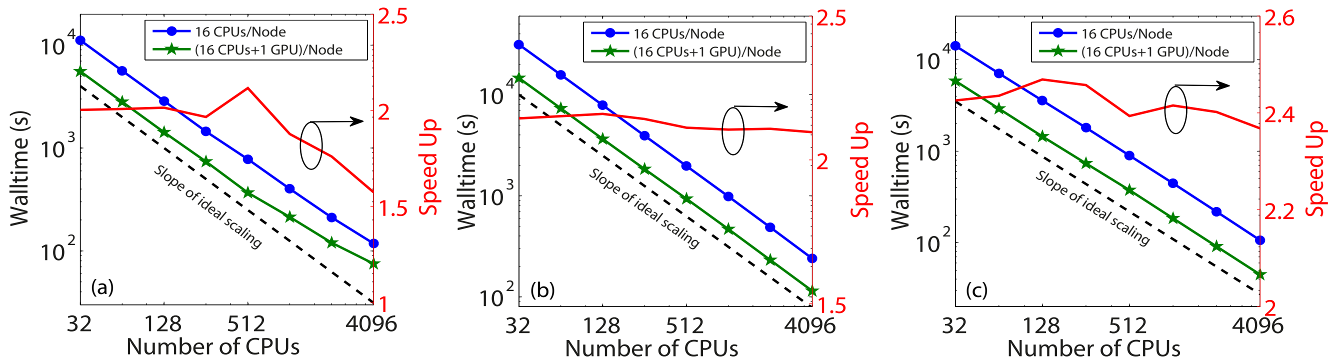

Fig. 4. Walltime vs. number of CPUs scaling curves to compute 1 Schrödinger-Poisson iteration for the (a) nanowire FET, (b) non-flat GNR, and (c) bilayer TFET shown in Fig. 1. Todi at CSCS is used: it contains 16 CPUs and 1 GPU per node. Two different types of numerical experiments are conducted: simulations with (green lines with stars) or without (blue lines with circles) the GPUs. In both cases, all the CPUs per node are utilized. The red curve indicates the speed up factor obtained when 16 CPUs and 1 GPU per node are used as compared to 16 CPUs only. Note that for the Si NW FET and Ge EHBTFET, 10 orbitals per atom are considered ($sp^3d^5s^*$ nearest-neighbor tight-binding model without spin-orbit coupling), 9 for the GNR (sp^3d^5). The largest Hamiltonian matrix amounts therefore to 876960 (GNR), then 426000 (TFET), and finally 313720 (NW).

Accelerated parallel computing of carrier transport simulation utilizing graphic processing units

A. Suzuki [1], T. Kamioka [1, 3], H. Imai [1], Y. Kamakura [2, 3], and T. Watanabe [1, 3]
[1] Faculty of Science and Engineering, Waseda University, Japan,
[2] Graduate School of Engineering, Osaka University, Japan,
[3] Japan Science and Technology Agency (JST), CREST, Japan.
e-mail: suzuki@watanabe.nano.waseda.ac.jp

INTRODUCTION

As the scaling down of Si MOSFET proceeds, the discreteness of the impurity distribution and the number of transported carriers emerges, so that the variability of device characteristics and intrinsic current noise arise as serious concerns [1, 2]. To address these issues, particle-based carrier transport simulation technique, e.g. molecular dynamics (MD), is a powerful method which allows us intuitive insight into the effect of the discreteness of impurity ions and carriers. However, the MD simulation requires huge computation resources to calculate the interaction forces acting on each pair of particles. This is a great obstacle to simulate the entire device structure including source and drain regions with high carrier and impurity density.

In recent years, graphics processing unit (GPU) has attracted much attention due to its large-scale parallelism ability. Many successful implementations on GPU have been reported for MD and Monte Carlo (MC) algorithms [3, 4]. However, to our knowledge, no application to the carrier transport simulation has been reported so far.

In this work, we demonstrate that the Ensemble Monte-Carlo/Molecular Dynamics (EMC/MD) method [5, 6] is successfully accelerated by GPU. The present result shows that EMC/MD simulation can be easily applied to the practical nano-scale device simulation including source and drain regions.

SIMULATION METHOD

In the EMC/MD method, carriers are treated as classical particles, and their real-space trajectories under the Coulomb point-to-point potentials are calculated by the MD algorithm. The acoustic and optical phonon scattering are described as stochastic changes in the momentum of carriers according to the standard energy-dependent formulations [6].

In this work, the EMC/MD algorithm is parallelized by utilizing GPU. Single GPU thread is assigned to the calculations associated with one electron, so that the number of thread is equal to the number of electrons. We employed NVIDIA GeForce GTX560Ti and GeForce GTX690, and compared the execution time with the single core calculation with Intel core i7 3930k CPU.

Figure 1 shows the simulated bulk n-type Si model. All electrons and ions are randomly placed inside the unit cell, on which the 3D periodic boundary condition is adopted. An external electric field of 1kV/cm is applied along the <100> axis. The time step is 10^{-17} s. We evaluate the execution time changing the number of electrons with keeping the total electron density. The execution time is defined as the duration to complete the 10^5 steps calculation.

Since carriers and impurity ions are treated as point charges in EMC/MD, a singular point of the Coulomb potential appears at zero distance. This is problematic in deal with the majority carriers in the source and the drain regions. To solve this problem, softened Coulomb potential is employed between electron and positively charged ions:

$$\varphi = -\frac{e^2}{4\pi\varepsilon}\frac{1}{\sqrt{r^2+\alpha^2}} \tag{1}$$

where e is the elementary charge, ε is the permittivity of semiconductor, and α is the softening factor. Eqn. 1 is commonly used formula in the field of gravity calculation [7].

RESUITS AND DISCUSSION

Figure 2 shows the execution time of the EMC/MD simulation using CPU and GPU. In the case of CPU calculation, the execution time is $O(N^2)$. By parallelizing with GPU computing, the execution time is successfully reduced to $O(N)$. A cross point of the execution times appears at 200

978-3-901578-26-7 © 2013 Society for Micro- and Nanoelectronics

electrons. Above 200 electrons, the computation speed with GPU exceeds that of CPU, and the benefit of the parallel computation increases as the number of elections increases. For small number of electrons, GPU computation gives no speed up, due to the overhead of parallelism and the poor performance of single GPU thread compared with that of the single CPU core.

Figure 3 shows the speedup rate, which is the ratio of the execution time with GPU to that with CPU. The GPU parallel computation speed is enhanced by more than 10 times in the case of several thousand particles. Thus the GPU computation is suitable for the practical nano-scale device simulation including source and drain regions. GeForce GTX690 shows better performance and scalability than GeForce GTX560Ti, mainly due to the difference in the number of Stream processors of these GPUs.

Figure 4 shows the calculated low field mobility in n-type Si plotted versus the impurity concentration. The mobility is determined by the mean travel distance along <100> under the external field of 1kV/cm. To reproduce the experimental mobility [8], the softening parameter should be changed between lower and higher electron densities.

CONCLUTION

We demonstrate that the GPU parallel computing is effective to accelerate the EMC/MD simulation involving large number of electrons and impurity ions. The nano-scale devices including source and drain regions can be fully simulated in a reasonable execution time by utilizing GPU.

ACKNOWLEDGEMENT

This work was supported by Grant-in-Aid for Scientific Research (B) (24310082) from Japan Society for the Promotion of Science and CREST from Japan Science and Technology Corporation (JST).

REFERENCES

[1] T. Kamioka et al.: IEDM Extd. Abs. 17.2.4 (2012).
[2] N. Sano et al.: IEDM Tech. Dig., 275 (2000).
[3] E. Alerstam et al.: J. Biomed Opt., 13:060504 (2008).
[4] J.A. Anderson et al.: J. Comp. Phys., 227, 5342 (2008).
[5] C. Jacoboni et al.: Rev. Modern Phys., **55**, 645 (1983).
[6] Y. Kamakura et al.: IEICE Trans. Elec. E-86-C, 357 (2003).
[7] A.E. Evrard, Mon. Not. R. astr. Soc., 235, 911 (1988).
[8] D.M. Caughey et al.: Proceeding of the IEEE, 55, 12, 2192 (1967).

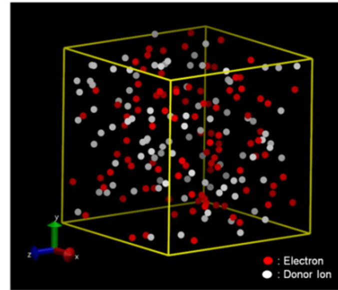

Fig. 1. Schematic view of the simulation system for electron transport in bulk-Si. Electrons and impurity ions are randomly placed inside a box.

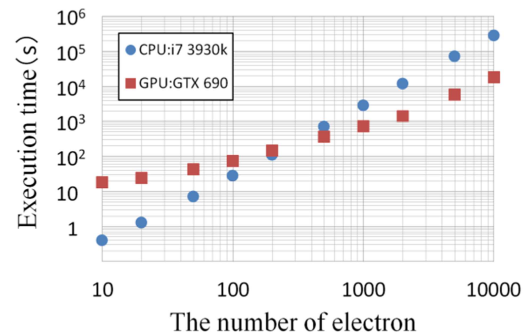

Fig. 2. The results compering the execution time of the CPU used only single core and GPU**.** The time step is 10^{-17}, and 10^5steps simulated. The electron density D is 1.0×10^{18} cm^{-3}, and the number of electron is from 10 to 10000.

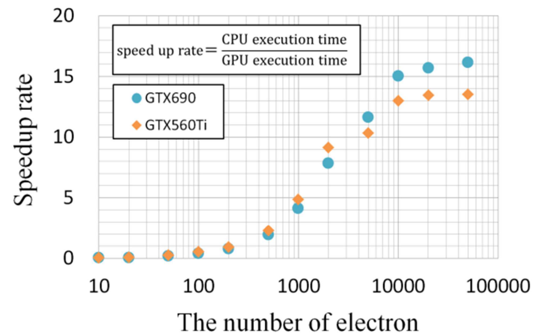

Fig. 3. The speed up rate of which is ratio between the execution time of CPU and that of GPU. The speedup rate reaches more than 10 times in several thousand particles.

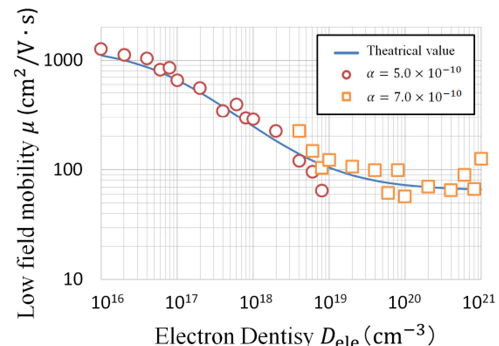

Fig. 4. The impurity concentration dependence of the low field mobility. The simulation is performed for a long time enough to reach the convergence. The low field mobility is simulated 100 ps with 100 elections and impurity ion.

Effect of Interface Roughness on Carrier Transport in Asymmetric Channel: An EMC/MD Simulation Study

H. Imai[1,5], T. Kamioka[2,5], Y. Kamakura[3,5], K. Ohmori[4,5], K. Shiraishi[4,5], M. Niwa[4,5], K. Yamada[4,5] and T. Watanabe[2,5]
[1]Faculty of Science and Engineering, Waseda University, Tokyo, Japan
[2]Waseda University, Institute of Nanoscience and nanotechnology, Tokyo, Japan
[3]Division of Electronic and Information Engineering, Osaka University, Osaka, Japan
[4]Graduate School of Pure and Applied Science, University of Tsukuba, Ibaraki, Japan
[5]Japan Science and Technology Agency (JST), CREST, Saitama, Japan
e-mail: h.y-imai@toki.waseda.jp

INTRODUCTION

Surrounding-gate metal-oxide-semiconductor (MOS) transistors have been attractively studied as promising devices for logic and memory LSIs [1]. In such vertical transistors, it is expected that the channel geometry tends to become asymmetric, e.g. taper shaped, due to the difficulties in the fabrication process [1].

In our previous work, it is found that mean current of an asymmetric horn-shaped channel, which widens from the source to the drain side, increases compared those of a symmetric straight channel [2]. The work, however, assumed the roughness at the sidewalls of channel is so small that the scattering is considered to be specular. This work reports on the effect of roughness at sidewalls on carrier transport in asymmetric channels, by using the ensemble Monte-Carlo/ molecular dynamics (EMC/MD) method [3,4].

SIMULATION METHOD

The carrier transport is simulated by EMC/MD method [3,4]. Carriers are treated as classical particles, and their real-space trajectories under the Coulomb point-to-point potentials are calculated by MD algorithm. The acoustic and optical phonon scatterings are taken into account as stochastic changes in the momentum of carriers according to the standard energy-dependent formulations.

We have examined three types of Si channels as illustrated in Fig. 1. One is a symmetric straight channel which corresponds to a conventional channel. The others are asymmetric horn-shaped and reserved-horn-shaped channels whose widths vary linearly from source to drain sides. These channels are characterized by a flare angle. Each device has the same volume so as to have the same resistance. Each channel is assumed to be intrinsic, containing no impurity ions. Only conduction electrons are considered as carriers. The carrier densityis the same (4.7×10^{18} cm^{-3}) for each device.

In order to reproduce the scattering at the sidewalls, the cylindrical objects are introduced as building units of the sidewall [2]. Carriers are repelled from the cylindrical objects. The interaction between carriers and the cylindrical object is described as a repulsive potential with cylindrical symmetry, whose axis is oriented perpendicular to the longitudinal direction. When a carrier approaches the interface, the carrier is elastically scattered at the sidewall. The roughness of the sidewall can be controlled by changing the radius of the cylindrical object, $\boldsymbol{r_{core}}$.

In these conditions, the current under the constant electric field of 5 kV/cm along the channel is estimated by counting the number of carriers transporting at a cross section of the channel per unit time.

RESULTS AND DISCUSSION

Fig. 2 shows the relation between mean current and flare angle for different roughness values. Although the mean current in every channel slightly decreases with the increase in the roughness, the mean current is enhanced in horn-shaped channels.

Fig. 3 shows the distribution of carrier velocity of longitudinal component along channel. For horn-shaped channels, the distribution shifts to higher velocities compared to the straight channel. Thus, the increase in the mean current in horn-shaped channels can be attributed to the enhancement in the carrier velocity.

978-3-901578-26-7 © 2013 Society for Micro- and Nanoelectronics

It is noted that a hump appears at high velocity side in the distribution, as indicated by the arrow in Fig. 3. This suggests the existence of carriers with quasi-ballistic transport [5], since the distribution does not obey a Gaussian. The enhancement in the hump intensity for horn-shaped channels means that carrier energy is not well relaxed due to suppression of scattering.

The hump intensity is weakened with the increase in roughness (the inset in Fig. 3), indicating the decrease in the number of carriers with ballistic transport. This is due to the increase in the probability of the back scattering towards the source side.

From above results, it is found the roughness at the sidewalls does not have a significant impact on the conductivity of horn-shaped channels. Even if the scattering becomes diffusive at the interface, the momentum of carriers in average kept collimated to the drain side by the tilted walls

CONCLUSION

The advantage of the horn-shaped channels in the conductivity is preserved even with the increase in the roughness at the sidewalls. The direction of current flow is important for device performance in the introduction of asymmetric channel geometries.

ACKNOWLEDGEMENT

This work was supported by Grant-in-Aid for Scientific Research (B) (24310082) from Japan Society for the Promotion of Sience and CREST from JST.

REFERENCES

[1] K. Sakui et al., *A new vertical MOSFET "Vertical Logic Circuit (VLC) MOSFET" suppressing asymmetric characteristics and realizing an ultra compact and robust logic circuit,* Solid-State Electronics, **54**, 1457 (2010).

[2] T. Kamioka et al., *Impact of channel Shape on Carrier Transport Investigated by Ensemble Monte Carlo/ Molecular Dynamics Simulation*, SISPAD proc., 83 (2011).

[3] C. Jacoboni et al., *The Monte Carlo method for the solution of charge transport in semiconductors with applications to covalent materials*, Rev. Mod. Phys., **55**, 645 (1983).

[4] Y. Kamakura et al., *Ensemble Monte Carlo/Molecular Dynamics Simulation of Inversion Layer Mobility in Si MOSFETs Effects of Substrate Impurity*, IEICE Trans. Electron., **E86-C**, 357 (2003).

[5] M. Lundstrom et al., *Essential Physics of Carrier Transport in Nanoscale MOSFETs*, IEEE Trans. Electron. Dev., **49**, 133 (2002).

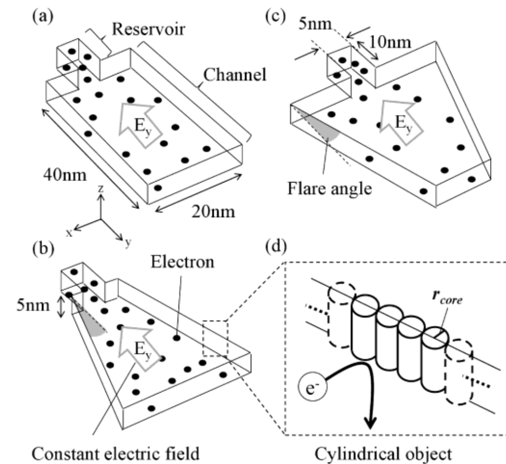

Fig. 1. Device models simulated in this study: (a) symmetric straight channel, (b) asymmetric horn-shaped channel, (c) asymmetric reserved-horn-shaped channel, and (d) cylindrical objects as building blocks of sidewalls. Carriers are injected from a reservoir connected to the channel.

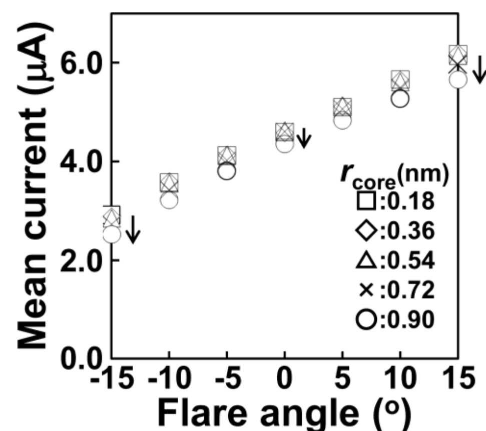

Fig. 2. Relation between mean current and flare angle for different roughness values.

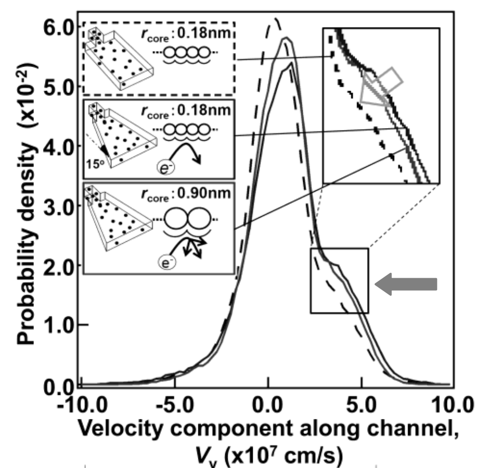

Fig. 3. Distribution of carrier velocity of longitudinal component along channel.

Deterministic DG Solvers for EPM-Boltzmann-Poisson Transport

Jose A. Morales Escalante*, Irene M. Gamba*, Armando Majorana†,
Yingda Cheng‡, Chi-Wang Shu§, and James R. Chelikowsky*
*ICES, The University of Texas at Austin, USA. e-mail: jmorales@ices.utexas.edu
† Dipartamento di Matematica e Informatica, Universitá degli Studi di Catania, Italy.
‡ Department of Mathematics, Michigan State University, USA.
§ Division of Applied Mathematics, Brown University, USA.

INTRODUCTION

The purpose of this work is to incorporate full electronic band structure computed by Empirical Pseudopotential Methods (EPM) in Discontinuous Galerkin (DG) transport schemes in order to solve the Boltzman-Poisson transport along numerical energy surfaces generated by EPM.
The dynamics of electron transport in modern semiconductor devices can be described by the semiclassical Boltzmann-Poisson (BP) model:

$$\frac{\partial f_i}{\partial t} + \frac{1}{\hbar}\nabla_k \varepsilon_i \cdot \nabla_x f_i - \frac{q_i}{\hbar} E \cdot \nabla_k f_i = \sum_j Q_{i,j} \quad (1)$$

$$\nabla_x \cdot (\epsilon \nabla_x V) = \sum_i q_i \rho_i - N(x), E = -\nabla_x V \quad (2)$$

where $f_i(x,k,t)$ is the probability density function over phase space (x,k) of a carrier in the i-th energy band in position x, with crystal momentum $\hbar k$ at time t. The collision operators $Q_{i,j}(f_i, f_j)$ model i-th and j-th carrier recombinations, collisions with phonons or generation effects. $E(x,t)$ is the electric field, $\varepsilon_i(k)$ is the i-th energy band surface, the i-th charge density $\rho_i(t, \mathbf{x})$ is the k-average of f_i, and $N(\mathbf{x})$ is the doping profile. Deterministic solvers using the Discontinuous Galerkin (DG) method have been proposed in [1], [2] to model electron transport along the conduction band for 1D diodes and 2D double gate MOSFET devices with the energy band $\varepsilon(k)$ given by analytical models valid close to a local minimum, such as the parabolic or the Kane models. These solvers are shown to be competitive with Direct Simulation Monte Carlo methods.
This preliminary work is focused on simulations for electron transport along a single conduction band for Si computed by EPM, which gives a full band structure spectral approximation in k-space [3] for a crystal lattice model as the sum of potentials due to individual atoms and associated electrons, with few parameters fitting empirical data such as optical gaps, absorption rates, etc.

WORK & PRELIMINARY RESULTS

When the approximation $\varepsilon(k) = \varepsilon(|k|)$ for the conduction band is assumed (as in the parabolic or Kane band approximations), computations for collision terms using Fermi's Golden Rule are significantly reduced. However, this assumption simplifies band structure details and hinders the application to transport of electrons in relative strong Electric fields which induce a flow in phase space that requires values of the band structure that not only are far from the conduction band minimum, but where also the band structure becomes anisotropic (Fig. 1). In this preliminary work, we calculated the EPM-Boltzmann-Poisson transport with a spherically averaged EPM calculated energy surface and compared the output to the classical analytical band models. We observed a significant correction in moments, exhibiting a computational strategy as a midpoint in between an analytical radial and full conduction band model.
To this end, the calculated EPM band structure was averaged by means of Gaussian quadrature on angular space over k-spheres around the local energy minimum $k_0 = (0.8562, 0, 0)2\pi/a$. In this way we obtain a band model that not only represents the variation of the conduction band in the k-space, but also has radial dependence $\varepsilon(|k|)$, retaining then desired advantages. These EPM spherical averages

978-3-901578-26-7 © 2013 Society for Micro- and Nanoelectronics

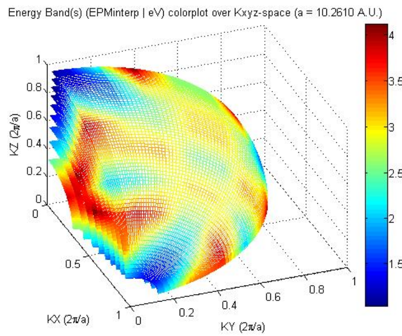

Fig. 1. Conduction Band (CB) for Si (E) Color Plot in k-space by Local EPM. First Quadrant Si Brillioun Zone. CB Min: $k_o = (0.8562, 0, 0)(2\pi/a)$

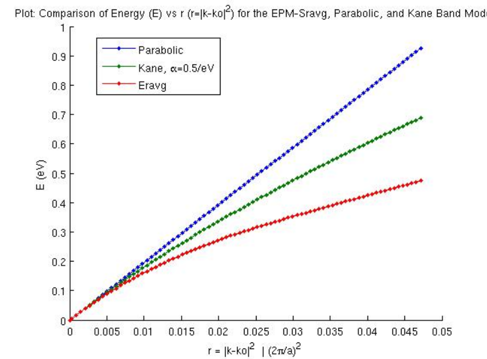

Fig. 2. Energy (E) vs. $r = |k - k_o|^2$ for the Parabolic, Kane, and EPM Radial Average Band Models. $\frac{dE}{dr}$ at the center-point of each k-cell calculated by cubic splines

of the first conduction band are shown in Fig. 2 vs $r = |k - k_0|^2$ for Si (in red), along with the parabolic (blue) and Kane (green) conduction band models. Following the computational strategy in [2], a spherical coordinate transformation over k is applied to (1). In this work we consider 1D $n^+ - n - n^+$ $1\mu m$ Si diodes with either a $400nm$ or a $50nm$ channel in the middle, with doping of $5 \times 10^{23}/m^3$ in the $n+$ region and $2 \times 10^{21}/m^3$ in the n region. Since for the approximated $\varepsilon(k) = \varepsilon(|k|)$, then, when the initial condition also depends on $|k|$, the problem retains azimuthal symmetry in k-space, which is suitable for dimensionality reduction for one dimensional x-space transport.

We compare the transport calculated on three different conduction band models: the EPM spherical average, parabolic, and Kane (Fig. 2). The derivative for the EPM average is interpolated by splines. Plots of average kinetic energy (Fig. 3) and momentum (current, Fig. 4) (moments of f) are shown for a $400nm$ channel with a 0.3 V potential bias at $t = 5.0ps$. There is a clear quantitative difference particularly for these moments, calculated as $\varepsilon(k)$-weighted averages in k-space between the different used band models.

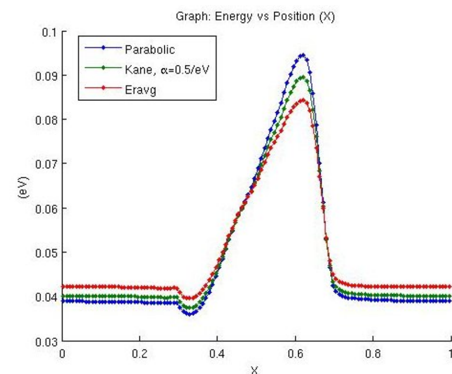

Fig. 3. Comparison of Average Energy (ε) vs. Position (x) for different Conduction Band Models: Parabolic, Kane, EPM Average. Bias: 0.3 Volt. $t = 5.0ps$.

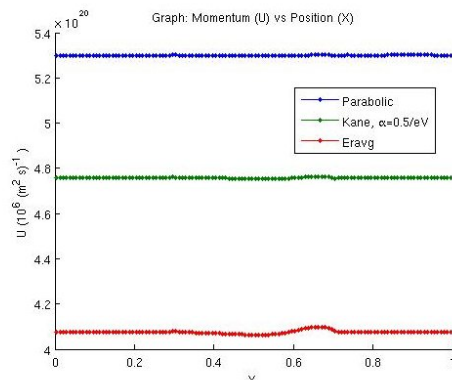

Fig. 4. Comparison of Current (Momentum) vs. (x, t) plots for different Conduction Band Models: Parabolic, Kane, EPM Average. Bias: 0.3 Volt. $t = 5.0ps$.

REFERENCES

[1] Y. Cheng, I. M. Gamba, A. Majorana, and C.W. Shu *A Discontinous Galerkin solver for Boltzmann-Poisson systems in nano-devices*, CMAME **198**, 3130-3150 (2009).

[2] Y. Cheng, I. M. Gamba, A. Majorana and C.-W. Shu, *A discontinuous Galerkin solver for full-band Boltzmann-Poisson models*, IWCE13 Proceedings (2009).

[3] J. Chelikowsky, and M. Cohen, *Electronic Structure of Silicon*, Physical Review B **10**, 12 (1974).

New self-consistent phonon-electron BTE solver for the simulation of ultra-small DG-MOSFET

T.T. Trang Nghiêm, J. Saint-Martin, P. Dollfus
Institute of Fundametal Electronics, University of Paris Sud, F91405 Orsay cedex, France
e-mail: jerome.saint-martin@u-psud.fr

ABSTRACT

To study the self-heating effects, we have developed a new efficient tool that solves self-consistently the Boltzmann transport equation (BTE) for both electrons and phonons. A Monte Carlo solver for electrons is coupled with a direct solver for the phonon transport (pBTE). In this work, this simulator is used to investigate the self-heating in a 20 nm-long double gate MOSFET.

For electrons, the Monte Carlo model used is a semi-classical ensemble simulator self-consistently coupled with a 2-D Poisson solver. All details of the analytic band structure and the scattering parameters may be found in [1,2]. This approach evaluates very accurately the phonon emission and absorption spectra in both real and energy space.

In the relaxation time approximation, for each phonon polarization s (i.e. LA, TA, LO, TO), the BTE for phonons can be expressed as

$$\vec{v}_{g,s} \cdot \nabla_{\vec{r}} N_s(\vec{r},\vec{q}) = -\frac{N_s(\vec{r},\vec{q}) - N_{s,T_{Fourier}}(\vec{r},\vec{q})}{\tau_s(T_{Fourier}(\vec{r}),\vec{q})} + G(\vec{r},\vec{q}) \quad (1)$$

where $v_{g,s}$ is the group velocity, $N_s(\vec{r},\vec{q})$ is the particle number, $\vec{r}$ is the position and $G(\vec{r},\vec{q})$ is the phonon generation term provided by the electron transport solution. $N_{s,TFourier}$ is the equilibrium phonon number at temperature $T_{Fourier}$, where $T_{Fourier}$ is the temperature obtained by solving the heat equation. τ_s is the total relaxation time computed via the Mathiessen's rule including three-phonon, phonon-impurity [3] and phonon-boundary scattering [4] mechanisms. The optical decay into acoustic phonon modes is considered too [5]. An analytical parabolic dispersion was used for phonons [6]. An out-of-equilibrium effective temperature T_{eff} is derived from the local phonon energy density, and is reinjected in the electron MC simulator via the update of electron-phonon scattering rates. The loop is repeated until a convergence is reached.

Fig. 1 shows the simulated Silicon-based DG-MOSFET with film thickness of 20 nm. In Fig. 2 the potential profiles along the device reveal the presence of high electric field at the drain-end of the channel, where, under high drain bias, hot electrons can emit many high-energy phonons, as shown in Fig. 3. In Fig. 4 the profile of effective temperature is plotted for different numbers of loops. We observe that the temperature evolves significantly between the 1st loop and the 2nd loop. However, after the 3rd loop the convergence is reached. Finally, the temperature in the channel reaches 430 K, which has an impact on the electron transport in the channel. For instance, Fig. 6 shows that the fraction B_{int} of electrons that cross the channel ballistically [1] is reduced when taking the self-heating effect into account. This leads to a significant reduction of current, as shown in Fig. 7. In this device, the reduction reaches 16% for $V_{DS} = 1.5$ V.

Our new self-consistent electron-phonon Finally, BTE solver provides very detailed insight into electro-thermal effect at the nano-scale.

REFERENCES

[1] J. Saint Martin et al., *On the ballistic transport in nanometer-scaled DG MOSFETs*, IEEE Trans. Electron Devices, **51**, 1148 (2004).

[2] V. Aubry-Fortuna et al., *Electron effective mobility on strained-Si/Si$_{1-x}$Ge$_x$ device using Monte Carlo simulation*, Solid-State Electronics **49**, 1320 (2005).

[3] M. G. Holland, *Analysis of lattice thermal conductivity*, Phys. Rev. **132**, 2461 (1963).

[4] S. B. Soffer, *Statistical model for the size effect in electrical conduction*, J. Appl. Phys. **38**, 1710 (1967).

[5] J. Rowlette, K. E. Goodson, *Fully coupled nonequilibrium electron-phonon transport in nanometer-scale silicon FETs*, Trans. Electron Devices **55**, 220 (2008).

[6] E. Pop et al., *Analytic band Monte Carlo model for electron transport in silicon including acoustic and optical phonon dispersion*, J. Appl. Phys. **96**, 4998 (2004).

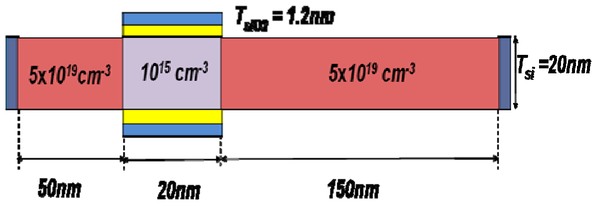

Fig. 1. Simulated Double-Gate MOSFET.

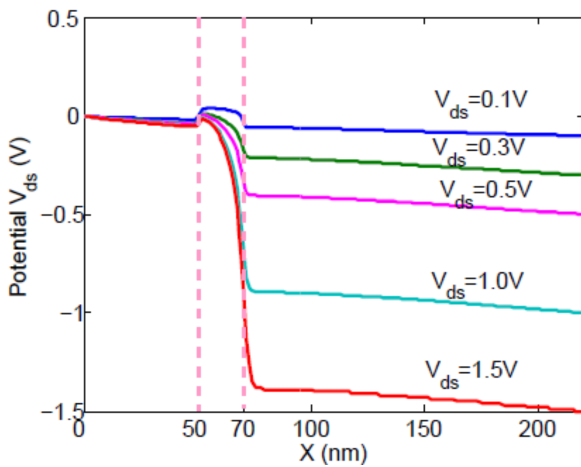

Fig. 2. Potential profile (bottom of conduction band) for various V_{DS} at $V_G = 0.5$ V (isotherrmal simulations).

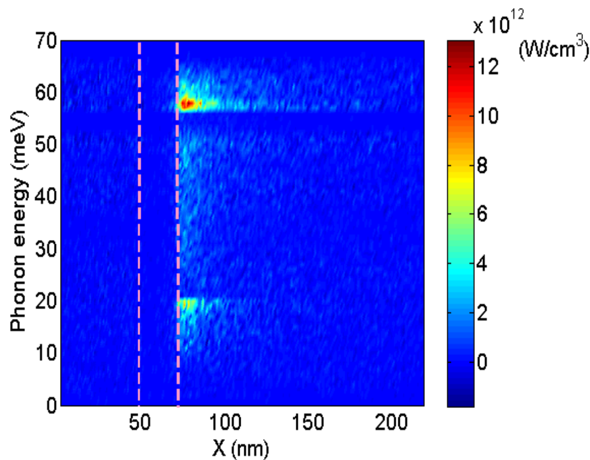

Fig. 3. Energy spectrum of generated phonons along the device at $V_G = 0.5$ V and $V_{DS} = 1.5$ V.

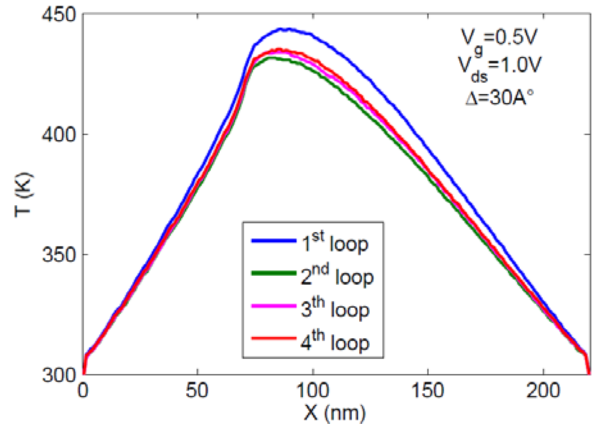

Fig. 4. Profile of effective temperature T_{eff} along the device obtained at a given bias point after different loop numbers.

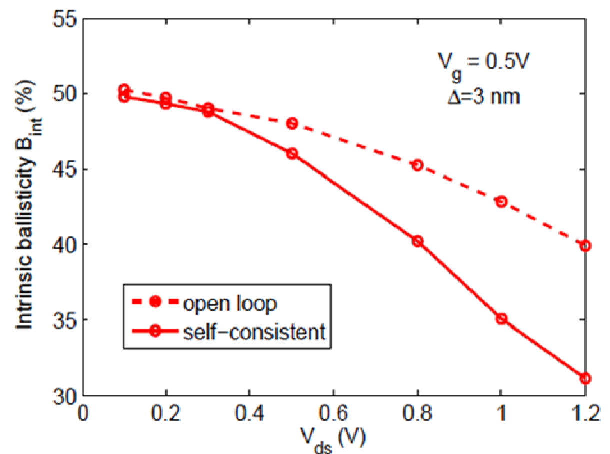

Fig. 5. Intrinsic ballisticity as a function of V_{DS} for V_G=0.5V. Isothermal–open loop (dashed line) and self-consistent simulation (continuous line).

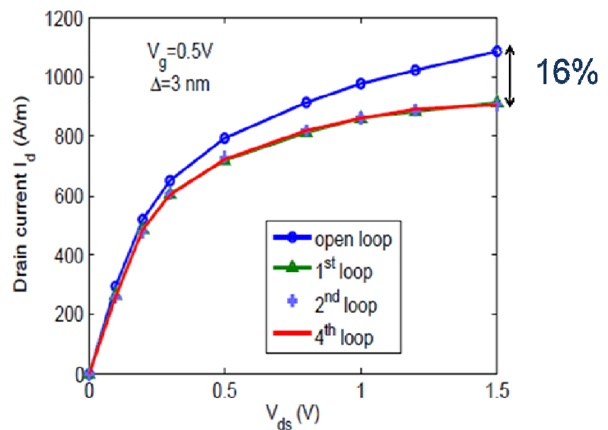

Fig. 6. I_D-V_{DS} characteristics for $V_G = 0.5$ V for different numbers of loops of electron and phonon transport simulation.

Device Simulation of Hall Effect around Grain Boundaries in Poly-Si Films

M. Kimura, M. Hirako, T. Yamaoka, and S. Tani
Department of Electronics and Informatics, Ryukoku University, Seta, Otsu 520-2194, Japan
e-mail: mutsu@rins.ryukoku.ac.j

INTRODUCTION

Device simulation has been recognized as a powerful tool to develop and design semiconductor devices. However, few simulation algorithms have been published to calculate carrier transport subject to Lorentz force due to magnetic field. On the other hand, Hall effect arising from the Lorentz force have been utilized to evaluate material properties and diagnose fabrication processes. Recently, it was found that the evaluation technique using the Hall effect can be utilized also for poly-Si films [1]. Moreover, it was proposed that the micro poly-Si Hall cells can be applied to high-resolutional real-time magnetic sensors [2]. However, complicated Hall effect may occur because of uneven structures in poly-Si films, and no detailed discussion has been executed for carrier transport subject to the Lorentz force.

In our research, we have developed a simulation algorithm of carrier transport subject to Lorentz force in semiconductor films [3]. The Lorentz current is discretized with the drift and diffusion currents, and the simulation algorithm is implemented in finite difference methods. Hall effect around grain boundaries in poly-Si films is evaluated as a simulation example, and it is found that high Hall voltages are generated at the grain boundaries. Particularly in this presentation, we compare the Hall effect around the grain boundaries with different values of trap density.

DEVICE STRUCTURE

The device structure for the device simulation of the Hall effect around the grain boundaries in the poly-Si films is shown in Fig. 1. Here, the dopant species is n-type, the dopant density is 1×10^{18} cm^{-3}, the carrier mobility is 100 cm^{2}V^{-1}s^{-1}, a grain boundary exists at the center of the poly-Si film, the trap density at the grain boundary is 0.5×10^{13} or 1×10^{13} cm^{-2}, the film width is 100 nm, the film length is 400 nm, the applied voltage is 1 mV, and the magnetic field is 0.1 T.

SIMULATION RESULTS

The spatial distributions of the electric potentials are shown in Fig. 2. It is found that high potential barriers are generated at the grain boundaries and spread to a few tens nm. Although this phenomenon has been reported in the previous article, it is confirmed that the simulation algorithm of carrier transport subject to Lorentz force does not spoil the conventional algorithm for the Poisson equation and drift and diffusion currents. Moreover, it is also found that as the trap density increases, the potential barrier becomes higher.

The spatial distributions of the Hall voltages are shown in Fig. 3. Here, the Hall voltages are defined as the difference of the electric potentials with and without the magnetic field. It is found that higher Hall voltages are generated at the grain boundaries than those in the grains. This is because the hall voltages are proportional to the carrier velocity, i.e. $V_H=vBW$. The carrier densities are lower owing to the potential barriers at the grain boundaries, and the carrier velocities are higher to maintain the conservation law of the electric current, i.e., Kirchhoff Law. Although the carrier mobility is the same, the electric fields at the grain boundaries are higher than those in the grains. As a result, the Hall voltages are higher at the grain boundaries. Moreover, it is also found that as the trap density increases, the potential barrier becomes higher, the carrier velocity becomes slower, and the Hall voltage becomes smaller. This phenomenon should be noted when the Hall effect is utilized to evaluate material properties in poly-Si films. The carrier mobility may be overestimated, and the carrier density may be underestimated.

REFERENCES

[1] M. Kimura, et al., Electrochem. Solid-State Lett. **13**, J96 (2010).
[2] Y. Yamaguchi, M. Kimura, et al., IEEE Electron Device Lett., **31**, 1260 (2010).
[3] M. Kimura, et al., Solid State Electronics, **63**, 137 (2011).

978-3-901578-26-7 © 2013 Society for Micro- and Nanoelectronics

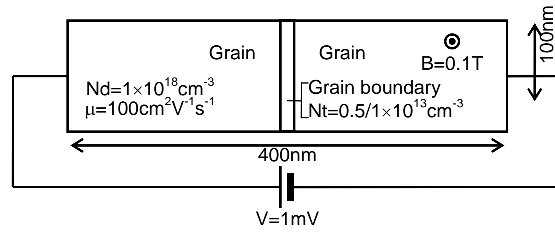

Fig. 1. Device Structure for the Device Simulation of the Hall Effect around the Grain Boundaries in the Poly-Si Films

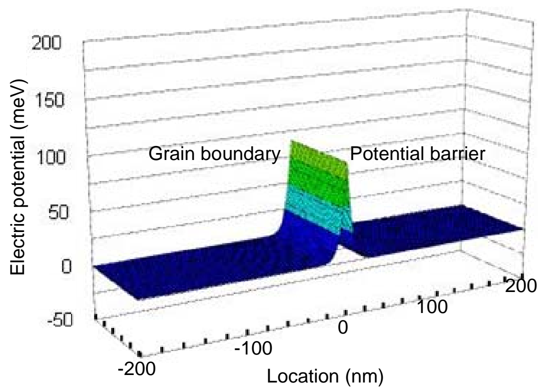

(a) Trap density = 0.5×10^{13} cm^{-2}

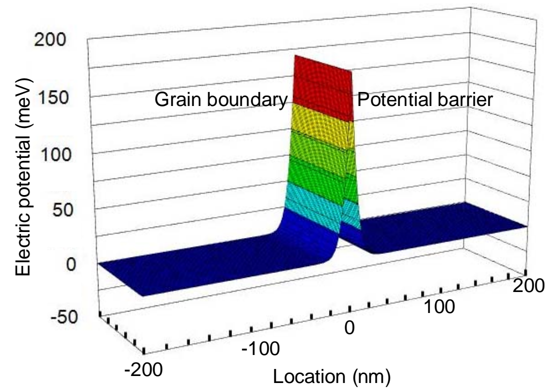

(b) Trap density = 1×10^{13} cm^{-2}

Fig. 2. Simulation Results of the Spatial Distributions of the Electric Potentials around the Grain Boundaries

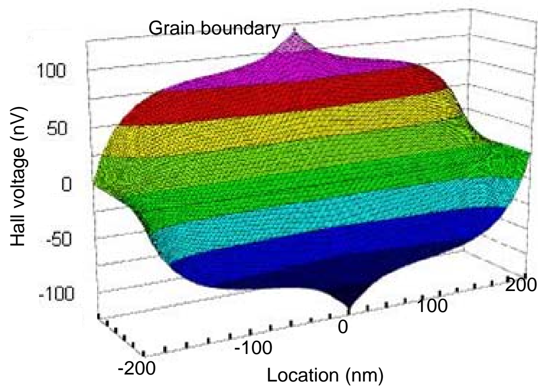

(a) Trap density = 0.5×10^{13} cm^{-2}

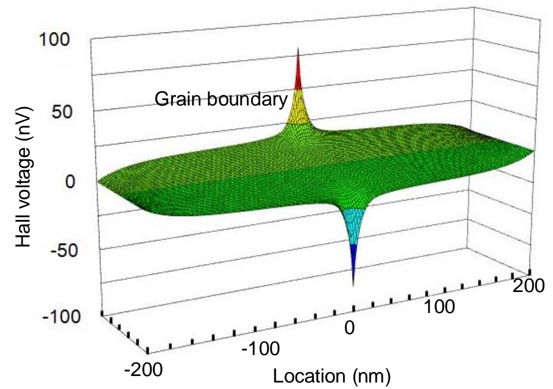

(b) Trap density = 1×10^{13} cm^{-2}

Fig. 3. Simulation Results of the Spatial Distributions of the Hall Voltages around the Grain Boundaries

Comparison of Off-Leakage Current between LTPS and HTPS TFTs using Activation Energy and Device Simulation

M. Kimura and A. Nakashima
Department of Electronics and Informatics, Ryukoku University, Seta, Otsu 520-2194, Japan
e-mail: mutsu@rins.ryukoku.ac.j

INTRODUCTION

Poly-Si thin-film transistors (TFTs) have been widely utilized for flat-panel displays (FPDs), such as liquid-crystal displays (LCDs), organic light-emitting diode displays (OLEDs), and electronic papers (EPs). Although the reduction of the off-leakage currents is also important, the mechanism of the off-leakage currents has not yet sufficiently discussed. In this presentation, we will compare transistor characteristics between low-temperature processed poly-Si (LTPS) TFTs [1] and high-temperature processed poly-Si (HTPS) TFTs [2], which are two typical kinds of TFTs, using activation energies and device simulation and clarify the mechanism of the off-leakage currents.

TRANSISTOR CHARACTERISTIC

LTPS TFTs are fabricated using the usual fabrication processes including excimer laser crystallization (ELC) [1]. HTPS TFTs are fabricated using the usual fabrication processes including solid-phase crystallization (SPC) [2]. Both the TFTs have the lightly-doped drain (LDD) structure. Although the device dimensions are slightly different between them, we think that we can compare them in the following sections.

The temperature dependences of the transistor characteristics are shown in Fig. 1. The field effect mobility (μ_{FE}) of the LTPS and HTPS TFTs are 67 and 38 $cm^2V^{-1}s^{-1}$, respectively. It is found that the temperature dependences of the off-leakage currents are larger than those of the on currents for both the TFTs.

The activation energies (E_a) of the transistor characteristics are shown in Fig. 2. In the off states, E_a for V_{ds}=0.1V is higher than that for V_{ds}=5V for both the LTPS and HTPS TFTs. E_a for V_{ds}=5V decreases as $|V_{gs}|$ increases only for the LTPS TFT.

MECHANISM ANALYSIS

The simulation results of the hole density and electric field around the junctions between the channel, LDD, and drain regions are shown in Fig. 3. It is found that a hole channel is lightly formed at the front-insulator interface in the LDD region, which originates from the carrier diffusion from the channel region. A pseudo p/n junction and a depletion layer appear at the junction between the LDD and drain regions, which make the electric field strong. The off-leakage current will be caused by the carrier generation there.

We will assume that the carrier generation is caused by the phonon-assisted tunneling with Poole-Frenkel effect (PAT) [3]. The simulation results of the energy band around the junction between the LDD and drain regions and PAT mechanism are shown in Fig. 4. A, B, and C in Fig. 2 roughly correspond to A, B, and C in Fig. 4. First, in the A state, the electric field exists due to the built-in potential. Because both |Vgs| and Vds are small, the electric field is gentle. An electron (e^-) is activated from a trap state in the bandgap to a certain energy level by the thermal activation and transported to the conduction band (E_c) by the tunneling. A hole (h^+) is activated from the trap state to a certain energy level and likewise transported to the valence band (E_v), and vice versa. Roughly speaking, the generation rate is approximated to be proportional to $\exp(-E_a/kT)$. Next, in the B state, because V_{ds} increases, the electric field becomes steeper, and E_a decreases. Finally, in the C state, because $|V_{gs}|$ increase, the electric field becomes further steep, and E_a further decreases for the LTPS TFT. For the HTPS TFT, E_a does not decrease so much. We think that this is due to the short tunneling length, which should be discussed in the future.

ACKNOWLEDGEMENT

This work is partially supported by a collaborative research with Seiko Epson.

REFERENCES

[1] A. Nakashima and M. Kimura, IEEE Electron Device Lett., **32**, 764 (2011).
[2] M. Kimura, et al., IEEE Electron Device Lett., **33**, 682 (2012)
[3] M. Kimura, et al., Electrochem. Solid-State Lett., **13**, H409 (2010).

978-3-901578-26-7 © 2013 Society for Micro- and Nanoelectronics

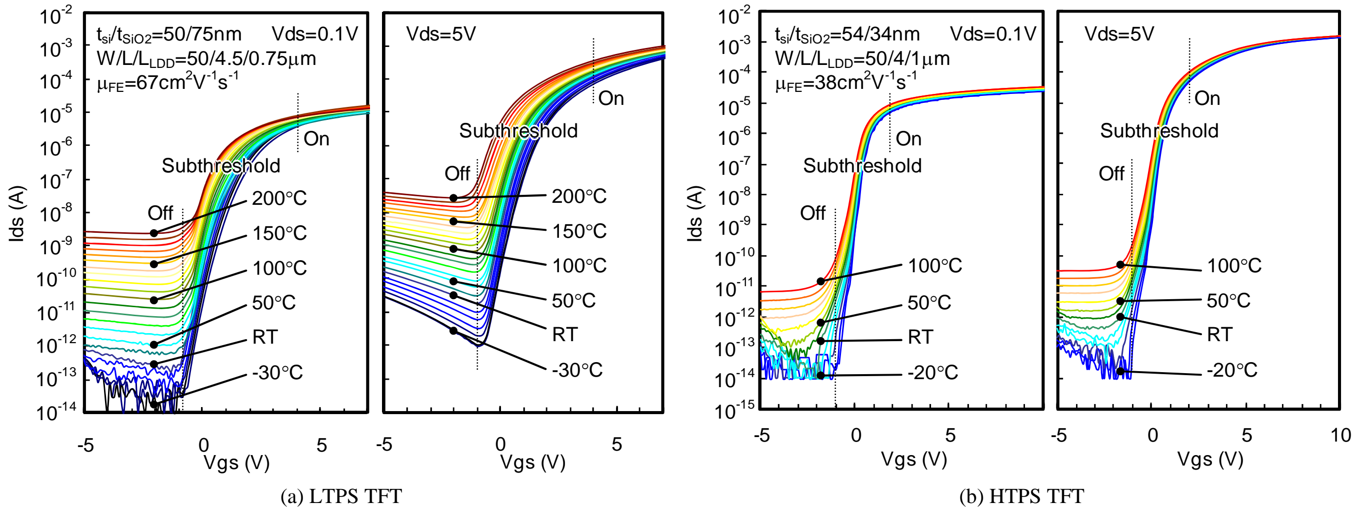

(a) LTPS TFT (b) HTPS TFT

Fig. 1. Temperature Dependences of the Transistor Characteristics

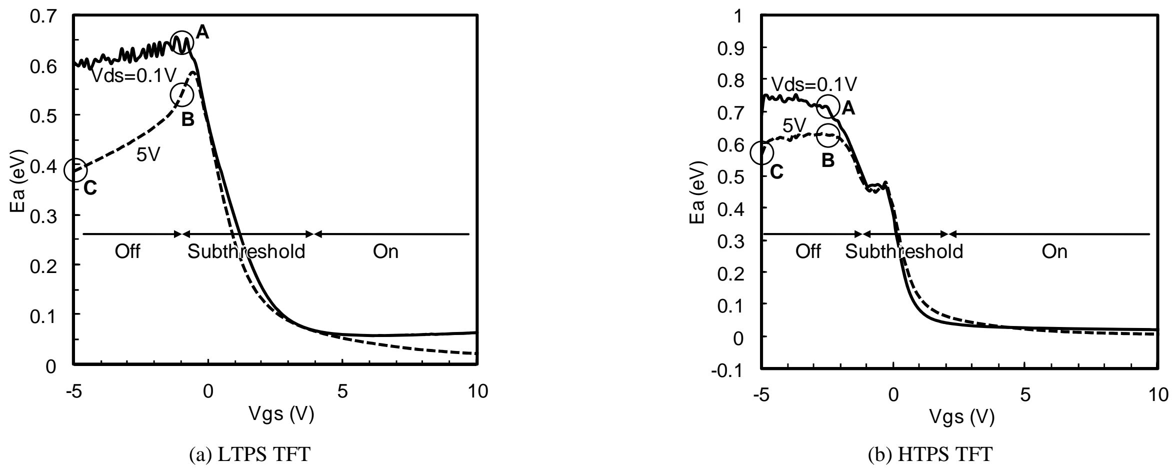

(a) LTPS TFT (b) HTPS TFT

Fig. 2. Activation Energies of the Transistor Characteristics

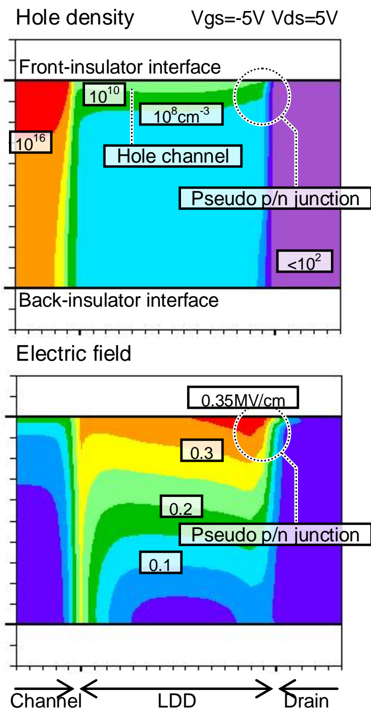

Fig. 3. Simulation Results of the Hole Density and Electric Field around the Junctions between the Channel, LDD, and Drain Regions

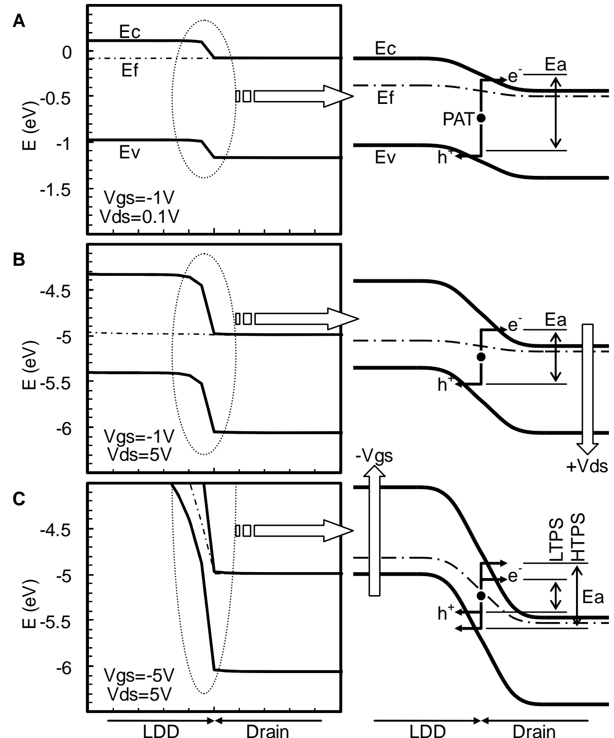

Fig. 4. Simulation Results of the Energy Band around the Junction between the LDD and Drain Regions and PAT Mechanism

Mixed-mode Simulation of Reconfigurable Si Nanowire Schottky Barrier Transistors Based Circuits

Juncheng Wang, Gang Du*, Kangliang Wei, Lang Zeng, Xiaoyan Liu *
Institute of Microelectronics, Peking University, Beijing, 100871, China
*e-mail: gangdu@pku.edu.cn, xyliu@ime.pku.edu.cn

Introduction

The reconfigurable Si nanowire Schottky barrier transistors (RFETs) are presented recently which show the variable electric characteristics and high on/off current ratio [1-3]. In contrast to conventional Schottky barrier Si nanowire transistors (SB-Si-NWTs) with metal/silicide as source/drain, the separate two gates in RFETs are located at the two Schottky junctions. Here we focus on the performance of RFETs base circuit. Some important parameters such as gate capacitance and cut-off frequency, which determine the behavior of RFETs in the analog/digital circuits are studied and compared with conventional SB-Si-NWTs.

The mixed-mode circuit simulation has been done for RFETs Inverter. Results of these simulations can give insights into the in-circuit behavior of these future generation devices.

Simulation Method and Device Structure

In our work, the performance of SB-Si-NWTs and RFETs is simulated with 3D device simulator Synopsys Sentaurus TCAD tool. The small-signal AC simulation and mixed-mode circuit simulation are carried out with it. We have considered drift diffusion transport within the Si region, thermionic emission and quantum mechanical tunneling at the Schottky junctions [4].

The schematic structures of the SB-Si-NWTs and RFETs for the simulations are plotted in Figure 1(a, b), with parameters given in Table Ⅰ. The circuit of RFET Inverter for mixed-mode circuit simulation is shown in Figure 1(c). Compared with conventional SB-Si-NWTs with metal/silicide as source/drain, the separate two gates in RFETs are located at the two Schottky junctions: program gate (Vg2) is to select p-/n-type configuration, control gate (Vg1) is to control the injection of the desired carriers into the channel. Intrinsic SB-Si-NWTs are used in our simulations. The silicide Schottky barrier height (SBH) is chosen to be 0.9 eV (such as PtSi) and 0.66eV (such as $NiSi_2$, the Fermi level of which aligns near the intrinsic Fermi level of Si [1]).

Results and Discussion

The transfer curves of SB-Si-NWT and RFETs when SBH=0.9 eV and 0.66 eV are simulated in Fig. 2 (a), (b). Fig. 2 (a) shows that the Schottky Barrier transistors suffer from their ambipolar nature which leads to lower on/off current ratio about 1×10^5 when Vds= −0.8V. The Drain Source voltage bias has much effect on the SB-Si-NWT, resulting in a shift of minimum drain-source current and lower on/off current ratio. Fig. 2 (b) plotted the transfer curves of RFETs when SBH=0.66eV. Due to the separated two gates in RFETs located at the two Schottky junctions, the RFETs can achieve much lower off-state current and higher on/off current ratio about 1×10^{15}. Besides, the Drain Source voltage bias has little influence on the RFETs compared with SB-Si-NWT.

The gate capacitance Cg of pSB-Si-NWT and p-type RFET as a function of gate voltage bias under different frequencies are shown in Fig. 3(a), (b). Cg of SB-Si-NWT and RFETs both decrease with the increasing frequency. For the ambipolar nature, Cg vs. gate voltage characteristic of pSB-Si-NWTs is almost symmetrical. However, when gate voltage changes from the negative to the positive, RFET is from on-state to off-state, and RFET decreases more slowly when on-state because it is easier for the inversion layer to form in the surface. Fig. 4 shows the high-frequency performances of SB-Si-NWT and RFETs.

To give insights into the circuit behavior of RFETs, we have carried out the mixed-mode circuit simulation for RFETs inverter. Fig. 5 shows us the voltage transfer characteristic of RFETs inverter when Vdd=1, 1.2, 1.5V. Transient analysis of RFETs inverter with a load capacitance of 0.05 fF is plotted in Fig. 6. The results show the delay of about 75ps and the inverter overshoot of about 10% Vdd in RFETs inverter.

Conclusion

The device characteristics and mixed-mode circuit behavior of RFETs are investigated through simulation. Gate capacitance and cut-off frequency of RFETs are studied and compared with SB-Si-NWTs. Our simulation results show the variable electric characteristics and higher on/off current ratio of the RFETs. Transient analysis shows the delay of about 75ps and the inverter overshoot of 10% Vdd in RFETs inverter.

978-3-901578-26-7 © 2013 Society for Micro- and Nanoelectronics

ACKNOWLEDGEMENT

This work is supported by the National Fundamental Basic Research Program of China (Grant No. 2011CBA00604).

REFERENCES

[1] A. Heinzig, et al, Nano Letters, **12**,119 (2012)
[2] D. Sacchetto, et al, IEEE Electron Device Lett., **33**, 143(2012)
[3] J. Wang, et al, ICSICT, 2012.
[4] TCAD Sentaurus Device User's Manual, Synopsys, 2010

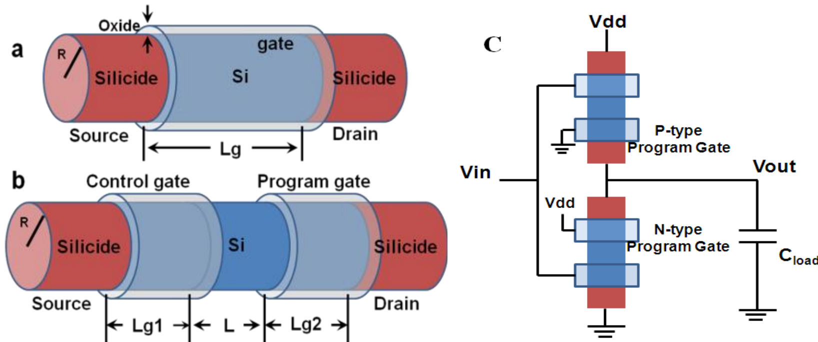

Fig. 1 The schematic structures of (a) SB-Si-NWTs and (b) RFETs for the simulations; (c) Circuit of RFET Inverter for mixed-mode circuit simulation.

TABLE I DEVICE PARAMETERS

PARAMETERS	VALUE
Gate Length (Lg/Lg1/Lg2)	30 nm
Length Between Two Gates (L)	30 nm
EOT(Tox)	1 nm
NWT Radius (R)	8 nm
Silicide Schottky barrier height (SBH)	0.9 eV, 0.66eV

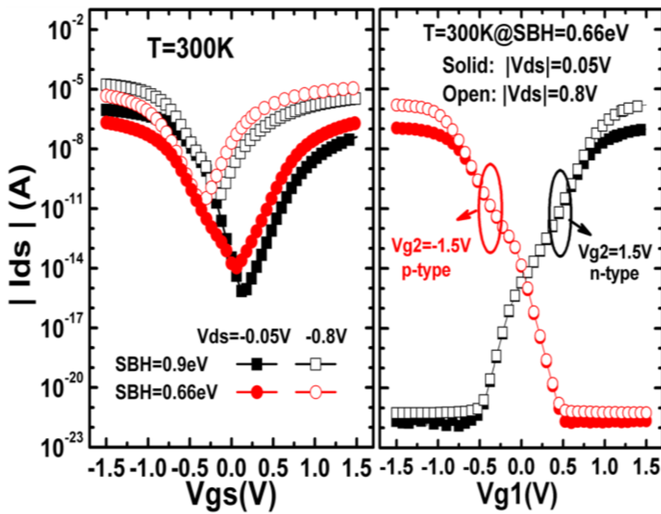

Fig. 2 The transfer curves of (a) SB-Si-NWTs and (b) RFETs.

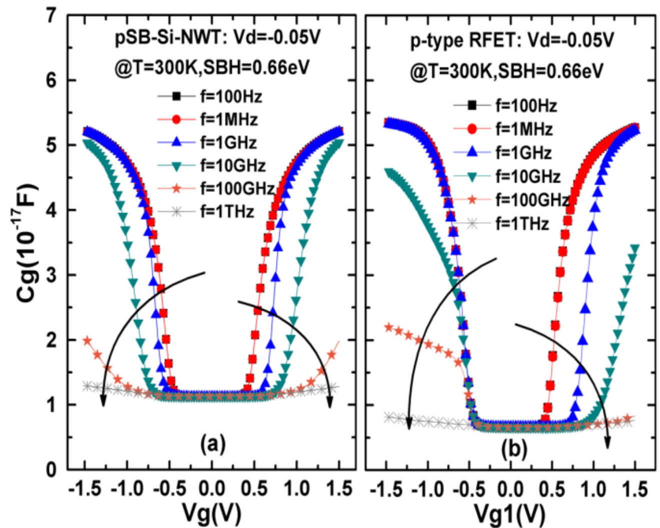

Fig. 3 Gate Capacitance vs. gate voltage characteristics of (a) pSB-Si-NWT and (b) p-type RFET when SBH=0.66eV under different frequencies.

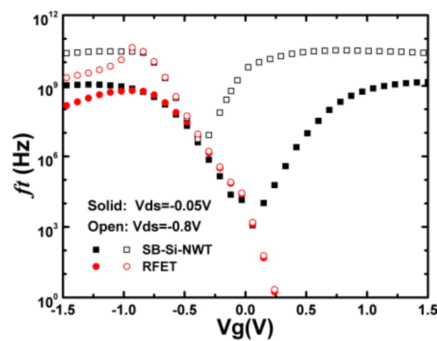

Fig. 4 The Cut-off frequency f_T vs. gate voltage characteristics of pSB-Si-NWT and (b) p-type RFET.

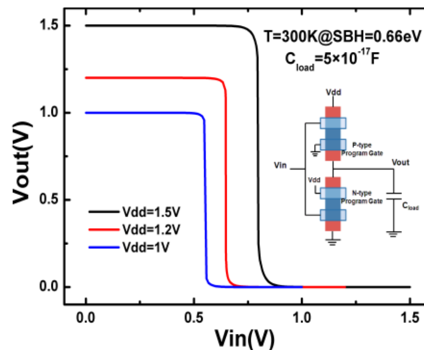

Fig. 5 Voltage transfer characteristic of RFETs inverter

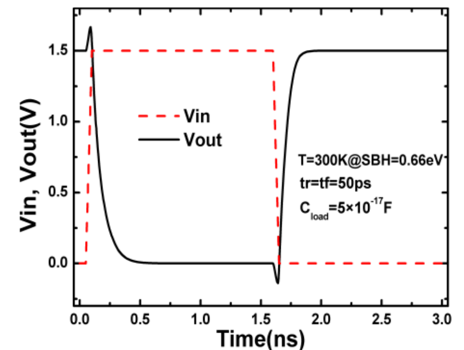

Fig. 6 Transient analysis of RFETs inverter

SNM Improvement for SRAMs Composed of High Mobility Channel MOSFETs

Mizuki Ono and Tsutomu Tezuka
Green Nanoelectronics Center in National Institute of Advanced Industrial Science and Technology
e-mail: mizuki.ono@aist.go.jp

With an increase in demand for high speed and/or low power operation of CMOS devices, high mobility channel MOSFETs, such as Ge- and $In_xGa_{1-x}As$ MOSFETs, for instance, are being intensively investigated. Comparing these MOSFETs with Si ones under a condition of the same operation speed, the cutoff characteristics are expected to be improved because $|V_{TH}|$ can be set higher than the Si ones. Therefore, SNM of SRAMs with the high-mobility MOSFETs is also expected to be improved. In this paper, 6T-SRAM cells composed of MOSFETs having a Si-, Ge-, and $In_{0.53}Ga_{0.47}As$ channel are comparatively studied from a viewpoint of SNM and power consumption using device and circuit simulations.

Current-voltage characteristics for planar MOSFETs with a semiconductor-on-insulator structure were calculated using a device simulator HyENEXSS™ [1]. Device parameters are summarized in Table I. Figure 1 shows calculated relationships between the off-state current, I_{OFF}, and the effective drive current, I_{eff} [2], at a given operation voltage, V_{DD}. Here, I_{eff} was introduced as an index of the operation speed. The result shows that I_{OFF} for the Ge- and the $In_{0.53}Ga_{0.47}As$ FETs are lower than the corresponding values for the Si FETs at a fixed I_{eff}. This is because $|V_{TH}|$ was set higher for the high-mobility FETs. In the following calculation, parameters for the Ge- and the $In_{0.53}Ga_{0.47}As$ FETs were adjusted so that their I_{eff} matched to the value for the Si FETs with I_{OFF} = 100 nA/μm. Voltage transfer characteristics were calculated for Si-, Ge-, and Hybrid ($In_{0.53}Ga_{0.47}As$ nFET/Ge pFET) inverters using a circuit simulator SmartSpice [3] (Fig. 2). The reason for the steep switching of the Ge- and the Hybrid inverters is the lower I_{OFF} of FETs in these inverters than that of FETs in the Si inverter (Fig. 1). Butterfly curves of Si-, Ge-, and Hybrid SRAMs were calculated (Fig. 3). SNM of the Si/Ge/Hybrid SRAMs was calculated to 0.14/0.18/0.19 V. The reason for the large SNM of the Ge- and the Hybrid SRAMs is the steeper switching of the Ge- and the Hybrid inverters than that of the Si inverter.

In order to study influences of V_{TH} variation on SNM, V_{TH} of 6 FETs in the SRAM were shifted independently by an amount of ΔV_{TH}. SNM with V_{TH} variation was defined by a minimum SNM of the 2^6 = 64 cases (Fig. 4). Qualitatively equivalent results were obtained for V_{DD} of 1.0, 0.8, 0.6, and 0.4 V. Even in the case that V_{TH} variation is taken into consideration, SNM of the Ge- and the Hybrid SRAMs is larger than that of the Si SRAM. Extrapolating the relationships between ΔV_{TH} and SNM in Fig. 4, ΔV_{TH} at which SNM = 0 V was calculated, which is considered to be a maximum permissible V_{TH} variation in the SRAM (Fig. 5). Using a reported value of 25 mV as a standard deviation of V_{TH} (σV_{TH}) [4] and assuming that ΔV_{TH} = 3 x σV_{TH} = 75 mV, lowest V_{DD} values of the Si/Ge/Hybrid SRAMs were calculated to be 0.93/0.72/0.63 V. Standby power ($\propto I_{OFF} \times V_{DD}$) of the Ge/Hybrid SRAMs was estimated to be 1.1/0.39% of the Si SRAM due to the lower I_{OFF}.

In conclusion, high mobility channel MOSFETs are effective for SRAMs in SNM improvement, resulting in standby power reduction.

ACKNOWLEDGEMENT

The authors are grateful to Dr. K. Fukuda of National Institute of Advanced Industrial Science and Technology and Dr. C. Tanaka of Toshiba Corporation for their useful comments.

This research is granted by the Japan Society for the Promotion of Science (JSPS) through the "Funding Program for World-Leading Innovative R&D on Science and Technology (FIRST Program)," initiated by the Council for Science and Technology Policy (CSTP).

REFERENCES

[1] HyENEXSS™, ver. 5.5, Selete, 2011
[2] M. H. Na, et al., *The Effective Drive Current in CMOS Inverters*, IEDM Tech. Dig., 121 (2002)
[3] http://www.silvaco.com/products/circuit_simulation/smartspice.html
[4] Z. Ren, et al., *Assessment of Fully-Depleted Planar CMOS for Low Power Complex Circuit Operation*, IEDM Tech. Dig., 366 (2011)

978-3-901578-26-7 © 2013 Society for Micro- and Nanoelectronics

Table I. Device parameters.

Gate Length	25 nm
Thickness:	
Channel Layer	10 nm
Buried Insulator	20 nm (SiO_2)
Gate Insulator	1 nm (SiO_2)
Gate Sidewall	20 nm (Si_3N_4)
Handle Wafer	100 nm (Si)
Impurity Concentration:	
Channel Region	1×10^{15} cm^{-3}
Handle Wafer	1×10^{18} cm^{-3}
Source and Drain Regions:	
Peak Impurity Concentration	3×10^{20} cm^{-3}
Offset Spacer Thickness (Varied in order to adjust I_{OFF})	0 to 20 nm
Channels: [110] direction in (001) surface, unstrained.	

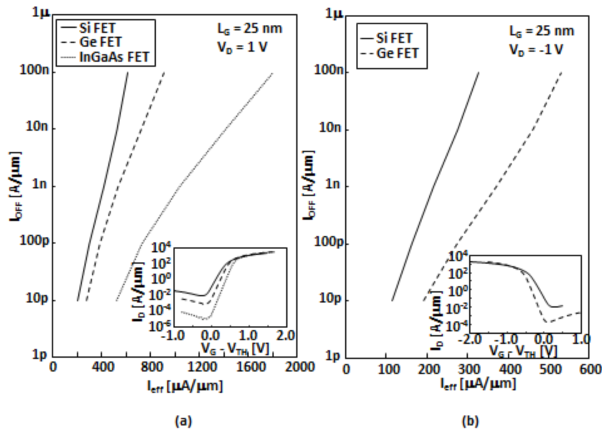

Fig. 1. Relationships between I_{OFF} and I_{eff} (= $\{I_D(|V_G| = V_{DD}, |V_D| = V_{DD}/2) + I_D(|V_G| = V_{DD}/2, |V_D| = V_{DD})\}/2$) [2] for (a) nFETs and (b) pFETs. Insets show I_D-V_G characteristics; I_{eff} are set equal to that of the Si FETs with I_{OFF} = 100 nA/μm.

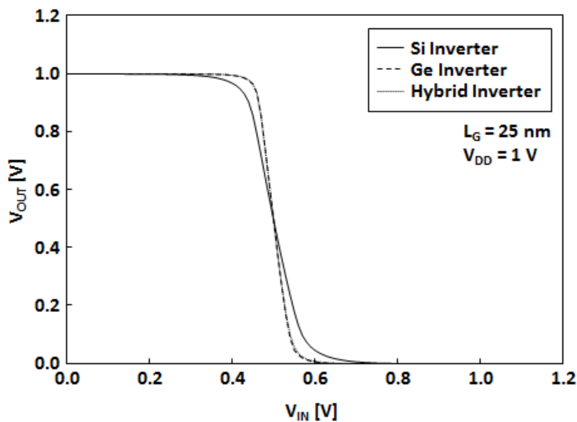

Fig. 2. Voltage transfer characteristics of Si-, Ge-, and Hybrid inverters.

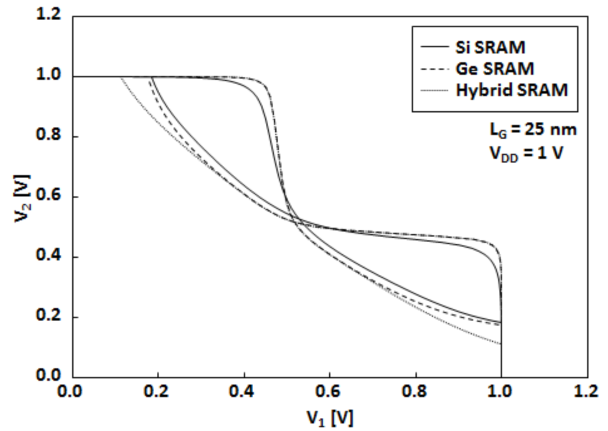

Fig. 3. Butterfly curves of Si-, Ge-, and Hybrid SRAMs.

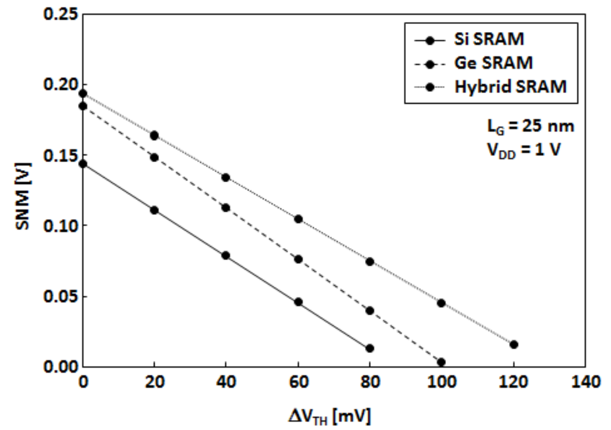

Fig. 4. Dependences of SNM on amount of V_{TH} variation (ΔV_{TH}) for the Si-, the Ge-, and the Hybrid SRAMs.

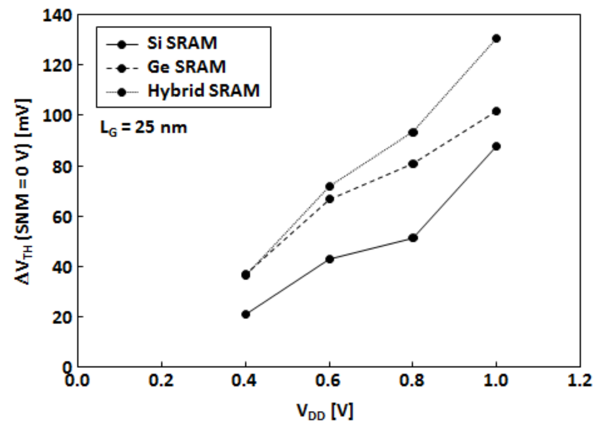

Fig. 5. Dependences of amount of V_{TH} variation (ΔV_{TH}) at which SNM = 0 V on V_{DD} for the Si-, the Ge-, and the Hybrid SRAMs.

Effect of Fin Tapering in Nanoscale Si FinFETs

Saumitra R. Mehrotra*, Abhijeet Paul†, Jin Cho†, Michael Povolotskyi and Gerhard Klimeck
School of Electrical and Computer Engineering, Purdue University, West Lafayette- IN, USA
†GLOBALFOUNDRIES, Albany-NY, USA
*e-mail: smehrotr@purdue.edu

INTRODUCTION

For the past 40 years scaling has enabled a sustained improvement in the transistor performance while increasing transistor density. The historically planar MOSFET has evolved into a 3D FinFET at the 22nm node to mitigate short channel effects [1, 2].The TEM images reveal that the 'fin' deviates from a popularly assumed rectangular shape to a tapered sidewall structure attributed to the process conditions used for fabrication [1, 2]. Such loss of control on the final shape of the FinFET may lead to unwanted variations in MOSFET performance. The present paper investigates the impact of fin tapering, in nanoscale FinFETs, on its DC performance using atomistic simulations in the ballistic limit.

DEVICE SIMULATION APPROACH

The effect of tapering is studied in unstrained, Si FinFETs with <110> channel orientation fabricated on a (100) wafer (Fig.1). The fin height is fixed at 10 nm while the base width is set to 6 nm. The effect of sidewall slanting is taken into account by introducing a taper angle, θ (Fig. 1). An effective oxide thickness of 1.2 nm as assumed (Fig. 1). Id-Vg characteristics are simulated using the 'Top-of-the-Barrier' transport model solved in a self consistent fashion (Fig. 2) [3, 4]. To capture the quantum effects accurately 10 band $sp^3d^5s^*$ (including SO-coupling for valence bands) tight binding (TB) model is employed for solving the Schrodinger equation [5]. A zero electric field (Neumann) boundary condition is used at the base of the Fin for the Poisson solution. The ON state is defined as the drain current (I_{DS}) at$V_{GS}=V_{DS}=0.7V$, with the fixed OFF state at $I_{DS}=100nA/\mu m$. Current values are normalized by the base width (=6nm).

RESULTS

Fig. 3 shows the Id-Vgplots for n/p- FinFETs with different W_{TOP}. Interestingly, p-FinFETs exhibit negligible variation in current, unlike n-FinFETs.This phenomenon is well explained by the interplay between the ON state charge (N_{inv}) and carrier injection velocity (v_{inj}). Holes show a preferential movement towards the (110) sidewalls (Fig. 4b) whereas electrons prefer reside near the (100) top-gate (Fig. 4a) [6]. Since the (110) side gates are much longer than the (100) top-gate, it leads to higher inversion charge in p-FinFETs compared to n-FinFETs at the ON state (Fig. 5a). Tapering of the fin reduces the perimeter where the gate acts leading to a reduction in the effective gate to channel capacitance thus, reducing the N_{inv} for both n and p-type FinFETs. With fin tapering the electron v_{inj} is not modulated much however, for holes,v_{inj} increases with fin tapering (Fig. 5). This nearly cancels the degradation in charge leading to negligible effect on the p-FinFET ON-current. v_{inj} is almost unaffected with tapering in n-FinFET which ultimately causes the final ON state current to degrade by nearly 30% as taper angle reduces from 90 to 77.3 degrees.

CONCLUSION

FinFET tapering severely degrades the ballistic ON current in n-FinFETs (coefficient of variation =15%) with negligible change in p-FinFETs (coefficient of variation =2%).

ACKNOWLEDGEMENT

nanoHUB.org computational resources operated by the Network for Computational Nanotechnology funded by NSF under EEC-0228390 and MSD FCRP are acknowledged.

REFERENCES

[1] Jan, C-H. et al. *IEDM 2012*.
[2] C. C. Wu et. al, *IEDM 2010*
[3] S. Steiger , et al. Nanotechnology, IEEE Transactions on, vol. 10, no. 6, nov. 2011.
[4] A. Paul et al, *IWCE 2009*
[5] Boykin, T. B., Klimeck, G., & Oyafuso, F.. *Physical Review B*, *69*(11), 115201 (2004).
[6] Neophytou, Neophytos, and Gerhard Klimeck. *Nano letters* 9.2 (2009): 623-630.

978-3-901578-26-7 © 2013 Society for Micro- and Nanoelectronics

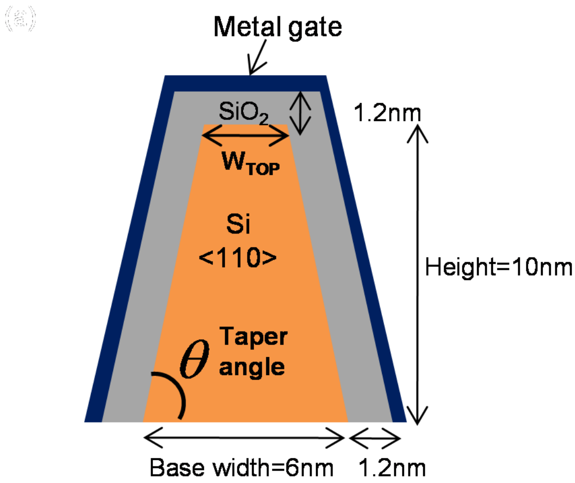

Fig. 1 Si FinFET structure considered in this study.

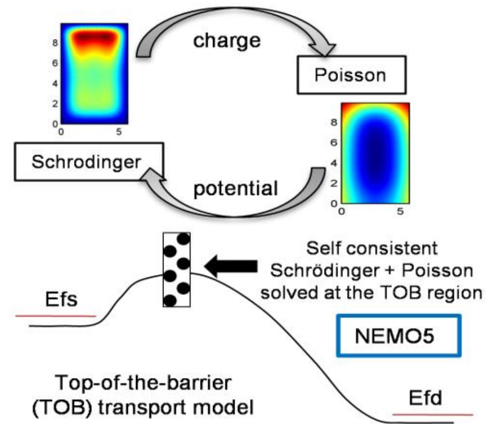

Fig. 2. Schematic description of the semi-classical top of the barrier transport model.

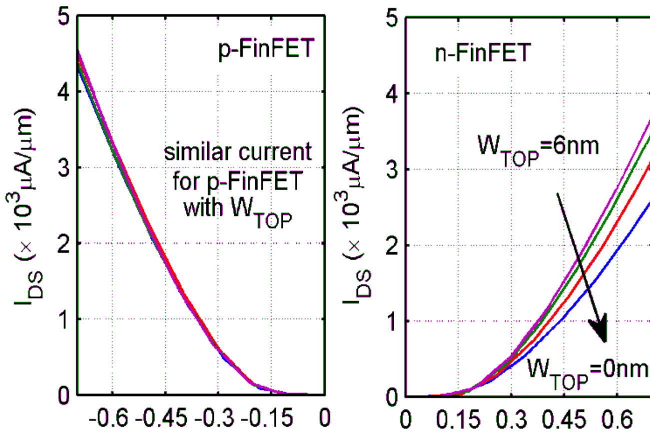

Fig. 3. . Ballistic Id-Vg plots for n-type and p-type Si FinFETs. Current values are normalized by the base width (=6nm)

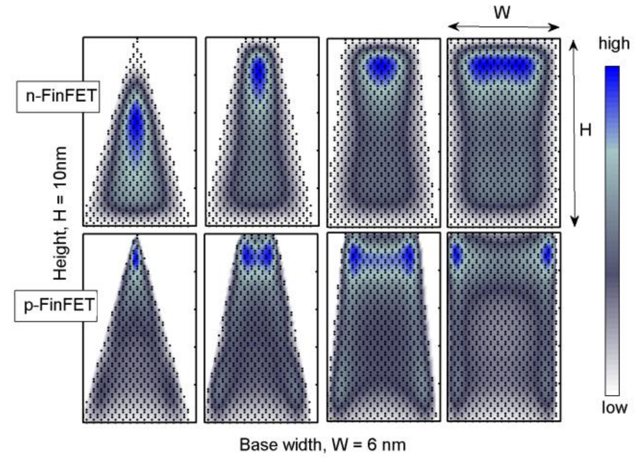

Fig. 4. Normalized charge distribution in (a) n-type (top row) and, (b) p-type (bottom row) Si FinFETs at the ON state (Vgs=Vds=0.7V).

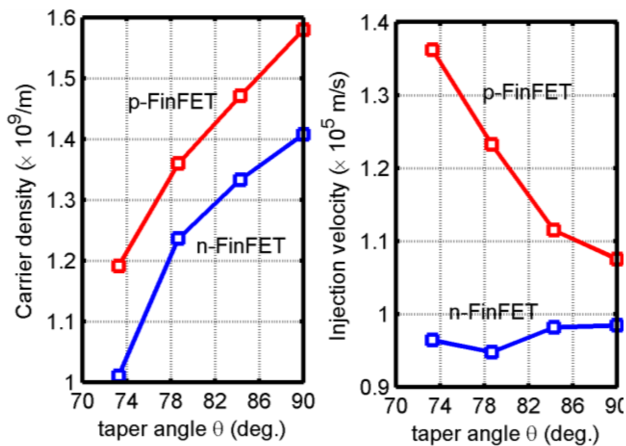

Fig. 5. ON state carrier density (left) and injection velocity (right) for n-type and p-type Si FinFETs.

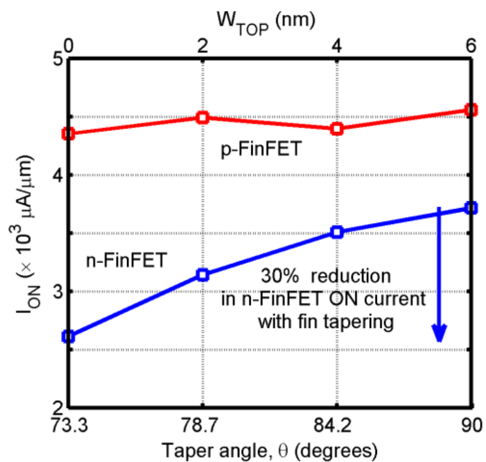

Fig. 6. Variation in ballistic ON current with taper angle (or W_{TOP}).

On Rounding and Taper Fins of FinFET Varactors

Chien- Hung Chen[1], Yiming Li[2,*], and Sheng- Yuan Chu[1,*]
[1]Department of Electrical Engineering National Cheng- Kung University, Tainan 701, Taiwan
[2]Department of Electrical and Computer Engineering, National Chiao Tung Universit, Hsinchu 300, Taiwan
e-mail: n2894104@mail.ncku.edu.tw (C.-H. Chen); * ymli@faculty.nctu.edu.tw (Y. Li); * chusy@ncku.edu.tw (S.-Y. Chu)

I. INTRODUCTION

Bulk FinFET is one of the candidates for device in sub-22 nm technology node, because of its good cut-off characteristics, short channel effect control and better scalability by miltiple gate mode operation [1-3]. Recent studies on FinFET devices were reported (see, for examples, [4-7], and references therein), but the influence of fin profile on device's capacitance has not yet clearly been investigated.

In this work, we experimentally fabricate and characterize HKMG bulk FinFET devices and simulated the fin profile with different tapers and rounding. The influence of the fin taper and rounding profile on C-V characterization is assessed, where the fabrication parameters are extracted accordingly.

II. EXPERIMENT AND SIMULATION

The devices we studied are the HKMG bulk FinFETs on (100) p-substrate, where the C-V curves are measured as shown in Fig. 1. To fabricate the devices, the advanced 193 nm immersion lithography and optimized etching processes are then utilized for silicon fin and STI formation. Then, a 1.5-nm-thick chemical oxide and a 3-nm-thick HfO_3 film are deposited by chemical vapor deposition. Finally, we use sputter to form 12-nm-thick TiN film, as shown in Fig. 2. Fig. 2 further indicates the profile of fin with taper and rounding due to the fabricated etching process.

Fig. 3 shows that 3D computational device model, where a set of quantum-mechanically transport equations is solved to calculate the device's characteristic. Notably, the right plots are the model cross section views of the fin profiles which are with respect to different taper and rounding. The taper varies from 0, 1, 3, and 5 degrees and the radius is from 1, 3, 6, 7, and 8 nm.

III. RESULTS AND DISCUSSION

As shown in Fig. 4, the simulated device's capacitance with different taper profiles, where the Radius = 0 and the Taper = 0, 1, 3 and 5. The capacitances are 8.20, 8.10, 7.78 and 7.55 fF, respectively at accumulation region. Their C_{min} are 2.31, 1.60, 1.32 and 1.25 fF, respectively. When the fin profile is more taper, the device is with smaller capacitance. As shown in Fig. 5, the simulated capacitance with different rounding profile devices (Taper = 0, Radius = 1, 3, 5, 7 and 8 nm) are 8.20, 8.03, 7.73, 7.48 and 7.37 fF, respectively, at accumulation region. Also, their C_{min} are 2.31, 2.18, 2.38, 1.63 and 1.61 fF, respectively. When the fin profile is with a larger taper, the device will be with a relatively smaller capacitance.

From the C-V curves simulated, we can extract the parameter of fin profile by fitting the measured C-V curves. As shown Fig. 6, the matching between the simulation and characterization is well. The extracted taper of the fabricated HKMG bulk FinFET sample is 5 deg. and the rounding radius is 8 nm. The extracted taper angle and the rounding radius owing to process variation effect can be modeled into device model for variability simulation of FinFET circuits.

IV. CONCLUSIONS

The 3D device simulation of FinFET varator devices with different taper and rounding profile has been demonstrated. The findings of this study have been calibrated with the silicon data by matching the measured capacitance, where the fabrication parameters haven been extracted.

ACKNOWLEDGEMENT

This work was supported in part by the Taiwan National Science Council (NSC) under Contract No. NSC-101-2221-E-009-092.

REFERENCES

[1] Y. Li et al,, *Tech. Dig. IEDM* (2011) 5.5.
[2] Y. Li et al., *Nanotechology 21* (2010) 095203.
[3] Y. Li et al, *IEEE TED. 54* (2007) 3426-3429.
[4] N. Fasarakis et al., *IEEE TED. 59* (2012) 3306-3312.
[5] N. Chevillon et al., *IEEE TED. 59* (2012) 60-71.
[6] H.-W. Su et al., *Proc. DRC* (2012) 109-110.
[7] T. Matsukawa et al., *Tech. Dig. IEDM* (2012) 8.2.

978-3-901578-26-7 © 2013 Society for Micro- and Nanoelectronics

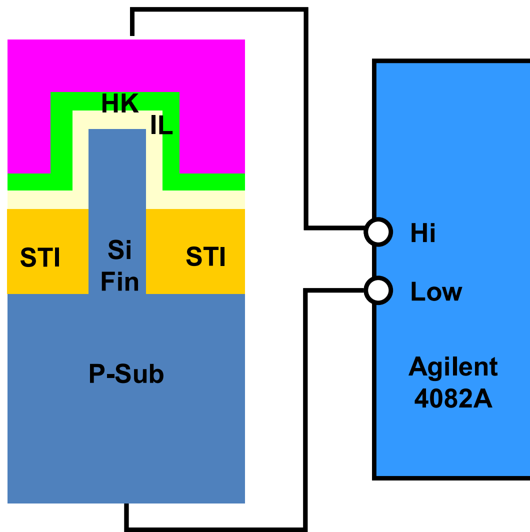

Fig. 1. Cross-section view of the fin MOSCAP and the measurement configuration of C-V curves, we measure the device's C-V curves by the 4082A Parametric Test System.

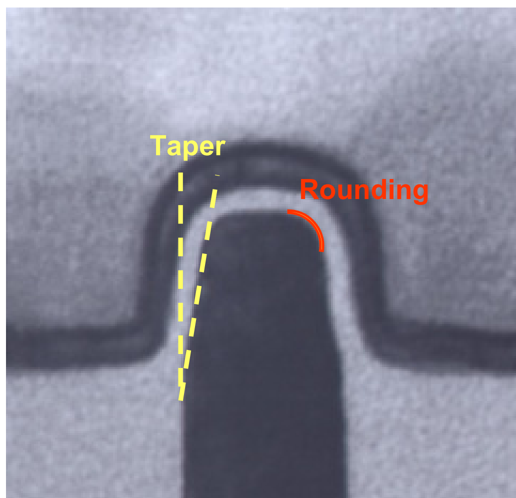

Fig. 2. The TEM of the fabricated Fin-type varator with a 20-nm fin width. Notably, the taper and rounding fin profiles are obviously.

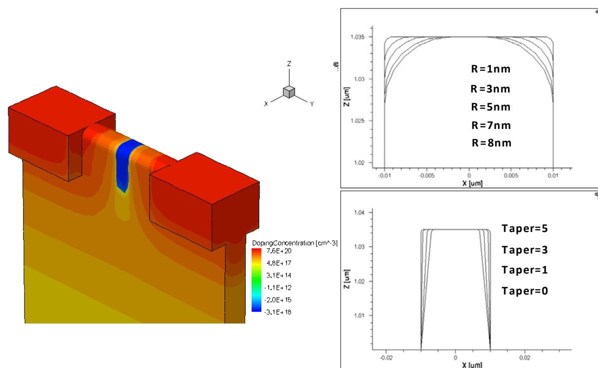

Fig. 3. The 3D simulation structure; the left plot is a 3D fin, and the right lots are the cross sections of the model with different angles of taper (θ = 0, 1, 3, and 5 deg.) and the rounding radius = 1, 3, 5, 7, and 8 nm.

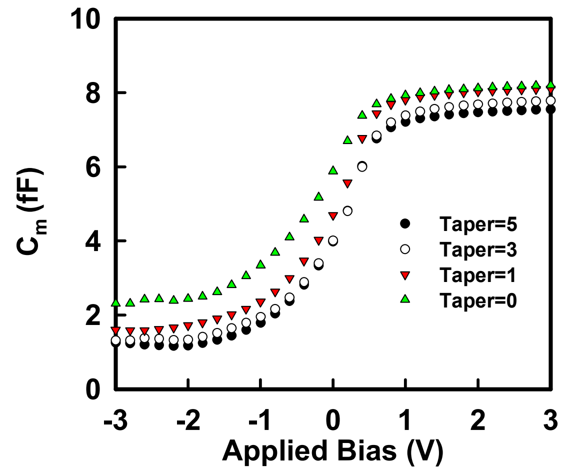

Fig. 4. The simulated C-V with different taper profile devices. When the fin profile is with a larger taper, the device is with a smaller C_{min} at the accumulation region.

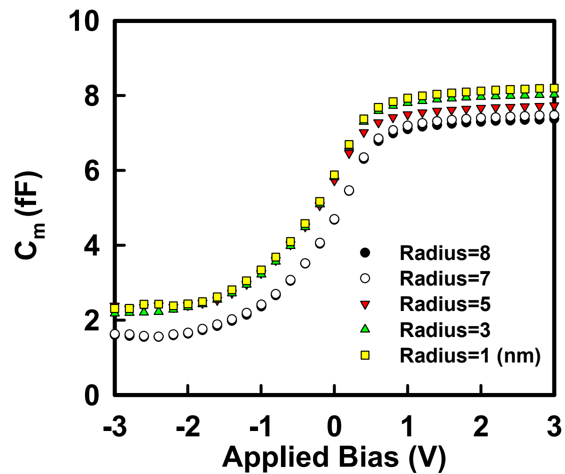

Fig. 5. The simulated C-V with different rounding profile devices. When the fin profile is with a larger rounding, the device is with a smaller C_{min} at the accumulation region.

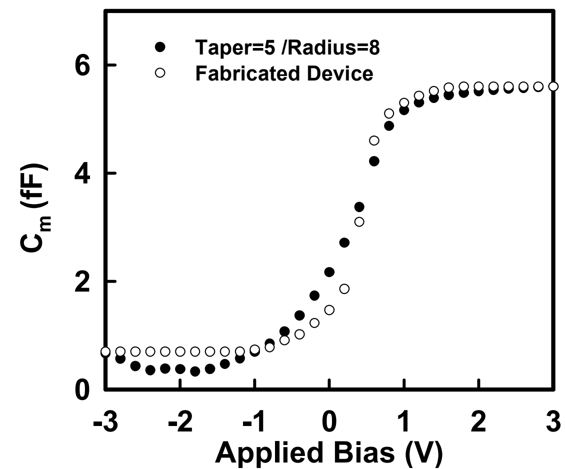

Fig. 6. The simulated and the measurement capacitances. The matching of the C-V curves is validated for the sample with the extracted taper and rounding.

Modeling of Stress-induced Effects on Depletion Layer Capacitance in MOS Capacitor

Kazunori Matsuda
Tokushia Bunri University at Kagawa, 1314-1 Shido, Sanuki, Kagawa, Japan
e-mail: kmatsuda@fe.bunri-u.ac.jp

INTRODUCTION

Stress-induced effect on the depletion layer capacitance of siliicon becomes important as the semiconductor devices scale down and the switching speed of logic gate becomes higher [1]. Gauge factor of this effect has been reported to be almost comparable with the piezoresistance effect [2]. In the present study, a model which reproduces the stress-induced effects on the depletion layer capscitance of MOS will be discussed.

MODEL

In the present model, the maximum depletion layer (w) of MOS capacitor is expressed as follows (Fig.1):

$$w = \sqrt{\frac{2\varepsilon_{Si}\varphi_S}{qN_A}} \qquad (1)$$

where $\varphi_S = 2(E_i - E_F)/q$ is he surface potential, N_A is the impurity concentration. The depletion layer capacitance is expressed with the maximum layer width: $C_{dep} = w/\varepsilon_{Si}$. The intrinsic Fermi energy (E_i) comprises two terms, i.e. the midgap effect and the density-of-state (DOS) change :

$$E_i = E_{g/2} + \frac{3}{4}kT\ln\left(\frac{m_h^*}{m_e^*}\right) \qquad (2)$$

According to the deformation potential theory, strain splits the fourfold valence bandedge into a pair of degenerate Kramars doublets; heavy and light hole bands. While six folded band minima in the conduction band splits into four and two folded band minima (Fig.2) [3]. As a result, the middle level of the bandgap, that is, the midgap effect changes proportionally to the magnitude of strain as follows,

$$\Delta E_{g/2} = \begin{cases} -2.5 \cdot e_l \text{ (eV)} & \text{for tension} \\ 2.3 \cdot e_l \text{ (eV)} & \text{for compression} \end{cases} \qquad (3)$$

where e_l is the strain when uniaxial stress is applied.

The DOS effective masses of electrons and holes in silicon are expressed as $m_e^*=6^{2/3}(m_l m_t^2)^{1/3}$ and $m_h^* = (m_{lh}^{3/2} + m_{hh}^{3/2})^{2/3}$, respectively. Hence, the ratio (m_h^*/m_e^*) without strain is estimated as 0.52. When tensile <110> stress is applied, the DOS effective mass of holes becomes the heavy-holes mass, and that of electrons becomes the DOS effective mass of twofold valley. So the ratio rises to $(m_{hh}^*/m_{\Delta 2}^*) = 0.98$. Similarly, when compressive <110> stress is applied, the ratio reduce to $(m_{lh}^*/m_{\Delta 4}^*) = 0.19$. As a result change of the second term is,

$$\Delta\left\{\frac{3}{4}kT\ln\left(\frac{m_h^*}{m_e^*}\right)\right\} = \begin{cases} 0.012 \text{ (eV)} & \text{for tension} \\ -0.020 \text{ (eV)} & \text{for compression} \end{cases} \qquad (4)$$

DISCUSSION

As shown in Fig.3 and Fig.4, the stress effects on the DOS of each valence band depend on stress in different manner for weak stress region and have anisotropy. However, they become nearly equal for large stress region. Table 1 shows the gauge factors of the stress effects on capacitance in weak stress region for three independent crystallographic directions. The characters of the gage factors are discussed by the stress effects on the DOS of valence band.

REFERENCES

[1] J-S. Lim, S. E. Thompson and J. G. Fossum, "Comparison of Threshold-Voltage Shifts for Uniaxial and Biaxial Tensile-Stressed n-MOSFETs, " IEEE Electron Device Lett., 25, 731, 2004.
[2] K. Matsuda and Y. Kanda, "Stress-induced effects on depletion-layer capacitance of metal-oxide-semiconductor capacitors," Appl. Phys. Lett., 83, 4351, 2003.
[3] C. Herring, "Transport properties of a many-valley semiconductor, " The Bell System Technical Journal, XXXIV(2), 237, 1955.

978-3-901578-26-7 © 2013 Society for Micro- and Nanoelectronics

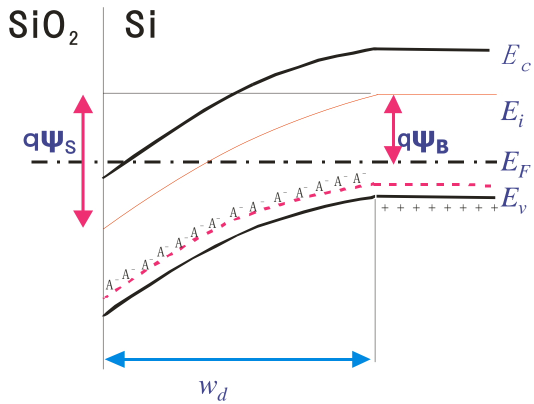

Fig. 1. Band diagram of p-type MOS capacitor with a positive voltage applied to the gate when a stress is applied.

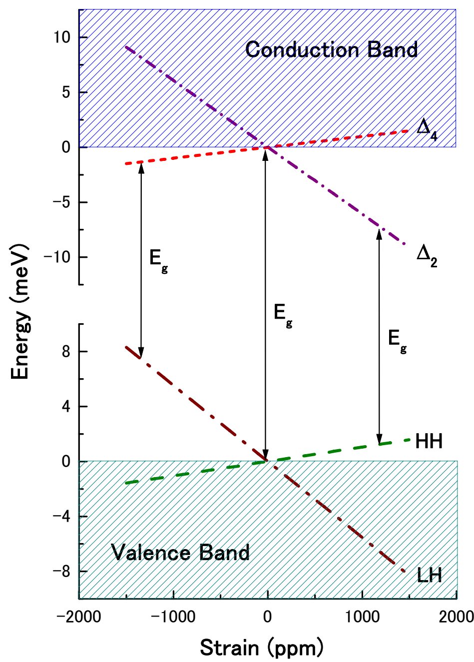

Fig. 2. Schematic drawing of the band splitting of silicon by the application of uniaxial <110> stress. Here E_g denotes the band gap between the band edge of the conduction band and the valence band.

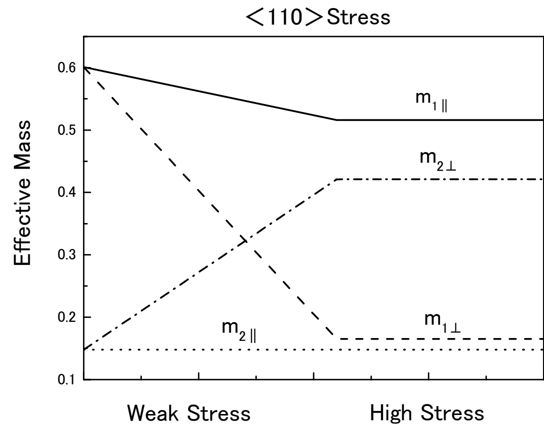

Fig. 3. Schematic drawing of the stress-dependent hole effective masses when <110> uniaxial stress is applied.

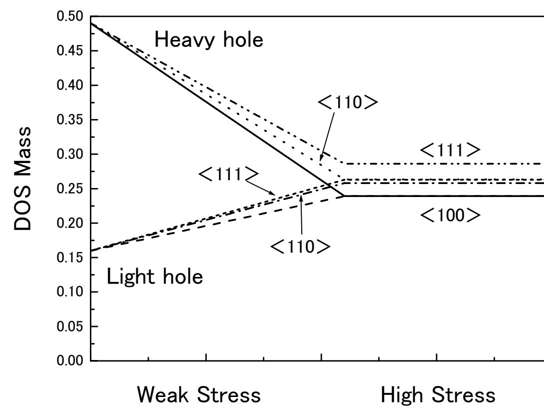

Fig. 4. Schematic drawing of the stress-dependent DOS mass of valence band edge.

Table 1: Gage factors of the stress-induced effects on depletion layer capacitance for three independent crystallographic directions.

Stress	Direction	Gauge Factor			
		DOS Change		Midgap Effect	
		n-type	p-type	n-type	p-type
<100>	Tension	5.5	8.0	-1.3	-
	Compress.	-17	-26	-0.6	-
<110>	Tension	19	32	-1.9	3.0
	Compress.	-30	-48	1.7	2.7
<111>	Tension	-3.1	-5.3	-0.92	-
	Compress.	-39	-61	-0.92	-

Gate Leakage Reduction of Vertical MOSFET with High-k Dielectric Film Employing Gate Dielectric Capacitance Oriented Design

T. Sasaki[1,2] , and T. Endoh[1,2]
[1]Graduate School of Engineering, Tohoku University, [2]JST-CREST
Aramaki aza Aoba 6-6, Aoba-ku, Sendai, Japan, 980-8579
e-mail: endoh@riec.tohoku.ac.jp

INTRODUCTION

Gate dielectric capacitance per unit area (C_{ox}) and equivalent oxide thickness (EOT) are one of the key design parameters of MOSFET to reduce gate leakage with high driving current in continuing scaling of the replacing gate dielectric material thermal silicon dioxide to high permittivity dielectrics. The Vertical MOSFET (VMOS) [1] has been intensively studied due to the strong gate controllability caused by its cylindrical silicon pillar and gate stack. This letter addresses the importance of the cylindrical structure of the VMOS and shows the significant gate leakage reduction by 99.2% with 1.67 times larger driving current in the case of the same C_{ox} of the Double Gate MOSFET (DG) at EOT=0.3nm.

GATE DIELECTRIC CAPACITANCE OF VERTICAL MOSFET WITH HIGH-K DIELECTRIC FILM

The C_{ox} of the VMOS ($C_{ox,VMOS}$) [1] as eq. (1),

$$C_{ox} = k \times \left[R \ln\left(1 + \frac{t_{ox}}{R}\right) \right]^{-1} \qquad (1)$$

where R is the silicon pillar radius, t_{ox} is the gate dielectric thickness, and k is the dielectric constant of the gate dielectric materials. The ratio (α) of the $C_{ox,VMOS}$ to the C_{ox} of the DG ($C_{ox,DG}=k/t_{ox}$) is plotted versus k at the same EOT=0.3nm in Fig. 1(a). The EOT is defined by EOT=$t_{ox}/(k/3.9)$. In the case of the same EOT, $C_{ox,VMOS}$ is the α times larger than $C_{ox,DG}$. Therefore, the t_{ox} of the VMOS is α times thicker than that of the DG at the same $C_{ox,VMOS}$ as the $C_{ox,DG}$ in Fig. 1(b).

INVESTIGATION OF THE GATE DIELECTRIC CAPACITANCE ORIENTED DESIGN

The gate leakage and driving current performances of the VMOS is investigated through Sentaurus device simulator [2]. Figure 2 shows the simulated device structures and Table I shows the device parameter settings. In the case that the $C_{ox,VMOS}$ is the same as the $C_{ox,DG}$, the gate leakage current density of the VMOS is reduced by 99.2% applied at the high gate voltage ($V_{gate}-V_{th}$=0.340V) in the comparison with the DG due to the α times thicker (0.56nm) t_{ox} than that of the DG in Fig. 3. The driving current normalized by channel width of the VMOS is increased by 1.67 times than that of the DG in Fig. 4. The increase of the driving current in the VMOS is caused by high electron density in the channel region in Fig. 5. The VMOS obtains higher electron density by 3.1 times than that of the DG at the silicon pillar center in Fig. 6. Therefore, the C_{ox} oriented design in the VMOS with high-k gate dielectric can obtain the reduction of the gate leakage with high driving current.

CONCLUSION

The gate leakage and driving current performances of the VMOS with high-k dielectric film is investigated in the comparison with the DG at the EOT=0.3nm. The VMOS reduces the gate leakage by 99.2% due to its cylindrical nature. The results are fruitful for the future high performance and low gate leakage device design with ultra-thin higher-k gate dielectrics.

ACKNOWLEDGEMENT

This work has been supported in part by a grant from "Research of Innovative Material and Process for Creation of Next-generation Electronics Devices" of CREST under the Japan Science and Technology Agency (JST).

REFERENCES

[1] T. Endoh, T. Nakamura, and Fujio Masuoka, IEICE TRANS. ELECTRON., **E80-C**, NO. 7 (1997).

978-3-901578-26-7 © 2013 Society for Micro- and Nanoelectronics

[2] Sentaurus manuals, http://www.synopsys.com Synopsys Inc..

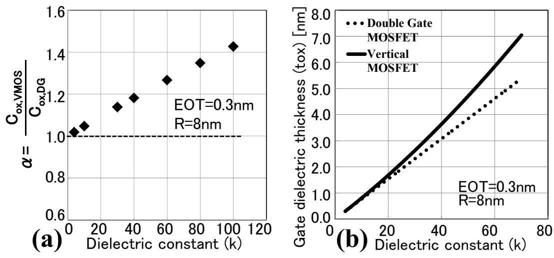

Fig. 1. (a) The ratio (α) of the C_{ox} of the VMOS to that of the DG versus k at the same EOT=0.3nm. (b) The α times thicker t_{ox} of the VMOS than that of the DG at the same C_{ox} in the EOT=0.3nm.

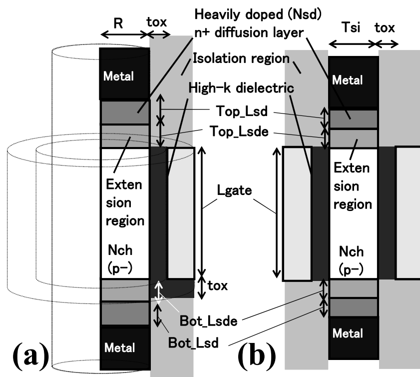

Fig. 2. Simulated device structures. (a) Vertical MOSFET, (b) Double Gate MOSFET. The VMOS and the DG was numerically solved in cylindrical coordinates and in two-dimensional simulation, respectively.

Table I. Device parameter settings.

Device parameters	VMOS	DG
Silicon pillar diameter (2R)	16nm	
Silicon thickness (Tsi)		16nm
Gate length (Lgate)	24nm	
Gate dielectric thickness (tox)	0.3～3.64nm	
Gate dielectric constant (k)	3.9～40	
Gate workfunction	4.4eV	4.6eV
Channel concentration (Nch)	1e17cm^{-3}	

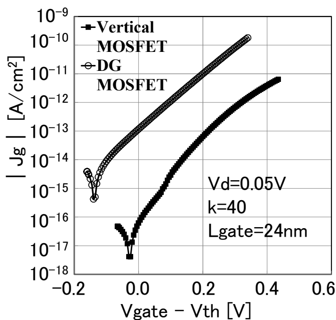

Fig. 3. Reduction of the gate leakage current density of the VMOS in the comparison with the DG in the case of the same C_{ox}. The V_{th} in Fig. 3 is extracted by constant-current method at I_d/(channel width)=100nA/μm in the linear region (V_d=0.05V).

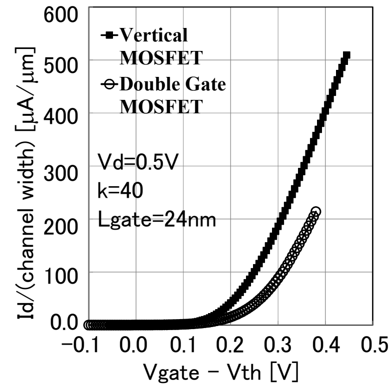

Fig. 4. Driving current normalized by channel width characteristic of the VMOS and the DG in the case of the same C_{ox}. The V_{th} in Fig. 4 is extracted by constant-current method at I_d/(channel width)=100nA/μm in the saturation region (V_d=0.5V).

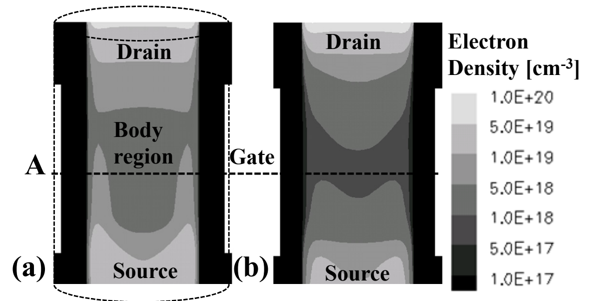

Fig. 5. Electron density distribution in the channel (a) VMOS and (b) DG at the V_{gate}-V_{th} =0.380V in the saturation region (V_d =0.5V). Even if the thicker t_{ox} than α times that of the DG, the electron density in the body region is larger than that of the DG, which leads to high driving current of the VMOS.

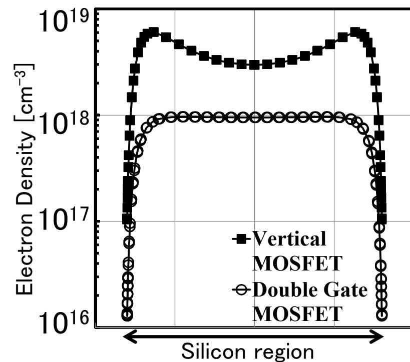

Fig. 6. High electron density of the VMOS in the body region at the dashed line A in Fig. 5.

Intrinsic Region Length Dependence of Vertical Double Gate IMOS

A. Itagaki[1, 2], M. Muraguchi[1, 2] and T. Endoh[1, 2]
[1]Graduate School of Engineering, Tohoku University
[2]JST-CREST
Aramaki Aza-Aoba 6-6, Aoba-ku, Sendai, Japan, 980-8579, E-mail: endoh@riec.tohoku.ac.jp

INTRODUCTION

CMOS technology has been scaling down in size following the Moore's law for over 40 years. As the size of the MOSFET is reduced rapidly into the nano scale region, they begin to suffer from a few critical issues. One of them is the increase of the subthreshold swing (S-Factor). Under ideal conditions, in which the gate oxide capacitance is infinite, S-Factor of the MOSFET becomes about 60 mV/dec at room temperature. As a result, short channel effect (SCE) brings the increase of S-Factor, the leakage current of the MOSFET increases substantially. At the same time, the threshold voltage (Vth) and supply voltage cannot be shrunken while keeping a sufficiently low off state current.

In order to solve the above problems, the I-MOS [1] is widely investigated as one of the promising approaches. In this paper, we investigated Vertical Double Gate IMOS (DGIMOS) as one of Multi-Gate type structures. The parameter dependences of Vertical DGIMOS are investigated. The variance of parameter characteristics of S-Factor, Vth and Ioff is analyzed with the decreasing of intrinsic region length (Li) of Vertical DGIMOS for the first time.

DEVICE STRUCTURE

Figure 1 and Table I show structure of vertical DGIMOS and the device parameters. Vertical DGIMOS structure is a kind of a gated p-i-n diode. Source/Drain doping concentration and p-type body concentration set to be 10^{20} cm^{-3} and 10^{17} cm^{-3} respectively. In the simulation, band-to-band tunnelling and impact ionization are considered.

RESULTS AND DISCUSSIONS

Figure 2 shows simulated I_{DRAIN} versus V_{GATE} characteristics of the Vertical DGIMOS under the condition that some of Li are 40, 34, 18 and 10 nm. Source voltage and Drain voltage are fixed -3V and 0V. In this paper, the definition of Vth is the gate voltage at which S-Factor is minimum, because S-Factor of vertical DGIMOS which is different from S-Factor of the MOSFET, isn't linear. Ioff is defined by the drain current when the gate voltage is zero. The S-Factor dependence of Li, the Vth dependence of Li, and the Ioff dependence of Li are given in Fig.3, Fig.4 and Fig.5 respectively. In the range that Li is set from 40 nm to 34 nm, S-Factor is improved with the reduction of Li and Vth becomes lower, Ioff becomes higher at the same time. In the range that Li is set from 34 nm to 18 nm, S-Factor is degenerated with the reduction of Li and Vth becomes lower, Ioff becomes higher at the same time. In the range that Li is set from 18 nm to 10 nm, S-Factor is degenerated with the reduction of Li and Vth becomes higher, Ioff becomes higher at the same time. As a result, the device simulation results clarify that parameter dependences of Li can be divided into 3 regions depend on impact ionization in intrinsic region and variance of channel potential.

CONCLUSION

The parameter dependences of Vertical DGIMOS are analyzed in detail in this paper. As important design guideline of DGIMOS, we found that parameter characteristics of S-Factor, Vth and Ioff show different behaviour in the three regions with the decreasing of Li.

ACKNOWLEDGEMENT

This work has been supported in part by a grant from "Research of Innovative Material and Process for Creation of Next-generation Electronics Devices" of CREST under the Japan Science and Technology Agency (JST).

 © 2013 Society for Micro- and Nanoelectronics

REFERENCES

[1] K. Gopalakrishnan *et al.*, IEDM Tech. Dig., pp.289-292, 2002.

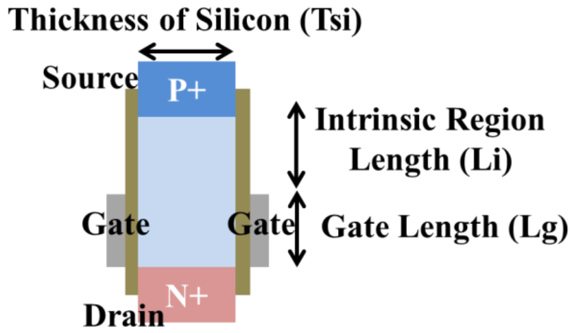

Fig. 1. Structure of the vertical double gate IMOS (DGIMOS).

Table I. Device parameters and values in Vertical DGIMOS

Device Parameter	Value
Intrinsic Region Length (Li)	10~40 nm
Gate Length (Lg)	40 nm
Gate Width (W)	1.0 μm
Thickness of Silicon (Tsi)	20 nm
Thickness of Oxide (Tox)	1.2 nm

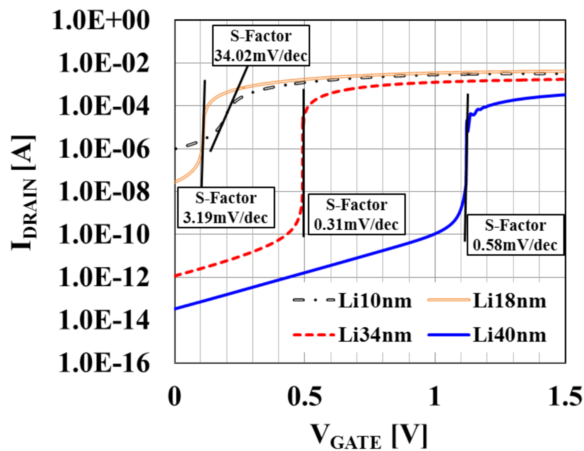

Fig. 2. Simulated I_{DRAIN} versus V_{GATE} characteristics of the vertical DGIMOS with V_D=0V and V_S=−3V.

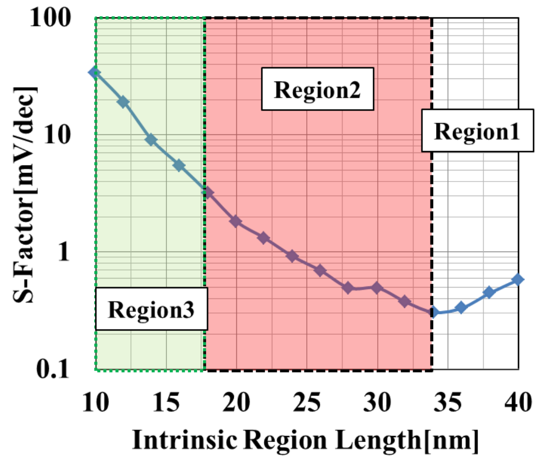

Fig. 3. The S-Factor dependence of Li in vertical DGIMOS.

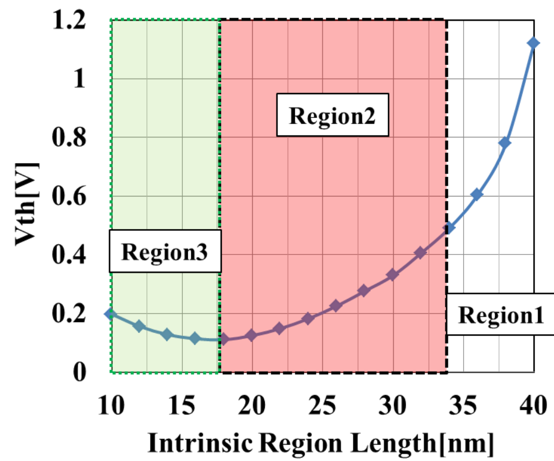

Fig. 4. The threshold voltage (Vth) dependence of Li in vertical DGIMOS.

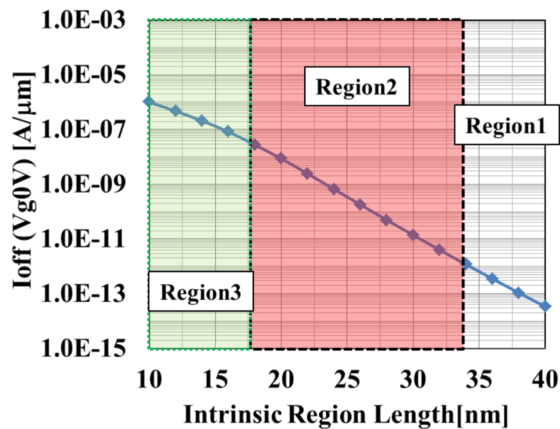

Fig. 5. The Ioff dependence of Li in vertical DGIMOS.

Junction Leakage Variability Simulation Considering Random Discrete Dopants

Hiroshi Takeda, Kazuya Uejima, Kiyoshi Takeuchi, and Masami Hane

LSI Research Laboratory, Renesas Electronics Corporation
1120 Shimokuzawa, Chuou-ku, Sagamihara, Kanagawa, Japan
E-mail: hiroshi.takeda.pz@renesas.com

Abstract

Junction leakage current variability due to random discrete dopants (RDD) has been simulated. Quantum corrected coulomb potential has been considered for discrete dopants. The effect of the RDD profiles on the electric field and the trap assisted tunneling (TAT) current due to single discrete trap has been discussed.

Introduction

For low stand-by power ULSIs, junction leakage current and its variability is an important issue to be addressed [1]. Junction leakage current due to trap assisted tunneling (TAT) process is one of the main sources of such off-state leakage in high temperature. Thus, it is important to evaluate the variability of the TAT current for improving the reliability and yields of ULSIs.

TAT current fluctuation caused by the randomness of discrete trap number and location (Fig. 1) has been already simulated [2],[3]. On the other hand, it is well known that the randomness of discrete dopants (RDD) is a major cause of threshold voltage variation [4]. Therefore, RDD can also strongly affect TAT current variability. In this paper, we have numerically evaluated the TAT current variability considering the effects of RDD.

Simulation Method

In order to evaluate the TAT current variability due to RDD fluctuations, potential and carrier density profiles with RDD are calculated by a drift-diffusion simulation. Using the obtained device profiles, TAT junction leakage current is calculated based on the Shockley-Reed-Hall (SRH) model [5] (Fig. 2). About 4500 nMOSFETs with different RDD distributions were generated. Then, TAT current caused by a single discrete trap was calculated, while changing the position of the discrete trap within each FET. The energy level of the discrete trap was fixed at the mid-gap for evaluating the variability of the maximum TAT current caused by the electric field fluctuation due to RDD.

In order to represent the discrete dopant potential, an analytical effective potential model [6] is used as a quantum corrected coulomb potential. The cut-off radius, r_c, of the analytical effective potential model is calibrated to reproduce a quantum corrected coulomb potential (Fig. 4). In order to include the effects into the drift-diffusion simulation, the discrete dopant potential is converted into a doping density distribution based on Poisson's equation in an isolated system.

Results and Discussions

Fig. 4(a) shows surface electric field profiles along the source-drain direction for devices with different RDD profile. The off-state electric field tends to be the highest around the surface of the channel/drain interface region, and the highest electric field varies about 2 times within the simulated devices. The highest electric field is obtained in device A, which has more discrete donors around the channel/drain interface (Fig. 4(b)). Because of the concentration of discrete donors around the channel/drain interface, the depletion region from the drain region reaches the channel region, and the large potential difference between the depletion region and the gate electrode causes the high electric field. Compared with device A, devices B (medium electric field) and C (low electric field) has fewer discrete donors around the channel/drain interface (Fig. 4(c),(d)).

Such electric field fluctuation by the difference of RDD profiles causes large difference in TAT junction leakage current calculated by the SRH model. Fig. 5 shows the distribution of J_{leak}, which is the maximum calculated TAT leakage current caused by a single trap for each device. J_{Leak} can vary about 2 orders of magnitude around the median value ($J_{\mathrm{Leak}}^{\mathrm{median}}$) by the electric field fluctuation due to RDD. These results show that RDD can accidentally cause extremely large junction leakage, and must be taken into account for leakage variability simulation, though the probability of such occurrence is low.

Conclusions

Variability of TAT junction leakage current due to RDD has been numerically evaluated. The TAT junction leakage current can be enhanced about 2 orders of magnitude from the median value because of the electric field enhancement caused by the discrete donor concentration in the channel region. Device structures should be designed considering such off-state leakage variability especially for low power ULSI applications.

References

[1] S. Shimizu *et al.*, Proc. of VLSI Symp., 196 (2011).
[2] A. Hiraiwa *et al.*, IEDM Tech. Dig., 157 (1998).
[3] S. Jin *et al.*, IEEE Trans. Electron. Dev. **52**, 2422 (2005).
[4] M. Miyamura *et al.*, Proc. of VLSI Symp., 22 (2007).
[5] G. Hurkx *et al.*, IEEE Trans. Electron. Dev. **39**, 331 (1992).
[6] C. Alexander *et al.*, IEDM Tech. Dig. (2006).

978-3-901578-26-7 © 2013 Society for Micro- and Nanoelectronics

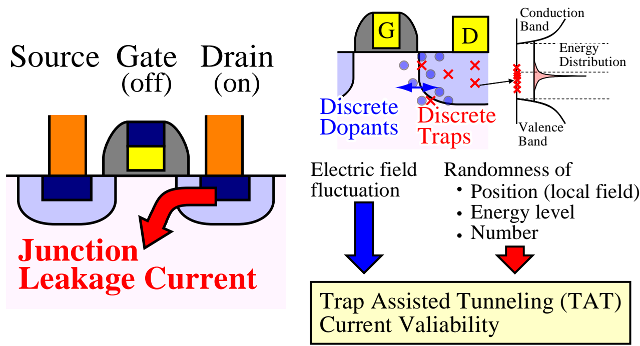

Fig. 1: Off-state junction leakage current fluctuation is investigated. Trap assisted tunneling (TAT) current is calculated as the junction leakage current in high temperature. The fluctuation of the TAT current can be enhanced by electric field fluctuation due to random discrete dopants (RDD) in addition to the randomness of discrete traps (trap position, density, energy level).

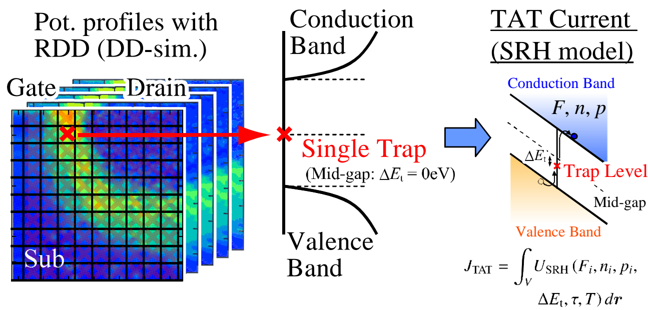

$$J_{TAT} = \int_V U_{SRH}(F_i, n_i, p_i, \Delta E_t, \tau, T)\, dr$$

Fig. 2: Variability of TAT current due to electric field fluctuation caused by RDD is evaluated. In order to eliminate the randomness of discrete traps, TAT current due to a single discrete trap is considered. The single discrete trap is located at all mesh points of the potential profiles with RDD calculated by drift-diffusion simulation. The TAT current is calculated based on SRH model. The trap energy level is fixed to be mid-gap in order to evaluate the fluctuation of maximum TAT current due to RDD.

$$V_{eff}(r) = e/4\pi\varepsilon\,(r^2+r_c^{\,2}/2)^{1/2}$$

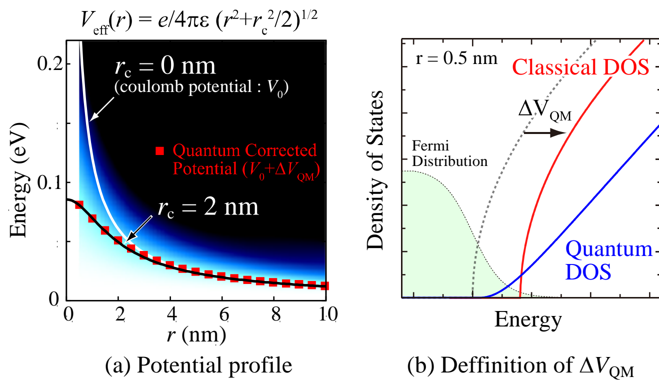

(a) Potential profile (b) Deffinition of ΔV_{QM}

Fig. 3: Analytical effective potential model[6], $V_{eff}(r)$, is used as the discrete dopant potential. (a) The cut-off radius r_c of $V_{eff}(r)$ is calibrated to reproduce a quantum corrected coulomb potential. (b) The quantum corrected potential is defined as the potential with which the quantum electron density (calculated by solving Schoredinger equation) is obtained based on classical density of states. The discrete dopant potential is converted to the doping density profile to include into drift-diffusion simulation.

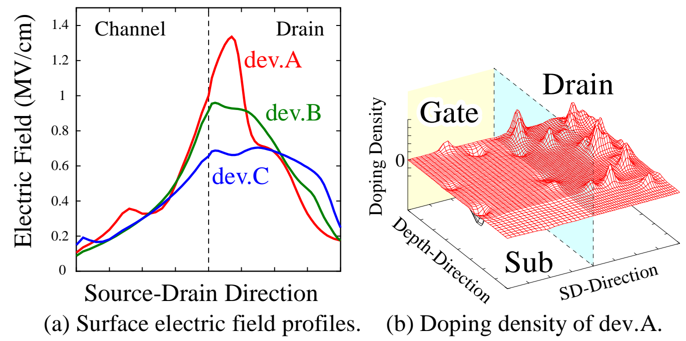

(a) Surface electric field profiles. (b) Doping density of dev.A.

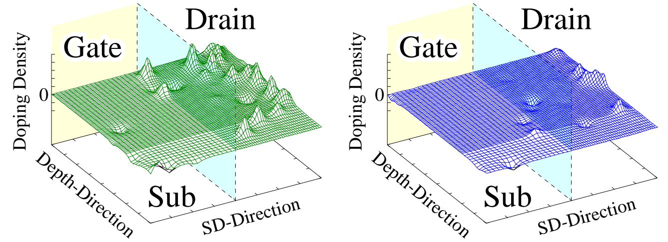

(c) Doping density of dev.B. (d) Doping density of dev.C.

Fig. 4: (a) Electric field profiles along source-drain direction at the substrate surface for devices with different RDD profiles. (b) Doping density profile of dev.A, which shows strong surface electric field. Compared with doping profiles of other devices ((b) dev.B with medium electric field, (c) dev.C with low electric field), dev.A has more discrete donors in the channel region which causes large potential difference between channel and gate electrode. Large TAT current fluctuation can be caused by such electric field difference if discrete traps are located around the regions.

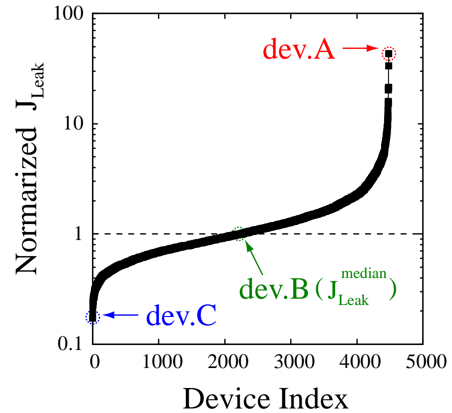

Fig. 5: The maximum junction leakage current within each device profile, J_{Leak}. J_{Leak} is normalized by median J_{Leak} (J_{Leak}^{median}) and plotted in ascending order. J_{Leak} is strongly affected by electric field fluctuation and enhanced to about 2 orders larger magnitude than the median device.

Impact of Scaling on the Variability in Multigate Transistors

M. Aldegunde, A. Martinez, and J. R. Barker*
College of Engineering, Swansea University, Swansea SA2 8PP, United Kingdom
e-mail: m.a.aldegunderodriguez@swansea.ac.uk
*School of Engineering, Glasgow University, Glasgow G12 8LT, United Kingdom

Three-dimensional device architectures are strong candidates for the scaling of MOSFETs into the next technology nodes [1]. Two of the most important sources of fluctuations in ultrascaled devices are *random discrete doping* and *surface roughness*. Previous studies of variability have been concentrated in generic nanowire structures or used semiclassical models. In this work we study the impact of scaling on the effect of both sources of variability in two Si multigate MOSFETs scaled according to the ITRS.

We carried out non-equilibrium Green's functions (NEGF) transport simulations including all relevant phonon scatterings [2]. We study two different devices with channel lengths of 11.8 and 6.6 nm and body thicknesses of 5.8 and 4.2 nm, respectively. In both cases the ratio between the body height and thickness is 2:1. Random discrete doping (RDD) and surface roughness (SR) are introduced using the same methodology and the same parameters as in [3]. We have simulated five different configurations for each device, which should provide an estimation for the range of variability expected in a larger ensemble. Figs. 1 and 2 show the $I_D - V_G$ characteristics at a high drain bias V_D=700 mV for both simulated transistors under the combined influence of RDD and SR. The characteristics with a smooth geometry and doping are shown as a reference. For both geometries we see a shift towards higher threshold voltages due to a change in the width and height of the barrier induced by the different variability sources. This shift is smaller for the larger device, where it ranges from 6 to 22 mV, than for the shorter one, where it ranges from 20 to 77 mV. The main effect of the RDD in the low gate bias region is a change in the subthreshold slope. The variability is much larger in the case of the shorter device, where the slopes vary between 84 and 101 mV/dec, whereas in the longer device they vary between 76 and 81 mV/dec. Fig. 3 presents the local density of states and the subbands for the smooth device and the highest current configuration in the shorter device at V_G=0.6 V. The small amplitude ripples of the subbands close to source and drain reflect the SR while the large amplitude ones correspond to the RDD which are close to the source/channel and drain/channel interfaces. We can also see how the potential fluctuations induced by RDD and SR break the interference fringes in the LDOS seen in the smooth device. Fig. 4 shows the electron density and electrostatic potential energy for the highest current configuration of the 6.6 nm device at V_G=0.5 V. At the source cross-section, the electron density has two maximums due to the large electron electrostatic energy at the middle of the cross section. These two maximums merge in the middle of the source/channel interface cross-section due to the RDD concentration there. Finally, Figs. 5 and 6 show the spectral current density for the two geometries in the lowest and highest current configurations (V_G=0.3 V). For the longer device, there is a small difference in the barrier width and therefore in the tunnelling current. The main difference in the $I_D - V_G$ characteristics is a shift of about 16 mV, which comes mainly from the difference in barrier height (around 20 mV). For the shorter devices we can see a clear difference in the barrier width coming from RDD close to the channel, which reduce the effective gate length. This notably increases the tunnelling current and therefore the subthreshold slope. This increase is also strengthened by the lower height of the barrier induced by the SR (around 25 mV).

References

[1] T. Chiarella *et al.*, Solid-State Electron. **54**, 855 (2010).
[2] M. Aldegunde *et al.*, J. Appl. Phys. **110**, 094518 (2011).
[3] A. Martinez *et al.*, IEEE Trans. Electron Devices **58**, 2209 (2011).

978-3-901578-26-7 © 2013 Society for Micro- and Nanoelectronics

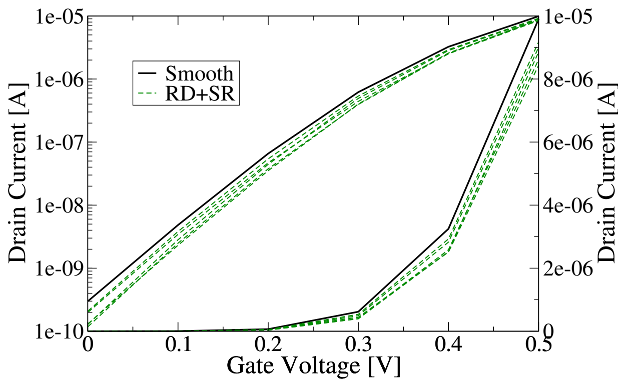

Fig. 1. $I_D - V_G$ characteristics of the 11.8 nm gate length MOSFET under the influence of discrete dopants and surface roughness. The smooth device (continuous black line) is also shown as a reference.

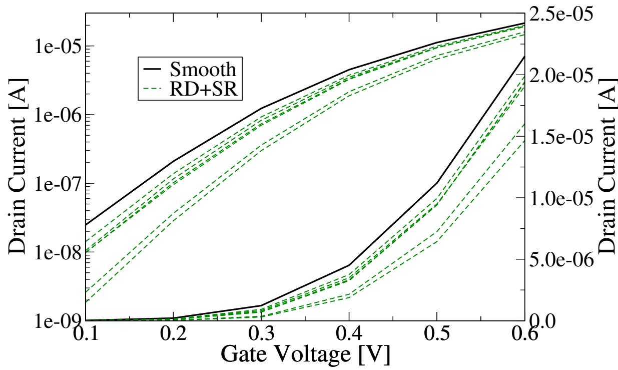

Fig. 2. $I_D - V_G$ characteristics of the 6.6 nm gate length MOSFET under the influence of discrete dopants and surface roughness. The smooth device (continuous black line) is also shown as a reference.

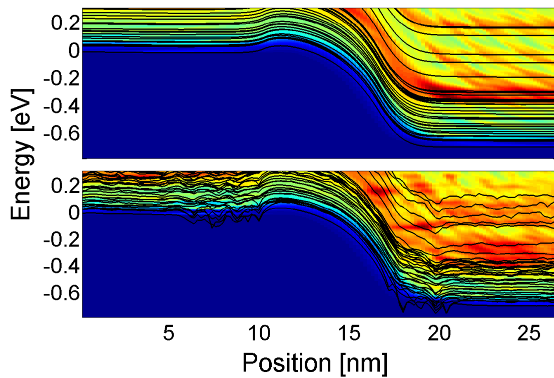

Fig. 3. Local density of states in the 6.6 nm gate length MOSFET for the smooth device (top) and under the influence of discrete dopants and surface roughness (bottom) at V_G=0.6 V.

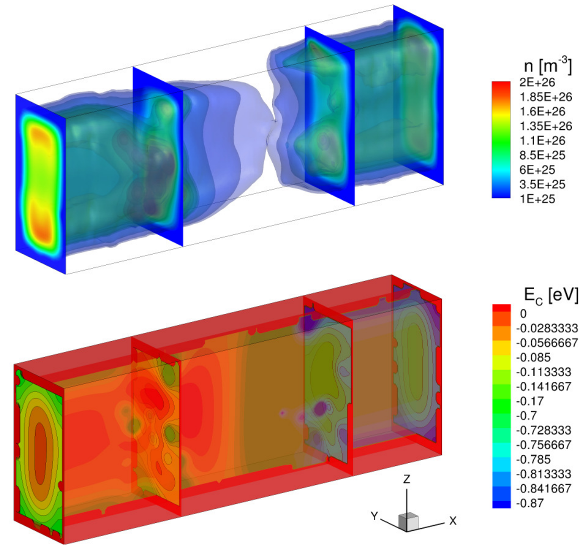

Fig. 4. Electron density (top) and electrostatic potential energy (bottom) for one random configuration of the 6.6 nm gate length MOSFET.

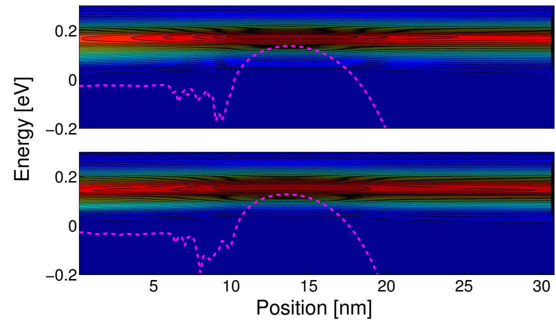

Fig. 5. Spectral current for the configurations with lowest (top) and highest (bottom) drain current for the 11.8 nm gate length MOSFET.

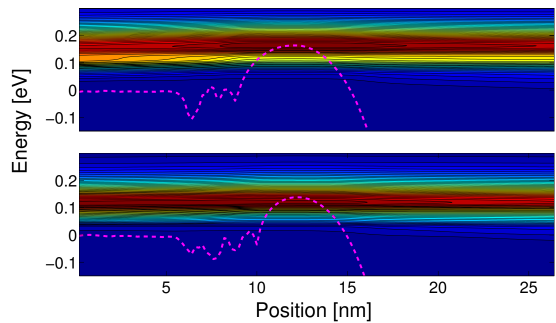

Fig. 6. Spectral current for the configurations with lowest (top) and highest (bottom) drain current for the 6.6 nm gate length MOSFET.

Surface Roughness and Electron Transport Statistics in Si Nanowires

G. Mil'nikov*‡, T. Zushi†, M. Tomita†, T. Watanabe†‡, Y. Kamakura*‡, and N. Mori*‡
*Graduate School of Engineering, Osaka University, 2-1 Yamada-oka, Suita, Osaka 565-0871, Japan
†Faculty of Science and Engineering, Waseda University, Shinjiku, Tokyo 169-8555, Japan-0075, Japan
‡CREST, JST, 7 Gobancho, Chiyoda-ku, Tokyo 102-0075, Japan
gena@si.eei.eng.osaka-u.ac.jp

Semiconductor nanowires (NW) has been recently considered as promising building blocks for future nanoelectronic devices and integrated circuits. One of the key issues for their practical applications is sample-to-sample variability caused by structural disorder at the wire interface. Application of the first-principle calculations to statistical modeling in realistic NW devices is prohibitively time-consuming. In this work we analyze statistics of electron transport in Si wires with surface disorder and propose a numerically cheap approximate model for statistical transport studies.

The model under consideration has been extracted from a realistic oxidized SiNW with interface atomic disorder obtained by the MD simulations [1]. Si atoms in the core part of the wire with moderate local strain $< 3\%$ have been used to construct NW samples for our statistical analysis (Fig. 1). We use the $sp^3d^5s^*$ tight-binding (TB) Hamiltonian of a strain Si crystal [2] with H termination model for the dangling bonds and employ the NEGF formalism for transport calculations. The obtained transport data are compared with the results calculated by using the equivalent model (EM) representation [3] which is an analog of the basis expansion approach for discrete systems with arbitrary band structure. The EM method enables a small atomistic basis of most relevant modes to be extracted from the original set of atomic orbitals. In the present case, the 24D EM representation has been constructed based on a periodic reference Si wire with the averaged local strain distribution (Fig.2). The EM was found to give similar fluctuations in the band structure and well reproduce the behavior of the transmission coefficient $T(\varepsilon, L)$ along the SiNW samples (Fig. 3).

Qualitative statistical analysis has been performed by fitting the computed averaged transmission $\langle T \rangle$ and its variance $var(T)$ by the "universal" L-dependent statistics calculated from the DMPK equation (β=1) [4] or its multidimensional generalization [5] (Fig. 4). We have confirmed the quasi-one-dimensional universal statistical behavior (Fig.5) which can be characterized by a single length parameter (Fig.6). The larger fluctuations in short samples cannot be explained by the dimensionality effects and are likely to be caused by the enhanced reflection at the contacts with leads.

Our results show that the localization of the electronic states due to the surface roughness scattering is an important factor effecting the NW device performance. The universal one-parameter transport statistics also suggests that one can predict their statistical properties without time consuming transport simulations at atomistic level and the EM may provide an effective tool for statistical device modeling. This study is currently in progress.

References

[1] T. Onda, T. Watanabe, and I. Ohdomari, *Crystal orientation dependency of oxidation-induced strain in silicon nanostructures: A molecular simulation study*, ISSS-5, Tokyo, Japan, 2008.
[2] Y. M. Niquet, D. Rideau, C. Tavernier, H. Jaouen, and X. Blase, *Onsite matrix elements of the tight-binding Hamiltonian os a strain crystal: Application to silicon, germanium, and their alloys*, Physical Review B **79**, 245201 (2009).
[3] G. Mil'nikov, N. Mori, and Y. Kamakura, *Equivalent transport models in atomistic quantum wires*, Physical Review B **85**, 035327 (2012).
[4] G. Mil'nikov and N. Mori, *Random evolution approach to universal conductance statistics*, Physical Review B **87**, 035434 (2013).
[5] G. Mil'nikov and N. Mori, unpublished.

978-3-901578-26-7 © 2013 Society for Micro- and Nanoelectronics

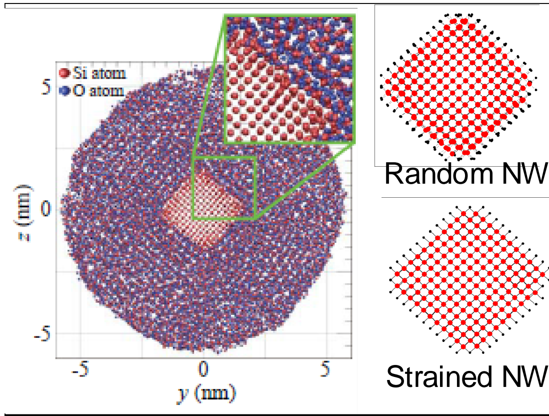

Fig. 1. Realistic nanostructure obtained in the MD simulations. The right panels show the core part of the wire used in the present simulations and the corresponding periodic NW with averaged strain.

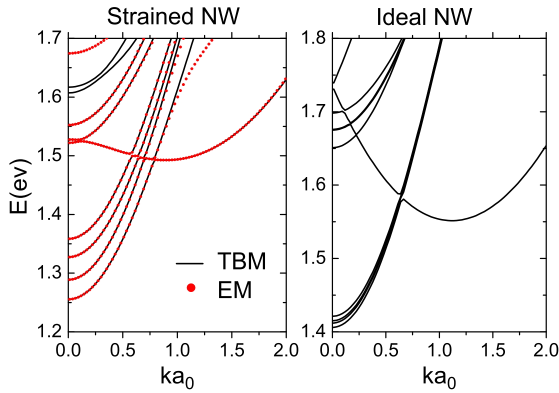

Fig. 2. The band structure in the strained NW in Fig. 1. The dots correspond to the 24D EM for the bottom part of the conduction band within $\sim$ 0.3 eV energy interval. The band structure in the corresponding ideal [100] SiNW is shown for comparison.

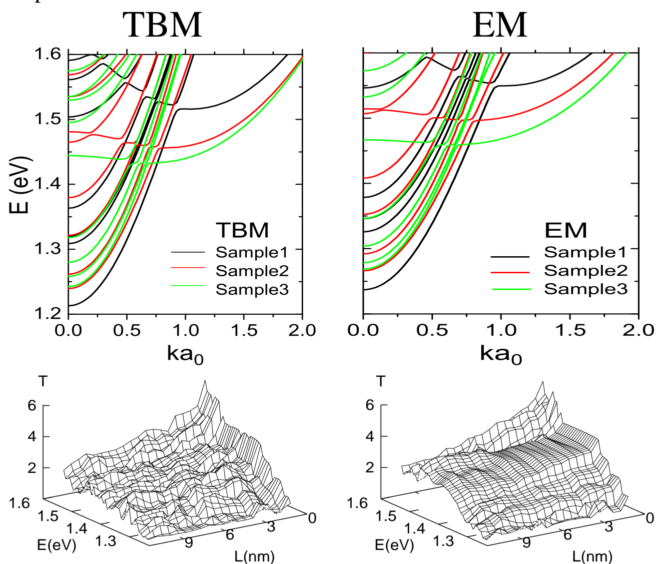

Fig. 3. Fluctuation of the band structure calculated by taking various blocks of the random wire (upper panels) and transmission function in a sample composed from such blocks (lower panels) in the TBM and EM representation.

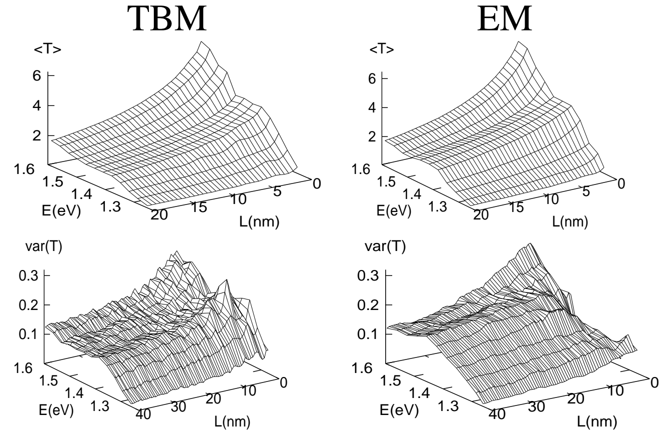

Fig. 4. The averaged transmission coefficient and its variance in the TBM and EM representation.

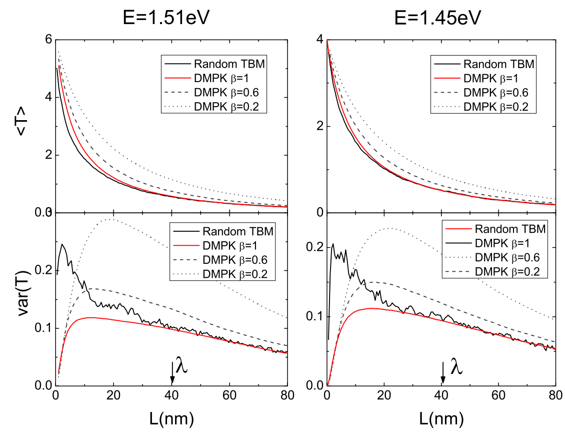

Fig. 5. Fitting $\langle T \rangle$ and $var(T)$ in Fig.(4) at two energy values by the universal functions of L/λ calculated from the DMPK equation (red line). The corresponding solutions of the DMPK equation with fractional βs are shown for comparison.

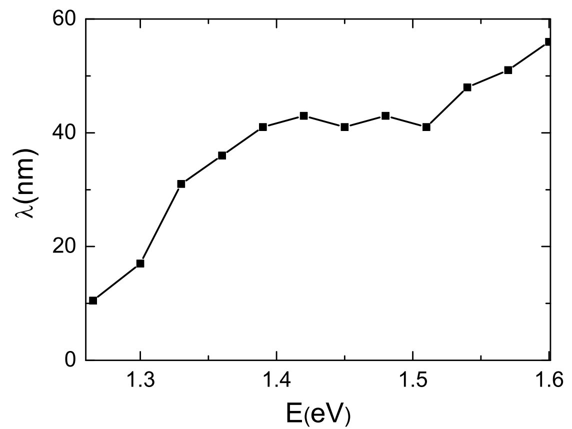

Fig. 6. The localization length as a function of energy.

Effect of the size and the separation of metal nanodots on the electromagnetic enhancement to surface-enhanced Raman spectroscopy

M.S. Choi, M.A. Stroscio*, and M. Dutta
Dept. Electrical and Computer Engineering, University of Illinois at Chicago, Chicago, IL 60607, USA
*Email: stroscio@uic.edu

INTRODUCTION

Surface-enhanced Raman spectroscopy (SERS) has been intensively researched in the past two decades due to its capability and usefulness as one of the most sensitive detecting tools of high levels of molecular specicity [1], [2], [3]. However, localized surface plasmon resonance (LSPR), which is a major contributor to the electromagnetic (EM) enhancement of SERS, depends on the composition, shape, size, the separation of nanodots, etc [4], their assembly has been studied in detail both experimentally [5] and theoretically. In the latter case, computational electromagnetic methods such as the finite-difference time-domain (FDTD) method and the finite element method (FEM) are often used [6]. Herein, we use the FEM, using an modified version of open-source FEM code, JFEM2D [7], to calculate the electromagnetic enhancement of various assemblies of Au nanodots with SiO_2 coating to predict optimal assemblies for a given incident wavelength. Furthermore, a selected number of $|\mathbf{E}|^4$ at the incident wavelength that give the maximum enhancement for a given geometry will be analyzed to predict "hot spots"[10], which are locations where the maximum EM enhancement occurs.

METHODS

The details on FEM code is described in a code author's article [6]. However, the permittivity values of Au and SiO_2 is modified in accordance with the Mie scattering the correction to nano-scaled metals with coating[8] and with a model dielectric function appropriate to SiO_2 [9], respectively. Figure 1 shows the assembly of interest. Herein, various separations (-5 nm to 10 nm) and radii (60 nm to 120 nm) are used.

DISCUSSION

A sample result is shown in Figure 2. With the separation fixed at 1 nm, assemblies with diameters of 90 nm and 100 nm have maximum EM enhancement when the wavelength of incident field is 813.8 nm. The result also shows that the two Au nanospheres with diameters of 100 nm give higher enhancement than one with diameters of 90 nm at 813 nm. On the other hand, the assembly with diameters of 80 nm give the maximum enhancement at 793 nm, which is a little bit lower than that from assemblies with larger diameters. For the assembly, the contour plot of $|\mathbf{E}|^4$ at 793 nm is plotted in log scale in Figure 3. It shows that the "hot spots" (geometrical locations with the highest enhancement) for the assembly are located between two Au nanospheres.

CONCLUSION

The effect of size and placement of Au nanospheres on the EM enhancement of SERS was studied. The application of these results to quantify the SERS enhancements effects observed for cylindrical dielectrics coated with Au nanodots will be illustrated.

REFERENCES

[1] T. Vo-Dinh, M. Y. K. Hiromoto, G. M. Begun, and R. L. Moody, *Surface-Enhanced Raman Spectrometry for Trace Organic Analysis*, Anal. Chem. 56, 1667-1670 (1984).
[2] S. E. J. Bell and N. M. S. Sirimuthu, *Quantitative surface-enhanced Raman spectroscopy*, Chem. Soc. Rev., 37, 1012-1024 (2008).
[3] T. Vo-Dinh, *Surface-enhanced Raman spectroscopy using metallic nanostructures* Trends in Analytical Chemistry, vol. 17, nos. 8+9, (1998).
[4] X. Lin, Y. Cui, Y. Xu, B. Ren, and Z. Tian, *Surface-enhanced Raman spectroscopy: substrate-related issues* Anal Bioanal Chem 394:1729-1745 (2009).
[5] W. Li, F. Ding, J. Hu, and S. Y. Chou, *Three-dimensional cavity nanoantenna coupled plasmonic nanodots for ultrahigh and uniform surface-enhanced Raman scattering over large area* Optics Express Vol. 19, No. 5, 3925 (2011).
[6] J. M. McMahon, A. Henry, K. L. Wustholz, M. J. Natan, R. G. Freeman, R. Van Duyne, and G. C. Schatz, *Gold nanoparticle dimer plasmonics: finite element method calculations of the electromagnetic enhancement to surface-enhanced Raman spectroscopy* Anal. Bioanal. Chem. 394:1819-1825 (2009).

978-3-901578-26-7 © 2013 Society for Micro- and Nanoelectronics

[7] J. M. McMahon, *JFEM2D (2009)* Available from: <http://www.thecomputationalphysicist.com>.

[8] R. D. Averitt, D. Sarkar, and N. J. Halas, *Plasmon Resonance Shifts of Au-Coated Au_2S Nanoshells: Insight into Multicomponent Nanoparticle Growth* Phys. Rev. Lett. Vol. 78 No. 22 (1997).

[9] M. V. Fischetti, *Long-range Coulomb interactions in small Si devices. Part II. Effective electron mobilirt in thin-oxide structures* J. Appl. Phys. Vol. 89 No. 2 (2011).

[10] C. Farcau and S. Astilean, *Mapping the SERS Efficiency and Hot-Spots Localization on Gold Film over Nanospheres Substrates* J. Phys. Chem. Vol. 114, 11717-11722 (2010).

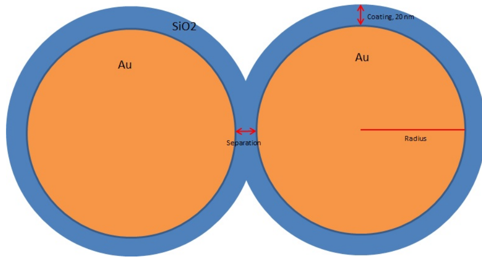

Fig. 1. Assembly of interest. Two gold nano spheres with SiO_2 coating are given

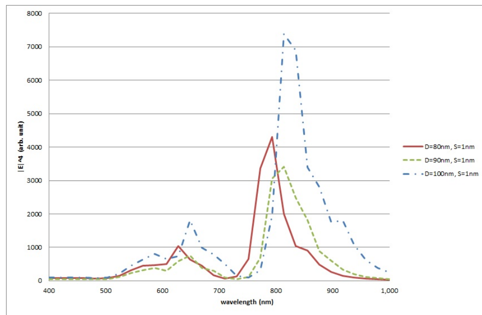

Fig. 2. Maximum electromagnetic enhancements ($|\mathbf{E}|^4$) for nanospheres of 80, 90, 100nm with separations of 1 nm

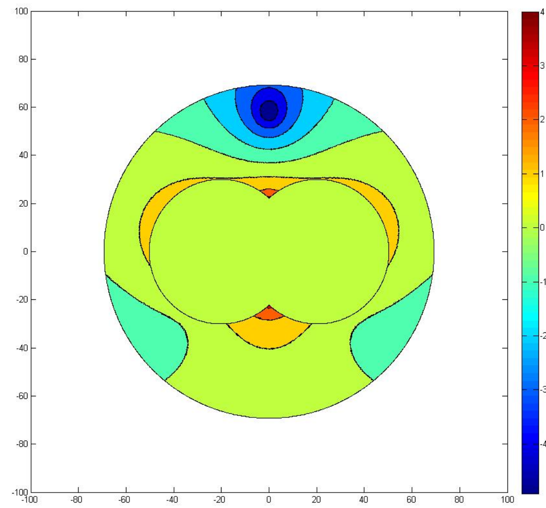

Fig. 3. Contour plot of $|\mathbf{E}|^4$ at the incident wavelength of 793 nm for the assembly with diameter of 80 nm and separation of 1 nm

Terahertz quantum cascade laser using AlGaAs wells for higher-temperature operation

Hiroaki Yasuda
National Institute of Information and Communications Technology,
4-2-1, Nukui-Kitamachi, Koganei, Tokyo 184-8795, Japan
e-mail: yasuda@nict.go.jp

INTRODUCTION

Remarkable progress on terahertz quantum cascade lasers (THz-QCLs) has been made using GaAs/$Al_xGa_{1-x}As$ multi-quantum-well structures. However, the maximum operation temperature was limited to 200 K. Realization of room-temperature operation of THz-QCLs is remained as a challenging issue. The main degradation mechanism of population inversions at high temperatures is thought to be thermally activated longitudinal optical (LO) phonon scattering [1, 2], where electrons in the upper lasing level 3 acquire sufficient in-plane kinetic energy to emit LO phonons and relax to the lower lasing level 2 as depicted in Fig. 1. To reduce the thermally activated phonon scattering, use of AlGaAs instead of GaAs as the well material might be promising because the LO phonon energy of AlAs-like modes is higher than that of GaAs-like modes [3]. In this study, we calculated the performance of an $Al_xGa_{1-x}As/Al_yGa_{1-y}As$ THz-QCL using the non-equilibrium Green's function (NEGF) method to find an appropriate Al composition of well layers for higher-temperature operations.

RESUTLTS AND DISCUSSIONS

Details of our NEGF calculation method were explained elsewhere [4, 5]. The Fröhlich interaction Hamiltonian was used for the self-energy of the LO phonon-electron coupling. The self-energy for the LO phonon scattering in $Al_xGa_{1-x}As$ layers was introduced as linear combinations of those in GaAs layers and AlAs layers as expressed in equation 1.

$$\Sigma_{\mathrm{LO(Al_xGa_{1-x}As)}} = x\Sigma_{\mathrm{LO(AlAs)}} + (1-x)\Sigma_{\mathrm{LO(GaAs)}} \tag{1}$$

One period of the calculated THz-QCL sequence is **5.1**/9.6/**2.3**/7.3/**4.0**/15.8 nm as shown in Fig. 2. The bold and regular numbers represent quantum barrier and well layers, respectively. The 15.8-nm-thick quantum well is n-doped with $n = 1.9 \times 10^{16}$ cm^{-3}. Only the Γ-valley electron states are taken into consideration for simplicity. The conduction band discontinuity, the LO phonon energies of GaAs-like and AlAs-like modes are set to be constant as 120, 36, and 46 meV, respectively.

Figure 3 shows the optical gain averaged over one period of the THz-QCL at 200 K. The gain for the $Al_{0.85}Ga_{0.15}As$/AlAs QCL increased as much as 17 cm^{-1} at 12 meV (2.9 THz). Figure 4 shows the electron distributions in the active region as a function of energy. The distribution curve has a dip around 160 meV, which is caused by the thermally activated phonon scattering due to the GaAs-like LO phonon mode. For the $Al_{0.85}Ga_{0.15}As$/AlAs THz-QCL, the dip becomes small and the other dip appears around 170 meV, which corresponds to the thermally activated phonon scattering by the AlAs-like LO phonon mode. Further calculations and designs should be made including X-valley electron states.

CONCLUSION

We investigated the performance of an $Al_xGa_{1-x}As/Al_yGa_{1-y}As$ THz-QCL by using the NEGF method to realize higher-temperature operations. We found that the optical gain improved by using $Al_{0.85}Ga_{0.15}As$ wells due to the reduction of the thermally activated phonon scattering by GaAs-like LO phonons.

ACKNOWLEDGEMENT

We thank S. Birner and T. Kubis for helpful discussions.

REFERENCES

[1] B. S. Williams, *Terahertz quantum-cascade lasers,* Nature Photonics **1**, 517 (2007).

[2] H. Yasuda, T. Kubis, P. Vogl, N. Sekine, I. Hosako, and K. Hirakawa, *Nonequilibrium Green's function calculation for four-level scheme terahertz quantum cascade lasers*, Appl. Phys. Lett. **94**, 151109 (2009).

[3] O. K. Kim and W. G. Spitzer, *Infrared reflectivity spectra and Raman spectra of Ga_{1-x} Al_x As mixed crystals*, J. Appl. Phys. **50**, 4362 (1979).

[4] T. Kubis, C. Yeh, P. Vogl, A. Benz, G. Fasching, and C. Deutsch, *Theory of nonequilibrium quantum transport and energy dissipation in terahertz quantum cascade lasers*, Phys. Rev. B 79, 195323 (2009).

[5] H. Yasuda, T. Kubis, I. Hosako, and K. Hirakawa, *Non-equilibrium Green's function calculation for GaN-based terahertz-quantum cascade laser structures*, J. Appl. Phys. **111**, 083105 (2012).

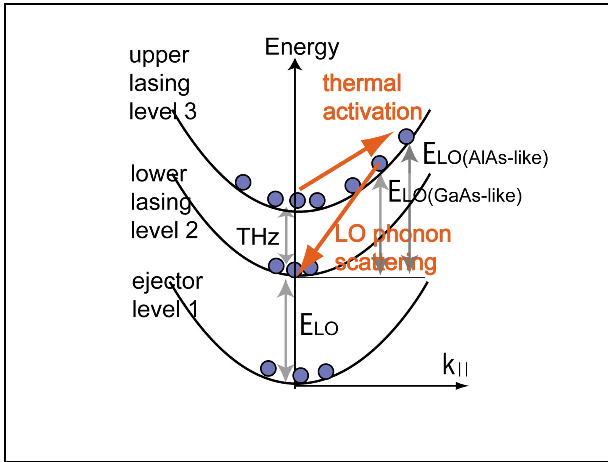

Fig. 1. Schematic of thermally activated LO phonon scattering.

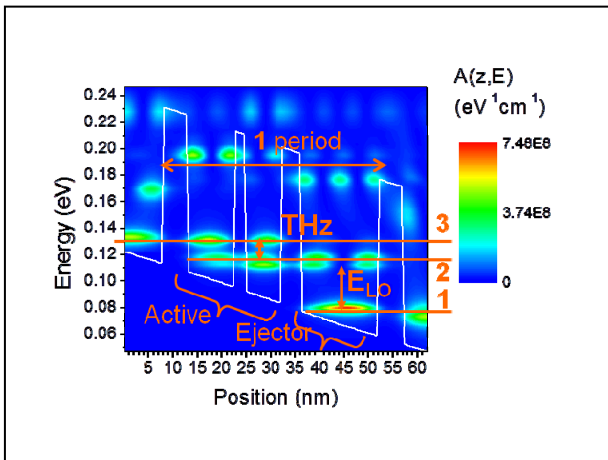

Fig. 2. Conduction band diagram and spectral functions $A(z, E)$ of the calculated THz-QCL at 12 kV/cm.

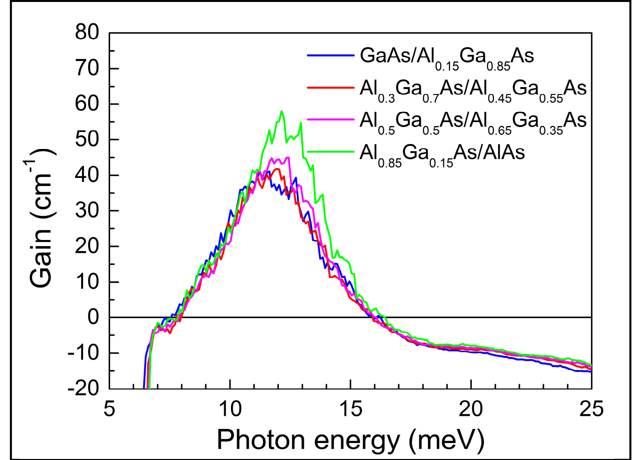

Fig. 3. Calculated gain averaged over one period of the THz-QCL structure at 200 K. The Al composition of wells was changed from 0 to 0.85.

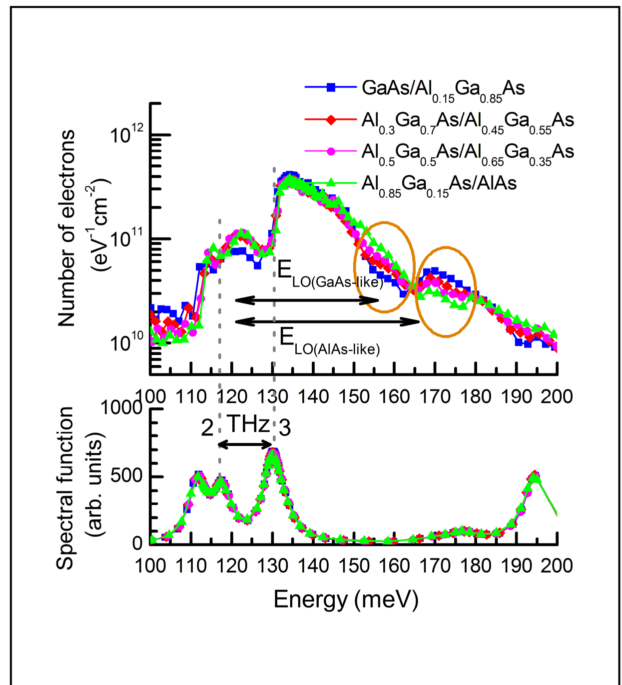

Fig. 4. Calculated electron distributions and spectral functions in the active region at 200 K.

Polarization dependent optical absorption properties of quantum dot superlattices

T. Kotani*†, H. Yoshikawa†, T. Miyake†, P. Lugli*, and C. Hamaguchi†
*Institute for Nanoelectronics, Technische Universität München, D-80333 Munich, Germany
†Advanced Technology Research Laboratories, Sharp Corporation,
2613-1 Ichinomoto-cho, Tenri, Nara 632-8567, Japan, e-mail: kotani.teruhisa@sharp.co.jp

Introduction

Recently, the closely stacked periodic quantum dots (QDs), which is often called quantum dot superlattices (QDSLs), have been attracting much interest due to their unique properties[1]. For the optical device application, understanding the absorption spectrum as well as the optical polarization is very important. In this study, we theoretically investigate the polarization dependence of the optical absorption properties of InAs/GaAs QDSLs.

Calculation Method

We consider z- ([001]-) stacked InAs/GaAs QDs with a truncated pyramidal shape having (101), $(\bar{1}01)$, (011) and $(0\bar{1}1)$ as side facets. The dot height is 3 nm, the base length is 15 nm and the wetting layer width is 0.5 nm. The plane-wave expanded 8-band k·p Hamiltonian [2], [3] with periodic boundary condition is solved to obtain the electronic structures. Strain and piezoelectric effect are also included. The optical absorption spectrum $\alpha(\omega)$ is calculated by

$$\alpha = \frac{e^2}{2n_r c_0 \epsilon_0 m_0^2 \omega L_x L_y} \int \mathrm{d}K_z \sum_{a,b} |M|^2 (f_a - f_b) G \tag{1}$$

, where $|M|$ is the optical matrix element, a and b are the miniband index, n_r is the refractive index, c_0 is the light speed, ϵ_0 is the dielectric constant of vacuum, m_0 is the free electron mass, $L_x(L_y)$ is the unit cell length in x-(y-) dimension, K_z is the superlattice vector, $f_i(i = a, b)$ is the distribution function, G is the Gaussian broadening (5 meV) due to the size or compositional fluctuation.

Result and Discussion

Figures 1 (a) – (d) show the absorption spectra of electron-hole transition in InAs/GaAs QDSLs. We assume the valence subbands are completely filled by electron and the conduction subbands are empty. The optical polarization of the main peak near the absorption edge strongly depends on the inter-dot spacing (L_z). For L_z = 1 nm, transverse magnetic- (TM-:E_{001}) polarization is dominant and the spectrum is similar to the quantum wires. For L_z = 3 nm, TM- and transverse electric- (TE-:E_{100}) polarization are almost the same. For $L_z \geq$ 5 nm, TE-polarization is dominant. The spectrum is similar to the single QD for L_z = 10 nm. We find this polarization properties are attributed to the strain-modified valence band structures. As L_z decreases, the biaxial tensile strain in the barrier increases. The biaxial tensile strain pulls up LH and then the mixing rate of LH in the lower state of valence subband increases. This results in the strong TM-polarized absorption for small L_z.

Conclusion

We have theoretically investigated optical properties of InAs/GaAs QDSLs. We find that the optical absorption spectrum strongly depends on L_z and the optical polarization switches at L_z = 3 nm. These findings provide an additional degree of freedom for the design of optical devices.

References

[1] C. Pryor *Quantum Wires Formed from Coupled InAs/GaAs Strained Quantum Dots*, Phys. Rev. Lett. **80**, 3579 (1998).
[2] C. Hamaguchi, *Basic Semiconductor Physics, 2nd. ed*, Springer-Verlag, (2010).
[3] S. Tomić, *Intermediate-band solar cells: Influence of band formation on dynamical processes in InAs/GaAs quantum dot arrays*, Phys. Rev. B **82**, 195321 (2010).

978-3-901578-26-7 © 2013 Society for Micro- and Nanoelectronics

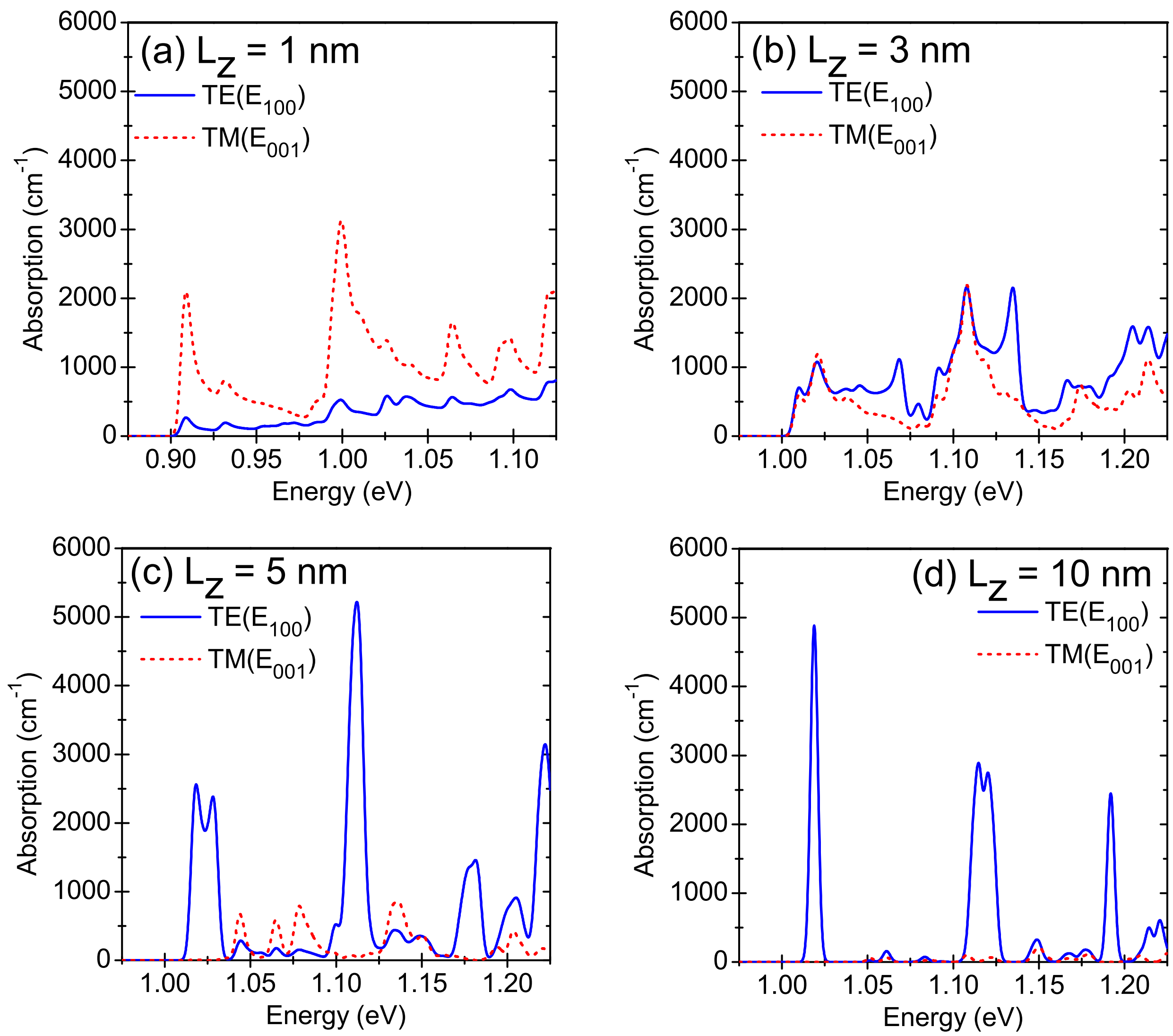

Fig. 1. TE (solid line) and TM (dashed line) polarized absorption spectra of InAs/GaAs QDSLs with inter-dot spacing of (a) L_z = 1 nm, (b) L_z = 3 nm, (c) L_z = 5 nm and (d) L_z = 10 nm.

Optical Absorption in InAs/$In_{0.48}Ga_{0.52}P$ Quantum Dot Superlattices

H. Yoshikawa, T. Kotani, Y. Kuzumoto, M. Izumi, Y. Tomomura, and C. Hamaguchi
Advanced Technology Research Laboratories, Sharp Corporation,
2613-1 Ichinomoto-cho, Tenri, Nara 632-8567, Japan
e-mail: yoshikawa-hirofumi@sharp.co.jp

INTRODUCTION

Recently, semiconductor quantum dot (QD) array-based intermediate band solar cells (IBSCs) have received much attention as ultrahigh efficiency solar cells[1]. The concept of IBSCs is to increase the photocurrent by the additional two-step photon-absorption via the intermediate band (IB or QD minibands) states as illustrated in Fig. 1. Although InAs/GaAs IBSCs are widely studied, the optical properties are not suitable for solar spectra, because the wavelength of absorbed light from IB (MB_0: first miniband) to the conduction band is too long. Instead we propose solar cells based on InAs/$In_{0.48}Ga_{0.52}P$ which provides higher efficiency of sunlight absorption. $In_{0.48}Ga_{0.52}P$ is lattice-matched material to GaAs with wider bandgap than GaAs. We present theoretical calculations of the absorption spectra of InAs/$In_{0.48}Ga_{0.52}P$ IBSCs.

CALCULATION METHOD

We consider z-stacked InAs/$In_{0.48}Ga_{0.52}P$ QD superlattices (QDSLs) with a pyramidal shape. The dot height is 3 nm, and the base length is 8 nm. The inter-dot spacing in z-direction is 3 nm. We calculated the electronic and optical properties by solving the plane-wave expanded 8-band k p Hamiltonian [2], [3] with periodic boundary condition. We also took into account of strain and piezoelectric effects. The electronic and optical properties of InAs/$In_{0.48}Ga_{0.52}P$ QDSLs are also compared with those of conventional InAs/GaAs QDSLs. For the valence band (VB) to IB (MB_0) or CB transitions (VB $\rightarrow$ IB or VB $\rightarrow$ CB), we assume the VB subbands are completely filled with electrons and the IB and CB subbands are empty. For the IB $\rightarrow$ CB transitions, we assume the IB is completely filled and the CB subbands are empty.

RESULT AND DISCUSSION

Figs. 2 (a)–(d) show the TE (x- and y- direction) and TM (z-direction) polarized absorption spectra of InAs/GaAs QDSLs and InAs/$In_{0.48}Ga_{0.52}P$ QDSLs, where we find the absorption spectra of InAs/$In_{0.48}Ga_{0.52}P$ QDSLs are blue-shifted compared to InAs/GaAs QDSLs. In addition, the absorption band of InAs/$In_{0.48}Ga_{0.52}P$ QDSLs is narrowed compared to InAs/GaAs QDSLs. These results indicate InAs/$In_{0.48}Ga_{0.52}P$ QDSLs have the strong quantum confinement effect due to the large conduction band offset, and thus the IB width become narrower. In the IB $\rightarrow$ CB transitions for the TE polarization, the peaks due to the transition between IB (MB_0) and MB_1, MB_2 become narrower. This result is not only due to the narrower IB width but also due to the change of MB_1 and MB_2 from the continuum states to the localized states below the effective potential barrier.

CONCLUSION

We find that the IB $\rightarrow$ CB transition energy gap can be widened by changing a barrier material from GaAs to lattice-matched $In_{0.48}Ga_{0.52}P$. This suggests that $In_{0.48}Ga_{0.52}P$ is a good candidate for a barrier material of ultrahigh efficiency IBSCs.

REFERENCES

[1] K. Tanabe, *et al.*, *High-efficiency InAs/GaAs quantum dot solar cells by metalorganic chemical vapor deposition,* Appl. Phys. Lett. **100**, 193905 (2012).
[2] C. Hamaguchi, *Basic Semiconductor Physics, 2nd. ed*, Springer-Verlag, (2010).
[3] S. Tomić, *Intermediate-band solar cells: Influence of band formation on dynamical processes in InAs/GaAs quantum dot arrays*, Phys. Rev. B **82**, 195321 (2010).

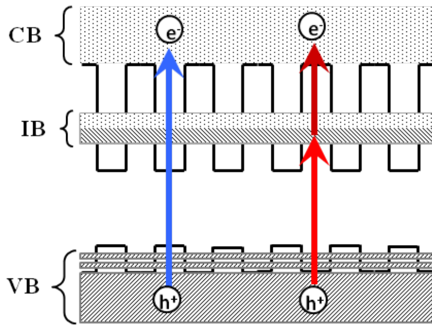

Fig. 1. Schematic view of the VB → IB (MB_0), VB → CB, and IB (MB_0) → CB transitions.

(a)

VB → IB and VB → CB transitions
TE polarization

(c)

IB → CB transitions
TE polarization

(b)

VB → IB and VB → CB transitions
TM polarization

(d)

IB → CB transitions
TM polarization

Fig. 2. The absorption spectra of InAs/GaAs QDSLs (dashed line) and InAs/$In_{0.48}Ga_{0.52}P$ QDSLs (solid line) (a) TE polarized in the VB → IB (MB_0) and VB → CB transitions, (b) TM polarized in the VB → IB (MB_0) and VB → CB transitions, (c) TE polarized in the IB (MB_0) → CB transitions, and (d) TM polarized in the IB (MB_0) → CB transitions.

Optical coupling between whispering-gallery mode and waveguide mode in photonic crystal

A. Tanaka*, M. Morifuji, and M. Kondow
Graduate School of Engineering, Osaka University, Suita, Osaka 565-0871, Japan
e-mail: ayano231@e3.eei.eng.osaka-u.ac.jp

INTRODUCTION

We study optical coupling between whispering-gallery mode (WGM) and waveguide mode in photonic crystal. Figure 1 shows photonic crystal structure we studied. WGM formed in cavity as shown in Fig. 1. It shows high quality factor and is nondegenerate. By controlling radius R of cavity, it is possible to shift resonance frequency for wavelength division multiplexing (WDM) communications. However, difference in light extraction efficiency between different size cavities is unfavorable for practical operation. We theoretically address the issue by tuning waveguide parameter.

STRUCTURE

The cavity resonator consists of 19 missing air holes aligned hexagonally. We modified positions of the air holes on the periphery of the cavity so that these air holes align on a circle (modified H3 defect). Waveguide (line defect) is set aside the cavity. We can change waveguide modes by letting both sides of the air holes line lessen by ΔW. We evaluated coupling efficiency defined

$$\eta = \frac{[\text{Light loss from waveguide}]}{[\text{overall loss}]} \qquad (1)$$

by carrying out two-dimensional finite-difference time-domain (FDTD) calculations, so as to examine correlation between η and structural parameters such as R and ΔW.

RESULTS AND DISCUSSION

First, we investigate relation between the coupling efficiency and shrinkage width of waveguide ΔW. Fig. 2 shows the coupling efficiency plotted as a function of ΔW for the cavity R=2.85a. The coupling efficiency shows a remarkable peak at $\Delta W \simeq 0.08a$. We found that the peak appears when inclination of the waveguide mode is approximately zero at resonance frequency in photonic band diagram. This result shows that coupling strength depends on the density of state of waveguide modes.

Next, we investigate the coupling efficiency for different radius cavities. For cavity of R=2.76a, 2.80a, 2.85a, and 2.90a, we shrink waveguide width by ΔW=0.20a, 0.14a, 0.10a, and 0.05a, respectively to couple waveguide mode 11 on each WGMs strongly. In Fig.3, filled circles denote η when the WGM strongly couples to waveguide mode labelled 11, shown in the inset.

Furthermore, we investigated coupling to the mode 12 by ΔW= -0.005a, -0.035a, -0.069a, and -0.105a, for each size of cavity resonators. Open circles denote η relating to the mode 12. Fig. 3 shows that η with mode 11 is larger than that with mode 12 in all resonators. This difference between mode 11 and 12 can be explained by symmetry of waveguide mode profile. Fig. 4 shows waveguide magnetic field amplitude of mode 11 and 12. They are totally symmetric and antisymmetric with respect to the center of the WGM, respectively. WGM can more easily excite mode 11 than mode 12. From this, optical coupling to the mode 11 is stronger than that to the mode 12.

In summary, we found that strength of optical coupling between WGM and waveguide modes depends on symmetry of the modes as well as on the density of states of the waveguide mode.

The present results are useful to suppress the difference of the light extraction efficiency to realize WDM devices.

REFERENCE

[1] K.Nagahara, et al, *Optical coupling between a cavity mode and a waveguide in a two-dimensional photonic crystal,* Photon. Nanostr. Fundam. Appl. **9**, 261 (2011)

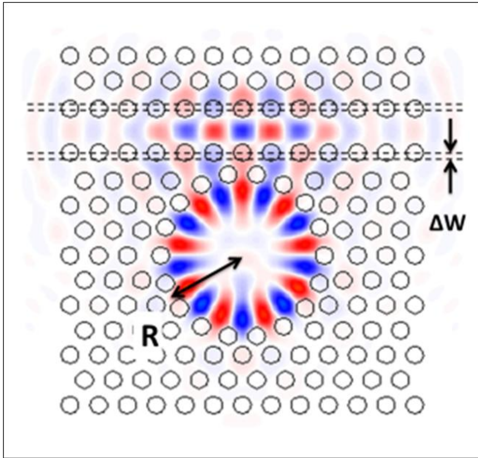

Fig. 1. Photonic crystal structure we studied. Magnetic field amplitude of the WGM and the waveguide mode are also shown.

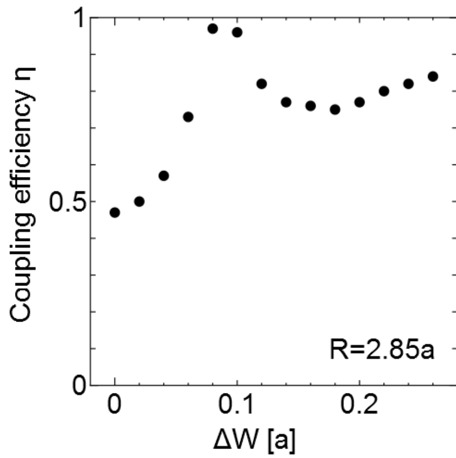

Fig. 2. Coupling efficiency between the cavity mode and the waveguide mode as a function of shrinkage width of waveguide ΔW at R=2.85a.

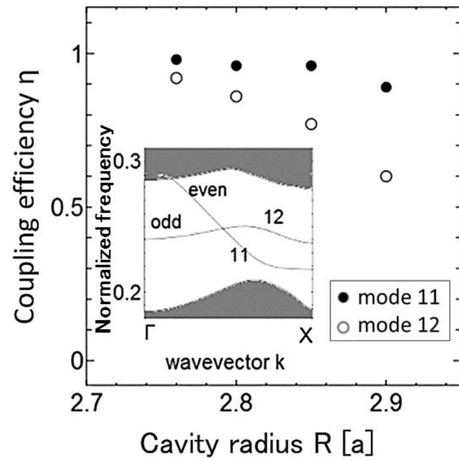

Fig. 3. Coupling efficiency of cavity radius R=2.76a, 2.80a 2.85a, and 2.90a. Filled circles and open circles denote the coupling efficiency related to the mode 11 and 12. Inset: Photonic band diagram. The curves labeled as 11 and 12 are waveguide modes.

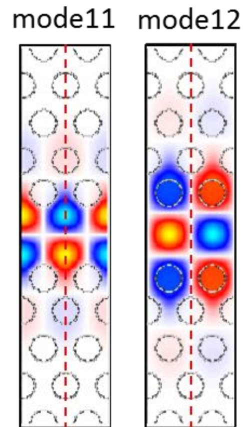

Fig. 4. Calculated magnetic field amplitude of mode 11 (left) and 12 (right) for wave vector X. Mode 11 and 12 have even and odd symmetry, respectively with respect to the center of the WGM (red dash line).

Coupled Monte Carlo–drift-diffusion simulation of transport in III-N LEDs

Pyry Kivisaari, Toufik Sadi, Jani Oksanen, and Jukka Tulkki
Department of Biomedical Engineering and Computational Science
Aalto University, P.O. Box 12200, 00076 Aalto, Finland
email: pyry.kivisaari@aalto.fi

INTRODUCTION

III-N LEDs have started a revolutionary change in the lighting industry, but many problems stand in the way of further improvements. One of the most serious problems is the efficiency droop, which has been studied and discussed for several years without a clear conclusion on its cause [1], [2]. The two most widely accepted possible explanations are a form of electron leakage [3] and direct or indirect Auger recombination [4]. One of the solution methods proposed to avoid droop is to use multi-quantum well (MQW) devices. However, in a typical device this does not help, since only one of the quantum wells (QWs) emits all the light [5], [6]. In spite of numerous theoretical and experimental attempts to explain the origins of the droop, discussion has not advanced for some time. The discussion is further complicated due to difficulties in fitting various theoretical and experimental results together. Therefore advanced physical models are needed for further investigations.

We introduce a coupled Monte Carlo–drift-diffusion (MCDD) device simulation method to study the efficiency droop in III-Nitride MQW LEDs. We apply the method to answer two relevant questions: (i) the importance of electron leakage in the efficiency droop of MQW LEDs and (ii) the causes of uneven carrier distribution between the QWs. The novelty of our work lies in applying the Monte Carlo (MC) method [7]: by employing a self-consistent MC simulation for the electron gas we gain accurate information of the droop mechanisms based on the device physics. This cannot be fully done by using the conventional DD model which relies on the assumption of carrier thermalisation. In this work, we also report the discrepancies between the DD model and the more sophisticated MC method in these specific devices.

METHOD, RESULTS AND DISCUSSION

In the MCDD method we model the electron gas by direct simulation of the Boltzmann equation with the MC method, which accurately describes nonequilibrium transport in nanodevices. We model the hole gas with the DD equations. The MC and DD are connected through Poisson's equation and the conventional ABC model for electron-hole recombination. The hole distribution is calculated with Fermi distribution, and the coupled simulation is run until convergence is reached, resulting in steady-state solutions.

Fig. 1 shows the MQW LED device including three QWs. Figs. 2, 3, and 4 show the band diagram, carrier densities, and recombination rate density in the structure, calculated with the DD model. Microscopic analyses using the MCDD method confirm the existence of the hot electron population. As demonstrated experimentally in the literature, our simulations confirm that only one QW emits almost all light.

Efficiency droop is still a very important open question in research of III-Nitride LEDs, and our numerical results help in understanding its origins in more detail. The MCDD method introduced in this work can be extended for more accurate studies of current transport in lasers and novel optoelectronic device concepts such as freestanding nanowires, plasmonic optoelectronic structures, and organic LEDs.

REFERENCES

[1] M.-H. Kim, M. F. Schubert, Q. Dai, J. K. Kim, E. F. Schubert, J. Piprek, and Y. Park, "Origin of efficiency droop in

978-3-901578-26-7 © 2013 Society for Micro- and Nanoelectronics

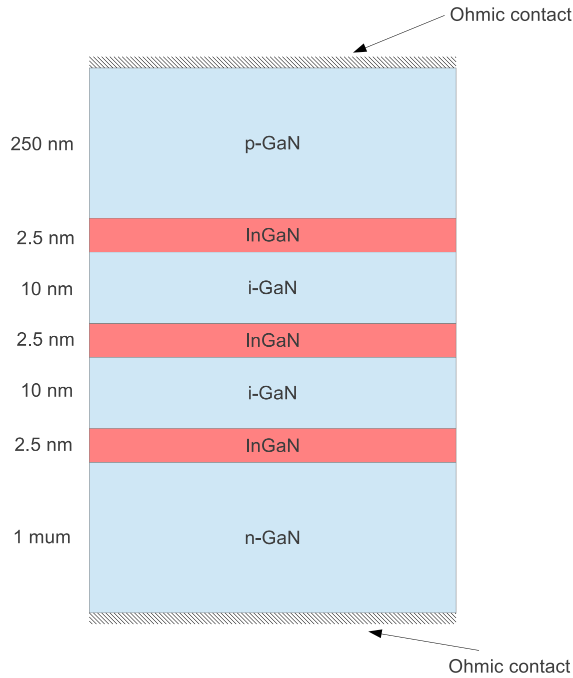

Fig. 1. The III-Nitride MQW structure simulated in this paper.

GaN-based light-emitting diodes," Applied Physics Letters, vol. 91, no. 18, pp. 183507–183507-3, Oct. 2007.

[2] J. Piprek, "Efficiency droop in nitride-based light-emitting diodes," physica status solidi (a), vol. 207, no. 10, pp. 2217–2225, 2010.

[3] G.-B. Lin, D. Meyaard, J. Cho, E. Fred Schubert, H. Shim, and C. Sone, "Analytic model for the efficiency droop in semiconductors with asymmetric carrier-transport properties based on drift-induced reduction of injection efficiency," Applied Physics Letters, vol. 100, no. 16, pp. 161106–161106-4, Apr. 2012.

[4] E. Kioupakis, Q. Yan, and C. G. Van de Walle, "Interplay of polarization fields and Auger recombination in the efficiency droop of nitride light-emitting diodes," Applied Physics Letters, vol. 101, no. 23, pp. 231107–231107-4, Dec. 2012.

[5] A. David, M. J. Grundmann, J. F. Kaeding, N. F. Gardner, T. G. Mihopoulos, and M. R. Krames, "Carrier distribution in (0001)InGaN/GaN multiple quantum well light-emitting diodes," Applied Physics Letters, vol. 92, no. 5, pp. 053502–053502-3, Feb. 2008.

[6] P. Kivisaari, J. Oksanen, and J. Tulkki, "Effects of lateral current injection in GaN multi-quantum well light-emitting diodes," Journal of Applied Physics, vol. 111, no. 10, pp. 103120–103120-9, May 2012.

[7] T. Sadi, R. W. Kelsall, and N. J. Pilgrim, "Investigation of Self-Heating Effects in Submicrometer GaN/AlGaN HEMTs Using an Electrothermal Monte Carlo Method," IEEE Transactions on Electron Devices, vol. 53, no. 12, pp. 2892–2900, Dec. 2006.

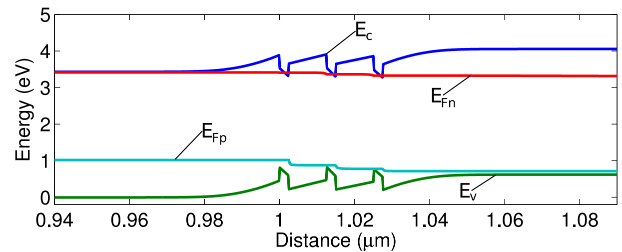

Fig. 2. Band diagram of a MQW LED with 3 QWs at 2.7 V, calculated with the DD model.

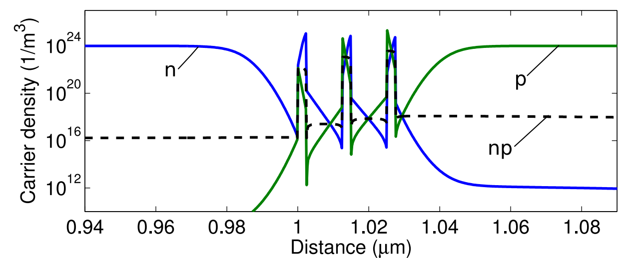

Fig. 3. Carrier densities of a MQW LED with 3 QWs at 2.7 V, calculated with the DD model.

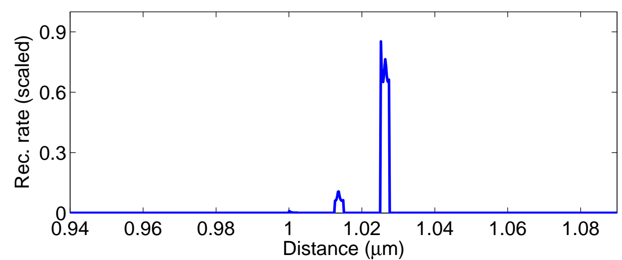

Fig. 4. Scaled recombination rate density in a MQW LED with 3 QWs at 2.7 V, calculated with the DD model. Only one of the QWs emits almost all the light, and one of the QWs is so dim that its recombination rate cannot even be seen on this scale.

Numerical Analysis on the Electrical and Optical Properties in Multilayer OLED Device

Young Wook Hwang[1], Hyeon Gi Lee[2], and Tae Young Won*,
Department of Electrical Engineering, Inha University, Nam-Gu, Incheon, South Korea
e-mail: {hyw, lhg, twon}@hsel.inha.ac.kr

ABSTRACT

In this paper, we report our numerical study on the electrical and optical properties in multilayer organic light emitting diode (OLED) device structure. Our finite element method (FEM) model includes the transport behavior of electrons and holes, the generation and decay of excitons, and emission and extinction properties of excitons. We made a focus on the charge balance in host material comprising a phosphorescent OLED (PHOLED). Finally, we investigated the variation of charge density and recombination density, which affect exciton density.

NUMERICAL MODEL

The electrical and optical characteristics of multilayer OLEDs critically depend on the device structure, which includes the species of LUMO and HOMO, the thicknesses of each layer, and sequence of layers.[1],[2] In order to analyze each element, we need to employ a numerical model which allows us to optimize the OLED structure.

$$\frac{\partial E(x)}{\partial x} = \frac{e}{\varepsilon\varepsilon_0}(p(x) - n(x) + p_t - n_t + A_{Doping} - D_{Doping}) \quad (1)$$

Equation (1) is the Poisson equation that yields the electric field distribution. *n(x)* is the density of electrons, *p(x)* is density of holes, and *E(x)* is the electric field.

$$\frac{\partial n(x)}{\partial t} = \frac{1}{e}\frac{\partial J_e(x)}{\partial x} - r(x)\cdot p(x)\cdot n(x) \quad (2)$$

Equation (2) is continuity equation for electrons determines the time evolution of the system. *r(x)* means Langevin recombination rate coefficient.

SIMULATION RESULTS

We use the multilayer structure that consists of 1,1-bis[(di-4-tolylamino) phenyl] cyclohexane (TAPC); 4,4′-bis[N-(1-naphthyl)-N-phenyl-amino] biphenyl (α-NPD); 4,4′-bis[N-(p-tolyl)-N-phenylamino] biphenyl (TPD) as a hole transport layer, 3,5′-N,N′-dicarbazole-benzene (mCP) as an emissive layer, 2,9-dimethyl-4,7-diphenyl-1,10-phenanthroline (BCP); 4,7-diphenyl-1,10-phenanthroline (BPhen) as an electron transport layer. Fig. 1 is a schematic diagram illustrating the multilayer structure for organic light emitting diodes under this work. Referring to Figs. 2 (a) and (b), we can see how the density of carriers change as time continues. Fig. 3 (a), (b) are plots in case when the energy level of HTL and ETL has been changed. Keeping the energy level of the other layers unaltered, we varied the HOMO energy level of TAPC from 5.3eV to 5.7eV and LUMO energy level of Bphen from 3.0eV to 3.4eV. While the injection barrier height is raised by the increment of the HOMO energy level of TAPC, the internal barrier height is reduced. Fig. 4 shows a plot illustrating the recombination density for the wide range of devices.

CONCLUSION

Our simulation exhibits that the recombination density varies with the energy level. Furthermore, we could demonstrate that the charge balance has a strong effect on the recombination density profile.

ACKNOWLEDGEMENT

This work was supported by Korea National Research Foundation 2011-0014911.

REFERENCES

[1] Z. Wu, S. Chen, H. Yang, Y. Duan, Y. Zhao, J. Hou, S. Liu, *Improving the current efficiency of organic light-emitting device utilizing the well structure*, Opt. Quant. Electron. **37**, 4 (2005).

[2] J. Wu, M. Agrawal, H. A. Becerril, Z. Bao, Z. Liu, Y. Chen, Organic light-emitting diodes on solution-processed graphene transparent electrodes, P. Peumans, ACS nano **4**, 1 (2009).

978-3-901578-26-7 © 2013 Society for Micro- and Nanoelectronics

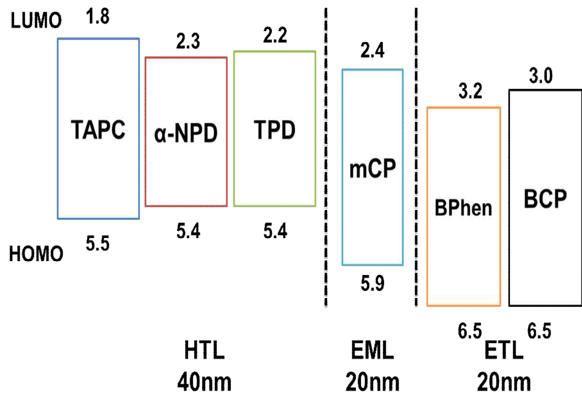

Fig. 1. Schematic diagram illustrating the multilayer structure under this study.

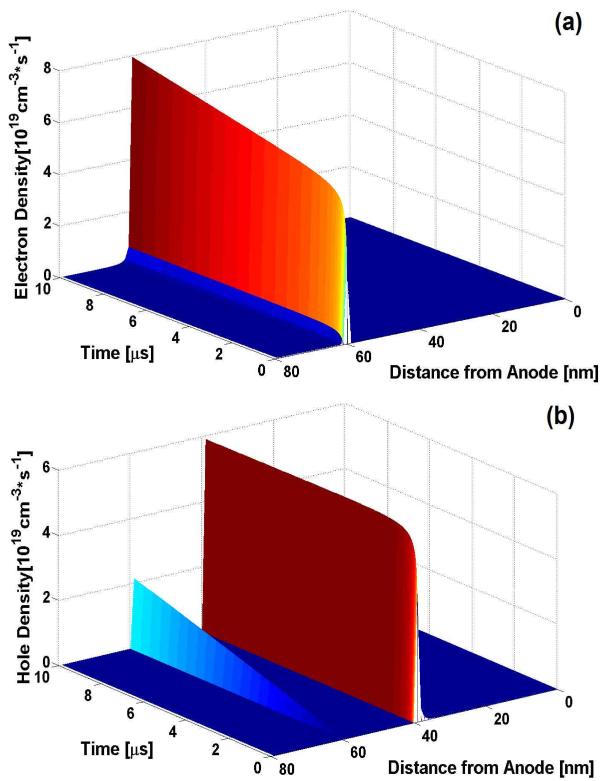

Fig. 2. (a) Calculated electron density profile in OLED after turn-on [10μs]

(b) Calculated hole density profile in OLED after turn-on [10μs].

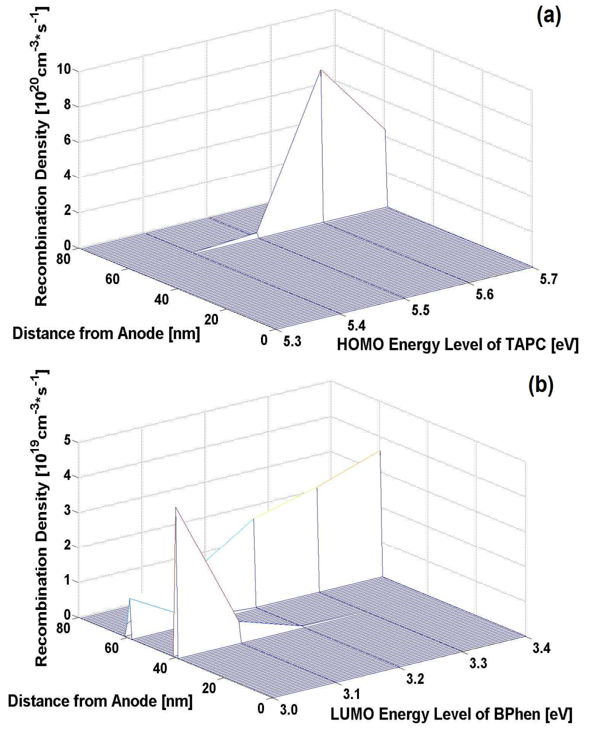

Fig. 3. (a) Recombination density profile for different HOMO energy level of TAPC [eV].

(b) Recombination density profile for different LUMO energy level of BPhen [eV].

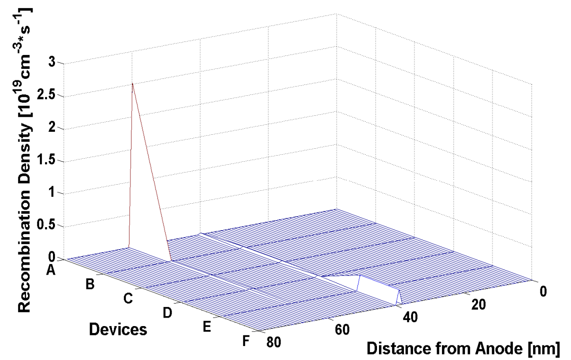

Fig. 4. Calculated recombination density profile for the variation of material.

Computational Analysis on Recombination Rate for Organic Light Emitting Diodes

Hyeon Gi Lee[1], Young Wook Hwang[2], and Tae Young Won,*
Department of Electrical Engineering, Inha University, Nam-Gu, Incheon, South Korea
e-mail: {lhg, hyw, twon}@hsel.inha.ac.kr

ABSTRACT

We report our numerical study on the carrier injection and exciton transport for organic light emitting diodes (OLEDs) structure with material basis on tris (8-hydroxyquinolinato) aluminum (Alq3). Since the charge accumulation at the interfaces between emission layer (EML) and transport layer is considered to raise the recombination rate, which also increases the exciton density, we numerically investigated the effect of inserting the EML in the bilayer structure.

DEVICE STRUCTURE

In Fig.1 is shown the multilayer OLED structure in this work. The device comprises ITO (Anode) / NPB (HTL) / EML / Alq3 (ETL) / Al (Cathode). The thickness of ITO and Al is 100nm, respectively. Emission layer (EML) is BAlq (aluminum (III) bis (2-methyl-8-quninolinato)-4-phenylphenolate) which is emitting cool blue color [15]. We investigated the effect of inserting the EML in bilayer structure. In this article, we investigated 9types of device presented in Table1.

SIMULATION RESULTS AND DISCUSSION

Referring to Fig. 2(a), in basic bilayer device A, the electric field peaks at the interface between electron transport layer and hole transport layer. In case of device B and C, a trilayer with emission layer, a change of electric field occurs between interfaces of each layer. Device B contains a high band gap in the EML, which causes the charges to accumulate on either interface and hence enhance the electric field across the EML. On the other hand, Device C represents an ideal structure in terms of both current balance and recombination since electrons and holes can enter the EML without overcoming the energy, this is shown Fig. 2(b). We also simulate transient response of Device A, B, and C to know which device structure is more efficient, this is shown Fig. 3. For a quantum efficiency of device, we define the current balance factor. Numerically, the factor can be evaluated using the electron, hole, recombination current. The current balance factor b is defined as follows:

$$b = \frac{\int_0^L eR(x)dx}{J} = \frac{J_{e,cathode} - J_{e,anode}}{J} \qquad (1)$$

It is important for recombination kinetics to figure out how many excitons are generated for each device structure. In Fig. 4 is shown the exciton density as a function of carrer injection barrier height in Device C

CONCLUSION

We investigated the design parameters which influence the efficiency or optical properties such as alignment of LUMO and HOMO of EML, thickness of each layer, injection barrier height, and doping concentration for optimization of OLEDs. As trade-off relationship of design parameters considered, engineer can choose electrical and optical properties.

ACKNOWLEDGEMENT

This work was supported by Korea National Research Foundation 2011-0014911.

REFERENCES

[1] S.L.M. van Mensfoort, R.J. de Vries, V. Shabro, H. P. Loebl, R.A.J. Janssen, and R. Coehoorn, *Electron transport in the organic small-molecule material BAlq — the role of correlated disorder and traps,* Organic Electronics. **11**, 8, 1408 **(**2010**).**

978-3-901578-26-7 © 2013 Society for Micro- and Nanoelectronics

Device Structure	Layer	HOMO (eV)	LUMO (eV)
Device A	HTL	2.8	5.3
	ETL	3.0	5.6
Device B	HTL	2.8	5.3
	EML1	3.0	5.3
	ETL	3.0	5.6
Device C	HTL	2.8	5.3
	EML2	2.8	5.6
	ETL	3.0	5.6

Table. 1. Energy level parameters for the materials of trilayer devices in our simulations.

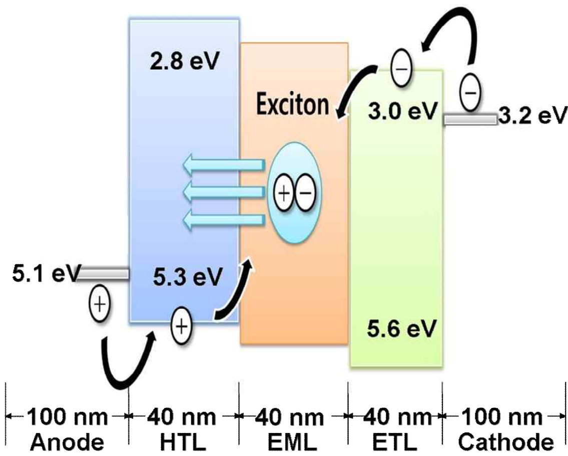

Fig. 1. A schematic diagram of a 3-layer OLED structure which comprises ITO (Anode) / NPB (HTL) / EML / Alq3 (ETL) / Al(Cathode).

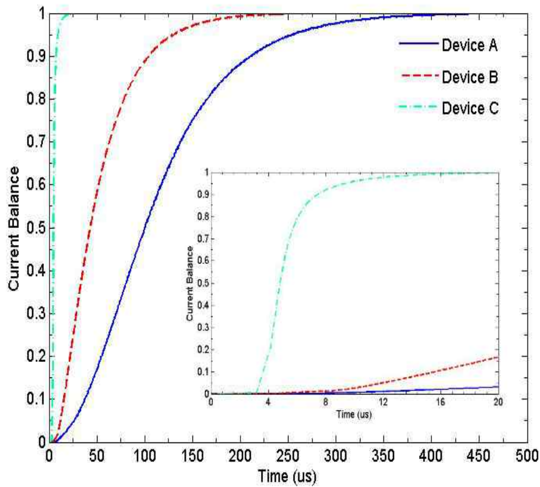

Fig. 3. A plot of the transient current balance which uses measure of recombination efficiency of device A, B, and C.

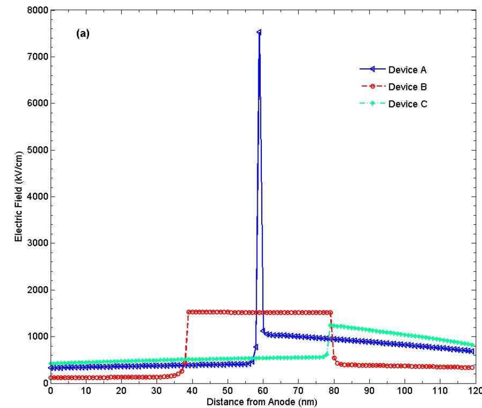

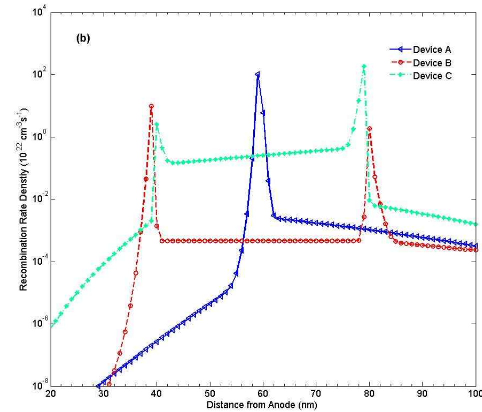

Fig. 2. Polts of calculated distribution of (a) electric field and (b) recombination rate density in basic bilayer device A, trilayer charge-blocking device B, and trilayer charge-confining device C.

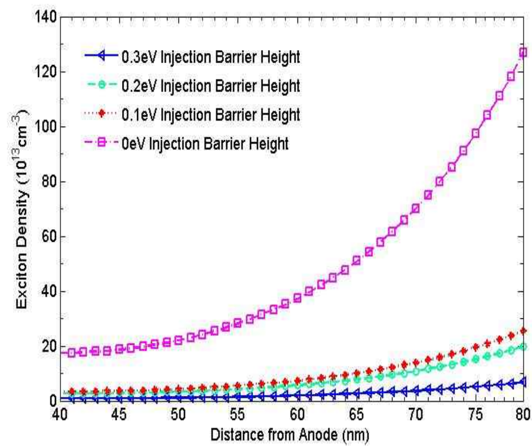

Fig. 4. A plot of exciton density distribution as a function of carrer injection barrier height in Device C.

Comprehensive Study on Reflectance of Si_3N_4 Subwavelength Structures for Silicon Solar Cell Applications Using 3D Finite Element Analysis

Ming-Yi Lee and Yiming Li*
Parallel and Scientific Computing Laboratory, Department of Electrical and Computer Engineering,
National Chiao Tung University, 1001 Ta-Hsueh Road, Hsinchu 300, Taiwan
e-mail: mylee@mail.ymlab.org (M.-Y. Lee) * ymli@mail.ymlab.org (Y. Li)

1. Introduction

Semiconductor solar cell is one of promising renewable energy technologies to relieve the impact of the climate change. In semiconductor based solar cells, electron-hole pairs are generated via absorption of impinging photons. Due to high refraction index of semiconductor materials, especially silicon, the incident sunlight power is largely reflected back, resulting in the reduction of light absorption and poor energy conversion efficiency. Bases on the theory of impedance matching, single layer and multilayer of antireflection coating are proposed for reduced reflectance property; however, the resulting reflectance spectra meet the demand only within a narrow spectral domain. Subwavelength structure's dimensions are much smaller than the wavelengths of light; therefore, using SWS on the surface of silicon solar cells (Fig. 1) can substantially reduce the reflectivity and improve the capability of light trapping [1-4].

In this study, 3D FE simulation for the reflectance of Si_3N_4 SWS with three types of structural shapes: the cylinder, the right circular cone, and the square pyramid shapes is conducted with respect to different geometry parameters and lighting angles for quantitative understanding of reflectance property.

2. SWS and Optical Model

Fig. 2(a) illustrates a periodical structure of Si_3N_4 SWS which is used in our 3D FE simulation without loss of generality, based upon our recent experimental characterization [4]. We study Si_3N_4 SWS with the cylinder, the right circular cone, and the square pyramid shapes, as shown in Figs. 1(b)-(d), respectively. Throughout the paper, we consider time-harmonic fields assuming a time-dependence in $e^{-j\omega t}$. The diffraction problem is governed by the well-known Maxwell equations. A repeated pattern is applicable to use periodic boundary conditions, thus the Floquet theorem is adopted to simulate the boundary condition of periodic structure:

$$\overline{E}_2(\overline{r}) = \overline{E}_1(\overline{r} + \overline{L}) = \overline{E}_1(\overline{r})e^{-j\theta}, \quad (1)$$

where r is position vector, L is the distance between the periodic boundaries, and θ is a phase factor.

3. Results and Discussion

To verify the effect of Floquet boundary condition in 3D FE analysis, as shown in Fig. 3, we compare the difference between the simulated unit cells of 1x1 and 2x2 array of Si_3N_4 SWS. We find at the wavelengths above 600 nm, the reflectance of 1x1 array of Si_3N_4 SWS as unit cell is almost consistent with unit cell of 2x2 array, meanwhile insignificant discrepancy occurs at wavelengths shorter than 600 nm.

Fig. 4 shows the reflectance spectra with incident angles of 0°, 30° and 60° for the cylinder-, right circular cone-, and square pyramid-shaped Si_3N_4 SWS, respectively. For the normal incidence case, the lowest average reflectance among three structural shapes is 3.47% of square pyramid-shaped structure. Fig. 5 shows the reflectance dependence on the structural height and wavelength. The pyramid-shaped Si_3N_4 SWS has lower reflectance and less sensitivity on structure height in comparison with the cylinder-shaped Si_3N_4 SWS. Hence, the impact of process variation of structure height on solar cell performance is relatively smaller for the pyramid-shaped Si_3N_4 SWS.

Based on solar spectrum at the sea level revealed in ASTM Standard Tables for Reference Solar Spectral Irradiances [5], we further estimate the reflected power density defined by reflectance times incident power density, as shown in Fig. 6(a). The higher reflected power density of cylinder-shaped Si_3N_4 SWS (red line) indicates the less efficiency in the solar cell application. Fig. 6(b) shows the normalized reflectance for three structure shapes of Si_3N_4 SWS. The square pyramid-shaped Si_3N_4 SWS again shows the lowest normalized reflectance 3.13% while the cylinder- and the right circular cone-shaped Si_3N_4 SWSs have 6.66% and 4.12%, respectively.

4. Conclusions

The reflective property of unit cell with a validated Floquet boundary condition has been calculated using a full 3D FE simulation. Considering various incidence angles and height effect on three experimentally observed structural shapes of Si_3N_4 SWS, we have concluded that the pyramid-shaped Si_3N_4 SWS has best reflective property in the analysis of morphological effect for silicon solar cell applications.

Acknowledgement

This work was supported in part by the Taiwan National Science Council (NSC) under Contract No. NSC-101-2221-E-009-092.

References

[1] K. C. Sahoo, Y. Li, E. Y. Chang, *Comput. Phys. Commun.*, Vol. 180, pp. 1721-1729, 2009.

978-3-901578-26-7 © 2013 Society for Micro- and Nanoelectronics

[2] K. C. Sahoo, M. K. Lin, E. Y. Chang, T. B. Tinh, Y. Li, and J. H. Huang, *Jpn. J. Appl. Phys.*, Vol. 48, pp. 126508 1-4, 2009.

[3] K. C. Sahoo, Y. Li, M.-K. Lin, E. Y. Chang, and J.-H. Huang, in: Proc. *IEEE 9th Nanotech. Conf.*, Geneoa, Italy, pp. 127-130, 2009.

[4] K. C. Sahoo, Y. Li, and E. Yi Chang, *IEEE Transactions on Electron Devices*, Vo. 57, No. 10, Oct. 2010, pp. 2427-2433.

[5] ASTM Standard G173-03, 2008: Standard Tables for Reference Solar Spectral Irradiances: Direct Normal and Hemispherical on 37° Tilted Surface.

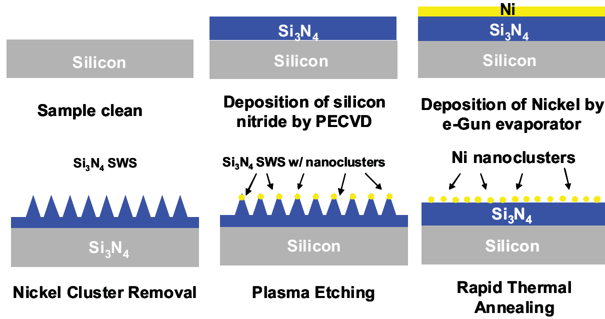

Fig. 1. Schematic illustration of the fabricated silicon solar cells with Si_3N_4 SWS. [4].

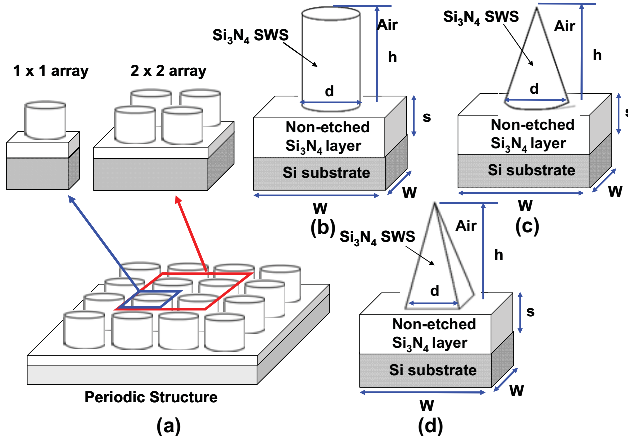

Fig. 2. (a) Illustration of periodic structure of Si_3N_4 SWS with 1x1 and 2x2 array as unit cell. Schematic of (b) cylinder-, (c) right circular cone-, (d) square pyramid-shaped structure.

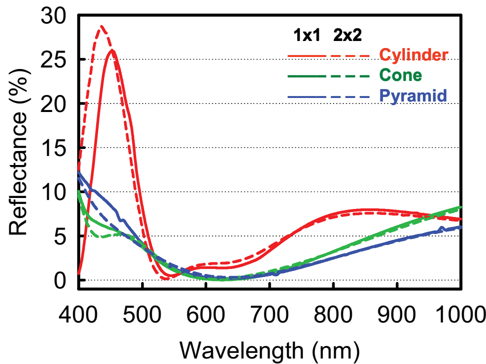

Fig. 3. Plot of the reflectance spectrum of Si3N4 SWS with three structural shapes as well as two different periodical configurations: 1x1 and 2x2 arrays in the 3D FEM simulation

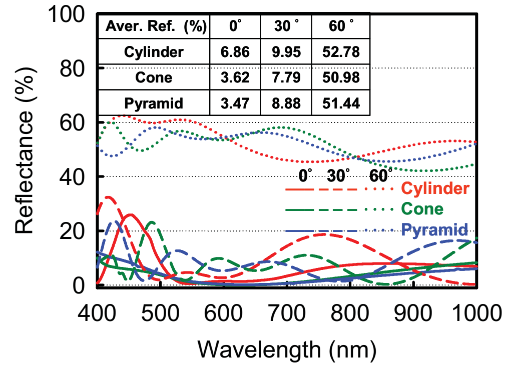

Fig. 4. Plot of reflectance spectrum of three structural shapes of Si_3N_4 SWS with incident angles of 0°, 30°, and 60°.

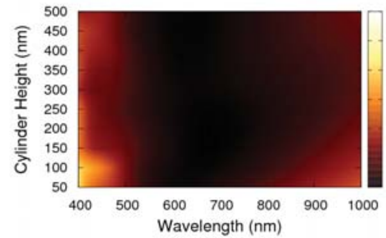

(a)

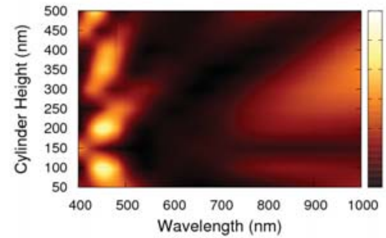

(b)

Fig. 5. 3D view for the height effect on the reflectance with respect to different wavelength. (a) The pyramid-shaped Si_3N_4 SWS has lower reflectance and less sensitivity on structure height in comparison with (b) the cylinder-shaped Si_3N_4 SWS.

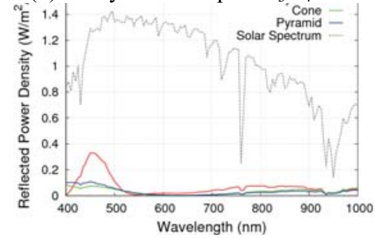

(a)

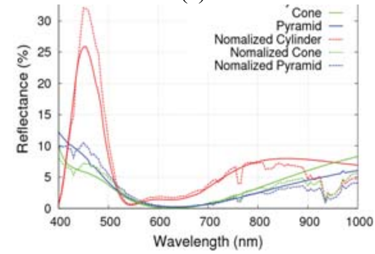

(b)

Fig. 6. (a) Plot of the reflected power density among three different shapes. (b) Plot of reflectance with and without considering incident solar spectrum at sea level.

Interface Phonon Modes of Dual-Gate MOSFET System

Nanzhu Zhang, M. Dutta and M. A. Stroscio
Dept. Electrical and Computer Engineering, University of Illinois at Chicago, Chicago, IL 60607, USA
e-mail: stroscio@uic.edu

INTRODUCTION

As we all know, silicon dioxide is a popular material for gate dielectrics. However, the thickness of silicon dioxide cannot be decreased below the 1.5-1.0 nm range as required by device scaling because leakage current increases. This leads us to search for new materials to replace silicon oxide. Indeed, high-k dielectrics are introduced into use since they have even larger dielectric constants, k, than silicon oxide, leading to an increase in the overall capacitance. However, a high-k dielectric is a material with a high dielectric constant κ. The dielectric constant of a solid results from both the ionic and the electronic polarization. A higher dielectric constant can come from a large ionic polarization for high-k material. The large ionic response dominates at low frequency which causes a large scattering strength and as a result leads to a reduction of the effective electron mobility in the inversion layer of a MOS system. [1] The mechanism of this effect is the starting point of the idea to use dual-gate MOSFET system to avoid the scattering yielded by the phonon modes in the system.

THEORY

As shown in Fig 1, the dielectric function of the semiconductor in the structure under study is ε and the thickness is 2t (from -t to t). The metal in this treatment is not an ideal metal with zero Thomas-Fermi screening length. Herein, we consider the Thomas-Fermi screening length, δ, of the non-ideal metal. Let the phonon potentials, Φ, for the given structure be defined as follow [2]:

$$\begin{cases} \Phi = Ae^{\frac{-(z-d)}{\delta}} & \text{when } z>d \\ \Phi = Be^{q(z-t)} + Ce^{-q(z-t)} & \text{when } t\leq z<d \\ \Phi = De^{qz} + Ee^{-qz} & \text{when } -t\leq z<t \\ \Phi = Fe^{q(z+t)} + Ge^{-q(z+t)} & \text{when } -d\leq z<-t \\ \Phi = Ae^{\frac{(z+d)}{\delta}} & \text{when } -z<-d \end{cases} \quad (1)$$

From this equations we can get the following results:

$$\begin{cases} \Phi' = -\frac{A}{\delta}e^{\frac{-(z-d)}{\delta}} & \text{when } z>d \\ \Phi' = Bqe^{q(z-t)} - Cqe^{-q(z-t)} & \text{when } t\leq z<d \\ \Phi' = Dqe^{qz} - Eqe^{-qz} & \text{when } -t\leq z<t \\ \Phi' = Fqe^{q(z+t)} - Gqe^{-q(z+t)} & \text{when } -d\leq z<-t \\ \Phi' = \frac{A}{\delta}e^{\frac{(z+d)}{\delta}} & \text{when } -z<-d \end{cases} \quad (2)$$

At the heterointerface of region 1 and region 2, the following two conditions have to be satisfied [3]:

$$\Phi_1(Z) = \Phi_2(Z) \quad (3)$$

$$\varepsilon_1 \frac{\partial \varepsilon_1}{\partial z} = \varepsilon_2 \frac{\partial \varepsilon_2}{\partial z} \quad (4)$$

Substituting equation (3) into equation (1) one finds:

$$\begin{cases} A = Be^{q(d-t)} + Ce^{-q(d-t)} & \text{at } z=d \\ B + C = De^{qt} + Ee^{-qt} & \text{at } z=t \\ De^{-qt} + Ee^{qt}) = F + G & \text{at } z=-t \\ Fqe^{q(-d+t)} + Gqe^{-q(-d+t)} = A & \text{at } z=-d \end{cases} \quad (5)$$

Substituting equation (4) into equation (2) leads to:

$$\begin{cases} \varepsilon_m(-\frac{A}{\delta}) = \varepsilon_{ox}(Bqe^{q(d-t)} - Cqe^{-q(d-t)}) & \text{at } z=d \\ \varepsilon_{ox}(Bq - Cq) = \varepsilon(Dqe^{qt} - Eqe^{-qt}) & \text{at } z=t \\ \varepsilon(Dqe^{-qt} - Eqe^{qt}) = \varepsilon_{ox}(Fq - Gq) & \text{at } z=-t \\ \varepsilon_{ox}(Fqe^{q(-d+t)} - Gqe^{-q(-d+t)}) = \varepsilon_m \frac{A}{\delta} & \text{at } z=-d \end{cases} \quad (6)$$

where ε_m is the dielectric function of metal, ε_{ox} is the dielectric function of the insulator, and ε is the dielectric function of semiconductor.

Solving these equation sets one obtains the following secular equation for the system:

$$(1-\frac{\varepsilon_m}{\varepsilon_{ox}}\frac{1}{\delta q})(1+e^{-2qt}+2e^{2q(2t-d)}-e^{2q(2t+d)}$$
$$+\frac{\varepsilon}{\varepsilon_{ox}}(e^{-2qd}-2e^{2q(2t-d)}+1))+(1+\frac{\varepsilon_m}{\varepsilon_{ox}}\frac{1}{\delta q}) \quad (7)$$
$$(e^{2q(d-t)}+e^{-2qd}-e^{2qt}+2e^{-4qt}+\frac{\varepsilon}{\varepsilon_{ox}}(e^{-2qd}+$$
$$2e^{2qd}-3e^{2q(d-2t)}-e^{-4qt}+e^{2qt}))$$

In the secular equation:

$$\varepsilon_m = 1 - \frac{\omega_{p,m}^2\tau^2}{1-\omega^2\tau^2} \quad (8)$$

where $\omega_{p,m}$ and τ are the plasma frequency and the dielectric relaxation time for the metal. [3] Moreover,

$$\varepsilon = \varepsilon^{\infty}(1-\frac{\omega_{p,s}^2}{1-\omega^2}) \quad (9)$$

where $\omega_{p,s}$ is the plasma frequency of the 2DEG, and ε^{∞} is the optical permittivity of the semiconductor. In addition,

$$\varepsilon_{ox} = \varepsilon_{ox}^{\infty}\frac{(\omega_{LO2}^2-\omega^2)(\omega_{LO1}^2-\omega^2)}{(\omega_{TO2}^2-\omega^2)(\omega_{TO1}^2-\omega^2)} \quad (10)$$

where $\varepsilon_{ox}^{\infty}$ is the optical permittivity of the insulator; ω_{LO1} and ω_{LO2} are the longitudinal-optical phonon modes while ω_{TO1} and ω_{TO2} are the angular frequencies of the phonon modes in the insulator [1].

RESULTS AND DISCUSSION

Herein, the secular equation is solved by substituting the dielectric functions to obtain the interface phonon modes for dual-gate MOSFET system. Herein, the metal is considered to be a non-ideal metal with a non-zero screening length, δ. In the interesting limit of an ideal metal, we can set the screening length is the secular equation to zero. In this case, it is demonstrated that in the symmetrical dual-gate MOSFET structure, that no interface optical phonon modes survive as a result of the boundary conditions. Similar symmetry-related phonon mode suppression of phonon modes and the related suppression of carrier-phonon scattering processes have been discussed previously. [4] Thus, through the introduction of a symmetrical dual-gate MOSFET structure, unwanted interface-phonon-related scattering effects associated with high-k dielectrics may be eliminated.

REFERENCES

[1] Massimo V. Fischetti, Deborah A. Neumayer and Eduard A. Cartier, *Effective electron mobility in Si inersion layers in metal-oxide-semiconductor systems with a high-k insulator: The role of remote phonon scattering*, Journal of Applied Physics **90**, 4587-4608 (2001).

[2] N. Mori and T. Ando, Physical Review B **40**, 6175 (1989).

[3] A. R. Bhatt, K. W. Kim, M. A. Stroscio, G. J. Iafrate, Mitra Dutta et al, *Reduction of interface phonon modes using metal-semiconductor heterosturctures*, Journal of Applied Physics **73**, 2338 (1993).

[4] Michael A. Stroscio and Mitra Dutta, Phonons in Nanostructures (Cambridge University Press, Cambridge, 2001).

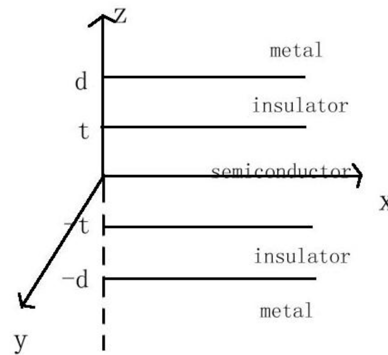

Fig. 1. Structure of Dual-gate MOSFET system

Impact of the Phonon Confinement and Geometry on the Mobility of Si-Nanowires

F. G. Ruiz, I. M. Tienda-Luna, A. Godoy, L. Donetti and F. Gámiz
Departamento de Electrónica y Tecnología de Computadores, University of Granada, Spain
* Email: franruiz@ugr.es

INTRODUCTION

The continuous reduction of device dimensions imposed by the Moore's Law has focused the attention on non-planar devices such as Trigate MOSFETs or Gate-All-Around Silicon Nanowires (NWs). Therefore, the study of the transport properties in 2D-confined nanowires with sizes ranging in a few nanometers is a research field of high interest [1], [2]. As the size of the devices decreases, the modification in the acoustic phonon spectrum becomes more pronounced, making mandatory the inclusion of acoustic phonon confinement in the mobility calculation [3], [4]. In this work we assess the influence of the phonon confinement on the mobility of Si NWs with different sizes and geometries.

RESULTS

To study the confined phonon-limited mobility in arbitrarily shaped NWs we have simulated devices like those in Fig. 1, with SiO_2/HfO_2 as gate insulator (T_{SiO_2}=0.5nm, T_{HfO_2}=2nm), midgap metal gate, undoped body and different sizes with the standard orientation ([100]). For NWs with W_{Si} larger than 5nm, the effective mass approach provides accurate enough results [5]. The Kubo-Greenwood formula and the momentum relaxation time approach [2] have been used to estimate the phonon-limited low-field mobility which is evaluated utilizing the confined acoustic phonons under freestanding (FSBC) and clamped surface (CSBC) boundary conditions (applied at the Si/SiO_2 interface) as well as bulk acoustic phonons (NC). In order to calculate the confined phonon spectrum we solve the elastic wave equation [6], [7]

$$\rho\omega^2 u_i + \sum_l \frac{\partial \sigma_{li}}{\partial x_l} = 0 \tag{1}$$

where ρ is the material density, ω is the angular frequency, u_i is the i-th component of the displacement vector, σ_{li} is the stress tensor and x_l can be the x, y or z coordinate. For the FSBC we have used the xyz algorithm proposed in [7] whereas for the CSBCs, we have selected a set of basis functions that vanish at the Si/SiO_2 interface to satisfy the boundary conditions ($u_i|_S$=0). Both methods can be employed regardless the geometry of the device.

Figure 2 shows the phonon dispersion for a W_{Si}=5nm square NW using the FSBC and the CSBC. Only the lowest phononic subbands are depicted. As can be seen, the use of CSBC makes the nearly linear phonon mode disappear provoking an increase in the carrier mobility as can be noticed in Fig. 3 where the phonon-limited mobility has been depicted for the same device when FSBC, CSBC and NC phonons are taken into account.

Figure 4 depicts the phonon-limited mobility of square devices with different sizes at $N_i = 5 \times 10^6 cm^{-1}$. As can be seen, the smaller the device, the bigger the effect of the different boundary conditions. As expected, in the limit of a large size, the FSBC and the CSBC curves approach the NC one.

Finally we have assessed the effect of the geometry on the mobility through the simulation of NWs with different percentage of curvature in their corners. Figure 5 depicts the mobility calculated when FSBC, CSBC and NC phonons are taken into account for a W_{Si}=5nm device with a percentage of curvature of 50% (left) and 100% (right). When compared to Fig. 3 (square NW), we have observed a decrease in the phonon-limited mobility as the rounding of the corners increases regardless of the phonon description employed.

978-3-901578-26-7 © 2013 Society for Micro- and Nanoelectronics

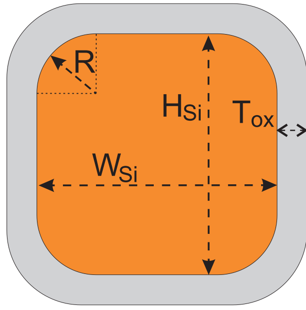

Fig. 1. Geometry of the devices under study. $W_{\rm Si}$ and $H_{\rm Si}$ are the device width and height, T_{ox} is the insulator thickness and R determines the percentage of curvature of the device as $100 \cdot 2R/W_{\rm Si}$.

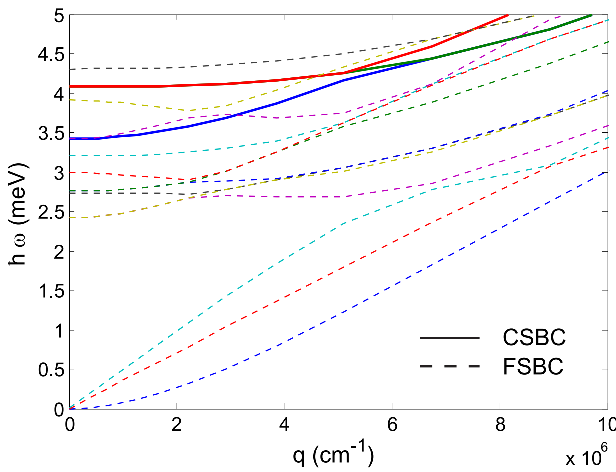

Fig. 2. Phonon dispersion relation for a W_{Si}=5nm square (R=0) NW when FSBC (dashed lines) and CSBC (solid lines) are considered.

Acknowledgment

Work supported by the Spanish Government under project FIS2011-26005, and the Junta de Andalucía under project P09-TIC-4873. F.G. Ruiz and I.M. Tienda-Luna also acknowledge the start-up project PYR-2012-5 of the CEI-BioTIC GENIL program.

References

[1] E. Ramayya et al., IEEE T. Nanotechnol. **6**, 1 (2007).
[2] S. Jin et al., J. Appl. Phys. **102**, 5 (2007).
[3] L. Donetti et al., J. Appl. Phys. **100**, (2006).
[4] A.K. Buin et al., J. Appl. Phys. **104**, (2008).
[5] J. Wang et al., IEEE T. on Electron Dev. **52**, 7 (2005).
[6] N. Nishiguchi et al., J. Phys.: Condens. Matter 2124, **9** (1997).
[7] W. M. Vissicher et al., J. Acoust. Soc. Sm. 90, **4** (1991).

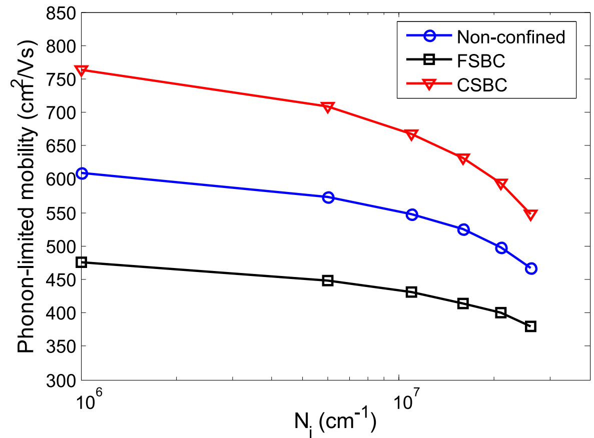

Fig. 3. Phonon-limited mobility vs. N_i for a W_{Si}=5nm square (R=0) NW when NC phonons (circles), FSBC (squares) and CSBC (triangles) are considered.

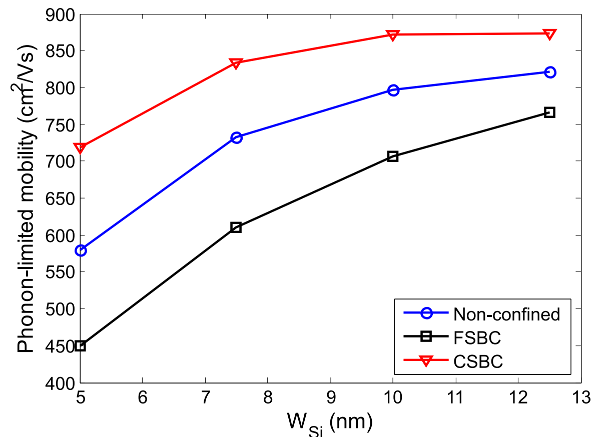

Fig. 4. Phonon-limited mobility vs. size for square (R=0) NWs at $N_i = 5 \times 10^6 \text{cm}^{-1}$ when NC phonons (circles), FSBC (squares) and CSBC (triangles) are considered.

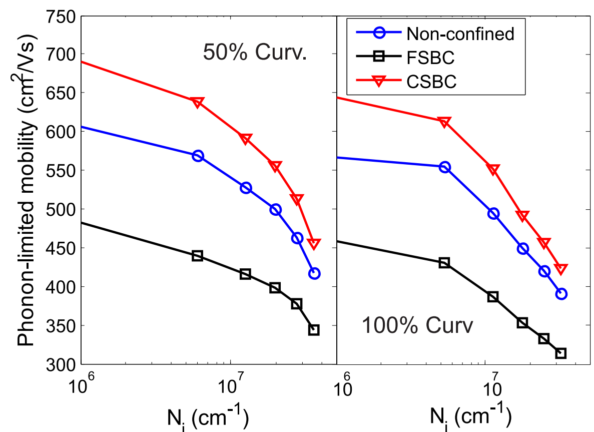

Fig. 5. Phonon-limited mobility vs. N_i for W_{Si}=5nm NWs with 50% (left) and 100% (right) percentage of curvature when NC phonons (circles), FSBC (squares) and CSBC (triangles) are considered.

Dependence of Matthiessen's Rule on Complex Phonon Self–Energies: A NEGF Study

M. Aldegunde*, R. Valin*, A. Martinez*, and J. R. Barker†
*College of Engineering, Swansea University, UK
†School of Engineering, University of Glasgow, G12 9YH, UK
e-mail: M.A.AldegundeRodriguez@swansea.ac.uk

Matthiessen's rule is a useful tool to estimate mobilities, however at nanoscales it should be used with care. Previous work on the validity of the Matthiessen's rule [1], [2] using only the imaginary part of the phonon self–energies was carried out. Ref. [2] estimated a 13% breakdown of the rule. Refs. [3], [4] showed that when the real part of the self-energy is not taken into account the Density of States (DOS) is underestimated, and as a consequence, the drain current is lower when only the imaginary part of the self–energy is considered. In this work the impact of the full self–energy (real+imaginary) in the current voltage characteristics of a gate–all–around Si nanowire transistor has been studied at low drain bias. In addition, the deviation of the Matthiessen's rule considering the full self–energy has been calculated and the results have been compared with our previous work [2]. The simulated device has a 20 nm channel length and a 2.2×2.2 nm^2 cross–section with an oxide thickness of 0.8 nm. The source and drain regions are 15 nm long with doping concentration of 10^{20} cm^{-3}. The I_D–V_G characteristics at V_D=1 mV with different phonon mechanisms are shown in Fig. 1. The low drain bias has been chosen in order to evaluate the Matthiessen's rule under low field conditions. At low gate bias, the current for the case of full self–energy is larger than the case with only imaginary self–energies. At high gate bias the situation is reversed. The contribution of each scattering mechanism to the total phonon scattering process has also been calculated and compared with the ballistic case. Fig. 1 shows that the largest contribution to the scattering process corresponds to the acoustic phonons and the lowest one to the f phonons. Fig. 2 shows the first sub–band along the channel at low and high gate bias (V_G = 0.3 V and V_G = 0.7 V) for the case of full self–energy and for the case of the imaginary part only. The gate barrier height relative to the source is similar for both cases and gate bias. Fig. 3 shows that the spectral current density for the full self–energy and imaginary cases in the middle of the channel. The curve for the full self–energy case is shifted to the left relative to the imaginary case curve and it has a large area at low gate bias. This implies a larger current for the full self–energy case. Fig. 4 shows an smaller shift but the area of the curve for the full self–energy case is larger than the corresponding area of the other case. Finally, we have calculated the resistances as a function of the gate bias for the full and the imaginary self–energies cases in order to evaluate the deviation of Matthiessen's rule. Fig. 5 shows the extracted resistances as a function of gate bias, we observe the exponential dependence of the inversion charge. The resistance values of the full self–energy case is lower than the other case at low gate bias. The Matthiessen's rule deviation has been calculated using $100\times(1-R_{Mat}/R_{NEGF})$, where R_{Mat} is the total resistance, which is obtained by adding the resistances from the simulations with each individual scattering mechanism and R_{NEGF} is the resistance obtained from simulation considering all the scattering mechanisms. The Matthiessen's rule deviation has been calculated for the full self–energy and with only the imaginary part. Fig. 6 shows the Matthiessen's deviation as a function of the inversion charge. The deviation is larger for the case of only imaginary self–energy at very large inversion charges. At low inversion charge Matthiessen's rule over–estimates the resistance. In conclusion, the off-current for the full self–energy case is two times larger than the corresponding current of the imaginary case but at high bias the difference is only 7%.

References

[1] M. Aldegunde, A. Martinez, and A. Asenov. *J. Appl. Phys.*, 110, 094518, (2011).
[2] M. Aldegunde, A. Martinez, and J. R. Barker. *J. Appl. Phys.*, 113, 014501, (2013).
[3] A. Svizhenko and M. Anantram. *Phys. Rev. B*, 72, 085430, (2005).
[4] A. Esposito, M. Frey, and A. Schenk. *J. Comput. Electron.*, 8, 336, (2009).

978-3-901578-26-7 © 2013 Society for Micro- and Nanoelectronics

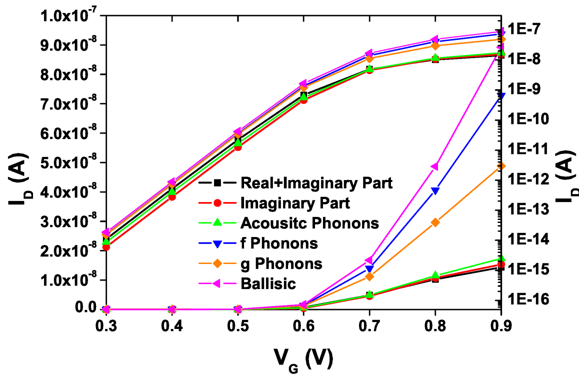

Fig. 1: I_D–V_G characteristics at V_D = 1 mV for the 20 nm gate length silicon nanowire transistor with different phonon mechanisms in operation for the full self–energy and its comparison with only the imaginary part of the self–energy when all the phonon mechanisms are active.

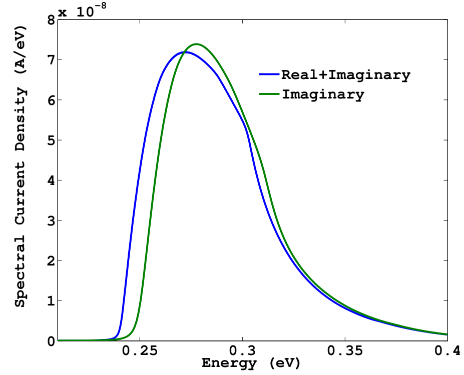

Fig. 4: Spectral current density in the middle of the channel for the the full self–energy and imaginary cases at high voltage (V_G = 0.7 V).

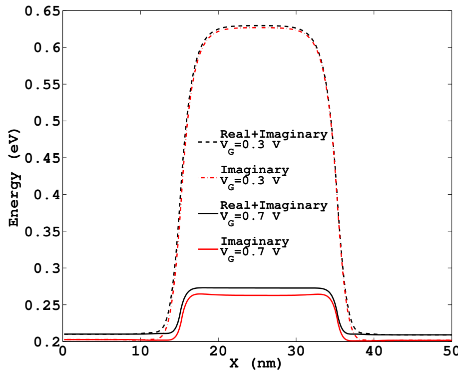

Fig. 2: First sub–band along the transport direction at low (V_G = 0.3 V) and high (V_G = 0.7 V) gate bias.

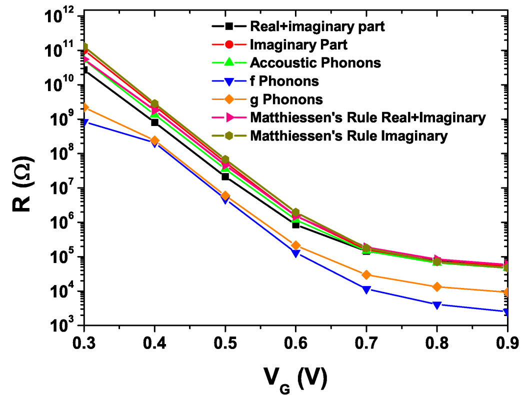

Fig. 5: Resistances of the silicon nanowire and comparison with Matthiessen's rule for both cases.

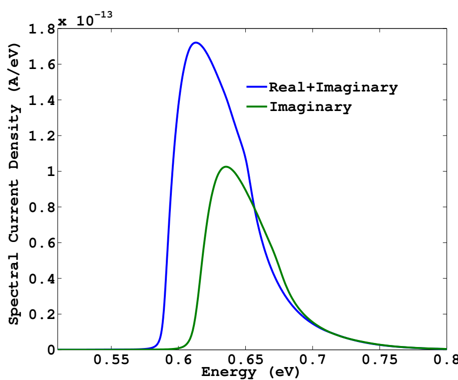

Fig. 3: Spectral current density in the middle of the channel for the the full self–energy and imaginary cases at low gate voltage (V_G = 0.3 V).

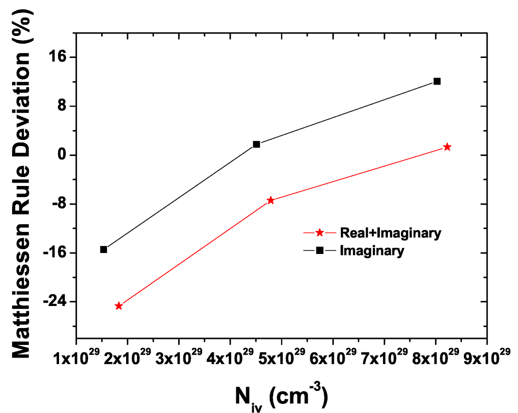

Fig. 6: Matthiessen's rule deviation as a function of the inversion charge for the cases of Fig. 5.

Phonon scattering at the interface between elastically dissimilar materials

Jung Hyun Oh, Moon-Gyu Jang*, and Mincheol Shin
Department of Electrical Engineering, Korea Advanced Institute of Science and Technology, Daejeon 305-701, Korea
* Electronics and Telecommunication Research Institute, Daejeon 305-350, Korea
e-mail:ohsimon@kaist.ac.kr

In recent years there have been growing interests in Si and Ge nanowires as promising structures for future electronics. Among these, the application to thermoelectric devices has attracted particular attention because it is found experimentally that the thermal conductivity of Si nanowires becomes largely suppressed as the cross-section decreases.[1] Low thermal conductivity is beneficial for maintaining temperature difference of thermoelectric devices and thus enhances the thermoelectric efficiency when associated with high electrical conductivity and large Seebeck coefficients. The underlying principle to reduce thermal conductivity is the introduction of phonon scattering centers because major heat transport in semiconductors is carried by phonon. The schemes include surface roughness, void defects, nanoparticles, alternate stacking of two different layers, and coated nanowires into devices.

In this work, we examine another structural defect that may be easily realized in experiments; several elastically-dissimilar layers are inserted into Si nanowires as shown in Fig. 1-(a). Silicides such as PtSi and W_2Ni_3Si are good candidates because they have different acoustic impedance from Si as well as give good electrical conductivity. The theoretical formalism is based on a continuum elastic wave equation, which provides relatively smaller computational burdens than atomistic calculations. From the isotropic elasticity theory the Lagrangian is given by,

$$\mathcal{L} = \int dV \left[\rho\omega^2 u^{(i)} u^{(i)} - (\partial_j u^{(i)}) C_{ijkl} (\partial_k u^{(l)})\right] \quad (1)$$

where ρ is the mass density, C_{ijkl} is the elasticity tensor, and $u^{(i)}$ is the ith coordinate of the displacement. Since our system contains structural defects, the elasticity tensor and the mass density are position-dependent. In order to study the phonon propagation, we calculate phonon transmission using a Green's function method derived from the Lagrangian of Eq. (1).[2]

The calculated transmission for a single layer is shown in Fig. 2. Due to the different elasticity of a host material Si and the dissimilar layer, the overall transmission becomes smaller. For the case of a PtSi silicide layer, the phonon transmission is suppressed by approximately 20% at $E = 10$ meV. It is found that the suppression depends on detailed crystal parameters rather than a simple acoustic impedance ratio between host and dissimilar layers; a SiC layer with a acoustic impedance ratio $\alpha_{SiC}/\alpha_{Si} = 1.77$ results in more suppressed behavior than for a PtSi layer $\alpha_{PtSi}/\alpha_{Si} = 2.66$. As the number of layers increases, the transmission function is more reduced as plotted in Fig. 3. We find that the transmission exhibits Ohm's behavior with the number of the dissimilar layer even though elastic scattering at the interfaces is assumed. In this case the inverse of the transmission function increases linearly with the number of layers as shown in Fig. 4.

Acknowledgment

This work was supported by the Basic Science Research Program through the NRF of Korea funded by the Ministry of Education, Science and Technology(2012039886) and ETRI.

References

[1] A. I. Boukai, et al., Y. Bunimovich, J. Tahir-kheli, J. Yu, W. A. Goddard III, and J. R. Heath, Nature (London) **451**, 168 (2008). Nature (London) **451**, 163 (2008).
[2] J. H. Oh, M. Shin, and M. G. Jang, J. Appl. Phys. **111**, (2012).

978-3-901578-26-7 © 2013 Society for Micro- and Nanoelectronics

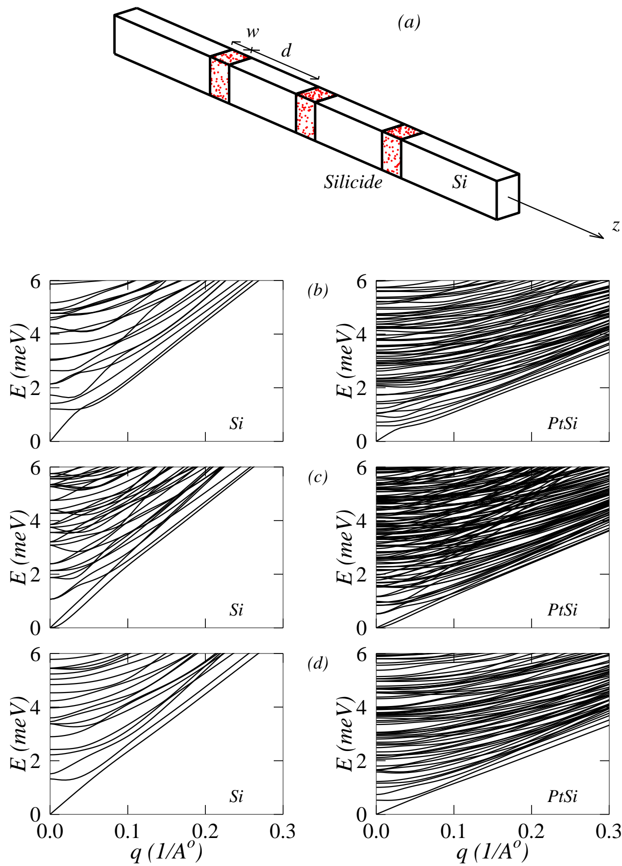

Fig. 1. (a) Schematic representation of a Si nanowire with three elastically dissimilar layers. The nanowire is assumed to have a rectangular cross-section and extends infinitely. Energy dispersions of dilatational(b), flexural(c), and shear/torsional(d) modes are shown for infinitely long Si (left) and PtSi (right) nanowires with a 8 nm × 8 nm cross-section.

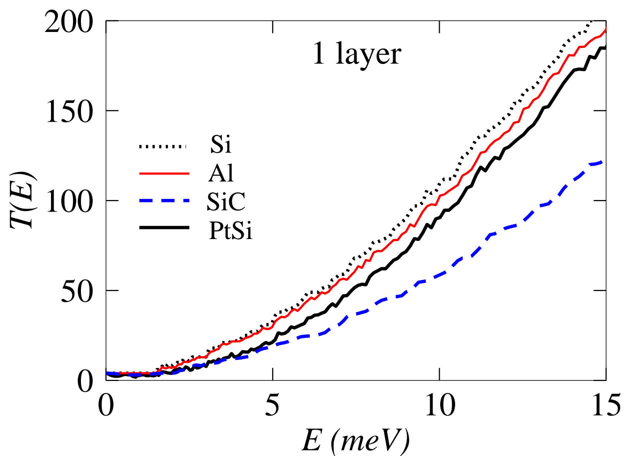

Fig. 2. Calculated transmissions of elastic waves are plotted as a function of incident energy for the case of a single dissimilar layer; PtSi (thick solid), SiC (dashed), Al (thin solid), and Si (dotted, corresponds to the no-layer case). We assume that nanowire cross-sections are a 8 nm × 8 nm and a layer thickness is $w = 10$nm.

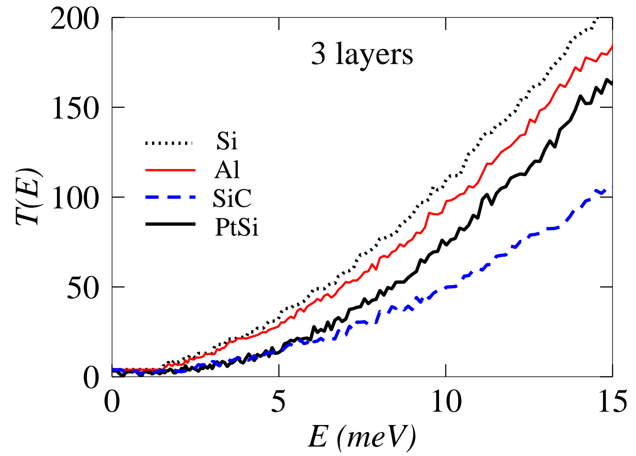

Fig. 3. Calculated transmissions of elastic waves are plotted as a function of incident energy for the case of three dissimilar layers; PtSi (thick solid), SiC (dashed), Al (thin solid), and Si (dotted, corresponds to the no-layer case). A 8 nm × 8 nm nanowire cross-section is used with a layer thickness, $w =$ 10nm, and a distance between layers, $d = 20$ nm.

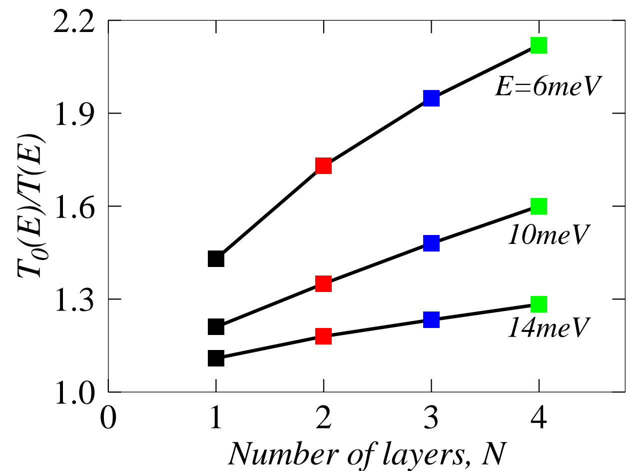

Fig. 4. The suppression of the transmission function relative to the result $T_0(E)$ of a pristine Si nanowire is emphasized as the number of layers increases for three different energies. The layer is assumed to be PtSi with a cross-section 8 nm× 8 nm, $w = 10$ nm, and $d = 20$ nm.

Effective Deformation Potential in Ultrathin SOI

T, Tanaka, and K. M. Itoh
School of Fundamental Science and Technology, Keio University, Yokohama 223-8522, Japan
e-mail: tt112157@z7.keio.jp

INTRODUCTION

Recent downsizing of Si MOSFETs face problems of short channel effects. To suppress these effects, ultrathin Silicon-on-Insulator (UTSOI) MOSFETs have attracted much attention. For bulk Si and bulk Si MOSFETs, deformation potentials (DPs) Ξ_d=1.1 eV and Ξ_u=10.5 eV or simplified effective DP D_{ac}=12.0 eV have been used to calculate the relaxation time of intravalley acoustic phonon scattering [1,2]. However, increase of D_{ac} in UTSOI MOSFETs was experimentally reported recently [3]. There are still uncertainties of effective DP approximated from anisotropic DPs and elastic approximation of intravalley acoustic phonon scattering in UTSOI MOSFETs. Thus, it is important to validate the DPs Ξ_d=1.1 eV and Ξ_u=10.5 eV to apply nanoscale devices. In this paper, we report the calculation of effective DPs from the anisotropic values (Ξ_d=1.1 eV and Ξ_u=10.5 eV) in UTSOI MOSFETs.

CALCULATION

Before the calculation of effective DPs, mobility in the bulk Si MOSFET was calculated to check our simulation. Parabolic subband structures were calculated by self-consistent solver of one-dimensional Poisson and Schrödinger equations. Then, transition probabilities and transport relaxation times were obtained from Fermi's Golden rule. For four-fold degenerated valleys, transport relaxation times in the same constant energy surface were approximated by same value. Acoustic phonons, surface optical phonons and surface roughness were considered as intravalley scatterings [4]. Three f-type and three g-type phonon scatterings were included as intervalley scatterings [4]. Mobility was calculated from the energetically averaged transport relaxation time. Figure 1 shows the comparison between our simulation and experimental mobility [5]. Roughness parameters were Δ=0.51 nm and Λ=1.0 nm, and doping concentration was N_A =3.9×10^{15} cm^{-3}. Then, effective DPs in UTSOI MOSFETs were determined by comparing between two mobility calculated from anisotropic DPs and the effective DP. In addition to elastic scatterings, inelastic scatterings of intravalley acoustic phonons were also calculated by

$$W(E_i) = \frac{2\pi}{\hbar} \sum_{q,f,j} \frac{\hbar q^2}{2\rho V \omega_q} D_j(\boldsymbol{q}) \left[N_q + \frac{1}{2} \mp \frac{1}{2} \right] \times \left| \langle f | \exp(i\boldsymbol{q}\cdot\boldsymbol{r}) | i \rangle \right|^2 \delta(E_i \pm \hbar\omega_q - E_f), \quad (1)$$

where $W(E_i)$ is the transition probability at initial electron energy E_i, q is the magnitude of phonon wavevector, ρ is the mass density, V is the crystal volume, $\omega_q=s_jq+c_jq^2$ is the isotopically approximated phonon frequency, s_j (j=LA or TA) is the sound velocity, c_j is the constant in Ref. [6], $D_j(\boldsymbol{q})$ is the anisotropic DP, N_q is the phonon occupation factor, and i (f) represents the initial (final) state index. Figure 2 shows the calculated transport relaxation time of the first subband in the 6.0 nm UTSOI MOSFET. The surface inversion carrier concentration was N_S =4.0×10^{12} cm^{-2}. Using these result, mobility was calculated. Calculated mobility from anisotropic DP and empirical DP in Ref. [3], and experimental mobility in Ref. [7] were shown in Fig. 3. Finally, Fig. 4 shows obtained effective DPs.

SUMMARY

We calculated effective DPs in UTSOI MOSFETs from the anisotropic DPs with considering inelastic scatterings of intravalley acoustic phonon scatterings. Lower effective DP than empirical DP in Fig. 4 suggests the change of DPs in UTSOI MOSFETs. However, nonparabolicity of conduction band have not been included in calculations yet. Until the conference, we include this effect and improve our calculation.

978-3-901578-26-7 © 2013 Society for Micro- and Nanoelectronics

ACKOWLEDGEMENT

This work has been supported in part by the Grant-in-Aid for Scientific Research and Project for Developing Innovation Systems by CREST-JST.

REFERENCES

[1] M. V. Fischetti, and S. E. Laux, *Band structure, deformation potentials, and carrier mobility in strained Si, Ge, and SiGe alloys*, Journal of Applied Physics **80**, 2234 (1996).

[2] S. Takagi, J. L. Hoyt, J. J. Welser, and J. F. Gibbons, *Comparative study of phonon-limited mobility of two-dimensional electrons in strained and unstrainedSi metal-oxcide-semiconductor field-effect transistors*, Journal of Applied Physics **80**, 1567 (1996).

[3] T. Ohashi, T. Takahashi, N. Beppu, S. Oda, and K. Uchida, *Experimental evidence of increased deformation potential at MOS interface and its impact on characteristics of ETSOI FETs*, IEDM Tech. Dig., 2011, pp. 16.4.1–16.4.4.

[4] M. V. Fischetti, and S. E. Laux, *Monte Carlo study of electron transport in silicon inversion layers*, Physical Review B **48**, 2244 (1993).

[5] S. Takagi, A. Toriumi, M. Iwase, and H. Tango, *On the universality of inversion-layer mobility in Si MOSFETs. Part I-Effect of substrate impurity concentration*, IEEE Transactions of Electron Devices **41**, 2357 (1994).

[6] E. Pop, R. W. Dutton, and K. E. Goodson, *Analytic band Monte Carlo model for electron transport in Si including acoustic and optical phonon dispersion*, Journal of Applied Physics **96**, 4998 (2004).

[7] K. Uchida, J. Koga, and S. Takagi, *Experimental study on electron mobility in ultrathin-body silicon-on-insulator metal-oxide-semiconductor field-effect transistors*, Journal of Applied Physics **102**, 074510 (2007).

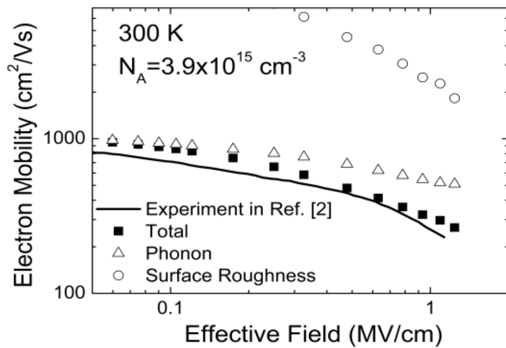

Fig. 1. Comparison between experimental (solid line Ref. [5]) and simulated mobility in bulk Si MOSFET.

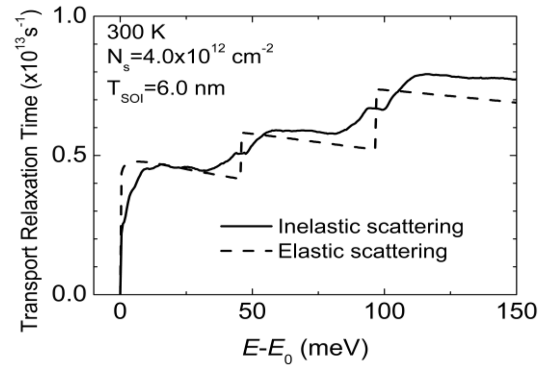

Fig. 2. Calculated transport relaxation times of the first subband.E-E_0 is the energy from the bottom of the subband.

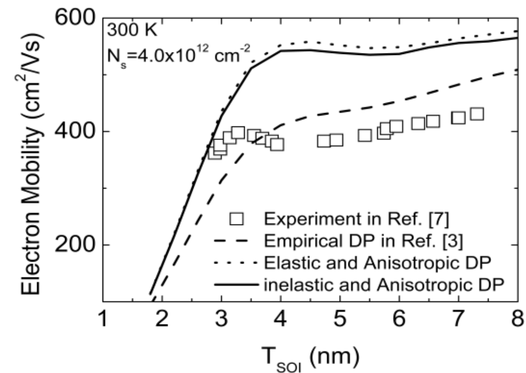

Fig. 3. Comparison between experimental (blank square Ref. [7]) and simulated mobility in UTSOI MOSFETs.

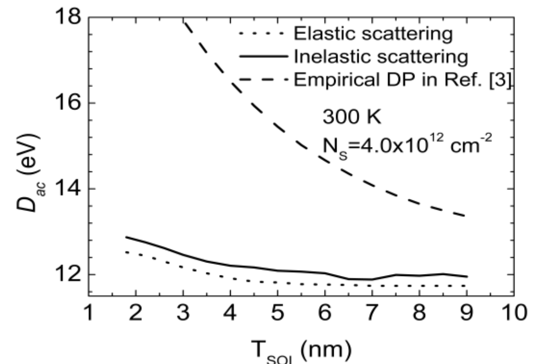

Fig. 4. Comparison between empirical DP in Ref. [3] and effective DPs calculated from elastical and inelastical intravalley acoustic phonon scattering.

Thermoelectric properties of Si-based Single-electron Transistors

V. Talbo, J. Saint-Martin, D. Querlioz, S. Retailleau, and P. Dollfus
Institute of Fundametal Electronics, CNRS, Univ. of Paris-Sud, Orsay, France
e-mail: jerome.saint-martin@u-psud.fr

Abstract

The thermoelectric properties of Single Electron Transistors (SETs) in sequential transport regime are investigated. By including the effect of energy level broadening, we assess the potentiality of semiconducting SETs in view of application in nanoscale thermoelectric metrology.

Introduction

Specific properties of nanostructures have generated a recent revival of interest in thermoelectric devices [1,2]. Thanks to their delta-like density of states, devices based on quantum dots are expected to exhibit high Seebeck coefficient, nearly zero electronic thermal conductance and ultra-low phononic thermal conductance if embedded in an oxide matrix, but to the price of low electronic conductance. The single-electron tunneling across discrete levels in the QD occurring in such devices behaves as a quasi-ideal energy filter providing these incomparable thermoelectric properties [3,4]. Moreover, the Seebeck coefficient in a single electron transistor (SET) thanks to its material-independent characteristics has been proposed as a reference in nanoscale metrology [5].

Model

In this work, we perform self-consistent 3D Poisson/Schrödinger simulation within the Hartree approximation, which captures the details of charging and tunneling effects in semiconductor quantum dots [6]. From the computation of tunneling rates within the Bardeen's formalism, we use a Monte-Carlo algorithm to solve a master equation and to extract the current-voltage characteristics for different temperature gradients applied between the source/drain electrodes of the device schematized in Fig. 1. Fig. 2 shows typical diamond stability diagram that are commonly obtained in SETs due to the effect of Coulomb blockade. The effect of collisional broadening of energy levels is accounted by introducing a Lorentzian function for the spectral function of the level instead of the Dirac function commonly used to describe unperturbed states. The width of the Lorentzian function can be obtained from the calculation of the self energy of the electron-phonon interaction [7].

Results

The influence of a temperature gradient applied to the SET on its current-voltage characteristics (Fig. 3) allows us to check that the linear approximation may be used to study the SET as a thermoelectric generator.

We plot in Fig. 4 the evolution of the Seebeck coefficient, the electronic conductance and the thermoelectric power factor resulting from a temperature gradient for SETs with both spherical and cubic quantum dot. It is shown that the power factor of such SET can reach the value of about 1 kW/m^2 at $T = 77$ K with small $\Delta T = 10$°K.When including realistic energy level broadening H at 77 K $\left(\text{i.e. } H \le 0.1kT\right)$, the evolution of the Seebeck coefficient remains very close to its ideal material-independent value. This demonstrates the good potential of semiconducting SETs for nanoscale thermoelectric metrology.

References

[1] P. Pichanusakorn and P. Bandaru, Mat. Sci. Eng. R. **67**, 19 (2010); R. Kim, S. Datta and M.S. Lundstrom, J. Appl. Phys. **105**, 034506 (2009).
[2] L. D. Hicks and M. S. Dresselhaus, Phys. Rev. B **47**, 16631 (1993).
[3] T. C. Harman, P. J. Taylor, M. P. Walsh, and B. E. LaForge Science **297**, 2229 (2002).
[4] M. Tsaousidou and G. P. Triberis, J. Phys.: Condens. Matter **22**, 355304 (2010).
[5] P. Mani, N. Nakpathomkun, E. A. Hoffmann, and H. Linke, Nano Letters **11**, 4679 (2011).
[6] V. Talbo, A. Valentin, S. Galdin-Retailleau and P. Dollfus, IEEE Trans. Electron Devices **58**, 3286 (2011).
[7] A. Valentin, S. Galdin-Retailleau and P. Dollfus, J. Appl. Phys. **106**, 044501 (2009).

978-3-901578-26-7 © 2013 Society for Micro- and Nanoelectronics

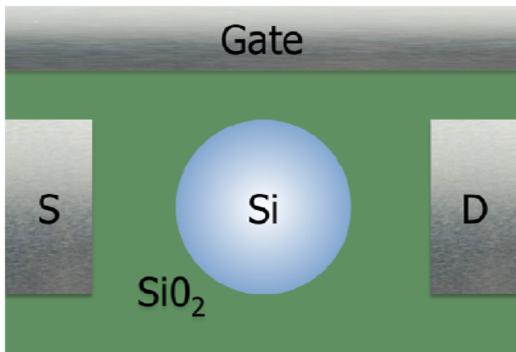

Fig. 1. Schematic cross-section of simulated Single Electron Transistors.

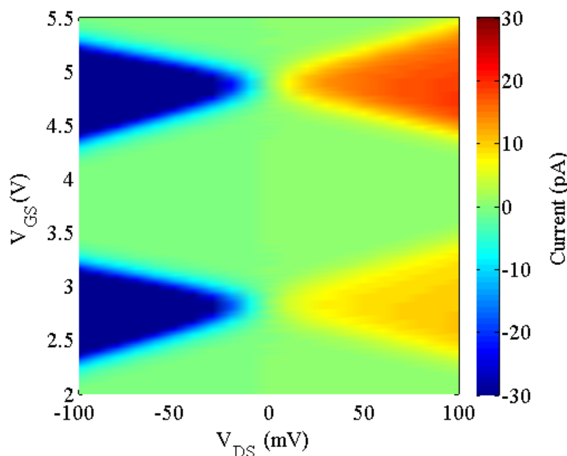

Fig. 2. Drain current stability diagram of the cubic SET at $T = 77$ K.

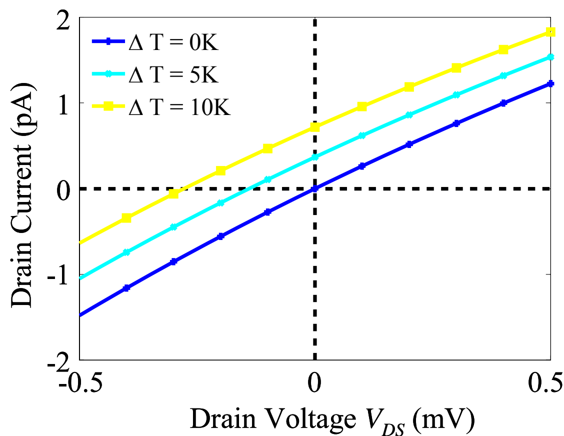

Fig. 3. Drain current-bias voltage characteristics for different temperature gradients around $T = 77$ K at $V_G = 3.4$ V.

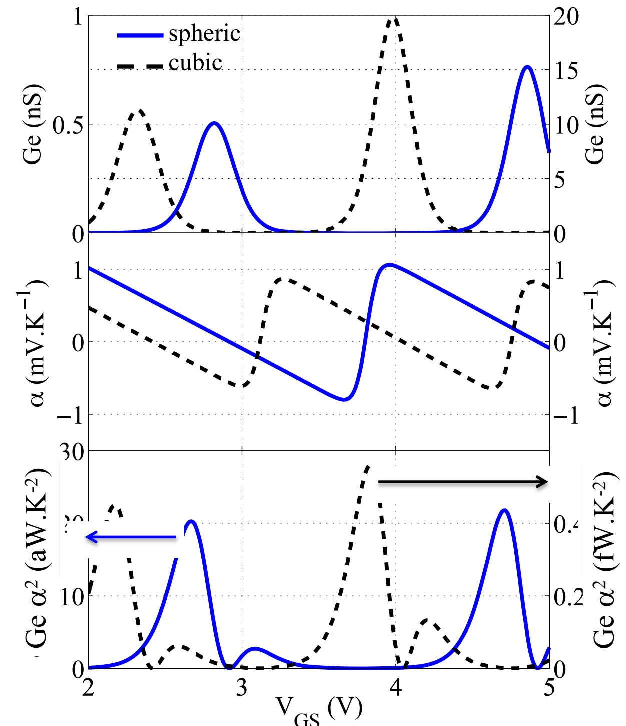

Fig. 4. Electronic conductance, Seebeck coefficient and power factor as a function of gate voltage, for the spherical-dot and cubic-dot SETs.

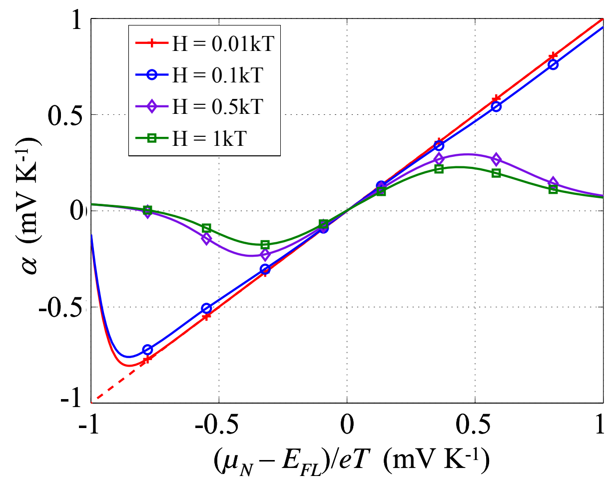

Fig. 5. Evolution of the Seebeck coefficient for different energy level broadenings H and comparison with the ideal linear function $\alpha_{ideal} = (\mu_N - E_{FL})/eT$ (dashed line)

Symmetry-dependent conductance behavior in graphene-based double-dot structures

P. Marconcini, D. Logoteta, and M. Macucci
Dipartimento di Ingegneria dell'Informazione, Università di Pisa, Via G. Caruso 16, I-56122 Pisa, Italy
e-mail: p.marconcini@iet.unipi.it

INTRODUCTION

Some of us have recently found and investigated an interesting effect, consisting in a strong symmetry-dependence of the conductance of two quantum dots in series separated by a tunnel barrier and connected to the external leads through input and output constrictions [1]. The conductance reaches a maximum value, which can counterintuitively be much larger that that in the absence of the constrictions, when the system is completely symmetric, i.e. the two constrictions are in positions symmetric with respect to the barrier, and no magnetic field is present. Any symmetry-breaking action makes the conductance decrease significantly. This effect derives from the constructive interference of many transport paths that in a symmetric structure share the same length and thus the same phase. The effect was studied in a semiconductor heterostructure and an application for sensors of position or magnetic field was suggested.

The fabrication of analogous sensors in graphene would be very attractive, because it would make possible to exploit specific properties of graphene, such as the high mobility at room temperature. However, transport in graphene has peculiar characteristics leading to a different behavior. For example, transport through a barrier in graphene exhibits Klein tunneling, which makes the barrier perfectly transparent in the case of normal incidence and derives from the relativistic-like behavior of electrons, or, equivalently, from the matching of the electron states outside the barrier with the hole states inside it.

Here we show the results of a study, in the ideal case without disorder, of double-dot structures defined in monolayer graphene, and we show that the mentioned symmetry-related effect does appear.

METHOD AND RESULTS

We consider an idealized structure with the geometry and the potential landscape sketched in Fig. 1. We numerically study this structure solving, in the Fourier space, the Dirac envelope equation in each region with longitudinally constant potential, and then applying a recursive scattering matrix method.

We have studied several device configurations. For example, in Figs. 2 and 3 we show the results obtained considering a structure with two 2 μm $\times$ 2 μm dots, with 400 nm wide constrictions and a 55 nm thick and 50 meV high tunnel barrier. In Figs. 4 and 5 we have instead considered 1 μm $\times$ 1 μm dots, with 200 nm wide constrictions and a 30 nm thick and 50 meV high tunnel barrier. In Figs. 2 and 4 we report the conductance, as a function of the electron Fermi energy, of the barrier and of the cavity alone, and of the cavity with the barrier in the central and 10 nm shifted positions. In all of the considered cases we see that the presence of the cavity reduces the transmission of the structure with respect to the barrier alone, but the conductance remains clearly dependent, in a large range of energies, on the position of the tunnel barrier and thus on the symmetry in the structure. This is even clearer in Figs. 3 and 5, where we show, for a Fermi energy of 30 meV, the dependence of the conductance on the shift of the tunnel barrier with respect to the central position.

These results show that, at least in the absence of significant disorder, the dependence of the conductance on symmetry survives in graphene coupled dots.

REFERENCES

[1] R. S. Whitney, P. Marconcini, M. Macucci, Phys. Rev. Lett. **102**, 186802 (2009).

978-3-901578-26-7 © 2013 Society for Micro- and Nanoelectronics

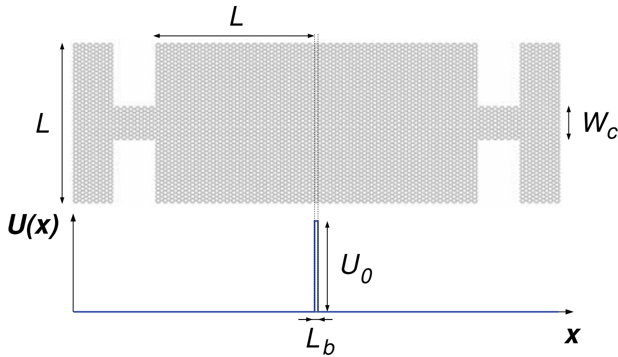

Fig. 1. Sketch of the considered graphene-based double-dot structure, and dependence of the potential energy U on the longitudinal position x.

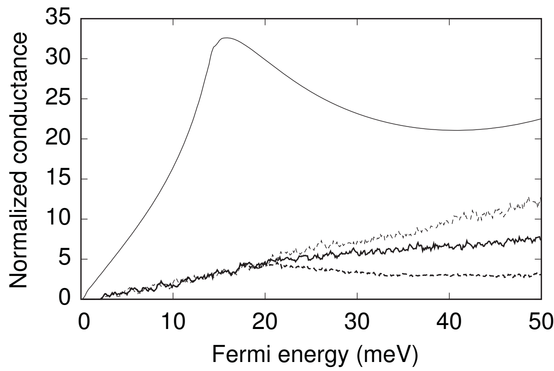

Fig. 2. Conductance (normalized with respect to the conductance quantum) as a function of the electron Fermi energy, for the barrier alone (thin solid curve), for the cavity alone (thin dashed curve), and for the cavity with the barrier in the center (thick solid curve) and in a 10 nm shifted position (thick dashed curve). These results have been obtained for a structure with (see Fig. 1) $L = 2\ \mu\mathrm{m}$, $W_c = 400$ nm, $L_b = 55$ nm and $U_0 = 50$ meV, with a transversal number of dimer lines in the two dots corresponding to a semiconductor armchair ribbon.

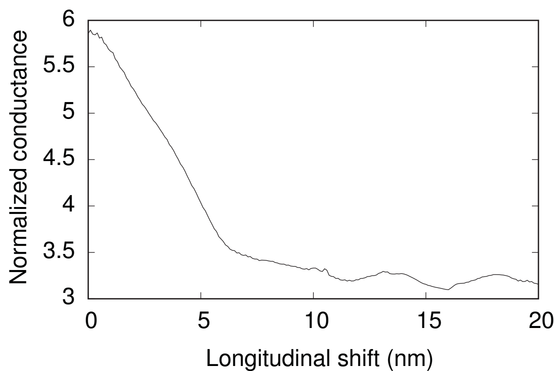

Fig. 3. Normalized conductance of the structure considered in Fig. 2 as a function of the shift of the tunnel barrier from the central position, for a Fermi energy of 30 meV.

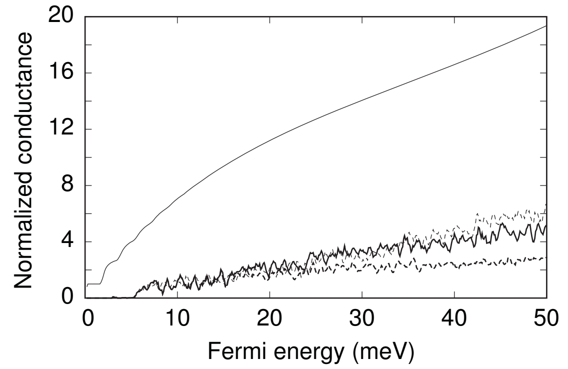

Fig. 4. Normalized conductance as a function of the electron Fermi energy, for the barrier alone (thin solid curve), for the cavity alone (thin dashed curve), and for the cavity with the barrier in the center (thick solid curve) and in a 10 nm shifted position (thick dashed curve). These results have been obtained for a structure with (see Fig. 1) $L = 1\ \mu\mathrm{m}$, $W_c = 200$ nm, $L_b = 30$ nm and $U_0 = 50$ meV, with a transversal number of dimer lines in the two dots corresponding to a metallic armchair ribbon.

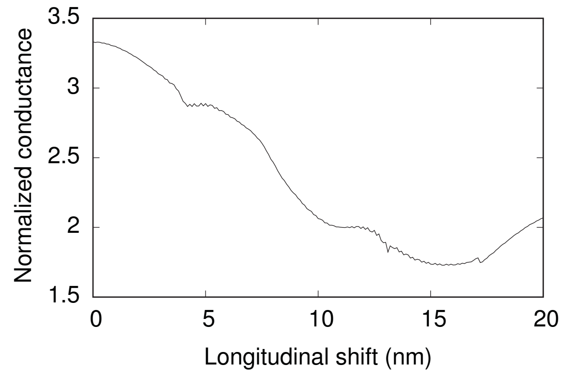

Fig. 5. Normalized conductance of the structure considered in Fig. 4 as a function of the shift of the tunnel barrier from the central position, for a Fermi energy of 30 meV.

Change of the Electronic Properties of Carbon Nanotubes Cause by Three-Dimensional Strain Field

M. Ohnishi, K. Suzuki*, and H. Miura*
Department of Nanomechanics, Graduate School of Engineering, Tohoku University,
6-6-11-716, Aoba, Aramaki, Aoba-ku, 980-8579, Sendai, Japan
*Fracture and Reliability of Research Institute, Graduate School of Engineering, Tohoku University
e-mail: masato.ohnishi@rift.mech.tohoku.ac.jp

INTRODUCTION

Since carbon nanotubes (CNTs) have superior properties both mechanically and electronically, there have been many efforts to develop electronic devices or various kinds of sensors based on carbon nanotubes [1-2]. We have revealed the possibility of the high sensitive strain sensor using popular resin in which multi-walled CNTs (MWNTs) are dispersed uniformly [2]. It is a critical issue to understand how the electronic state of CNTs is effected by a deformation [3-4]. In this study, we focused on orbital hybridization, one of the main factor causing the change of the electronic state of CNTs. In order to understand how orbital hybridization occur around strained areas, we analyzed the electronic state of CNTs and graphene nanoribbons (GNRs), unzipped CNTs by using the density functional theory.

CHANGE IN ELECTRONIC STATE OF CNTS AND GNRS CAUSED BY DEFORMATION

We analyzed the electronic structure of armchair GNRs (N = 10, 16, 18, 20) folded on the center line and (n, 0) zigzag CNTs (n = 9, 11, 12, 13) under axial and radial strain. Models of a GNR and a CNT are shown in Fig. 1(a), (b), respectively. The radial strain of the CNTs was considered to the deformation of the circular cross-sectional shape to the deformed elliptical CNT. The semi-major axis of the ellipse can be written $R = (1 + \varepsilon_R) R_0$, where ε_R is defined by the radial strain and R_0 is the radius of the CNT without strain. The amplitudes of the axial and the radial strains were varied 0% to 10% and 0% to 30%, respectively. In order to summarize the results, we used the dihedral angle which is an angle between π orbitals of adjacent atoms as shown in Fig. 1(c).

The analyses were performed by Accelrys' density functional theory (DFT)-code DMol[3]. The generalized gradient approximation (GGA) of PW91 was applied in this analysis. The total energy was converged to within 0.5 meV with a Monkhorst-Pack *k*-point mesh of $1 \times 1 \times 50$. The longitudinal direction of the GNRs and CNTs was taken that along *c* axis and vacuum separations along both *a* and *b* axes were more than 50 Å, which was large enough to neglect the interaction of next cells. The length along *c* axis was equal to the transverse vector of CNTs, 4.26 Å in the case of GNRs and CNTs without strain.

The band gap changes of GNRs and CNTs with the increase in the maximum dihedral angle are shown in Fig. 2(a), (b), respectively. As shown in these figures, the band gap remained a small value when a GNR or CNT has initially a small band gap. On the other hand, when a GNR or CNT has a large band gap, the band gap changed drastically. Although band gaps were almost constant when the applied strain was small, band gaps decreased almost linearly as the increase in the maximum dihedral angle when the maximum dihedral angle exceeded the critical value. The decreasing rate of the band gap of CNTs was larger than that of GNRs. This should be because the area of large dihedral angle was larger than that of GNRs, and thus, the orbital hybridization occur at larger areas in the CNTs.

In order to discuss how orbital hybridization occur around the areas of large dihedral angles, the change of the band structure of GNR (N = 10) is

978-3-901578-26-7 © 2013 Society for Micro- and Nanoelectronics

shown in Fig. 3. As shown in this figure, the highest occupied molecular orbital (HOMO) energy did not change significantly as the increase in the maximum dihedral angle. On the other hand, the lowest unoccupied molecular orbital (LUMO) energies changed significantly. When the maximum dihedral angle was small, the second LUMO energy decreased as the increase in the maximum dihedral angle while the LUMO energy did not changed significantly. After the second LUMO energy merged into the LUMO energy at the maximum dihedral angle of 14 degrees, the LUMO energy started to decrease which resulted in the decrease in the band gap. Because the LUMO and the second LUMO indicate π and σ orbitals, this result indicate that the band gap started to decrease after π orbitals hybridized with σ orbitals and that the decrease in the σ orbital energy caused the orbital hybridization. Therefore, by analyzing the second LUMO energy around strained areas, the estimation of the local band gap of CNTs under complicated strain should be possible.

CONCLUSION

The electronic state of GNRs and CNTs under three-dimensional strain field was analyzed by using the DFT calculation in order to understand how orbital hybridization is induced around strained areas. We found that the decrease in the second LUMO energy resulted in the orbital hybridization which caused the decrease in the band gap. The structural dominant factor which caused the bad gap change was the distribution of dihedral angle.

ACKNOWLEDGMENT

This research was partly supported by the Grants-in-Aid for Scientific Research and the Japanese special coordination funds for promoting science and technology.

REFERENCES

[1] W. Zhang, et al. J. Nanoscience and Nanotechnology, **6,** 960-964, (2006).

[2] M. Ohnishi, K. Ohsaki, Y. Suzuki, K. Suzuki, and H. Miura, Proc. Of the ASME 2010 International Mechanical Engineering Congress & Exposition, IMECE2010-37277, 1-7, (2010).

[3] L. Yang and J. Han. *Electronic Structure of Deformed Carbon Nanotubes*, Physical Review Letters, **85**, 1, (2000) 154-157.

[4] T. W. Tombler, et al., *Reversible electromechanical characteristics of carbon nanotubes under local-probe manipulation*, Nature, **405**, (2000), 769-772.

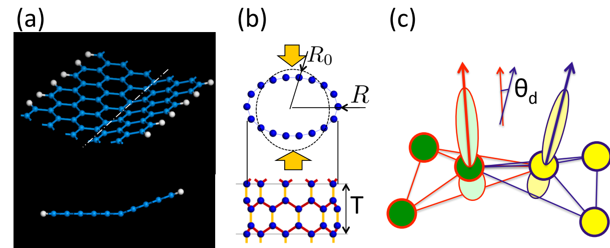

Fig. 1 Examples of the analysis model of (a) GNRs and (b) CNTs, and (c) dihedral angle.

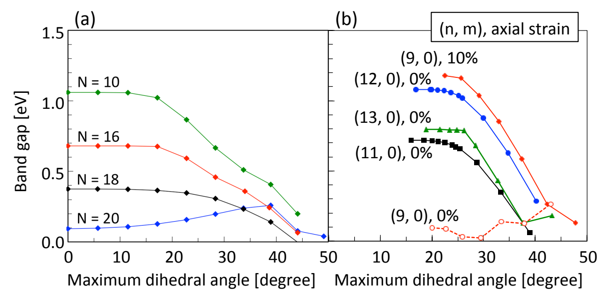

Fig. 2 Change in the band gap of GNRs and CNTs caused by orbital hybridization

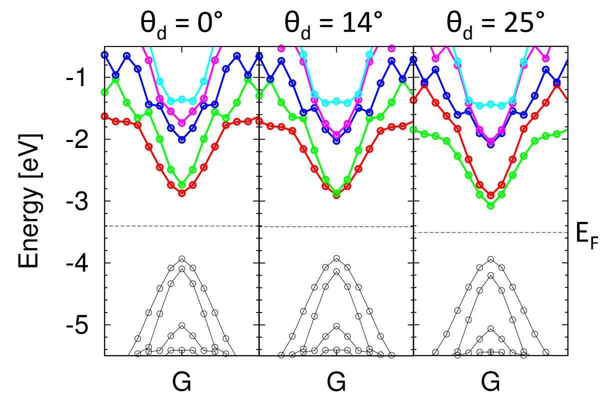

Fig. 3 Change in electronic band structure of AGNR (N=10) with the increase in the maximum dihedral angle

Effect of σ-band for Conduction of Metal/Graphene/Metal Junctions

S. Honda, K. Inuduka, and N. Sano
Faculty of Pure and Applied Sciences, University of Tsukuba, Tsukuba 305-8573, Japan
e-mail: honda@hermes.esys.tsukuba.ac.jp

INTRODUCTION

Graphene, which is composed of a two-dimensional honeycomb lattice of carbon atoms, has a characteristic electronic structure near the Fermi level: its conduction and valence bands meet at only two states called Dirac points in the Brillouin zone and its energy momentum dispersion is linear near the Dirac points, that is, graphene is a gapless semiconductor in which electrons behave as massless electrons. The characteristics of electronic transport of such massless electrons have been intensively studied in graphene of infinite size as well as in finite-size nano-ribbons. The graphene has a zigzag edge and an arm-chair edge. The magnetization appears at the zigzag edge in the spin polarized graphene. The σ-band is neglected in the several theoretical studies for graphene because the σ-band is formed far the Fermi level. We show that the σ-band influence on the conduction in the graphene junctions.

MODEL and METHOD

Figure 1 shows the calculated structure of metal/graphene/metal lateral junctions with arm-chair edge contacts are shown in Figure 1. The zigzag edge of GNR is hydrogenated. The edge state of graphene disappears by hydrogenating. The width of GNR is 8 chains. The arm-chair edge of GNR is contacted the metal edge. We have used a sp^3 tight-binding model. The nearest-neighbor sp^3 model: s, p_x, p_y, and p_z orbital, or a p_z model: p_z orbital is used for the GNR. The metal lead is 2D semi-infinite square lattice with s-orbital. For the band parameters of the tight-binding model, we use are taken from Harrison's textbook. The conductance is calculated by using a recursive Green's function method and the Kubo formula [1].

RESULTS

The dispersions of 8 chains GNR with the sp^3 model are shown in figure 2. Fig. 2(a) and (b) show the non-spin-polarized GNR and the spin-polarized GNR, respectively. Fermi level is 0 eV. The almost sub-bands are consisted of the π-band of p_z orbital. We find the σ-band of s, p_x, p_y orbitals around 4.5 eV and –4.5 eV. In the spin-polarized GNR, a band gap of 0.84 eV opens (Fig. 1(b)). The band gap decrease with increasing the width of GNR. We use the spin-polarized GNR for the conduction calculation. Figure 3 and 4 show the calculated results of the conductance per spin around the conduction band bottom in the junction with the 50 and 500 lengths GNR, respectively. The light gray bold curve shows the conductance with sp^3 orbitals and a black thin curve shows the conductance with only p_z orbital for the graphene. When the graphene length is 50 chains, the conductance with sp^3 model is smaller than p_z model and the effective band gap is large. When the graphene length is 500 chains, the magnitude of effective band gap is nearly equal. However, the peak and dip of the magnitude of quantized conductance are different. In the sp^3 model, the s, p_x and p_y orbital of the graphene hybridize the p_z orbital of graphene via the metal lead. As a result, the calculated results of the conductance in the metal and graphene junctions differ between the sp^3 model and the p_z model.

REFERENCES

[1] S. Honda, A. Yamamura, T. Hiraiwa, R. Sato, J. Inoue, and H. Itoh, Phys. Rev. B **82**, 033402 (2010).

978-3-901578-26-7 © 2013 Society for Micro- and Nanoelectronics

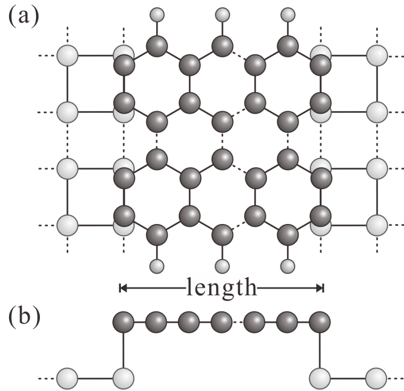

Fig. 1. (a) Top view and (b) side view of structure of metal/ graphene/ metal junction. The graphene hydrogenate. The black and gray and small gray spheres are carbon atoms and s-orb metals and hydrogen atoms, respectively. In this figure, the width and length of graphene are 4 chains and 3.5 chains, respectively.

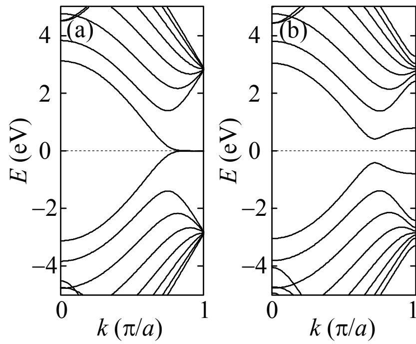

Fig. 2. The dispersion relations of (a) non-spin polarized and (b) spin polarized graphene nanoribbon. The width of graphene is 8 chains.

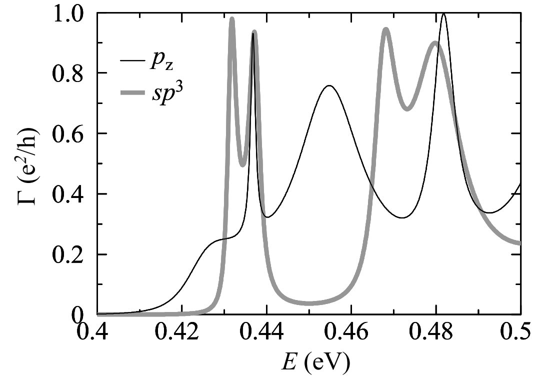

Fig. 3. Conductance of metal / graphene/ metal junction. The width and length of graphene nano ribbon are 8 chains and 50 chains, respectively.

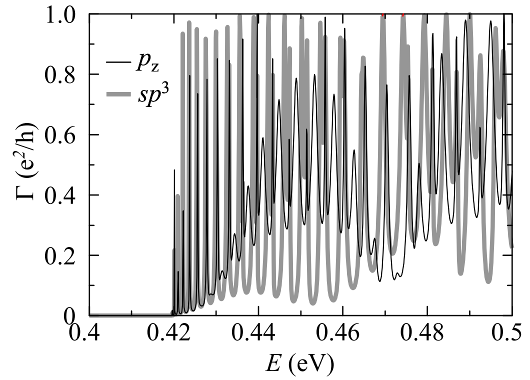

Fig. 4. Conductance of metal / graphene/ metal junction. The width and length of graphene nano ribbon are 8 chains and 500 chains, respectively.

Effect of Axial Strain on Switching Behavior of Carbon Nanotube Tunneling Field Effect Transistors

S. Souma, T. Nakano, H. Nagai, and M. Ogawa
Department of Electrical and Electronic Engineering, Faculty of Engineering,
Kobe University 1-1 Rokkodai, Nada, Kobe 657-8501, Japan
email: ssouma@harbor.kobe-u.ac.jp

Introduction

The integration density of integrated circuits has been increasing with amazing speed, and the critical issue of high off-state power dissipation comes along together. In fact, while the conventional MOSFETs operate with power supply voltages as low as two volts, now high performance transistors operating at practically lower voltages are desired. One of the important options to fulfill such demand is to use carbon nanotube tunneling field effect transistors (CNT-TFETs), since they not only are expected to operate with the sub-threshold swing below 60mV/decade at room temperature due to band-to-band tunneling [1], but also enables us to modify their electrical properties simply by changing their geometrical shapes. For instance, it is known that the on-current can be enhanced while reducing off-current in CNT-TFETs by applying the strain along the axial direction [2]. Motivated by such background, we study the influence of axial strain on the electronic transport for a model CNT-TFETs connected to electrodes.

Method

We assume that the source and the drain electrodes are p-type and n-type CNTs, where the band structures are assumed to be shiftd upper and lower in energy by means of the gate voltage (Fig. 1). In order to perform efficient simulation of such electromechanical phenomena in CNT, we employ the tight-binding model for electronic structure calculations [3]. We first analyze the band structures of semiconducting CNT under various strength of the axial strain (Fig. 2), and then calculate the transmission probabilities (Fig. 3) and the electrical transport properties by using the non-equilibrium Green's function method.

Results and discussions

Figure 2 shows the changing trend of bandgap energy by the axial strain for various semiconducting CNTs. This result means that the strain applied along the axial direction of CNT is effective for opening the bandgap. In Fig. 3 we plotted the transmission probability in (7,0) CNT-TFET, where we can clearly observe the band-to-band tunneling current. In Fig. 5-7, the gate voltage dependences of the drain current are plotted for two different dopin levels and three different axial strain ratios. These results demonstrate that the axial strain applied in the channel region of CNT is to be of benefit for reducing the subthreshold swing (SS) without reducing the on-current significantly when the heavy dopin level condition is achieved in the electrode.

Conclusion

We have investigated the effect of axial strain on the performance of CNT-TFET. Our simulations have demonstrated that the axial strain applied in the channel region of CNT-TFET is to be of benefit for reducing the subthreshold swing (SS) without reducing the on-current significantly when the heavy dopin level condition is achieved in the electrode.

References

[1] S. O. Koswatta, M. S. Lundstorm, and D. E. Nikonov, Appl. Phys. Lett. 92, 043215 (2008).
[2] K. Uchida and M. Saitoh. Appl. Phys. Lett. 91, 203520 (2007).
[3] C. H. Xu, C. Z. Wang, C. T. Chan, and K. M. Ho, J. Phys. Condens. Matter 4, 6047 (1992).

978-3-901578-26-7 © 2013 Society for Micro- and Nanoelectronics

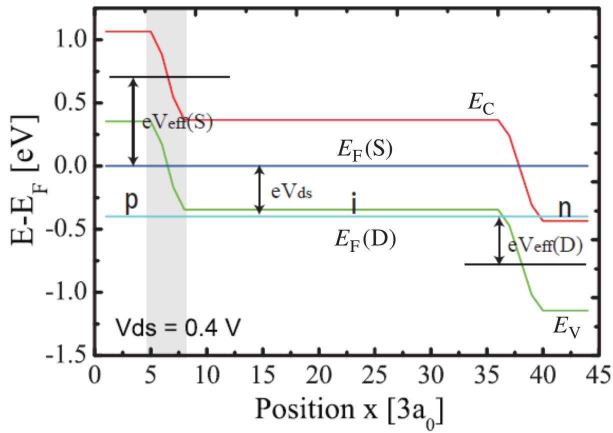

Fig. 1. Sketch of band profile in the p-i-n CNT-TFET structure, where the central channel region is composed of 30 unit cells.

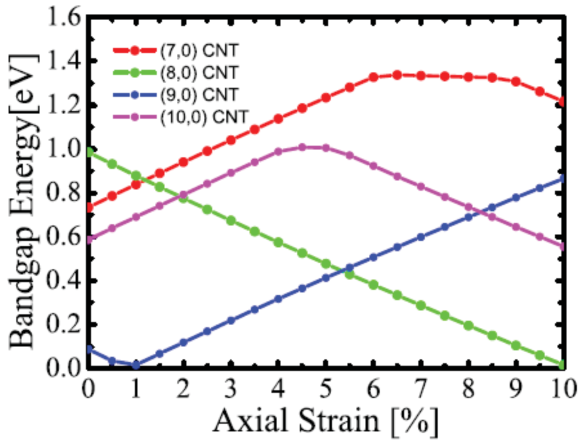

Fig. 2. Strain dependence of the bandgap energy in zigzag CNT with various diameters.

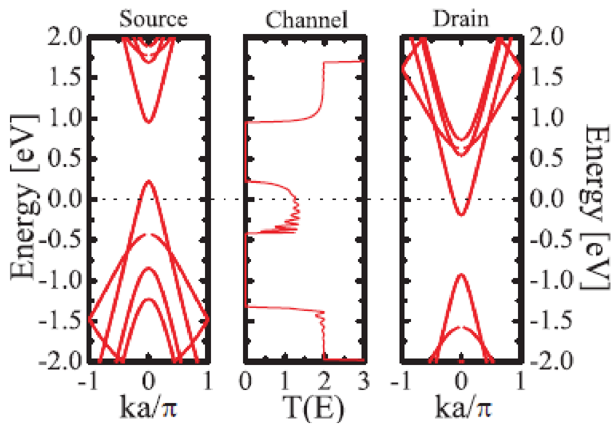

Fig. 3. Band structures in the source (left panel) and drain (right panel) (7,0) CNT electrodes, where the Fermi levels are 0.2 eV below E_V and 0.2 eV above E_C, respectively. The central panel is the transmission probability between two electrodes.

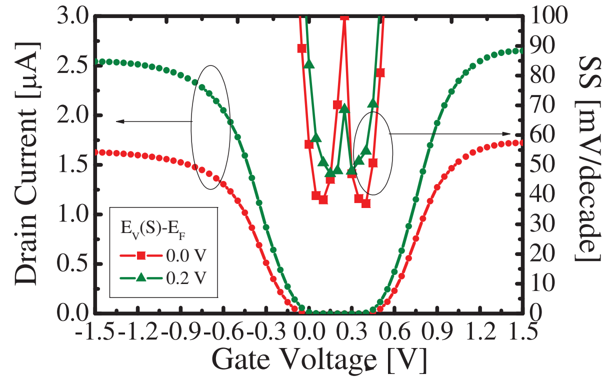

Fig. 4. Gate voltage dependence of the drain current in the absence of the strain. Results for two different doping levels are compared: small and large current magnitudes correspond to the light and heavy doping levels.

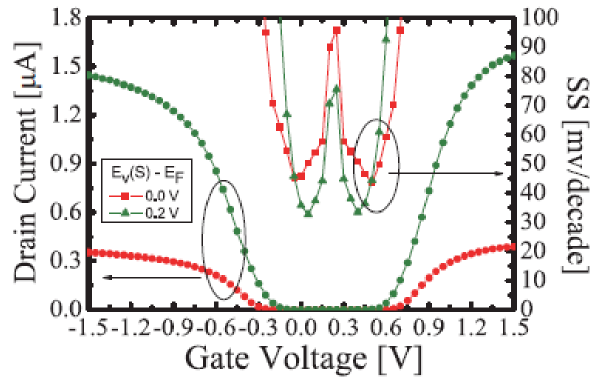

Fig. 5. Gate voltage dependence of the drain current in the presence of 2% axial strain.

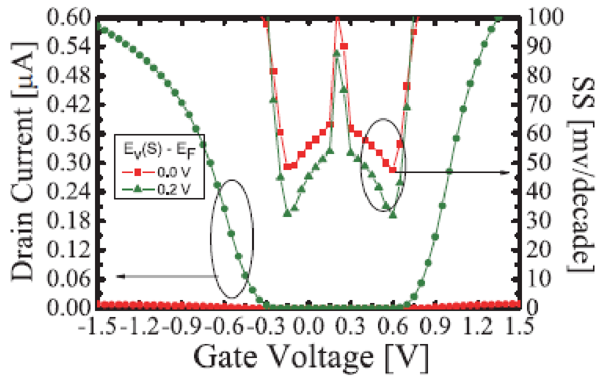

Fig. 6. Gate voltage dependence of the drain current in the presence of 4% axial strain.

Quantum Dynamical Simulation of Photo-Induced Graphene Switch

T. Akiyama, M. Ueyama, E. Nishimura, M. Ogawa, and S. Souma
Department of Electrical and Electronic Engineering, Faculty of Engineering,
Kobe University 1-1 Rokkodai, Nada, Kobe 657-8501, Japan
email: ssouma@harbor.kobe-u.ac.jp

Introduction

The long-continued advance of the performance of information processing technologies has been based on miniaturization of electronic components. Fundamental limits imposed by the laws of physics, however, threaten to halt the continued miniaturization, clouding the future of silicon-based semiconductors. A possible scenario for this "post-miniaturization" is superseded by new material of "graphene", an ultimately monoatomically layered graphite sheet. Although many researchers focus on the ultra-high electron mobility of graphene, absence of the band gap in graphene sets limitation on using for current switching devices. But it have been gradually found out that band gap of graphene can be created by effect of external field or structural change. In this study, we focus on the way of applying a time dependent external field (e.g., laser light irradiation) as a method of modulating electrical characteristic of graphene [1]. With such motivation, we study numerically the effect of laser irradiation on the electronic transport through single layer graphene, where we employ the wave packet dynamics to take into account the effect of laser field with various polarizations irradiated only through the finite channel region of graphene device.

Model and Method

In Fig. 1 we show the schematic illustration of the device assumed in this work. The laser field with the electric field intensity E_0 and the frequency ω is irradiated only through a central finite region of graphene, while the left and the right electrode regions are doped by electrons so that the band structure is shifted lower in energy by 1 eV. In prior to the simulation of electronic transport, the electronic property of the laser irradiated graphene is explored by analyzing the dynamical band structure, which is obtained by Fourier transforming the real time evolution of the wave function for a given set of the $\mathbf{k} = (k_x, k_y)$ (electronic wavenumber), E_0, and ω. The transmission of an electron through the central laser irradiated region is analyzed by the real-time evolution of the incident Gaussian wave packet through the device shown in Fig. 1.

Results and Discussions

As shown in Fig. 2-4, the calculated dynamical band structures are strongly dependent on the polarization of the irradiated light. In particular, the finite bandgap can be induced at the Fermi level $E = 0$ when the circularly polarized light is irradiated as shown in Fig. 4. When such circularly polarized light is irradiated through a finite region of graphene, the incident wavepacket is strongly reflected at the laser irradiated region, in a way dependent on the field intensity E_0.

Conclusion

Our simulations have shown that the transmission through graphene can be significantly modulated by irradiating the laser field with the circular polarization, in a way consistent with the generation of the dynamical band gap by the circularly polarized light plotted. The detailed discussion on the channel length dependence of the transmission will be given in the presentation.

References

[1] T. Oka and H. Aoki, Phys. Rev. B 79, 081406(R) (2010)..

978-3-901578-26-7 © 2013 Society for Micro- and Nanoelectronics

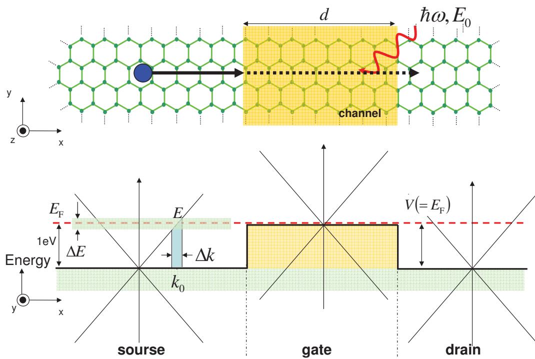

Fig. 1. Schematic illustration of the device assumed in this work. The laser field with the electric field intensity E_0 and the frequency ω is irradiated only through a central finite region of graphene, while the left and the right electrode regions are doped by electrons so that the band structure is shifted lower in energy by 1 eV.

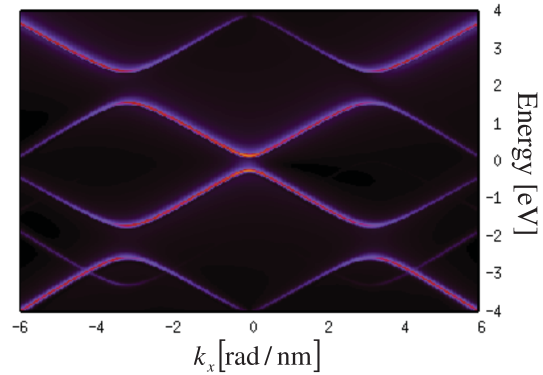

Fig. 4. Dynamical band structure of graphene irradiated by the circularly polarized light with $E_0 = 6.0$ V/nm and $\omega = 6.28$ rad/fs.

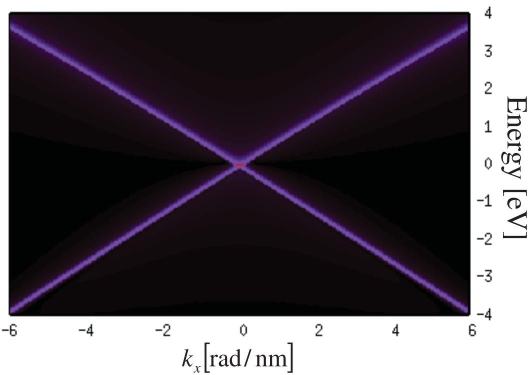

Fig. 2. Dynamical band structure of graphene near the Fermi level $E = 0$ calculated for the vanishing laser field. Brighter color corresponds to the higher intensity of the Fourier transformed wavefunction data.

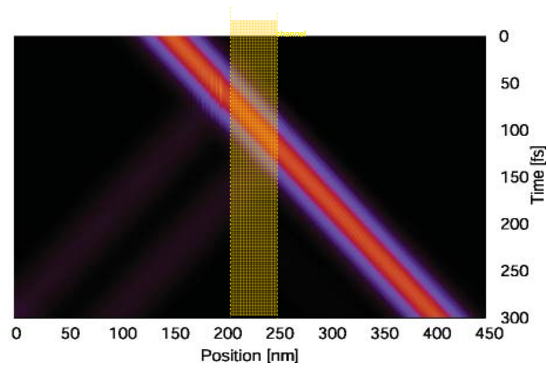

Fig. 5. Time propagation of the Gaussian wave packet through the graphene in the vanishing laser field.

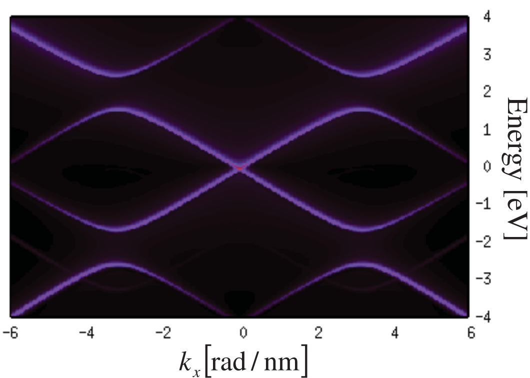

Fig. 3. Dynamical band structure of graphene irradiated by y-polarized light with $E_0 = 6.0$ V/nm and $\omega = 6.28$ rad/fs.

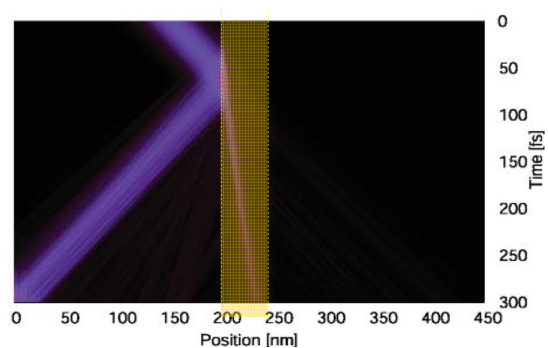

Fig. 6. Time propagation of the Gaussian wave packet through the graphene irradiated by the circularly polarized light through the central shaded region.

Switching Optimization of an Electrically Read- and Writable Magnetic Logic Gate

T. Windbacher, O. Triebl, D. Osintsev, A. Makarov, V. Sverdlov, and S. Selberherr
Institute for Microelectronics, TU Wien, Gußhausstraße 27–29/E360, 1040 Wien, Austria
e-mail: {Windbacher | Triebl | Osintsev | Makarov | Sverdlov | Selberherr}@iue.tuwien.ac.at

Introduction

The continuously growing demand for bigger bulk memory at decreasing prices pushes scaling efforts and leads to the introduction of new device types and materials. Spin based technologies are auspicious due to their fast switching, high endurance, and non-volatility. They additionally permit the use of spin as a degree of freedom to join information storage and processing in a single device, thus enabling a fully non-volatile information processing system. Recently, a fully electrical read-write device out of a ferromagnetic semiconductor has been shown [1]. It was also contemplated to extend this device to a logic XOR gate, which offers the combination of memory storage and logical operations within a single unit. We proposed a way to extend the functional capabilities of the logic gate to further logic functions and carried out a simulation study showing that the switching of the gate is feasible for horizontal as well as diagonal current flow [2] (see Fig. 1). We also found that it is much harder to reset the structure with a diagonal current flow as reliably and fast as for a horizontal current flow, due to the impediment at the constriction connecting the two disks (see Fig. 4). Therefore, we propose an alternative switching path which avoids the passage of the constriction (cf. Fig. 1, Fig. 2, and Fig. 3).

Methods

Analogously to [2] we assume disk radii of 30, 40, and $80\,\mathrm{nm}$, a fixed constriction length and width of $15\,\mathrm{nm}$, a saturation magnetization M_S of $32\,\mathrm{kA/m}$, a cubic anisotropy with the easy axis oriented parallel to the leads and a cubic anisotropy constant K_C of $2\,\mathrm{kJ/m^3}$ for the $(Ga, Mn)As$ film (cf. [3], [4]). Furthermore, to improve the accuracy of the results, all data points shown are an average over several simulations (in the range of $\pm 5\%$ of the corresponding current density) and the error bars depicted in Fig. 5 and Fig. 6 state the respective standard deviation $\pm\sigma$.

Results/Discussion

Comparison between Fig. 5 and Fig. 6 reveals that for an alternative current flow path the switching occurs for a broader range of current densities. At the same time the switching speed has also increased, provided the current densities for the diagonal and alternative flow paths are the same. In general, for higher currents the switching occurs faster. Deviations from this rule are due to the formation of nontrivial spin texture excitations or vortices which delay relaxation of the total magnetization towards its equilibrium orientation. The alternative current flow path also leads to an increase of the switching probability to 65% as compared to 43% for the case of diagonal current flow.

Conclusion

The proposed alternative current flow path enables higher switching speed as well as higher switching probabilities.

Acknowledgment

This research is supported by the European Research Council through the Grant #247056 MOSIL-SPIN.

References

[1] S. Mark, P. Dürrenfeld, K. Pappert, L. Ebel, K. Brunner, C. Gould, and L. W. Molenkamp, "Fully electrical read-write device out of a ferromagnetic semiconductor," *Physical Review Letters*, vol. 106, p. 057204, Jan 2011.
[2] T. Windbacher, O. Triebl, D. Osintsev, A. Makarov, V. Sverdlov, and S. Selberherr, "Simulation study of an electrically read- and writable magnetic logic gate," *Microelectronic Engineering*, 2013.
[3] H. Ohno, A. Shen, F. Matsukura, A. Oiwa, A. Endo, S. Katsumoto, and Y. Iye, "$(Ga, Mn)As$: A new diluted magnetic semiconductor based on $GaAs$," *Appl.Phys.Lett.*, vol. 69, no. 3, pp. 363–365, 1996.
[4] M. Abolfath, T. Jungwirth, J. Brum, and A. H. MacDonald, "Theory of magnetic anisotropy in $\mathrm{III}_{1-x}\mathrm{Mn}_x\mathrm{V}$ ferromagnets," *Physical Review B*, vol. 63, p. 054418, Jan 2001.

 © 2013 Society for Micro- and Nanoelectronics

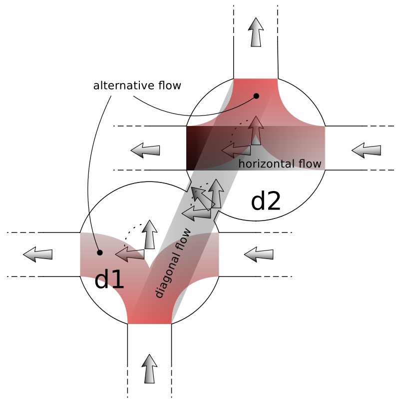

Fig. 1. The magnetization in the leads is fixed and oriented along 180° for the horizontal leads and along 90° for the vertical leads. The disks $d1$ and $d2$ can be set back to their initial magnetization state either by applying a current diagonally passing the constriction or by applying the alternative current path avoiding the constriction. Horizontal current paths were used in [2] to switch $d1$ and $d2$ independently.

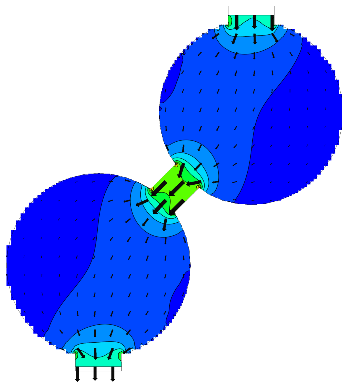

Fig. 2. Current density profile for two 40 nm disks and diagonal flow path.

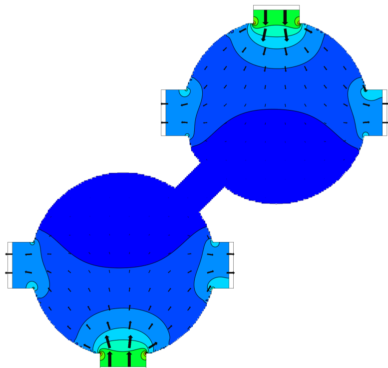

Fig. 3. Current density profile for two 40 nm disks and alternative flow path.

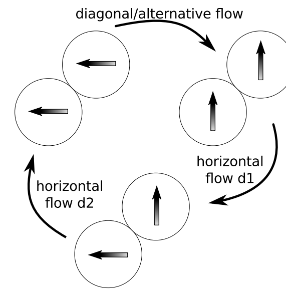

Fig. 4. The different initial and ending states and the corresponding current paths needed for transition between these states are depicted. The cycle begins with both disks exhibiting a magnetization along 90° and applying a horizontal current flow through disk $d1$ to reach the state, where the magnetization in $d1$ is flipped to 180°, while in disk $d2$ the magnetization is still oriented along 90°. From there a horizontal current flow is applied through $d2$ to orient the disk in the same direction as $d1$). In order to reset the two disks to their initial state a diagonal (alternative) flow path through (avoiding) the constriction is applied.

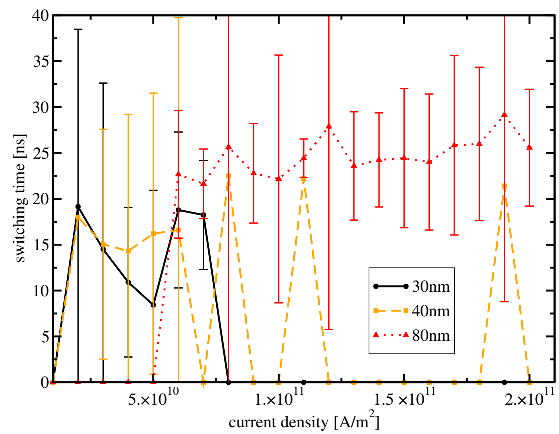

Fig. 5. Switching times for diagonal flow at 30, 40, and 80 nm.

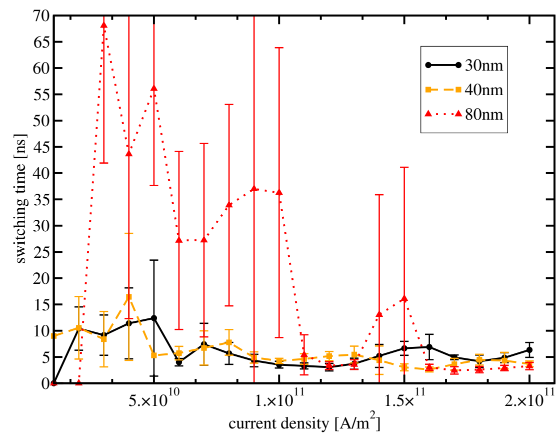

Fig. 6. Switching times for alternative flow at 30, 40, and 80 nm.

Modeling the effect of nanowire size on the piezoelectric nanogenerators output

M. Purahmad, M. A. Stroscio* and M. Dutta
Dept. Electrical and Computer Engineering, University of Illinois at Chicago, Chicago, IL 60607, USA
*Email: stroscio@uic.edu

INTRODUCTION

The emergence of portable and light-weight mobile devices has led to the need for alternative power sources instead of conventional batteries. In many applications such as biomedical drug-delivery implants, implantable medical electronic devices and wireless micro-sensors in remote locations, batteries are not feasible. So harvesting energy from the environment is becoming essential for self-powered devices. One of the promising methods of energy harvesting is the use of piezoelectric materials to capitalize on the ambient vibrations [1-4]. The conversion of mechanical energy to electrical energy has been well demonstrated using piezoelectric cantilever-based MEMS devices [5]. However, the large unit size, large triggering force and specific high resonance frequency of the traditional cantilever-based energy harvesters limit their applicability and adaptability in nanoscale devices and systems. From this point of view, nanostructure materials such as nanowires and nanofibers have been the focus of much research as promising nanogenerators [6]. However, due to the presence of free carrier in semiconductor piezoelectric materials, the physics underlying such semiconductor nanogenerators such as ZnO NWs has not been completely or universally applied [7]. Hence, the application of piezoelectric semiconductor nanowires (NWs) requires a good understanding of their electrical and piezoelectric properties. Herein, one of the main concepts for design of ZnO NWs-based nanogenerators (NGs) is addressed.

RESULTS AND DISCUSSIONS

By determining the piezoelectric induced charge density, in terms of an equivalent density of charges, the effect of piezoelectric charges on the distributed electric potential in the nanowire have been investigated. The surface potential is derived by considering a non-depleted region and a surface depleted region and solving the Poisson equation [8]. Figure 1 shows the surface potential of ZnO NWs with different radii. As shown in case of the ZnO NWs with smaller radius, a higher surface potential is seen. Figure 2 presents the effect of piezoelectric charges on the surface potential of ZnO NWs. The numerical results demonstrate that induced piezoelectric charges result in a stronger surface potential perturbation in ZnO NWs with smaller radius.

CONCLUSION

The effect of ZnO NWs size on surface potential modulation caused by piezoelectric charges was investigated. It was shown that ZnO NWs with a radii around the critical radius are the best candidates for use as nano-generators.

REFERENCES

[1] Z. L. Wang, "Energy Harvesting for Self-Powered Nanosystems," J. Nano Research, vol. 1, pp. 1- 8, 2008.

[2] S. Saadon, O. Sidek, "Ambient Vibration-based MEMS Piezoelectric Energy Harvester for Green Energy Source," IEEE Conference proceeding ICMSAO, 2011.

[3] Sumon Dey, Mohsen Purahmad, Suman Sinha-Ray, Alexander L. Yarin, Mitra Dutta, "Investigation of PVDF-TrFE Nanofibers for Energy Harvesting", Proceeding of 2012 IEEE conference on nanotechnology material and devices conference (NMDC), 2012.

[4] J. Chang, M. Dommer, C. Chang, L. Lin, "Piezoelectric nanofibers for energy scavenging applications," J. Science Direct Nano Energy, vol. 1, pp. 356–371, 2012.

978-3-901578-26-7 © 2013 Society for Micro- and Nanoelectronics

[5] E. E. Aktakka, R. L. Peterson, K. Najafi: 'A Self-Supplied Inertial Piezoelectric Energy Harvester with Power-Management IC', IEEE proceeding of ISSCC, pp. 120-121, 2011.

[6] G. Zhu, R. Yang, S. Wang, and Z. Lin Wang, "Flexible High-Output Nanogenerator Based on Lateral ZnO Nanowire Array", J. Nano Lett. Vol. 10, pp. 3151–3155. 2010,

[7] Alexe M, Senz S, Schubert M A, Hesse D and Gosele U, "Energy Harvesting Using Nanowires?", Adv. Mater. vol. 20 pp.4021–4026, 2008.

[8] Mohsen Purahmad, Michael A Stroscio and Mitra Dutta, "A theoretical study on the effect of piezoelectric charges on the surface potential and surface depletion region of ZnO nanowires", IOP Semicond. Sci. Technol. Vol. 28, no. 1, pp. 015019 (6pp), 2013.

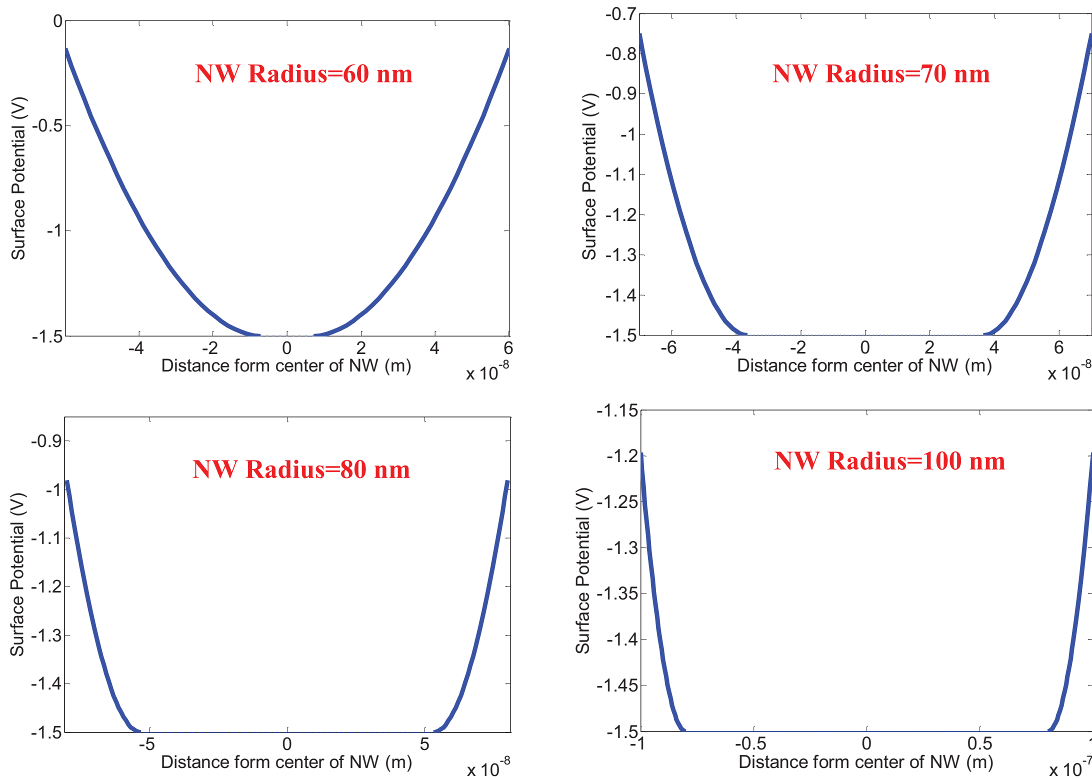

Fig.1. The surface potential of ZnO NWs with different radii.

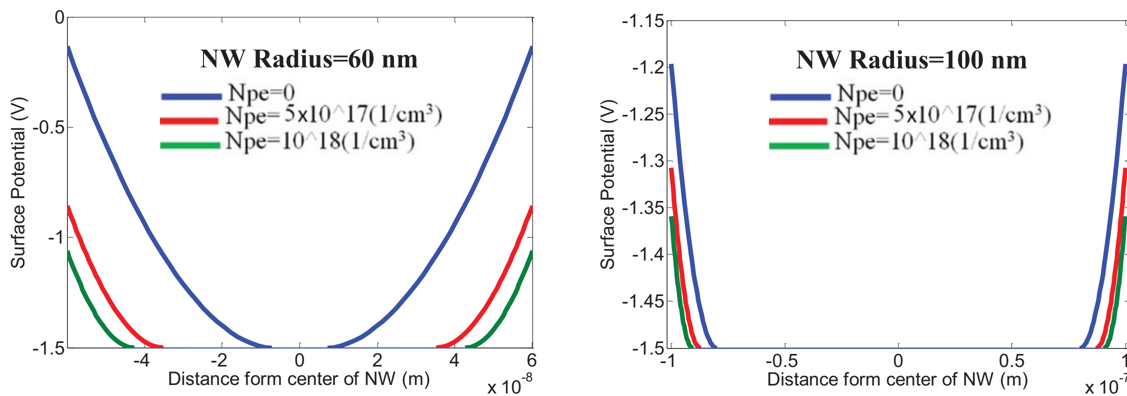

Fig.2. The surface potential of ZnO NWs with two different radius (60 nm and 100 nm) at presence of different piezoelectric charge densities.

Modeling of Current Distribution through Metal-Insulator-Metal Diodes with Tunnel Barrier Roughness

Yuki Hiramatsu*, Nobuya Mori*†, and Yoshinari Kamakura*†
*Graduate School of Engineering, Osaka Univ., 2-1 Yamada-oka, Suita, Osaka 565-0871, Japan
†Japan Science and Technology Agency (JST), CREST, Kawaguchi, Saitama 332-0012, Japan
e-mail: kamakura@si.eei.eng.osaka-u.ac.jp

Since the tunnel current is very sensitive to the tunneling distance, the barrier thickness variability is one of the concerns for integrating the large number of tunnel junctions, e.g., in MRAM [1]. In this study, we numerically investigate the current distribution through metal-insulator-metal diode structures considering the effect of tunnel barrier roughness [2,3], and also discuss the analytical formalism for describing its statistical properties [4] depending on the various parameters.

Figure 1 shows the numerically generated roughness pattern assuming the Gaussian spectral density. We then cut out the samples as shown in Fig. 2, and evaluated the average roughness height $\langle \delta \rangle$ and the average current density $\langle j \rangle$ over each sample area. Figure 3 shows the probability distributions of $\langle \delta \rangle$ plotted as a function of the sample area A. The distributions follow a normal distribution, and the variance $\sigma^2_{\langle \delta \rangle}$ decreases with A due to the statistical averaging effect. Since the spacial correlation is taken into account in the present roughness model, $\sigma^2_{\langle \delta \rangle}$ becomes constant when $A \ll \pi\Lambda^2$ (where Λ is the correlation length), while is inversely proportional to A in the large area limit. As shown in Fig. 4, we have approximated this behavior to the analytical form:

$$\sigma^2_{\langle \delta \rangle} = \Delta^2 [1 + A/(\pi\Lambda)^2]^{-1}. \quad (1)$$

Figure 5 shows the probability distributions of $\langle j \rangle$, exhibiting quite distorted form particularly in the small area samples. Since the tunneling current exponentially depends on the barrier thickness, it is lognormally distributed if the thickness is normally distributed. However, with increasing A, the distribution becomes narrower and symmetric in accordance with the central limit theorem.

To analytically describe such behavior, Fenton-Wilkinson approximation [5] was employed. This assumes that when X_i $(i = 1 \ldots N)$ are distributed according to a lognormal distribution: $X_i \sim LN(\mu, \sigma^2)$, then the sum distribution is well approximated by another lognormal distribution: $\sum_i X_i/N \sim LN(\tilde{\mu}, \tilde{\sigma}^2)$, where

$$\tilde{\sigma}^2 = \ln\left(\frac{e^{\sigma^2}}{N} + 1\right), \quad (2)$$

$$\tilde{\mu} = \mu + \frac{\sigma^2 - \tilde{\sigma}^2}{2}, \quad (3)$$

and μ and σ are the mean and the standard deviation of X_i, respectively. Figure 6 shows the numerically simulated distributions of $\langle j \rangle$ together with the results calculated with Eqs. (1)–(3). Note that the analytical approach well describes not only the area dependent peak positions, but also the tail distributions, which are important information for considering, e.g., the scaling limit of the magnetic tunnel junctions used in MRAM.

References

[1] W. S. Zhao et al., *Failure and reliability analusis of STT-MRAM*, Microelectron. Reliab. **52**, 1848 (2012).
[2] V. Serin et al., *TEM and EELS measurement of interface roughness in epitaxial Fe/MgO/Fe magnetic tunnel junctions*, Phys. Rev. B **79**, 144413 (2009).
[3] K. M. Bhutta, *Characterization of MgO barrier by conducting atomic force microscopy*, Microscopy: Science, Technology, Applications and Education **3**, 2022 (2010).
[4] V. Da Costa et al., *Statistical properties of currents flowing through tunnel junctions*, J. Magn. Magn. Mater. **258-259**, 90 (2003).
[5] L. Fenton, *The sum of log-normal probability distributions in scatter transmission systems*, IRE Trans. Comm. Sys., **8**, 57 (1960).

978-3-901578-26-7 © 2013 Society for Micro- and Nanoelectronics

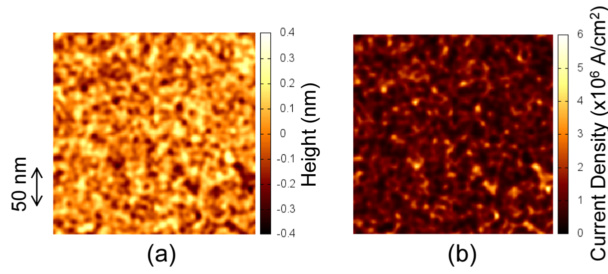

Fig. 1. Roughness pattern generated with a Gaussian spectral density $S(q) = \pi\Delta^2\Lambda^2 \exp(-q^2\Lambda^2/4)$ ($\Delta = 0.1$ nm, $\Lambda = 6$ nm). (a) Distribution of the roughness height $\delta(\mathbf{r})$ and (b) the local current density $j(\mathbf{r})$ are plotted.

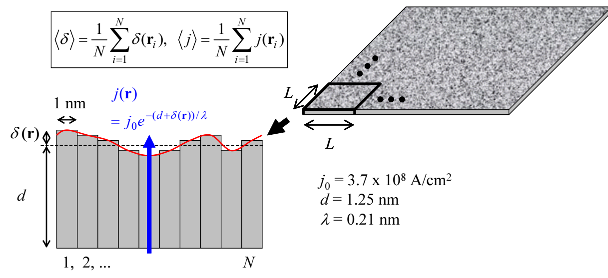

Fig. 2. Calculation method for the distribution of the tunneling current through the samples. (a) The samples with an area of $A = L^2$ are cut out from the generated roughness pattern, and (b) in each sample the average roughness height $\langle\delta\rangle$ and the average current density $\langle j\rangle$ are evaluated by discretizing the sample area into small sections ($\ll \Lambda^2$).

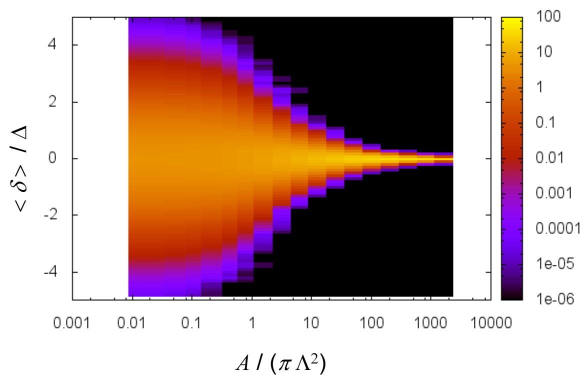

Fig. 3. Probability distributions of the average roughness height $\langle\delta\rangle$ simulated for various sample area A.

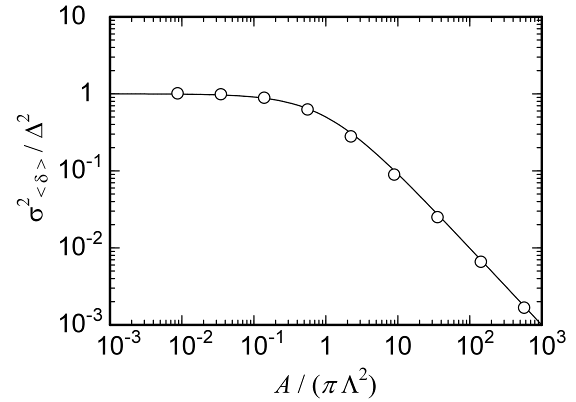

Fig. 4. Variance of $\langle\delta\rangle$ plotted as a function of A. Dots represent the numerical simulation results, which are well fitted by the analytical form given in Eq. (1) (solid line).

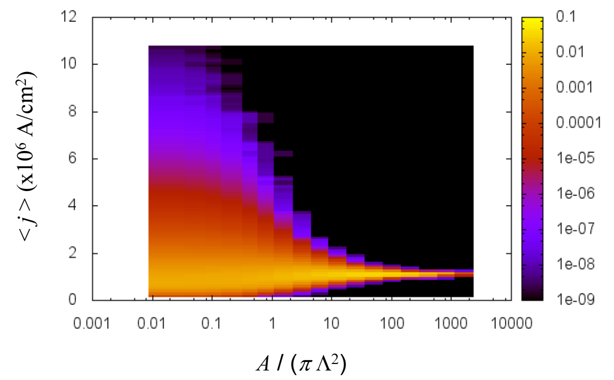

Fig. 5. Probability distributions of the average current density $\langle j\rangle$ simulated for various sample area A.

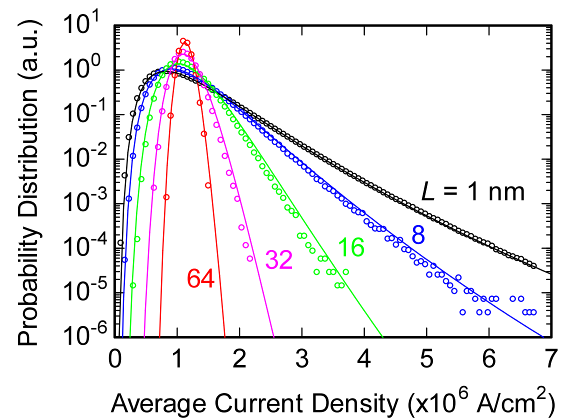

Fig. 6. Probability distributions of $\langle j\rangle$ simulated for various sample size L. Dots represent the numerical simulation results, and the solid lines are the analytically calculated results.

Optimization of Spin-Transfer Torque Magnetic Tunnel Junction-Based Logic Gates

H. Mahmoudi, T. Windbacher, V. Sverdlov, and S. Selberherr
Institute for Microelectronics, TU Wien, Gußhausstraße 27–29/E360, 1040 Wien, Austria
e-mail: {Mahmoudi | Windbacher | Sverdlov | Selberherr}@iue.tuwien.ac.at

INTRODUCTION

By offering zero standby power, non-volatile logic is a promising solution to overcome the leakage losses which have become an important obstacle to scaling of CMOS technology [1]. Magnetic tunnel junctions (MTJs) offer a great potential, because of their unlimited endurance, CMOS compatibility, and fast switching speed. Recently, several realizations of MTJ-based logic gates have been demonstrated using spin-transfer torque (STT) MTJs for which the MTJ devices are used simultaneously as memory and logic gates [2], [3]. This intrinsically enables logic-in-memory architectures with no need for extra hardware [4]. The error probabilities in these gates depend significantly on device and circuit parameters. Here, we present a method to optimize the device and circuit parameters by minimizing the errors.

ERROR PROBABILITY CALCULATION

Fig. 1a and Fig. 1b show the STT-MTJ-based reprogrammable [2] and implication (IMP) [3] logic gates, respectively. Depending on the resistance (logic) states of the input (source) MTJ devices, these gates provide a conditional switching behavior on the output (target) MTJs. The error probability of the realized conditional switching behavior, which is corresponding to a specific Boolean logic operation, depends on the desired switching/non-switching event probabilities as

$$P_{\mathrm{err}} = \frac{1}{N}\sum_{i=1}^{N}\left\{\sum_{j=1}^{n_{\mathrm{u}}} P_{\mathrm{s}}(j) + \sum_{k=1}^{n_{\mathrm{d}}}[1 - P_{\mathrm{s}}(k)]\right\}, \quad (1)$$

where N is the total number of possible input states, n_{u} (n_{d}) is the number of undesired (desired) switching events, and P_{s} is the switching probability of the MTJ defined as [5]

$$P_{\mathrm{s}} = 1 - \exp\left\{-\frac{t}{\tau_0}\exp\left[-\Delta_{\mathrm{I}}\left(1 - \frac{I}{I_{\mathrm{C0}}}\right)\right]\right\}. \quad (2)$$

Δ_{I} is the thermal stability factor associated with the STT switching [6], t is the pulse width, and I is the current flowing through the MTJ. In order to calculate the current (I) passing through each MTJ the bias voltage dependence of the TMR ratio [5] must be taken into account [3].

RESULTS AND DISCUSSION

Fig. 2 shows P_{err} for different logic operations based on the reprogrammable gate as a function of V_{A}. It illustrates that for each operation there is an optimal V_{A} and the AND (NAND) operation demonstrates a lower error probability as compared to the OR (NOR) operation. Similar circuit parameter optimizations can be performed for IMP gate [3].

The minimum in total error probability is because of a trade-off between the probabilities of the desired and undesired switching events as shown in Fig. 3. As the state dependent modulation (SDM) increases with the tunnel magnetoresistance (TMR) ratio, the error probability decreases with the increase of the TMR (Fig. 4). Another important device parameter is Δ_{I} according to (2), higher Δ_{I} provides sharper switching dynamics, smaller SWs, and thus lower error probabilities (Fig. 5).

Note that a larger Δ_{I} is also needed for reliable operation of large STT-MRAM memory arrays [6]. From Fig.4 and Fig.5 we conclude that the implication logic architecture provides smaller error for probabilities logic operation and is thus preferred for logic-in-memory implementation.

ACKNOWLEDGMENT

The work is supported by the European Research Council through the grant #247056 MOSILSPIN.

References

[1] N. S. Kim et al., *Leakage Current: Moore's Law Meets the Static Power*, Computer **36**, pp. 68-75 (2003).

[2] A. Lyle et al., *Magnetic Tunnel Junction Logic Architecture for Realization of Simultaneous Computation and Communication*, IEEE Trans. Magn. **47**, pp. 2970-2973 (2011).

[3] H. Mahmoudi et al., *MTJ-based Implication Logic Gates and Circuit Architecture for Large-Scale Spintronic Stateful Logic Systems*, ESSDERC, pp. 254-257 (2012).

[4] W. Zhao et al., *High Speed, High Stability and Low Power Sensing Amplifier for MTJ/CMOS Hybrid Logic Circuits*, IEEE Trans. Magn. **45**, pp. 3784-3787 (2009).

[5] M. Hosomi et al., *A Novel Nonvolatile Memory with Spin Torque Transfer Magnetization Switching: Spin-RAM*, IEDM Tech. Dig., pp. 459-462 (2005).

[6] E. Chen et al., *Advances and Future Prospects of Spin-Transfer Torque Random Access Memory*, IEEE Trans. Mag. **46**, pp. 1873-1878 (2010).

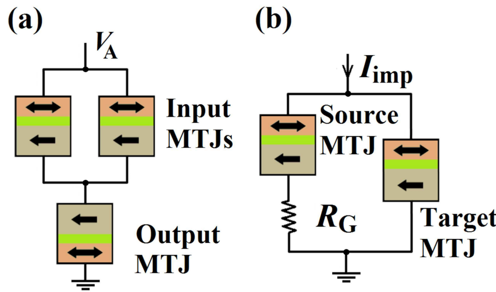

Fig. 1. (a) MTJ-based reprogrammable logic gate [2]. Depending on the preset state of the output MTJ and the polarity and amplitude of the applied voltage (V_A), the result of a logic operation (AND, OR, NAND, or NOR as shown in Fig. 2) between the inputs will be written in the output MTJ. (b) Current-controlled implication [3] logic gate. The resistance states of the target and source MTJs are the logical inputs and the final state of the target MTJ holds the output.

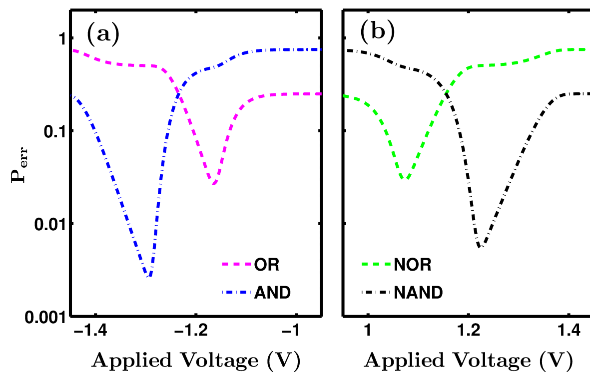

Fig. 2. Average error probabilities for different logic operations using the reprogrammable gate as a function of V_A based on physical MTJ devices characterized in [5]. The value of the circuit parameters (V_A in the reprogrammable gate and I_{imp} and R_G in the IMP gate) can be optimized to minimize the error probability (P_{err}).

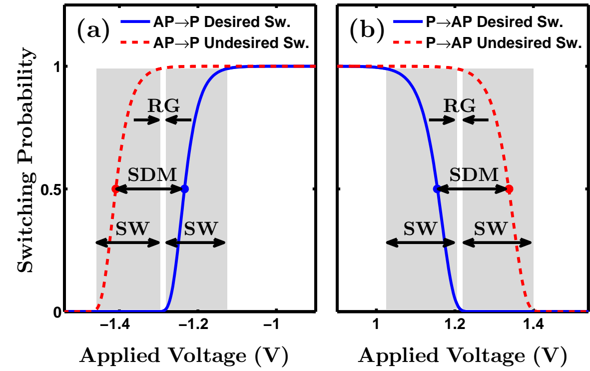

Fig. 3. Switching probabilities of the output MTJ (Fig. 1a) plotted for desired and undesired switching events in AND (a) and NAND (b) operations with the reprogrammable gate. A high enough state dependent modulation (SDM) can open a reliable gap (RG) between the switching windows (SWs).

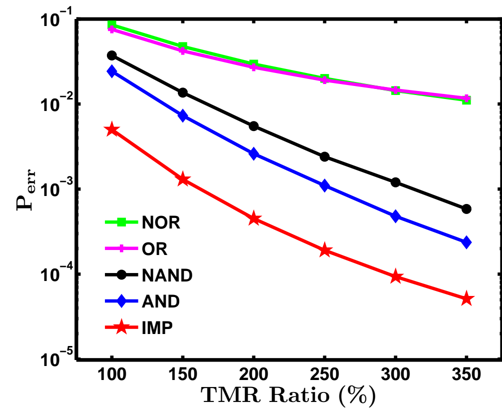

Fig. 4. Average error probabilities for implication and reprogrammable logic gates as a function of the TMR ratio plotted for optimized circuit parameters and $\Delta_I = 40$. Increasing the TMR ratio increases the SDMs shown in Fig. 3. Therefore, it increases RG and thus decreases P_{err}.

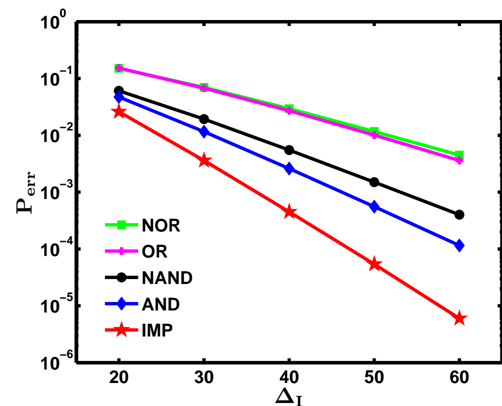

Fig. 5. Average error probabilities for implication and reprogrammable logic gates as a function of Δ_I plotted for optimized circuit parameters and TMR=200%. Increasing Δ_I decreases the SWs shown in Fig. 3 and therefore decreases P_{err}. The implication logic architecture significantly improves the reliability as compared to the reprogrammable logic architecture.

Verification of Simulation Time Improvement for SPICE Simulator using Built-in MTJ Model

H. Koike[1], T. Ohsawa[1], and T. Endoh[1,2,3]
[1] Center for Spintronics Integrated Systems, [2] Graduate School of Engineering,
[3] Center for Innovative Integrated Electronic Systems, Tohoku University,
Aramaki Aza-Aoba 6-6-05, Aoba-ku, Sendai 980-8579, Japan. E-mail: endoh@riec.tohoku.ac.jp

Introduction

In order to introduce spintronics devices into general CMOS LSI design, a high-speed and accurate circuit simulator is highly required. There has been reported an MTJ macro model for SPICE simulator [1]. On the other hand, we have proposed a high-speed SPICE simulator incorporating the model parameters, which describe MTJ's behavior [2]. In this paper, the simulation times are compared for both the developed SPICE simulator, which is a "built-in MTJ model" type, and conventional MTJ simulator, which uses an "MTJ macro model".

Simulators under Evaluation

We take a 2-terminal MTJ, shown in Fig.1, for consideration. Our SPICE simulator with built-in MTJ model can describe DC R-V and switching characteristics of MTJ. An example of MTJ characteristics is shown in Fig. 2. Its model parameters are categorized into 3 levels. Each level supports the following characteristics.

Level 1: only DC R-V.
Level 2: Level 1
+ Switching in Thermal Activation Region.
Level 3: Level 2
+ Switching in Precession Region.

The MTJ characteristics in Fig. 2 are described using level 3 model parameters.

Meanwhile, a simple MTJ macro model was created for evaluation. Figure 3 shows the macro model circuit. It can describe only 2-state resistance switching between Rp (parallel) and Rap (anti-parallel) without the bias dependency of the MTJ resistances, as shown in Fig. 4. In order to support the detailed characteristics like the above-mentioned level 1 to 3, a complicated macro circuit including several tens of components is needed, resulting in obviously requiring much more simulation time than that of the macro circuit composed of only 4 components in Fig. 3.

Simulation and Discussion

Simulations were carried out to compare the simulation time between the SPICE simulator with built-in MTJ model [2] and that with the simple MTJ macro model in Fig. 3. The circuit used in the simulation is shown in Fig. 5. It can perform switching operations of 100 ~ 50000 MTJs using an ideal driver. Simulation time was measured for both two simulators.

Figure 6 shows the simulation result. It can be seen that the simulation time for our built-in MTJ model simulator is below the time for the conventional simulator with the simplest circuit in all cases, even for the highest modelling level 3. This is mainly because the increased internal nodes by the macro model circuit increase the matrix calculation time in the SPICE simulation. Thus the result means that the SPICE simulator with built-in MTJ model has an essential advantage in simulation speed and accuracy, compared to that with the MTJ macro model.

Conclusion

The SPICE simulator with built-in MTJ model is advantageous in simulation time and accuracy compared to the simulator with MTJ macro model.

Acknowledgement

This research was supported by the JSPS through the FIRST Program.

References

[1] J. D. Harms et al, *IEEE Transactions on Electron Devices*, vol.57, no. 6, pp. 1425-1430, Jun. 2010.
[2] N. Sakimura et al, *2012 IEEE International Symposium on Circuits and Systems (ISCAS)*, pp. 1971-1974.
[3] K. Yagami et al, *IEEE Transactions on Magnetics*, vol.41, no. 10, pp. 2615-2617, Oct. 2005.

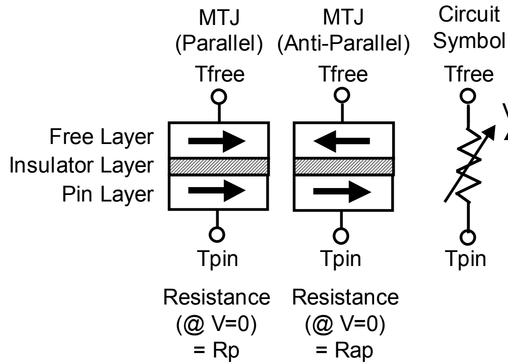

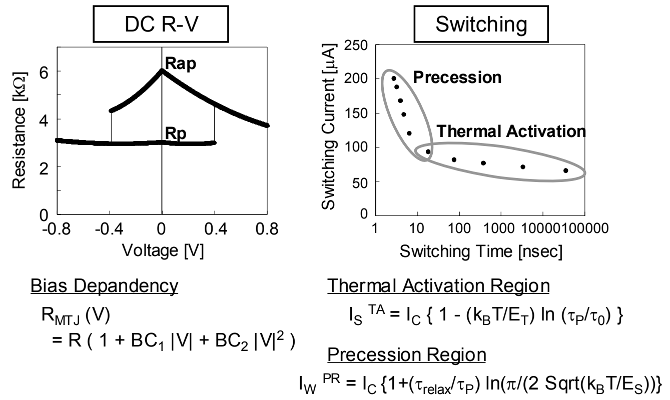

Fig. 1. 2-terminal MTJ device. An MTJ is composed of Free/Insulator/Pin layers. If the magnetization directions for Free and Pin layers are parallel, the resistance is Rp. If they are anti-parallel, then the resistance is Rap (Rap>Rp).

Fig. 2. MTJ characteristics supported by the developed SPICE simulator with "built-in MTJ model" [2]. The switching model equations for both thermal activation and precession region are reported in reference [3].

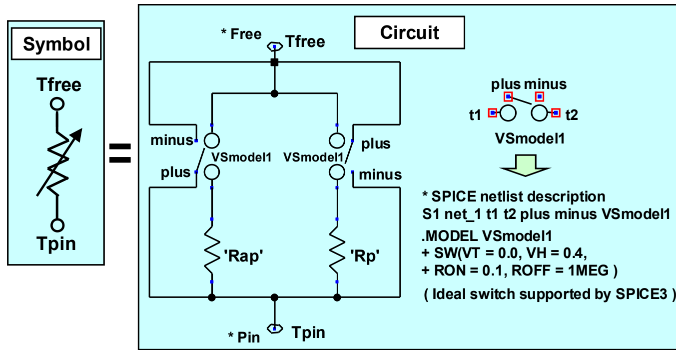

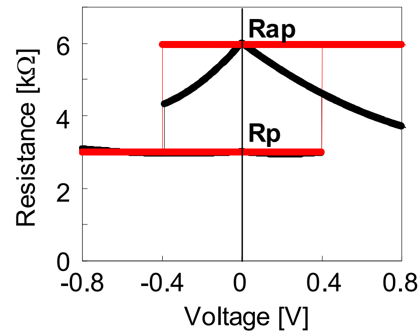

Fig. 3. Simple MTJ macro model circuit. It uses 2 linear resistors and 2 ideal switches supported by SPICE3. Simple 2-state switching can be described by this circuit.

Fig. 4. DC R-V characteristics simulated using the SPICE with built-in model (black line) and the SPICE with macro model (red line).

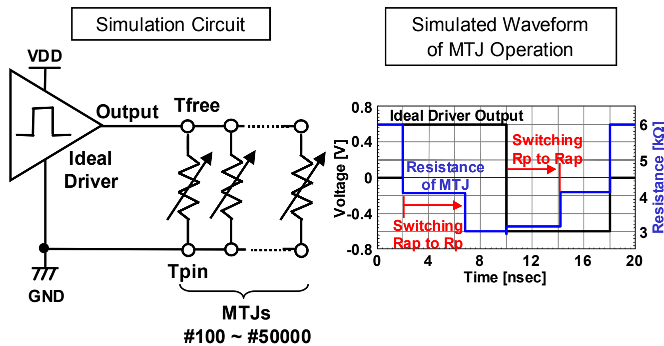

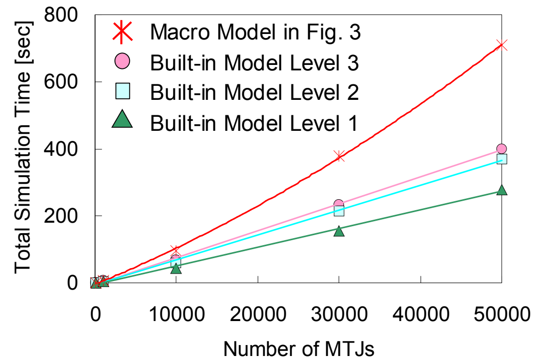

Fig. 5. Simulation circuit and its typical simulated waveforms, which show Rap to Rp switching followed by Rp to Rap switching.

Fig. 6. Simulation result. In case of 30000 MTJs, for example, about 38% simulation time reduction is achieved by our built-in model simulator, although our built-in MTJ model simulator uses level 3 model and macro model simulator uses the simplest model as shown in Fig.3.

A Model Reflecting Preheat Effect by Two-step Writing Technique for High Speed and Stable STT-MRAM

Y. Yoshida[1], H. Koike[3], M. Muraguchi[1], S. Ikeda[2, 3], T. Hanyu[2, 3], H. Ohno[2, 3], and T. Endoh[1, 3, 4]
[1]Graduate School of Engineering, Tohoku University
[2]Research Institute of Electrical Communication, Tohoku University
[3]Center for Spintronics Integrated Systems, Tohoku University
[4]Center for Innovative Integrated Electronic Systems, Tohoku University
Aramaki Aza-Aoba 6-6, Aoba-ku, Sendai, Japan 980-8579, E-mail: endoh@riec.tohoku.ac.jp

INTRODUCTION

Spin-transfer-torque MTJ based STT-MRAMs gather attention as nonvolatile working memory candidate. Especially, low switching current, high TMR, high thermal stability are available even at 40nm size by CoFeB/MgO based perpendicular MTJ (pMTJ) [1]. However, large current is needed to improve the switching probability as the write pulse width decreases. For this issue, a two-step writing method demonstrates that the switching characteristics are improved by a base pulse which preheats MTJ [2]. However, a model reflecting a preheat effect by two-step writing is necessary for optimization of a base pulse of two-step pulse. In this paper, a switching probability model reflecting an intrinsic critical current dependence on temperature is proposed to consider the preheat effect by base pulse.

RESULT AND DISCUSSION

Fig.1 shows R-H curve of measured CoFeB/MgO based pMTJ (100nmφ). Fig.2 (a) shows schematic pulse waveform applied to pMTJ. Pulse application trials were performed 50 times for each pulse condition in the switching probability measurement. Fig.2 (b) shows a schematic measurement setup. In this setup, current flowing through MTJ is observed as a voltage at an oscilloscope. Fig.3 shows an example of observed waveform which MTJ switched from parallel (P) state to anti-parallel (AP) state. We evaluated P→AP direction here. Fig.4 shows switching probabilities. In Fig.4, the plotted point is the measured result by two-step writing. The dashed line is the switching probability calculated from the switching probability in thermal activation region [3]

$$P(t_p) = 1 - \exp\left[-\left(\frac{t_p}{\tau_0}\right)\exp\left\{-\frac{E_b}{k_B T}\times\left(1-\frac{J}{J_{C0}}\right)\right\}\right] \quad (1)$$

Here, T is temperature, J is critical current density, J_{C0} is intrinsic critical current density, E_b is energy barrier, k_B is Boltzmann's constant, t_p is switching pulse width, and τ_0 is attempt time. τ_0 was assumed as 1ns. However, the calculated switching probability from eq. (1) is not matched to the measured probability. We assumed that this is because the preheat effect by base pulse is not conciderd. To evaluate the preheat effect due to base pulse, we took account for the temperature dependence of I_{C0} in eq. (1). We measured the I_{C0} (Fig.5). By substituting this temperature dependence to eq. (1), the switching probability is expressed as,

$$P(t_p) = 1 - \exp\left[-\left(\frac{t_p}{\tau_0}\right)\exp\left\{-\frac{E_b}{k_B T}\times\left(1-\frac{I}{-0.97\times(T-273)+288}\right)\right\}\right] \quad (2)$$

To evaluate the preheat effect due to base pulse, the temperature T in eq. (2) was fitted to the measured result by changing T. We estimated the preheated effect was 14K (solid line in Fig.6).

CONCLUSION

The model which reflect the preheat effect by two-step writing was proposed. In this model, the I_{C0} dependence on temperature was took account. We considered that the calculated switching probability was well fitted to the measured result with this model.

ACKNOWLEDGEMENT

This research is supported by JSPS through FIRST Program.

REFERENCES

[1] S. Ikeda, et al., Nat. Mater., **9**, 721 (2010).
[2] F. Iga, et al., SSDM, 963 (2011).
[3] Z. Diao et al., J. Phys. Condens. Matter 19 165209 (2007).

978-3-901578-26-7 © 2013 Society for Micro- and Nanoelectronics

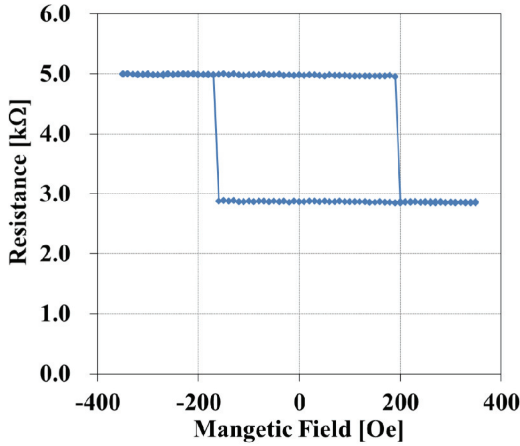

Fig. 1. R-H characteristic of measured MTJ.

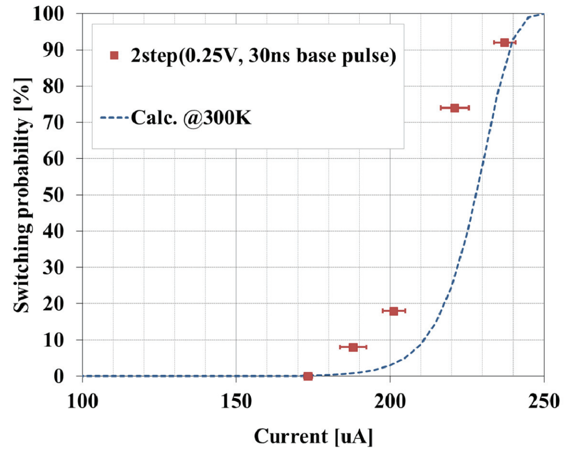

Fig. 4. Switching probabilities by two-step writing (P→AP).

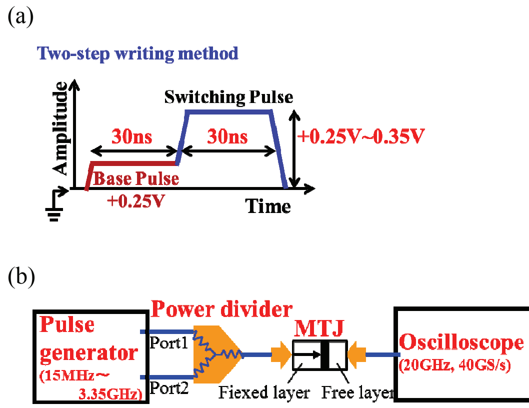

Fig. 2. (a) Schematic applied pulse. (b) Measurement setup.

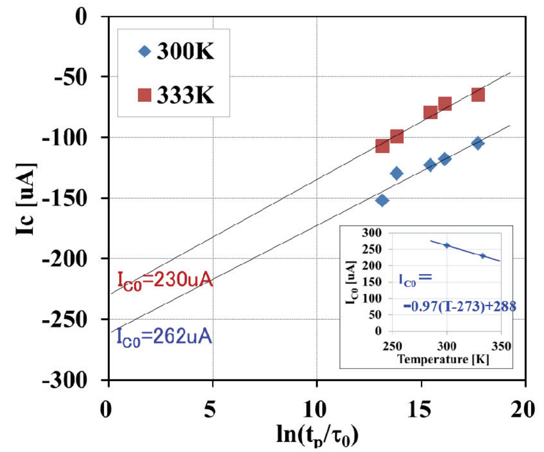

Fig.5. Critical current (I_C) vs. of $\ln(t_p/\tau_0)$. Inset is the intrinsic critical current (I_{C0}) dependence on temperature.

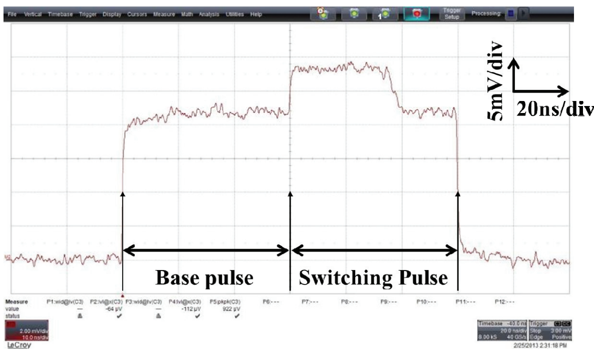

Fig. 3. Example of observed switching waveform (P→AP).

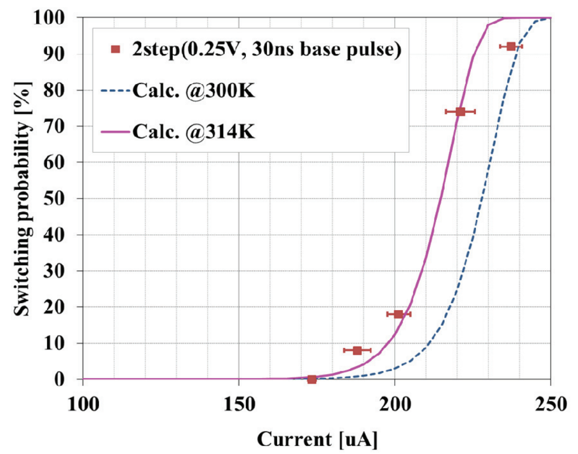

Fig. 6. Switching probabilities by two-step writing and the switching probability calculated by eq.(1) and eq.(2).

Structural and Electronic Properties of Threading Screw Dislocations in GaN

M. Matsubara, J. Godet*, L. Pizzagalli*, and E. Bellotti
Department of Electrical and Computer Engineering, Boston University,
8 Saint Mary's Street, Boston, Massachusetts 02215, USA
*Institut P′, UPR 3346 CNRS/Université de Poitiers, SP2MI, BP 30179,
86962 Futuroscope Chasseneuil Cedex, France
e-mail: matsubar@bu.edu

GaN is a promising material for applications to power electronics devices with its favorable high field and thermal transport properties [1]. However, the presence of high density of threading dislocations ($> 10^8$ cm^{-2}) in GaN is problematic. They limit the performance of power devices by reducing the photoluminescence intensity and the electron mobilities, and may end up leading to premature device breakdown. Therefore it is important to evaluate their impact on device performance and reliability. Here we focus on threading screw dislocation, which is a non-radiative recombination center with deep electronic states in the band gap, with different types of core structures and evaluate their energetics by the first-principles method using hybrid Hartree-Fock density functionals.

The core structure of threading screw dislocations in GaN is still under debate. Recently a new configuration of screw dislocation core is introduced by Belabbas *et al.* [2], where the dislocation line is located at the middle of bonds connecting two adjacent projected hexagons ("B" core), while it is located at the center of projected hexagon in the conventional screw core configuration ("A" core, see Fig. 1). We have investigated this new "B" full core structure as well as several types of "A" core structures: full (6:6), open (0:0), Ga-filled (6:0) and N-half-filled (6:3) structures, where the numbers in parenthesis, (n_{Ga}:n_{N}), denote the numbers of Ga and N atoms remaining in the core region.

Our calculations are performed using the projector augmented wave method with the Perdew-Burke-Ernzerhof (PBE) functional and Heyd-Scuseria-Ernzerhof (HSE) functional [3] implemented in the VASP code [4]. Ga $3d$ electrons are considered as valence electrons and energy cutoff is set to 425 eV. Our fully periodic supercell accommodates dislocation dipole and contains up to 288 atoms of Ga and N. The supercell for "A" open core structure is shown in Fig. 2.

Relative formation energies are shown in Fig. 3, which are calculated based on the Northrup formalism [5] and are expressed as a function of the Ga chemical potential (μ_{Ga}). In N-rich growth condition (at -1.17 eV) the most stable structure is the "B" full core. This result is consistent with the one by Belabbas *et al.*, who insist it is the most stable under any growth conditions within their calculations based on local density approximation [2]. However, in Ga-rich growth condition (at 0 eV), contrary to the findings by Belabbas *et al.*, the most stable structure is the Ga-filled (6:0) "A" core, which is originally proposed by Northrup [5]. We will show the detailed structural properties of these stable dislocation configurations and the electronic properties including their band structures calculated using the HSE hybrid functional (see Fig. 4).

References

[1] J. L. Hudgins, G. S. Simin, E. Santi, and M. Asif Khan, *An Assessment of Wide Bandgap Semiconductors for Power Devices*, IEEE Trans. Power Electronics **18**, 907 (2003).
[2] I. Belabbas, J. Chen, and G. Nouet, *A new atomistic model for the threading screw dislocation core in wurtzite GaN*, Computational Materials Science **51**, 206 (2011).
[3] J. Heyd, G. E. Scuseria, and M. Ernzerhof, *Hybrid functionals based on a screened Coulomb potential*, J. Chem. Phys. **118**, 8207 (2003); **124**, 219906(E) (2006).
[4] G. Kresse, and J. Furthmüller, *Efficient iterative schemes for ab initio total-energy calculations using a plane-wave basis set*, Phys. Rev. B **54**, 11169 (1996).
[5] J. Northrup, *Theory of intrinsic and H-passivated screw dislocations in GaN*, Phys. Rev. B **66**, 045204 (2002).

978-3-901578-26-7 © 2013 Society for Micro- and Nanoelectronics

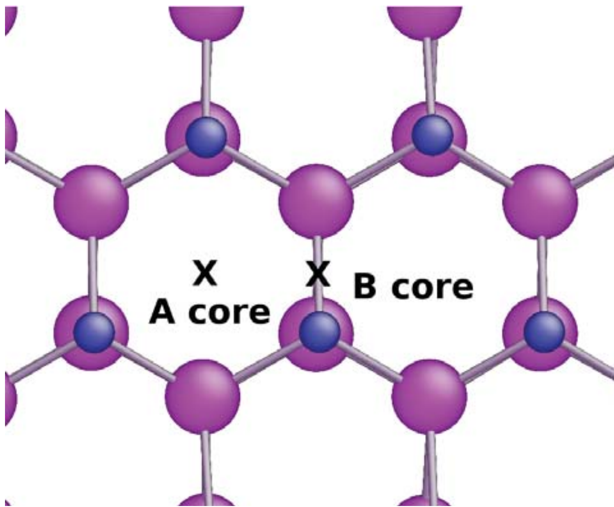

Fig. 1. Two different core configurations for threading screw dislocation projected onto the (0001) plane. The positions of dislocation lines are denoted by the cross marks. The "A" core is located at the center of projected hexagon and "B" core is at the middle of bonds connecting two adjacent hexagons.

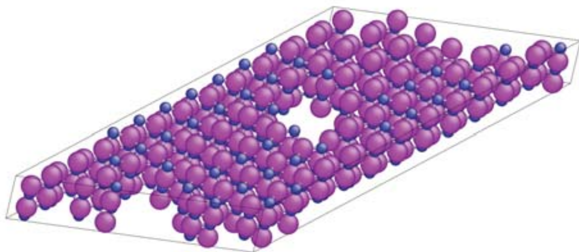

Fig. 2. Three dimensional view of our periodic supercell containing two open core screw dislocations.

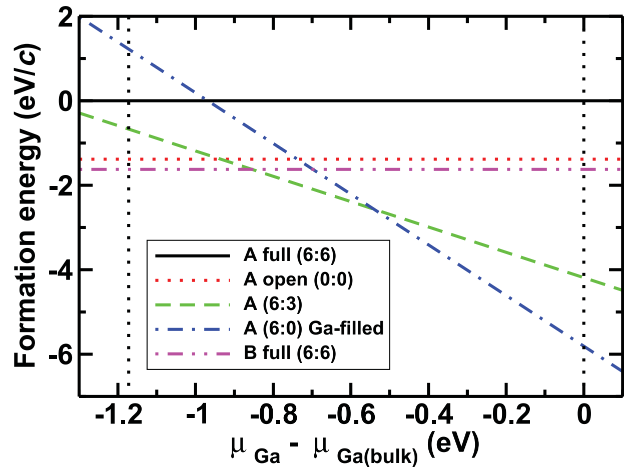

Fig. 3. Relative formation energies of different core structures as a function of the Ga chemical potential. The dotted vertical bars at 0 eV and -1.17 eV denote the Ga-rich limit and the N-rich (Ga-poor) limit, respectively.

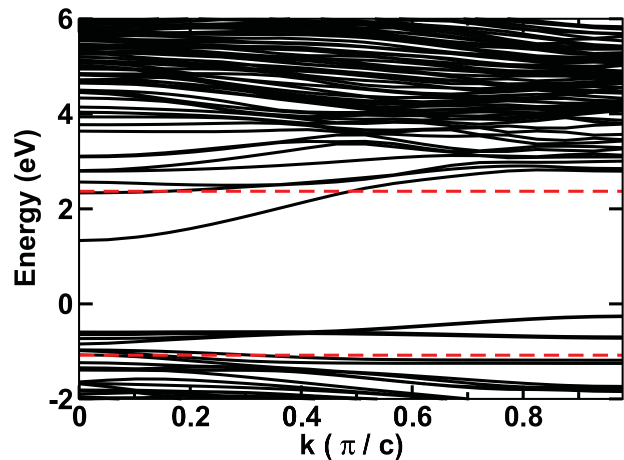

Fig. 4. Band structures of screw "B" core configuration along the [0001] direction calculated by HSE. Fermi energy is located at 0 eV. The red dashed lines at −1.1 eV and −2.4 eV correspond to the valence band maximum and the conduction band minimum of bulk (without dislocation) GaN, respectively.

Dependence of gate-to-drain distance on electron velocity in AlN/GaN HEMTs

Kazuki Kodama, Hirokuni Tokuda, and Masaaki Kuzuhara
Graduate School of Engineering, University of Fukui, 3-9-1 Bunkyo, Fukui, 910-8507, Japan
e-mail: k.kodama59@gmail.com

INTRODUCTION

GaN-based high-electron-mobility transistors (HEMTs) are receiving a considerable attention for ultra-high frequency applications [1]. A current gain cutoff frequency of 343 GHz has been achieved for the AlN/GaN HEMT with a scaled gate length of 20 nm [1]. For high frequency performance, the importance of scaling in gate length and source-to-drain distance has been pointed out. However, there is no theoretical study with respect to the impact of access region length.

In this paper, dependence of gate-to-drain distance on channel electron velocity has been investigated using a 2-D Monte Carlo simulator based on full-band model for AlN/GaN HEMTs. The results demonstrated enhanced velocity overshoot effects by the shrinkage gate-to-drain distance below 100 nm.

CALCULATION MODEL AND DEVICE STRUCTURE

In our full-band device model, Boltzmann transport equation was solved using an ensemble Monte Carlo algorithm coupled with 2-D Poisson equation. Band structures for wurtzite GaN, AlN, and AlGaN have been calculated based on an empirical pseudopotential method [2, 3]. The reciprocal wave vectors of 147 were employed for Fourier series expansions of the wave function.

Figure 1 shows band structure in GaN (a) and AlN (b). The bottom of conduction band was assumed to be electron energy of 0 eV. The scattering mechanisms considered were acoustic phonon scattering, polar and non-polar optical phonon scattering, and piezoelectric scattering [4].

Figure 2 shows the schematic cross section of an AlN/GaN/AlGaN HEMT simulated in this work. The structure consists of 3 nm undoped AlN top barrier, 20 nm undoped GaN channel, and 500 nm undoped $Al_{0.08}Ga_{0.92}N$ back barrier. The gate-to-drain distance (L_{gd}) was varied from 10 to 500 nm. For simplicity, source and drain ohmic contacts were placed directly on the channel layer.

RESULTS AND DISCUSSION

Figure 3 presents calculated I-V characteristics for the device with L_{gd} of 40 nm and L_g of 20 nm. The maximum drain current exceeded 4 A/mm at V_{GS}=2 V and V_{DS}=2 V. The peak transconductance was over 2 S/mm.

Figure 4 shows calculated potential distribution (V_{GS}=0.5 V and V_{DS}=5 V). The crowding in electric field is clearly observed near the gate edge in the drain side. At high electric fields (more than 3 MV/cm), band transition of hot electrons was observed from 1 to 2 (not shown here).

Figure 5 plots the channel electron velocity as a function of distance from the gate edge for varying L_{gd} from 10 to 200 nm. It was found that velocity overshoot effects are enhanced for devices with L_{gd} of sub-100 nm. A peak velocity of $7\text{x}10^7$ cm/s was achieved for L_{gd} =10 nm.

CONCLUSION

Full-band Monte Carlo simulations have been performed for AlN/GaN/AlGaN DH-HEMTs. The results demonstrated that the reduction in gate-to-drain distance is effective to enhance the velocity overshoot effect.

ACKNOWLEDGEMENT

This work was performed as a part of the project named “Development of Nitride-based Semiconductor Crystal Substrate and Epitaxial Growth Technology” by NEDO.

REFERENCES

[1] K. Shinohara et al., IEDM Tech. Dig. **453** (2011) 19.1.1..
[2] J. Chelikowskyl et al., J. Appl. Phys. **79** (1996) 2786.
[3] I. H. Oguzman et al., J. Appl. Phys. **80** (1996) 4429.
[4] S. Yamakawa et al., J. Comp. Electronics **2** (2003) 481.

978-3-901578-26-7 © 2013 Society for Micro- and Nanoelectronics

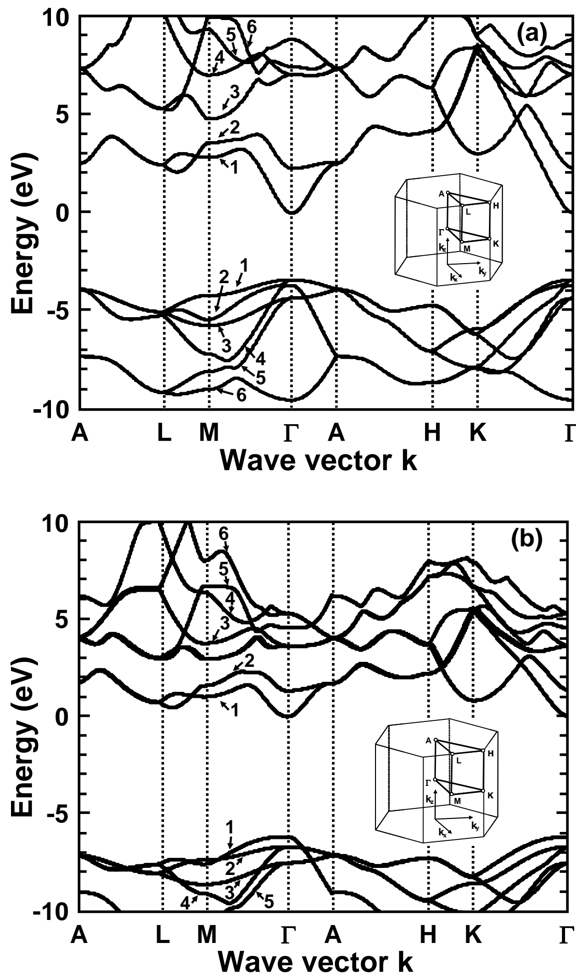

Fig. 1 Empirical pseudopotential band structure in wurtzite (a) GaN and (b) AlN. The insert in Fig. (a) shows the first Brillouin zone in wurtzite structure.

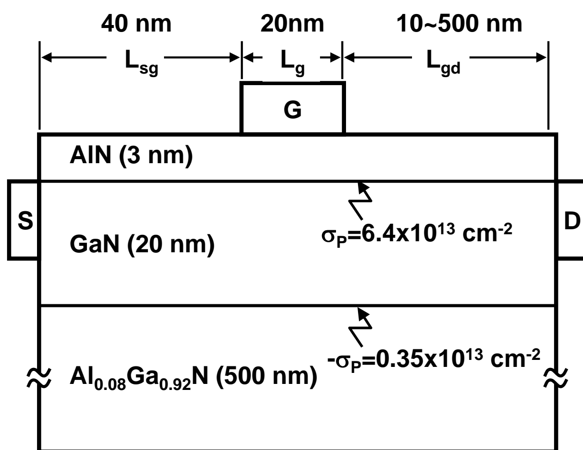

Fig. 2 Cross section of device structure simulated in this work. Neumann condition at all semiconductor surfaces was assumed to solve Poisson equation. The metal semiconductor interfaces was calculated based on Dirichlet condition.

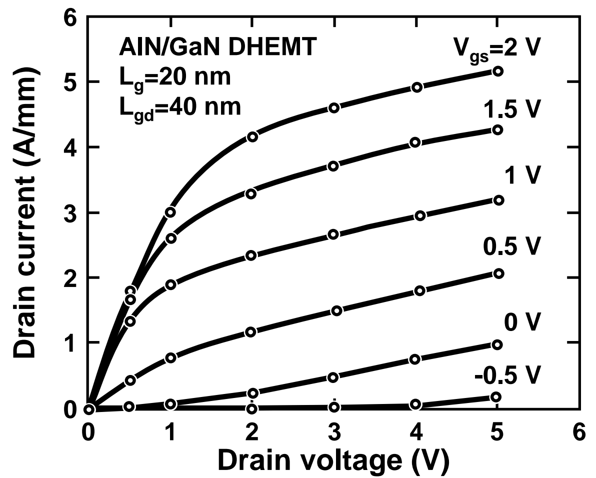

Fig. 3 I-V characteristics for AlN/GaN DHEMT with L_{gd} of 40 nm.

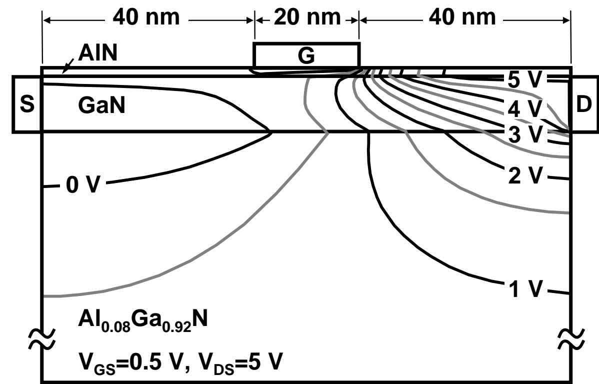

Fig. 4 Calculated potential distribution at V_{GS}=0.5 V and V_{DS}=5 V for the device with L_{gd} of 40 nm. The solid lines indicate equipotential with step of 0.5 V

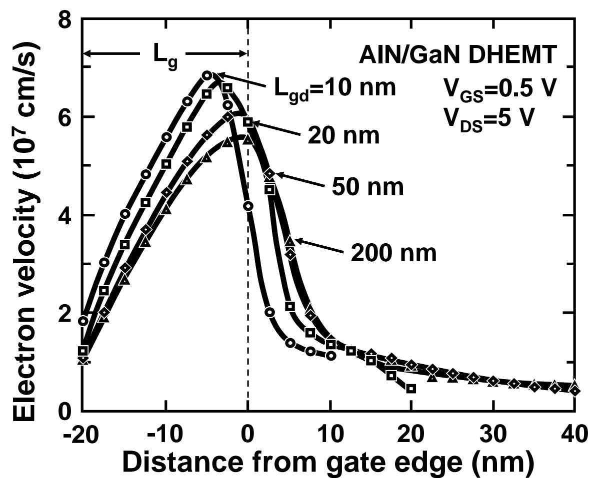

Fig. 5 Channel electron velocity as a function of distance from the gate edge for varying L_{gd} from 10 to 200 nm. Circle indicates the device with L_{gd} of 10 nm, square is L_{gd}= 20 nm, diamond is L_{gd}= 50 nm, and triangle is L_{gd}= 200 nm.

A Full-band Monte-Carlo Study of Carriers Transport in III-Nitrides Alloys

E. Bellotti*, S. Shishehchi*, and F. Bertazzi†
*ECE Department, Boston University, 8 Saint Mary's Street, 02215 Boston, MA
†DELEN and IEIIT-CNR, Politecnico di Torino, corso Duca degli Abruzzi 24, 10129 Torino, Italy
e-mail: bellotti@bu.edu

GaN and its compounds have made inroads into the application spaces normally dominated by both conventional III-V semiconductors and silicon. The availability of a rich family of ternary and quaternary alloys makes it possible to tailor these semiconductors to work as light emitters and detectors from the near infrared to the deep UV. Furthermore, the favorable high field transport properties make GaN and its ternary alloys materials of choice for a new generation of power devices that can enable the practical implementation of smart grids for energy distribution. In spite of these high expectations, significant problems exist, not only from the technological stand point but also due to the lack of understanding of the properties of this material system. In particular the knowledge of the high-field carrier transport coefficients, is sketchy at best. Consequently, understanding the carrier transport characteristics of $Al_xGa_{1-x}N$, $In_xAl_{1-x}N$, $In_xGa_{1-x}N$ alloys is one of the critical step needed to be able to design high voltage solid state switches, rectifiers, detectors and light emitters. The goal of this work is to present the results of a full band Monte Carlo (FBMC) investigation of the carrier transport and impact ionization processes in AlGaN, InGaN and AlInN alloys. Furthermore, we will elucidate the reasons that lead to a single carrier multiplication processes in some of these alloys.

Using a full-band Monte Carlo model we have computed[1] the carrier impact ionization coefficients in $Al_xGa_{1-x}N$ for seven alloy compositions between $x = 0$ (GaN) and $x = 1.0$ (AlN). We have found that holes dominates the impact ionization process for compositions below 50%, while electrons dominate for larger aluminum contents. The model also predicts that, due to the particular features of the $Al_xGa_{1-x}N$ valence band structure, holes impact ionization processes are effectively negligible for aluminum composition above 60%. Furthermore, we find that the electron-alloy scattering significantly reduces the electron ionization coefficients leading to the dominant behavior of holes in for an aluminum composition below 50%.

We have computed the electronic structure and developed a transport model for $In_{0.18}Al_{0.82}N$ that is lattice-matched to GaN[2]. Using this approach we have evaluated the electron and hole mobilities and drift velocities. We have found that the mobilities and drift velocity of both carriers are limited by the alloy scattering phenomenon. We have found that the hole impact ionization process is suppressed for this alloy composition. This is due to the particular features of the $In_{0.18}Al_{0.82}N$ valence band structure. Furthermore, we find that the electron-alloy scattering significantly reduces the electron ionization coefficients both for transport along the Γ-A and Γ-M direction.

ACKNOWLEDGMENT

This works has been supported by the U.S. Army Research Laboratory through the Collaborative Research Alliance (CRA) for MultiScale multidisciplinary Modeling of Electronic materials (MSME).

REFERENCES

[1] E. Bellotti and F. Bertazzi, "A numerical study of carrier impact ionization in $Al_xGa_{1-x}N$," *J. Appl. Phys.*, vol. 111, no. 10, p. 103711, 2012.
[2] S. Shishehchi, F. Bertazzi, and E. Bellotti, "A Full Band Monte-Carlo Study of Carrier Transport Properties of InAlN Lattice Matched to GaN," in *SPIE Photonics West, Physics and Simulation of Optoelectronic Devices XXI*, vol. 8619 Proceedings of the SPIE, San Francisco, CA, Jan. 2013.

978-3-901578-26-7 © 2013 Society for Micro- and Nanoelectronics

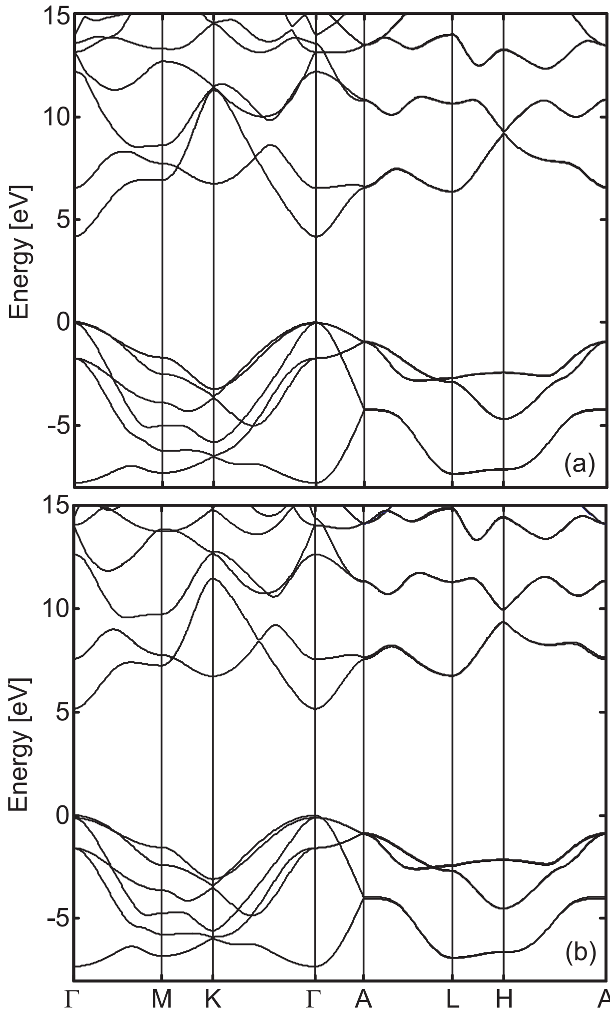

Fig. 1. Calculated electronic structure of (a) $Al_{0.4}Ga_{0.6}N$ and (b) $Al_{0.8}Ga_{0.2}N$

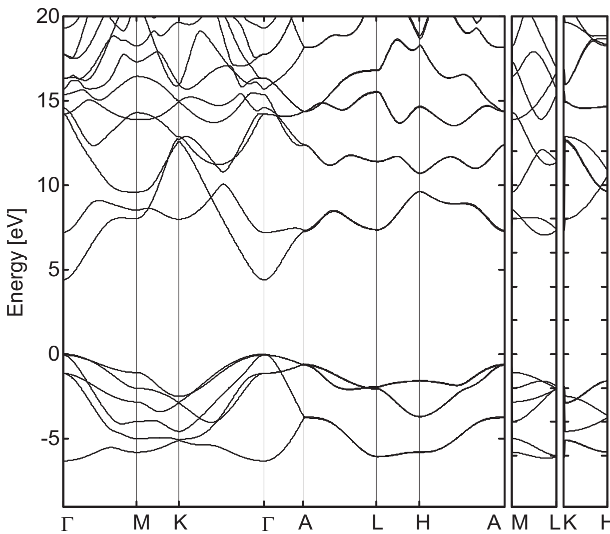

Fig. 2. Calculated electronic structure of $In_{0.18}Al_{0.82}N$

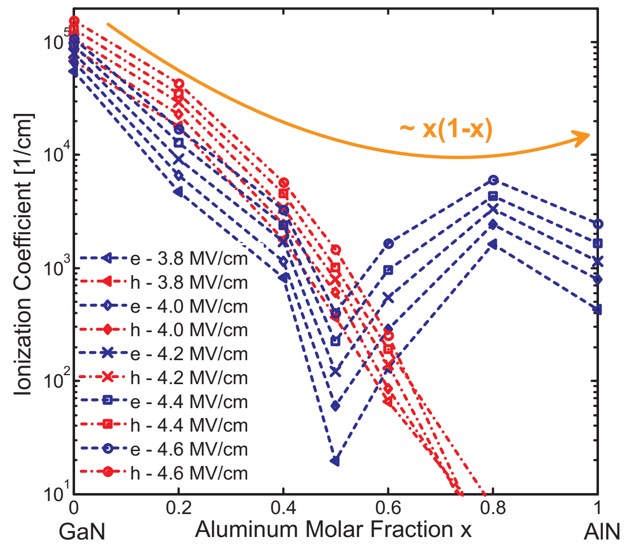

Fig. 3. Calculated electron (dashed lines, blue in color) and hole (dash-dot lines, red in color) impact ionization coefficients as a function of the aluminum molar fraction for five electric field strengths: 3.8 MV/cm (left triangles), 4.0 MV/cm (diamonds), 4.2 MV/cm (crosses), 4.4 MV/cm (squares) and 4.6 MV/cm (circles), including the alloy scattering.

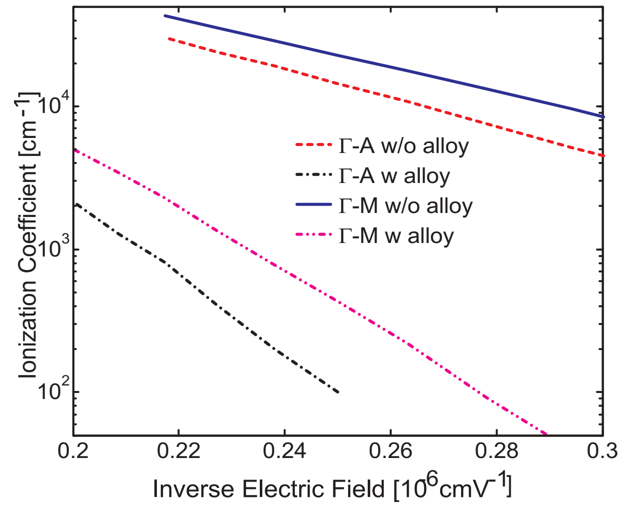

Fig. 4. Calculated electrons impact ionization coefficienst for $In_{0.18}Al_{0.82}N$ as a function of the crystallographic direction and the strength of the alloy scattering.

Effect of AlN Spacer Layer on AlGaN/GaN HEMTs

Niraj Man Shrestha[1], Yuen Yee Wang[1], Yiming Li[2,*], and E.Y. Chang[1,*]
[1]Compound Semiconductor Device Laboratory, Department of Material Science and Engineering
[2]Parallel and Scientific Computing Laboratory, Department of Electrical and Computer Engineering
National Chiao Tung University, 1001 University Road, Hsinchu 300, Taiwan
* ymli@faculty.nctu.edu.tw (Y. Li); edc@mail.nctu.edu.tw (E.Y. Chang)

Abstract - Two-dimensional electron gas (2DEG) formed at AlGaN/GaN interface is a critical part to tune the characteristic of AlGaN/GaN HEMT devices. AlN spacer layer is used between AlGaN and GaN layer to improve 2DEG density, mobility, and drain current. Our device simulation indicates the mobility and current will attain their maximum at the 0.5-nm- and 1.2-nm-thick AlN layers, respectively. For the spacer of device which is thicker than 1.2 nm, the ohmic resistance is increased. Recess ohmic electrodes help to significantly reduce the ohmic resistance.

I. Introduction

AlGaN/GaN high electron mobility transistors (HEMTs) have been the subject of many recent investigations because of their potential to use in high-temperature, high-power devices. One of the most unusual features of these HEMT is that very high 2DEG densities (10^{13} cm^{-2}) can be found in even nominally or undoped heterostructures [1-3]. However, the existence of scattering mechanism plays important role to limit the mobility of 2DEG of conventional AlGaN/GaN HEMT. An additional thin AlN spacer between AlGaN and GaN improves the mobility at low temperatures, where the thickness of AlN is an important parameter for the mobility in AlN/GaN heterostructures [4-6]. In this study, the electron transport for different AlN spacer thickness is simulated. In addition, Ohmic electrode is recessed in order to reduce the ohmic resistance.

II. Simulation and Result Discussion

Fig. 1 shows the schematic of explored device; the device characteristic is simulated by solving a set of quantum mechanically corrected transport equations. Mobility and carrier concentrations are calculated for both the conventional HEMT and the explored new HEMT which is with the AlN spacer layer between the layers AlGaN and GaN. Fig. 2 shows that carrier improved electron concentration on inserting AlN spacer layer, which is mainly due to the increase in the quantum well depth, as shown in Fig. 3. Not shown here, the carrier mobility is also increased significantly. Due to the increase in quantum well depth, the scattering is lowered. Alloy scattering is lowered because binary compound such as AlN has less alloy scattering in comparison to ternary compound [7]. As a result, the mobility is also increased; and, the current is thus increased. We further explore the effect of AlN spacer layer thickness on the device characteristic. Figs. 4(a) and 4(b) show that both the quantum well depth and electron concentration are increased with respect to the thickness of AlN layer. However, the electron mobility increases first, where the maximum appears at the 0.5-nm-thick of AlN layer, it then reduces on further increasing AlN layer, as shown in Fig. 5. This is owing to the Coulomb scattering between 2DEG carriers when very thick spacer layer is used. Fig. 6 shows the simulated drain current at the zero gate voltage. This shows that drain current is maximum when AlN is 1.2 nm thick. Fig. 7 shows that contact resistance is increased for the thick AlN layer. To overcome this effect recess ohmic electrodes are used as shown in Fig. 8.

III. Conclusions

The findings of the different thickness of AlN spacer layer conclude that electron concentration increases with the increases of AlN thickness. The device's mobility reaches the maximum at 0.5-nm-thick AlN layer and the drain current's maximum at 1.2nm thick spacer. The recess ohmic electrodes has been adopted to reduce the resistance.

Acknowledgement

This work was supported in part by the Taiwan National Science Council (NSC) under Contract No. NSC-101-Ec-17-A-05-S1-154. Y. Li in this work was supported in part by the Contract No. NSC-101-2221-E-009-092.

References

[1] I. Smorchkova, C.R. Elsass, J.P. Ibbetson et al., J. Appl. Phys. 86, 4520 (1999).
[2] R. Gaska, J. W. Yang, A. Osinski et al., Appl. Phys. Lett. 72, 707 (1998).
[3] E. T. Yu, G. J. Sullivan, P. M. Asbeck et al., Appl. Phys. Lett. 71, 2794 (1997).
[4] W. Hu, B. Ma, D. Li et al., Jpn. J. Appl. Phys. 49, 035701 (2010).
[5] Y. Cao et al., Appl. Phys. Lett. 90, 182112 (2007).
[6] M. Miyoshi, A. Imanishi, T. Egawa et al., Jpn. J. Appl. Phys. 44, 6490 (2005).
[7] D. Jena, I. Smorchkova , A. C. Gossard et. Al., phys. stat. sol. (b) 228, 617 (2001).

978-3-901578-26-7 © 2013 Society for Micro- and Nanoelectronics

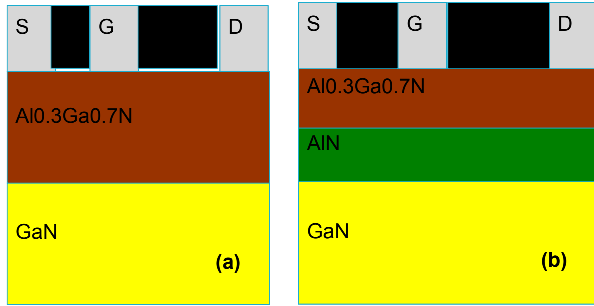

Fig. 1. The simulated structure of HEMTs, where the plots (a) and (b) are without and with the AlN spacer layer.

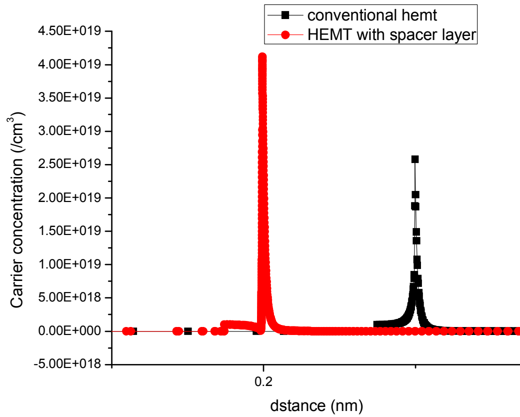

Fig. 2. The electron concentration for the device with and without AlN spacer layers.

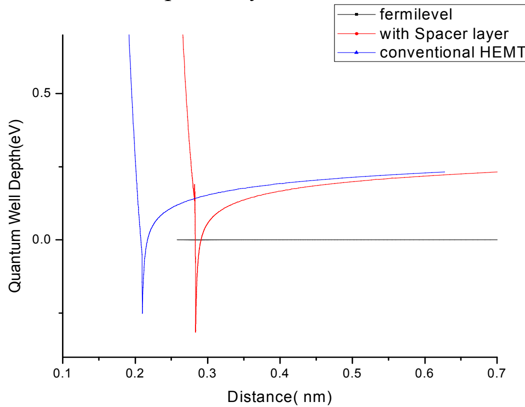

Fig. 3. The calculated quantum well depth for the device with and without AlN spacer layers.

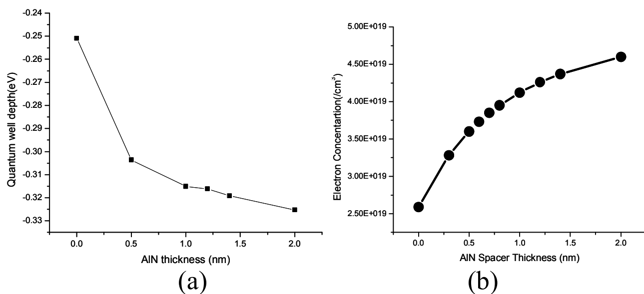

Fig. 4. (a) The quantum well depth and (b) the electron concentration with the AlN thickness.

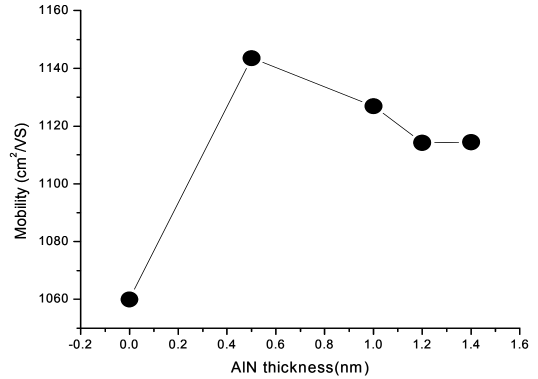

Fig. 5. The mobility versus the AlN thickness.

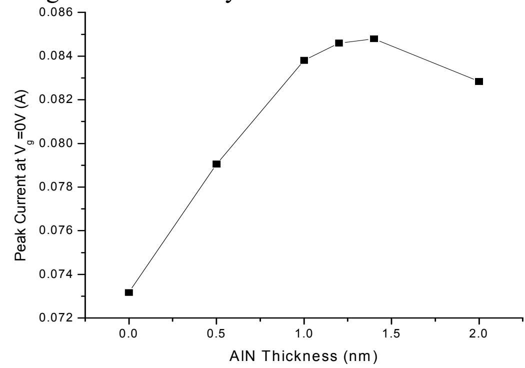

Fig. 6. The simulated current for the device with different AlN thicknesses.

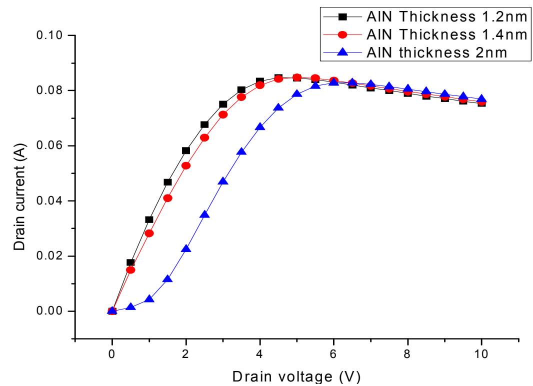

Fig. 7. The drain current versus the drain voltage, where three different AlN thicknesses are simulated.

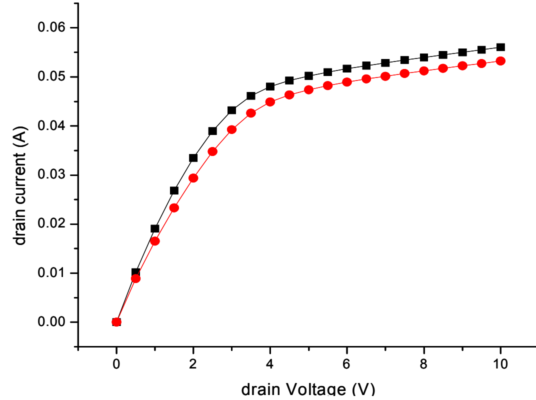

Fig. 8. The I-V for the device with the recess (black line) and without the recess ohmic (red line) electrodes, where the AlN spacer layer is at 1.2 nm.

A Fast Doping Profile Optimization Method for Power Devices

Katsuya Nomura, Tsuyoshi Ishikawa, Tsuguo Kondoh,
Atsushi Kawamoto, Tadayoshi Matsumori, Takahide Sugiyama, and Yuji Nishibe
Toyota Central R&D Labs., Inc. 41-1, Yokomichi, Nagakute, Aichi 480-1192, Japan
e-mail: e1579@mosk.tytlabs.co.jp

INTRODUCTION

In power devices such as power MOSFETs and insulated-gate bipolar transistors (IGBTs), the on-resistance and breakdown voltage are important device characteristics. In order to improve these characteristics, device structures with specific doping profiles have been proposed [1] [2]. These doping profiles lead to improvements of the on-resistance and breakdown voltage due to carrier accumulation and electric field reduction, respectively. Such doping profile design can be formulated as the optimization problem of doping profile. Several studies have been carried out on mathematical optimization of doping profile for submicron devices [3] [4], and a fast optimization approach using the adjoint method was reported [5]. However, no mathematical optimization for power devices has been reported because of the large-scale analysis required. In this paper, a fast doping profile optimization method for power devices is proposed.

METHODOLOGY

It is known that for power devices, there is a tradeoff between the on-resistance and the breakdown voltage [6]. In order to optimize this tradeoff, the present study attempts to decrease the peak value of the electric field while limiting the increase in the on-resistance. This is formulated as the following minimization problem, whose objective function is the peak electric field and whose constraint is the on-resistance:

$$\underset{C}{\text{minimize}} \ \max|E|, \text{ subject to } R_{\text{on}}^{\text{opt}} \leq R_{\text{on}}^{\text{init}}, \quad (1)$$

where C is the doping concentration, E is the electric field, and $R_{\text{on}}^{\text{opt}}$ and $R_{\text{on}}^{\text{init}}$ are the on-resistances of the optimal and initial structures, respectively.

A flow chart for the optimization method is shown in Fig. 1. The drift diffusion model is used as the fundamental equation for power devices, the adjoint method is used as a sensitivity analysis method to reduce the execution time, and the sequential quadratic programming method [7] is used to update the doping profile.

RESULTS

Fig. 2 shows the initial and optimal doping profiles for a p-n diode. It can be seen that in the optimal profile, an intrinsic layer appears near the p-n junction. As seen in the current-voltage curves Fig. 3, although the on-resistance is the same for both structures, the breakdown voltage is increased using the optimized profile. Thus, a better tradeoff between the on-resistance and breakdown voltage is obtained.

Fig. 4 shows the initial and optimal doping profiles for an edge termination. It can be clearly seen that for the optimal doping profile, the p-type region is expanded. Furthermore, the electric field distributions shown in Fig. 5 indicate that the high electric field concentration is eliminated as a result of the optimization process, corresponding to an improvement in the breakdown characteristics. The above results indicate that the proposed method is useful for developing novel device structures.

Table I shows the execution time for the adjoint method used in the present study and a conventional finite difference sensitivity analysis. It can be seen that the adjoint method can drastically reduce the execution time and enable fast optimization.

REFERENCES

[1] H. Takahashi, H. Haruguchi, H. Hagino, and T. Yamada, *Carrier stored trench-gate bipolar transistor (CSTBT)-a*

 © 2013 Society for Micro- and Nanoelectronics

novel power device for high voltage application, Proc. of ISPSD, pp. 349-352, 1996.

[2] T. Laska, M. Munzer, F. Pfirsch, C. Schaeffer, and T. Schmidt, *The field stop IGBT (FS IGBT). a new power device concept with a great improvement potential,* Proc. of ISPSD, pp,.355-358, 2000.

[3] M. Stockinger, R. Strasser, R. Plasun, A. Wild, and S. Selberherr, *A qualitative study on optimized MOSFET doping profiles*, Proc. of SISPAD, pp.77-80, 1998.

[4] M. Stockinger, R. Strasser, R. Plasun, A. Wild, and S. Selberherr, *Closed-loop MOSFET doping profile optimization for portable systems*, Proc. of MSM, pp. 411-414, 1999.

[5] M. Hinze and R. Pinnau, *An optimal control approach to semiconductor design*, Math. Mod. Meth. Appl. Sci., vol. 12, no. 1, pp. 89-108, 2002.

[6] R. P. Zingg, *On the specific on-resistance of high-voltage and power devices*, IEEE Trans. Electron Devices, vol. 51, no. 3, pp. 492-499, 2004.

[7] P. E. Gill, W. Murray, and M. A. Saunders, *Snopt: An SQP algorithm for large-scale constrained optimization*, SIAM J. Optim., vol. 12, no. 4, pp. 979-1006, 2002.

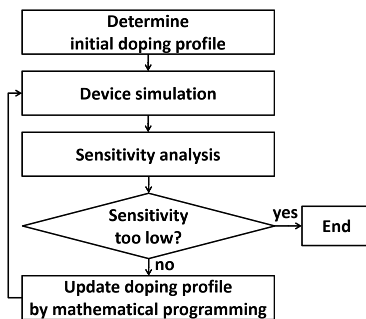

Fig. 1. Flow chart of doping profile optimization procedure. After the initial doping profile is determined, a device simulation is carried out. This is followed by a sensitivity analysis. If the sensitivity is too low, the calculation is stopped. If not, the doping profile is updated by mathematical programming to improve the objective function while satisfying the constraint. The optimal profile is determined by repeating the device simulation, sensitivity analysis and profile update steps.

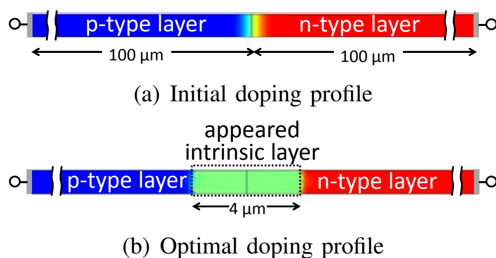

(a) Initial doping profile

(b) Optimal doping profile

Fig. 2. (a) Initial and (b) optimal doping profiles for a diode. Optimization leads to the appearance of an intrinsic layer near the p-n junction.

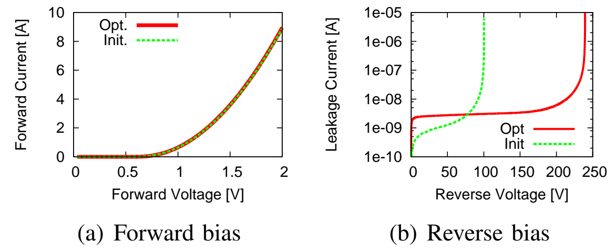

(a) Forward bias (b) Reverse bias

Fig. 3. Current-voltage curves for initial and optimal diode structures under (a) forward bias, where the curves are identical because of the on-resistance constraint, and (b) reverse bias, where the breakdown voltage is increased from 100 V to 240 V by optimization.

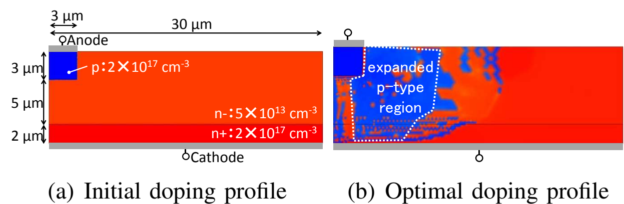

(a) Initial doping profile (b) Optimal doping profile

Fig. 4. (a) Initial and (b) optimal doping profile for edge termination. The p-type region is expanded following optimization.

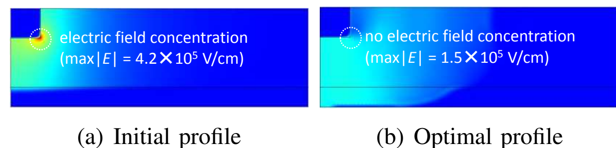

(a) Initial profile (b) Optimal profile

Fig. 5. Electric field distribution around an edge termination for (a) the initial structure, in which a high electric field concentration is present, and (b) the optimal structure, in which this concentration is eliminated. The peak value of the electric field is reduced from 4.2×10^5 V/cm to 1.5×10^5 V/cm, leading to an improvement in the breakdown characteristics.

TABLE I
EXECUTION TIME PER UPDATE.

Type	No. of Elements	Sensitivity analysis method	Exec. time per update [s]
1-D	108	adjoint	0.21
		finite difference	32
2-D	3140	adjoint	2.4
		finite difference	6788

Hydrodynamic and Drift-Diffusion modelling of GaN-based Gunn diodes

E. Momox*, N. Zakhleniuk, and N. Balkan
School of Computer Science and Electronic Engineering, University of Essex
Wivenhoe Park, Colchester CO4 3SQ, UK
e-mail: emomox@essex.ac.uk*

INTRODUCTION

The negative differential mobility caused by the transferred electron effect is one of the promising mechanisms in semiconductors capable, in principle, of generating microwave and possibly THz radiation. Development of Gunn microwave oscillators has hitherto been focused on the utilization of traditional III-V semiconductors like GaAs, achieving a maximum emission frequency around 100 GHz. The recent success of the III-V nitrides technology (in particular GaN, InN, AlN) has led to the development of a range of novel microelectronic and optoelectronic devices based on these materials that due to non-monotonous velocity-field (v-F) characteristics, record-high peak velocities and very high breakdown fields are able to generate high-power, and high-frequency radiation. In this work, we investigate the electron transport in GaN-based Gunn diodes in the transient regime using hydrodynamic (HD) and drift-diffusion (DD) transport models. A comparative analysis is presented.

METHODS

Two types of GaN-based Gunn diodes were simulated using Sentaurus Device: (i) one sample consisted of n^+-n^--n-n^+ regions in which the notch (n^-) length (L) is varied; see Fig. 1a, and (ii) another sample with a similar doping profile in which the notch region is detached (a distance d) from the n^+ region near the cathode; see Fig. 1d. HD and DD transport models were used for evaluating the electron transport in 2 μm thick samples under transient regime at room temperature. We have used the same material parameters and biasing method as the ones described in [1].

RESULTS AND DISCUSSION

Fig. 1b shows the electron density dynamics calculated with the HD (solid lines) and with the DD (dash-dotted lines), both models generate accumulation layers that propagate from the cathode (-) to the anode (+). This is, to the best of our knowledge, the first report of this situation using a HD approach in the context of GaN; other authors have also observed this situation with Monte Carlo simulations [2, 3]. Moreover, when the notch region is increased, dipole domains are created instead of accumulation layers and travel along the sample as depicted in Fig. 1c. Furthermore, we conducted simulations with a fixed notch length, that when attached to the n^+ region yields accumulation layers, and systematically detached it. When the separation is short, the HD yields weak domains during the first moments of time (Fig. 2e) whereas the DD produces dipole domains. In turn, when the separation is long enough, both the HD and DD generate dipole domains as seen in Fig. 2f.

CONCLUSION

For the nucleation and propagation of dipole domains in GaN-based Gunn diodes it is important to have a doping notch wide enough. As well, detaching the notch might produce sustained dipole domains.

REFERENCES

[1] E. Momox, N. Zakhleniuk and N. Balkan, "Overshoot mechanism in transient excitation of THz and Gunn oscillations in wide-bandgap semiconductors," *Nanoscale Research Letters,* vol. 7, no. 647, 2012.

[2] R. F. Macpherson and G. M. Dunn, "The use of doping spikes in GaN Gunn diodes," *Applied Physics Letters,* vol. 93, p. 062103, 2008.

[3] Y. P. Teoh, G. M. Dunn, N. Priestley and M. Carr, "Monte Carlo modelling of multiple-transit-region Gunn diodes," *Semiconductor Science and Technology,* vol. 17, p. 1090, 2002.

978-3-901578-26-7 © 2013 Society for Micro- and Nanoelectronics

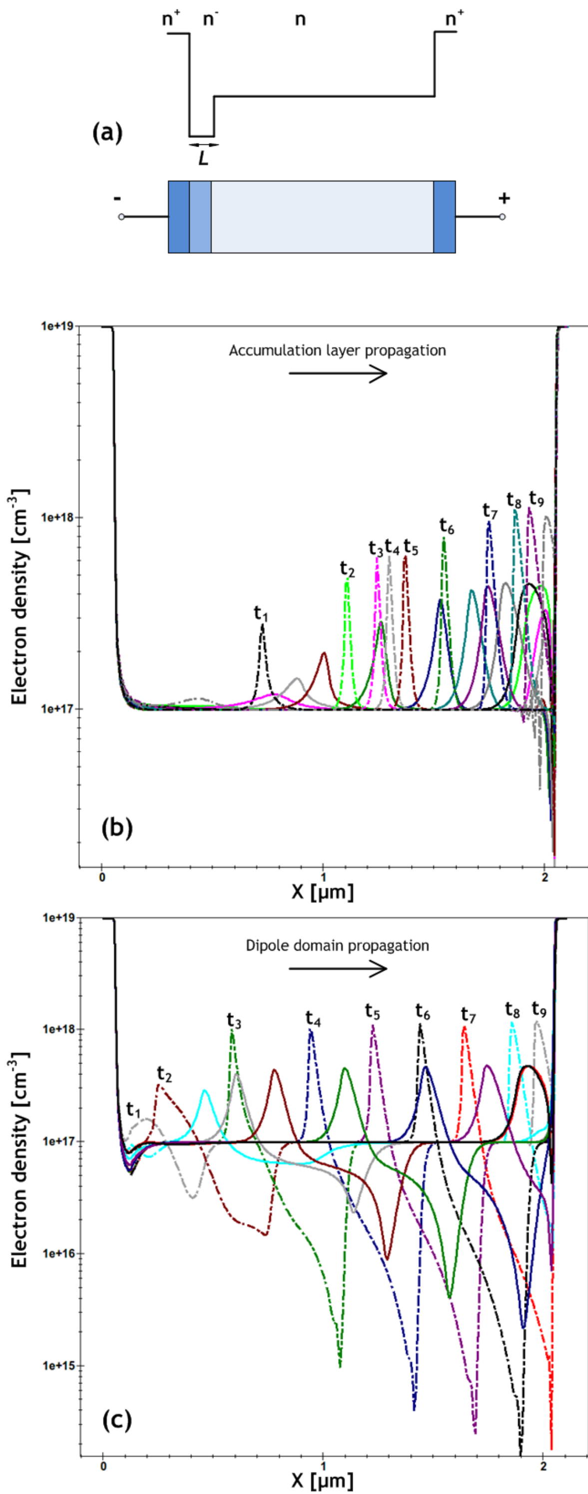

Fig. 1. (a) doping profile (b) HD (solid lines) and DD (dash-dotted lines) transient simulations of a GaN Gunn diode with a 0.2 µm wide notch, and (c) with a 0.8 µm wide notch for different instants in time (t_i).

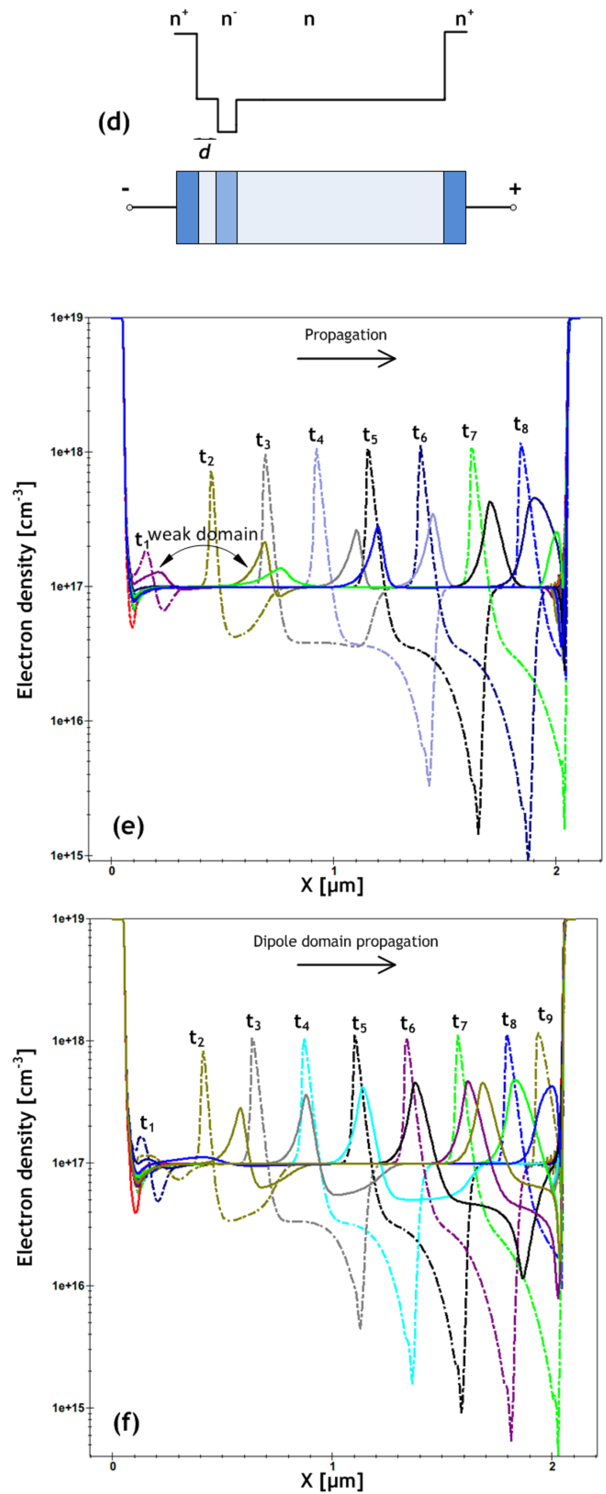

Fig. 2. (d) doping profile (e) HD (solid lines) and DD (dash-dotted lines) transient simulations of a GaN Gunn diode with a 0.4 µm wide notch detached by 0.015 µm, and (f) detached by 0.03 µm for different instants in time (t_i).

Investigation of SiC p-i-n Diode Reverse-Recovery Effect for Compact Modeling

K. Matsuura, M. Miyake, A. Ueno, and H. J. Mattausch
Hiroshima University, Higashi-Hiroshima, Hiroshima, Japan
e-mail: masataka-miyake@hiroshima-u.ac.jp

INTRODUCTION

Recently, many reports about power devices using the wide bandgap material silicon carbide (SiC) have been published, because SiC has many advantages in comparison to silicon (Si) as e.g. a 10 times higher critical electric field [1]. Among SiC-based power devices, the p-i-n diode is intensively developed as a key device for ultrahigh-voltage applications over 5 kV. In this work, we investigate the reverse-recovery effect [2] of SiC p-i-n diodes. Main focus is given on the specific features of the SiC material, such as the extremely low intrinsic carrier density (n_i) in comparison to Si, and the resulting effects on compact model construction for circuit simulation.

INVESTIGATION WITH 2D-DEVICE SIMULATION

The reverse recovery currents of Si and SiC p-i-n diodes with the same structure (see Fig. 1) are compared by 2D-device simulation under identical initial forward current condition in Fig. 2. Figure 3 shows the carrier distributions at the 4 time points indicated in Fig. 2. Even if the on-current is kept the same (100 A), differences are observed in three aspects, namely, carrier density at the p^+/n^- junction (n_j), carrier-distribution gradient (dn_j/dx), and depletion width (W_d). Since the lifetime is fixed to 1 μs for both diodes, it is concluded that n_j and dn_j/dx differences mainly result from mobility (μ) changes due to the different diffusion length. Regarding W_d, the different electric permittivity (ε) is considered as the reason. By setting μ and ε to the same values in the simulation experiments all above differences are eliminated, as verified in Fig. 4. In consequence, this agreement implies that the reverse recovery effect can be modelled based on the same fundamental physics, even at 10^{19} times lower n_i in SiC when compared to Si.

VERIFICATION WITH HiSIM-DIODE MODEL

HiSIM-Diode has been developed to model the reverse-recovery effect based on the dynamic carrier distribution using the non-quasi-static modelling method for carrier recombination [3, 4]. Here we verify that this modelling approach is also valid for SiC by considering its different material parameters from Si. As shown in Fig. 5, the 2D-device simulation results of Figs. 2 and 3 for the SiC diode are indeed reproduced by the compact model. In addition, the reproduction of measured data for a SiC p-i-n diode is verified in Fig. 6.

CONCLUSION

It is confirmed with 2D-device simulation that the reverse recovery effect in the SiC diode can be modelled based on the fundamental physics with the same concepts as applied for Si. Reproduction of measured reverse recovery data for a SiC p-i-n diode by HiSIM-Diode, which can properly handle the material parameters of SiC, makes this evident.

ACKNOWLEDGEMENT

The SiC p-i-n diodes have been fabricated by the National Institute of Advanced Industrial Science and Technology (AIST), Japan, and the measurements were performed by the Kansai Electric Power Co., Inc., Japan. Authors would like to express their sincere thanks. This research is supported by the Japan Society for the Promotion of Science (JSPS) through the “Funding Program for World-Leading Innovative R&D on Science and Technology (FIRST Program),” initiated by the Council for Science and Technology Policy (CSTP).

REFERENCES

[1] A. Elasser and T. P. Chow, "Silicon carbide benefits and advantages for power electronics circuits and systems," Proc. IEEE **90**, 6, 969 (2002).
[2] B. J. Baliga, *Fundamentals of Power Semiconductor Devices*, Springer (2008).
[3] M. Miyake, J. Nakashima, and M. Miura-Mattausch, "Compact Modeling of the p-i-n Diode Reverse Recovery Effect Valid for both Low and High Current-Density Conditions," IEICE Trans. Electron., **E95-C**, 1682 (2012).
[4] J. Nakashima, et al., "Dynamic-Carrier-Distribution-Based Compact Modeling of p-i-n Diode Reverse Recovery Effects," Jpn. J. Appl. Phys. **51**, 02BP06 (2012).

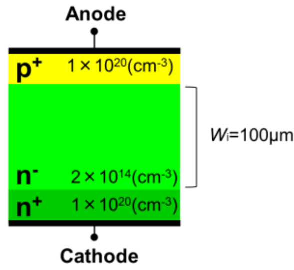

Fig. 1. Investigated p-i-n diode structure: In this work, the n- drift layer thickness and its impurity concentration are set to 100 μm and $2x10^{14}$ cm^{-3}, respectively.

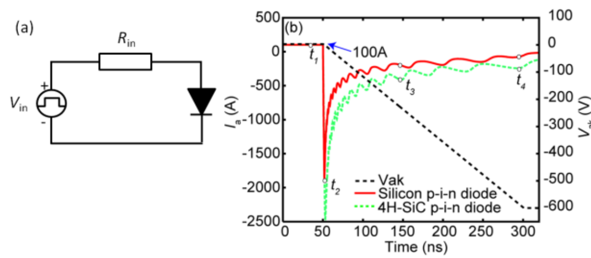

Fig. 2. (a) Test circuit. (b) Reverse recovery currents of Si and 4H-SiC diodes calculated by a 2D-device simulator, where the initial forward current is set to 100 A.

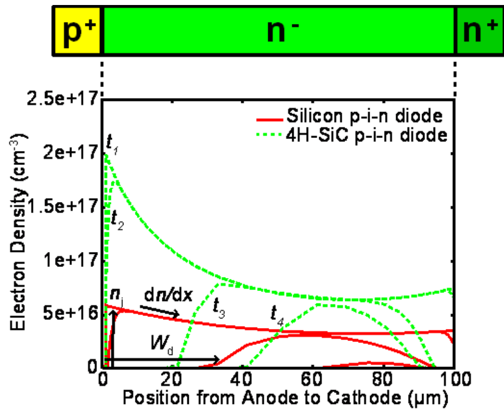

Fig. 3. Dynamic carrier distribution in the n- drift region calculated by a 2D-device simulator (Solid lines: Si diode, Dotted lines: 4H-SiC diode).

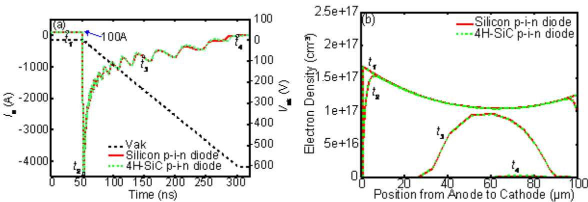

Fig. 4. (a) Reverse recovery currents and (b) the dynamic carrier distributions, with the same mobility and permittivity for both Si and 4H-SiC diodes.

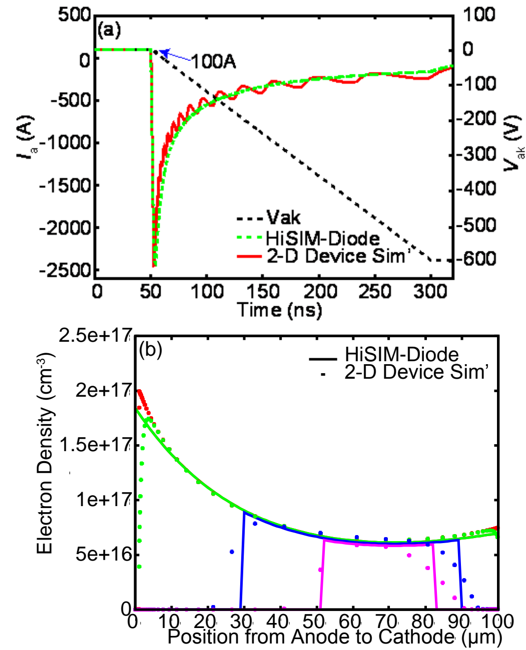

Fig. 5. Comparison of the 2D-device simulation results (shown in Figs. 2 and 3) and the HiSIM-Diode results. (a) Reverse recovery currents and (b) the dynamic carrier distributions of the 4H-SiC diode. The oscillation in the reverse recovery current with 2D-device simulation is also seen in the Si diode case of Fig. 2. (The reason for its occurrence is not yet confirmed.)

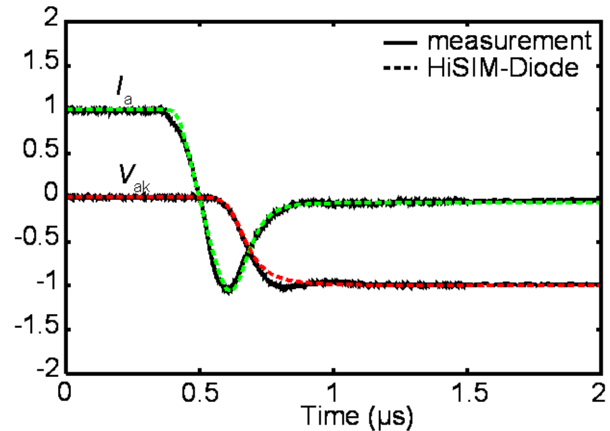

Fig. 6. Comparison of measured data and the HiSIM-Diode results for a 4H-SiC diode with a typical inductive-load test circuit at a voltage and current rating of 2000 V and 100 A/cm^2, respectively, where a Si IGBT is used as a switch. The reverse recovery currents and the voltage over the diode are shown on the vertical axis normalized by the rated current or voltage.

Author Index

Aboud S 48, 106
Adisusilo IN 68
Afzalian A 40
Akis R 150
Akiyama T 236
Alam K 136
Alarcón A 34
Aldegunde M 50, 194, 220
Amoroso SM 52
Anantram M 80
Ando T 14
Anh Le H 112
Asai Y 116
Asenov A 52, 64, 128
Aspera SM 146
Awano Y 62
Awaya N 146

Bae M-H 104
Balkan N 260
Barker JR 16, 50, 194, 220
Basu D 134
Baumgartner O 46, 86, 132
Behnam A 104
Bellotti E 250, 254
Berrada S 34
Bertazzi F 254
Bescond M 88, 92, 94
Bishop N 124
Bournel A 34
Boykin TB 114
Burnett AD 148

Carroll M 124
Cavassilas N 88, 92, 94
Chang EY 256
Charlier J-C 40
Chassat C 34
Chelikowsky JR 170
Chen C-H 184
Chen C-Y 56
Chen G 162
Chen Q 162
Chen Y-Y 56
Cheng Y 170
Cho J 182
Choi H 138
Choi MS 198
Choi W 156
Chu S-Y 184
Cooper JD 84
Cronin L 128
Csaba G 78

Dimov I 152
Dollfus P 34, 112, 172, 226
Donetti L 218
Dorgan VE 104
Du G 178
Duchemin I 60
Dutta M 198, 216, 240

El-Sayed AM 52
Endoh T 102, 140, 188, 190, 246, 248
Esseni D 60

Füshsle M 118
Ferry DK 150
Fischetti MV 18, 28, 44, 48, 106
Flandre D 40
Fu B 28, 48
Fukuda K 142

Gärtner K 158
Gámiz F 218
Gamba IM 170
Gao X 124
Garetto D 60
Georgiev VP 128
Gerrer L 52
Godet J 250
Godoy A 218
Goes W 46
Goodnick SM 66
Grasser T 46
Grier A 84
Grosse KL 104
Guo H 32, 144

Hagness SC 36
Hamaguchi C 20, 202, 204
Hanashiro Y 154
Hane M 192
Hanyu T 248
Harrison P 84
Hathwar R 66
Hattori J 100

He Y 42
Hetmaniuk U 80
Higo A 90
Hirako M 174
Hiramatsu Y 242
Hiroki A 160
Hollenberg LCL 118
Honda S 232
Hu W 90
Hung Nguyen V 34
Hwang YW 210, 212

Ikeda S 248
Ikonić Z 84, 148
Imai H 166, 168
Imamoto T 102
Indjin D 84
Inoue S 38
Inuduka K 232
Ishikawa T 258
Islam S 104
Itagaki A 190
Itoh KM 54, 224
Izumi M 204

Jang M-G 222
Jaouen H 60
Jeong C 156
Jiang Z 114, 134
Jin S 156

Kaczer B 46
Kamakura Y 68, 166, 168, 196, 242
Kamioka T 166, 168
Karamitaheri H 98
Karner M 132
Kasai H 146
Kawamoto A 258
Kelsall RW 148
Kharche N 134
Kim J 106
Kim Y-T 156
Kimura M 174, 176
Kishi H 146
Kivisaari P 208
Klimeck G 42, 114, 118, 134, 182
Knezevic I 22, 36
Kodama K 252
Koike H 246, 248
Kondoh T 258
Kondow M 206
Koprucki T 158
Kosina H 86, 98, 108, 132
Kotani T 202, 204
Kubis T 42, 114
Kukita K 68
Kuroda MA 114
Kuzuhara M 252
Kuzumoto Y 204
Kwon U-H 156

Lannoo M 92, 94
Lee HG 210, 212
Lee J 138
Lee K-H 156
Lee M-Y 214
Lee S 118
Lee Y 138
Lherbier A 40
Li C 92
Li Y 56, 90, 184, 214, 256
Lilly M 124
Lindskog M 82
Ling S 52
Liu B 150
Liu L 32, 144
Liu X 178
Logoteta D 26, 228
Lugli P 202
Luisier M 96, 164

Macucci M 26, 126, 228
Magyari-Köpe B 72
Mahapatra S 118
Mahmoudi H 70, 244
Majorana A 170
Makarov A 70, 74, 238
Mamaluy D 124
Manoharan M 38, 110
Marconcini P 26, 126, 228
Markov S 128
Martinez A 50, 194, 220
Martyna GJ 114
Masahara M 142
Matsubara M 250
Matsuda K 186
Matsumori T 258
Matsuura K 262
Mattausch HJ 262
Matthias Tan Y-H 118
Mehrotra SR 182
Meng L 162
Mera H 92, 94

Michelini F 88
Migita S 142
Mil’nikov G 54, 196
Minari H 54
Misawa T 62
Miura H 230
Miwa JA 118
Miyake M 262
Miyake T 202
Mizubayashi W 142
Mizuta H 38, 110
Momox E 260
Morales Escalante JA 170
Mori N 54, 196, 242
Mori T 142
Morifuji M 154, 206
Morita Y 142
Muller R 124
Muraguchi M 190, 248

Nagai H 234
Nakano T 234
Nakashima A 176
Nallet F 60
Nam Do V 112
Nayak SK 134
Nedjalkov M 152
Neophytou N 98
Newns DM 114
Nguyen VH 60
Nielsen E 124
Nier O 60
Niquet YM 60
Nishi Y 72
Nishibe Y 258
Nishimura E 236
Niwa M 168
Nomura K 258

Odanaka S 160
Ogawa M 234, 236
Oh JH 222
Ohmori K 168
Ohnishi M 230
Ohnishi S 146
Ohno H 248
Ohsawa T 246
Okada T 90
Oki S 62
Oksanen J 208
Ono M 180
Ono T 122

Osintsev D 70, 76, 238
Ota H 142

Palestri P 60
Papp A 78
Park H-H 156
Park S-H 134
Park Y 156
Paul A 182
Pizzagalli L 250
Pop E 104
Porod W 78
Pourfath M 108
Povolotskyi M 114, 182
Purahmad M 240

Querlioz D 34, 226

Rafferty HM 148
Rahman MM 90
Ravandi S 48
Reggiani L 24
Retailleau S 226
Rhyner R 96
Riddet C 64
Rideau D 60
Ruiz FG 218
Ryu H 118

Sadi T 58, 208
Saint-Martin J 34, 172, 226
Sakurai A 120
Salahuddin S 30
Samukawa S 90
Sano N 232
Saraniti M 66
Sasaki T 188
Schanovsky F 46
Scheinemann A 130
Schenk A 130
Schnass K 132
Schwaha P 152
Selberherr S 70, 74, 76, 152, 238, 244
Sellier JM 152
Serov AY 104
Shin M 138, 222
Shiraishi K 168
Shishehchi S 254
Shluge AL 52
Sho S 160
Shrestha NM 256

Shu C-W . . . 170
Silvestri L . . . 60
Simmons MY . . . 118
Smith L . . . 60
Souma S . . . 234, 236
Stanojević Z . . . 86, 132
Stroscio MA . . . 198, 216, 240
Sugiyama T . . . 258
Sule N . . . 36
Suzuki A . . . 166
Suzuki K . . . 230
Sverdlov V . . . 70, 74, 76, 238, 244

Takagi S . . . 136
Takeda H . . . 192
Takenaka M . . . 136
Takeuchi K . . . 192
Talbo V . . . 226
Tamai Y . . . 146
Tan Y . . . 114
Tanabe A . . . 142
Tanaka A . . . 206
Tanaka T . . . 224
Tani S . . . 174
Tanimura Y . . . 120
Tavernier C . . . 60
Tezuka T . . . 180
Tienda-Luna IM . . . 218
Tokuda H . . . 252
Toledano-Luque M . . . 46
Tomita M . . . 196
Tomomura Y . . . 204
Touski SB . . . 108
Towie EA . . . 64
Trang Nghiêm TT . . . 172
Triebl O . . . 238
Triozon F . . . 60
Trovato M . . . 24
Tulkki J . . . 208

Uejima K . . . 192
Uematsu M . . . 54
Ueno A . . . 262
Ueyama M . . . 236
Uno S . . . 100

Valavanis A . . . 84
Valin R . . . 220
Vandenberghe WG . . . 44, 48
Vilà-Nadal L . . . 128

Wacker A . . . 82
Wang A . . . 140
Wang Jian . . . 32, 144
Wang Juncheng . . . 178
Wang Yin . . . 144
Wang Yu . . . 42
Wang YY . . . 256
Watanabe T . . . 166, 168, 196
Watkins MB . . . 52
Weber CE . . . 134
Wei K . . . 178
Weinbub J . . . 70
Willis KJ . . . 36
Windbacher T . . . 70, 238, 244
Winge DO . . . 82
Won TY . . . 210, 212

Yamada K . . . 168
Yamaoka T . . . 174
Yasuda H . . . 200
Yasuda T . . . 142
Yin Z . . . 162
Yoshida Y . . . 248
Yoshikawa H . . . 202, 204
Young R . . . 124

Zahid F . . . 32, 144
Zakhleniuk N . . . 260
Zeng L . . . 178
Zhang N . . . 216
Zhao Y . . . 80
Zhu Y . . . 32, 144
Zushi T . . . 196

ISBN 978-3-901578-26-7
9 783901 578267 >